

WL-TR-93-3103

PROCEEDINGS OF DAMPING '93

VOL 1 OF 3

**AD-A274 226**



BONNIE L. PORTIS, COMPILER

CSA ENGINEERING, INC.  
2850 W. BAYSHORE ROAD  
PALO ALTO, CALIFORNIA 94303-3843

JUNE 1993

INTERIM REPORT FOR 02/01/93-02/28/93

APPROVED FOR PUBLIC RELEASE; DISTRIBUTION IS UNLIMITED.



**S** DTIC  
ELECTE  
DEC 23 1993  
**A**

FLIGHT DYNAMICS DIRECTORATE  
WRIGHT LABORATORY  
AIR FORCE MATERIEL COMMAND  
WRIGHT PATTERSON AFB OH 45433-7562

**93-31150**



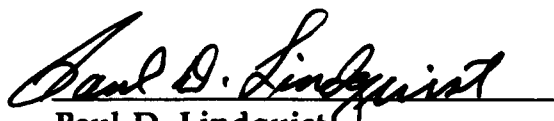
**93 12 23 007**

**Best  
Available  
Copy**

NOTICE

WHEN GOVERNMENT DRAWINGS, SPECIFICATIONS, OR OTHER DATA ARE USED FOR ANY PURPOSE OTHER THAN IN CONNECTION WITH A DEFINITELY GOVERNMENT-RELATED PROCUREMENT, THE UNITED STATES GOVERNMENT INCURS NO RESPONSIBILITY OR ANY OBLIGATION WHATSOEVER. THE FACT THAT THE GOVERNMENT MAY HAVE FORMULATED OR IN ANY WAY SUPPLIED THE SAID DRAWINGS, SPECIFICATIONS, OR OTHER DATA, IS NOT TO BE REGARDED BY IMPLICATION, OR OTHERWISE IN ANY OTHER PERSON OR CORPORATION; OR AS CONVEYING ANY RIGHTS OR PERMISSION TO MANUFACTURE, USE, OR SELL ANY PATENTED INVENTION THAT MAY IN ANY WAY BE RELATED THERETO.

THIS TECHNICAL REPORT HAS BEEN REVIEWED AND IS APPROVED FOR PUBLICATION.



Paul D. Lindquist  
Aerospace Engineer  
Acoustics and Sonic Fatigue



Ralph M. Shimovetz  
Section Leader  
Acoustics and Sonic Fatigue



John Ach, Acting Chief  
Aerospace Engineer  
Acoustics and Sonic Fatigue

IF YOUR ADDRESS HAS CHANGED, IF YOU WISH TO BE REMOVED FROM OUR MAILING LIST, OR IF THE ADDRESSEE IS NO LONGER EMPLOYED BY YOUR ORGANIZATION PLEASE NOTIFY WL/FIBG, WRIGHT-PATTERSON AFB, OH 45433-6553 TO HELP MAINTAIN A CURRENT MAILING LIST.

COPIES OF THIS REPORT SHOULD NOT BE RETURNED UNLESS RETURN IS REQUIRED BY SECURITY CONSIDERATIONS, CONTRACTUAL OBLIGATIONS, OR NOTICE ON A SPECIFIC DOCUMENT.

# REPORT DOCUMENTATION PAGE

Form Approved  
OMB No. 0704-0188

Public reporting burden for this collection of information is estimated to average 1 hour per response, including the time for reviewing instructions, searching existing data sources, gathering and maintaining the data needed, and completing and reviewing the collection of information. Send comments regarding this burden estimate or any other aspect of this collection of information, including suggestions for reducing this burden, to Washington Headquarters Services, Directorate for Information Operations and Reports, 1215 Jefferson Davis Highway, Suite 1204, Arlington, VA 22202-4302, and to the Office of Management and Budget, Paperwork Reduction Project (0704-0188), Washington, DC 20503.

1. AGENCY USE ONLY (Leave blank)		2. REPORT DATE JUN 93	3. REPORT TYPE AND DATES COVERED FINAL FEB 93 - FEB 93	
4. TITLE AND SUBTITLE PROCEEDINGS OF DAMPING '93 VOLUME I OF 3			5. FUNDING NUMBERS C F33615-89-C-3201 PB 63215C PR L502 TA 00 WU 20	
6. AUTHOR(S)  BONNIE L. PORTIS, COMPILER			8. PERFORMING ORGANIZATION REPORT NUMBER	
7. PERFORMING ORGANIZATION NAME(S) AND ADDRESS(ES)  CSA ENGINEERING, INC. 2850 W. BAYSHORE RD. PALO ALTO, CA 94303-3843			10. SPONSORING/MONITORING AGENCY REPORT NUMBER  WL-TR-93-3103	
9. SPONSORING/MONITORING AGENCY NAME(S) AND ADDRESS(ES)  WL/FIBGC (CAPT JOHN R. MACKAMAN) FLIGHTS DYNAMICS DIRECTORATE WRIGHT LABORATORY AIR FORCE MATERIEL COMMAND WRIGHT PATTERSON AFB, OH 45433-7006			11. SUPPLEMENTARY NOTES	
12a. DISTRIBUTION/AVAILABILITY STATEMENT  APPROVED FOR PUBLIC RELEASE; DISTRIBUTION UNLIMITED			12b. DISTRIBUTION CODE	
13. ABSTRACT (Maximum 200 words)  PRESENTED ARE INDIVIDUAL PAPERS OF DAMPING '93, HELD 24-26 FEBRUARY 1993 IN SAN FRANCISCO. THE SUBJECTS INCLUDED: PASSIVE DAMPING CONCEPTS; PASSIVE DAMPING ANALYSIS AND DESIGN TECHNIQUES; OPTIMIZATION; DAMPED CONTROL/STRUCTURE INTERACTION; VISCOELASTIC MATERIAL TESTING AND CHARACTERIZATION; HIGHLY DAMPED MATERIALS; VIBRATION SUPPRESSION TECHNIQUES; DAMPING IDENTIFICATION AND DYNAMIC TESTING; APPLICATIONS TO AIRCRAFT; SPACE STRUCTURES; MARINE STRUCTURES; AND COMMERCIAL PRODUCTS; DEFENSE APPLICATIONS; AND PAYOFFS OF VIBRATION SUPPRESSION.				
14. SUBJECT TERMS  VIBRATION DAMPING, PASSIVE DAMPING CONTROL/STRUCTURES INTERACTION			15. NUMBER OF PAGES 393	
			16. PRICE CODE	
17. SECURITY CLASSIFICATION OF REPORT UNCLASSIFIED	18. SECURITY CLASSIFICATION OF THIS PAGE UNCLASSIFIED	19. SECURITY CLASSIFICATION OF ABSTRACT UNCLASSIFIED	20. LIMITATION OF ABSTRACT  UL	

## Workshop Administration

### Director

Dr. Lynn C. Rogers  
Oak Ridge National Lab

### Technical Chairman

Dr. Conor D. Johnson  
CSA Engineering, Inc.

### Administrative Chairman

Bonnie L. Portis  
CSA Engineering, Inc.

## Session Chairmen

Dr. Mohan Aswani, *Aerospace Corporation*

Mr. Eric M. Austin, *CSA Engineering, Inc.*

Mr. L. Porter Davis, *Honeywell, Inc.*

Mr. William Driscoll, *3M*

Mr. Robert Dunning, *Lockheed*

Dr. John P. Henderson, *Materials and Vibration Engineering*

Dr. Darel E. Hodgson, *E\*Sorb Systems*

Dr. Robert Holman, *Hughes Aircraft Company*

Mr. J. Warren Hoskins, *Lockheed Missiles and Space Company*

Dr. Roy Ikegami, *Boeing Aerospace and Electronics*

Dr. Conor D. Johnson, *CSA Engineering, Inc.*

Dr. James Kelly, *EERC, University of California at Berkeley*

Dr. Edward Kerwin, *Bolt, Beranek and Newman, Inc.*

Dr. John Kirby, *McDonnell Douglas Aerospace Company*

Mr. Robert Krumme, *CMS, Inc.*

Lt. Col. Steve Lamberson, *AFWL/ARDI*

Capt. Vincent J. Levraea, *Wright Laboratory, Flight Dynamics Directorate*

Mr. Salvatore Liguore, *McDonnell Douglas Aerospace Company*

Mr. Paul Lindquist, *Wright Laboratory, Flight Dynamics Directorate*

Capt. John R. Mackaman, *Wright Laboratory, Flight Dynamics Directorate*

Mr. Rory Ninneman, *Phillips Laboratory*

Mr. Ted Nye, *TRW Space and Technology Group*

Mr. Jerome Pearson, *Wright Laboratory, Flight Dynamics Directorate*

Mr. Ken Qassim, *Phillips Laboratory*

Dr. Mohan Rao, *Michigan Technological University*

Mr. Stanley Sattinger, *Westinghouse Science and Technology Center*

Accession For		
NTIS	CRA&I	<input checked="" type="checkbox"/>
DTIC	TAB	<input type="checkbox"/>
Unannounced		<input type="checkbox"/>
Justification		
By		
Distribution /		
Availability Codes		
Dist	Availability for Special	
A-1		

DTIC QUALITY INSPECTED 3

**Dr. Daniel Segalman, Sandia National Labs**  
**Dr. Jaak Soovere, Lockheed Aeronautical**  
**Capt. Daniel Stech, United States Air Force Academy**  
**Mr. Ralph Tate, Loral Vought Systems**  
**Dr. John Tracy, McDonnell Douglas Aerospace Company**  
**Dr. Ben Wada, Jet Propulsion Laboratory**  
**Ms. Catherine Wong, Naval Surface Warfare Center**  
**Mr. Michael Zeigler, Wright Laboratory, Flight Dynamics Directorate**

## **FOREWORD**

**This publication includes individual papers of Damping '93 held February 24-26, 1993, San Francisco, California. The Conference was sponsored by the Air Force Wright Laboratory, Flight Dynamics Directorate, Wright-Patterson Air Force Base, Ohio.**

## TABLE OF CONTENTS

	<u>Paper No.</u>
<b>The Role of Damping and Durability in Secondary Structure for Air Vehicles</b> (Keynote Address) Dr. John W. Lincoln	AAA*
<b>Non-obstructive Particle Damping Technology</b> (Invited Speaker) Dr. Hagop Panossian	AAB
<b>SESSION BA - Various Vibration Suppression Technologies</b>	
<b>Energy Absorption Due to Cyclic Deformation of Shape Memory Alloys</b> Dr. Darel E. Hodgson	BAA
<b>Passive Damping Applications</b> Dr. Stepan S. Simonian	BAB
<b>Design of Passive Piezoelectric Damping for Space Structures</b> Dr. Andreas H. von Flotow, J. Aldrich, Nesbit Hagood, and David W. Vos	BAC
<b>SESSION CA - Space Applications I</b>	
<b>An Advanced Controls Technology Flight Experiment</b> R. A. Manning, R. E. Wyse, and S. R. Schubert	CAA
<b>Optimized Passive Vibration Isolator Design for the Space Station Freedom Exercise Treadmill</b> Richard Armentrout and Harold H. Doiron	CAB
<b>Design of Spacecraft Damped Precision Platform</b> Dennis Hill, John Molnar, John Chionchio, Clyde Stahle, and Michael Zeigler	CAC*
<b>Elastomeric Materials Applied Internally to Turbine Blades</b> Eric M. Austin and Lyn M. Greenhill	CAD*

\*Not available for publication

## TABLE OF CONTENTS (continued)

Paper No.

### **SESSION CB - Analysis and Design I**

- Consistent Damping Method for Space Structural Systems** CBA  
Wan T. Tsai, Joseph T. Leang, and Richard S. Chao
- Transient Solution of Coupled Structural Components Using System Modal Coordinates with and without Coupled System Damping** CBB  
Edwin E. Henkel and Raymond Mar
- Multiple Scales Methods for Structural Dynamics** CBC\*  
Wing Kam Liu
- Formulation of a Frequency Dependent Damping Matrix** CBD\*  
Antonio M. Claret and Fernando Venancio-Filho

### **SESSION CC - Viscoelastic Material Measurements**

- Fourier Transform Mechanical Analysis (FTMA) Technique to Determine Dynamic Mechanical Properties of Viscoelastic Materials** CCA  
Dr. Surendra N. Ganeriwala
- Dynamic Compressibility Apparatus** CCB  
Wayne T. Reader, N. Scott Emery, and Fred Schloss
- Dynamic Durometer Measurement of Young's Modulus and Loss Factor** CCC  
Dr. Walter Madigosky and Dr. Ralph Fiorito
- Integrated Direct Stiffness Test System for Viscoelastic Material Properties (Work in Progress)** CCD  
Bryce L. Fowler, Bradley R. Allen, and Dr. David A. Kienholz

### **SESSION DA - Space Applications II**

- Passive Damping Analysis for an Advanced Space Interceptor** DAA\*  
Eric M. Austin, Victor J. Wagner, and David H. Merchant

## TABLE OF CONTENTS (continued)

	<u>Paper No.</u>
<b>Variations in the Damping of Space Structures in One Gravity and Zero Gravity</b> Dr. A. S. Bicos, Dr. E. F. Crawley, M. S. Barlow, M. C. van Schoor, and B. Masters	DAB
<b>Impact of Interface Stiffness and Damping on Payload Responses in Space Systems</b> Dr. Wan T. Tsai	DAC

### **SESSION DB - Analysis and Testing**

<b>Modal Parameter Estimation Effects on Damping Matrix Identification</b> Dr. A. Agneni, Dr. L. Balis-Crema, Dr. A. Castellani, and F. M. Onorati	DBA
<b>The Relation Between Internal Friction in Metals and Elastic Wave Velocities</b> Dr. Augusto Capecchi	DBB
<b>Some Frequency and Damping Measurements of Laminated Beryllium Beams</b> Dr. Lynn C. Rogers and John Andriulli	DBC

### **SESSION DC - Characterization of Polymeric Materials**

<b>Accurate Characterization of Passive Damping Materials with Database Storage and Retrieval on Different Computer Platforms</b> Bryce L. Fowler and Dr. Lynn C. Rogers	DCA
<b>Results of Recent Analysis of the Frequency-Temperature Behavior of Polyisobutylene</b> Dr. David I. G. Jones	DCB
<b>Estimation of Dynamic Properties of Rubber Materials and their Applications to Vibration Isolation</b> Chun-hwa Ryu, Hyeong-oh Kweon, Gyu-Seop Lee, and Sang-Kyu Park	DCC

## TABLE OF CONTENTS (continued)

### Paper No.

#### **SESSION EA - Damping/Isolation for the Launch Environment**

- Performance/Sizing Tradeoffs in Active and Passive Launch Isolation** EAA  
David C. Cunningham
- A Launch Isolation System for the Shuttle Resupplied Hubble Space Telescope Solar Array** EAB  
L. Porter Davis, Terry Allen, and John Vise
- A New Structural Design Concept for Launch Vehicle Shrouds to Decrease Payload Noise Environment** EAC  
Jefferson Newton, Dr. Roy Ikegami, and Paul D. Nedervelt
- Protection of Attitude Control Thrusters Against Pyrotechnic Stage Separation Shock** EAD  
Dr. Ernst Hornung and Huba Oery

#### **SESSION EB - Analysis and Design II**

- A Boundary Element Formulation for Dynamic Analysis of Viscoelastic Fluid-Dampers** EBA  
Dr. Nicos Makris, Dr. G. F. Dargush, and Dr. M. C. Constantinou
- Vibration Responses of Viscoelastically Damped Plates** EBB  
Dr. Sung Yi, M. F. Ahmad, Dr. H. Hilton, and G. D. Pollock
- Damping Capacity of Scarf-Joints** EBC  
Dr. Mohan Rao and Haiming Zhou
- Similtude and Modelling Damping Forces in Bolted Connections** EBD\*  
Dr. M. Groper

## TABLE OF CONTENTS (continued)

### Paper No.

#### **SESSION EC - Shape Memory Alloys**

- Low Frequency Damping and Ultrasonic Attenuation in Ti<sub>3</sub>Sn-Based Alloys** ECA  
Catherine Wong and Rober L. Fleischer
- Fully Cyclic Hysteresis of a Ni-Ti Shape Memory Alloy** ECB  
Dr. Edward J. Graesser and Dr. Francis A. Cozzarelli
- Design and Seismic Testing of Shape Memory Structural Dampers** ECC  
P. R. Witting and Dr. Francis A. Cozzarelli
- The Vibration Characteristics of Composites with Embedded Shape Memory Alloy** ECD  
Lee Chin Hai and Dr. C. T. Sun

#### **SESSION FA - Aircraft Applications**

- A Magnetic Tuned-Mass Damper for Buffet-Induced Airfoil Vibration** FAA  
Joseph R. Maly and Kevin L. Napolitano
- Attenuation of Empennage Buffet Response Through Active Control of Damping Using Piezoelectric Material** FAB  
Jennifer Heeg, Jonathon Miller, and Robert V. Doggett, Jr.
- Analytical Evaluation of Damping Treatments for F-15 Wing** FAC  
Scott R. Schroeder

#### **SESSION FB - Nonlinear Structures**

- The Influence of Constrained-Layer Damping Treatment on Parametric and Autoparametric Resonances in Nonlinear and Internally Resonant Nonlinear Structures** FBA  
Lawrence D. Zavodney and Joseph Schudt

## TABLE OF CONTENTS (continued)

	<u>Paper No.</u>
<b>Incorporating a Full Damping Matrix in the Transient Analyses of Nonlinear Structures</b> J. Michael Chapman	<b>FBB</b>
<b>Treatment of Structural and Frequency Dependent Damping on Nonlinear Systems by a Step-by-Step Linearization Procedure in Frequency Domain</b> Dr. Antonio M. Claret	<b>FBC*</b>

### **SESSION FC - Friction**

<b>Analysis of Dry Friction Hysteresis in Cables under Uniform Bending</b> Dr. X. Huang and Dr. O. Vinogradov	<b>FCA</b>
<b>On the Linearization of Structures Containing Linear-Friction Dissipating Devices</b> Jose A. Inaudi and Dr. James M. Kelly	<b>FCB</b>
<b>Analysis of Dry Friction Hysteresis in Tension Cables</b> Dr. X. Huang and Dr. O. Vinogradov	<b>FCC</b>

### **SESSION GA - Tuned Mass Dampers/Vibration Energy Absorbers**

<b>Increasing the Impact Energy Absorption of Containment Structures with Viscoelastic Materials</b> R. G. Holm, M. A. Mendelsohn, and S. S. Sattinger	<b>GAA</b>
<b>The Effect of Viscoelasticity on the Performance of Reaction Mass Actuators</b> Dr. H. Hilton, L. A. Bergman, and T. C. Tsao	<b>GAB</b>
<b>Enhanced Passive Vibration Absorbers Using Acceleration Feedback</b> Capt. D. Stech and Dr. R. Quan	<b>GAC</b>
<b>Improved Precipitation Static Discharge (PSD) Unit Attachment Method</b> T. Gerardi, J. Weiher, Lt. G. Agnes, J. Shaw, and C. Hitchcock	<b>GAD*</b>

## TABLE OF CONTENTS (continued)

Paper No.

### SESSION GB - Smart Structures

- |   |             |
|---|-------------|
| <b>Finite Element Modeling of Sensors/Actuators for Smart Structure Applications</b><br>Salvatore L. Liguore and Jack H. Jacobs | <b>GBA*</b> |
| <b>Piezoelectric Composites for Use in Adaptive Damping Concepts</b><br>Wayne T. Reader and David F. Sauter                     | <b>GBB</b>  |
| <b>Damping in Smart Materials and Structures</b><br>Nisar Shaikh and Sam D. Haddad  | <b>GBC</b>  |
| <b>Actively Damped Piezoelectric Composite Wing</b><br>Dr. P. Santini, F. Betti, P. Gasbarri, and A. Rossi                      | <b>GBD</b>  |

### SESSION GC - Composites

- |  |             |
|--|-------------|
| <b>Stratified Layer Model for Composite Laminates</b><br>Capt. Vincent Levraca and Col. Ronald Bagley  | <b>GCA*</b> |
| <b>Damping Analysis for Thick Composite Laminates and Structures</b><br>Dr. D. A. Saravanos  | <b>GCB</b>  |
| <b>Vibration Responses of a Composite Shell Made of a Metallic Material with Damping Treatments</b><br>Dr. Y. P. Lu, A. J. Roscoe, and H. C. Neilson | <b>GCC</b>  |
| <b>Damping Thin-Walled Composite Structures with Embedded Constraining Layers</b><br>Stanley Sattinger and Z. N. Sanjana                             | <b>GCD</b>  |

### SESSION HA - Civil Structures

- |  |            |
|--|------------|
| <b>Analytical and Experimental Study of a Mass Damper Using Shape Memory Alloys</b><br>J. A. Inaudi, Dr. J. M. Kelly, W. Taniwangsa, and Robert Krumme | <b>HAA</b> |
|--|------------|

\*Not available for publication

## TABLE OF CONTENTS (continued)

	<u>Paper No.</u>
<b>High Damping of Antique Walls</b> Dr. Juval Mantel	HAB
<b>Temperature Control in Viscoelastic Dampers for Buildings</b> Dr. Warren C. Gibson, Kevin L. Napolitano, Bradley R. Allen, and Dr. Roger Scholl	HAC

### SESSION HB - Control Structure Interaction

<b>Response Study of Optimum Structural and Control Design</b> Dr. Narendra Khot	HBA
<b>Uniform Modal Damping of an Elastic Ring by the Natural Control Law</b> Dr. J. Q. Sun and Dr. J. Rossetti	HBB
<b>Two-DOF Small Structures-Optics-Controls System, A Parametric Study</b> Dr. Ernest B. Paxson, Jr.	HBC

### SESSION HC - High Damping Materials

<b>Damping Behavior of 6061 Al/SiC/Gr Metal Matrix Composites</b> Robert J. Perez, Jinmin Zhang, M. N. Gungor, and Dr. E. Lavernia	HCA
<b>Development of Room Temperature Vibration Damping Steel</b> Dr. Shian-Ing Chen	HCB*
<b>A Simple Approach to Design, Installation, and Testing of Passive Damping for an Optical System</b> Eric M. Austin and James C. Goodding	HCC

### SESSION IA - Industrial Applications

<b>Vibration Attenuation by Configuration Variation of Machines and Structures</b> Dr. Z. Parszewski, J. M. Krodkiewski, and K. Krynicki	IAA
---	-----

\*Not available for publication

## TABLE OF CONTENTS (continued)

	<u>Paper No.</u>
<b>Stiffness and Damping in Automobile Seats</b> Dr. W. M. Patten, Dr. B. Yang, and Li Liu	<b>IAB*</b>
<b>Noise Standardization in Machine Design</b> Ilya D. Tsukernikov and Boris A. Seliverstov	<b>IAC*</b>
<b>Damping in the Noise Reduction of Liquid Separators</b> Boris A. Seliverstov	<b>IAD*</b>

### SESSION IB - Active Damping

<b>Active Vibration Control Using Parallel Processing Techniques</b> Dr. G. S. Virk	<b>IBA</b>
<b>Active Constrained Layer Damping</b> Dr. Amr Baz	<b>IBB</b>
<b>Comparing Passive Damping and Active Control on Flexible Structures with Either Closely Spaced or Coincident Modes</b> Major Steven Webb and 2Lt Dean Cibotti	<b>IBC</b>
<b>Damping of Structural Vibration with Piezoelectric Materials and Parameter Optimization</b> T. Yongjie, Z. Shenbi, H. Xieqing, and H. Xuanli	<b>IBD</b>

### SESSION IC - Damping Properties and Materials

<b>Damping Properties of PTMG/PPG Blends</b> Gilbert Lee, John D. Lee, Dr. B. Hartmann, and Dr. D. Rathnamma	<b>ICA</b>
<b>Investigation of Damping Properties for the Fiber Enhanced Viscoelastic Damping Polymers</b> Dr. Thomas Alberts and Houchun Xia	<b>ICB</b>
<b>On the Dynamic Properties of Natural Rubber and Epoxidized Natural Rubber</b> H. A. Ahmadi, Dr. A. H. Muhr, and Dr. K. N. G. Fuller	<b>ICC</b>

\*Not available for publication

## TABLE OF CONTENTS (continued)

	<u>Paper No.</u>
<b>Effect of Long Space Exposure upon Properties of Viscoelastic Materials</b> Dr. John Kirby, Dr. Donald Edberg, and Dr. David I. G. Jones	<b>ICD</b>

### **SESSION JB - Analysis and Design**

<b>A Modal Strain Energy Approach to the Prediction of Resistively-Shunted Piezoceramic Damping</b> Christopher Davis and Dr. George Lesieutre	<b>JBA</b>
<b>A Refined Theory of Flexural Vibration for Viscoelastic Damped Sandwich Beams</b> J. M. Bai and Dr. C. T. Sun	<b>JBB</b>
<b>A Simple Approach to Design, Fabrication, and Testing of Passive Damping for an Optical System</b> Eric M. Austin and James C. Goodding	<b>JBC*</b>

### **SESSION JC - Characterization**

<b>A Constitutive Equation for Thermoviscoelastic Behavior of Polymeric Materials</b> Dr. Surendra Ganeriwala	<b>JCA</b>
<b>Relating the Complex Moduli of Viscoelastic Materials to the Complex Stiffness Characteristics of Anti-Vibration Mounts</b> Dr. S. O. Oyadiji and G. R. Tomlinson	<b>JCB*</b>
<b>Sensitivity Analysis For Estimation of Complex Modulus of Viscoelastic Materials by Non-Resonance Method</b> Dr. Kwang-Joon Kim and Tai-Kil Ahn	<b>JCC</b>

**The following is a list of authors and their addresses who where unable to submit their papers for publication in the Damping '93 Proceedings.**

**Dr. John W. Lincoln  
USAF/ASC/ENFS  
Area B, Building 125  
2335 Seventh Street, Suite 6  
Wright-Patterson AFB, OH 454433-7809  
telephone: (513) 255-2576  
fax: (513) 476-4546**

**John Molnar  
GE Astro Space  
P.O. Box 800  
MS NP 1A  
Princeton, NJ 94303-0800  
telephone: (609) 951-7804  
fax: (609) 951-7911**

**Eric M. Austin  
CSA Engineering, Inc.  
2850 West Bayshore Road  
Palo Alto, CA 94303-3843  
telephone: (415) 494-7351  
fax: (415) 494-8749**

**Wing Kam Liu  
Northwestern University  
Department of Mechanical Engineering  
Evanston, IL 60208-3111  
telephone: (708) 491-7094  
fax: (708) 491-3915**

**Antonio M. Claret  
Escola de Minas / UFOP  
Pc Tiradentes No. 20  
CEP 35400-000 Ouro Preto, MG  
Brasil  
telephone: (031) 551-1139  
fax: (031) 551-1689**

**Dr. Lynn C. Rogers**  
**Oak Ridge National Lab**  
**USAF/WL/FIBG (Center for Passive Damping)**  
**Area B, Building 24C, Room 220**  
**2145 Fifth Street, Suite 2**  
**Wright-Patterson AFB, OH 45433-7006**  
**telephone: (513) 255-6622 extension 252**  
**fax: (513) 255-6684**

**John Andriulli**  
**Oak Ridge National Lab**  
**K-25, Site/K-1225, MS-7294**  
**P.O. Box 2003**  
**Oak Ridge, TN 37831-7294**  
**telephone: (615) 576-0424**  
**fax: (615) 574-8481**

**Dr. M. Groper**  
**Western Michigan University**  
**College of Engineering and Applied Sciences**  
**Department of Mechanical and Aeronautical Engineering**  
**Kalamazoo, MI 49008-5065**  
**telephone: (616) 387-3380**  
**fax: (616) 387-4024**

**Salvatore L. Liguore**  
**McDonnell Douglas Aerospace**  
**P.O. Box 516**  
**St. Louis, MO 63166-0516**  
**telephone: (314) 232-3109**  
**fax: (314) 777-1171**

**Capt. Vincent Levraca**  
**WL/FIBG, Wright Laboratory**  
**2145 Fifth Street, Suite 2**  
**Wright-Patterson AFB, OH 45433-7006**  
**telephone: (513) 255-5229 extension 452**  
**fax: (513) 255-6685**

**Col. Ronald Bagley**  
**WL/FIB, Wright Laboratory**  
**Wright-Patterson AFB, OH 45433-7006**  
**telephone: (513) 255-5200 extension 457**  
**fax: (513) 255-6684**

**Dr. Shian-Ing Chen**  
**China Steel Corporation**  
**Lin Hai Industrial District**  
**P.O. Box 47-29**  
**Hsiao Kang, Kaohsiung**  
**81233 Taiwan, Republic of China**  
**telephone: 07-802-1111 extension 3353**  
**fax: 07-802-2511**

**Dr. W. M. Patten**  
**The University of Oklahoma**  
**School of Aerospace and Mechanical Engineering**  
**865 Asp Avenue, Room 212**  
**Norman, OK 73019-0601**  
**telephone: (405) 325-5011**  
**fax: (405) 325-1088**

**Ilya D. Tsukernikov**  
**Head of Vibroacoustics Sector**  
**123308 Moscow, Marshal Zhukov Avenue, 1**  
**Russia**  
**telephone: (095) 195-6974**  
**fax: (095) 195-1043**

**Boris A. Seliverstov**  
**Chief of Laboratory**  
**123308 Moscow, Marshal Zhukov Avenue, 1**  
**Russia**  
**telephone: (095) 195-6974**  
**fax: (095) 195-1043**

**H. A. Ahmadi**  
**Malaysian Rubber Producer's Research Association**  
**Brickendonbury**  
**Hertford SG13 8NL, England**  
**telephone: (0992) 584-966**  
**fax: (0992) 554-837**

**Dr. S. O. Oyadiji**  
**University of Manchester**  
**Engineering Department**  
**Simon Building**  
**Manshester M13 9PL, United Kingdom**  
**telephone: (44) 61-275-4444**  
**fax: (44) 61-275-3844**

# NON-OBSTRACTIVE PARTICLE DAMPING TECHNOLOGY

H. V. Panossian, Ph.D.  
Principal Engineer, Control/Structure  
System Dynamics  
Rockwell International  
Rocketdyne Division  
6633 Canoga Avenue  
Canoga Park, CA 91303  
(818) 586-9660

AAB-1



## ABSTRACT

Presented herein is a novel passive vibration damping technique that is referred to as Non-Obstructive Particle Damping (NOPD). The NOPD technique consists of making small diameter holes (or cavities) at appropriate locations in a non-obstructive manner inside the main load path of a vibrating structure without affecting its mass, and filling these holes to appropriate levels with particles yielding the maximum damping effectiveness for the desired mode or modes. Powders, spherical, metallic, non-metallic or liquid particles (or mixtures) with different densities, viscosities, and adhesive or cohesive characteristics can be used. Damping optimization can be carried out by selecting the location and size of cavities, based on modal analysis, and by filling the holes to appropriate levels with the right kind of particles, those having such relative sizes with respect to the cavities and that yield the optimal damping effectiveness. Experimental modal surveys were performed on damping various structures, and computer simulations were run on acoustic attenuation by using the NOPD technique. The results of these tests and analyses will be presented and briefly discussed. Heuristic evaluations will be made that will address the advantages and limitations of NOPD and potential applications in military and industrial structures.

The use of viscoelastic materials for vibration damping is presently precluded in many spacecraft and aircraft applications, lasers, rocket engines, and other structural systems due mainly to severe thermal flow and pressure, as well as other environmental conditions that contribute to the degradation of key damping characteristics. Therefore, it is extremely desirable to design some form of structural damping into high performance structures in order to be able to minimize changes of resonant instabilities or to avoid damage due to vibrations under severe environmental conditions. In order to decouple or detune resonant vibrations in high performance structures, the normal practice is to optimize the design such that the natural frequencies of the structure are widely separated from resonating frequencies. However, practical constraints usually lead to drastic measures for the accomplishment of such design changes via optimization or other means.

The attainable service life of any structure is a function of a combination of alternating and steady-state stress levels induced by vibrations and/or thermal and environmental loads. There is extensive evidence that reduction in the stress levels and cyclic loads amplitudes in structures via damping treatments increases their operating life, since the magnitude of the vibratory stresses under resonance is inversely proportional to the degree of damping in the structure. Inherent damping, especially in metallic structures, is relatively low, and as a consequence, any additional damping can be effective in reducing stress levels for almost all structural systems that experience high vibrations.

The effectiveness of damping treatments is related to the extent of vibration energy being converted into some other form of energy. In the case of viscoelastic materials, some of the vibration energy is dissipated in the form of heat through flexure. In other forms of damping treatments, various other mechanisms are involved in the energy absorption process. For instance, it is known that in impact damping applications, momentum exchange is the dominant mechanism.

Use of particles for vibration damping is an ancient method that has been practiced for many centuries. The techniques utilized previously, however, were either surrounding the vibrating structure with a mass of particles, developing special containers or sleeves and introducing the particles within the slot around the vibrating medium, or having one large particle within a cavity of a moving structure that absorbs energy by impact action. All of these techniques involve addition of mass and/or design changes that could influence the performance of the system at hand.

Non-obstructive particle damping is a new technique where particles of metals or non-metals in solid or liquid form, as powders, spheres, or irregular shaped particles, are introduced within small holes or cavities inside the walls of the vibrating structure in order to absorb or dissipate vibration energy. The novelty in this approach is the technique of putting the particles within small cavities in the main load paths of the vibrating structure non-obstructively and without affecting its mass. Experimental results have shown extensive vibration amplitude reduction caused by minute amounts of particles introduced within the cavities inside structures. The mechanisms involved in this method are more complex than those of existing techniques since there is the potential of energy absorption/dissipation via friction, momentum exchange between moving particles and vibrating walls, heat, and viscous and shear deformations, among others. This approach was first tested at Rocketdyne facilities on a rocket engine component.

# INTRODUCTION

- **MODERN STRUCTURAL/DYNAMIC SYSTEMS**
  - Have complex active control features
  - Require advanced instrumentation
  - Have stringent vibration criteria
  - Are designed based on strength/rigidity
  - Have their material selected prior to structural dynamic behavior analysis
- **FUTURE STRUCTURAL/DYNAMIC SYSTEMS NEEDS**
  - Design based on stiffness considerations and structural dynamics
  - High performance
  - High survivability/Reliability
  - Low vibration amplitudes
  - Easy maintainability
  - Good material properties

# ROLE OF ACTIVE/PASSIVE DAMPING

- **AS SEEN BY INDUSTRY:**
  - Limited knowledge
  - Limited consideration
  - Seen as nonexistent for cryogenic or hot environments
- **IN STRUCTURAL DYNAMICS APPLICATIONS:**
  - Level of importance = dimensional stability  
= specific stiffness

AAB-4

# **OPTIMUM STRUCTURAL DAMPING, VIBRATION SUPPRESSION & LOAD ALLEVIATION**

- **Right material (metal matrix, composites, etc.) for the structure**
- **Definition of environments (gusts , etc.) and loads (limit loads, cyclic load)**
- **Viscoelastic and other materials (tungston, ceramics, etc.) for coating surfaces**
- **Tradeoff studies for active/passive vibration suppression/isolation measures**
- **Cost and weight savings, reduction of system complexity, augmentation of energy dissipation by special means**

AAB-5

# SPACECRAFT/ROCKET PROPULSION SYSTEMS

- **VIBRATION/ACOUSTIC ENVIRONMENTS**
  - Cause high amplitude loading on payloads
  - Are more severe during lift-off and transonic portions of launch
  - Sources are: Vibro-Acoustic/fluctuating pressure fields generated by the rocket engine at life-off and boundary layer turbulence in atmospheric flight
- **PROPULSION SYSTEM CHARACTERISTICS**
  - Thrust ignition transients (shock & vibration) on pad and at lift-off
  - Maximum dynamic pressure flight regimes (wind and aerodynamics)
  - Thrust oscillations throughout burn

# COMMON DAMPING METHODS

## I ACTIVE (FOR VERY SPECIALIZED APPLICATIONS)

- Eddy current devices
- Piezoelectric devices
- Memory metals

## II PASSIVE: (1) MATERIAL

- Constrained layer
- Free layer
- Composites, alloys, etc.
- Viscoelastic materials

## (2) DESIGN OPTIMIZATION FOR VIBRATION REDUCTION

- Special design of blades/impellers
- Special design of seals/bearings
- Aero-thermo dynamic design
- Calculation of optimal design parameters for least vibration

## (3) VIBRATION REDUCTION BY ISOLATION

- Electronic components
- Controllers
- Payload

# DAMPING EFFECTS, MODELS & MECHANISMS

- DAMPING EFFECTS
  - LIMIT MOTIONS, INCREASE RATE OF DECAY, REDUCE RATE OF BUILD-UP, LIMIT AMPLITUDE.
  - INCREASE FATIGUE LIFE, INCREASE IMPEDANCE, REDUCE TRANSMISSION OF VIBRATIONS AND STRUCTURE.
  
- DAMPING MODELS: VISCIOUS       $F = Cx$   
FRICTION       $F = \mu \operatorname{sgn}(\dot{x})$   
POWERLAW       $F = kx^n$   
HYSTERIC       $F = -h\dot{x}$  (h = HYSTERETIC DAMPING)
  
- DAMPING MECHANISMS:
  - MECHANICAL HYSTERESIS (MATERIAL, INTERNAL FRICTION)
  - ELECTROMAGNETIC (EDDY CURRENTS)
  - EXTERNAL FRICTION (SOLIDS, FLUIDS)
  - TRANSPORT (ACOUSTIC, PUMPING, CONDUCTION)
  - FREQUENCY CONVERSION (IMPACT, GRANULAR MATERIALS)
  - INTERNAL FACTORS: MATERIAL TYPE, CHEMICAL COMPOSITION, INTERNAL STRUCTURE, ETC.
  - EXTERNAL FACTORS: TEMPERATURE, PRELOAD, INITIAL STRAIN
  - AMPLITUDE OF MOTION, STRESS, DEFORMATION, GEOMETRY, SCALE, BONDING, SURFACE CONDITION

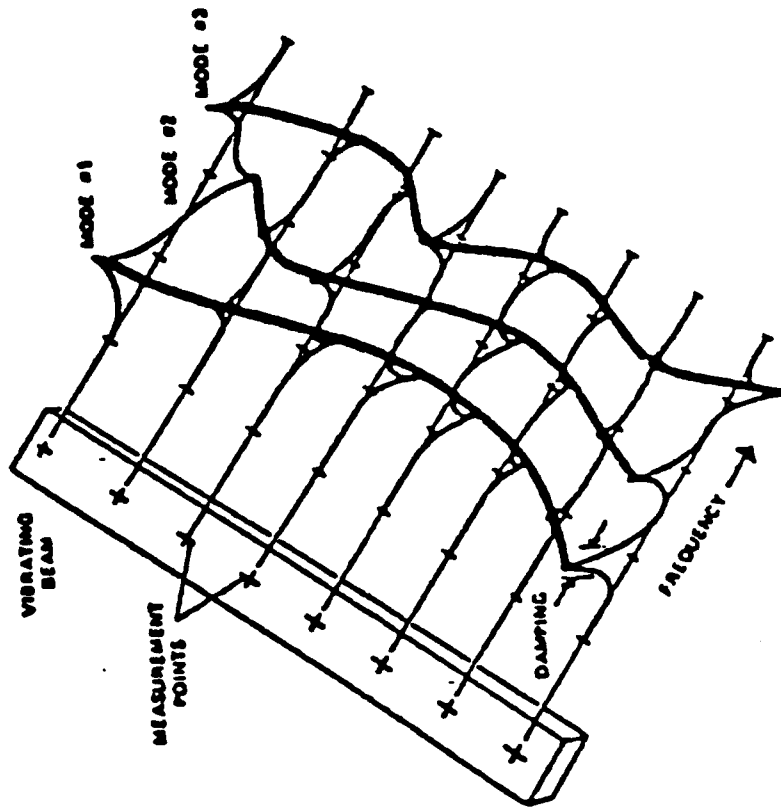
# APPROACH TO DAMPING DESIGN

- OPTIMAL DAMPING DESIGN:
  - PROBLEM AND ENVIRONMENT DEFINITION
  - STRUCTURAL DYNAMICS: VERIFY THAT THE PROBLEM IS ONE OF RESONANT VIBRATION
  - OPTIMAL DAMPING MATERIAL SELECTION AND DESIGN OPTIMIZATION
  - LABORATORY MOCK-UP AND EVALUATION TEST
  - FULL-SCALE APPLICATION AND TESTING
  - DEVELOPMENT OF TOOLING AND METHODOLOGY FOR MANUFACTURING
  
- STRUCTURAL DYNAMIC CHARACTERIZATION
  - DETERMINE FREQUENCY RANGE OF INTEREST
  - THOROUGH DYNAMIC INVESTIGATION/ENVIRONMENT DEFINITION
  - ACCURATE TEMPERATURE/PRESSURE DATA
  
- MATERIAL SELECTION/APPLICATION
  - TEMPERATURE RANGE FOR DAMPING
  - TEMPERATURE RANGE FOR SURVIVABILITY
  - FREQUENCY AND MODE SHAPES
  - WEIGHT ADDITION, DIMENSIONAL INCREASE, SYSTEM PERFORMANCE

# VIBRATION CONTROL & SUPPRESSION

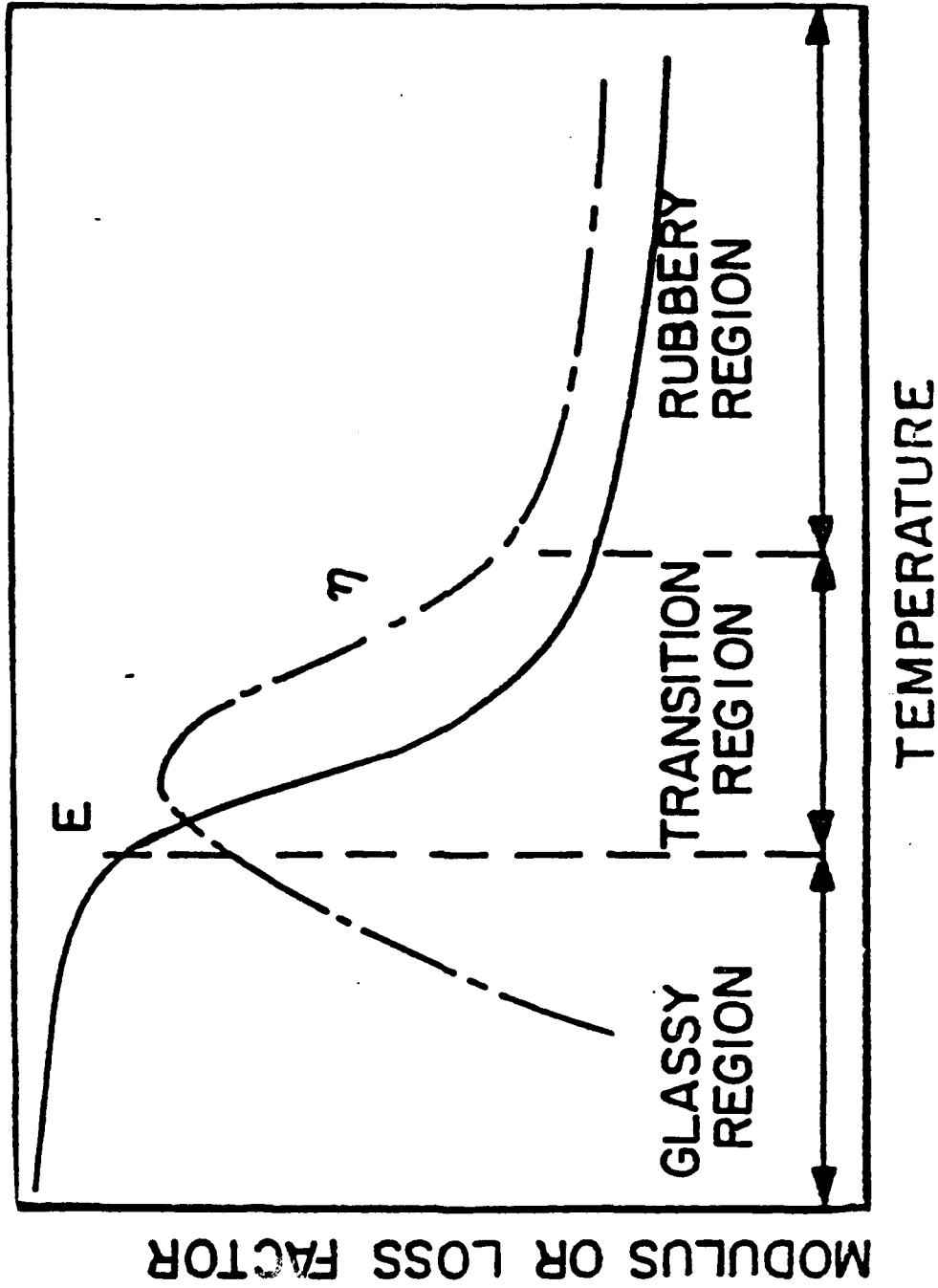
- THE VIBRATION CONTROLLER COUNTERACTS MODAL OSCILLATIONS AND RAPIDLY SETTLES THE STRUCTURE
  
- THREE WAYS TO PASSIVELY REDUCE VIBRATION:
  - 1) OPTIMAL SYSTEM DESIGN ADJUSTMENT: ARRANGE COMPONENTS TO MINIMIZE VIBRATION EFFECTS
  - 2) DISTURBANCE ISOLATION : STOP VIBRATION AT SOURCE
  - 3) STRUCTURAL DAMPING : ADJUST TRANSMISSION PATH TO ABSORB ENERGY
  
- THREE WAYS TO ACTIVELY REDUCE VIBRATION
  - 1) DISTURBANCE ISOLATION : STOP VIBRATION AT SOURCE
  - 2) DISTURBANCE COMPENSATION : INTRODUCE COUNTERACTING FORCE
  - 3) STRUCTURAL CONTROL : ABSORB STRUCTURAL VIBRATION ENERGY

# MODAL PARAMETERS OF A BEAM



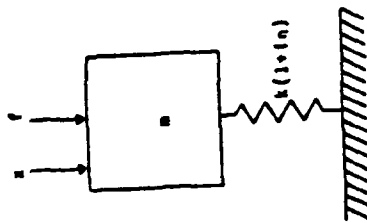
AAB-11

# DAMPING OF VISCOELASTIC MATERIALS

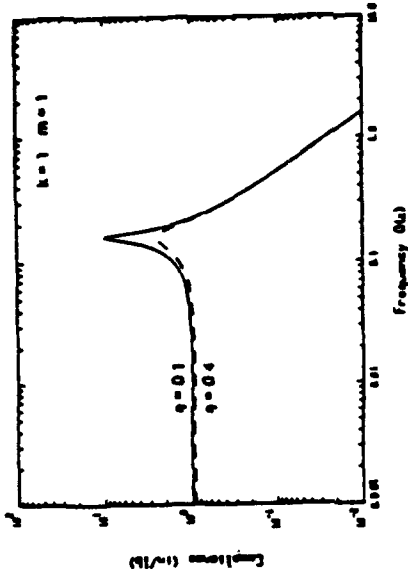


Variation of E and  $\eta$  with Temperature.

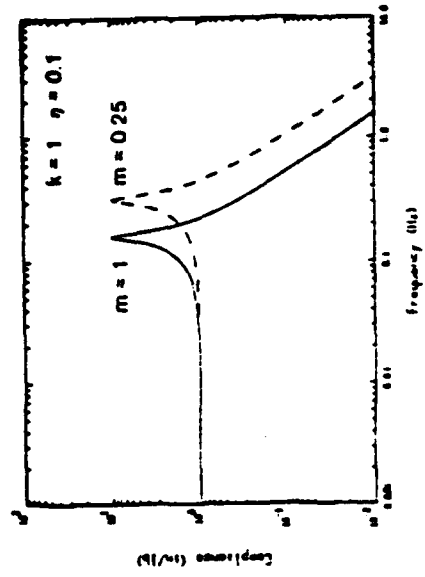
# EFFECTS OF MASS, STIFFNESS & DAMPING OF SDOF SYSTEM



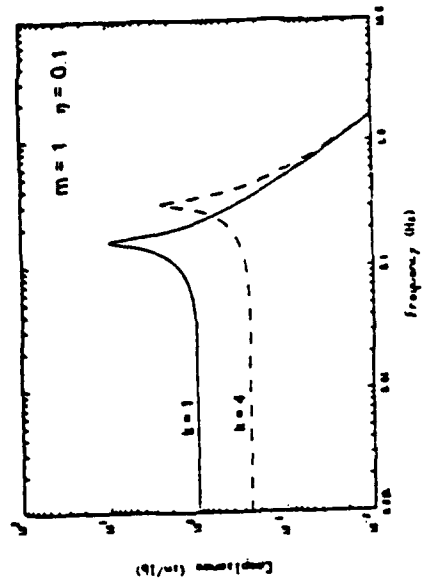
Forced excitation of a single-degree-of-freedom system.



Effect of damping changes.



Effect of mass changes.



Effect of stiffness changes.



# NON-OBSTRACTIVE PARTICLE DAMPING

## TECHNIQUE:

Make small holes at appropriate locations in the main load-path of a vibrating structure and fill these holes with various metallic or non-metallic particles in spherical, powder, irregular, liquid (or mixtures) forms to appropriate levels

## BENEFITS:

- NOPD will work under severe environments
- It is retrofittable on existing hardware
- Damping as high as 10% of critical is easily achievable
- Enhances working-life of structures thus saving cost
- It is easy to implement

# **APPLICATION TO TURBINE BLADE SIGNIFICANT DAMPING PER ANALYSIS**

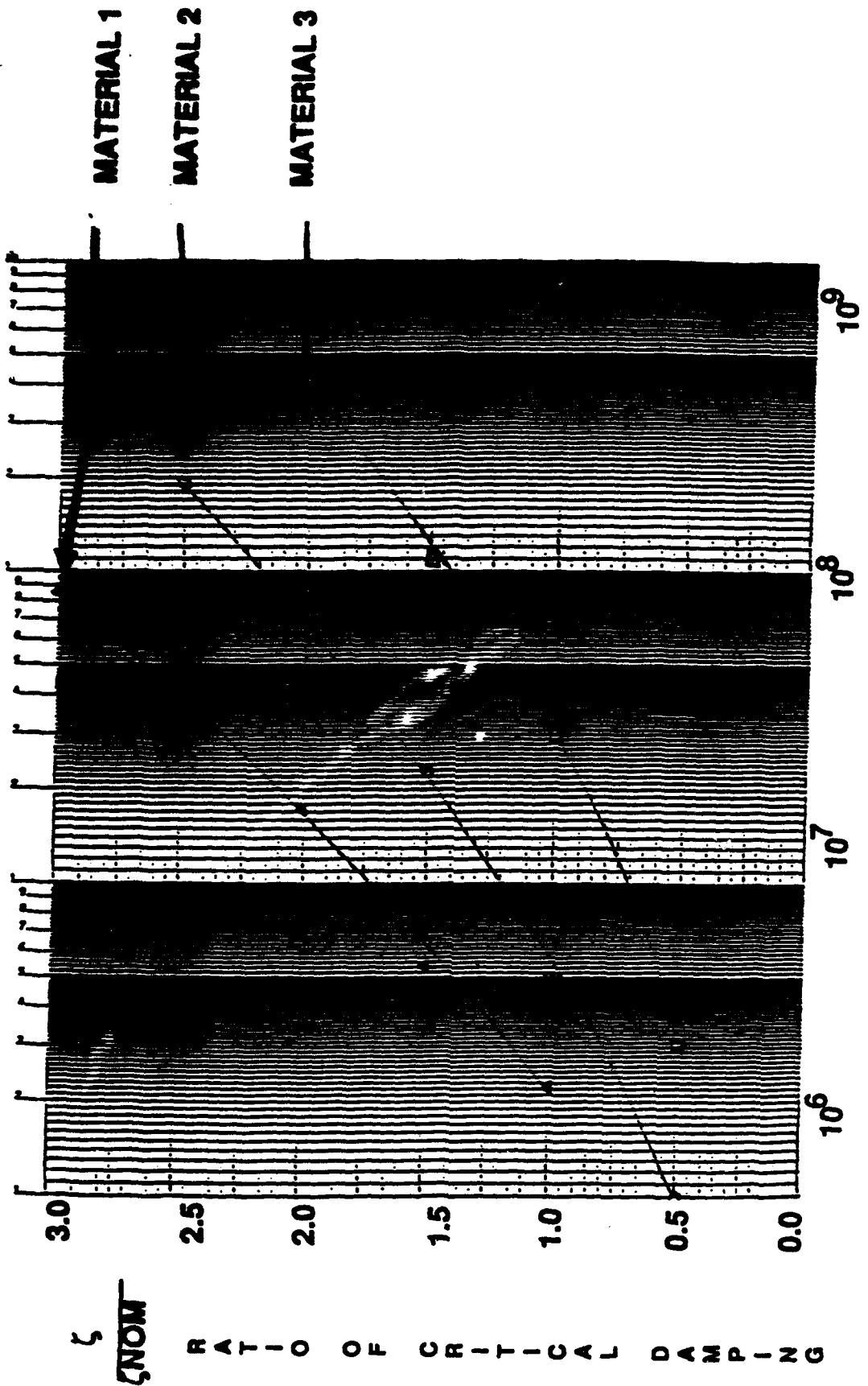
- **Rockwell IR&D funding used to develop technology**
  - **\$450,000 over last 3 years**
- **Technique verified in laboratory**
  - **Dynamic excitation tests**
  - **Multiple configurations**
- **Analytical models correlated with test results**
  - **Prediction/design capability**
- **Implementation on Rockwell products initiated**

AAB-16

# NON-OBSTRACTIVE PARTICLE DAMPING

TECHNIQUE	METHOD	ENERGY ABSORPTION		ADVANTAGES	DISADVANTAGES
		METHOD	ENERGY ABSORPTION		
VISCOELASTIC	SURFACE TREATMENT SANDWICHING	SHEAR/ EXTENSIONAL DEFORMATION	RELATIVELY EASY TO IMPLEMENT		DEGRADES, DISINTEGRATES, TEMPERATURE, ENVIRONMENT DEPENDENT
TUNED	MASS OF LINEAR SPRING	LOCAL DISPLACEMENTS OF STRUCTURE	CAN BE ADDED ON, GOOD FOR LOW FREQUENCY		DIFFICULT TO TUNE AND DEGRADES IN TIME
FRICITION	PIECE OF METAL TIGHTLY ATTACHED	FRICITION/HEAT	GOOD FOR HIGH AMPLITUDE/ FREQUENCY		WEARS OUT, DEGRADES
FLUID	SQUEEZE FILM, FLOW THROUGH ORIFICES	MASS FLOW AND ACOUSTIC EFFECTS	SHOCK ABSORPTION		LIMITED APPLICATIONS
IMPACT	METALLIC PARTICLE IN CAVITY	MOMENTUM EXCHANGE	GOOD FOR HIGH AMPLITUDES AND ALL TEMPERATURES		LIMITED ENERGY ABSORPTION
NOPD	MINUTE PARTICLES IN SMALL CAVITIES	FRICITION, MOMENTUM EXCHANGE, ETC.	GOOD FOR ALL ENVIRONMENTS, NON-OBSTRACTIVE DOES NOT ADD MASS		CAN CREATE STRESS CONCENTRATIONS

# INCREASED DAMPING RATIO INCREASES HARDWARE LIFE

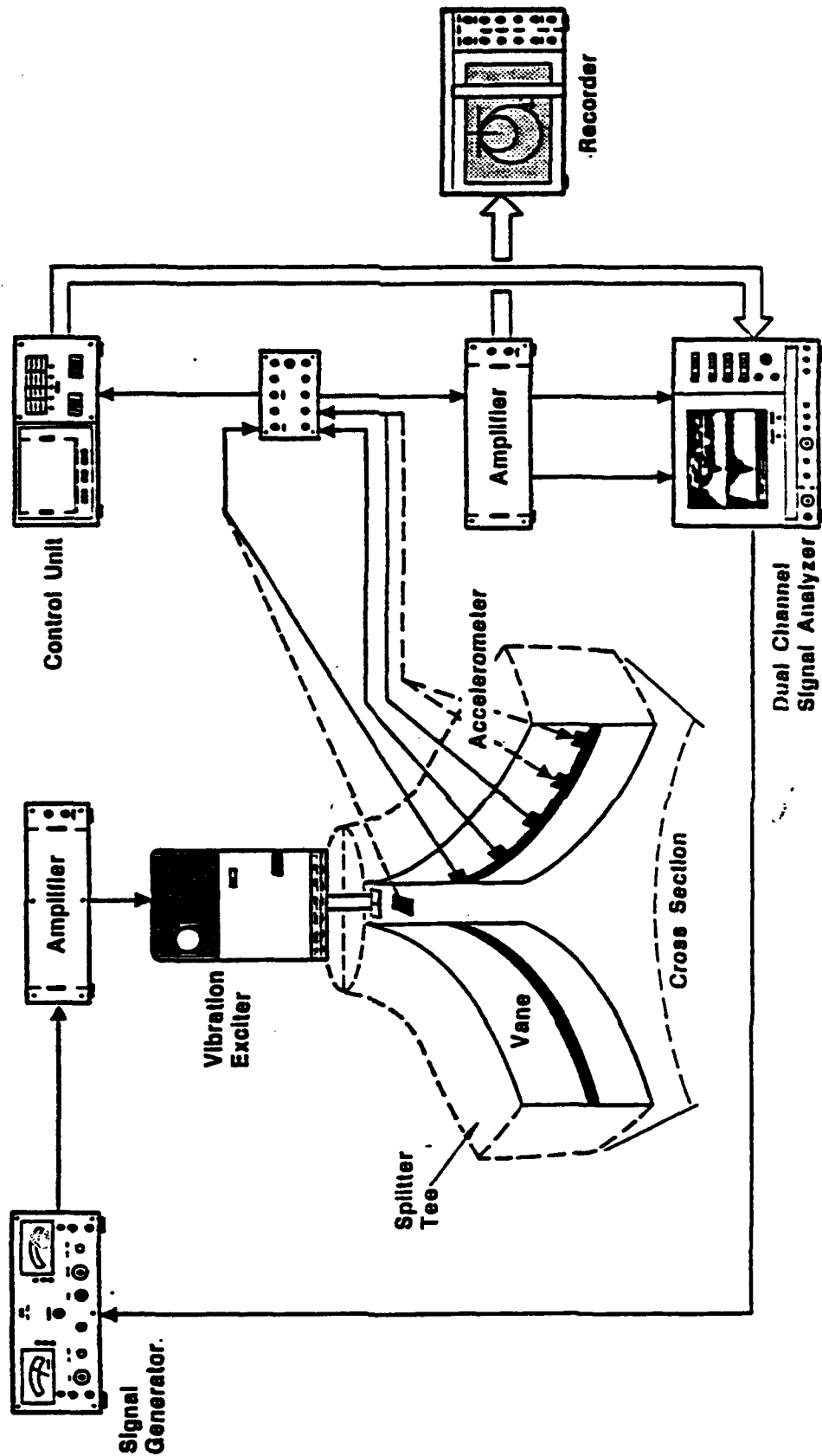


CYCLES TO FAILURE

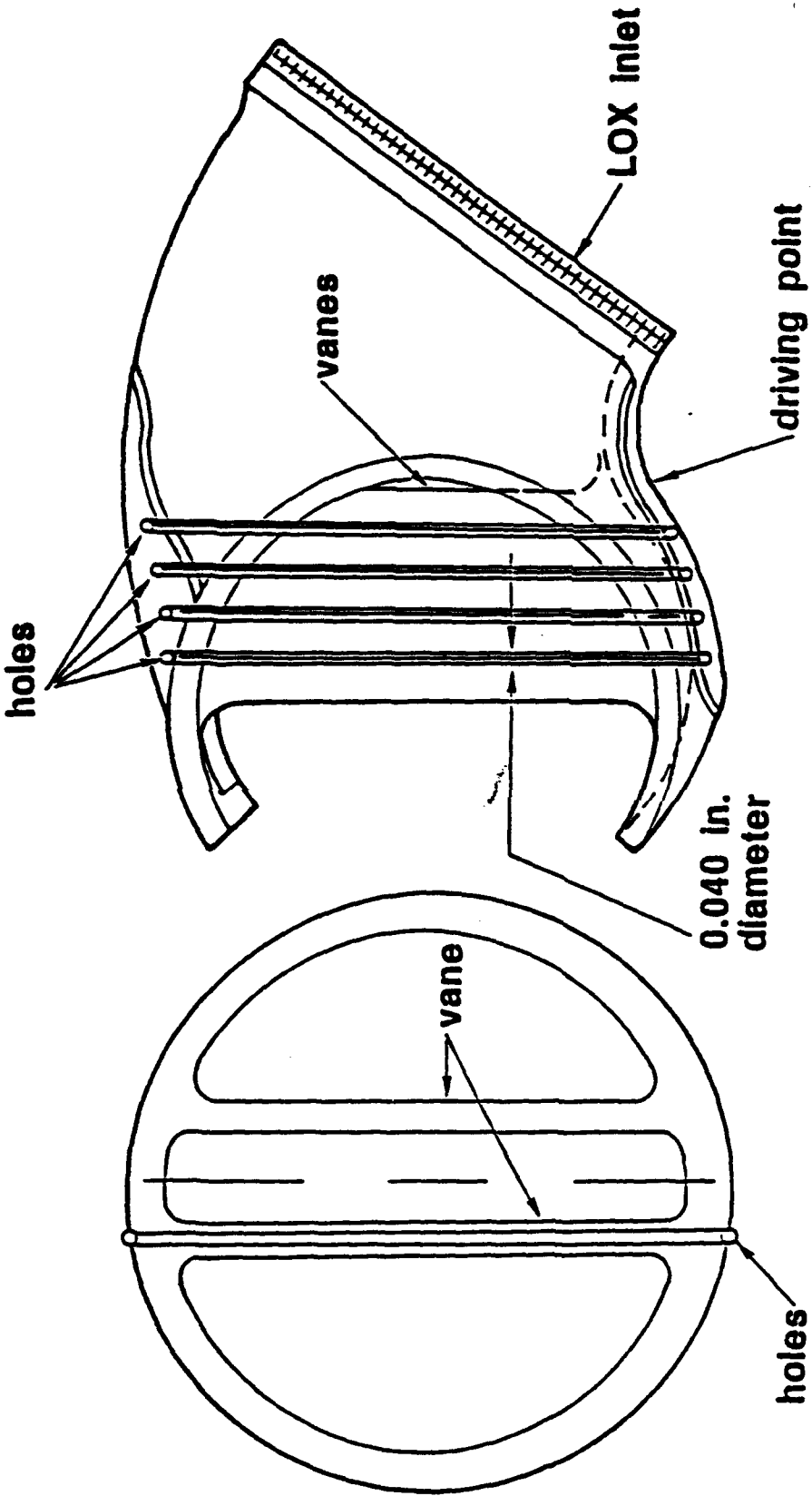
AAB-18



# MEASUREMENTS OF MODAL/VIBRATION TESTS

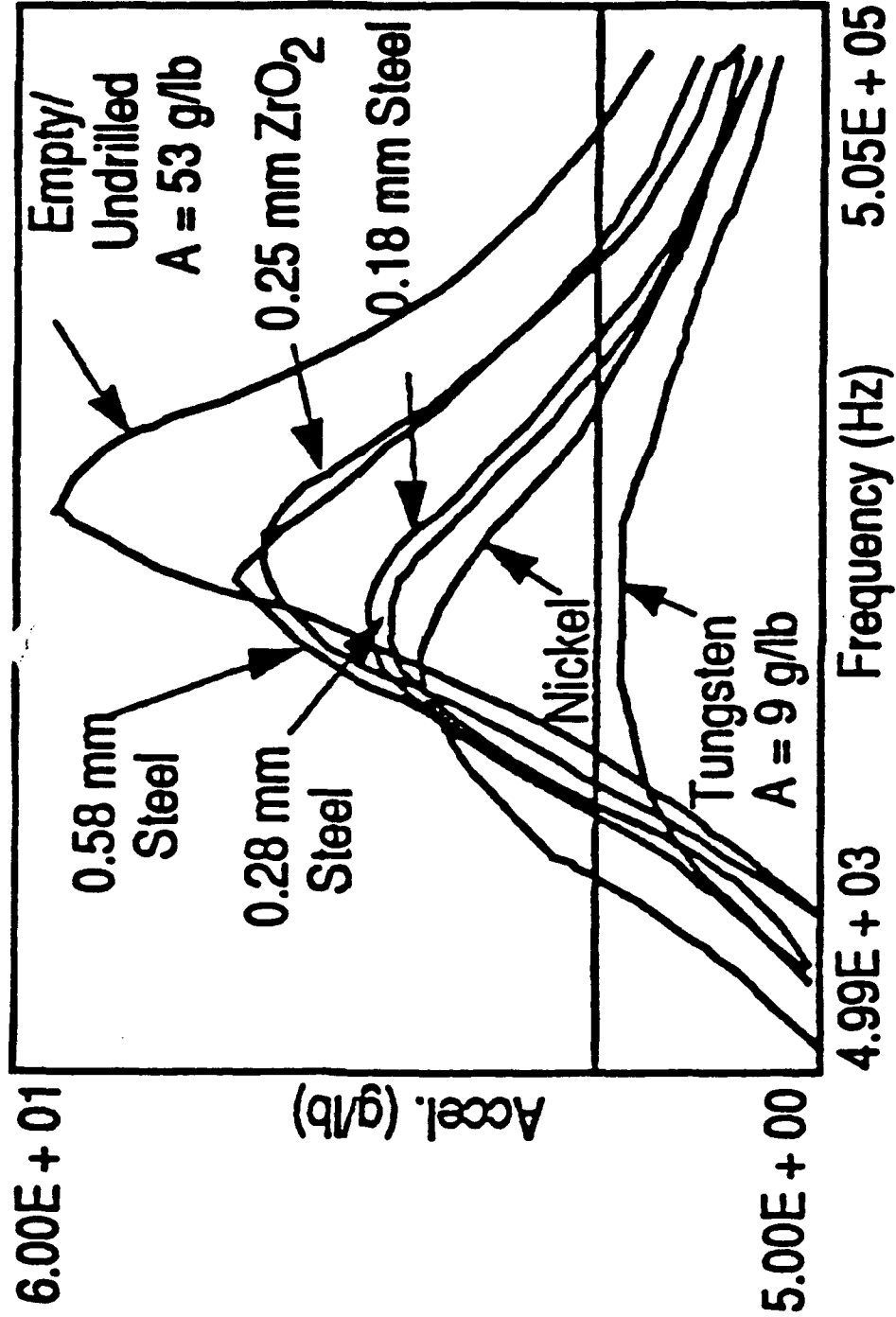


# SSME LOX INLET IEE

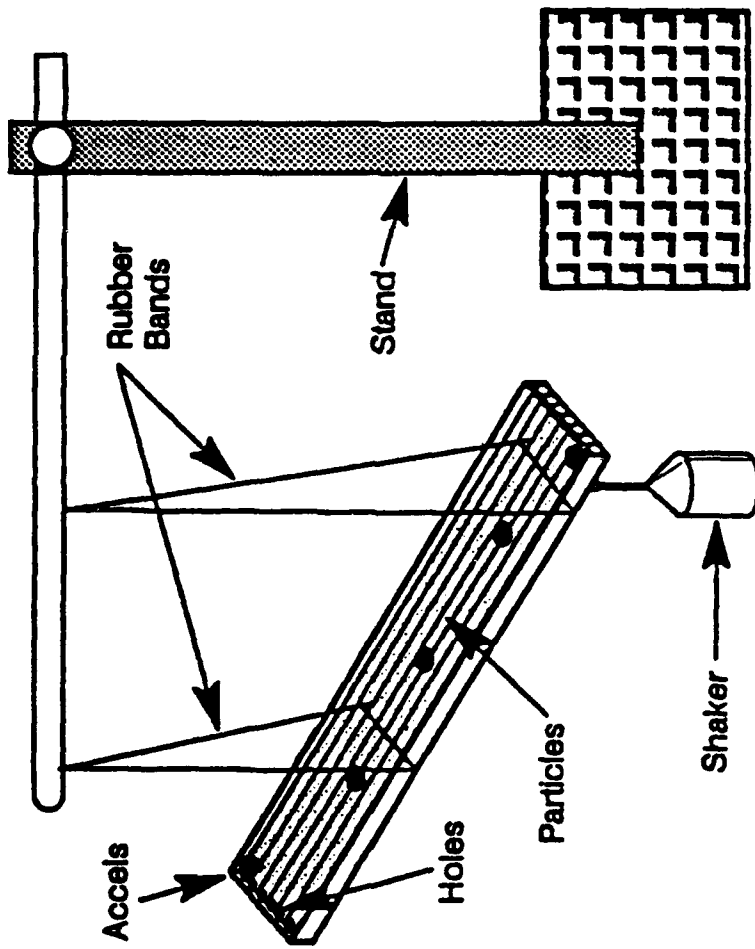


AAB-20

# EFFECTIVENESS OF VARIOUS MATERIALS ON TORSIONAL MODE SSME LOX INLET TEE



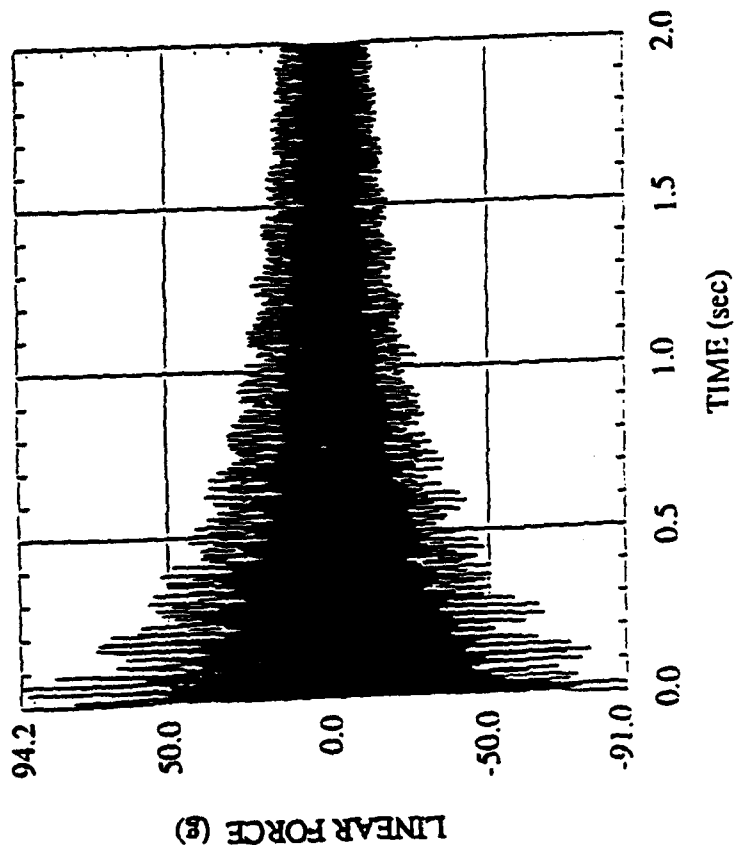
# NOPD FREE-FREE BEAM TESTS IN AIR



AAB-22

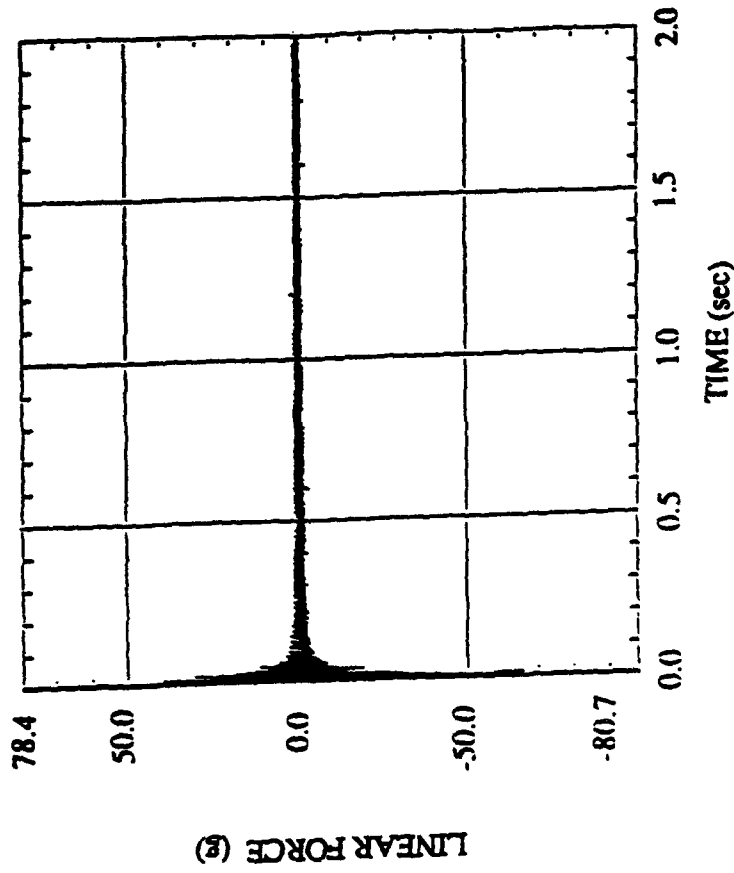
# SIGNIFICANT DAMPING OF ALUMINUM BEAM WITH NOPD

TIME RESPONSE



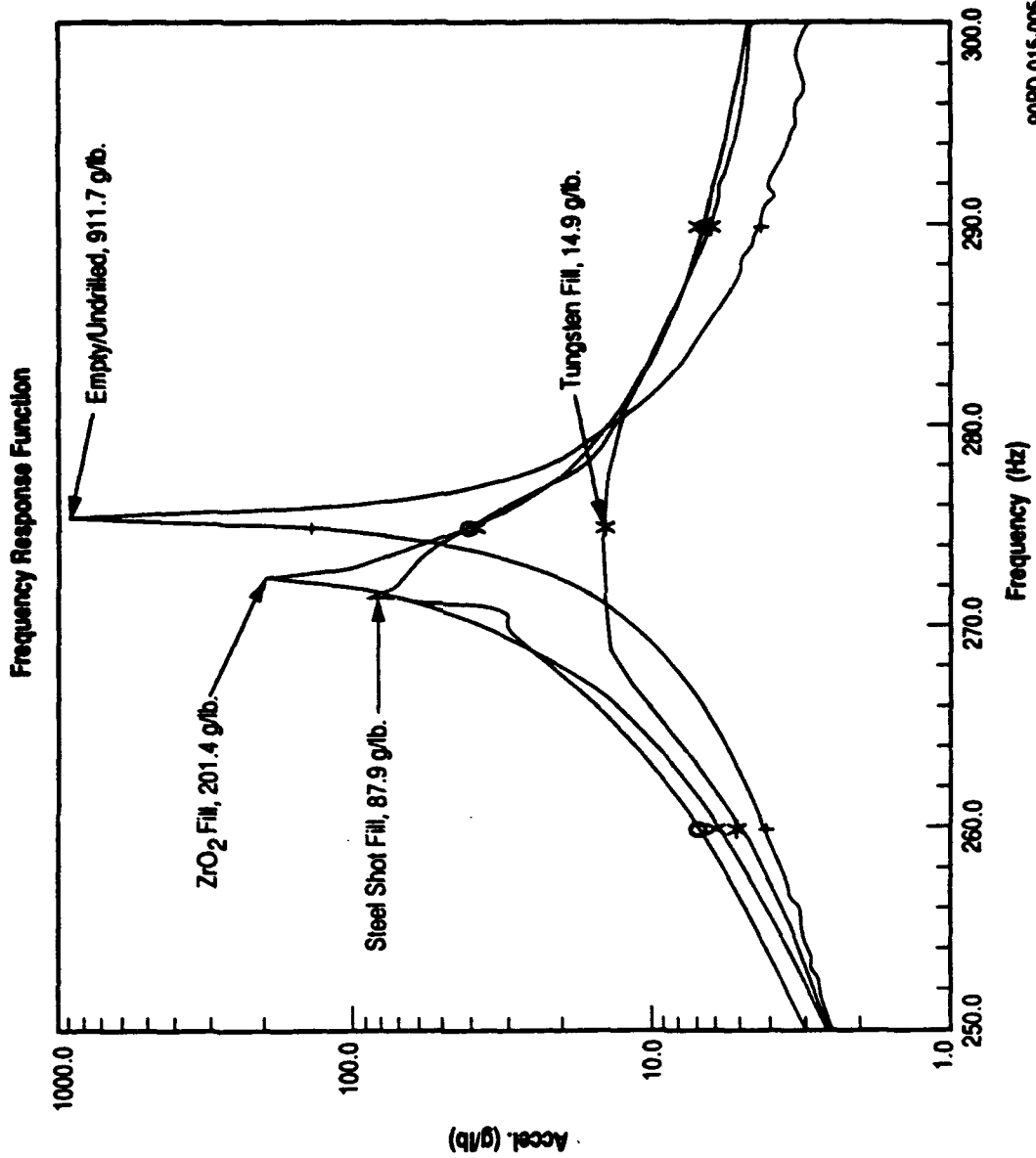
WITHOUT PARTICLES

TIME RESPONSE



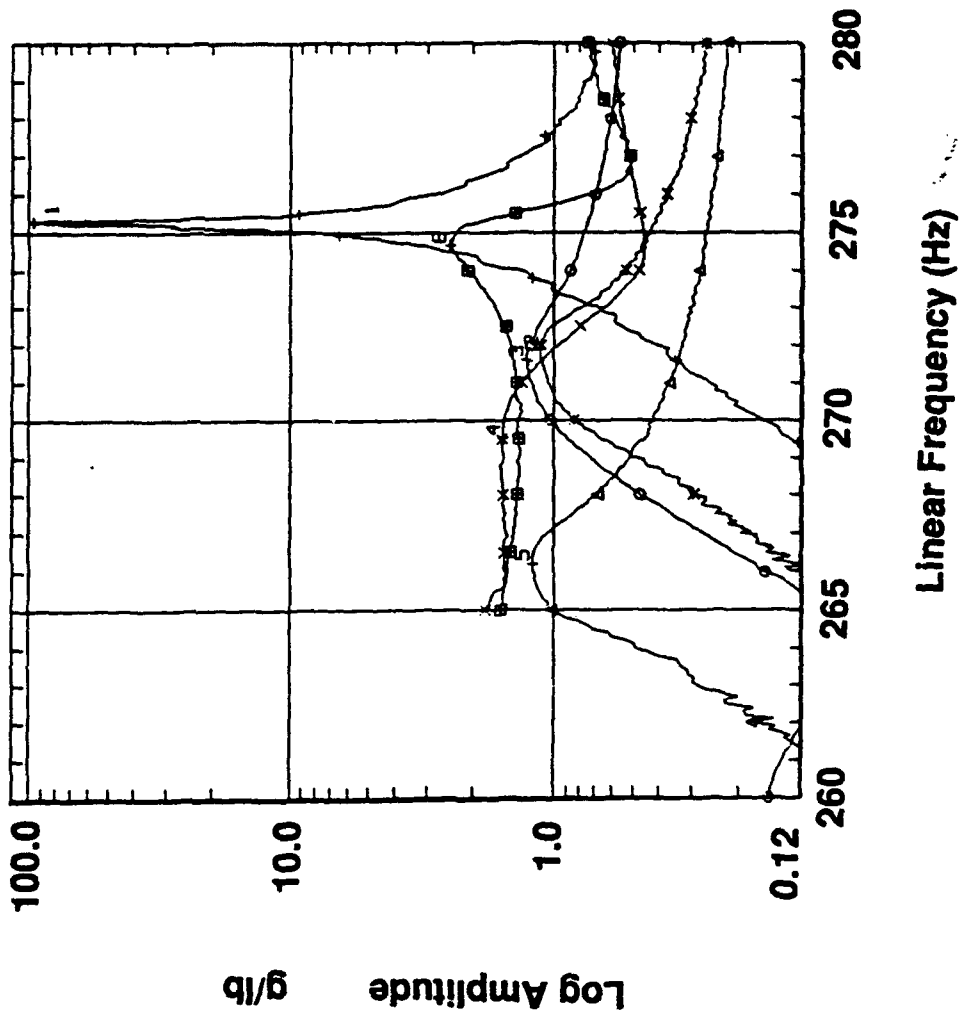
WITH PARTICLES

# FIRST FREE-FREE BENDING MODE (HAMMER RESPONSE)



90FD-015-005

# NOPD EFFECTIVENESS WITH VARIOUS MATERIALS



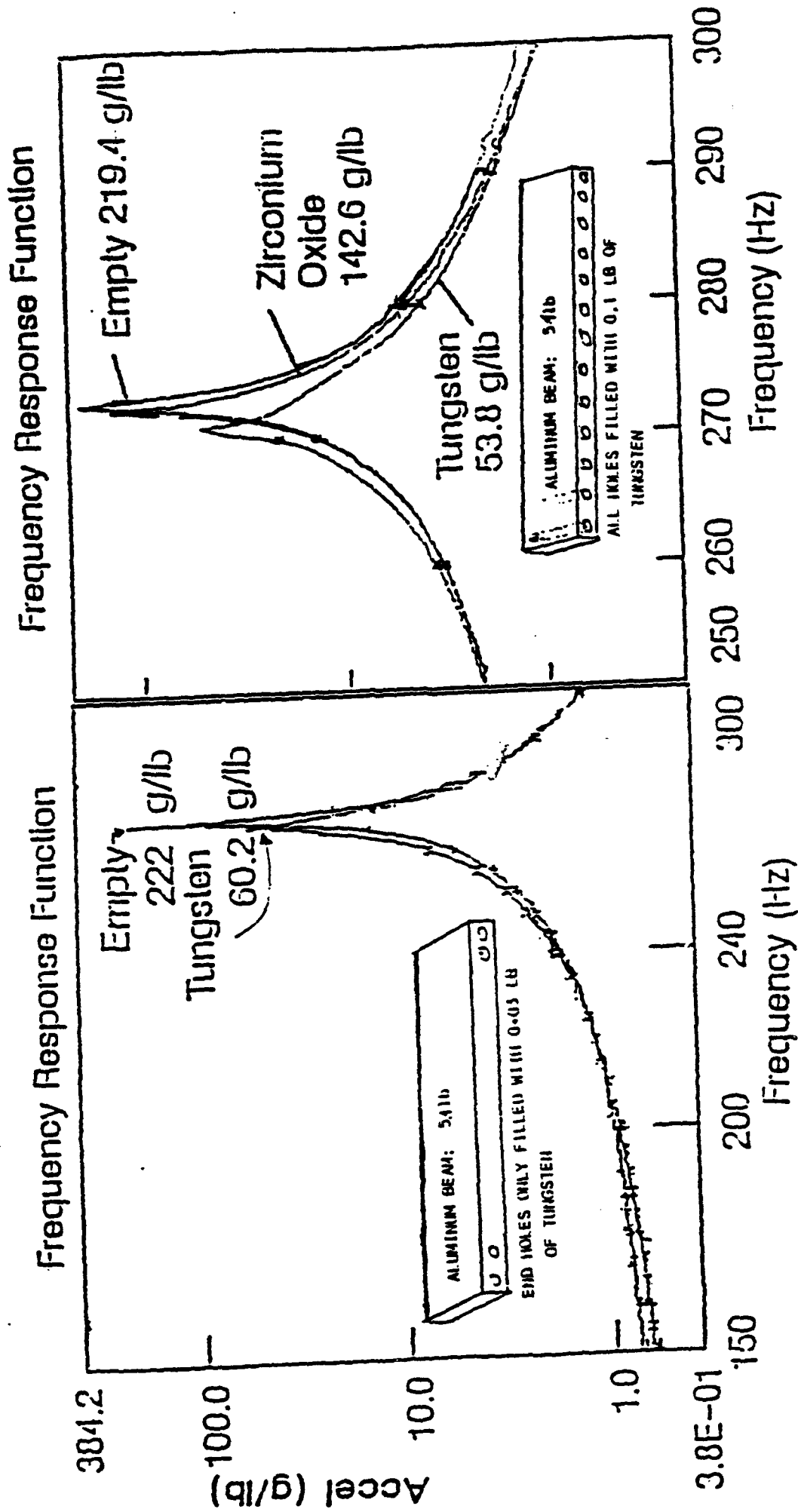
Aluminum Beam Tests  
Longitudinal Holes  
Sine Wave Input

NOPD Material

1. Empty
2. Steel Shot
3. Lead Shot
4. Copper
5. Tungsten
6. Sand

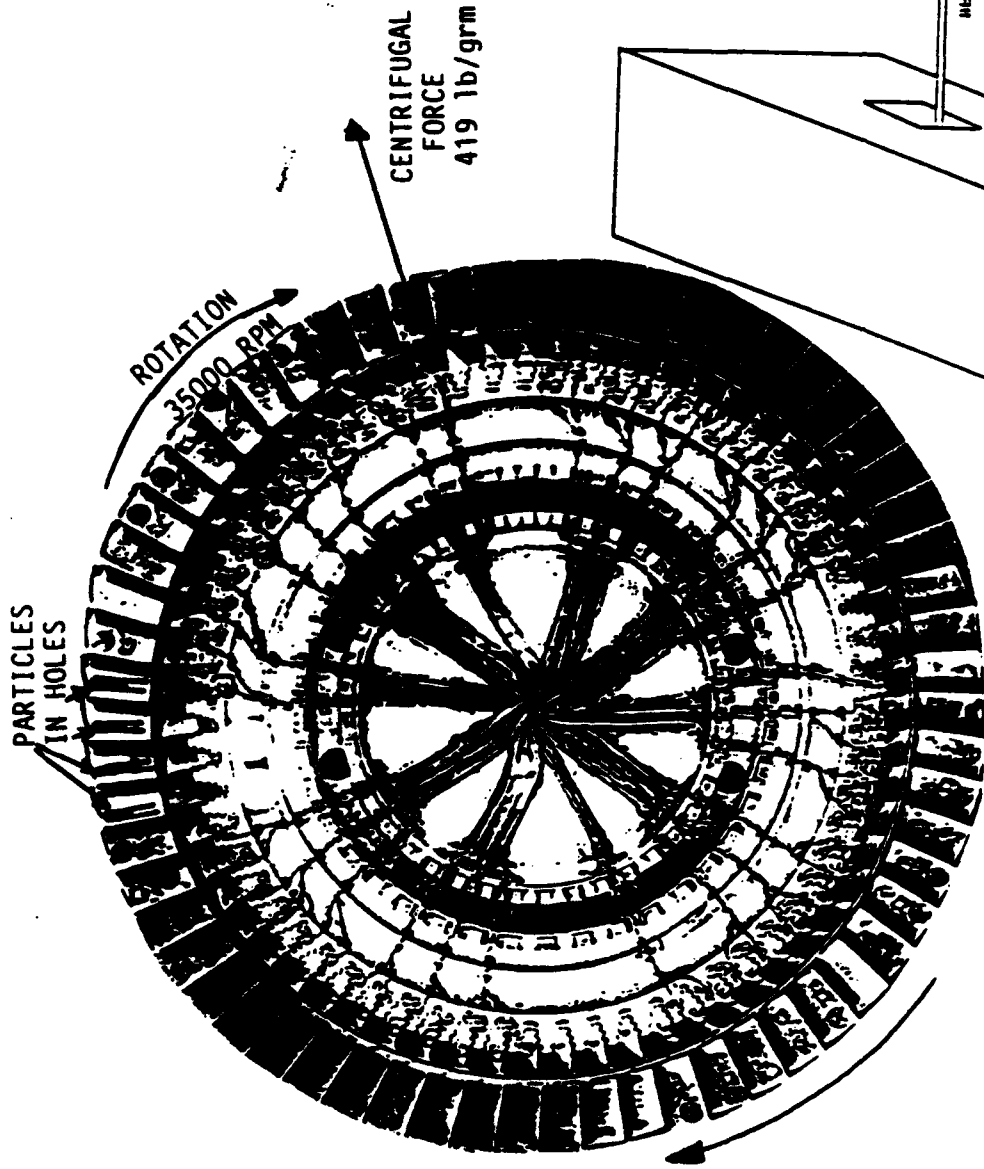
AAB-25

# FIRST FREE-FREE BEAM BENDING MODE: ALL HOLES VS END HOLES

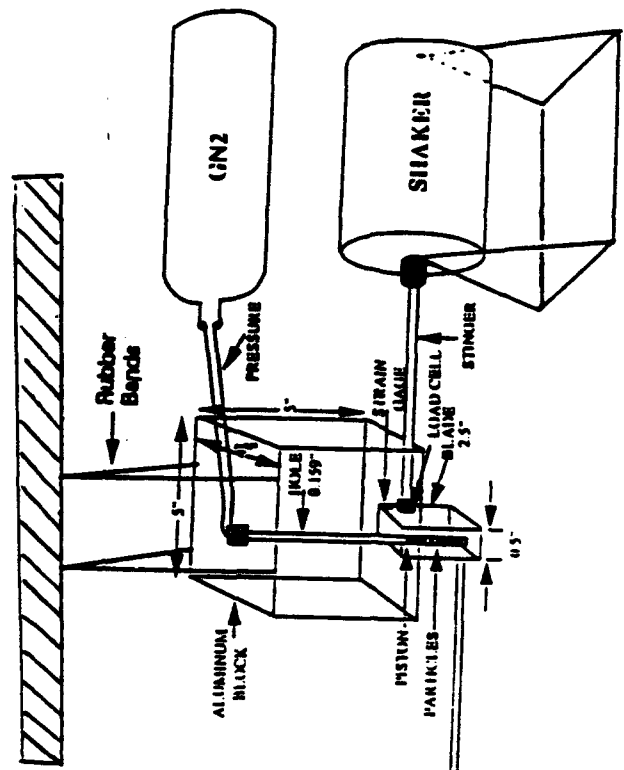


# NOPD COMPACTION TESTS

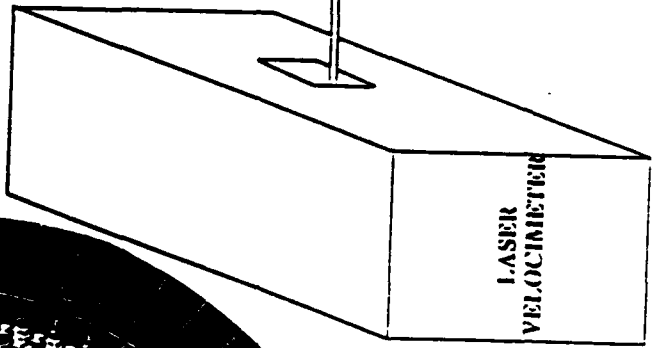
**TEST OBJECTIVE:**  
Simulate Compaction  
Force of Rotation



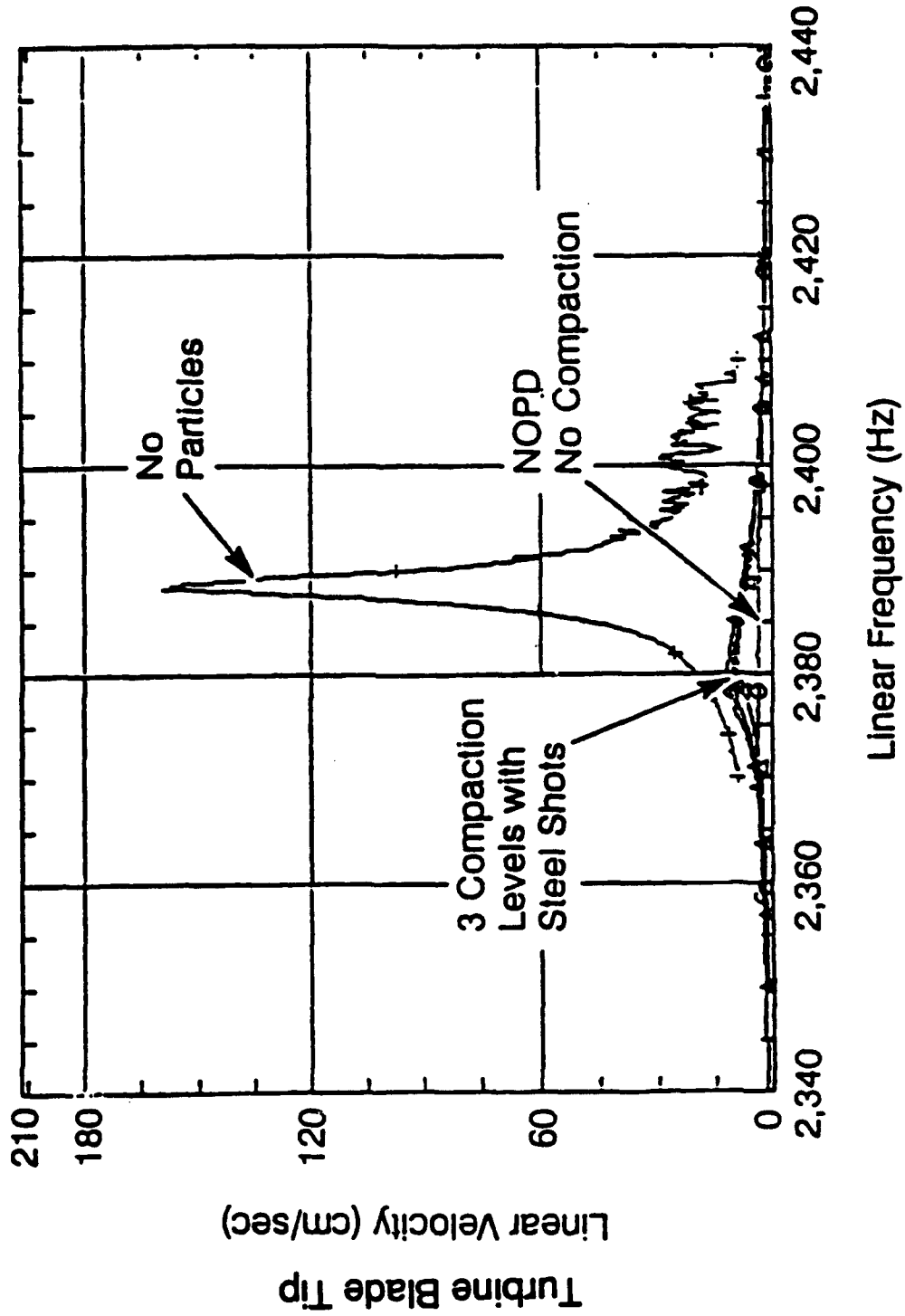
SSME HPFTP WHEEL  
WITH BLADES



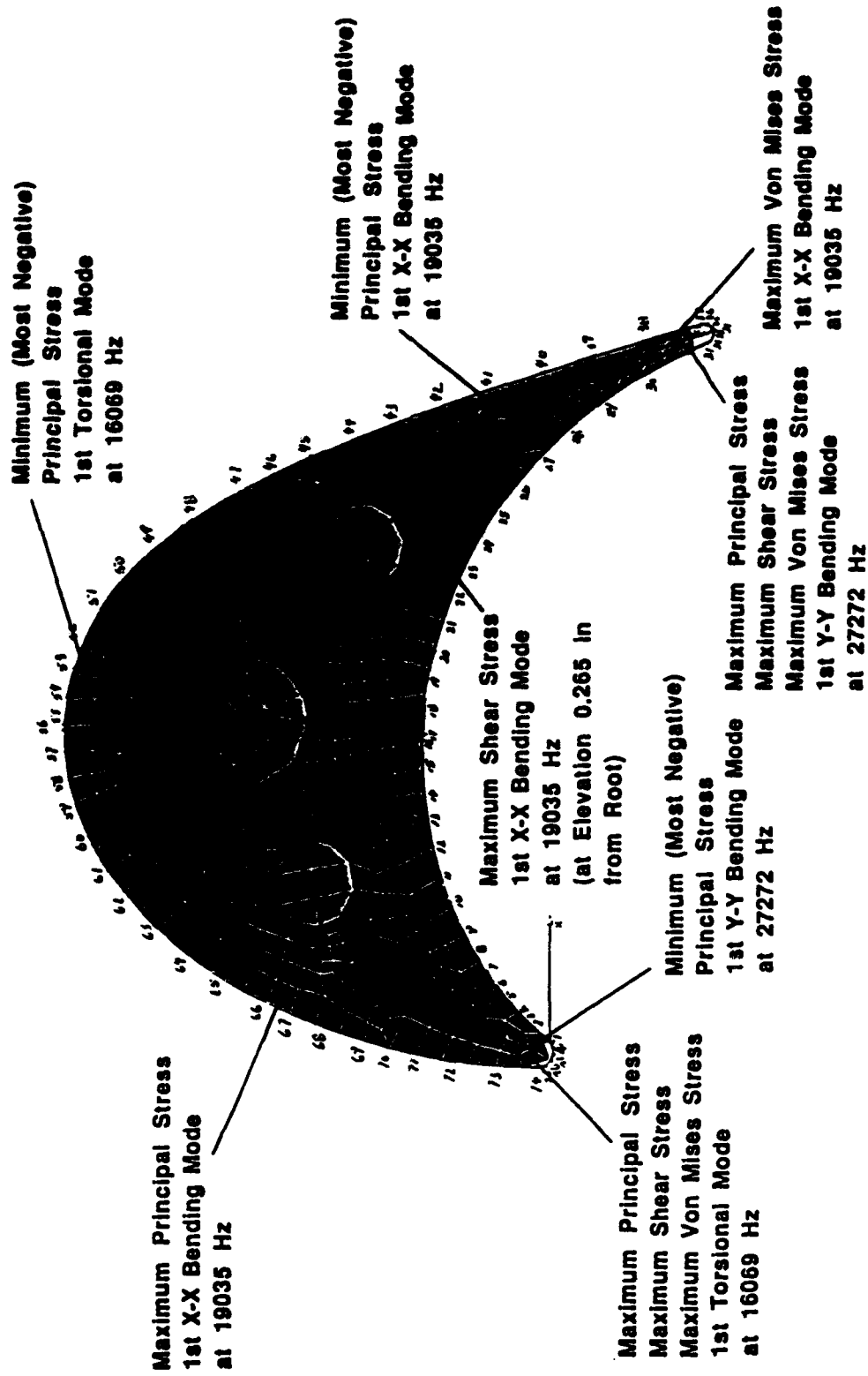
COMPACTION TEST  
SETUP



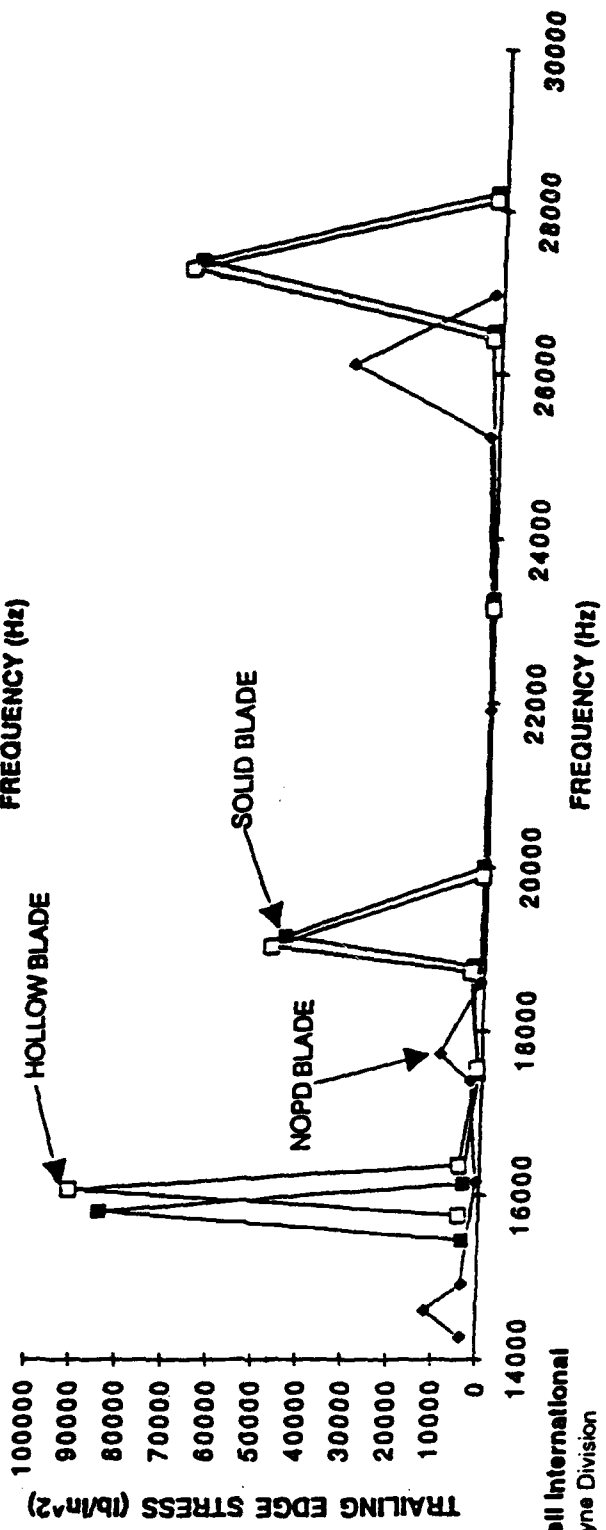
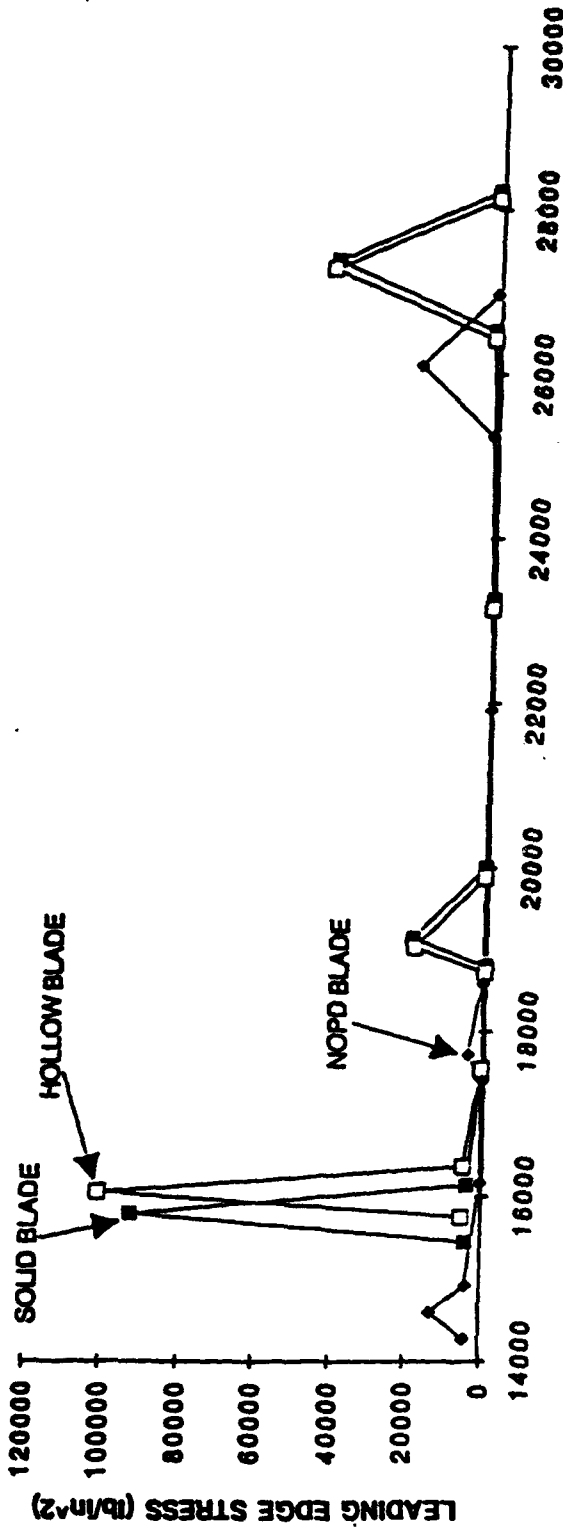
# EFFECT OF COMPACTION ON NOPD PERFORMANCE



# BLISK TURBINE BLADE MAXIMUM STRESS LOCATIONS



# COMPARISON OF STRESS (SZ) DISTRIBUTION AT BLADE HUB

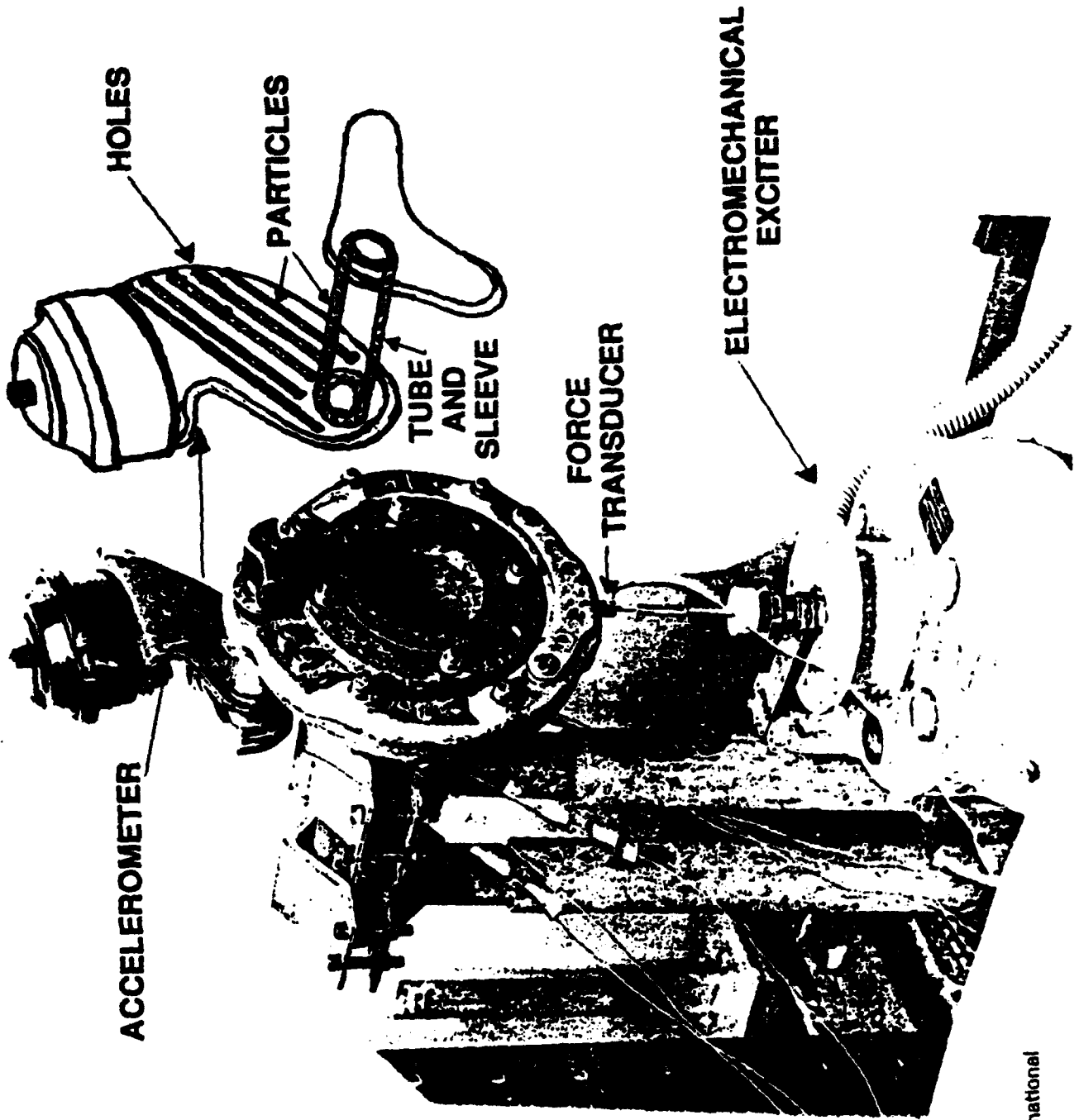


AAB-30



2LB CONCENTRATED FORCE APPLIED AT NODE 1123 AT 45 DEG WRT X-AXIS

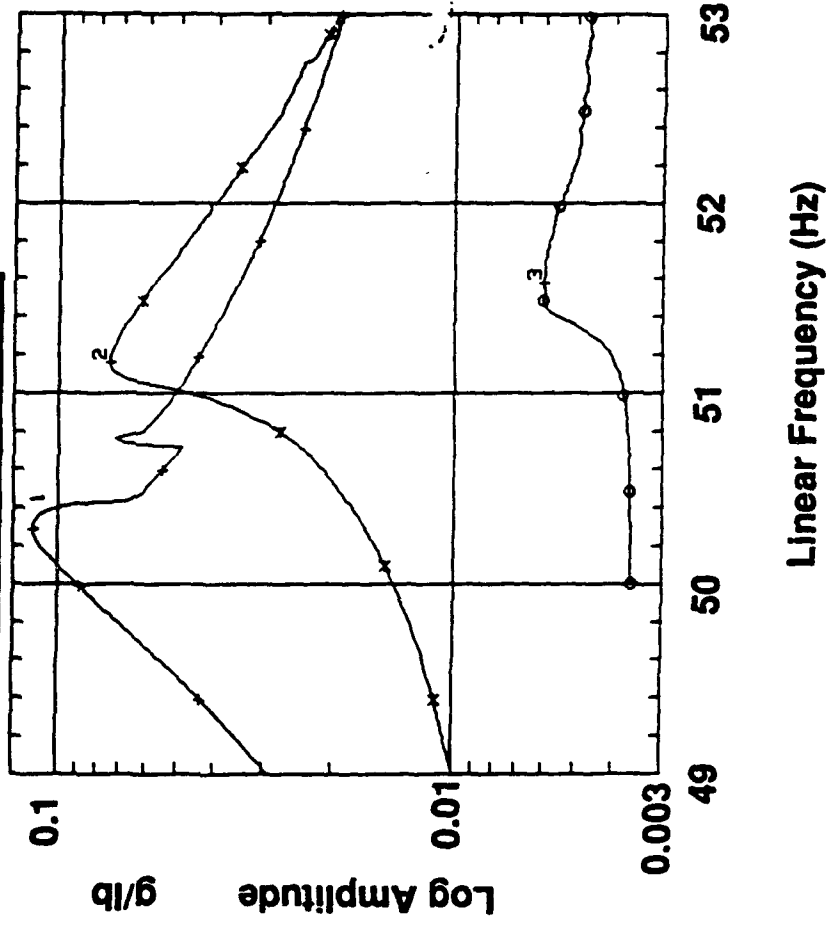
# AUTOMOTIVE BRAKE SYSTEM TEST SETUP



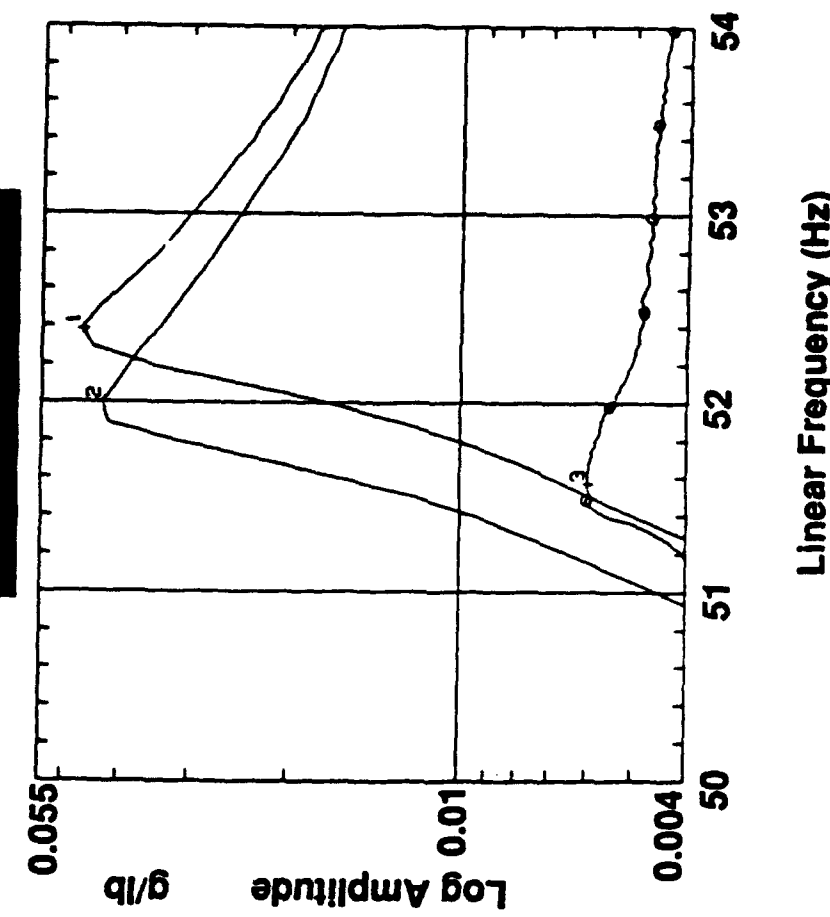
AAB-31

# BRAKE SYSTEM TESTS DEMONSTRATE INCREASED BENEFITS WITH LARGER FORCES

**With 20 Lb. Force:**  
 1. Unmodified  
 2. Empty  
 3. Tungsten



**With Variable Force:**  
 1. 5 Pounds  
 2. 10 Pounds  
 3. 20 Pounds

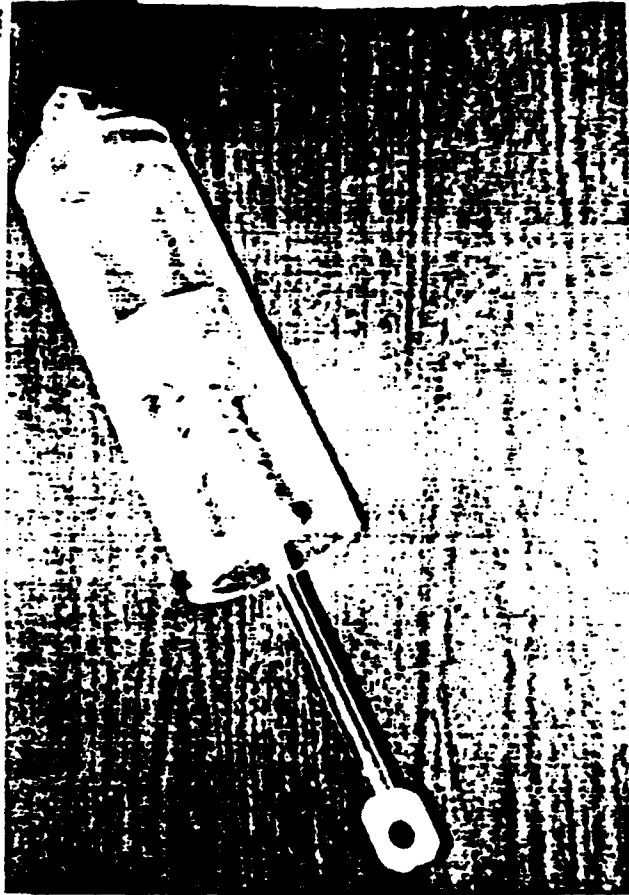
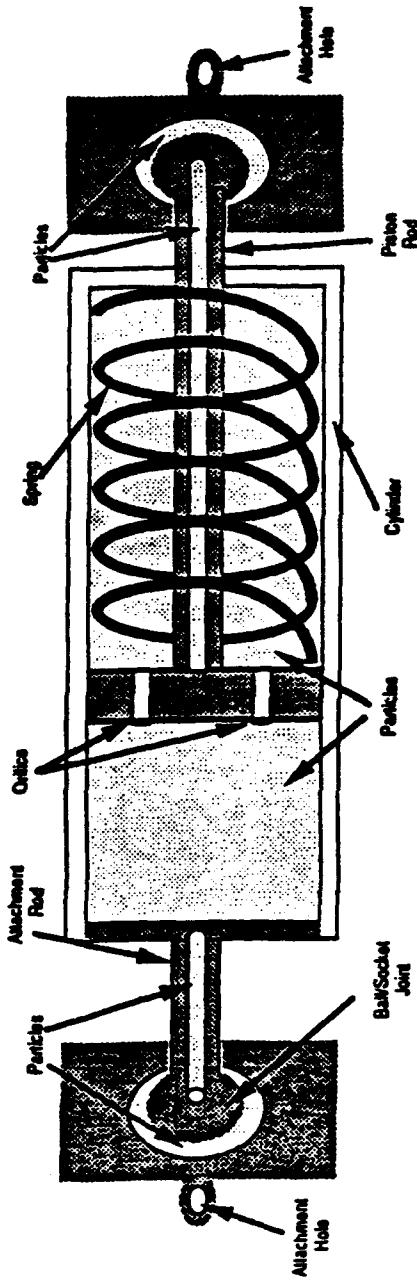


# SHOCK ISOLATION MOUNT WITH PARTICLES

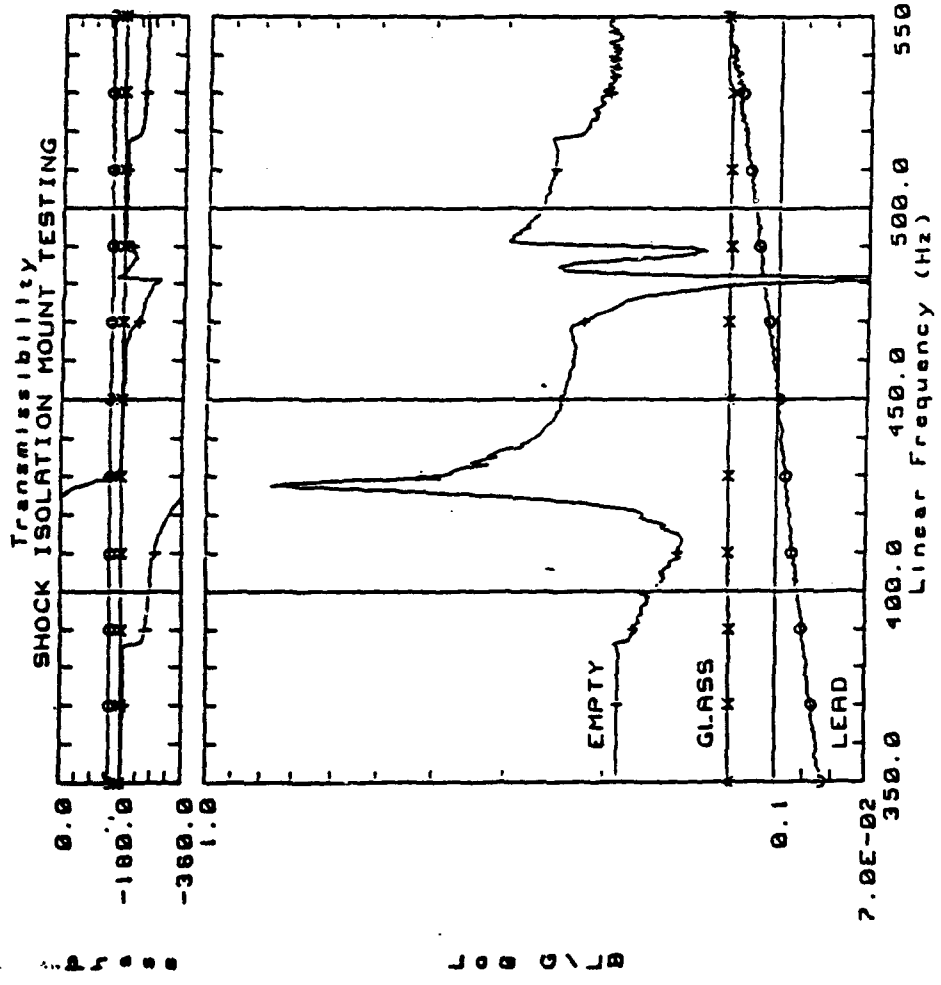
## CONCEPT DEFINITION:

- SAFE OPERABILITY OF SENSITIVE INSTRUMENTATION/EQUIPMENT REQUIRES ISOLATION FROM VIBRATION/SHOCK ENVIRONMENT
- EXISTING PASSIVE ISOLATOR MOUNTS ARE FLUID (GAS/LIQUID) FILLED, COMPLEX AND EXPENSIVE
- THE VIBRATION/SHOCK ISOLATION MOUNT FILLED WITH PARTICLES (VSIMFP) CONSISTS OF A CYLINDER FILLED WITH PARTICLES WITH A PISTON INSIDE SITTING ON A SPRING FOR CORRECT STIFFNESS. THE VIBRATORY LOADS WILL FORCE THE COMPRESSION/EXTENSION OF SPRING AND FORCE PARTICLES THROUGH THE ORIFICES FOR CONSISTENT DAMPING. THE ATTACHMENT BALL JOINT DAMPERS PROVIDE ADDED DAMPING AND CROSS-LOAD ATTENUATION (SEE FIGURE)
- DESIGN OF VSIMFP INVOLVES: 1) CYLINDER SIZING, 2) ORIFICE SIZING, 3) SPRING STIFFNESS/SIZE, AND 4) PARTICLE TYPE/SHAPE/SIZE

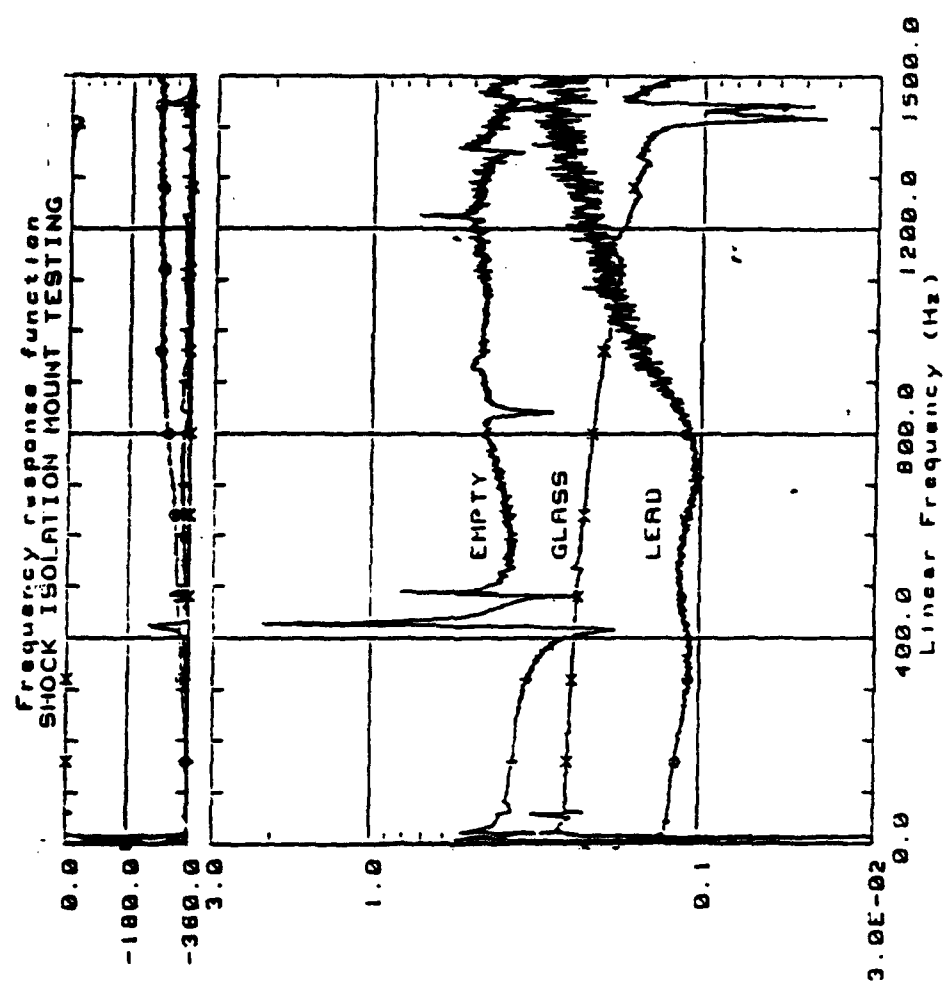
# SHOCK ISOLATION MOUNT WITH PARTICLES



# SHOCK ISOLATION MOUNT WITH PARTICLES



20 LB-F SINE



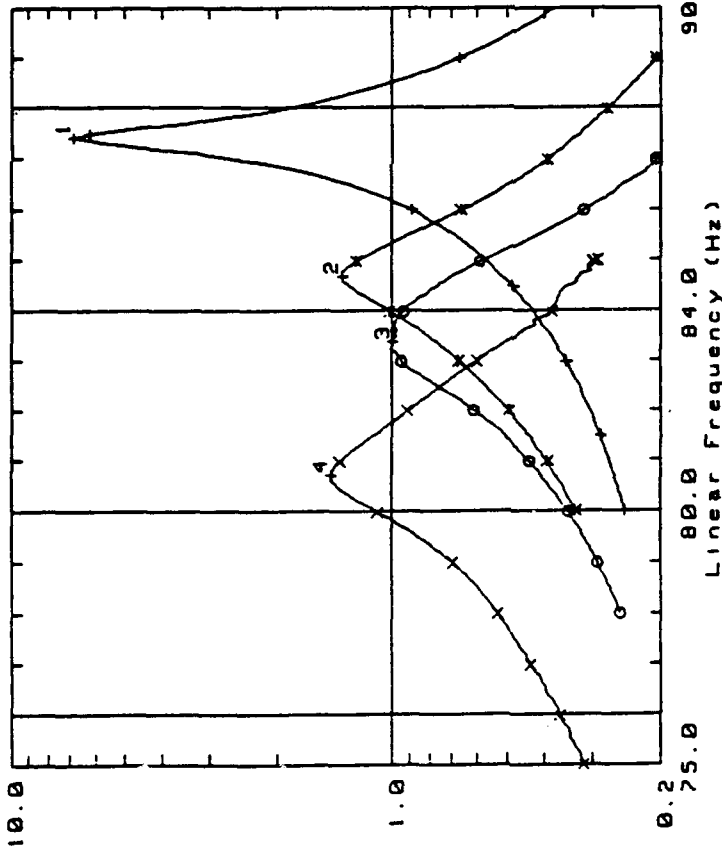
RANDOM  
20 LB-F RMS



35

# ACTIVE / PASSIVE VIBRATION DAMPING

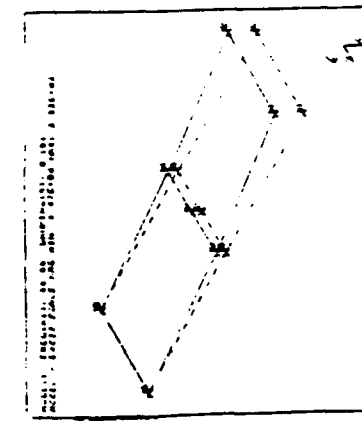
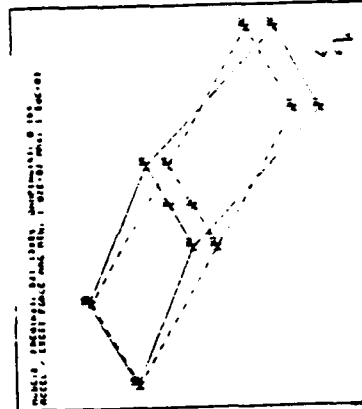
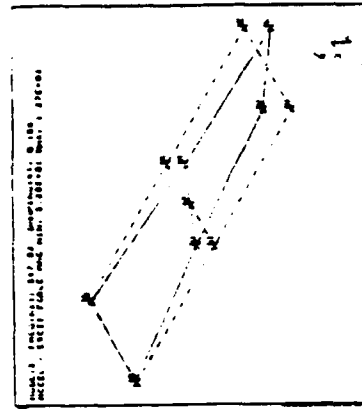
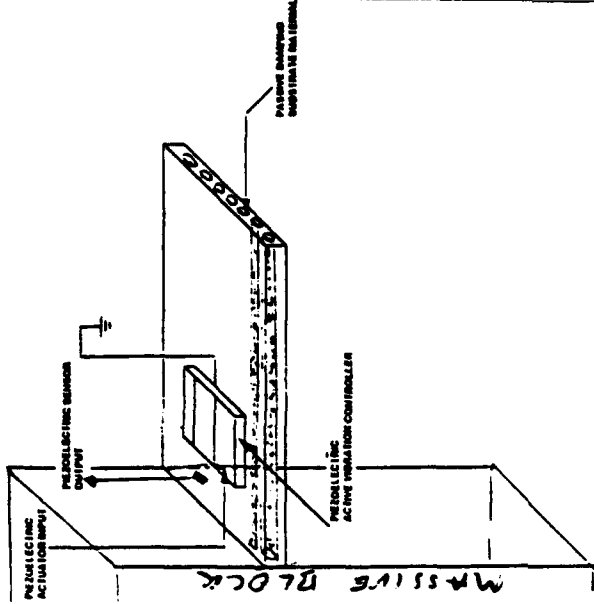
Transmissibility  
CANTILEVERED BEAM TESTING



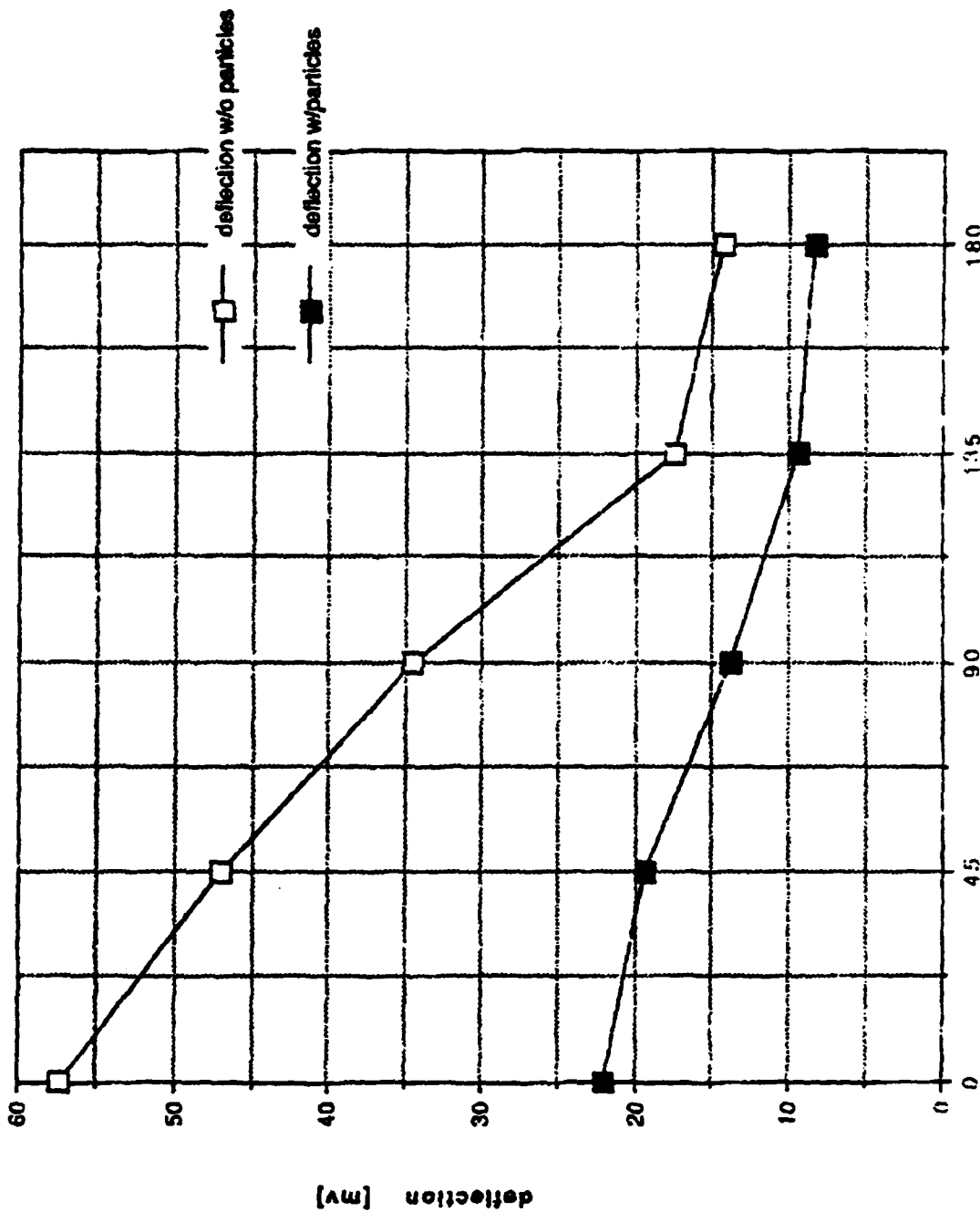
1 0 9 G \ LB

AAB-36

- 1 - EMPTY
  - 2 - LEAD POWDER
  - 3 - LEAD SHOT
  - 4 - TUNGSTEN
- 2 LB SINE
- 1X - 87.4
  - 1Y - 6.9
  - 2X - 84.7
  - 2Y - 1.3
  - 3X - 83.4
  - 3Y - 1.0
  - 4X - 80.7
  - 4Y - 1.4



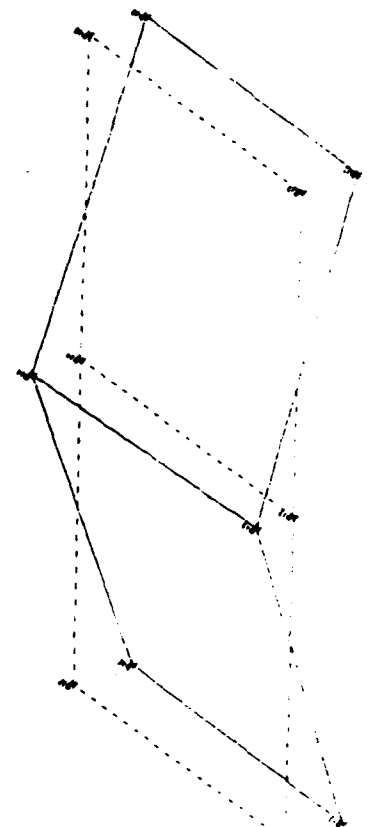
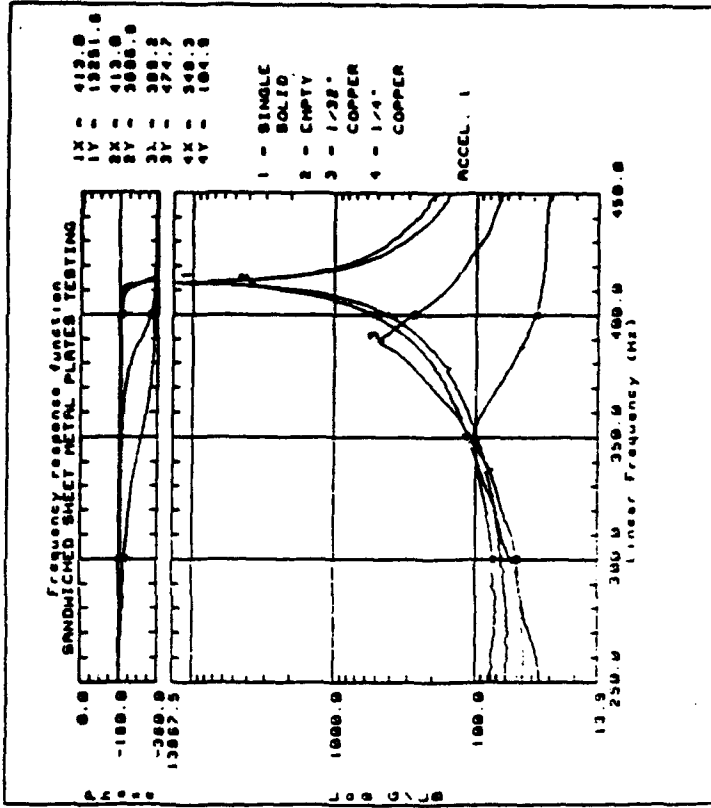
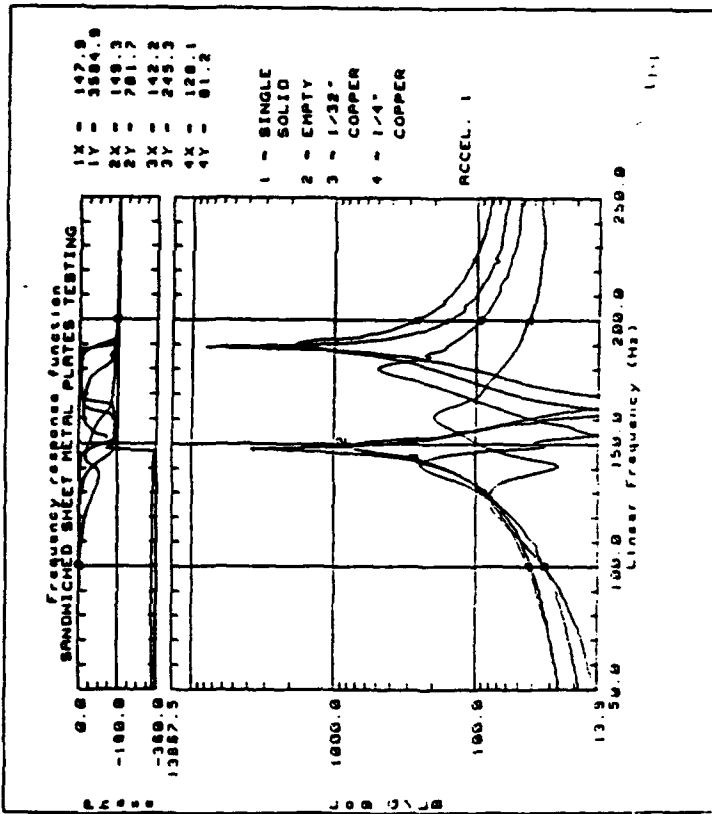
# ACTIVE / PASSIVE VIBRATION DAMPING



Phase difference (between shaker table & piezo plates)

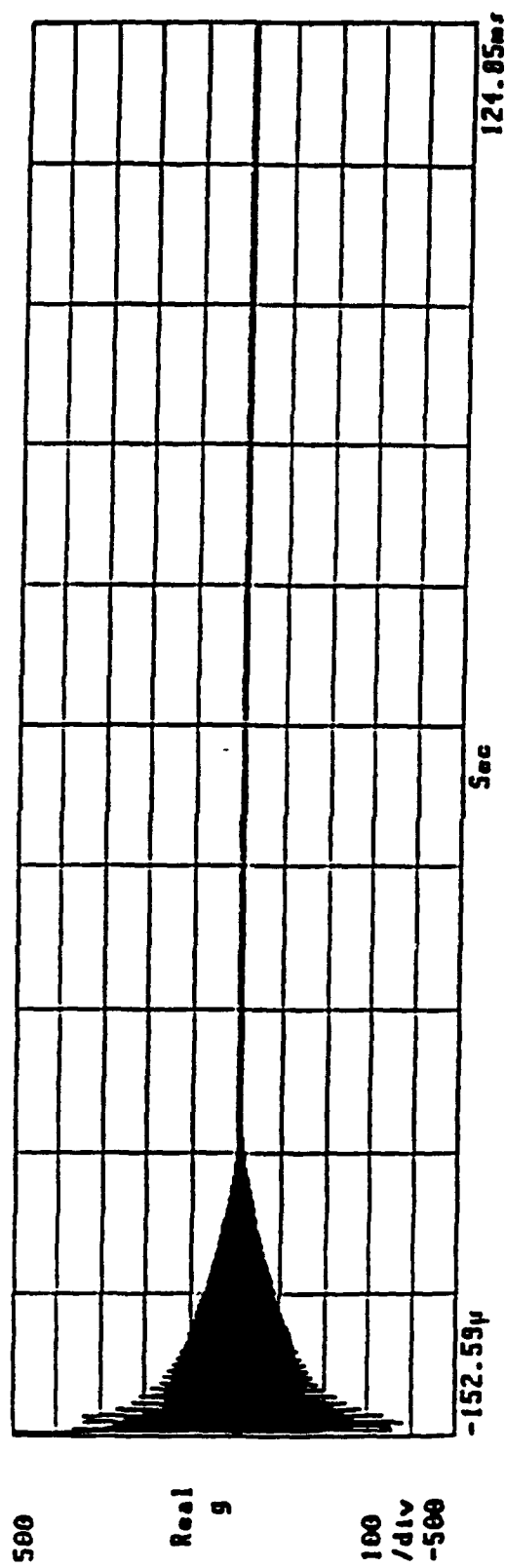
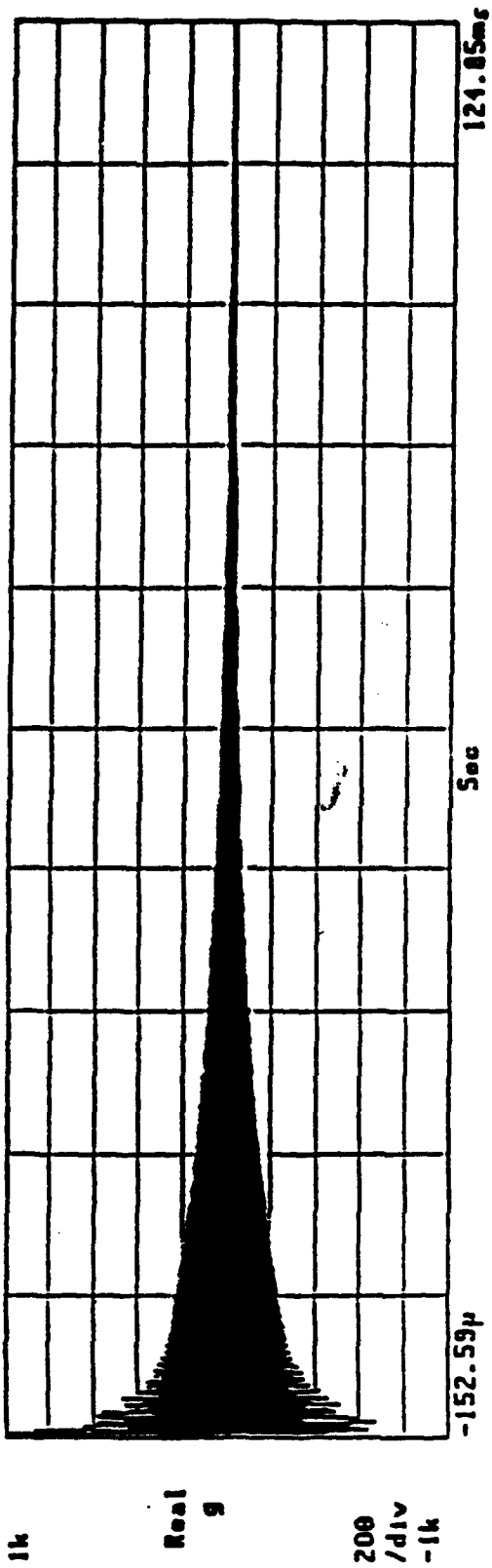
# NON-OBSTRACTIVE PARTICLE DAMPING

## SANDWICHING PARTICLES BETWEEN PLATES



 Rockwell International  
Rocketdyne Division

# TIME HISTORIES OF SILICON NITRIDE COMPOSITES WITH AND WITHOUT NOPD

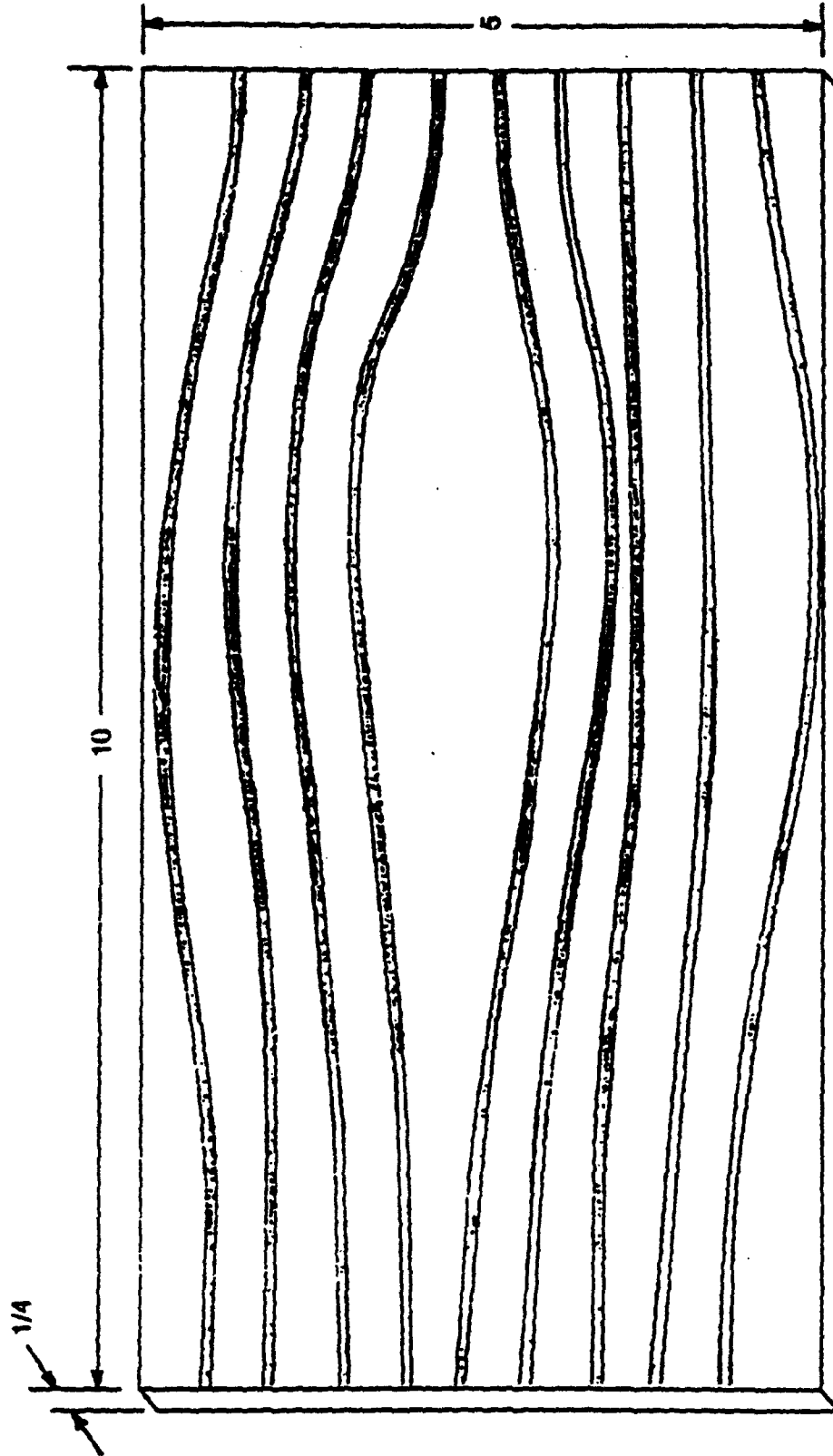


AAB-39

# **ABILITY TO CAST IN PLACE NOPD PARTICLES UNDER EVALUATION**

- Inco 718 plates cast - tubes protruding
- Use stainless steel tubes - warpage occurred
- Use quartz tubes - results excellent
- Does not eliminate the need for close-out
  
- Inco 718 plates cast - fully embedded tube grid with particles
- Stainless steel tubes
- No warpage
- Test results promising

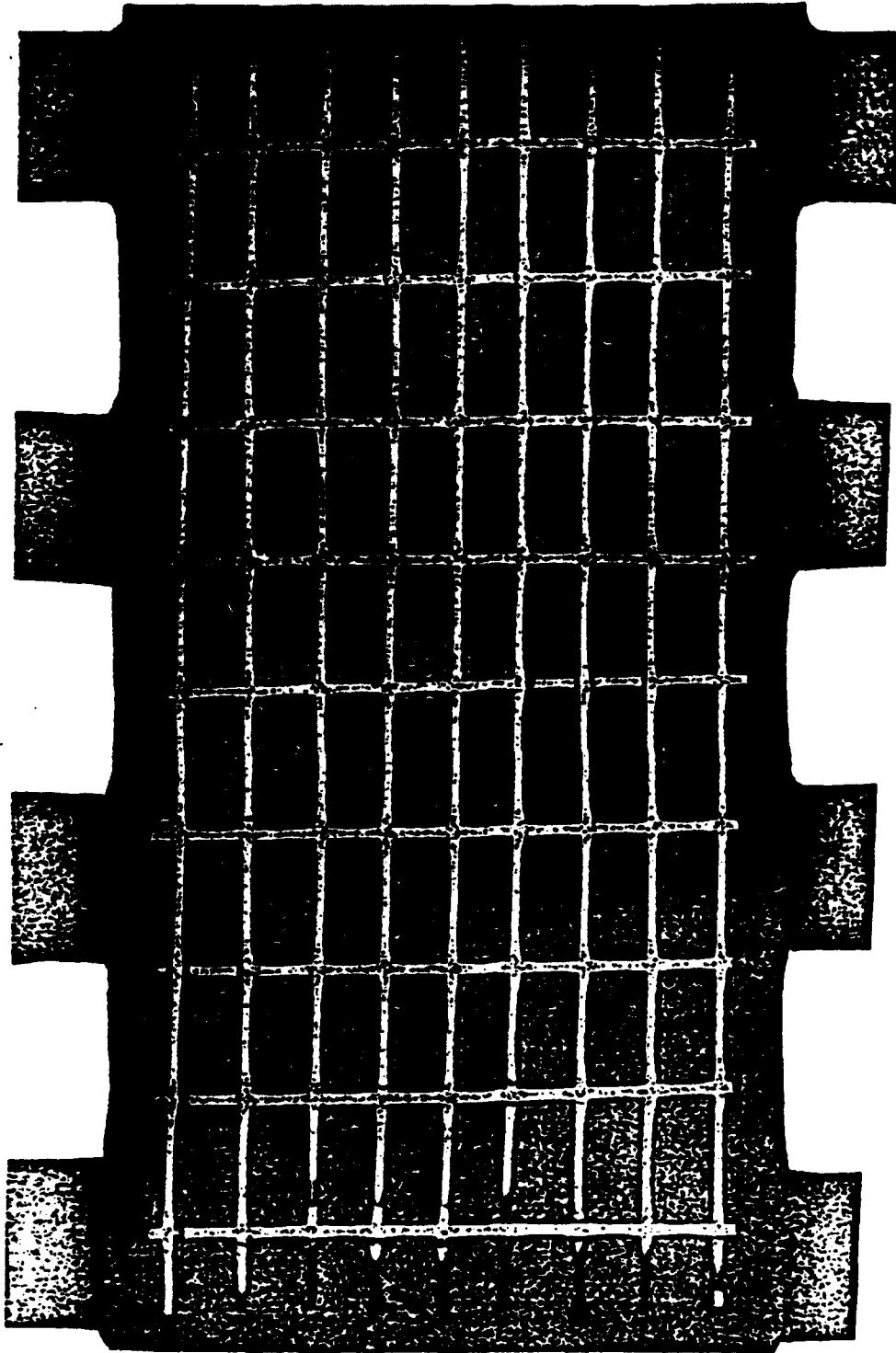
# EMBEDDED STAINLESS STEEL TUBES IN PLATE



Dimensions are in inches

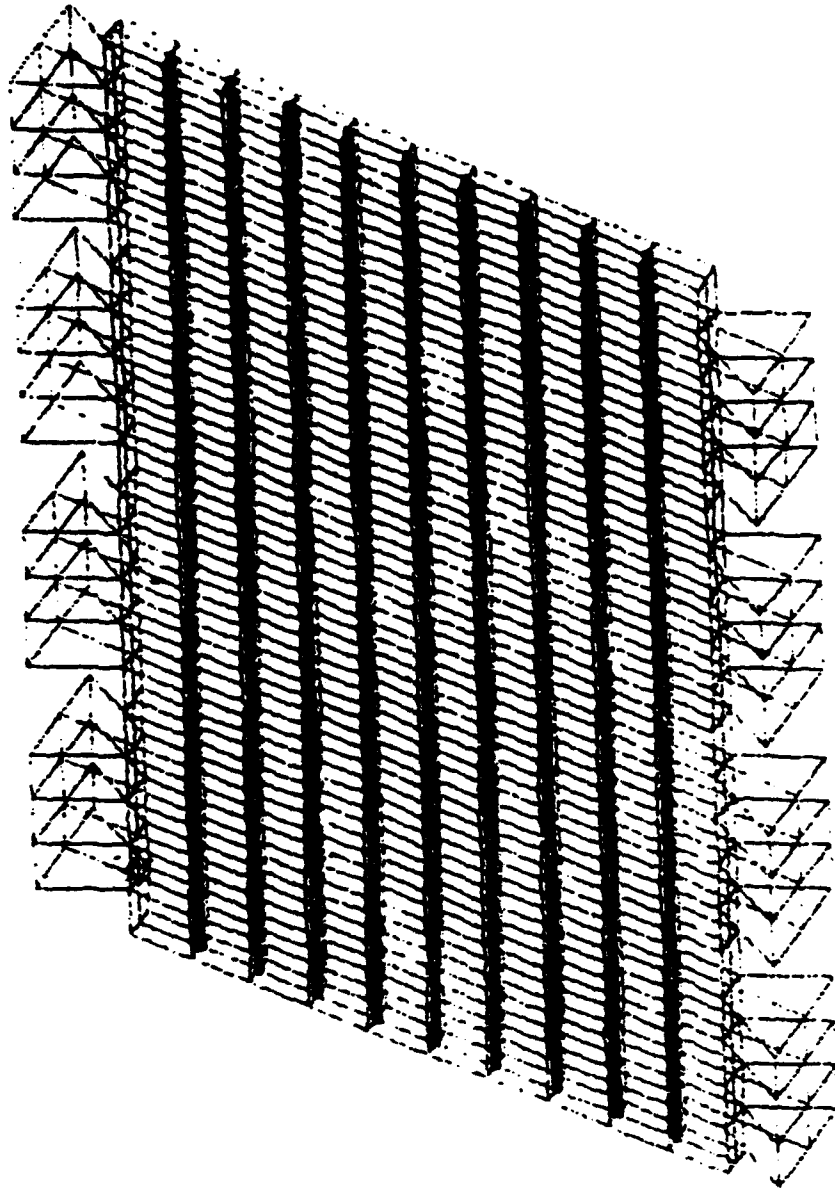
AAB-41

# GRID OF TUBES EMBEDDED IN PLATE



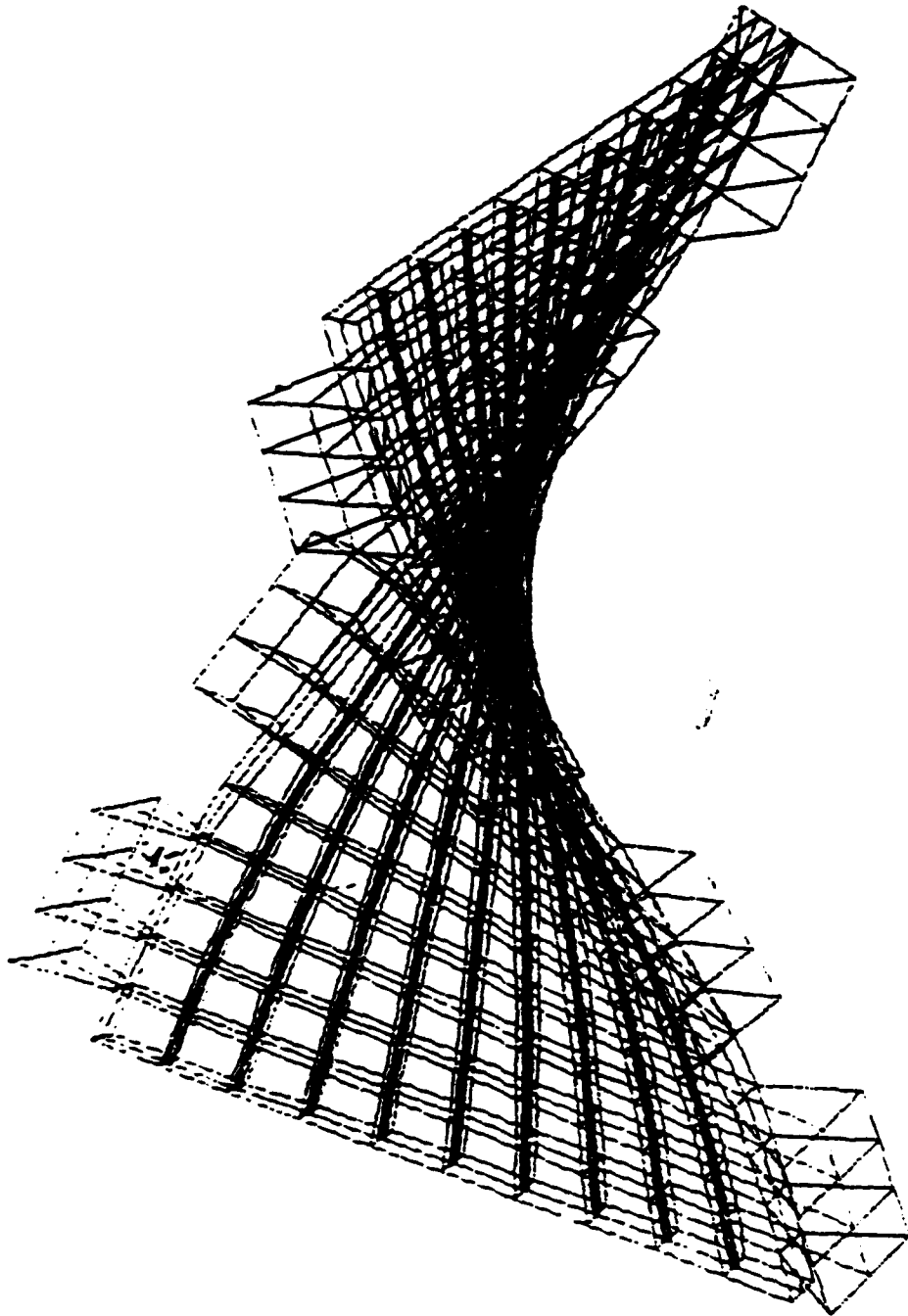
AAB-42

# FINITE ELEMENT MODEL OF PLATE WITH TUBES



AAB-43

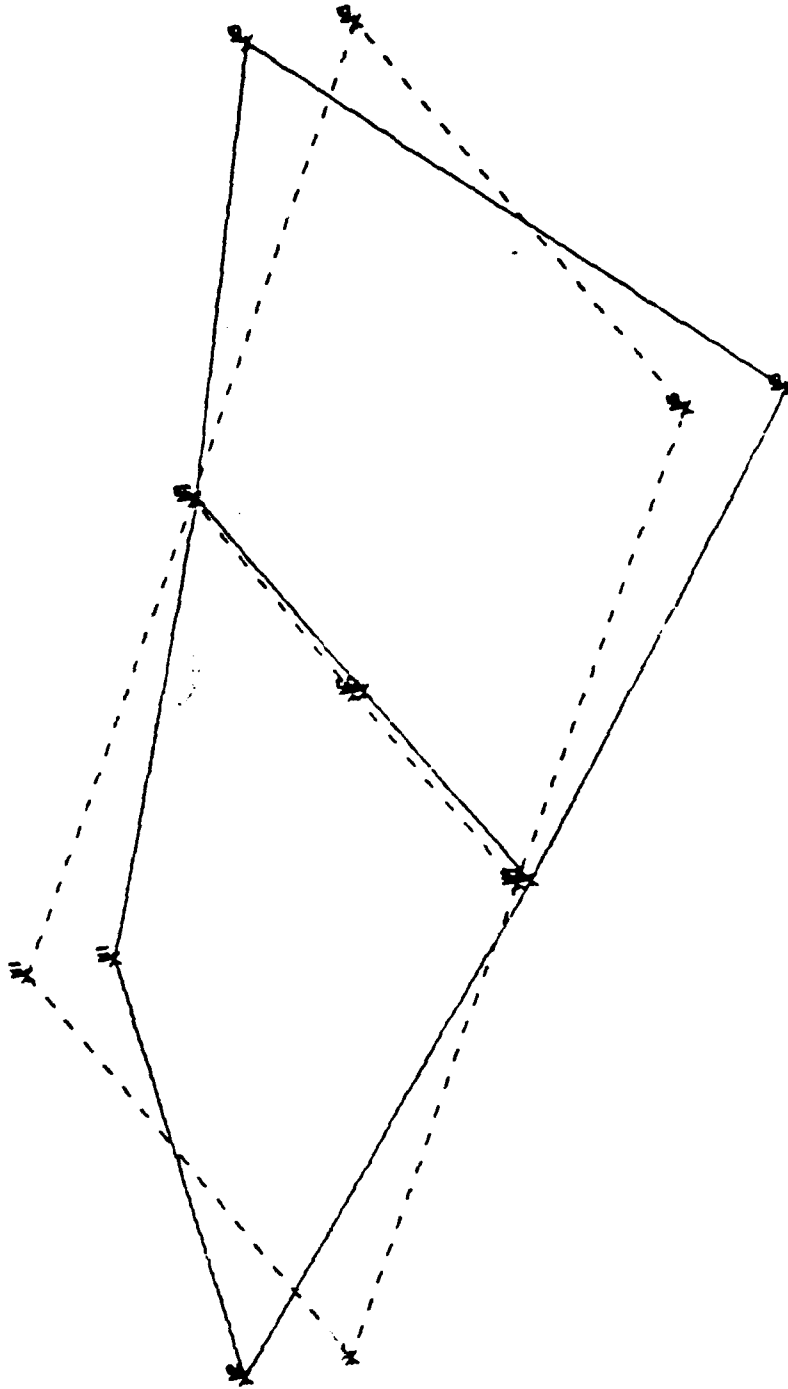
# FIRST TORSIONAL VIBRATION MODE



AAB-44

# FIRST MEASURED VIBRATION MODE (TORSIONAL)

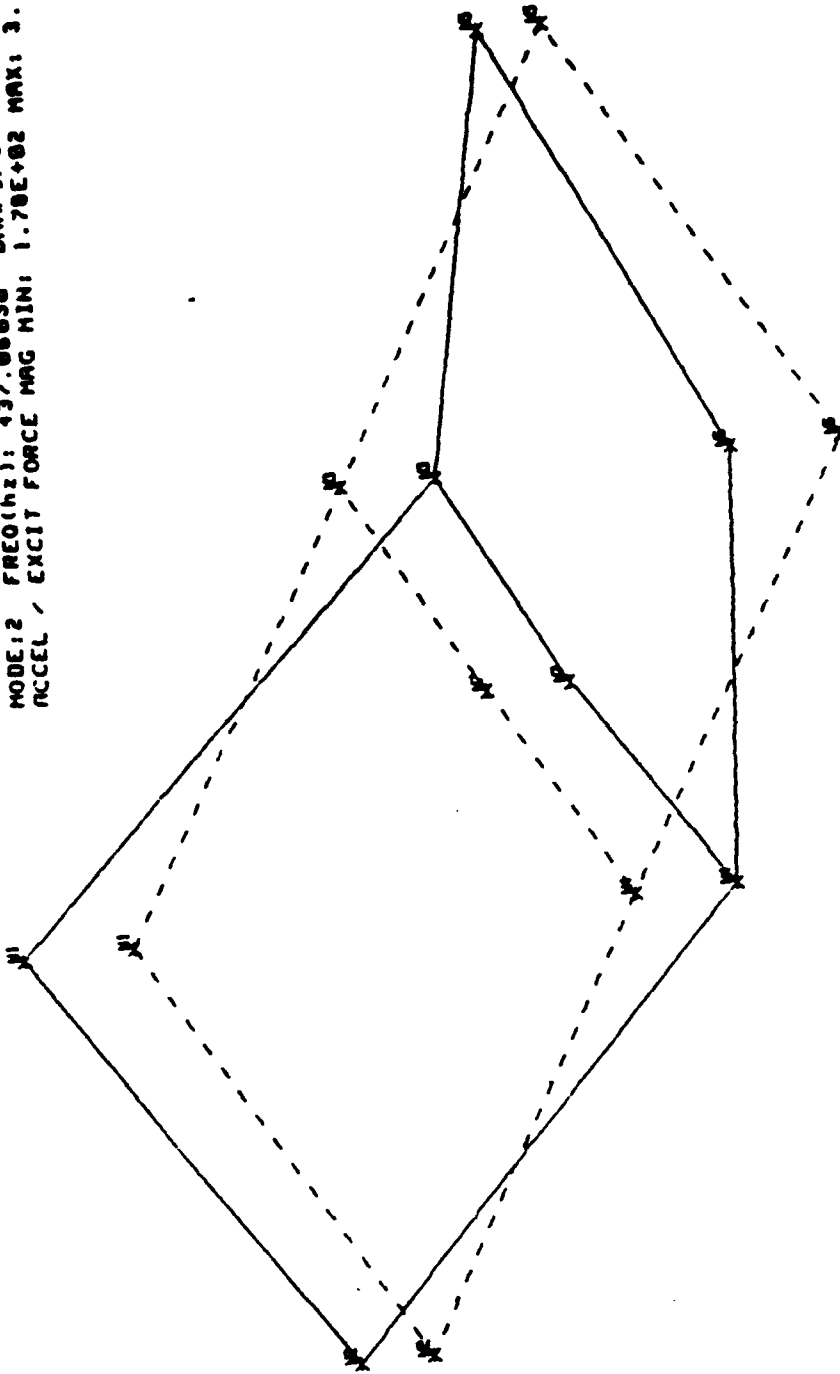
MODE: 1 FREQ(HZ): 487.823 DAMPING(%): 0.1488382  
ACCEL / EXCIT FORCE MAG MIN: 2.41E+00 MAX: 5.10E+01.



AAB-45

# SECOND MEASURED VIBRATION MODE (BENDING)

MODE:2 FREQ(hz): 437.86836 DRMPING(X): 0.17428678  
ACCEL / EXCIT FORCE MAG MIN: 1.78E+02 MAX: 3.10E+02

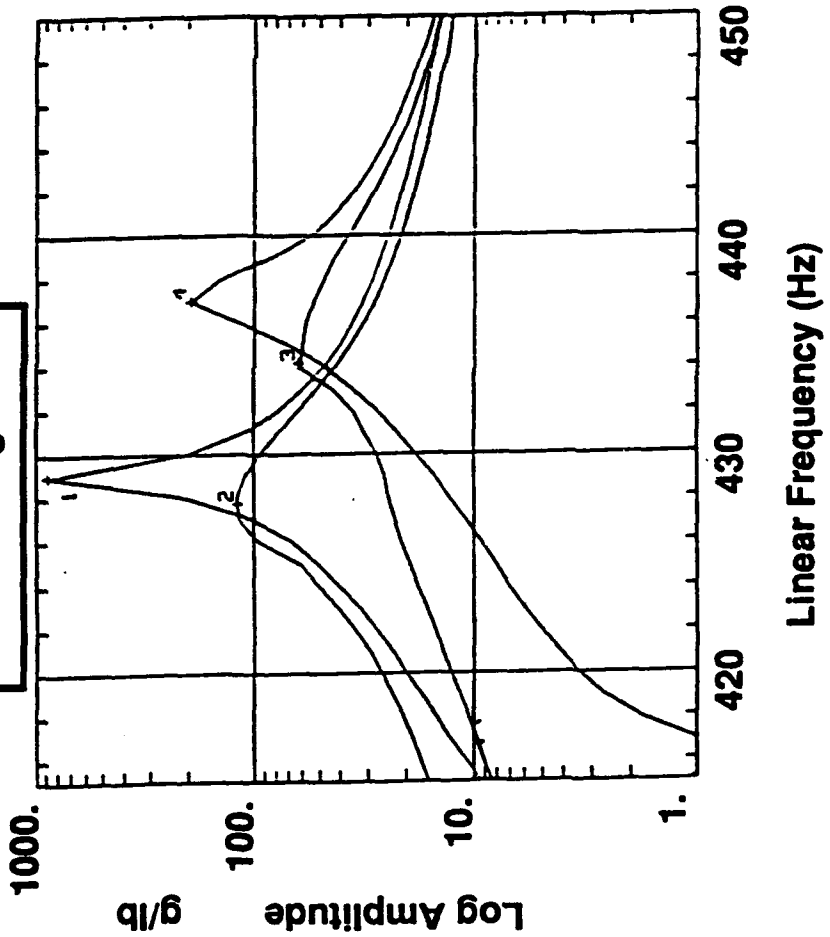


AAB-46

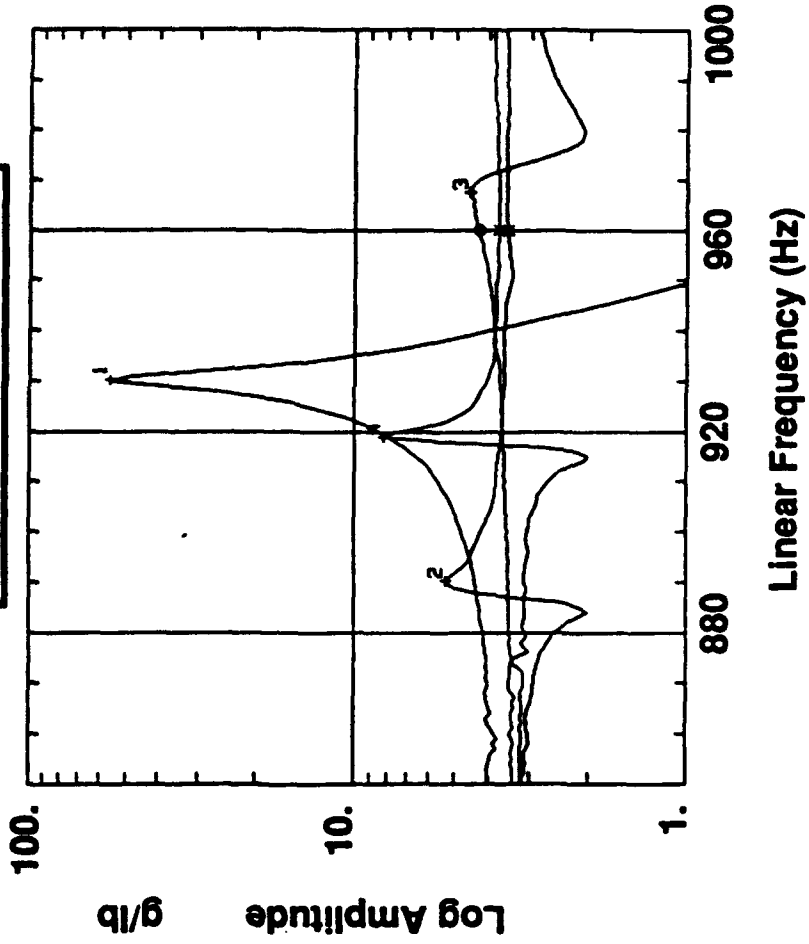
# PLATE VIBRATIONS WITH EMBEDDED NOPD TREATMENTS

- Treatment Type**
1. Solid Plate
  2. Cast Holes
  3. Tubes
  4. Embedded Grid

**First Bending Mode**

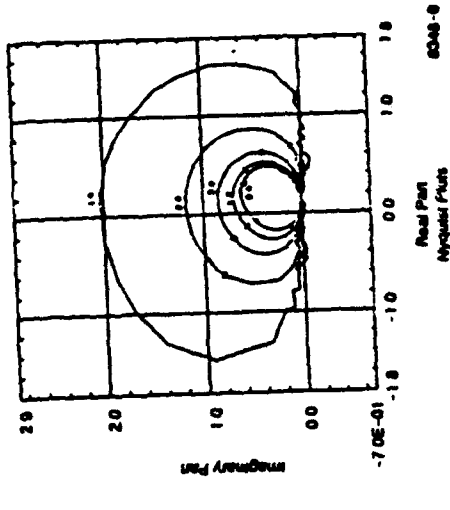
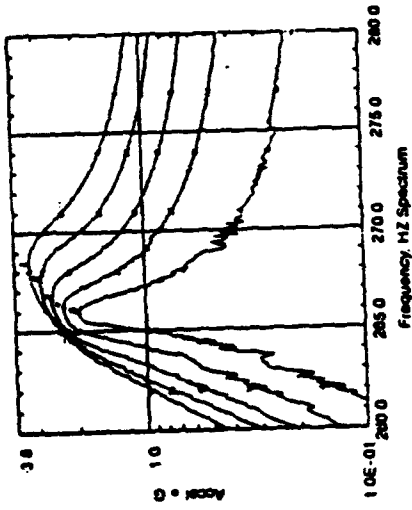


**Second Bending Mode**

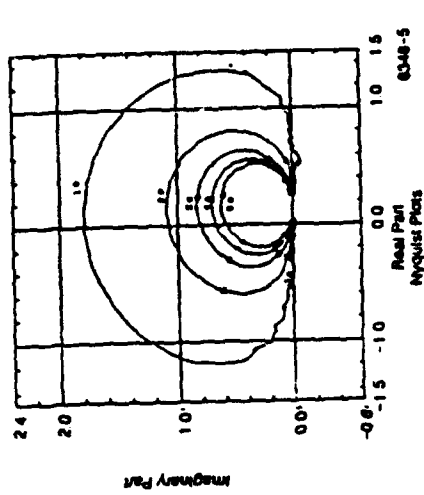
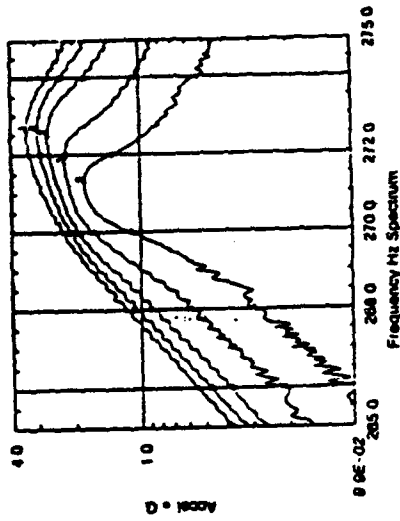


AAB-47

# NOPD NON-LINEARITIES WITH INPUT FORCE

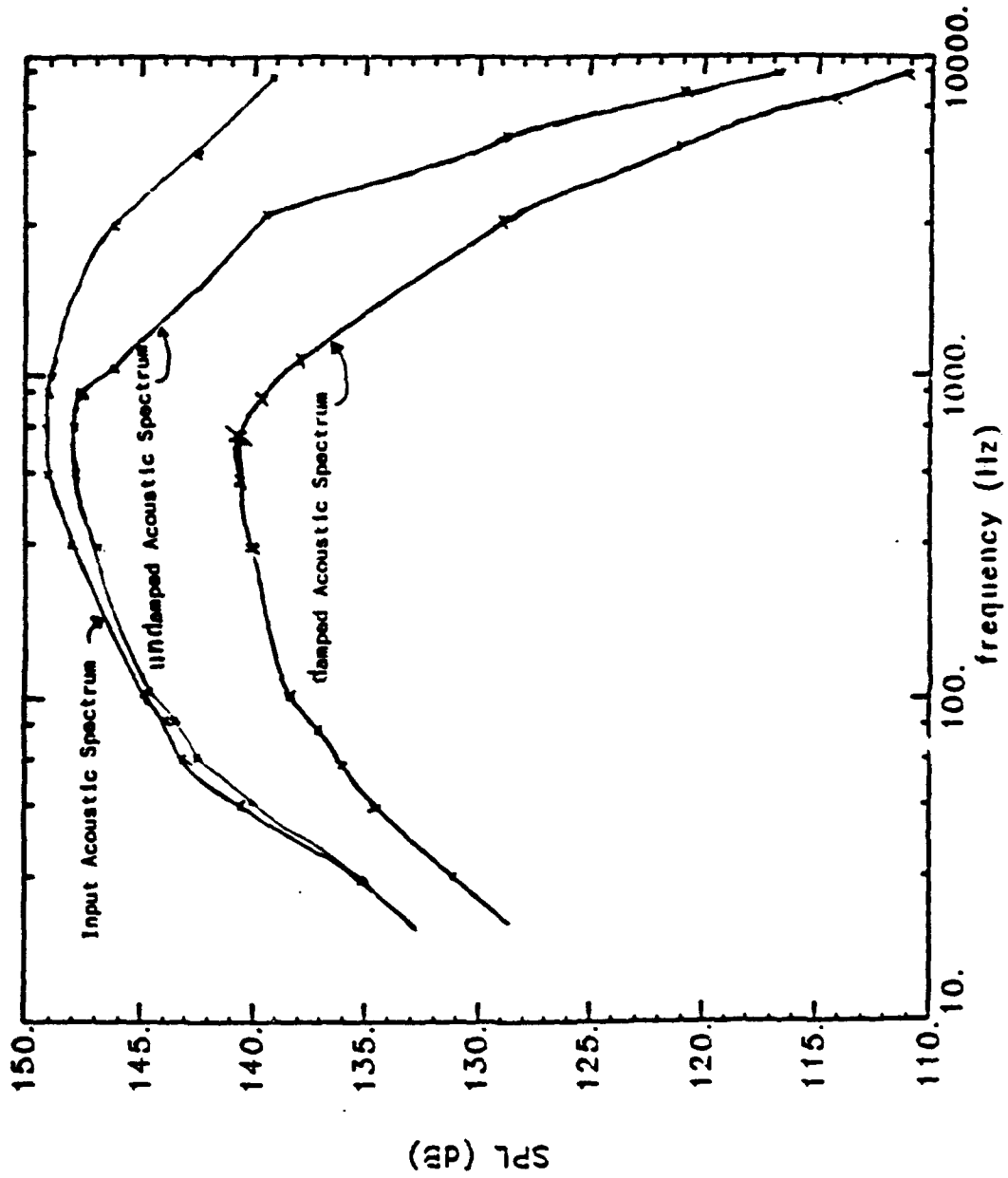


**Free-Free Beam Excitation  
Level Comparisons Under NOPD  
Treatment With Tungsten Powder.**



**Free-Free Beam Excitation  
Level Comparison Under NOPD  
Treatment With 0.011 in. Steel Shots.**

# ANALYTICAL PREDICTION OF NOPD ACOUSTIC PERFORMANCE

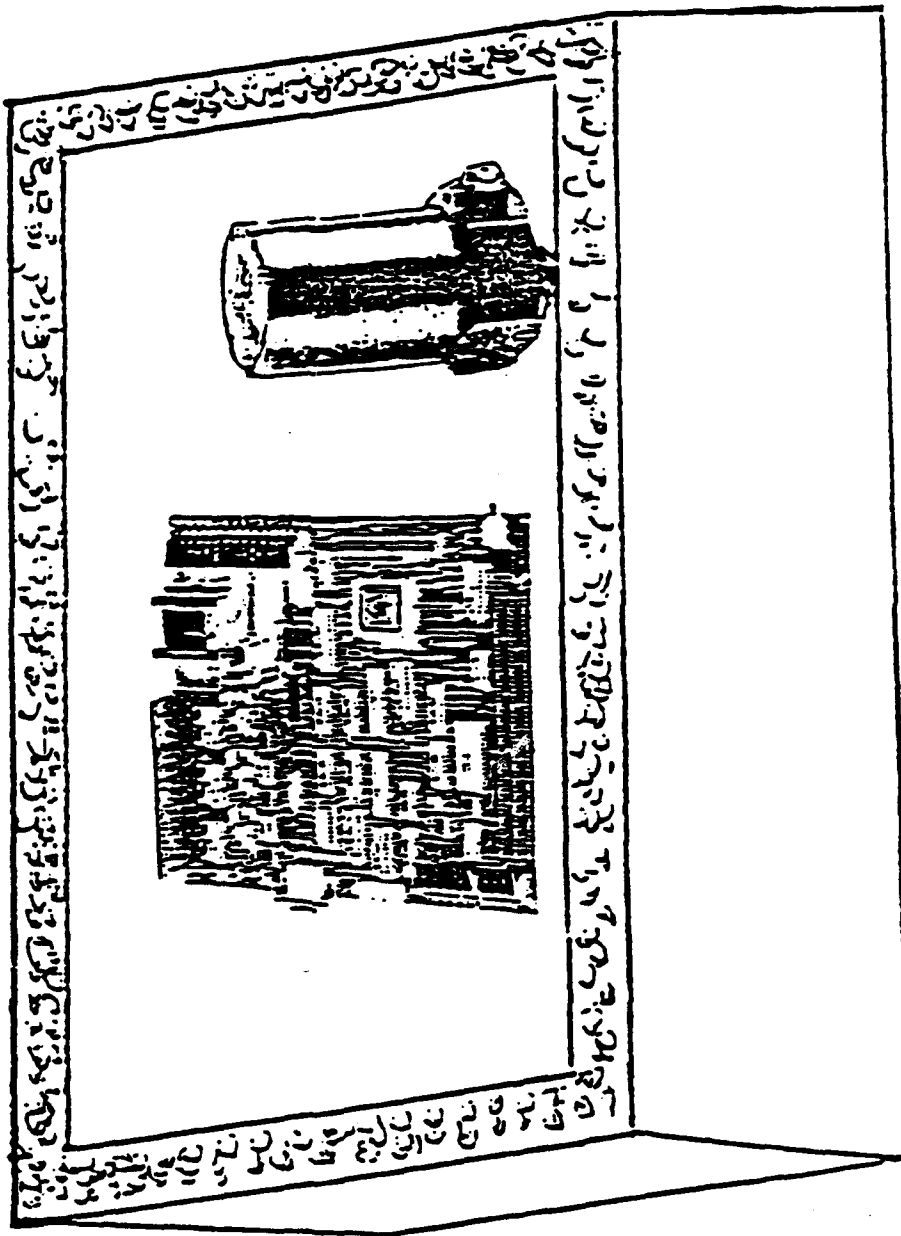


AAB-49

# NOPD CHARACTERISTIC FEATURES QUANTIZED (PRELIMINARY RESULTS)

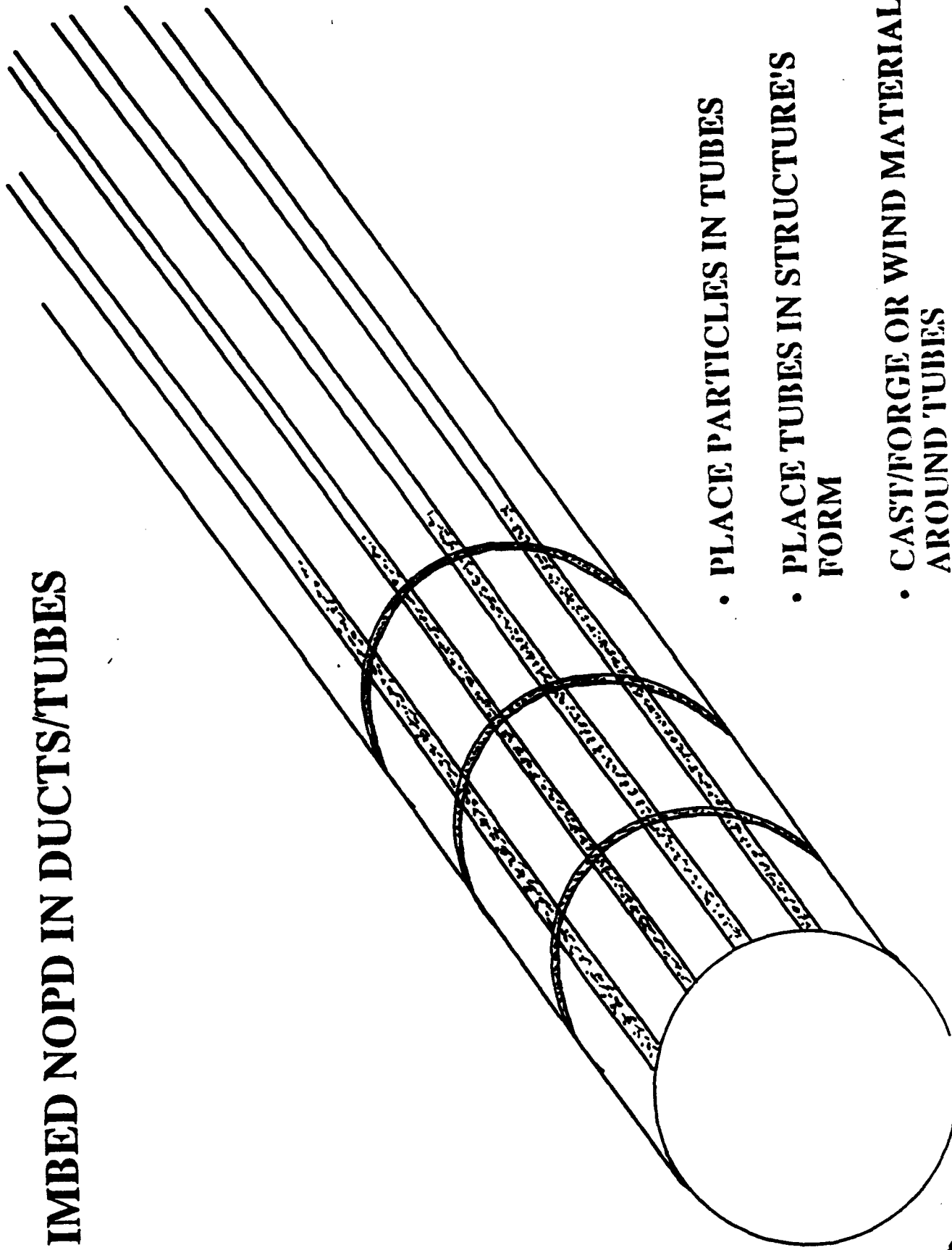
NOPD PARAMETERS	FREQUENCY	FORCE AMPLITUDE	VIBRATION MODE	VIBRATION ENVIRONMENT	STRUCTURE
PARTICLE DENSITY	X	X		X	
PARTICLE SHAPE					
PARTICLE SIZE	X	X			
HOLE LOCATION			X		X
RELATIVE MASS	X	X	X		X
HOLE SIZE	X				X
FILL LEVEL		X	X	X	

# PARTICLES FOR ACOUSTIC ISOLATION



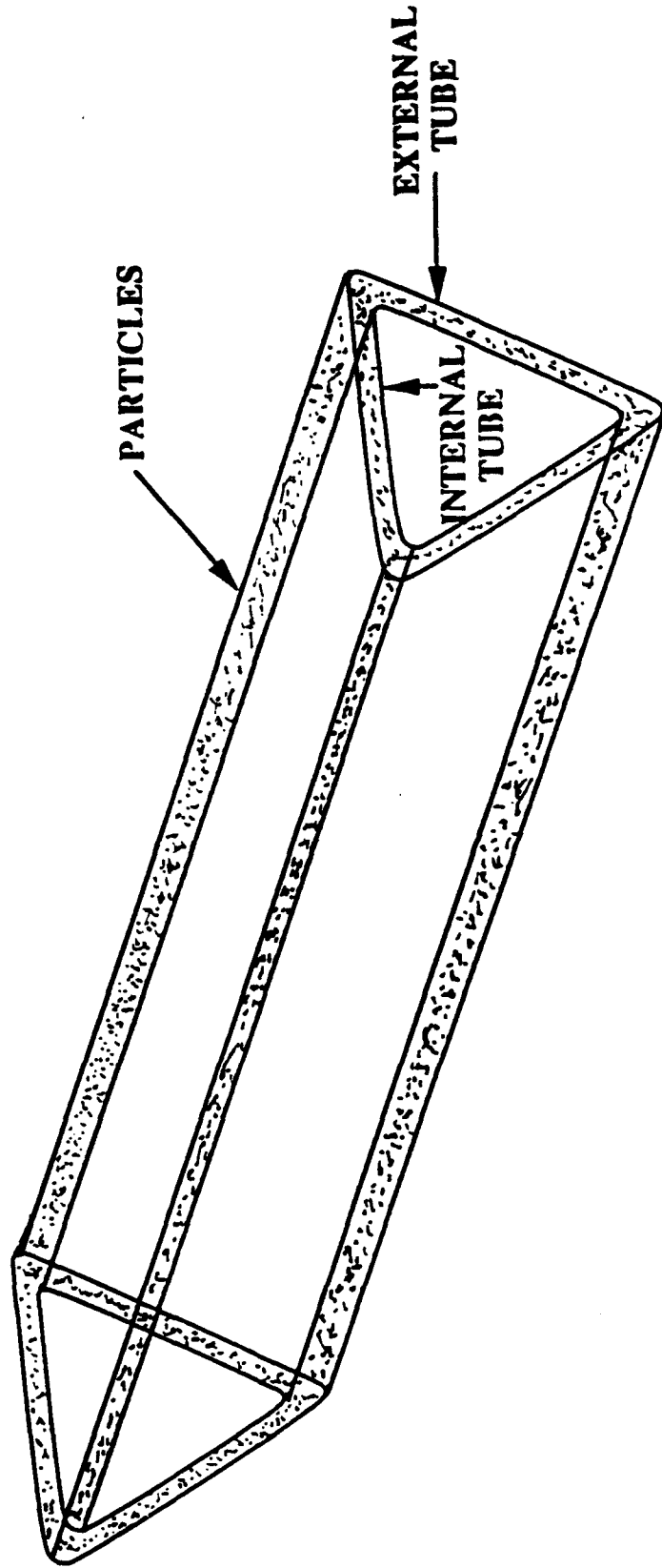
AAB-51

# IMBED NODP IN DUCTS/TUBES



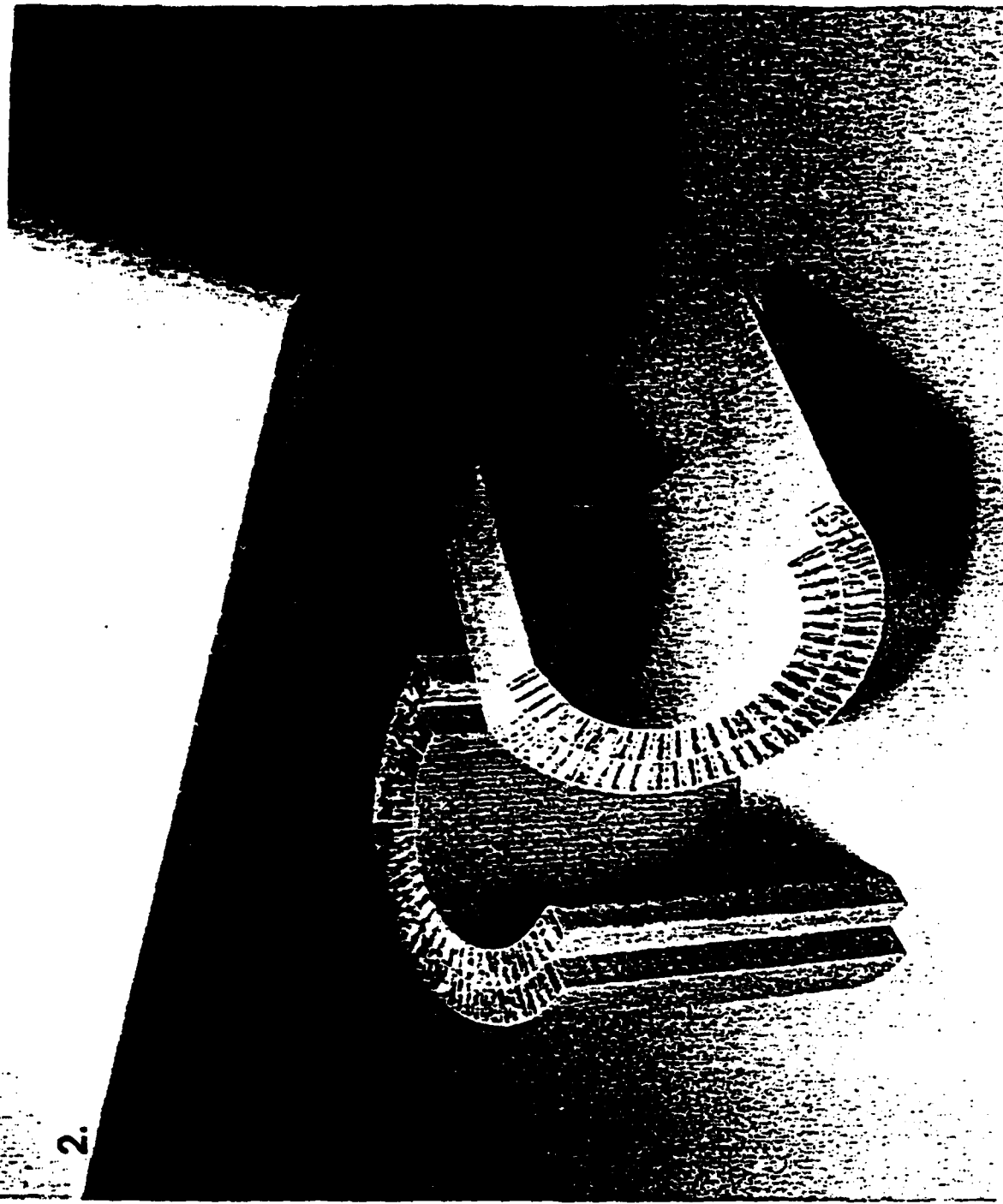
- PLACE PARTICLES IN TUBES
- PLACE TUBES IN STRUCTURE'S FORM
- CAST/FORGE OR WIND MATERIAL AROUND TUBES

**HIGH STIFFNESS/HIGH DAMPING TRIANGULAR CROSSSECTION  
DOUBLE-WALLED TUBES SANDWICHED WITH PARTICLES**



AAB-53

**HONEYCOMB/COMPOSITE STRUCTURES IDEAL FOR NOPD**



2.

AAB-54

**COMPOSITE SYSTEM**



Buckwell International

Buckwell Division

## CONCLUSIONS

- NOPD is effective, does not degrade in time, and is low cost
- Need to optimize damping through analysis for best location and size of holes and kind, size, shape and fill level of particles
- NOPD is easy to apply, does not add mass and seems environment independent
- Numerous applications of NOPD need to be explored
- Concerns for stress concentration can be minimized by appropriate design and manufacturing process

# **NOPD CHALLENGES**

- **Effects of material; shape, density, frequency range, amplitude, etc.**
- **Characterization and modeling of damping phenomenon of particles**
- **Environmental insensitivity**
- **Minimize stress concentrations created by cavities**
- **Identify damping mechanisms quantitatively**

# **Energy Absorption Due to Cyclic Deformation of Shape Memory Alloys**

by

Darel E. Hodgson  
E\*Sorb Systems

## **ABSTRACT**

The microstructural processes which absorb energy during the deformation of Shape Memory Alloys (SMA's) are markedly different than those occurring during the deformation of "normal" metals. In SMA's, two different processes can absorb energy. One is a very low strain, lattice softening effect which occurs only very near the transformation temperature. The other is due to the friction of creating and moving martensite platelets and occurs over a wide temperature range at significant deformations. Neither of these energy absorbing mechanisms creates permanent damage in the alloys, though, so no work hardening occurs. Also, the martensite platelet movement is limited in extent and allows only a few percent of deformation strain. Thus, the SMA tends to limit the strain that it undergoes during energy absorption.

---

1034 W. Maude Ave., Suite 603, Sunnyvale, CA 94086, (408) 730-5633

## INTRODUCTION:

The Shape Memory Alloys are a unique class of materials that display a number of dramatic mechanical properties due to the crystallographic transformation they undergo. This thermoelastic martensitic transformation from a higher temperature austenite to a lower temperature martensite changes the material reversibly from a cubic structure to a monoclinic phase. The martensite is composed of alternate twin bands and when examined microscopically has an "herringbone" appearance. The transformation change is shown schematically in Figure 1. The transformation

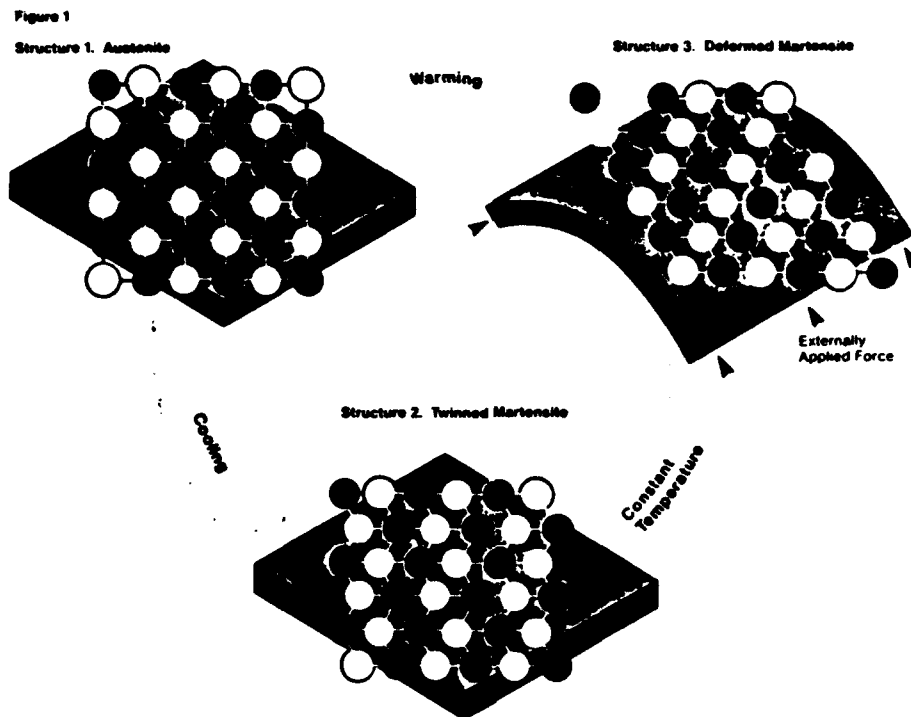


Figure 1. Schematic of Austenite ↔ Martensite Transformation in Shape Memory Alloys.

temperature can be adjusted for any alloy over a wide range of temperature by slight changes in the composition or changes in thermomechanical processing. In any case, the higher temperature cubic phase tends to be strong and to deform by normal dislocation processes which are irreversible. The martensitic phase, however, can be deformed up to several percent strain by changing the sense, or 'tilt' of some of the martensitic twin platelets. The strain absorbed by the structure due to changing the orientation of some of the twins can be eliminated by transforming all of the twinned material back to the parent austenite. This is called the Shape Memory Effect (SME).

The uniaxial stress-strain curves of a typical Shape Memory Alloy (SMA) above and below its Transformation Temperature (TTR) are shown in Figure 2. Because the phase transformation is thermoelastic, it can be stress induced as well as thermally induced<sup>2</sup>. This means that by applying the appropriate stress at a temperature somewhat above the TTR, one can form stress induced martensite which is strained as it forms. This martensite is not thermally stable at that temperature, though, so upon reduction of the stress the material will revert to austenite and 'unstrain' at a reversion stress<sup>3</sup>. This is shown in Figure 3.

Over twenty different alloy systems have been shown to exhibit the Shape Memory Effect<sup>4</sup>. Most are very narrow in compositional range because the basic composition which displays SME is an intermetallic compound, and most are composed of exotic metals and have minimal ductility or high cost. Three systems have found wide commercial application, however. These are the Nickel-Titanium based alloys and the copper based alloys, CuZnAl and CuAlNi.

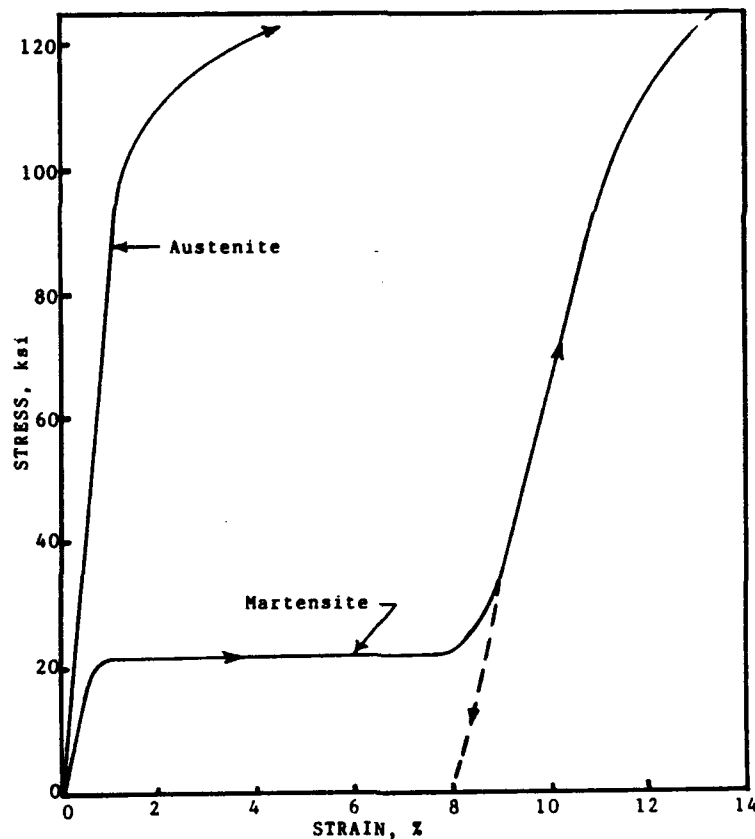


Figure 2. Typical Stress-Strain curves of NiTi Shape Memory Alloy above (Austenite) and below (Martensite) its Transformation Temperature (TTR).

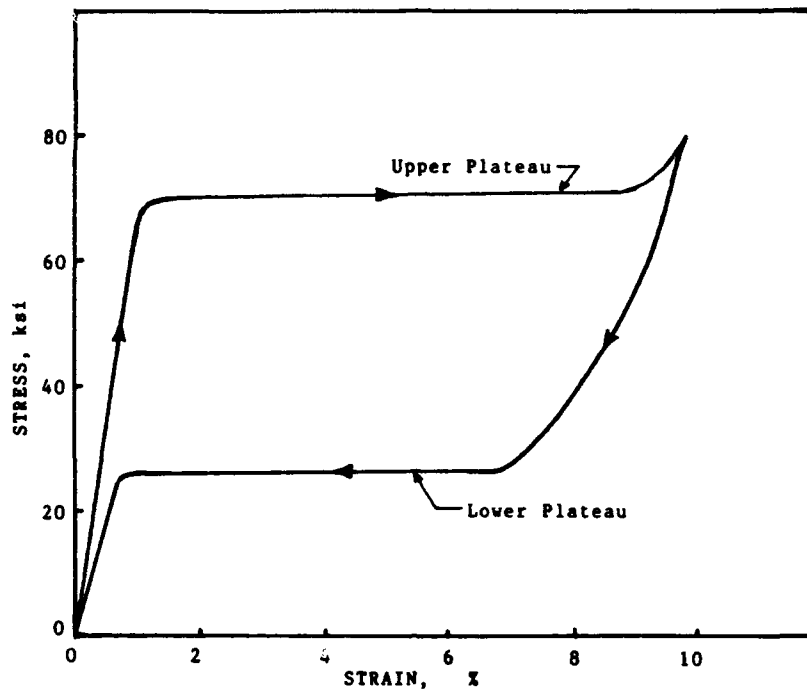


Figure 3. Stress-Strain behavior in uniaxial tension of the Stress Induced Martensite in NiTi Superelastic Alloy.

There are three specific damping mechanisms in the SMA's, and some discussion of the microstructural basis for each will be presented. If the strain amplitude is very low, and the temperature is very near TTR, an extreme internal friction peak is found due to lattice changes associated with the crystal phase change. If one strains the martensitic material at a temperature where it is stable, several percent deformation can be absorbed merely by shifting of twin orientations with no permanent damage being done to the material. Finally, stress inducing martensite at a temperature above the TTR will require a large amount of work and only a portion of that work will be returned when the material reverts to austenite, thus absorbing work in the alloy.

### LOW STRAIN DAMPING NEAR TTR

When an SMA is cooled toward its TTR, it reaches a point where the lattice is on the verge of transforming to martensite but has not yet transformed. The crystal structure is near instability, and dramatic 'lattice softening' occurs<sup>5</sup>. This takes the form of a sharp minimum in the elastic modulus and a hundredfold increase in the internal friction at temperatures very near the transformation. One can see this in Figure 4, where the elastic behavior is evidenced by the change in vibration period and the internal friction by the logarithmic decrement measurement from a torsional pendulum. The mechanistic basis for these changes is likely microscopic creation and

elimination of nuclei of the incipient phase or localized movements of twin boundaries over a few atom distances. In either case, the effect is large only in a narrow temperature range near the TTR, and utilizing it demands service conditions that don't vary by more than about 10°C from TTR. In that range, though, some SMAs have extraordinary damping against small amplitude and higher frequency vibrations.

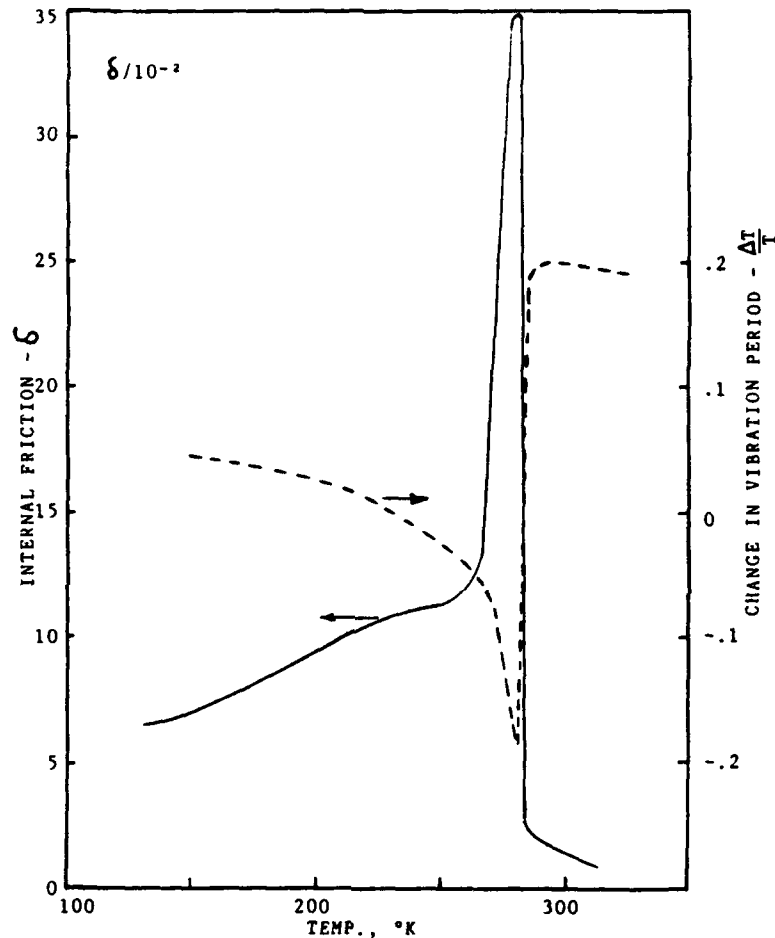


Figure 4. Internal friction,  $\delta$ , and  $\frac{\Delta T}{T}$ , the change in vibration period, versus temperature for a CuZnAl Shape Memory Alloy at TTR.

## DAMPING BY DEFORMATION OF THE MARTENSITE

If an SMA is in its martensitic condition, it can absorb shear strains up to several percent by the annihilation of some twin variants and the increase or creation of others. Reversing this shear strain will recreate the original mix of twin variants, and continuing the shear strain in the opposite direction will lead to twin variants of another sense altogether which accommodate that strain. There is an inherent resistance in

the structure to movement of these twin boundaries, however, so significant energy is absorbed in the SMA as the twin variants are created and annihilated<sup>6</sup>. If the stress-strain curve of the martensite shown in Figure 2 is extended into the other quadrants, we find an idealized behavior such as that shown in Figure 5.

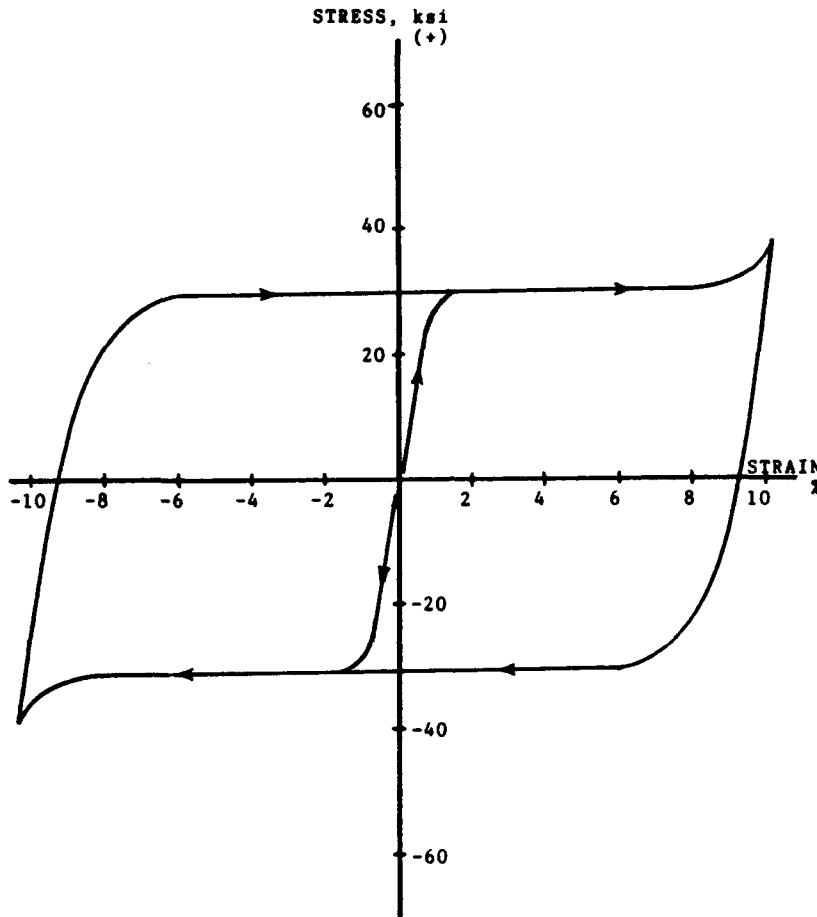


Figure 5. Four quadrant Stress-Strain behavior of the Martensite Phase in NiTi Shape Memory Alloy.

There are several features of Figure 5 which merit comment. The range of strain which can be accommodated by the SMA member is determined largely by which SMA alloy system is considered. For instance, the range with Nickel Titanium alloys is of the order of  $\pm 8\%$ , while with the copper based materials it is about half as much. Also, the range is changed somewhat by thermomechanical processing which may be used to optimize other aspects of the material's behavior. The height of the stress plateaus is also alloy system dependent, but different compositions and processing can have an even larger effect. In NiTi, for instance, the flat plateau may be from less than 10ksi to nearly 50ksi depending on small alloy variations and processing history. In the copper-based alloys, similar changes occur, plus the plateaus tend to be quite

sloped instead of flat. As shown in the figure, both the tension and compression quadrants are similar. In reality, there are some differences and these again rely on alloy and history variations. If one extends the strain beyond the range shown as plateaus, one finds one of the most desirable features of the SMA damping materials. Referring back to Figure 2, one sees that strain beyond the plateau will quickly increase the stress supported by the SMA material. In properly treated NiTi alloys, the increase in stress above the plateau level before one encounters significant permanent deformation (by dislocation processes) may be as great as ten times the plateau stress. This allows the designer a tremendous safety margin where he can use the SMA component to strain and absorb energy at a particular stress, but then act as its own safety element to prevent permanent deformation or fracture at significant overloads. Likely the most appealing feature of SMA material used to damp by deformation of the martensite is that the deformation process is non-damaging to the material. Because the movement of the twins occurs without dislocation motion or permanent slip processes within the microstructure, the reverse straining can occur innumerable times with minimal change in the material. This is in contrast to such materials as mild steel, for instance, where relatively few cycles to moderate strain will work harden the material to a point where it no longer absorbs the same amount of energy or may be subject to failure. Also, because the movement of the twin interfaces occurs on such a microscopic scale and is mostly stress dependent, the damping is nearly frequency independent throughout the realm of interest. It is possible with sufficient strain and cycling rate to heat the SMA internally to a level that might cause it to exceed its TTR, but this likely can be overcome with heat dissipation techniques.

### **DAMPING BY DEFORMATION OF SUPERELASTIC MATERIAL**

The third method by which deformation energy can be absorbed in an SMA material is to create stress induced martensite and then allow it to revert to austenite. This is different than merely moving different twin variants as in the previous section, because the martensite phase is created and disappears during each strain cycle. An idealized stress-strain curve such as shown in Figure 3 results from this process, and if carried into the four quadrants we find that behavior like that in Figure 6 results. The reason that the martensite is formed when stress is applied to the system is that the system will try to accommodate an applied stress, and it can do this by converting to the martensite and simultaneously deforming to the most favorable twin variant to absorb strain. The stress at which the martensite is formed is the 'upper plateau stress', and varies linearly with increasing temperature<sup>2</sup>. This stress induced martensite is not thermally stable, however, and as the stress is reduced it will revert to austenite, with elimination of the strain, at the 'lower plateau stress'. The difference between the stress level of the two plateaus is the stress hysteresis, and multiplied by the strain absorbed by the SMA element is a measure of the energy absorbed in the element during the strain cycle. Similar to the behavior of the deformed martensites in the previous section, the compression behavior is often found to be somewhat different from the tension behavior, alloy and processing variables have a large influence on the stresses and strains encountered, and the straining process is not damaging to the material so it can be repeated indefinitely. Also, internal heating of the SMA can occur

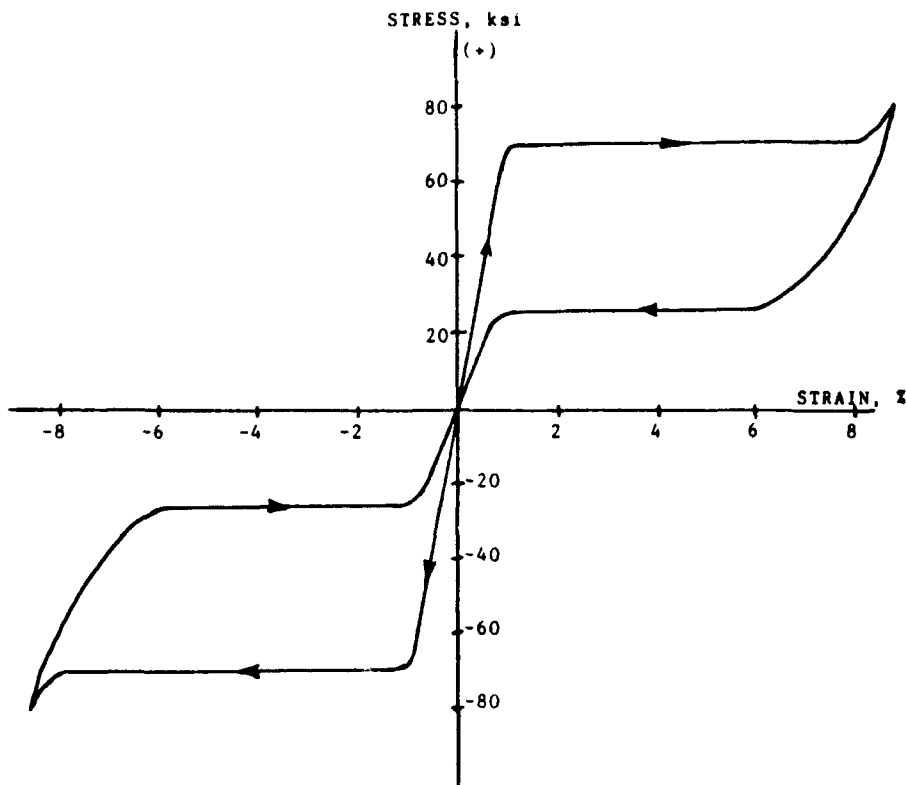


Figure 6 . Four Quadrant Stress-Strain behavior of the Stress Induced Martensite in NiTi Superelastic Alloy.

by sufficient strain and rapid cycling, but heat dissipation can usually be accomplished readily. In contrast to deforming martensite, though, we find that as the applied stress is reduced the SMA reverts to austenite and returns to its original shape at a significant stress. While the martensitic material stays in whatever shape one leaves it, the Superelastic material exerts considerable stress to return itself (and the structure) to original shape. This can be used advantageously in design.

## DAMPING DEVICE IMPLICATIONS

As there are three distinctly different realms of damping behavior in the Shape Memory Alloys, there are three different types of damping elements implied.

In the small strain region very near the TTR, SMAs make excellent sound dampers or higher frequency vibration deadeners due to their extreme internal friction peak. Contrary to a material like lead, they have significant structural strength and physical robustness. They are much more expensive, and have a narrow temperature range for optimum performance.

If the SMAs are used in their martensitic region, they can be used as elements to absorb large strains in tension, compression or torsion. They will absorb significant energy regardless of what type of strain is applied, are frequency and temperature insensitive (within reason), and can be very environmentally rugged. The energy absorbed per cycle is reliable, repeatable and time independent. Designs can be extremely flexible and able to handle whatever strain, stress or deformation mode one needs and components are surprisingly compact.

The mode in which the SMAs appear to have the greatest versatility in damping is in their Superelastic state. Consider, for example, using NiTi wire processed to have the type of stress-strain behavior shown in Figure 3. A damping component designed to use a multitude of wire ligaments in tension can be adjusted for load carrying by the number of wire elements, for the anticipated strain range by the active length of each ligament, and for overall size merely by how the ligaments are packaged. The NiTi wire has a reliable superelastic temperature range of over 100°F, is effectively corrosion proof, cannot leak or degrade in the environment and has an absolutely reliable level of energy absorption per strain cycle. The argument might be made that such a device will only work when stretched from its initial length in tension, so compression damping is inaccessible. Consider, however, if such a device in service had already been prestretched and held in the middle of its plateau strain range. In that case, cyclic motion which either lengthens or shortens the device will cause the SMA material to cycle through the hysteresis region of its stress-strain behavior and absorb energy. Likewise, other types of damping devices which utilize the SMA material can be created to satisfy torsional loading, shear loading and heavy load bearing if needed.

#### REFERENCES

1. Raychem Corporation Brochure, "Shape Memory Metal", Menlo Park, CA, 1981.
2. K. Otsuka and K. Shimizu, Proc. of ICOMAT 1979, Cambridge, MA, 1979, pp 607-618.
3. D.E. Hodgson, "Using Shape Memory Alloys", publ. by Shape Memory Applications, Inc., Sunnyvale, CA, 1988.
4. H. Funakubo, Shape Memory Alloys, Gordon and Breach Science Publishers, New York, 1987.
5. M. Morin, et. al., "Internal Friction of Cu-Zn-Al", Proc. of ICOMAT - '82, Leuven, Belgium, 1982, pp. C4-685-689.
6. L. MacDonald Schetky, "Proc. of Engineering Aspects of Shape Memory Alloys", Ed. by T. Duerig, et. al., Butterworth-Heinemann Publishers, London, 1990, pp. 170-177.

# **Passive Damping Applications**

**by**

**Stepan S. Simonian, PhD**

**TRW Spacecraft Technology Division  
Redondo Beach, California**

**Presented at Damping '93  
San Francisco, California  
February 24-26, 1993**

## **Introduction**

From the earliest days of spacecraft design, passive damping considerations have been an important element in their designs. The early satellites were of small size and of rigid construction and utilized three classes of dampers. The first class of dampers are of the type commonly referred to as wobble or nutation dampers. As the name implies, they were used to damp the rigid body spacecraft coning angles. To the next category belonged boom dampers, such as flexible gravity gradient booms. The third class of dampers were devices used to control the deployment velocities of deployables, such as antennas and solar arrays. The damping mechanism utilized in the above designs were either viscous fluids or of magnetic origin, such as eddy current in a number of different configurations. Due to evolving spacecraft design concepts, some of the above mentioned energy dissipating mechanisms are not used very often on present day spacecraft designs. However, the considerable increase in size in many current satellite designs, and often very stringent performance requirements, dictate the need for vibration suppression considerations. Currently, there are two approaches to vibration suppression: passive and active, or a combination of the two. In the present communication, only passive damping applications will be covered. In what follows, the author will briefly define the "jitter" problem and discuss spacecraft passive damping studies familiar to him in the last decade.

As mentioned above, many current space missions require stringent performance requirements. A satellite "jitter" problem may be defined as any on-orbit vibration which degrades the performance of on-board instruments. On-board instruments are those devices which transmit or reflect electromagnetic radiation; hence, by their very nature, instruments are sensitive to line-of-sight (LOS) errors induced by active on-board equipment. The sources of vibration may be quite varied and include environmental effects such as periodic thermal distortion, disturbances induced by rotating, scanning and reciprocating equipment.

To satisfy on-orbit performance requirements, it is necessary to damp the machinery induced vibrations. Depending on the magnitude of allowable sensor disturbances, the inherent damping capacity of flexible spacecraft vibration modes, may or may not satisfy the requirements. Many current space missions require passive damping levels greater than one percent of critical damping to satisfy the performance requirements. Due to current spacecraft design and fabrication practice, the required inherent damping levels will not be met. A survey of spacecraft damping measurements (see Ref. 1), under low amplitude vibrations similar to on-orbit conditions, show

that currently used 0.2 % damping for deterministic on-orbit vibration analysis is not unrealistic. The scattergram and a probability density fit of this data is reproduced from Ref. 1, and are depicted in Figures 1 & 2, respectively. Further details on this data, as well as a probabilistic jitter analysis using this data can be found in the above mentioned reference.

The above presented data therefore is the justification for the design of passive energy dissipating devices into spacecraft, when moderate and high damping levels are required to satisfy performance requirements.

In what follows, the damping devices described will be categorized under discrete and distributed techniques.

### **Discrete Dampers**

To this category belong vibration isolators and dampers. Three different vibration isolators will be described which use fluid, magnetic and viscoelastic materials (VEM) as the damping mechanisms. Theoretical developments will not be pursued here on isolator theory, since these are very well documented in the literature (see for instance Ref.2).

#### **Vibration Isolator: Fluid damped**

In 1983 TRW Dynamics Department anticipated that there would be numerous applications for a space qualified isolator of high performance. As a result a company funded effort was undertaken to demonstrate that:

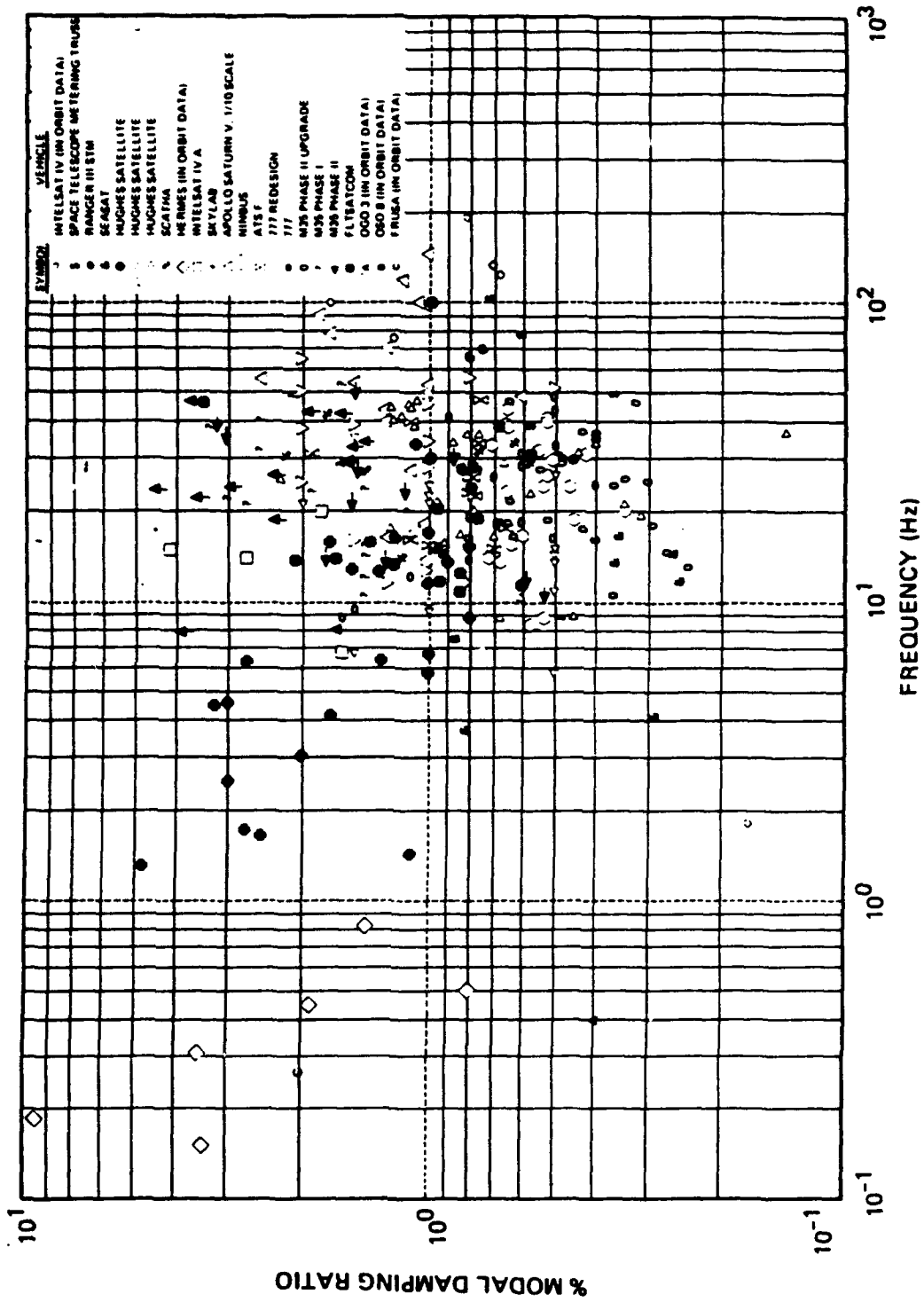
1. Isolator transmissibility can be analytically predicted.
2. The effects of isolator local modes can be analytically predicted.
3. Excellent transmissibility characteristics can be obtained over a wide frequency range.
4. Isolator transmissibility can be designed to be insensitive to a wide range of input levels.

To accomplish these goals the following tasks were performed:

1. Requirements for isolator transmissibility input levels were established.
2. A detailed isolator design was completed.
3. Analytical prediction of transmissibility, including isolator local modes, were developed.
4. Two complete demonstration model isolators were fabricated.
5. The isolators were tested to verify the analytical predictions.

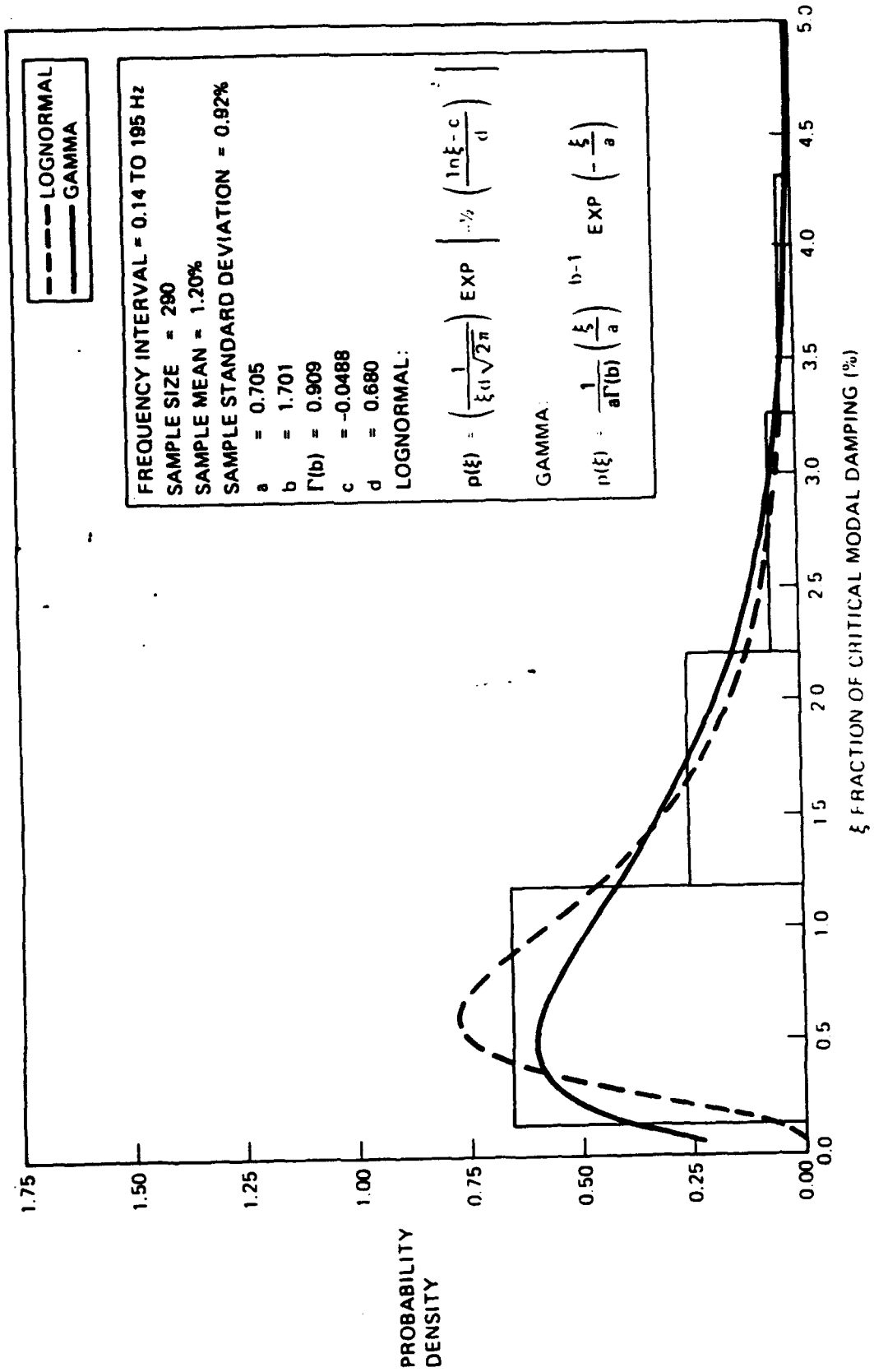
# Survey of Satellite Damping Measurements

Figure 1



# Damping Model for All Data

Figure 2



The requirements for isolator transmissibility is given in Figure 3. This was based on a desire to achieve the best possible isolation at high frequency, since it is assumed that small subsystems would have their sensitive modes primarily in the higher frequencies. A 10 Hertz resonance frequency was chosen for a reference design. An elastically coupled damper isolator concept was chosen because it offers the best performance of this group. A fluid damper was chosen for ease in producing a damper for the demonstration unit. Figures 4 & 5 show the exterior and cutaway view of the isolator. Testing validated the analytical model predictions, a comparison of which is depicted in Figure 6.

#### Vibration Isolator: Eddy-current damped

In 1985 responding to a compact 6 degree-of freedom isolator requirement, a concept was proposed which met all the requirements. The design concept consisting of six linear isolators were arranged in a Stuart platform configuration, yielding 6 nearly equal resonance frequencies. The elements of the design is illustrated in Figure 7. The required attenuation and performance prediction is depicted in Figure 8. As can be seen from the figure, attenuation will exceed the 20 dB requirement in 6 degrees-of-freedom so that substantial margin is forecasted over most of the frequency band. The materials selected are not sources of outgassing contaminants and are insensitive to space thermal vacuum environment. Similar to the fluid damped isolator discussed above, the design employs an elastically coupled concept for performance enhancement.

#### Vibration Isolator: Viscoelastically damped

In late 1989 in a crash program a viscoelastically damped isolation system was conceived, designed and fabricated in a matter of 2.5 months. The proposed system consisting of eight linear elastically coupled isolators were arranged in a configuration to provide 6 degree-of-freedom isolation to a reaction wheel. The baseline design is depicted in Figure 9. The unit section view of an isolator element is shown in Figure 10. The isolator mechanical model schematic appears on Figure 11. As can be seen from this figure, the design provides a stiffening spring mechanism to limit stroke during launch.

In addition to the above mentioned discrete isolator mechanisms, we present below a number of viscoelastically damped joints which have been designed, fabricated and tested starting from 1983 for a number of TRW programs.

The requirements for isolator transmissibility is given in Figure 3. This was based on a desire to achieve the best possible isolation at high frequency, since it is assumed that small subsystems would have their sensitive modes primarily in the higher frequencies. A 10 Hertz resonance frequency was chosen for a reference design. An elastically coupled damper isolator concept was chosen because it offers the best performance of this group. A fluid damper was chosen for ease in producing a damper for the demonstration unit. Figures 4 & 5 show the exterior and cutaway view of the isolator. Testing validated the analytical model predictions, a comparison of which is depicted in Figure 6.

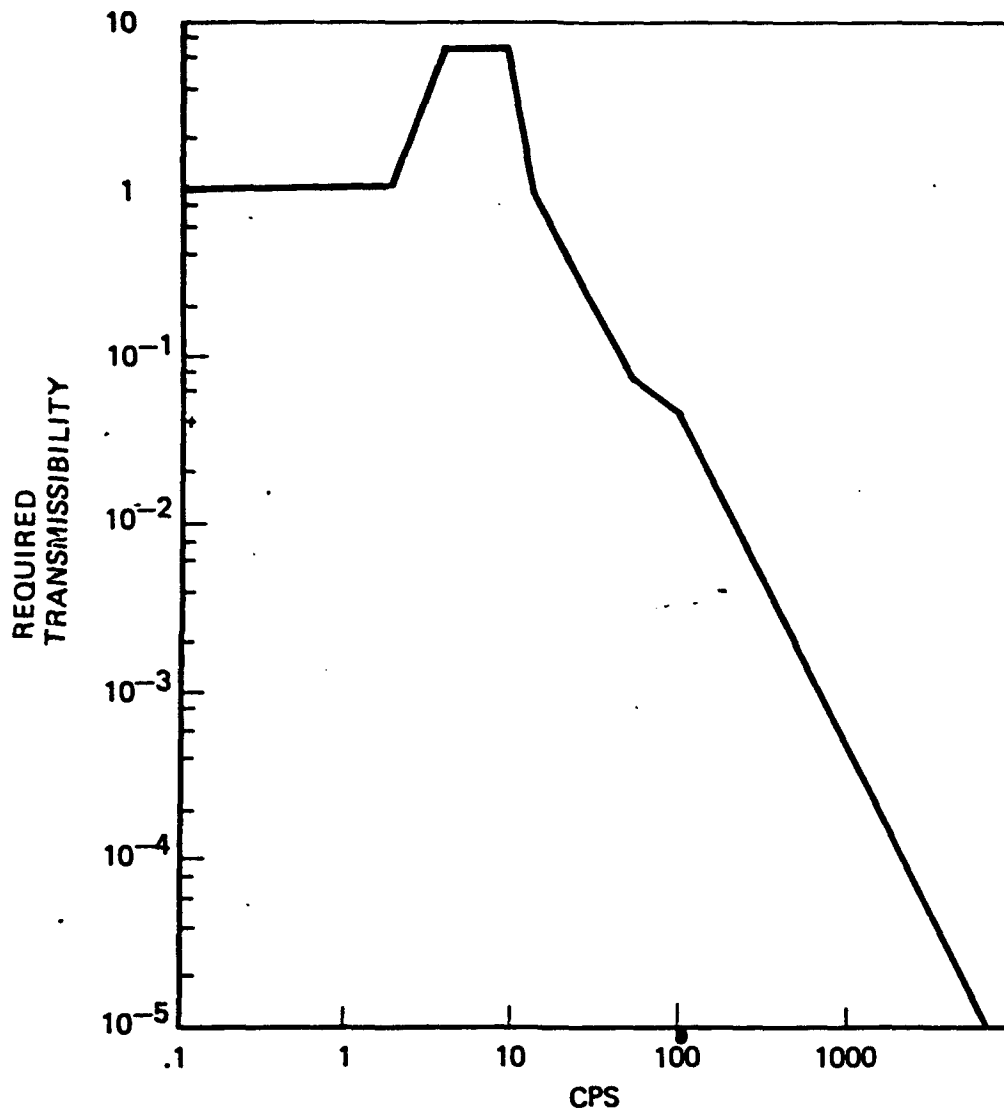
#### Vibration Isolator: Eddy-current damped

In 1985 responding to a compact 6 degree-of freedom isolator requirement, a concept was proposed which met all the requirements. The design concept consisting of six linear isolators were arranged in a Stuart platform configuration, yielding 6 nearly equal resonance frequencies. The elements of the design is illustrated in Figure 7. The required attenuation and performance prediction is depicted in Figure 8. As can be seen from the figure, attenuation will exceed the 20 dB requirement in 6 degrees-of-freedom so that substantial margin is forecasted over most of the frequency band. The materials selected are not sources of outgassing contaminants and are insensitive to space thermal vacuum environment. Similar to the fluid damped isolator discussed above, the design employs an elastically coupled concept for performance enhancement.

#### Vibration Isolator: Viscoelastically damped

In late 1989 in a crash program a viscoelastically damped isolation system was conceived, designed and fabricated in a matter of 2.5 months. The proposed system consisting of eight linear elastically coupled isolators were arranged in a configuration to provide 6 degree-of-freedom isolation to a reaction wheel. The baseline design is depicted in Figure 9. The unit section view of an isolator element is shown in Figure 10. The isolator mechanical model schematic appears on Figure 11. As can be seen from this figure, the design provides a stiffening spring mechanism to limit stroke during launch.

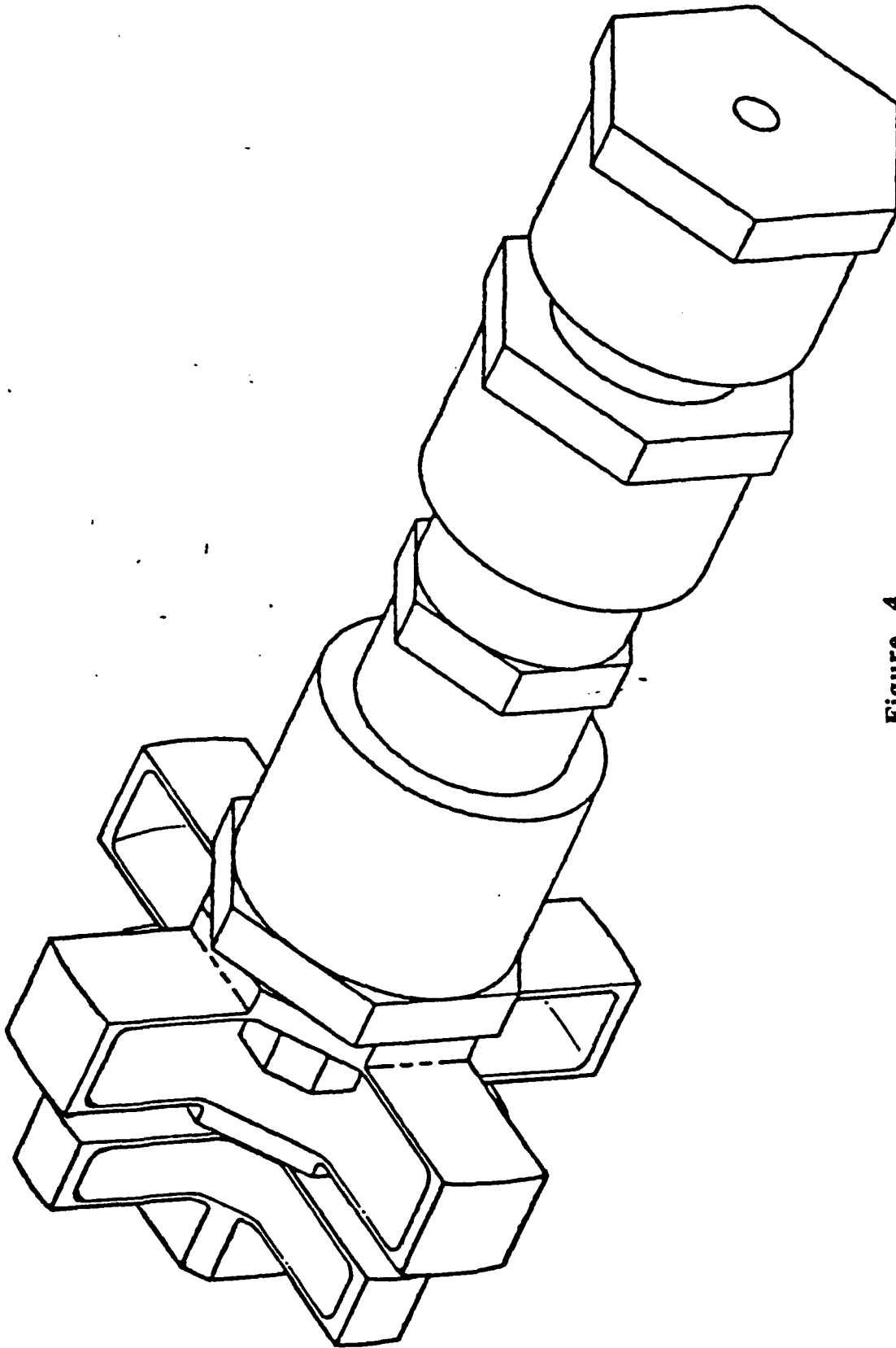
In addition to the above mentioned discrete isolator mechanisms, we present below a number of viscoelastically damped joints which have been designed, fabricated and tested starting from 1983 for a number of TRW programs.



Required Isolator Transmissibility

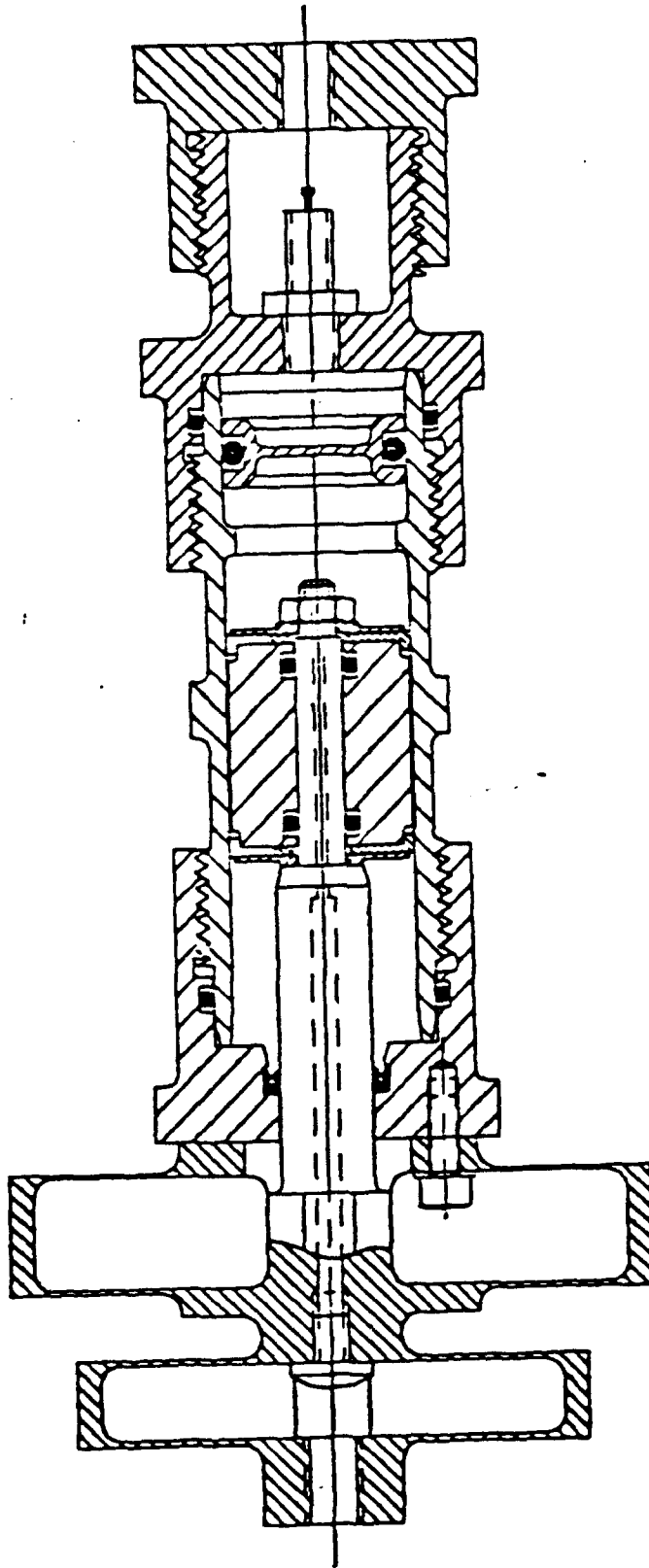
Figure 3

BAB-8



**Figure 4**

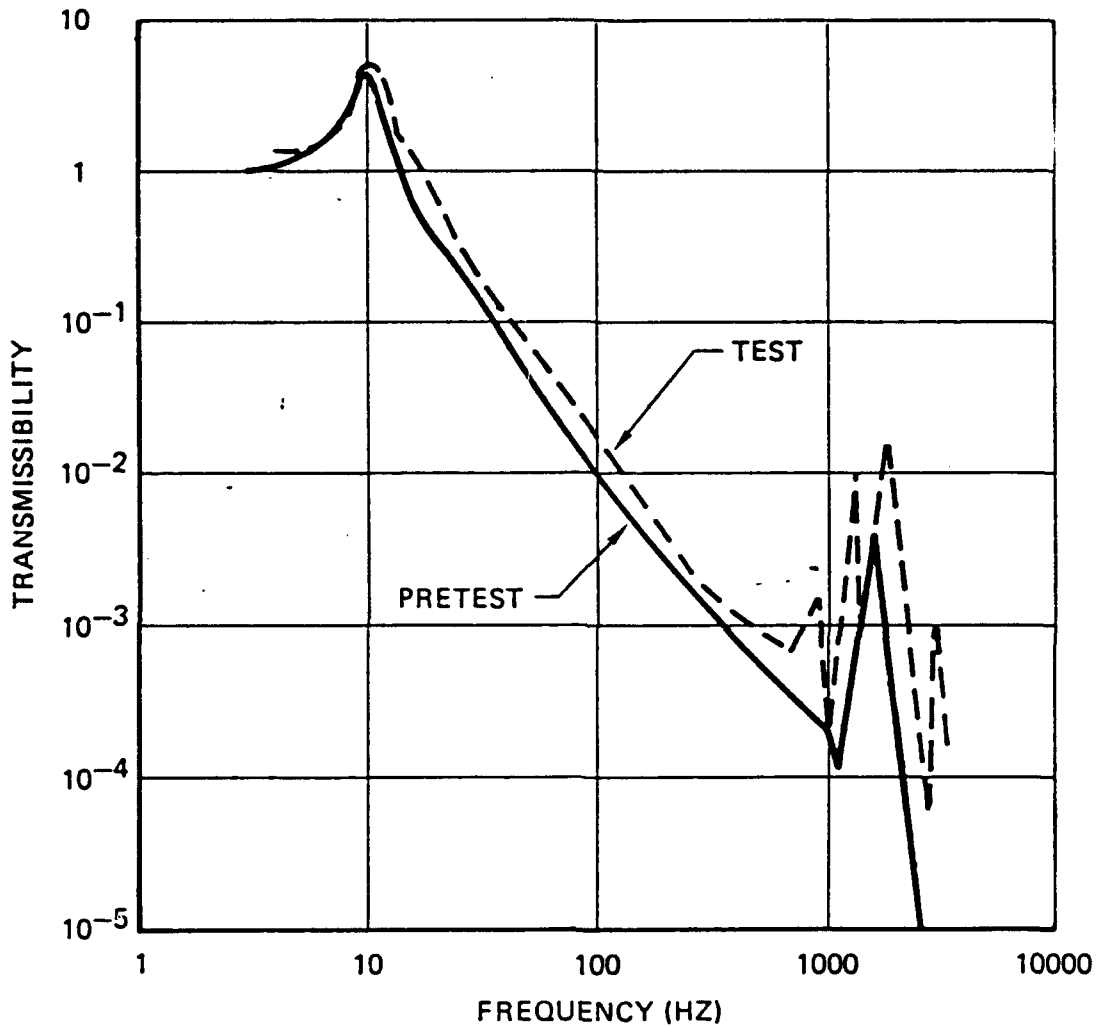
**Fluid Damped Dual Stage Spring Passive Vibration Isolator**



**Figure 5**  
Isolator Cross Section

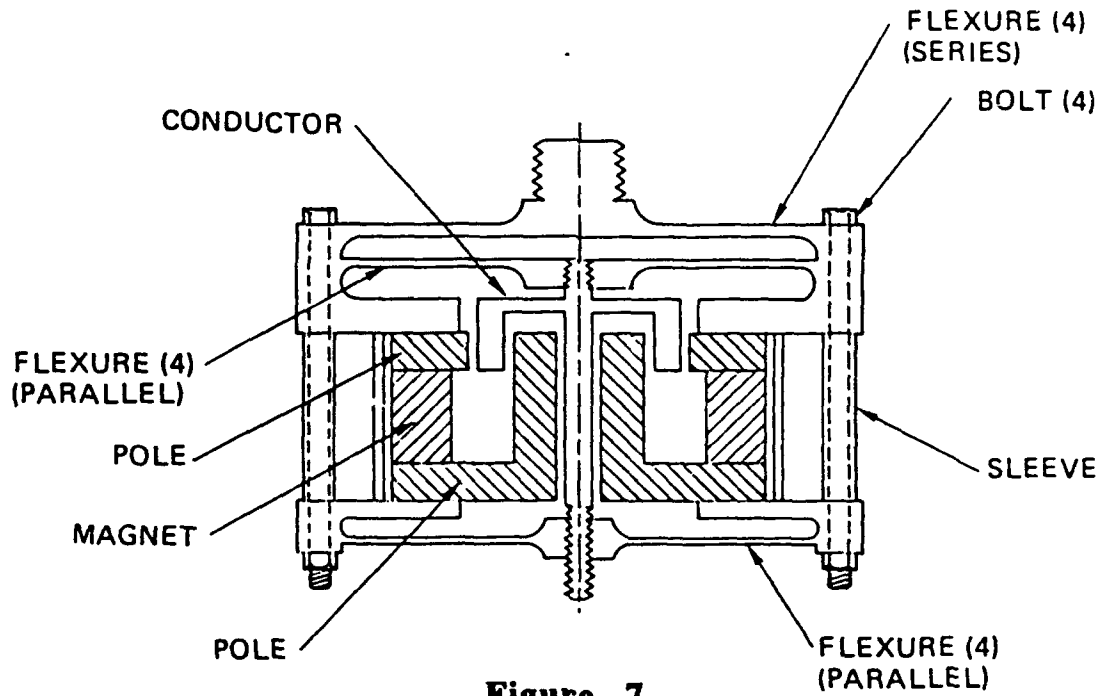
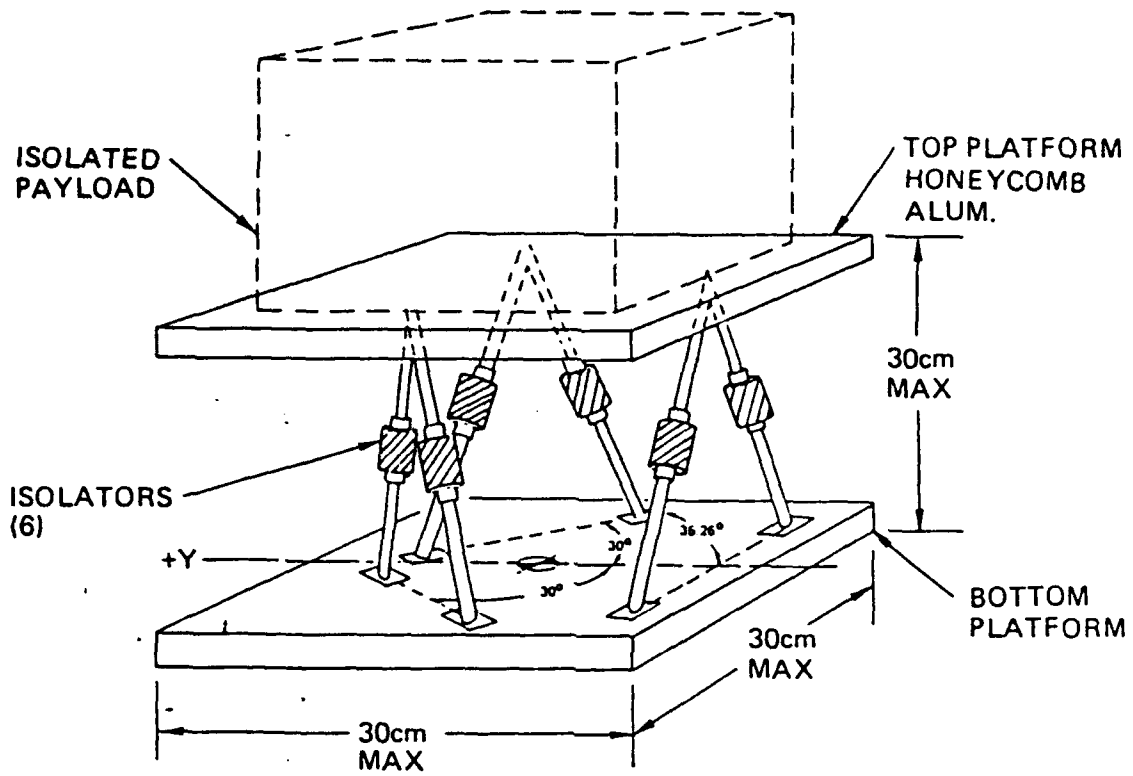
BAB-10

Development Test Results Validated  
the Mathematical Model



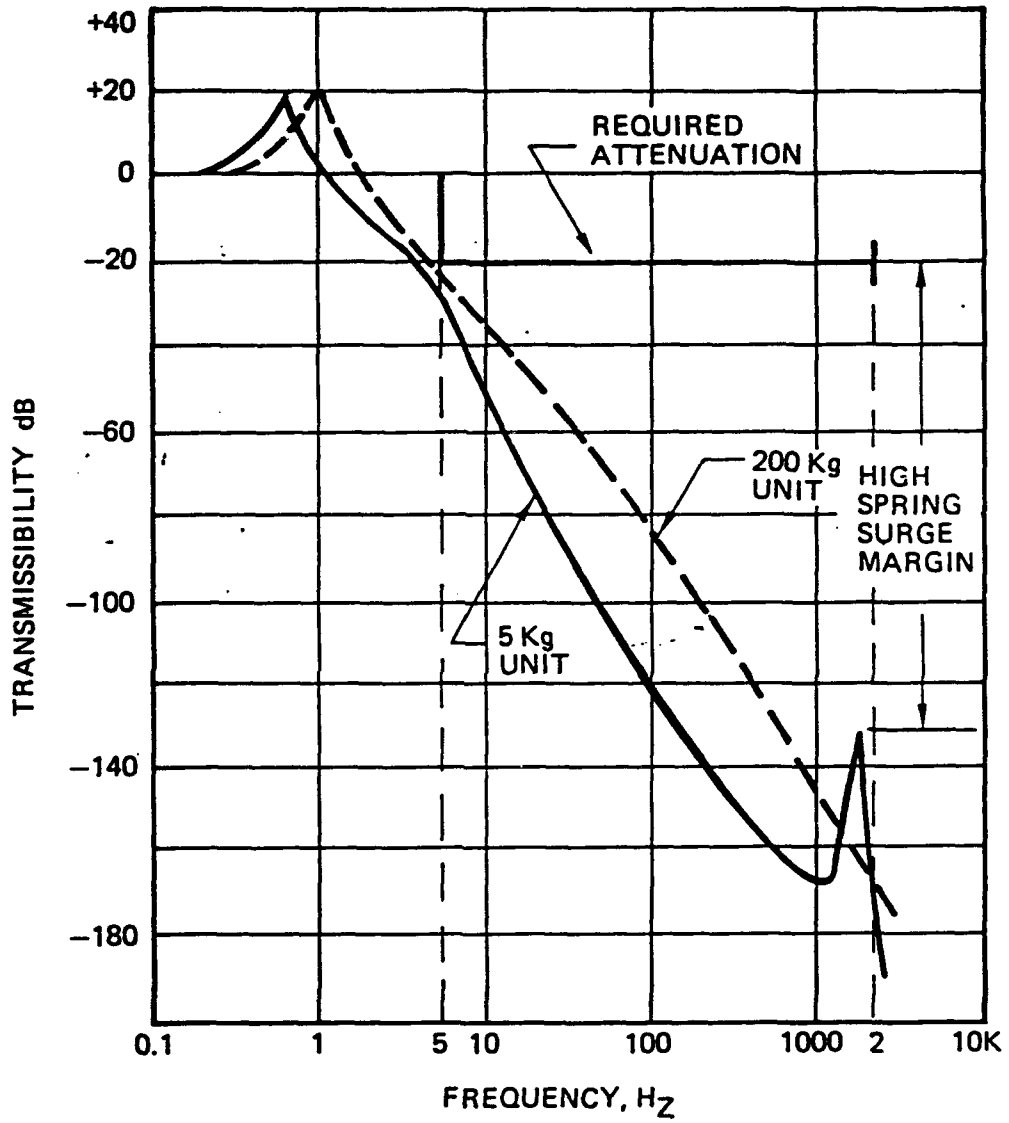
Comparison of Test and Analysis  
Showing Excellent Agreement

Figure 6



**Figure 7**

**Proposed Low Risk, Realizable Passive Vibration System**



Required Attenuation is Achieved by the 5 Kg and 200 Kg Isolator Components

Figure 8

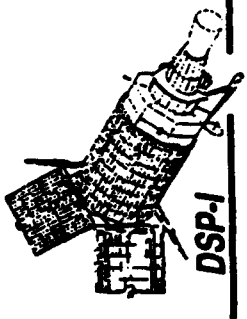
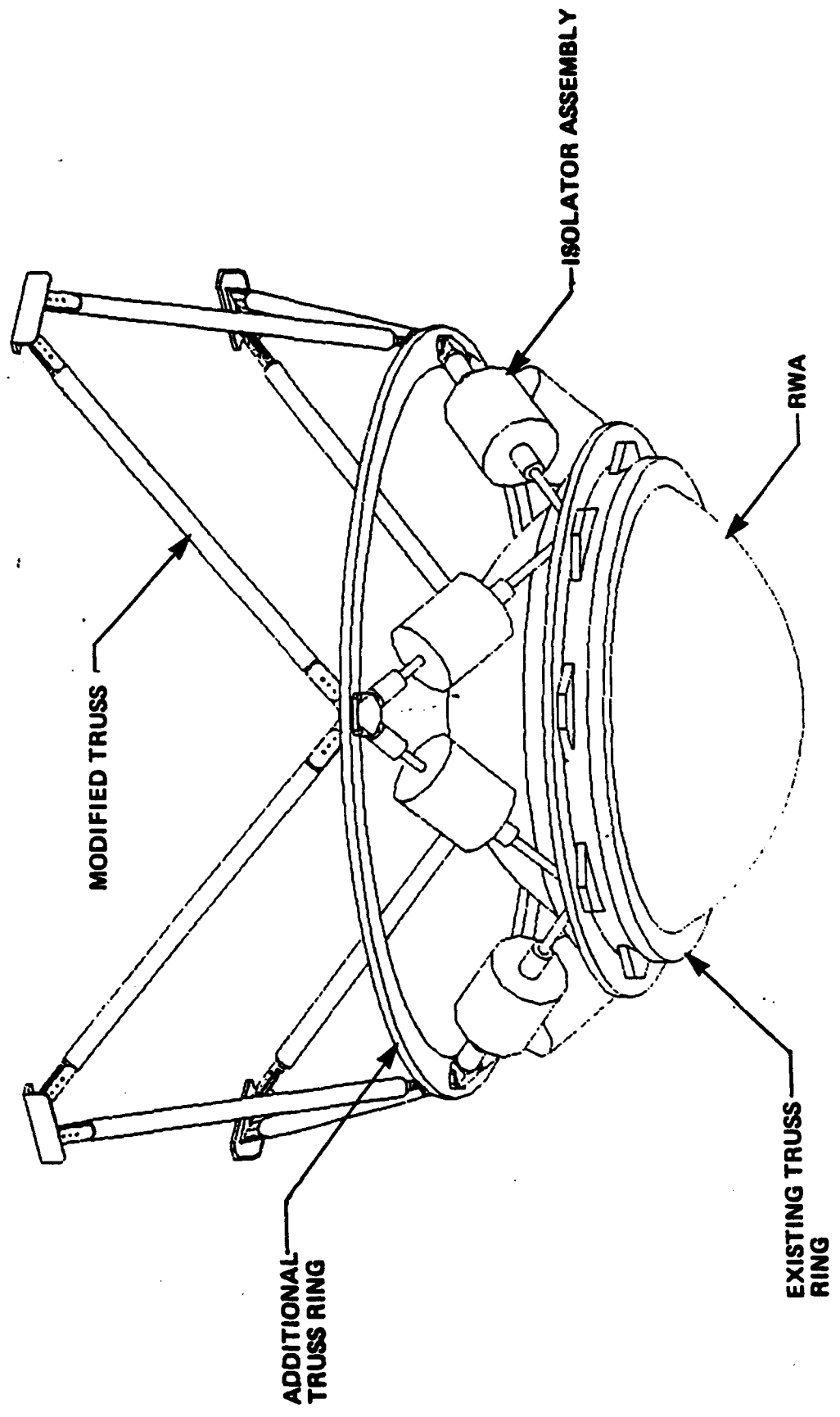


Figure 9

# Modified Truss Concept



82

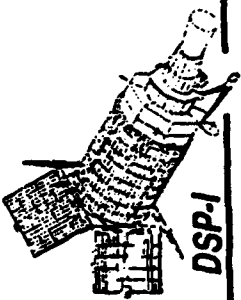


Figure 10  
Isolator Unit Section View

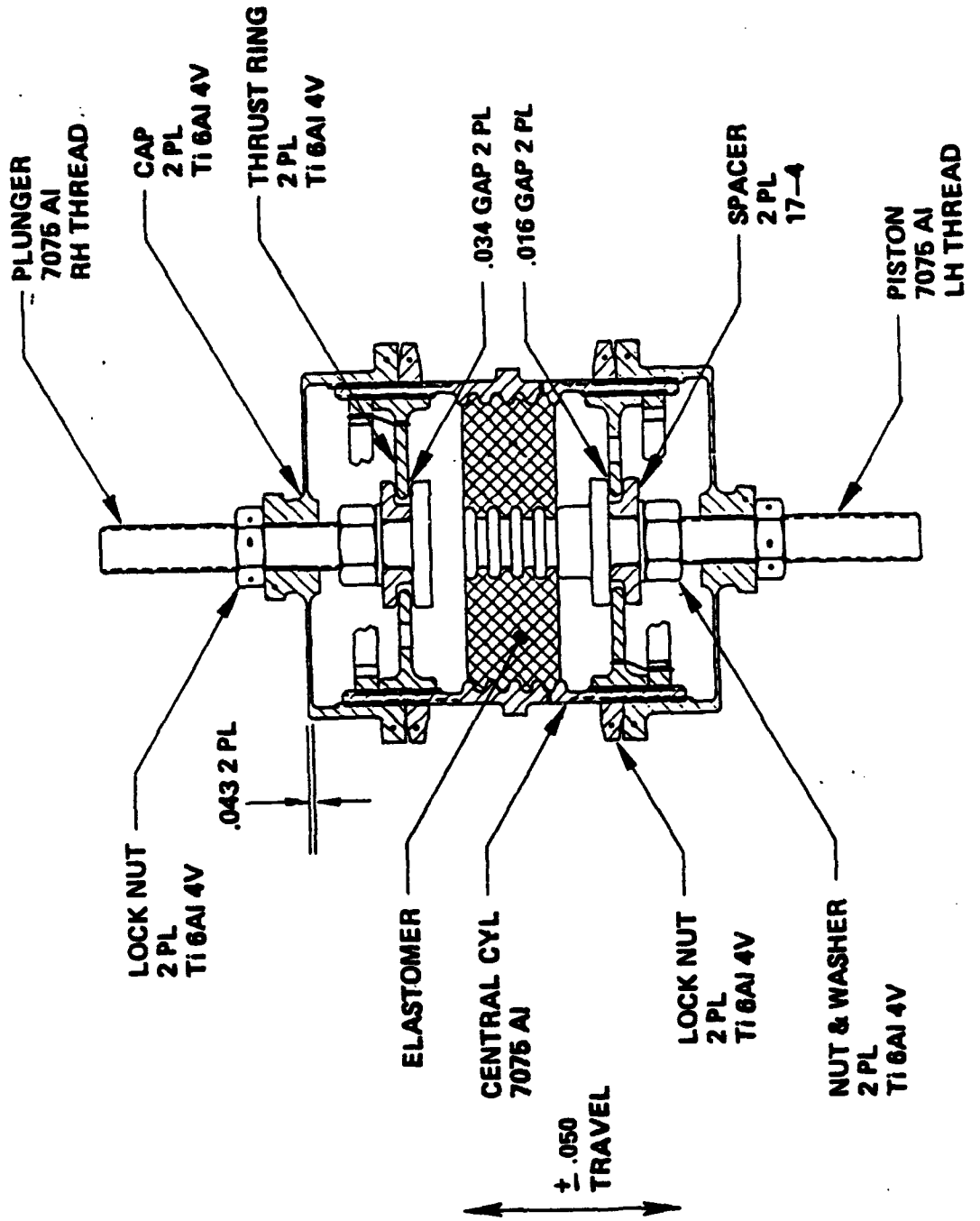
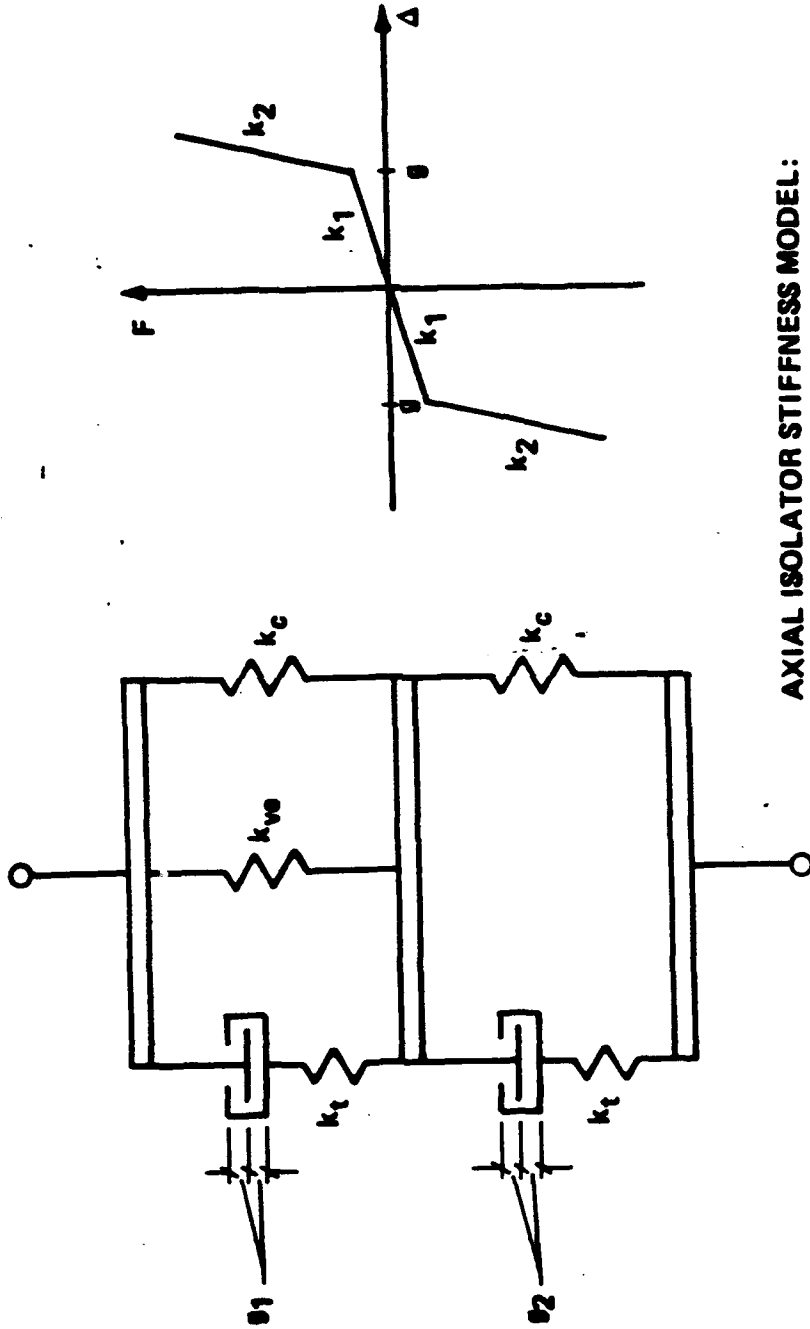
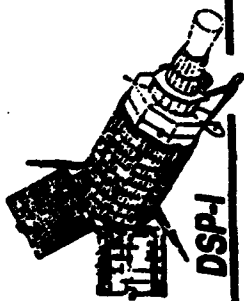


Figure 11  
**Isolator Mechanical Model  
 (Schematic)**



AXIAL ISOLATOR STIFFNESS MODEL:

- $k_c$  - ISOLATOR CAP STIFFNESS
- $k_{ve}$  - VISCOELASTIC SPRING STIFFNESS
- $k_t$  - THRUST RING STIFFNESS
- $\theta_1, \theta_2$  - GAPS

## Large Space Structure (LSS) IR&D

In 1983 an IR&D program was initiated to maximize vibration suppression/control of LSS at a minimum cost. Development drivers were studies involving optimal blend of passive damping and active control of LSS. Such studies were almost nonexistent at the time, also there were no experimental data on blended active control and augmented passive damping systems for LSS. Some of the details of the study are documented in Refs.2 through 5. The experiment configuration is depicted in Figure 12. The passively damped joint is shown in Figure 13. Each joint, as can be seen from the figure, is made up of four links arranged 90° from one another. The design is modular, such that any number of the dampers can be replaced with rigid links with no damping. The undamped rigid links are also shown in Figure 13. Figure 14 presents results of achieved damping for various damper configuration. Depending on the particular damper configuration 7-32 % of critical damping was achieved for the lateral bending modes of the structure !

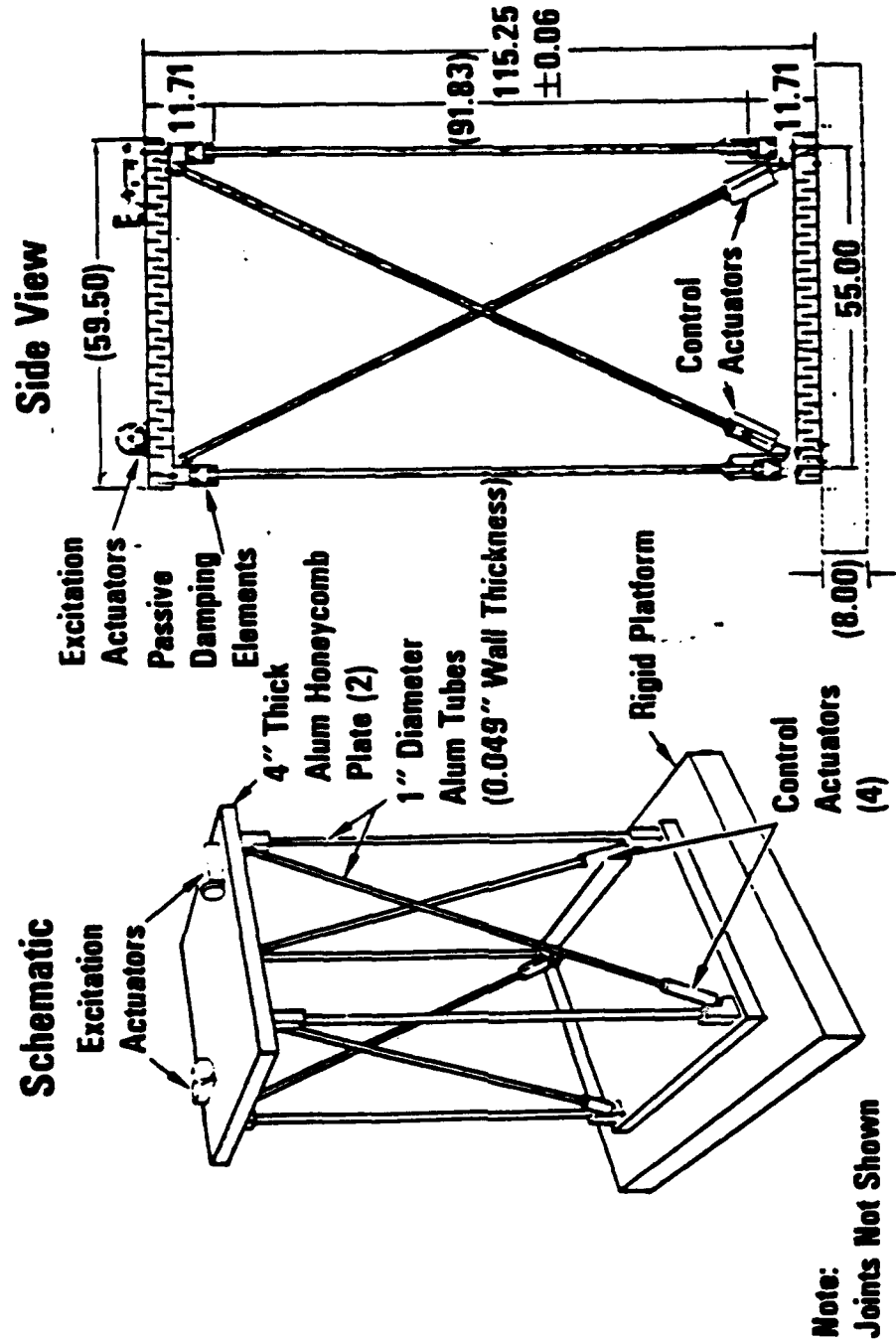
## Damping and Metal Matrix for Precision Structures (DAMMPS)

The objective of this Air Force Program was on the marriage of two key materials technologies: Metal matrix composites (MMC), and high loss viscoelastic materials. MMC's display very high specific stiffness, near zero CTE, no outgassing, high conductivity and no moisture absorption. Unfortunately, they possess very low vibration damping capacity. Modern viscoelastic materials on the other hand, display very high damping capacity. By incorporating viscoelastic materials in a controlled fashion into generic MMC truss structure joints, critical damping factors of 10-20% or greater are obtained. Thus the damping enhancement is at least two orders of magnitude over the inherent damping provided by MMC structures. It is predicted that this enhanced performance will be a key factor to the successful space deployment of various vibration sensitive devices and optical payloads.

The truss structure assembly is shown in Figure 15. It is equipped with six passive joints. The details of the damper are depicted in Figures 16 through 18. Figure 19 displays an alternate machined spring concept instead of the helical machined spring depicted in Figure 18. The mechanical model of the damper shown to the right in Figure 18 is similar in concept also used in all the isolator designs. The performance prediction of system damping for a nominal joint configuration is depicted in Figure 20. Damping levels of 2.5 to 15% can be achieved with only one viscoelastic material. With the use of multiple viscoelastic materials with different transition temperatures (this

# LSS Experiment

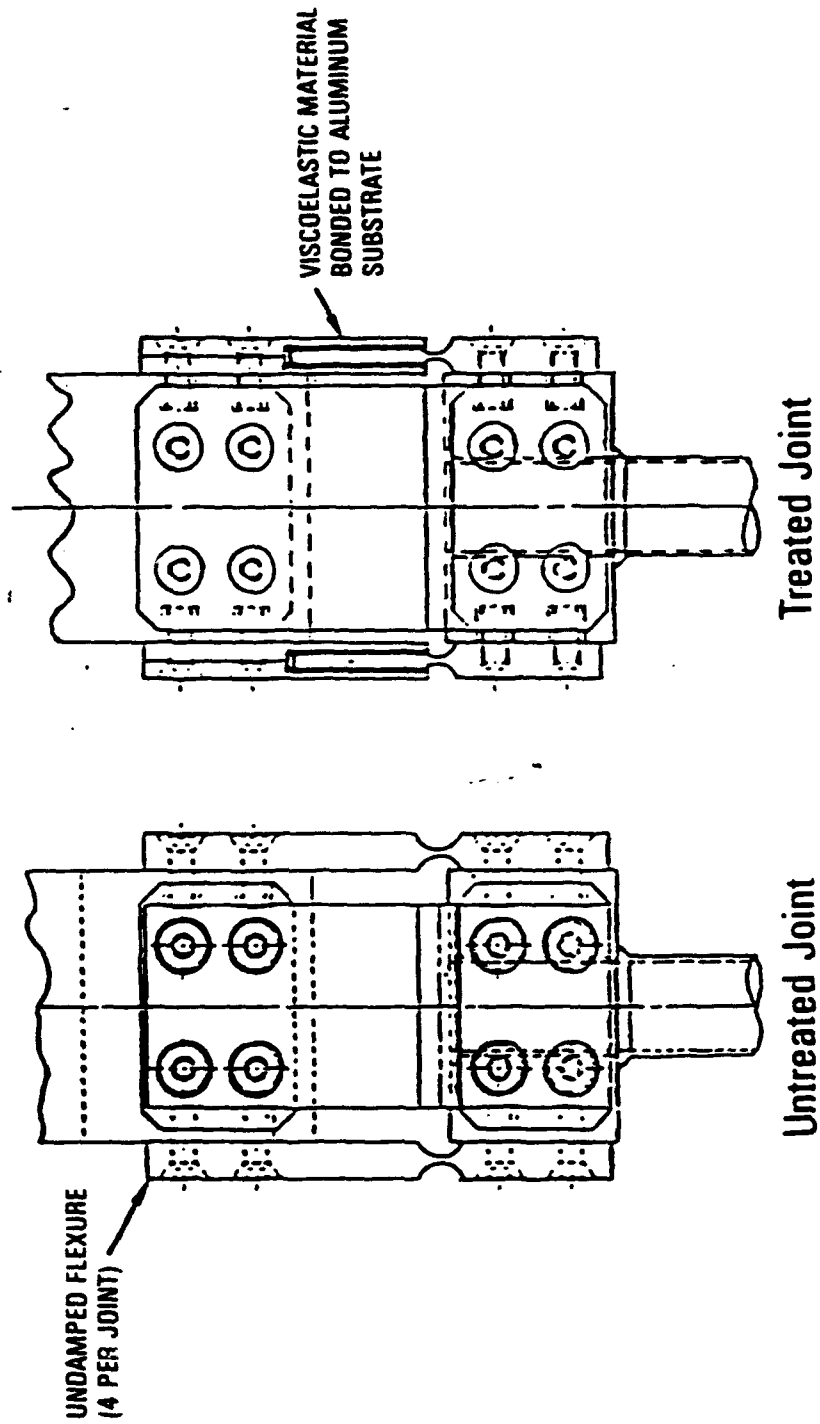
Figure 12



# Undamped and Damped Rectangular Joint

Figure 13

Modular Design Permits Interchangeability between Damped and Undamped Joints



85

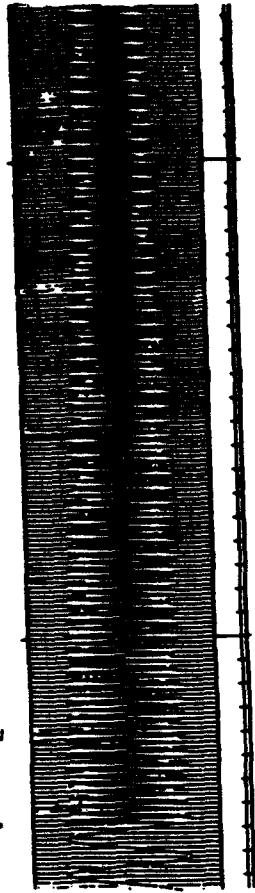
# System Damping Optimization

Figure 14

## Tested Damper Configurations Twang Test Data: Damper Configuration III

(a) No

Dampers 1 mm/sec:  $f = 0.65$  Hz

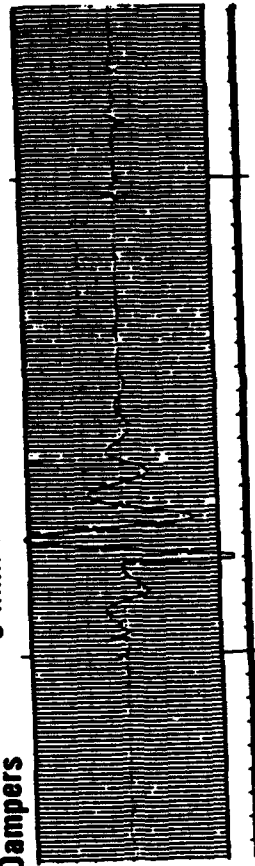


$$\zeta (\%) = \frac{1}{2\pi m} \ln \left( \frac{x_n}{x_{n+m}} \right) (100) = \frac{1}{2\pi(92)} \ln \left( \frac{17}{10} \right) (100) \approx 0.1 \%$$

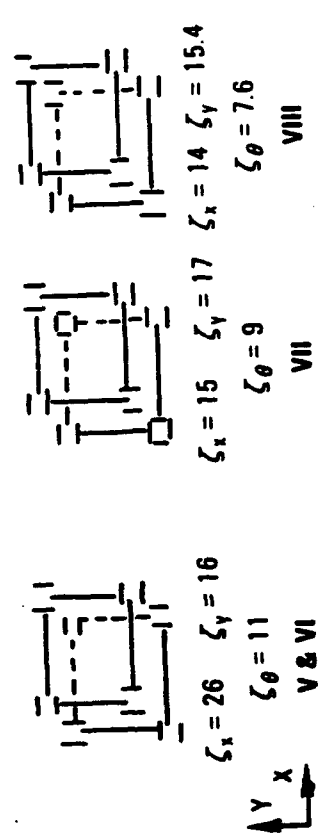
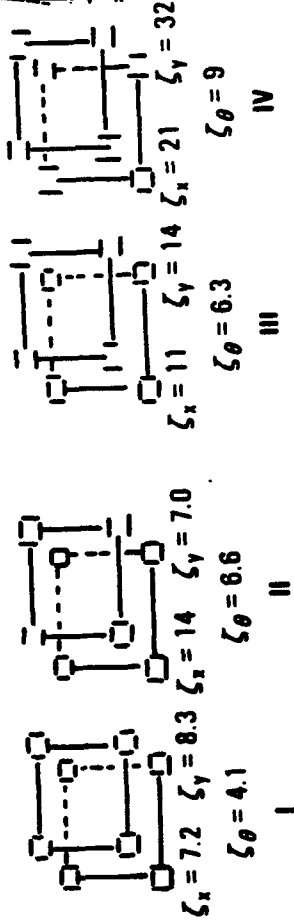
(b) With

Dampers

5 mm/sec:  $f = 0.54$  Hz



$$\zeta (\%) = \frac{1}{2\pi m} \ln \left( \frac{x_n}{x_{n+m}} \right) (100) = \frac{1}{2\pi(2)} \ln \left( \frac{26}{4} \right) (100) \approx 15 \%$$

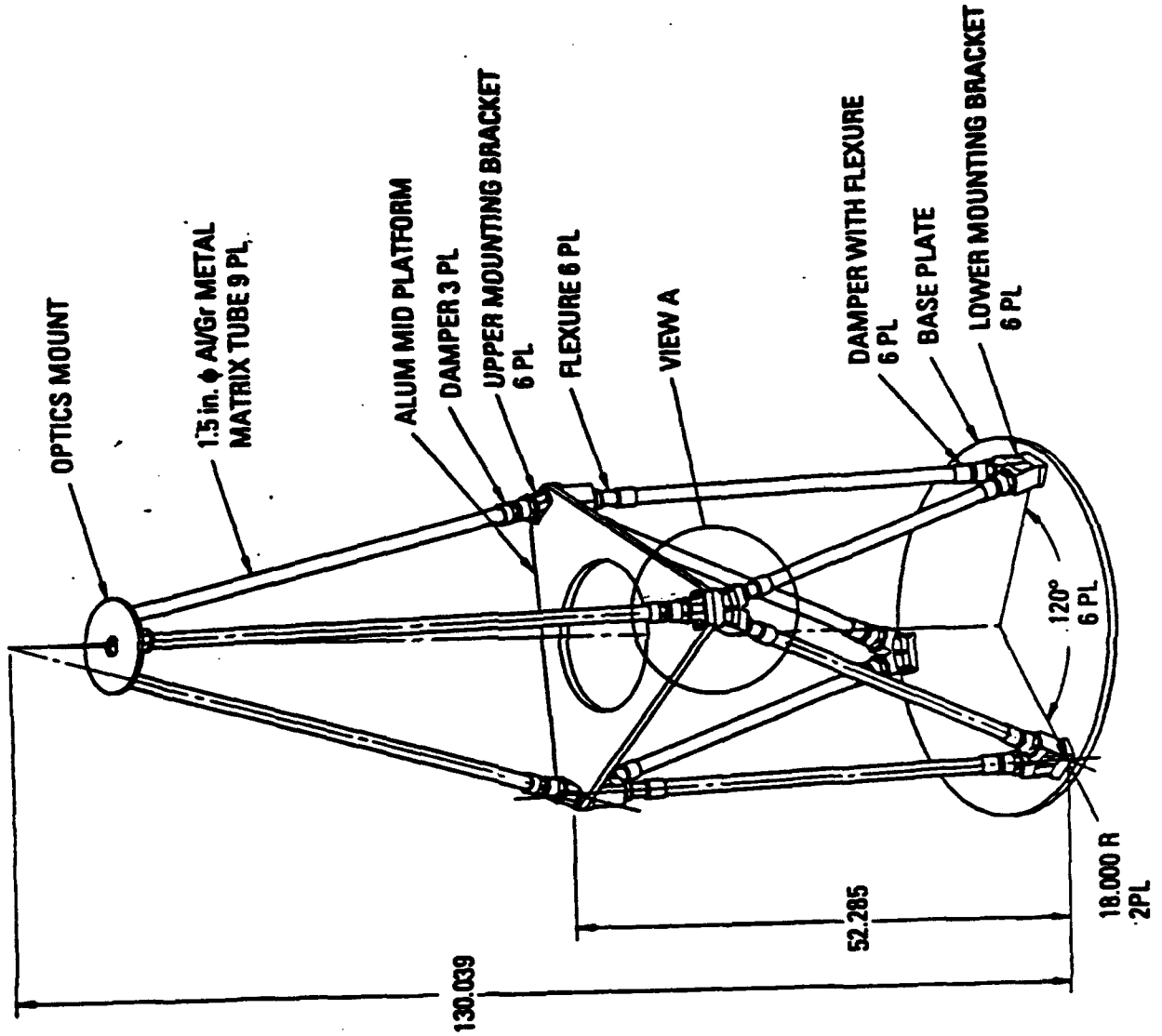




DAMMPS

Figure 15

# Truss Assembly



DAMMPS DEMONSTRATION STRUCTURAL ARTICLE (DSA)

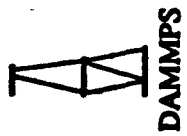
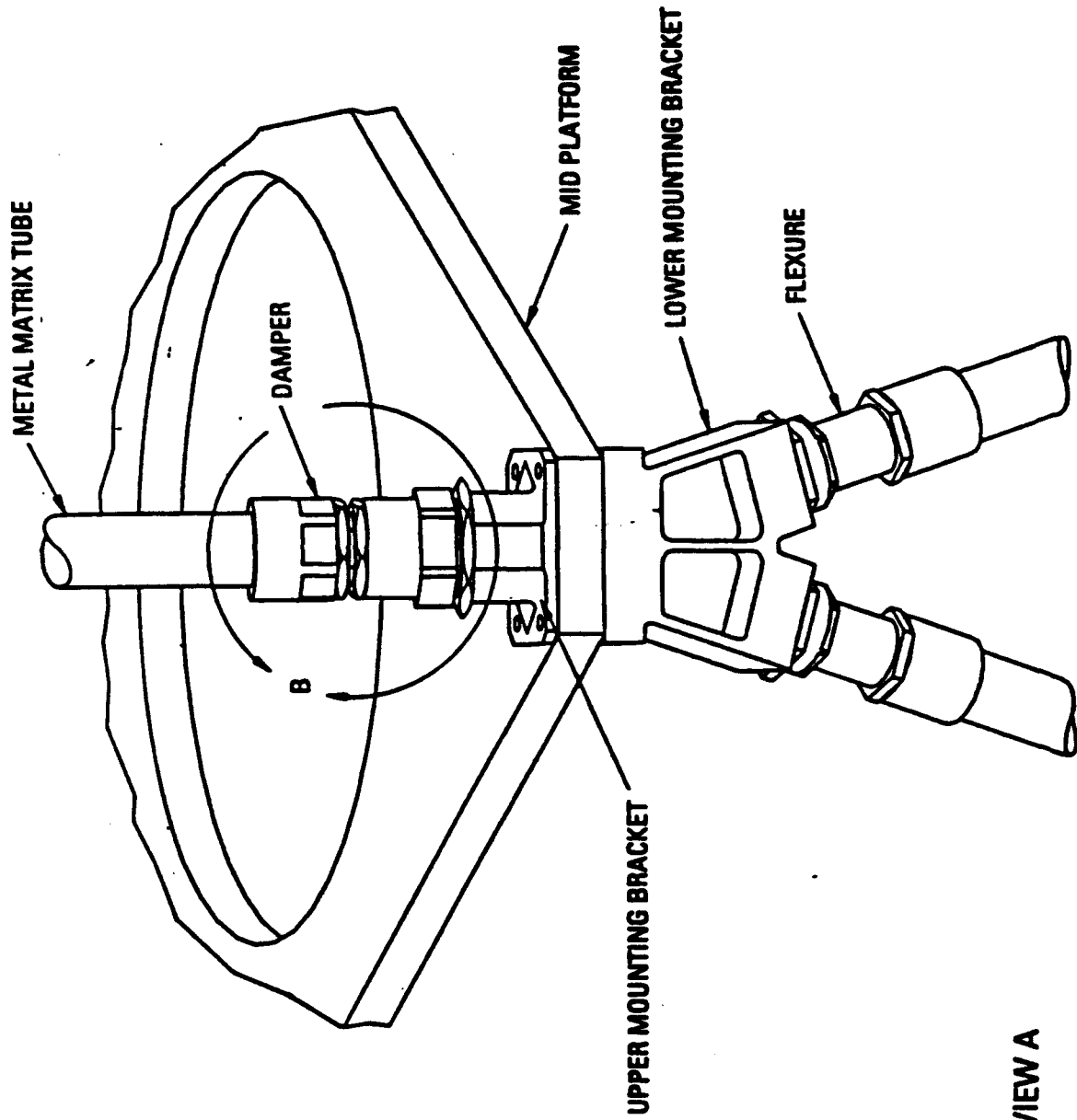


Figure 16

# Mid Platform



BAB-22

VIEW A

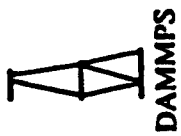
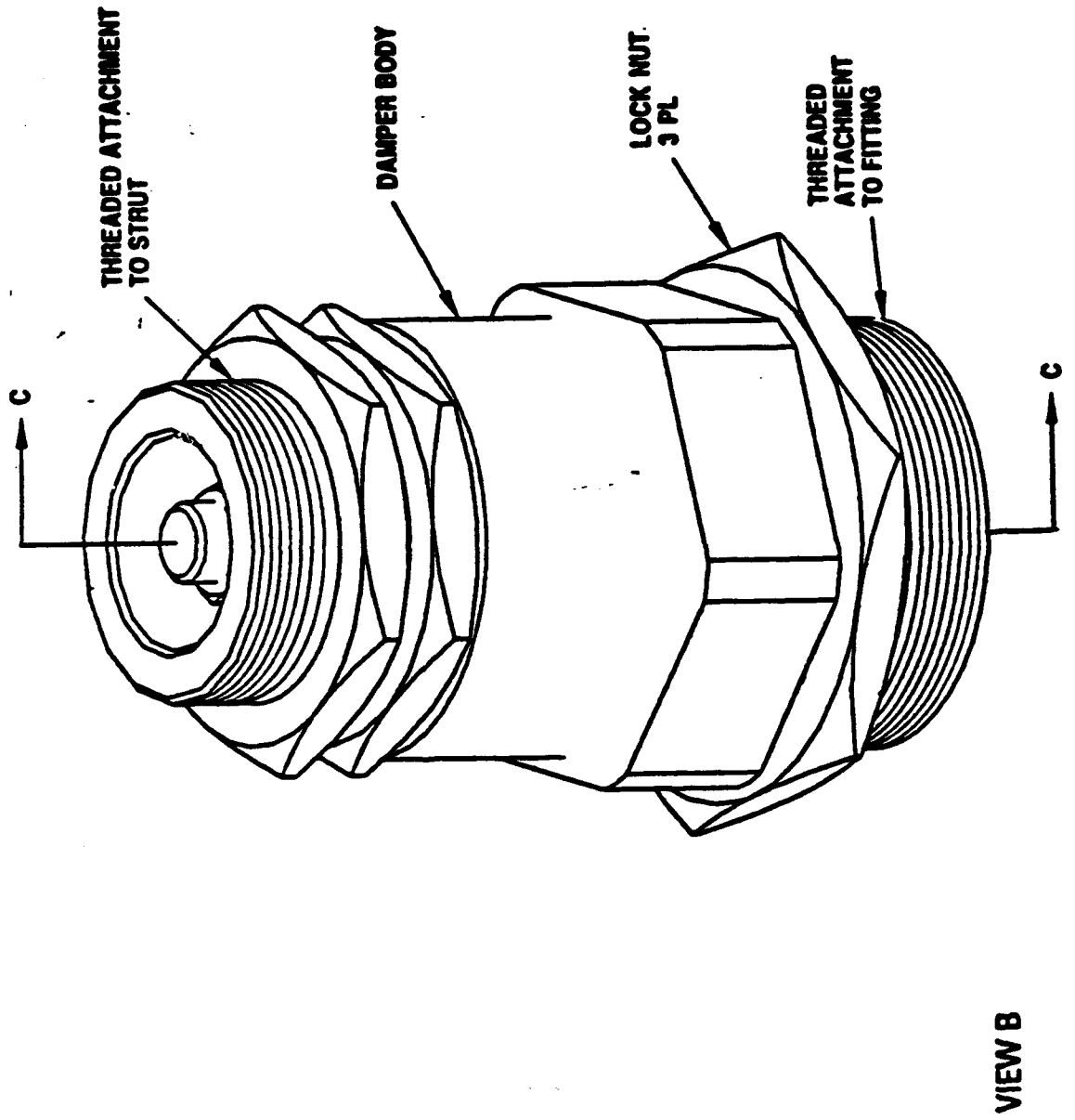


Figure 17

# Damper



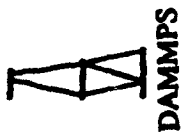


Figure 18  
**Damper Section View**

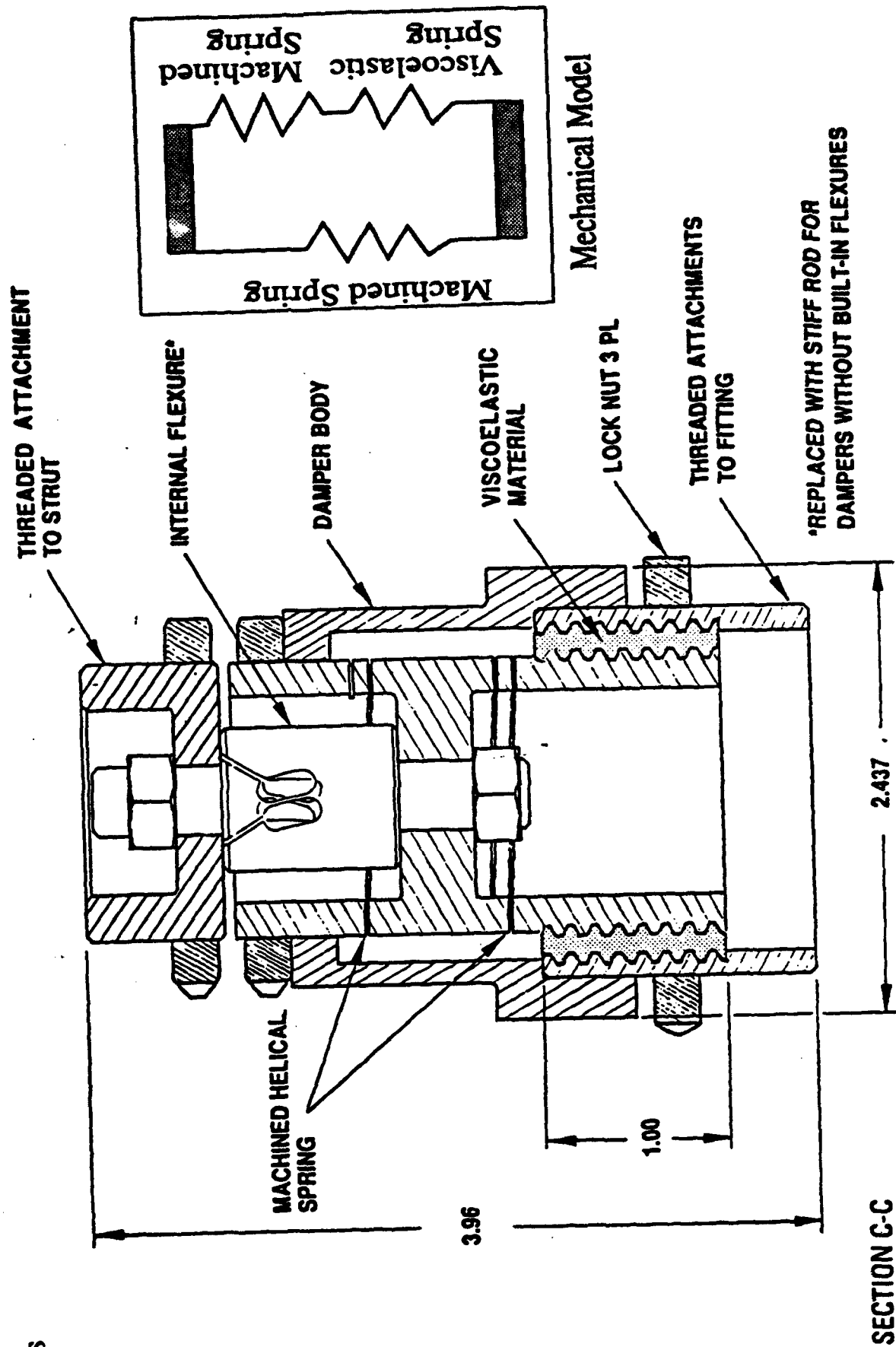
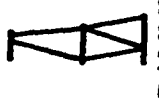
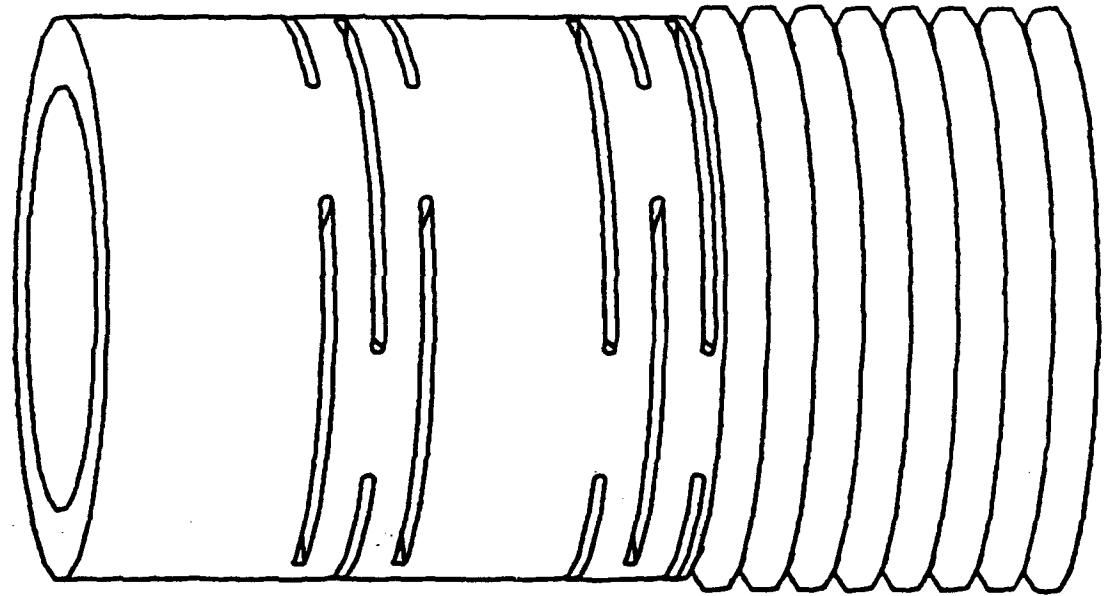
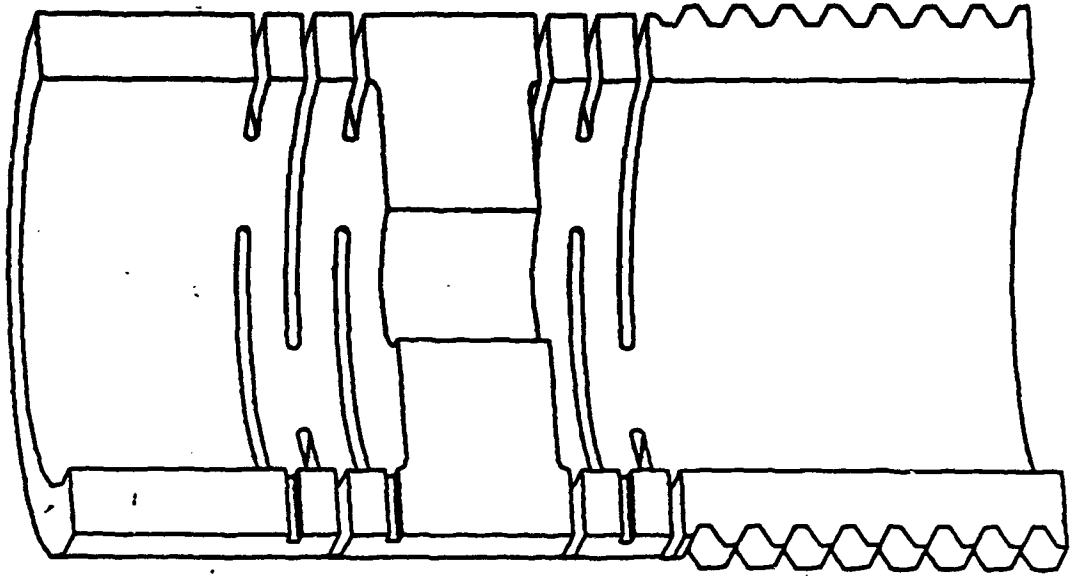


Figure 19

# Cantilever Beam Spring



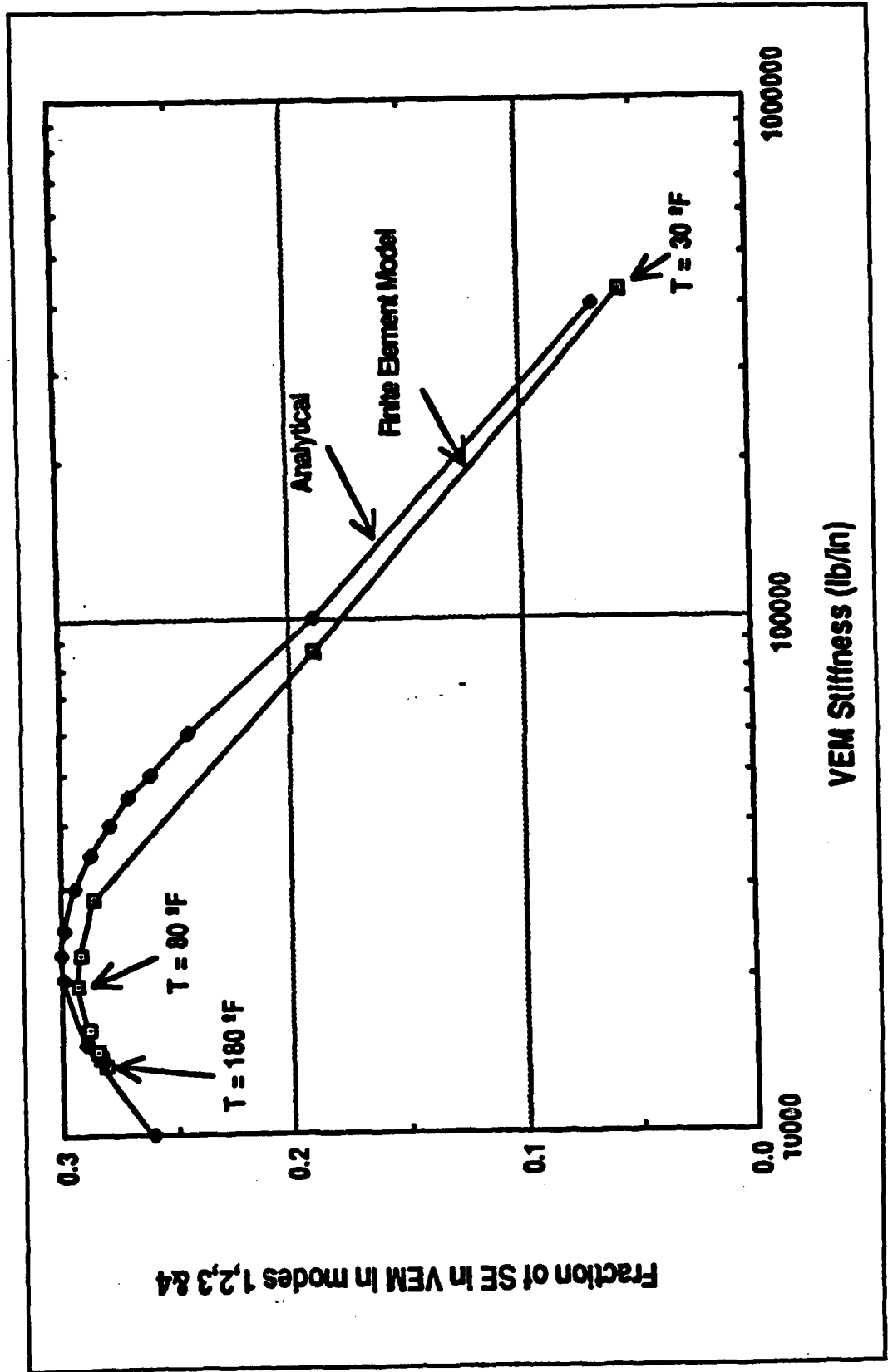
DAMMPS

BAB-25

# DESIGN DAMPING LEVEL

Figure 20

- Damper Parameters Have Been Optimized



will be demonstrated for the AMASS damper below), it is estimated that at least 10% damping can be achieved without any thermal control. With minimal passive thermal control, even higher damping designs can be achieved.

### Advanced Materials Applications to Space Structures (AMASS)

Appendage dynamics are very important to overall spacecraft pointing stability. Gimbaling a solar array to track the sun, for example, leads to disturbances from the stepper motor and harmonic-drive gear reducer, exciting the higher frequency vibration modes of the arrays. Rapid slews of the arrays or spacecraft excite the lower frequency modes of the spacecraft. The AMASS program developed and demonstrated a solar array support structure which employs both active and passive damping designs to achieve a system which possesses high damping characteristics over a broad frequency and temperature range. The AMASS solar array passive joint damper is based on the joint concepts developed from the DAMMPS program discussed above. The damper design is shown in Figure 21. Figure 22, based on measured damping data, shows the high damping and relative insensitivity of the damper over a wide temperature band.

### Modular Fluid Damper IR&D

The objective of this project was to design passive modular fluid dampers based on the design of the joint developed under the DAMMPS project discussed above. The fluid dashpot design concept is depicted in Figure 23. The design goal for the viscous damping coefficient was  $c = 50$  lb-sec/in. The configuration of the dashpot within the DAMMPS joint is depicted in Figure 24. Performance simulations using reaction wheel induced disturbances is displayed in Figure 25 using the fluid damper.

### Passively Damped Clips

Brake fluid lines or wire cable bundle fasteners and clips utilized in the automotive, aircraft, and rapid rail transportation systems often fail in fatigue due to the sustained vibration loads. Most of these parts are fabricated from injection molded plastics or stamped sheet metal. Designing passive damping into these fasteners will prolong their life.

In a proof-of-concept study, an elastomeric lining with high damping properties was added to a plastic clip used to attach the brake fluid lines in a truck application (see Figure 26). From Figure 27 it can be seen that a

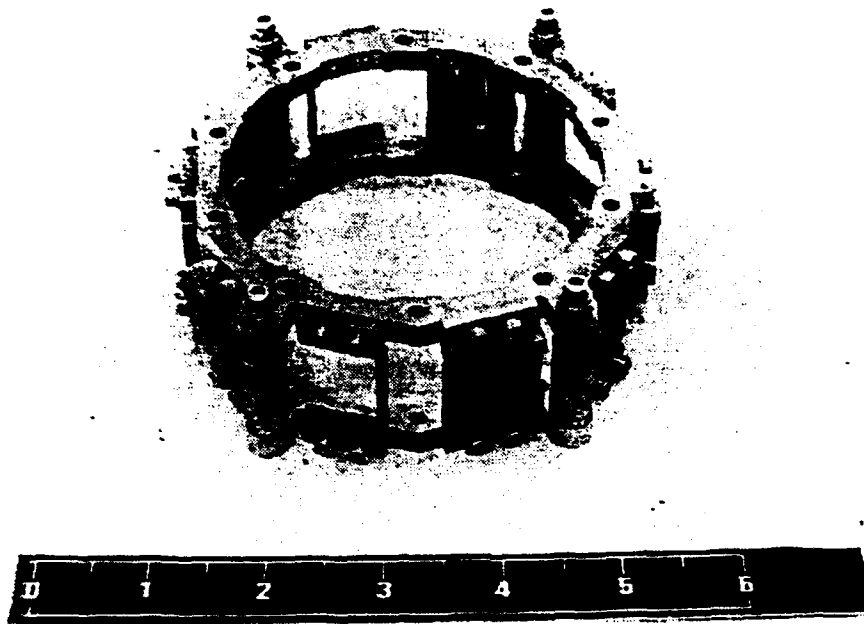
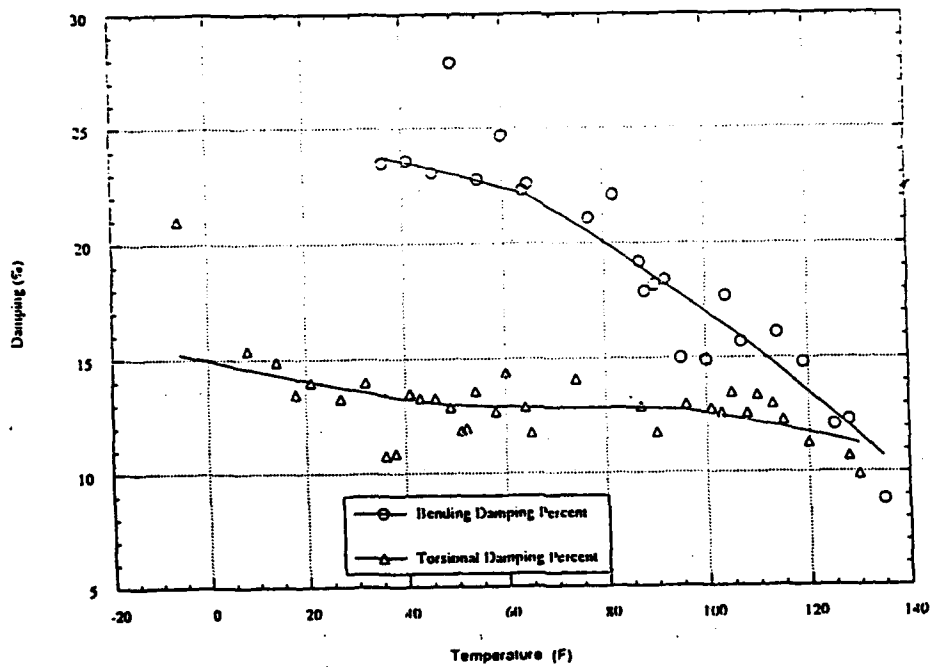


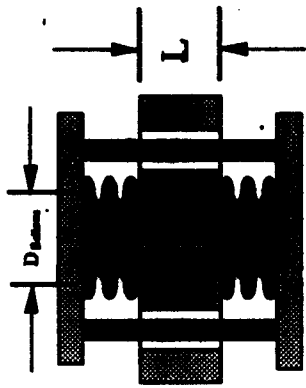
**Figure 21**  
Flight Version of the AMASS Passive Joint



Passive Joint Measuring Damping

**Figure 22**

**Figure 23**  
**FLUID DASHPOT DESIGN**



**Bellows:** Servometer electrodeposited nickel

**Fluid:** Dow corning 200

**Damping Force:**  $F_D = CV$

$$C = 8\pi\mu L \left(\frac{D_{\text{bellows}}}{d_{\text{orifice}}}\right)^4$$

**Damping coeff.**

$\mu$  = Fluid viscosity

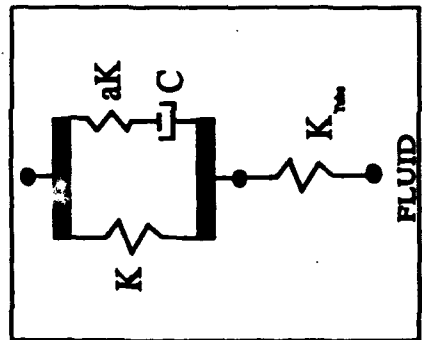
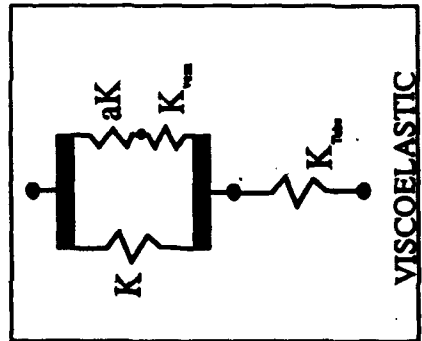
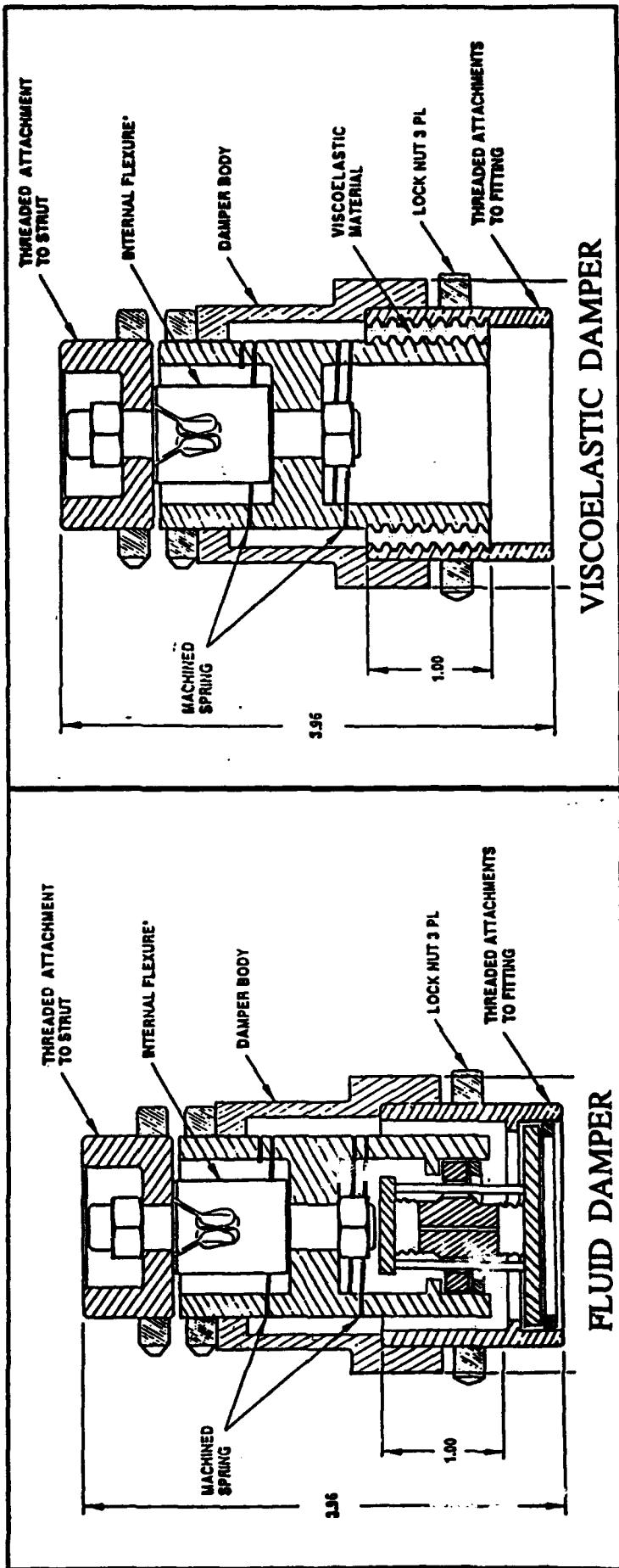
$L$  = Length of orifice

$D_{\text{bellows}}$ ,  $d_{\text{orifice}}$  = Diameter of Bellows and orifice

$V$  = Velocity

**Design goal:**  $C \approx 50$  lb-sec/in

Figure 24  
**FLUID AND VISCOELASTIC DAMPERS**

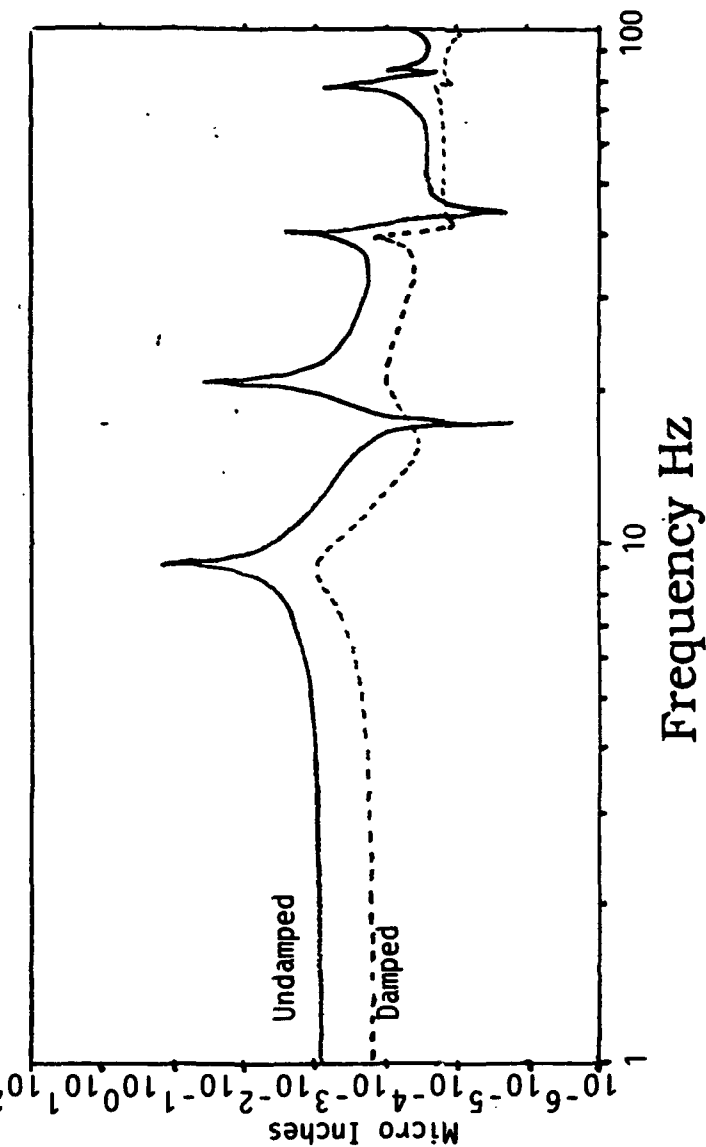


**Axial Mechanical Models**

$K, aK$  : Spring rates of machined springs  
 $K_{\text{vcm}}$  : Complex valued spring rate of viscoelastic material  
 $C$  : Viscous damping coefficient  
 $K_{\text{Tube}}$  : Tube axial stiffness

**Figure 25**  
**DYNAMIC ANALYSIS**

LOS X: Due to Reaction Wheel Induced Disturbances



- Undamped Structure: 0.2% Damping
- Damped Structure: 15-20% Damping - Fundamental Modes
- Viscous Damping coefficient  $C \approx 50$  lb-sec/in

**Figure 26**

*Brake line clip used in passive damping proof-of-concept test*

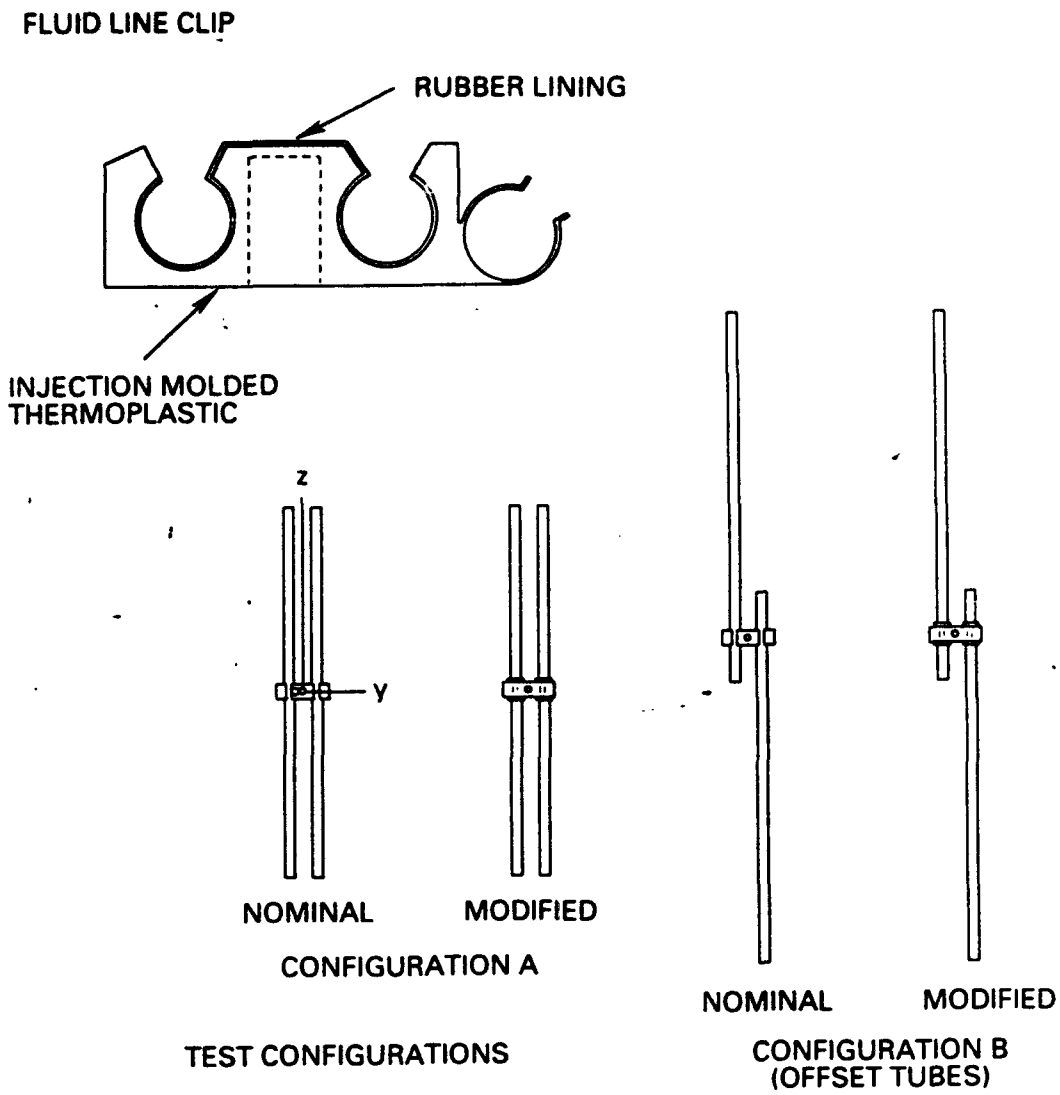
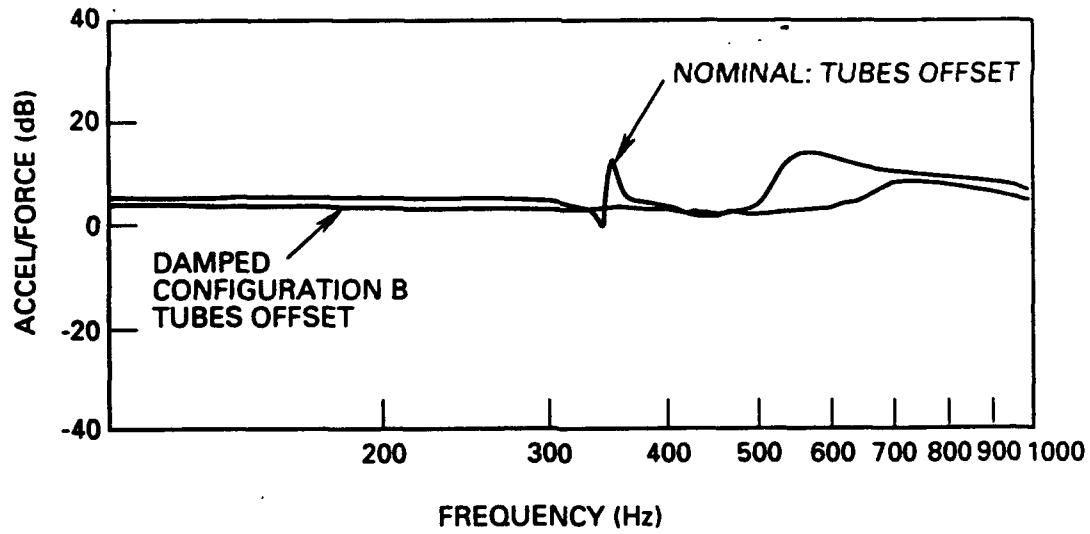
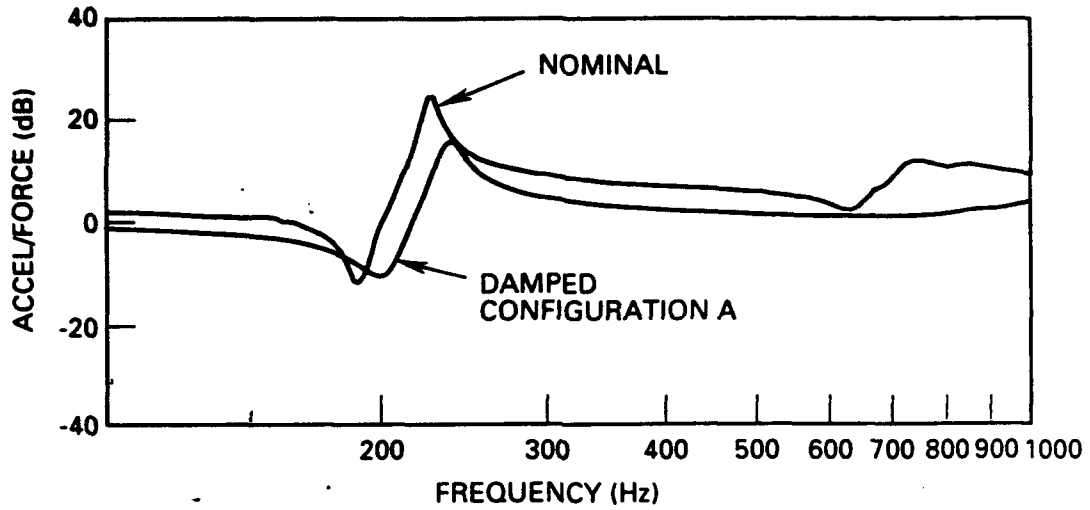


**Figure 27**

*Effect of passive damping material on brake line response*



reduction of over 7 dB was achieved at a peak response frequency. Even greater attenuation would be achieved with an integral optimized design.

### Distributed Damping Applications

Below we present applications of distributed damping to platelike and tubular structural components.

#### Tubular Members

During the course of the IR&D project: Vibration Suppression Design Techniques, in 1987, experimental investigations were conducted on aluminum tubes with constrained layer damping treatments and on integrally damped composite Gr/Ep tubes. During performance testing of the TRW Large Space Structure (LSS) it was observed that the control actuator excited the fundamental mode 105 in aluminum diagonal tubes on the structure. The sole purpose of these diagonal elements (see Figure 12) were to transmit actuator control forces to the upper plate whose motion was being controlled. An obvious band-aid approach was to wrap the tubes with constrained layer damping treatments. Figure 28 shows the results obtained using this technique. During this investigation it became obvious that segmenting the constraining layers yields improved results. This led to the development, fabrication and test of integrally damped composite tubes using segmentation techniques.

In graphite tubes, it was found that uniform segmented' constraining layers of graphite at 0 degree orientation was an effective constrained layer design. Initial experience with uniform segmented constraining layers lead to the more advanced design of alternating ply constrained layer concept. Even though the theoretical developments were based on axial behavior, experimentally it was verified that the designs are also effective for bending applications. Figure 29 displays cross-sections of both uniform segmented constrained layer as well as the alternating ply constrained layer concept.

#### Platelike Structures

Towards the end of 1991 viscoelastic damping techniques were integrated into two applications; printed circuit boards (PCB) and composite honeycomb panels. In both of these applications constrained layer techniques are utilized. However, no additional constrained layer has been

# Constrained Layer Damping Tests: Diagonal Element Damping

Figure 28

## Damping Test Results

No. Sheets	Configuration		HP Analyzer		Optron Analyzer	
	Bottom	Top	Frequency (Hz)	Damping (%)	Frequency (Hz)	Damping (%)
1			++	++	21.04	0.24
3			++	++	20.50	0.44
5			++	++	20.12	0.55
7			20.41+	0.848+	20.44	0.82
			20.37	0.864		
9			20.52	0.933	20.55	0.87
10			20.63	1.11	20.70	1.17
11			20.73	1.16	20.72	1.25
12			20.49*	1.24*	20.55	1.04**
			20.44	1.28		
13			20.24	1.36	++	1.39**
14			20.01	1.46	20.04	1.40**
15			20.11	1.51	++	1.39**

+ Measurements taken sequentially

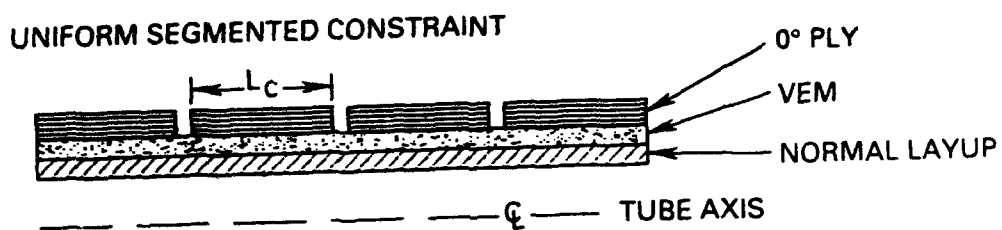
++ Measurement not taken

\* Measurements taken on consecutive days

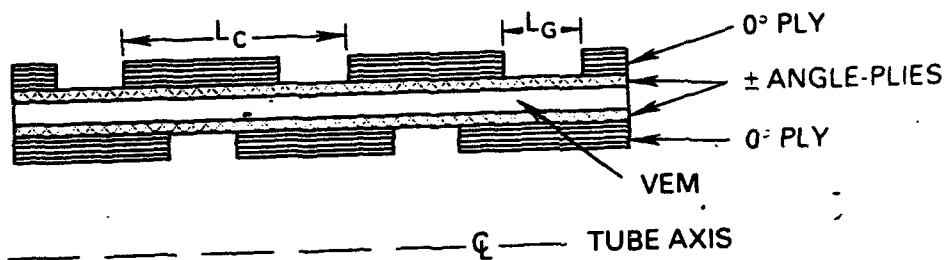
\*\* Large standard deviation in these measurements

**Figure 29**

*- Cross-Section of  
Alternating Ply Constrained Layer Concept*



ALTERNATING PLY CONCEPT\*



\*U.S. Patent # 5030490  
"Viscoelastic Damping Structure and Related Manufacturing Method"

added to the structure. Existing structural layers have been utilized to serve as the constraining layers.

### Damped Printed Circuit Board (D/PCB) Applications

A number of proof-of-concept multilayer PCB's were designed, fabricated and tested dynamically. Current design practice utilizes a thick conformal coating to reduce vibration induced loads on PCB mounted components and on solder joints. The conformal coating, often up to 1/8 in thick, adds a lot of weight to the board and makes it difficult to service. Since conformal coatings function as free layer damping treatments, they are not as effective as constrained layer damping treatments in reducing board vibrations.

The approach taken here is a variation of the constrained layer damping concept where the PCB layers are treated as the constraining layers. Vibration tests indicate that using this approach, the overall random vibration load on the PCB's can be halved compared to conformally coated boards, with no weight penalty. The comparisons of peak response reductions is depicted in the Table. The test board is shown in Figure 30. The random vibration environment is depicted in Figure 31. A typical plot of comparison of a conformally coated PCB with the present damping approach is shown in Figure 32. We believe that we have taken a successful first step in this important application. To completely qualify the concept, it will be necessary to measure the effect of the damping layer to other important PCB process parameters.

### Integrally Damped Honeycomb Panels

Due to favorable weight/stiffness characteristics, many structures in the aerospace and other commercial industries utilize honeycomb panels in their design. Due to the nature of the materials used, and fabrication practice, often these structures have very low inherent damping capacity. Thus, equipment mounted on these panels vibrate excessively, and at the same time the panels radiate high noise levels.

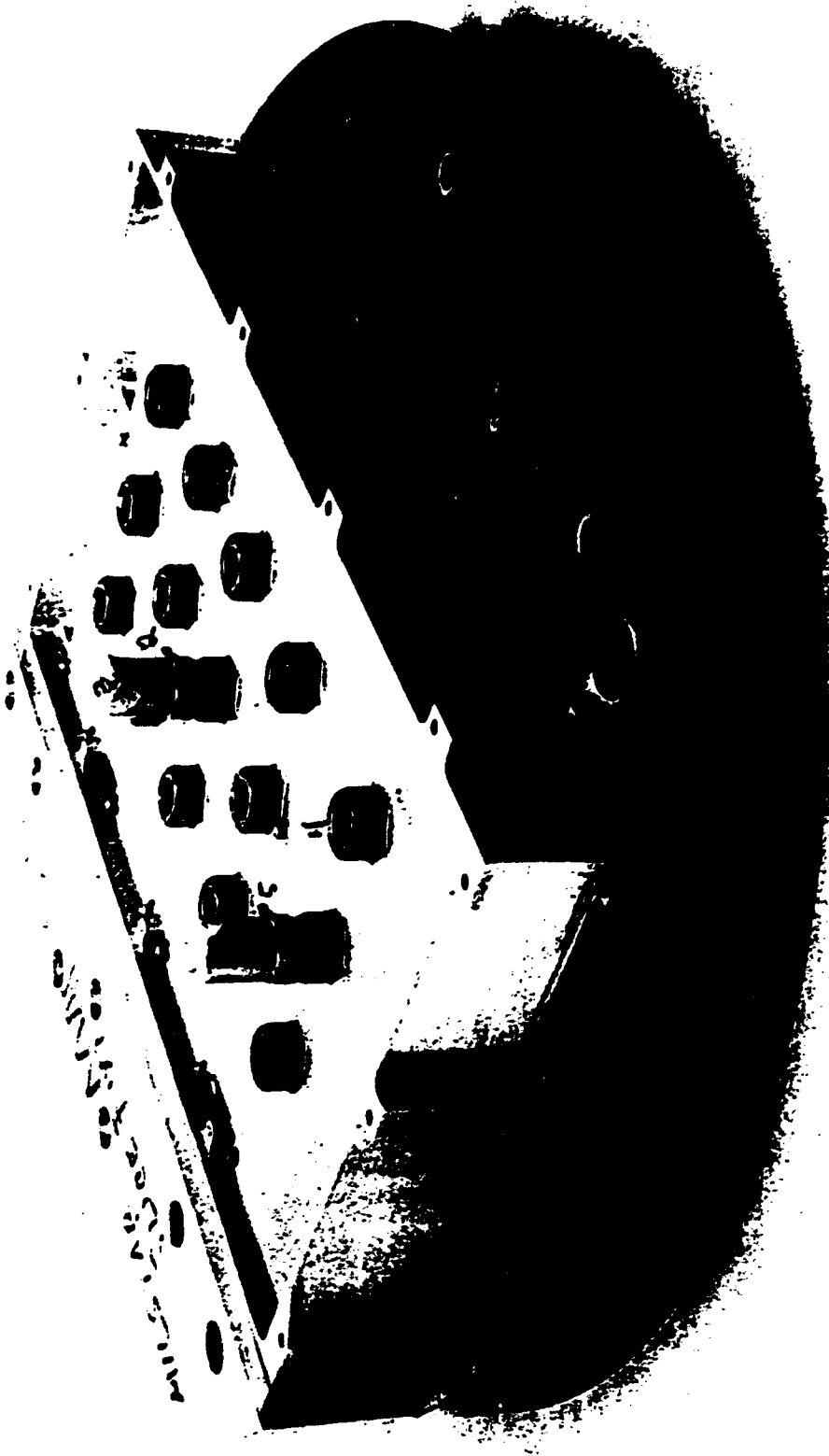
With the brief above mentioned background, the purpose of the present short evaluation study was to incorporate high damping viscoelastic material (VEM), and integrate it into the panel manufacturing process. Upon dynamic testing of a pair of panels, dramatic vibration and noise reduction were observed on the treated panel. Below a brief discussion of the design and test results are presented.

Table

MILSTAR Board Improvement Study  
Response from a Damped and Undamped Circuit Board  
20.3 Grms Input Spectrum Normal To the Board

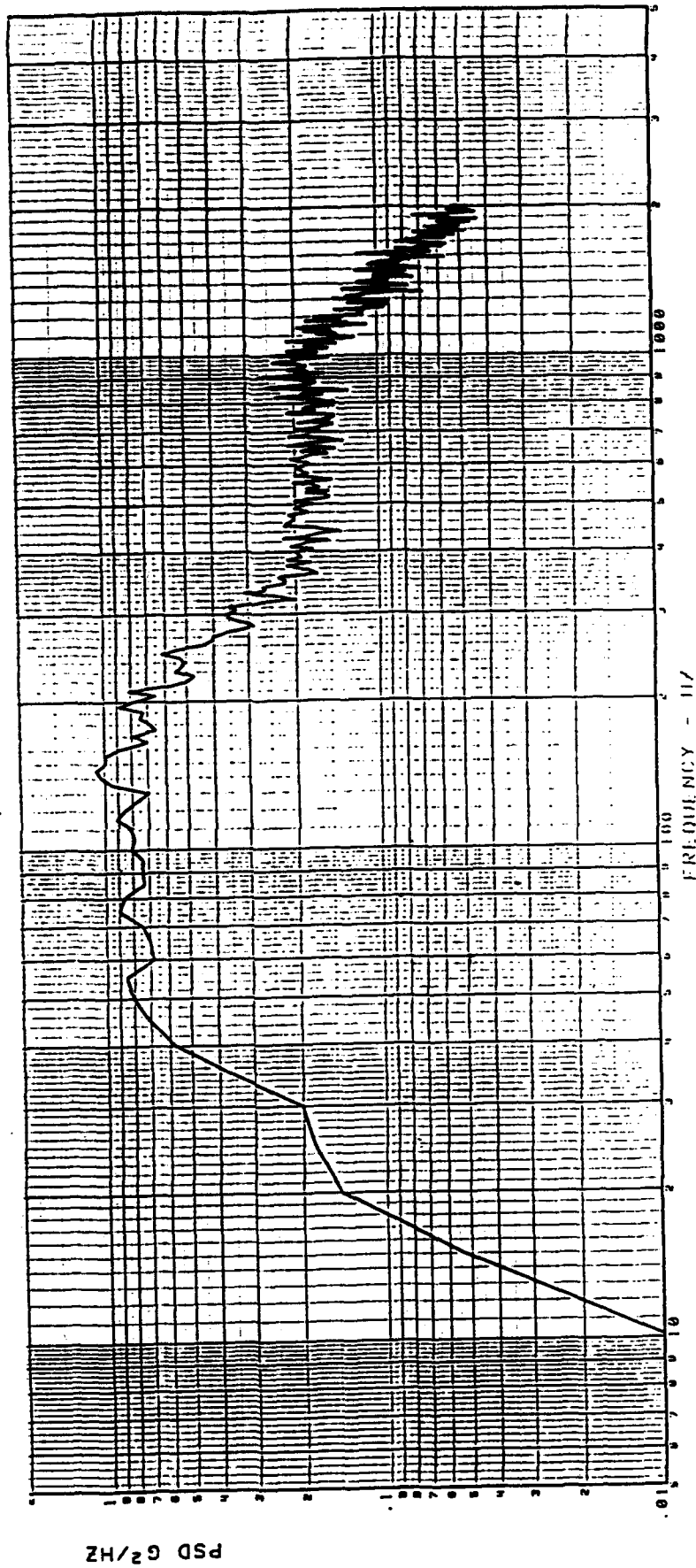
Accel No.	Overall Response (Grms)		Peak Response ( $g^2/hz$ )	
	Undamped	Damped	Undamped	Damped
2	72.1	44.8	102.	20.
3	93.0	57.5	180.	38.
4	72.6	45.5	160.	30.
5	58.8	35.5	70.	12.

Board Test Setup For Vibration Normal to the Board  
**Figure 30**



Note 4 Small Accelerometers Were Used For The Vibration Test  
The Two Large Accelerometers Were Used in Modal Hammer Tests

**Figure 31**  
20.3 Grms Test Spectrum Used For Board Damping Test  
(The Same Spectrum is Used For The MAP EM Qualification Test)



24814-1132-5141 -R 2-T 2-M 0-P IN

ROUGH DRAFT

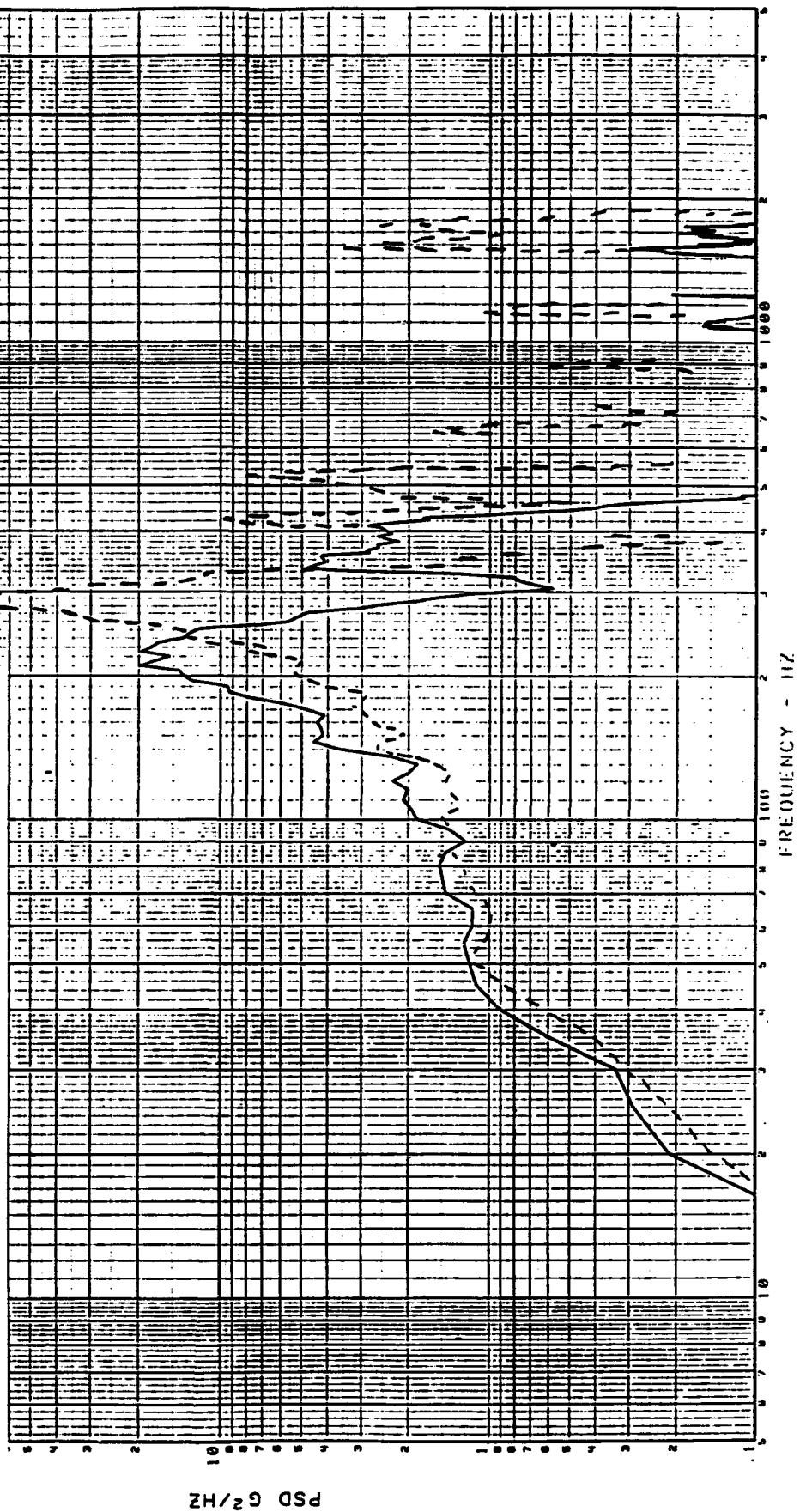
### Figure 32

Response Spectra For Accel #2

Damped 44.8 Grms

Undamped 72.1 Grms

—  
- - -



Two 12 in. x 12 in. honeycomb panels were fabricated. In the face sheets in one of the panels, made from several layers of P100 Gr/Ep tape plies, a viscoelastic (VEM) layer was incorporated. A quarter inch aluminum honeycomb core was utilized. The location, thickness and stiffness of the VEM was optimized using a finite element program. The damping treatment was integrated into the composite manufacturing process (see Figure 33). The other manufactured panel did not incorporate any damping material in its construction.

Both the damped and undamped panels were impact hammer tap tested in a free-free configuration depicted in Figure 34. Five cylindrical steel weights were bonded on each of the front and back surfaces of the panels to simulate mass loading to the panels. Both panels were suspended on a bungee cord supported on a rigid optical table. Each panel was instrumented with two accelerometers, one in the center of the panel and the other in the lower corner. A load cell and accelerometer instrumented hammer was utilized to excite the panel, by imparting an impact to the mass at the upper corner of the panel. The accelerometer responses were recorded and processed by a HP computer/software system. Typical time traces of the acceleration responses of the center and corner accelerometers are depicted in Figures 35 and 36, respectively.

Figures 35(a) and 36(a) depict the responses of the undamped panels, whereas Figures 35(b) and 36(b) show the response of the damped panel. As can be seen from these plots, the vibrations in the damped panel die down within 0.5 seconds, whereas for the undamped plate there is significant response even after 8 seconds (see Figures 35(a) and 36(a)). The transfer functions between the point of impact and accelerometer locations are depicted in Figures 37(a) and 37(b). The solid lines in these plots depict the transfer functions of the undamped board, whereas, the dotted lines represent the corresponding transfer functions for the damped board. Study of these figures reveals that there is an 11 fold reduction in vibration amplitude at the fundamental frequency of 44.6 Hz and a 13 fold amplitude reduction at the second fundamental mode of 87 Hz. In terms of damping, for the fundamental mode (45 Hz) we measured 0.2% of critical for the undamped panel and 2.3% damping for the damped panel. For the 2nd fundamental mode (87 Hz), the undamped panel had 0.35% damping, whereas the damped panel displayed 4.5% critical damping level. As for the higher frequency peaks, they have been effectively eliminated with the damping treatment as can be seen in Figure 37. The suppression of the higher frequency modes also dramatically reduced the radiated noise from an impact excited and treated panel.

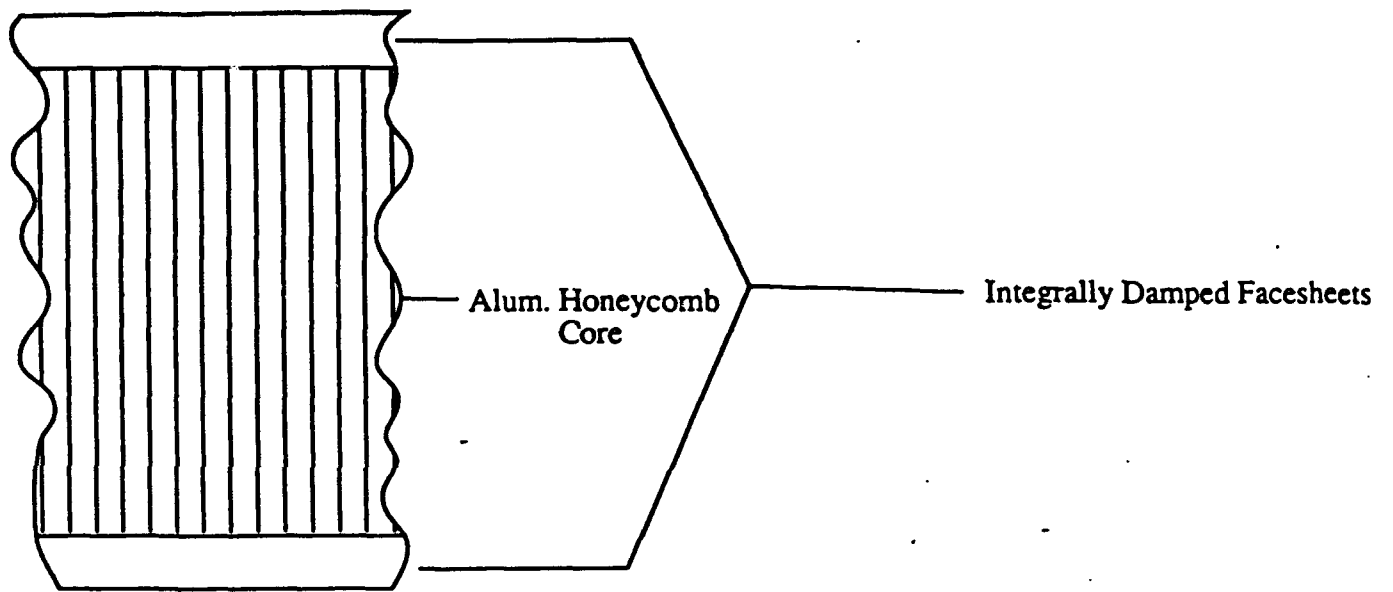


**Figure 33**  
**Damped Honeycomb Panel**

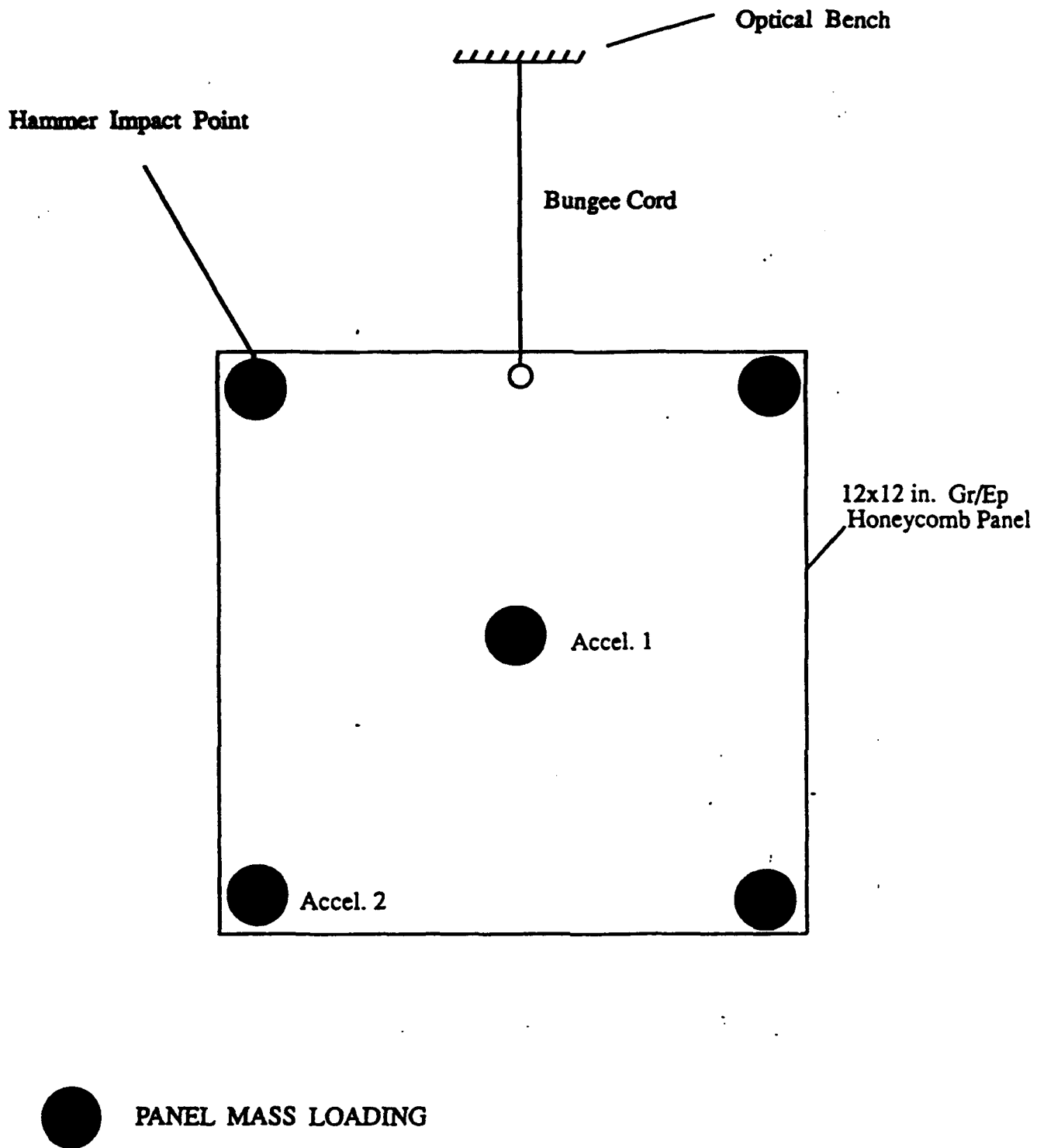
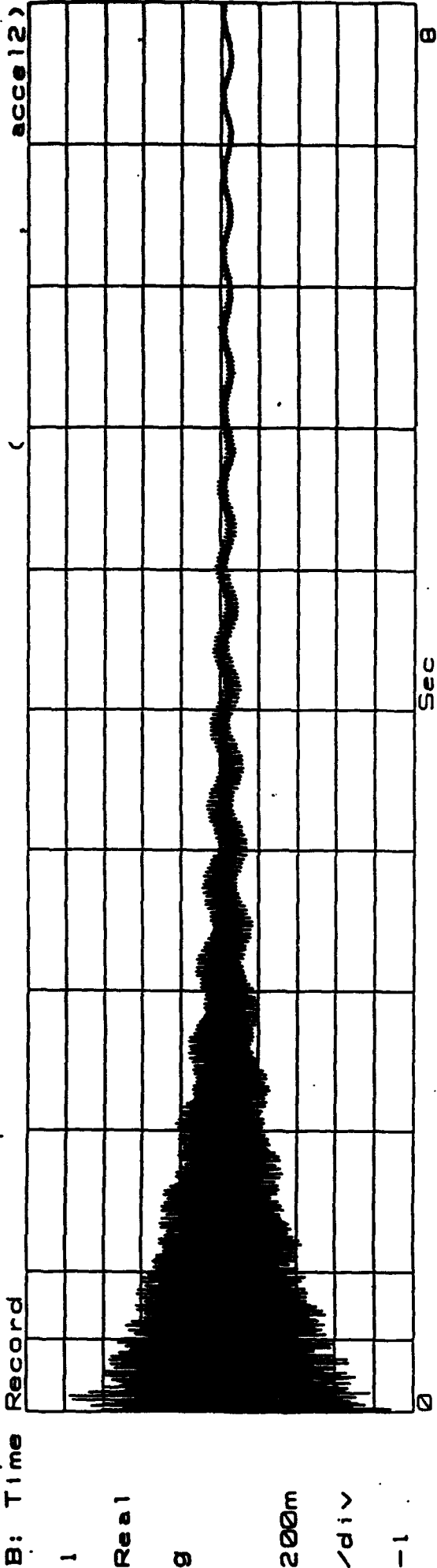


**Figure 34**  
**Panel Modal Hammer Test Configuration**

# Center Accelerometer Time Trace

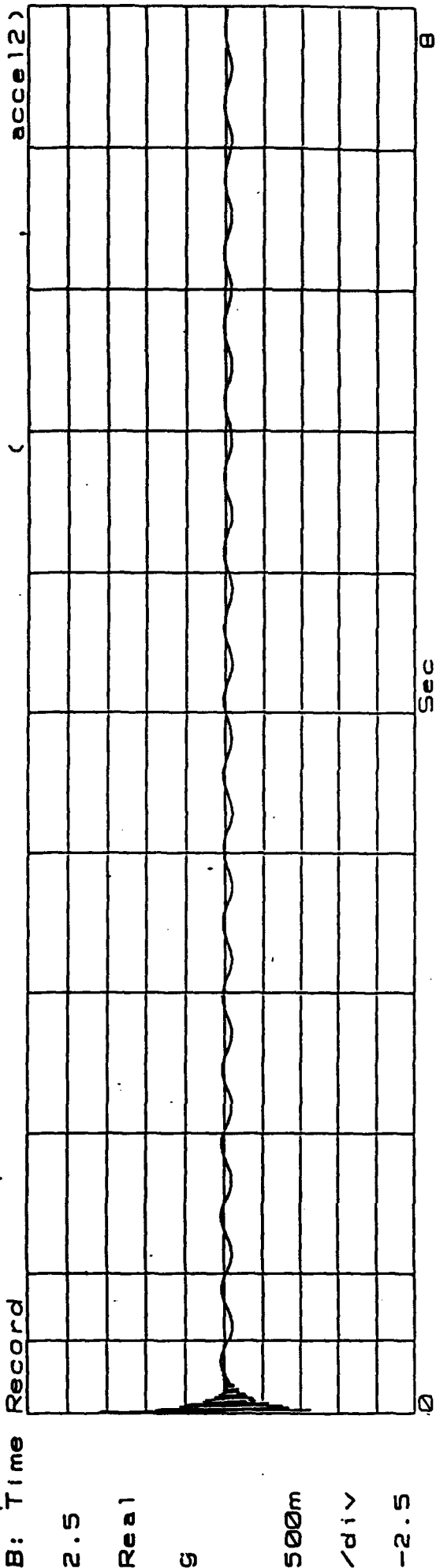
## Figure 35

Undamped Transient Response  
B: Time Record



(a) Panel without VEM

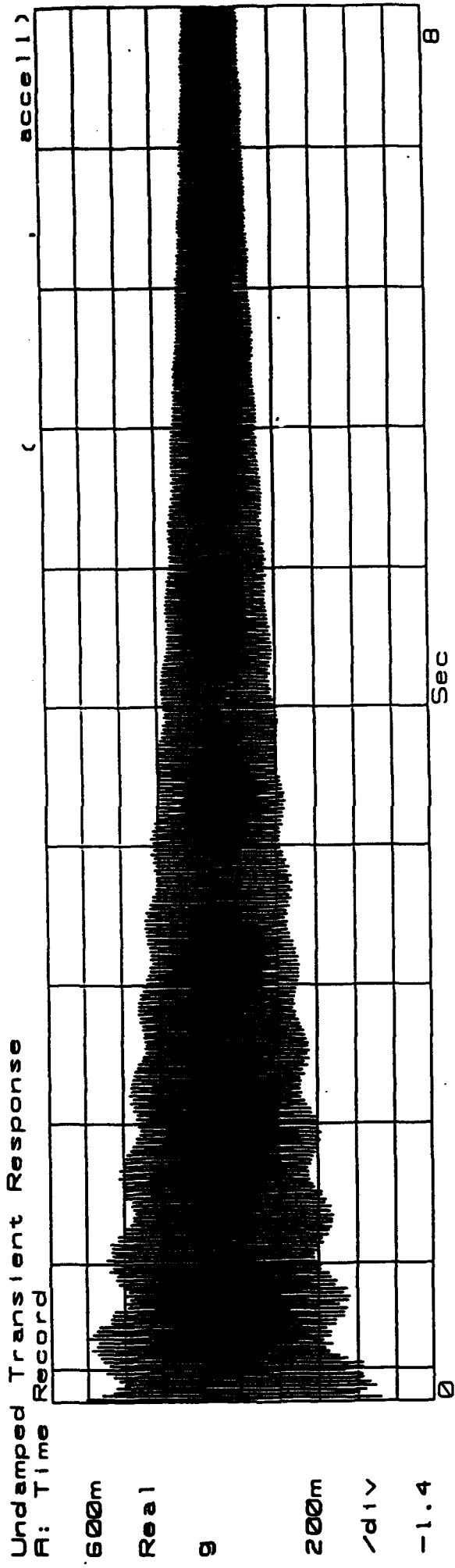
Damped Transient Response  
B: Time Record



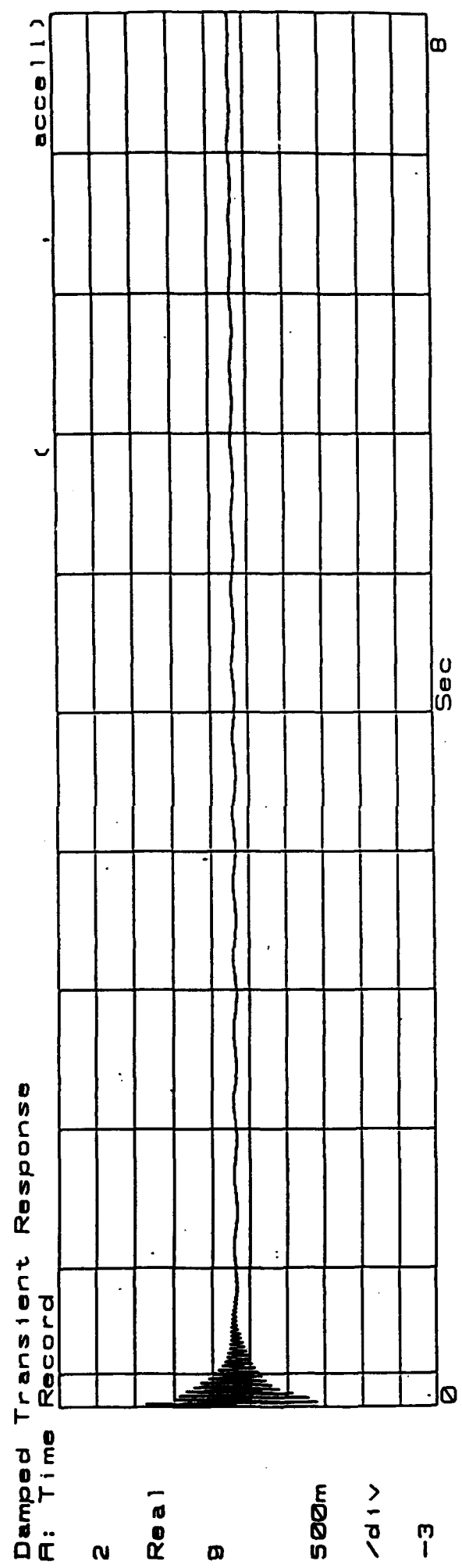
(b) Panel with VEM

# Corner Accelerometer Time Trace

Figure 36



(a) Panel without VEM

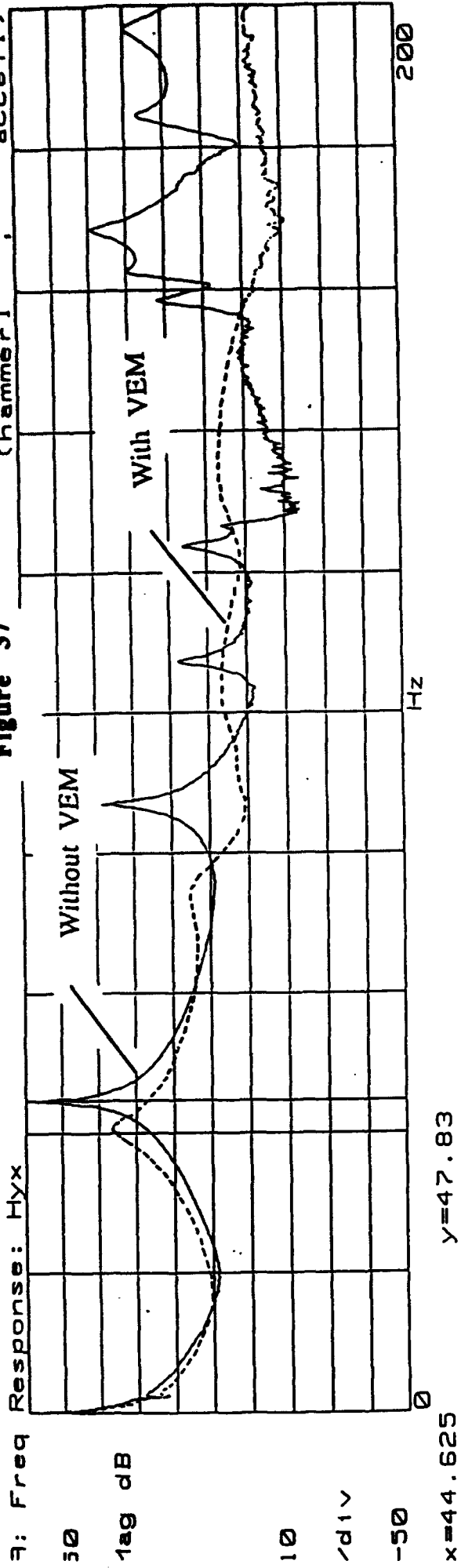


(b) Panel with VEM

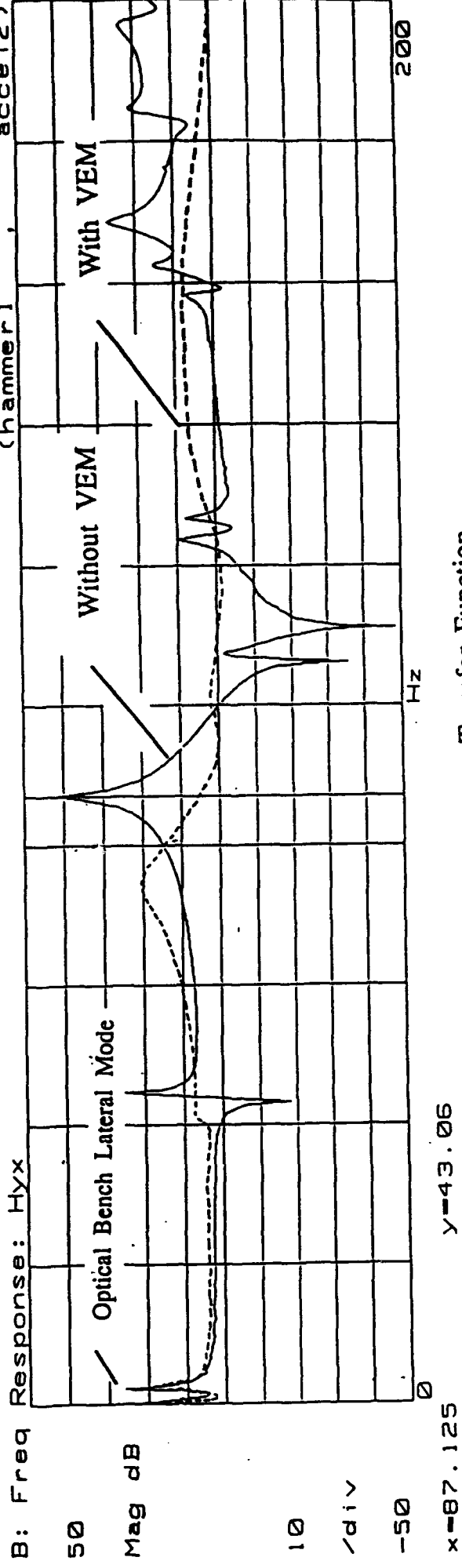
12

# Measured Transfer Functions

Figure 37



(a) Comer Accelerometer Transfer Function



(h) Center Accelerometer Transfer Function

53

Based on these observations, it is expected that there will be significant reduction in vibration response for equipment mounted on full size panels with damping treatment. Due to reduced vibration amplitudes, there will be less chance of vibration test failures and increase the fatigue life of the structure. More importantly, when the lowered vibration amplitudes are factored in the overall design and load cycle analysis, we can also expect important structure weight savings.

This novel application of passive damping technology in addition to significant reduction of vibration amplitudes is also 3-4 times lighter than the constrained layer damping treatment approach currently utilized in many applications. The reason for the weight reduction with this novel approach is that no constraining material is added, in fact the Gr/Ep layers above the VEM layer function as built-in constraining layers.

## **References**

1. Simonian, S.S., "Survey of Spacecraft Damping Measurements: Applications Electro-Optic Jitter Problems", ASME DE-Vol.5, The Role of Damping in Vibration and Noise Control, Sept., 1987. pp. 287-292.
2. Ruzicka, J.E., "Resonance Characteristics of Unidirectional Viscous and Coulomb-Damped Vibration Isolation Systems", Transactions of ASME Paper No. 67-Vibr-21, May 1967. pp. 1-12.
3. Simonian, S.S., C.S. Major, and R. Gluck, "An Experimental Study of Passive Damping and Active Control of Large Space Structures", Proceedings of the AFWAL Vibration Damping Workshop, Long Beach, CA, 27 Feb. 1984.
4. Major, C.S. and S.S. Simonian, "An Experiment to Demonstrate Active and Passive Control of a Flexible Structure", American Control Conference, Session TA-6, San Diego, CA, June 1984.
5. Simonian, S.S., "Synthesis of Discrete Passive Vibration Dampers", SAE Aerotech 85, Paper 851935, October 1985.
6. Major, C.S. and E.B. Shain, "Demonstration of Vibration Control of a Flexible Truss Structure", VPI&SU/AIAA Symposium, VI, Blacksburg, June 1985.

7. Simonian, S.S., M.S. Lukich and R. Gluck, "On a Balanced Passive and Active Vibration Suppression of Large Space Structures", AIAA/ASME/ASCE/AHS 28th Structures, Structural Dynamics and Materials Conference, Monterey, CA, April 1987.

# Design of Passive Piezoelectric Damping for Space Structures

Jack B. Aldrich, Nesbit W. Hagood, Andreas von Flotow, and David W. Vos  
Massachusetts Institute of Technology, Cambridge, MA 02139 USA

Passive damping of structural dynamics using piezoceramic electromechanical energy conversion and passive electrical networks is a relatively recent concept with little implementation experience base. This paper describes an implementation case study, starting from conceptual design and technique selection, through detailed component design and testing to simulation on the structure to be damped. About 0.5kg. of piezoelectric material was employed to damp the ASTREX testbed, a 5000kg structure. Emphasis was placed upon designing the damping to enable high bandwidth robust feedback control. Resistive piezoelectric shunting provided the necessary broadband damping. The piezoelectric element was incorporated into a steel flextensional device in order to concentrate damping into the 30 to 40Hz frequency modes at the rolloff region of the proposed compensator. The effective stiffness and damping of the flextensional device was experimentally verified. When six of these effective springs are placed in an orthogonal configuration, strain energy is absorbed from all six degrees of freedom of a 90kg. mass. The suspension modes of this vibration absorber was nominally tuned to 30Hz. A finite element model of the testbed was modified to include the six-axis damper. An analytical model was developed for the spring in order to see how the flex-tensional device and piezoelectric geometries effect the critical stress and strain energy distribution throughout the component. Simulation of the testbed demonstrated the damping levels achievable in the completed system.

## 1. INTRODUCTION

There are many applications where the addition of passive vibration damping to a structural system can greatly increase the system's performance or stability. The addition of passive damping can decrease peak vibration amplitudes in structural systems and add robustness to marginally stable active control systems[1]. Since the actual system modes are rarely in complete agreement with the model, even the modeled modes pose some threat to the stability of the closed loop system. In addition, lightly damped modes can exist in the rolloff region of the control system. Although these modes are not included in the model, they are still subject to control authority that has not yet rolled off. These rolloff modes pose another threat of instability to the control designer.

There are several sources of passive damping in space structures. The most common is material damping by which structural strain energy is dissipated. Damping is also provided by the friction and impacting that occur in the structural joints. The inherent damping in a truss can be increased by using damping enhancement schemes [3]. Several damping techniques are applicable to space structures. Some viscoelastic techniques have been developed for trusses in Ref. [4]. Proof-mass dampers (PMD's) have been applied previously to space structure damping in Ref. [5] and conceptually in Ref. [6]. Viscous damping struts were implemented in Ref. [7]. An active thermal damping scheme was used in Ref. [8]. Impact dampers were used in Ref. [9]. Truss structures with active piezoelectric members for vibration suppression are presented in Refs. [10] and [11].

In recent years, piezoelectric elements have been used as embedded sensors and actuators in smart structures by Crawley and deLuis[12] and Hagood[13], and as elements of active structural vibration systems by Fanson and Caughey[14], Hanagud *et al.* [15], and Bailey and Hubbard[16]. They have also been used as actuation components in wave control experiments by Pines and von Flotow [17]. Within active control systems, the piezoelectrics require complex amplifiers and associated sensing electronics. These can be eliminated in passive shunting applications where the only external element is a simple passive electrical circuit. Modelling of passive piezoelectric damping is described in Ref. [3]. Experimental verification of passive piezoelectric damping in a laboratory structure is described in Ref. [13]. The shunted piezoelectric itself could also be used as a damped structural actuator in a control system, as will be discussed later in this paper.

This work will present a passive piezoelectric damping implementation on ASTREX, a large space structure. The motivation behind this research is to provide as much passive damping as possible to facilitate line-of-sight control roll-off. Passively-shunted piezoelectrics were the chosen damping scheme because of their small implementation experience base relative to the viscoelastic or viscous damping schemes. Piezoceramic's high stiffness and temperature stability make it useful for structural damping applications.

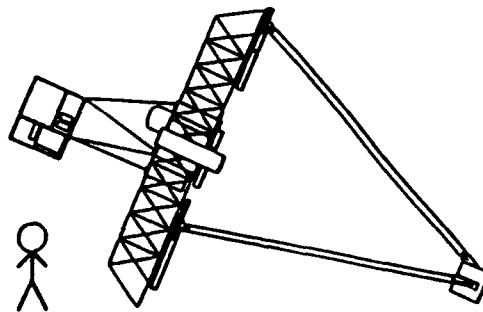


Figure (1) ASTREX space structure with scaled six-foot figure.

In Section 2, the modeling and passive damping issues of shunted piezoelectrics are defined. In Section 3, ASTREX and the control performance goals are introduced. In Section 4, two potential damping devices are compared. Section 5 explains the design, manufacturing and assembly details of the better device from the previous section. Section 6 describes analytical and finite element modeling techniques of the component. Section 7 gives the experimental verification of the component. Section 8 simulates the damping performance of the six-axis proof mass dynamic absorber in the ASTREX testbed. Conclusions are summarized in Section 9.

## 2. MODELING OF PIEZOELECTRIC PASSIVE DAMPING

### 2.1. Modeling of Shunted Piezoelectrics

Piezoelectric material can be used simultaneously as a passive damper, actuator and sensor. This paper focuses on its development as a passive damper. This function, however, is best understood in the context of its other two roles. The model in figure 2 shows that the passive damping shunting current, the actuation current and the applied stress can all be used to strain the piezoelectric. See equation (1). Once the piezoelectric is strained, mechanical energy is converted into electrical energy which is dissipated across a shunting circuit. Thus, the piezoelectric is depicted as an transformer in the network analog in Figure 2(b). This electromechanical coupling gives the piezoelectric its third role as a sensor.

It is possible to choose the shunting parallel circuit impedance,  $Z_i^{sh}(s)$ , to maximize the effective material loss factor,  $\eta$ . If an appropriate  $Z_i^{sh}(s)$  is selected, the cyclic voltage buildup is appropriately phased with the applied stress to yield piezoelectric passive damping. A complete treatment of this concept is given in Ref [3]. Once the shunting and electrical impedances are defined by passive damping performance considerations, the current-strain and stress-strain frequency dependent relationships are constrained by equation (1).

$$S = [s^2 - d_i L^{-1} Z_i^{sh} s A d] T + [d_i L^{-1} Z_i^{sh}] I \quad (1)$$

This equation gives the strain,  $S$ , for a given applied stress,  $T$ , and forcing current,  $I$ . Notice that shunting the piezoelectric does not preclude use of the shunted element as an actuator in an active control system but rather modifies the passive characteristics of the actuator.

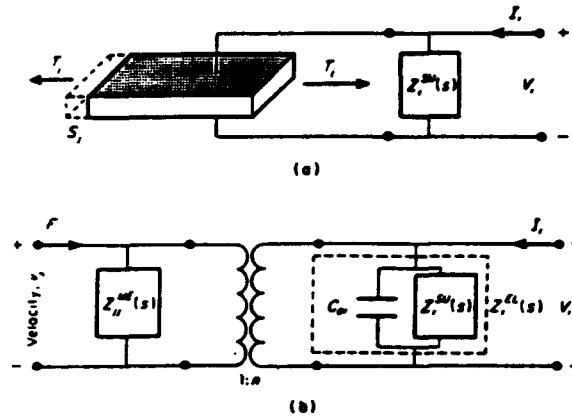


Figure 2. Simple physical model of a uniaxial shunted piezoelectric (a) and its network analog (b).

### 2.2 Resistive versus Resonant Shunted Piezoelectrics

In order to simplify the modeling, it is often possible in practical damping applications to load the piezoelectric in only one of the following three directions: *longitudinal case*, force and field in the "3" direction; *transverse case*, force in "1" or "2" direction, field in "3" direction; *shear case*, force in "4" or "5" direction (shear), field in "2" or "1" direction, respectively. If the designer desires broadband damping for the structure, the shunting circuit is a resistor. If the designer desires narrowband damping, both an inductor and a resistor must be shunted across the piezoelectric to form a resonant shunted LRC circuit.

In resistively shunted piezoelectric damping, the resistor is varied until the RC circuit time constant,  $\rho$ , is in the vicinity of modes to be damped. In resonant shunting, both the inductor and the resistor must be tuned. Such a scheme should only be considered for damping well-modeled structural modes that require excessive damping. Since broadband damping was needed, resonant circuit shunting was not investigated in this paper. Another option is to tune several inductor and resistor pairs to damp discrete modes.

### 2.3. Resistive Shunted Piezoelectric Material Properties

The resistor shunts the electrodes of a piezoelectric element as seen in figure 3.

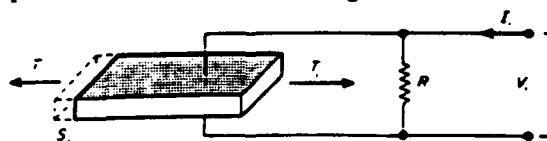


Figure 3. Resistor shunted piezoelectric assumed geometry with forcing in the  $j$ th direction and electric field in the  $i$ th direction.

Deriving the effective material properties from impedance yields the loss factor,  $\eta$ , and relative modulus,  $\bar{E} = \frac{E}{E_{sc}}$   $\therefore$

$$\eta_{\bar{E}}^m(\omega) = \frac{\rho k_p^2}{1 + \rho^2(1 - k_p^2)} \quad (2)$$

$$\bar{E}_{\bar{E}}^m(\omega) = 1 - \frac{k_p^2}{1 + \rho^2(1 - k_p^2)} \quad (3)$$

Where  $\rho$ , is the dimensionless frequency:

$$\rho_i = R_i C_{\mu} \omega = \frac{\omega}{\omega_d} \quad (4)$$

The loss factor and relative modulus equations have been plotted versus  $\rho$ , the dimensionless frequency (or the dimensionless resistance) in Figure 4 for a typical value of the longitudinal coupling coefficient. These curves are similar to the equivalent material curves for a standard linear solid. As illustrated by the graphs, for a given resistance the stiffness of the piezoelectric changes from its short circuit value at low frequencies to its open circuit value at high frequencies. The frequency of this transition is determined by the shunting resistance. The material also exhibits a maximum loss factor at this transition point.

As seen in figure 4, the material loss factor peaks at 42.5% in the longitudinal and shear cases. The transverse case has an 8% peak loss factor.

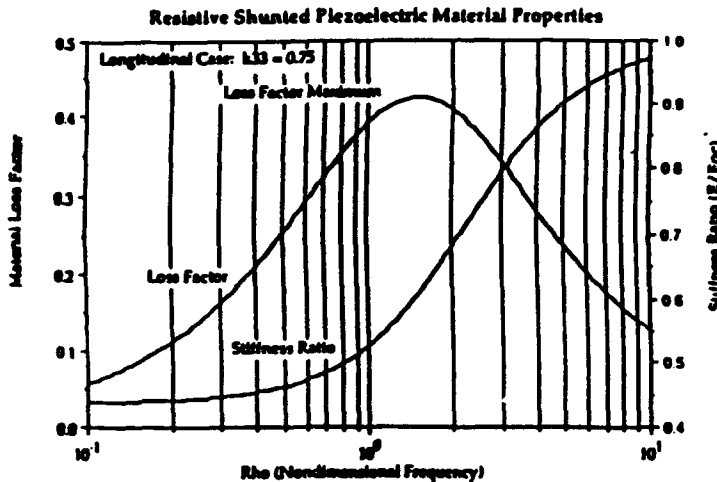


Figure 4. Effective material properties of a resistively shunted piezoelectric in the longitudinal case ( $k_{33}=0.75$ ) showing material loss factor and relative modulus.

## 2.4. Coupling Shunted Piezoelectrics to Structures

The peak loss factor for the piezoelectric in Figure 4 will decrease when it is coupled to its host structure, according to the fraction of the total strain energy that is actually in the piezoelectric, reference [18]

$$\eta^{TOT} = \sum_{i=1}^n \eta_i U_i / \sum_{i=1}^n U_i \quad (5)$$

where  $U_i$  is the strain energy in the  $i$ th element of the structure. The challenge is thus to employ the damping piezoelectric material in areas of high strain energy to take advantage of this weighting. Of course, the high strain energy locations must also be ranked by their influence on system performance objectives.

The strain energy sharing concept is first considered when designing the damper to be applied to the structure. Note that the word, damper, refers to the piezoelectric damping material and any necessary series or parallel stiffnesses that give the device structural integrity. All damping devices can be simplified to follow one of two different design procedures:

Case(1) If the damper is made up of 100% piezoelectric that is loaded in one direction the material properties in figure 4 apply. An example of this is a shear washer to be discussed in section 4.1. In this case, the appropriate resistor moves the peak of the component loss factor to the desired frequency:

$$\rho_i = R_i C_{\mu} \omega = \sqrt{1 - k_p^2} \quad (6)$$

Case(2) If the damper consists of a piezoelectric with series and/or parallel stiffnesses, the peak loss factor location can no longer be guided by equation (6). In this case, equation (6) is a good first iteration approximation if series stiffnesses are high and parallel stiffnesses are low compared to the piezoelectric. The short circuit stiffness,  $K_s$  and the open circuit stiffness,

$(K_1 + K_2)$  must be computed from an analytical or finite element model of the complete device. Assuming the component's effective material properties are analogous to the piezoelectric, a first order estimate of the effective coupling coefficient,

$$K_d^2 = \frac{K_{33}}{K_{33}} \quad (7)$$

is then used in (6) in place of  $K_d^2$  to size the resistor. An example of this is the flex-tensional device described in section 4.2.

Regardless of the design case, the short and open circuit stiffnesses of the damper determine two of the minimum three points necessary to describe the first-order stiffness curve of the damper (Figure 5(a)). The third parameter, conveniently given by the transition frequency,  $\rho$ , is determined by the value of the shunting resistor.

## 2.5. Finite Element Modeling of Piezoelectric-based Dampers

In order to determine the performance of a given piezoelectric damping scheme in its host structure, the damper's stiffness and loss factor curves from figure 5(a) must be modeled. This behavior is captured by the following spring and dashpot finite element configuration (Figure 5(b)).

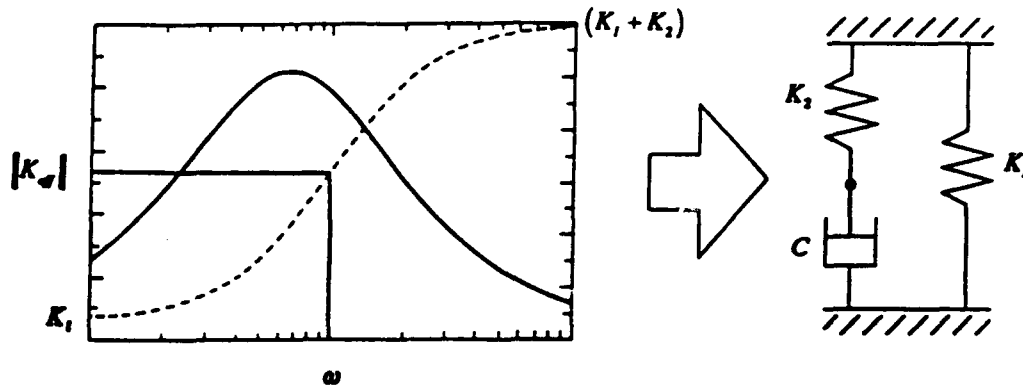


Figure 5. (a) Effective damper properties of a resistively shunted piezoelectric damper in the longitudinal case ( $k_{33}=0.75$ ) showing damper loss factor (solid) and the damper's stiffness (dash). (b) Equivalent model of the piezoelectric-based damper.

The complex stiffness of the three element configuration is modeled with two linear spring stiffnesses,  $K_1$ ,  $K_2$  and one complex dashpot stiffness,  $Ci\omega$  as follows:

$$K_{eff} = K_1 + \left( \frac{1}{K_2} + \frac{1}{Ci\omega} \right)^{-1} \quad (8)$$

Given  $K_1$  and  $K_2$  from static structural models,  $C$  is the only unknown constant needed to complete the dynamic model. Simple algebraic manipulations yield the appropriate value of  $C$  such that the transition from low-frequency short-circuit stiffness to high-frequency open-circuit stiffness occurs at the correct transition frequency,  $\rho$ . This is accomplished by arbitrarily selecting a third coordinate point,  $(\omega, |K_d|)$ , near the transition of the stiffness curve.

Figure 5 shows an equivalent mechanical model of the resistively-shunted piezoelectric damper (including series and parallel stiffnesses). This mechanical equivalent model is suitable for inclusion in commercial finite element software.

The real and imaginary parts of the complex stiffness are separated in (9) to calculate the real magnitude in (10):

$$K_{eff} = \left( \frac{K_1 K_2^2 + (C\omega)^2 (K_1 + K_2)}{K_2^2 + (C\omega)^2} \right) + i \left( \frac{C\omega K_2^2}{K_2^2 + (C\omega)^2} \right) \quad (9)$$

$$|K_{eff}| = \sqrt{[Real(K_{eff})]^2 + [Imag(K_{eff})]^2} \quad (10)$$

The results of (10) are manipulated into the quadratic equation,  $C^4 \{a_1\} + C^2 \{a_2\} + \{a_3\} = 0$  and solved for the only unknown,  $C$ .

$$\begin{aligned} & C^4 \left\{ \omega^4 [(K_1 + K_2)^2 - (|K_{eff}|)^2] \right\} + \\ & C^2 \left\{ \omega^2 [2K_1 K_2^2 (K_1 + K_2) + K_2^4 - 2(|K_{eff}|)^2 K_2^2] \right\} + \\ & \left\{ K_2^4 (K_1^2 - (|K_{eff}|)^2) \right\} = 0 \end{aligned} \quad (11)$$

### 3. ASTREX AND CONTROL PROBLEM OVERVIEW

Before the piezoelectric-based damper or actuator can be designed and analyzed, the characteristics and performance criteria of the undamped structure, ASTREX, must be considered. ASTREX includes a tripod that supports a mirror known as the secondary (see figure 6). The primary consists of over a hundred 1 meter backplane struts that form a hexagonal-shaped lattice truss. The tertiary, located a couple of meters behind the secondary, houses the electronics. Thrusters located on opposite sides of the primary, are available to perform rapid slewing maneuvers. Two control moment gyros are planned on the primary, as are two reaction wheels on the secondary.

ASTREX's original control-structures interaction performance-metric, involved minimizing the line-of-sight error from step input slewing maneuvers. For purposes of this project, we have assumed use of the two reaction wheels on the secondary as control actuators. The frequency response of this transfer function (from torque applied to line-of-sight) for the undamped structure is reproduced in figures 17 through 19. From considerations of practical bandwidth limits of the reaction-wheel actuators, together with knowledge of the capability of fast steering mirrors, we semi-arbitrarily selected 30 to 40Hz as a target closed-loop bandwidth for this control loop. Eigen-frequencies below this bandwidth would be actively controlled. Eigenfrequencies near the 30 to 40Hz cross-over would present robust stability problems. Eigenfrequencies far above this bandwidth will need enough passive damping for gain stabilization.

These heuristic considerations, codified in [2], lead us to emphasize passive damping treatments that target the decade centered about 30 to 40Hz, and target modes which contribute strongly to rotational motion of the secondary.

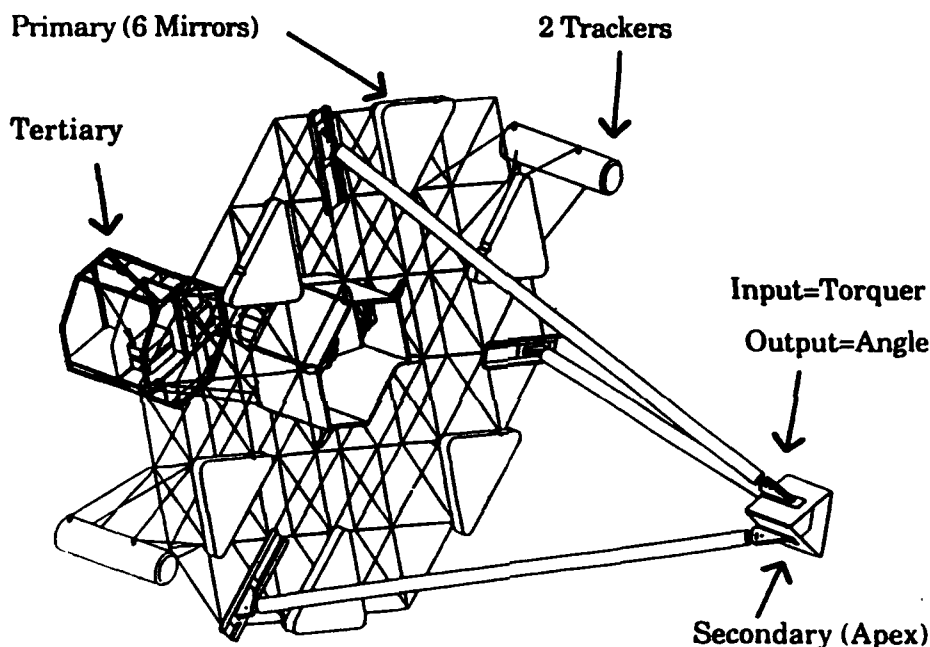


Figure 6. ASTREX space structure overview.

### 4. POTENTIAL PIEZOELECTRIC DAMPING IMPLEMENTATIONS FOR ASTREX

The problem of damping a complicated space structure with piezoelectric materials is open-ended. In trusses consisting of repetitious truss bays the problem is to optimize strut placement. In structures, like ASTREX, the ambiguity can be interpreted as a freedom to invent any conceivable device that has considerable influence in damping the modes that facilitate control rolloff.

Building struts for ASTREX was not considered for the following two reasons: 1. It was determined in reference 2 that replacing ASTREX's primary composite struts with piezoelectric struts offers insignificant damping with only a few struts being switched. Obviously, if too many struts are replaced, the structure becomes too heavy. 2. TRW has already built laminated piezoelectric/composite active struts which replaced the three tripod legs.

Two alternative damping schemes were considered. The "smart-node", active-joint or piezoelectric washer is addressed in section 4.1. The six-axis proof mass damper with piezoelectric actuators is addressed in section 4.2.

#### 4.1. A Potential Damping Device

The washer design consists of piezoelectric material that is strained in the shear mode under dynamic loading. As the tripod leg bends it exerts a reaction torque at the tripod mount, which behaves as a fixed boundary condition. Inserting piezoelectric washers between the ears of the tripod strut and the clamps of the mount, transforms the rigid boundary condition into a rotary spring as seen in figure 7.

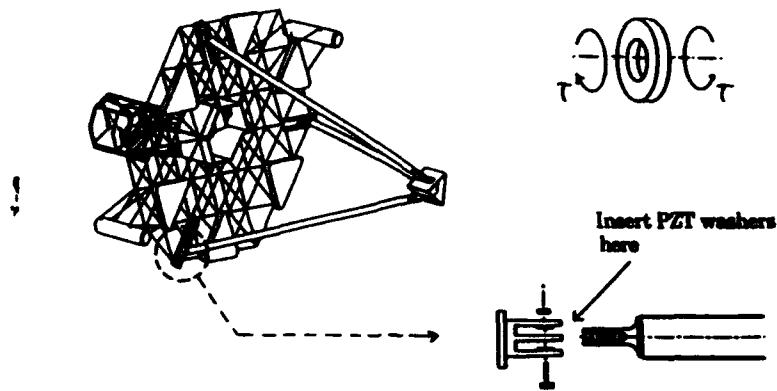


Figure 7. Piezoelectric "washer" design for tripod strut joints. Two washers per strut are each loaded in the shear mode.

The washer was modeled in ASTREX finite element code as a rotary spring with only one rotational degree of freedom aligned with the bolt. The washer's broadband resistive damping was designed so that the peak loss factor was located near 30Hz. An optimal rotary short-circuit stiffness value of 400,000 N/m<sup>2</sup> was attained from finite element iterations. This equates to a washer with a one inch outer diameter with a half-inch hole and one-eighth inch thickness. This design promises to absorb 10% of the total strain energy for a typical tripod bending mode at 29Hz. A loss factor of 4.2% can be computed from equation (5).

Stresses were computed from NASTRAN finite element program. If the input torquer disturbance source were activated at maximum output, finite element analysis showed that the design would either fail from brittle fracture and/or fail to damp due to excessive and/or permanent depolarization at stresses higher than 50MPa (See figure 8). Unlike other damping designs, there is no practical way to provide a mechanical stop to prevent excessive rotary motion. When modes skew to the plane of the washer are considered, the stress issue cannot be ignored. Thus, the design was discontinued. In addition, manufacturing the washers would involve inventing a circumferential poling machine. Such a task is out of the scope for this project.

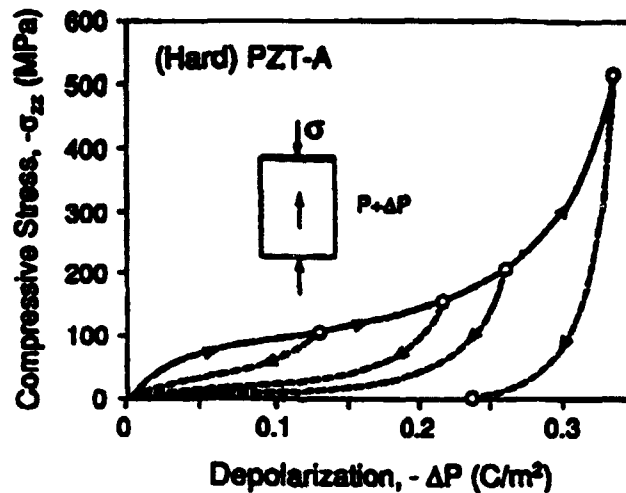


Figure 8. Percent depolariation versus applied stress in MPa for PZT Ch-5400. Note the permanent depolarization hysteresis loop.

#### 4.2. Another Potential Damping Device

The six-axis proof mass vibration absorber with six piezoelectric dampers was born out of the need to create an energy sink for the heavy (90kg) apex mass undergoing large displacements. Displacements over 4 times those found in the backplane, have been determined from ASTREX's eigenvectors. Finite element optimization of the stewart platform configuration indicated that an effective damper stiffness of 1.5N/μm would channel over 50% of the total strain energy in the piezoelectric material for several modes under 50Hz. Theoretically, this means that modal loss factors as high as 20% are attainable. Mode shapes and loss factors that are representative of their corresponding frequency region, are shown in table 1.

The six-axis proof mass damper design in figure 9 consists of a 90kg. mass suspended from the interior of the 24"x24"x24" triangular apex housing by six flex-tensional damping devices. It should be noted that the 90kg. mass primary purpose is to balance the ASTREX testbed on its air bearing ball joint. The ball joint is connected to the center of the hexagonal primary truss which is elevated above the floor by a twenty foot supporting post.

The six-axis configuration can be optimized by using the maximum stroke capability offered by the stewart-bridge geometry. This optimal stroke/actuation configuration was slightly modified to accommodate the geometrical constraints of the congested apex

interior. (see figure 9) If the distance,  $d$ , between adjacent struts in each of the three orthogonal strut pairs is decreased, the rotational eigenvalues of the proof mass decreases due to the decrease in the systems effective moment arm. This yields a more effective damper for the low frequency rotary movements. The tradeoff is the increase in static stresses of the dampers. The distance versus stress optimization for the modified Stewart bridge was not investigated, since the dimensions of the damping device prevented the aforementioned distance reduction.

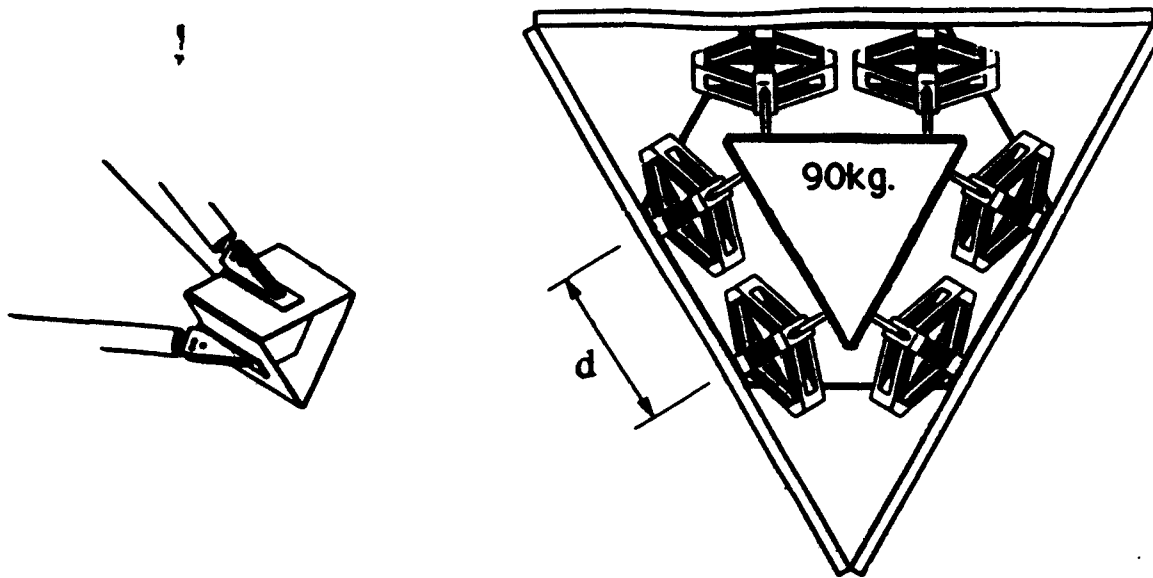


Figure 9. (a) Apex. (b) Six-axis vibration absorber with 90kg. proof mass attached to apex housing interior by 6 piezoelectric-based damper/actuators.

#### 4.3. Damping Performance: Washer versus 6-Axis Absorber

In order to decide which damping scheme to attempt to build, the two designs were evaluated according to their ability to absorb strain energy from performance-sensitive modal displacements. Recall equation (5), that states that the system loss factor is proportional to the fraction of the total strain energy in the piezoelectric for a given mode. Although only three modes are listed in figure 10, the trend of six-axis vibration absorber dominance is present in all modes. The potential merit of the six-axis absorber obviously exceeds that of the washer design.

Mode #13	Mode #23	Mode #40
$f = 29\text{Hz}$	$f = 42\text{Hz}$	$f = 77\text{Hz}$
$\eta_{\text{washer}} = 19.4\%$	$\eta_{\text{washer}} = 7.2\%$	$\eta_{\text{washer}} = 0.42\%$
$\eta_{\text{gizmo}} = 4.2\%$	$\eta_{\text{gizmo}} = 0.042\%$	$\eta_{\text{gizmo}} = 0.008\%$

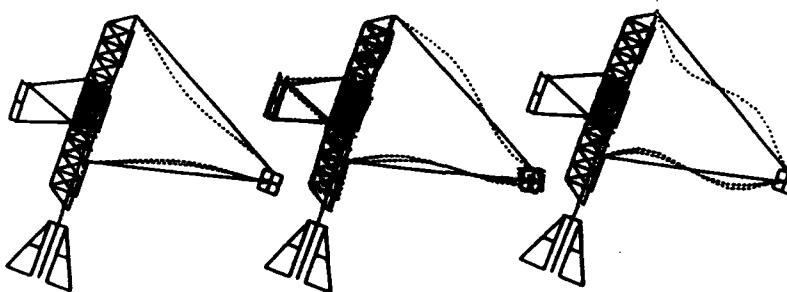


Figure 10. The washer and the six-axis gizmo design are compared.

#### 5. DESIGN DETAILS OF THE COMPONENT

The crux of six-axis proof mass damper design is the component design of the six damping devices. Piezoelectric material alone is too stiff and brittle to be used as a low-frequency damper with structural integrity. A 30Hz tuned vibration absorber will sag about  $250\mu\text{m}$  in a one-gee field. This is an enormous deflection for a small piece of piezoceramic. Thus, a properly designed stroke amplification device is essential in reducing the device's stiffness and increasing its travel.

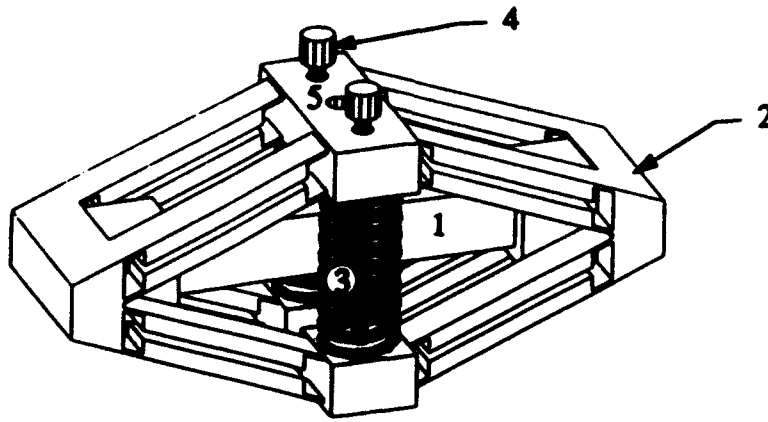


Figure 11. Drawing of the prototype flex-tensional piezoelectric stroke amplification device. Parts include: 1. One 16-layer piezoelectric stack with two steel shims. 2. One steel flex-tensional stroke amplifier. 3. Two preload springs. 4. Two threaded steel rods with adjustable mechanical stops. 5. Axial stinger. (only the stinger hole is shown here)

The role of each of the five parts described in figure 11 and their associated design, manufacturing and assembly considerations will be assessed in the following five paragraphs:

1. The role of the piezoelectric stack is to provide resistively-shunted passive damping. The design uses mechanical amplification to reduce the stiffness of the stack in order to meet the 30Hz target eigen-frequency. This, in turn, reduces large critical stresses in the stroke amplifier as described in the following paragraph. Reducing the stack's stiffness may also be achieved by increasing its length and decreasing its cross-sectional area until the material stresses are no greater than 50MPa to ensure minimal performance loss due to hysteretic depolarization. Buckling must also be considered for slender stacks. Another design consideration for the piezoelectric material is to have the appropriate number of capacitors (stacks) to balance the trade-off between glue-layer strain energy loss and large capacitor thickness flux-loss. A 16-wafer piezoelectric stack was the engineering judgement. The glue-layers gave the piezoelectric stack a coupling-coefficient,  $k_{33}$ , of 0.59 as opposed to the nominal material value of 0.71. This reduces the available piezoelectric peak loss factor from 35% to 21%.

2. The role of the steel flex-tensional stroke amplifier is to provide the necessary amplification to give the piezoelectric structural integrity and low stiffness. Stroke amplification at the device level equates to strain reduction in the piezoelectric. The ideal stroke amplifier would consist of beams with infinite axial stiffness connected by perfect hinges so that all the component's strain energy would be subject to the damping authority of the piezoelectric stack. A realistic component, however, has the following design criteria: 1. The lever angle is selected according to the analytical model, equation (12), so that the desired effective stiffness is realized. 2. The sum of the axial stiffness of the flexures is much greater than that of the stack. 3. The bending stiffness of the flexures is much less than that of the component. 4. The flexure stresses are less than their respective yield stresses. The stroke amplification device consists of a monolithic piece of steel, which is carved out of quenched and tempered 40 Rockwell steel by a machining process called: wire Electron Discharge Machining (wire-EDM).

3. The role of the two preload springs is to ensure that the piezoelectric stack remains in compression under normal loading conditions. This also keeps the flexures in tension. The optimal design for the spring is a mile high spring with negligible stiffness relative to the component's effective stiffness. When this type of spring is placed in the device, the preload requirement is met with negligible device stiffness contribution. This idealization is limited by practical assembly procedures which require pronged pliers insertion to shorten the spring temporarily for insertion into the EDM'ed part. Spring spacing must be large enough to allow for flattened-wrench adjustment of the mechanical stop nuts inside the springs. This also limits the ideal mile high spring idea.

4. The two mechanical stops are adjusted to prevent accidental overloading of the gizmo. The maximum operating input torque of 28 ft.lbs. plus gravity load yields the component's maximum axial displacement of 0.3mm. Motion in excess of this number is inhibited. The mechanical stops are adjusted by wrench and locked in place with adjacent locknuts.

5. The role of the axial stinger is to suspend the 90kg. mass according to the modified Stewart bridge configuration. High axial stiffness and low bending stiffness of the stinger minimizes strain energy sharing. Low bending stiffnesses can be obtained by using a pinned flexure at each end of the stinger.

## 6. ANALYSIS OF THE COMPONENT

### 6.1. Analytical Model of Component

A simple analytical model is used to estimate the stiffness of the component given the lever ratio, piezoelectric stiffness and lever arm stiffness. The lever arm stiffness consists of two flexure stiffnesses in series with the semi-rigid bar stiffness. The model in figure 12 assumes the flexure bending stiffness is negligible. Kinematic Equations describing the deformed and undeformed geometry are expanded and linearized to obtain the following expression:

$$K_{eff} = \left( \frac{1}{K_{bar}(\sin^2 \theta)} + \frac{2}{K_{flex}(\tan^2 \theta)} \right)^{-1} \quad (12)$$

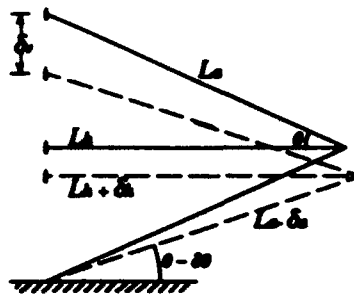


Figure 12. Deformed (dash) and undeformed (solid) geometry of the analytical model for the component.

## 6.2. Finite Element Component Model

In order to verify the assumption of negligible bending stiffness in the flexures, a finite element model was constructed. The finite element component model accounts for the bending stiffness of these components. The finite element program can output bending and axial stresses and strain energies in the flexures to aid in an iterative design optimization of the flexures. The following picture describes the boundary conditions and element geometry refinements for an one-eighth model of the component. The piezoelectric stack length is half and its area is a fourth of the full-model equivalent.

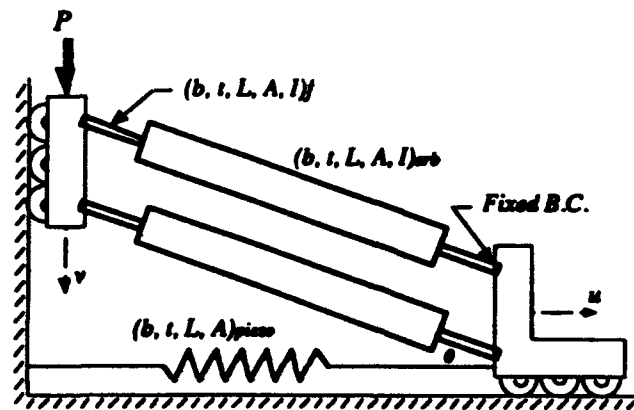


Figure 13. A finite element model of one-eighth of the component.

There are two undesired flexibilities in the above models that need to be addressed. The tensile stress in the smaller flexure, modeled as a single beam element, decays into the larger semi-rigid beam. The depth of the decay plus the original flexure's length yields the effective length of the flexure to be used in the models of section 6.1 and figure 13. The second undesired flexibility is caused by the smaller flexure's eccentricity with respect to the center of the larger semi-rigid beam. When the flexure is pulled in tension, the off-center axial force induces an undesirable bending moment and compressive bending stresses about the lever arm's neutral axis. The beam's curvature from the bending stresses reduces the overall axial stiffness of the lever arm.

In either case, the unmodelled flexibility,  $1/K_?$ , can be found by comparing the overapproximated two-beam junction with two-dimensional stress elements on any commercial finite element program. The total stiffness is calculated from the applied force and total displacement quotient.  $K_1$  and  $K_2$  are the nominal  $EA/L$  of the flexure and the semi-rigid beam, respectively. The mystery stiffness,  $K_?$ , is backed out of the following equation:

$$K_{total} = \left( \frac{1}{K_1} + \frac{1}{K_2} + \frac{1}{K_?} \right)^{-1} \quad (13)$$

This mystery stiffness was added to the component finite element model. It is essentially an unwanted flexibility in series with the piezoceramic stack. The finite element model in figure 14 shows the bending compressive stress that makes the outer beam material useless for transmitting strain energy into the piezoelectric. A symmetric beam eliminates this problem in section 9.

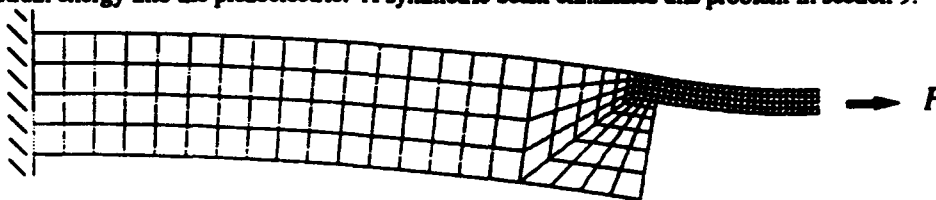


Figure 14. Deflected shape of flexure/semi-rigid beam interaction. The footprint length is 8.6 times the flexure thickness.

## 7. EXPERIMENTAL VERIFICATION OF COMPONENT PERFORMANCE

### 7.1. The Component Tester

The microcomponent tester in figure 15 was used to measure component stiffness and phase as a function of frequency and resistance. The piezoelectric actuator drives a user-input sinusoidal or random force through a load cell and into the component to be tested. A laser source inputs a light into a beam splitter which creates two separate beams of light. One beam, known as the reference beam is deflected into the laser sensor. The other beam is deflected onto the oscillating component mirror which then deflects the beam backwards along the same path back to the laser sensor. The laser measures the difference in phase between the two beams of light which is calibrated to the displacements of the component.

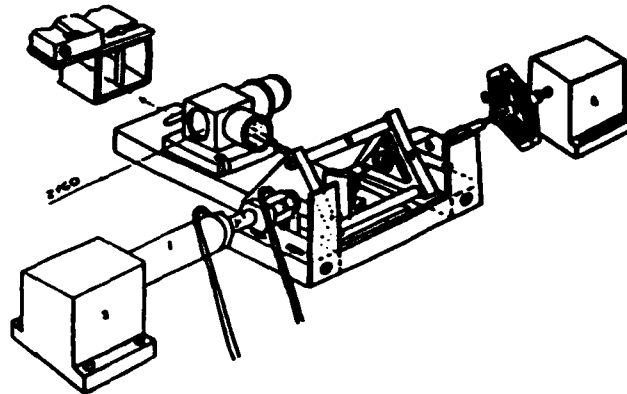


Figure 15. Interferometric microcomponent tester.

Component stiffness can be measured from these force and displacement measurements. Component loss factor can be measured from the tangent of the phase lag between these two measurements.

### 7.2. Component Test Data

In order to verify the component design, stiffness and loss factor test data was collected as follows. First, the effective capacitance of the piezoelectric was calculated. The resistor was selected from the following equation to tune the peak damping curve at 30Hz.

$$\rho = RC\omega \quad (14)$$

where  $\rho=1$ ,  $\omega=30\text{Hz}$ ,  $C=15\text{microfarads}$  and  $R=360\text{k}\Omega$ .

Second, forty logarithmically-distributed resistors were selected about the  $\rho=1$  center point. Forty stiffness and phase transfer functions were generated using a thirty count average. Two data points, 10Hz and 42Hz, were arbitrarily chosen to extract stiffness and loss factor data directly off the respective transfer functions. A seven-point discrete frequency average was computed about these two frequencies to smooth the noise on the transfer function. The following plots and experimental curve fits show the results of this procedure.

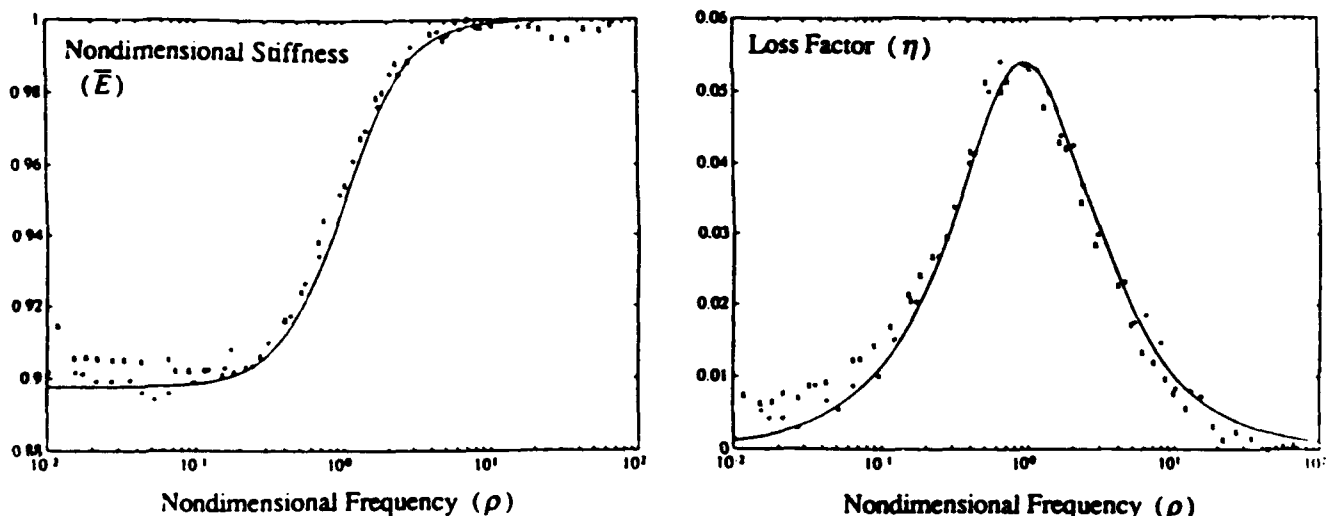


Figure 16. Nondimensional stiffness and loss factor data for experimental component data.

Although the stiffness change and loss factor are overestimated by the finite element model, the curves are clearly indicative of the predicted first-order frequency-dependent stiffness change and the Gaussian loss factor distribution. The results are summarized below.

### 7.3. Component Results Summary

	DATA	NASTRAN
$K_{ax}$ (N/ $\mu$ m)	9.57	9.71
$K_{ay}$ (N/ $\mu$ m)	10.66	12.12
$\eta_{pie}$ (%)	21.6	21.6
$\eta_{comp}$ (%)	5.4	11.1

Table 2. Component results summary for the experimental data and the finite element model.

Several conclusions can be made from the results. The component is much stiffer than intended. The two-dimensional finite element model's overestimate of the piezoelectric loss factor is attributed to unmodeled flexibility throughout the three-dimensional wire-EDMed part.

### 8. SIMULATED FREQUENCY RESPONSES IN THE TESTBED

The effect upon the plant transfer function (from control actuator to error sensor) of inserting a six-axis isolation stage to support the payload at the secondary mirror, is simulated in figure 17, using experimentally measured component characteristics. This simulation employs a NASTRAN dynamic model of the ASTREX structure. This model has not been tuned with a modal survey. The results are thus at best representative, and certainly not trustworthy in detail. A control engineer, faced with these two plants, will be happy with neither, but would certainly prefer to compensate the damped plant. The difference between the damped (solid) and undamped (dash) traces in figures 17, 19 and 20 is the effect of the six-axis vibration absorber with piezoelectric damping. The difference between the damped (solid) and short-circuit (dash-dot) traces in figures 17, 19 and 20 is the effect of piezoelectric damping.

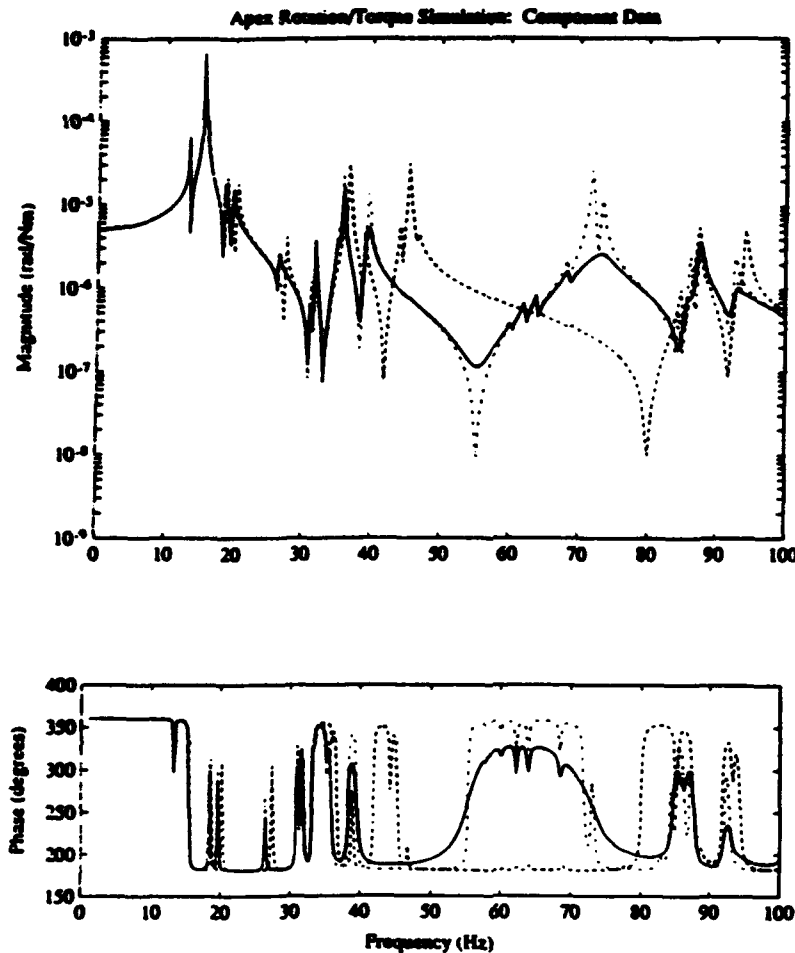


Figure 17. ASTREX simulation using experimental stiffness and damping data of the component.

## 9. THE NEW DESIGN

The new design would include five important modifications: 1. Quality control on piezoelectric stack manufacturing to ensure a  $k_{33}$  coupling coefficient of 0.75, not 0.59. 2. The lever angle would be halved to obtain the desired component stiffness of 1.5N/um. 3. Due to the extremely low bending strain energy in the flexures, the flexure lengths would be halved to channel more strain energy in the piezoelectric. 4. The entire lever arm width would be doubled to 2cm to increase the flexure's axial stiffness to bending stiffness ratio. 5. The thick semi-rigid beam would also be doubled in thickness. 6. The semi-rigid beam would be symmetric about the flexures in order to reduce the footprint length from 8.6 to 1.1 times the flexure length as pictured in figure 18.

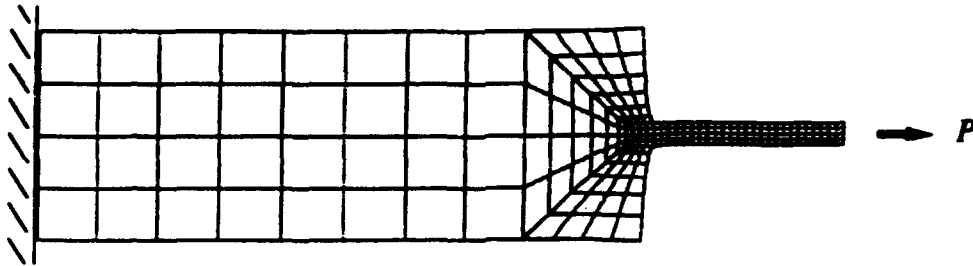


Figure 18. Deflected shape of flexure/semi-rigid beam interaction. Since, this design is symmetric, undesirable compressive stresses are eliminated. The footprint length is only 1.1 times the flexure thickness.

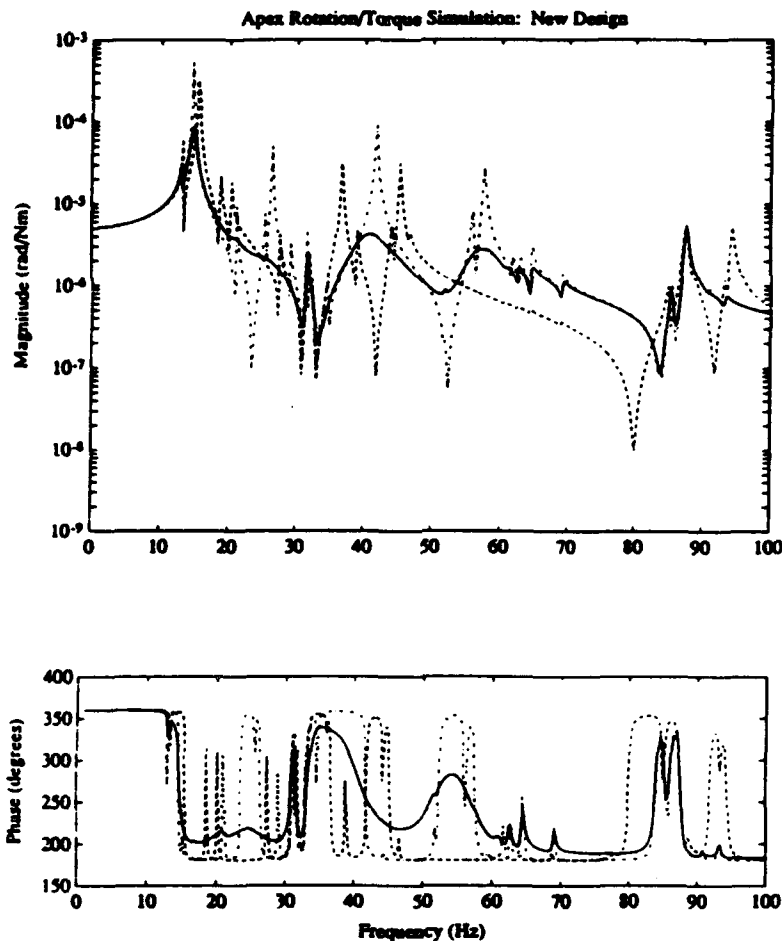


Figure 19. ASTREX simulation using the new design stiffness and damping values of the component.

An alternate use of the six-axis stage is for isolation; it is possible to isolate the control system from unpleasant structural dynamics of the ASTREX structure. This is summarized in figure 20, in which the actuator torque is applied not to the tripod apex but to the 90kg. suspended mass that is presumably supporting the secondary optics. In this plant, the isolation properties of the six-axis stage lead to very clean plant dynamics above 40Hz, and would permit robust closed-loop control.

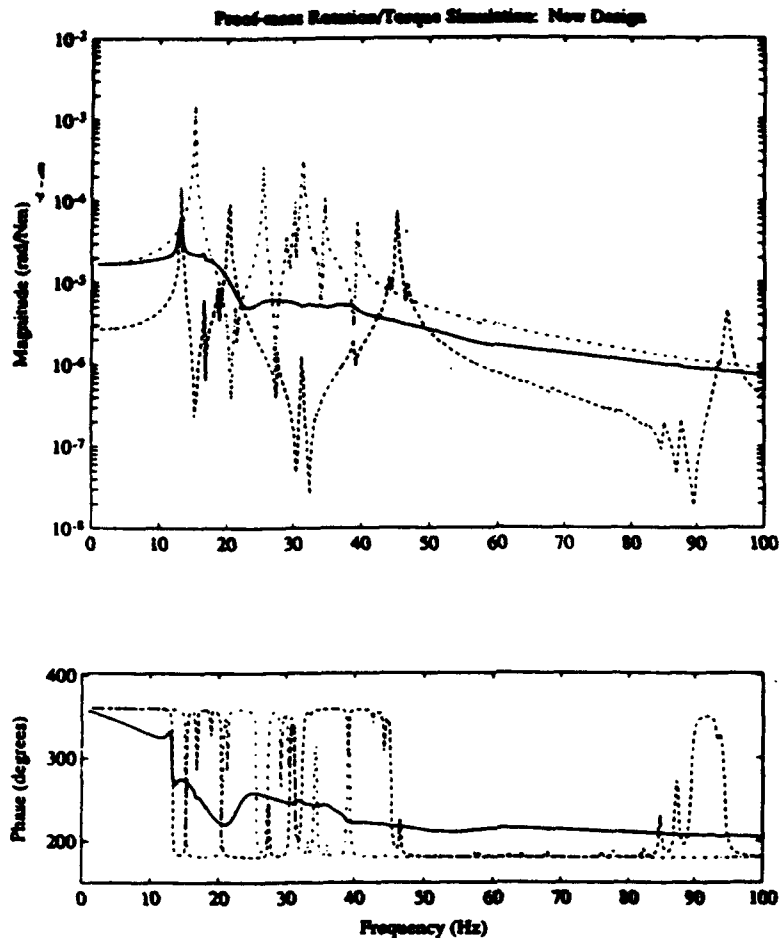


Figure 20. ASTREX simulation using the new design stiffness and damping values of the component.

## 10. CONCLUSIONS

Passive damping is important for space structure performance and controller stability robustness requirements. The ability of resistively-shunted piezoelectric damping to meet these requirements was investigated. This paper has presented the piezoelectric passive damping modeling approach and its modifications for finite element software implementation. The dynamic behavior and passive damping needs of the ASTREX testbed were addressed with a modal comparison of two potential damping design options: the piezoelectric joint and the tuned piezoelectric vibration absorber. The latter design was designed, manufactured and tested at the component level.

An analytical truss model was developed for the vibration absorber components. The model was used iteratively to optimize the lever ratio and piezoelectric strain energy of the component with respect to dimensional requirements and desired design features. A finite element model of the component was used to verify the design and to ensure stress limits were not exceeded. A local analysis of the beam was made to include the lever's "footprint" flexibility.

Test results indicate that it is challenging to channel a large fraction of the structural strain energy into the piezoceramic material without sacrificing some strain energy to residual parallel and series non-piezoelectric stiffnesses.

This paper has reported some of the practical considerations encountered when attempting piezoceramic passive damping of a large flexible structure. The paper presents a first iteration solution to these problems. Future work will use this as a starting point.

## References

<sup>1</sup>R. Guela, A. H. von Flotow, D. W. Vos, "Passive Damping for Robust Control of Flexible Structures," in press, *Journal of Guidance, Control and Dynamics*.

<sup>2</sup>A. H. von Flotow, N. W. Hagood, K. Napolitano, E. Austin, L. P. Davis, "A Case Study in Passive Piezoceramic, Viscous and Viscoelastic Damping," *Proceedings of the International Symposium on Active Materials and Adaptive Structures*, Alexandria, VA, November 4-8, 1991.

<sup>3</sup>N. W. Hagood, and A.H. von Flotow, "Damping of Structural Vibrations with Piezoelectric Materials and Passive Electrical Networks," *Journal of Sound and Vibration*, April-May, 1991.

<sup>4</sup>Chen, G., and Wada, B. K., "Passive Damping for Space Truss Structures," *Proceedings of the 29<sup>th</sup> AIAA/ASME/ASCE/AHS Structures, Structural Dynamics, and Materials Conference*, AIAA, AIAA Paper 88-2469, Washington, DC, May 1988, pp.1742-1749.

<sup>6</sup>J. Jaung, "Optimal Design of a Passive Vibration Absorber for a Truss Beam," *Journal of Guidance, Control, and Dynamics*, Vol. 7, No. 6, 1984, pp.733-739.

<sup>7</sup>J. F. Wilson and L. P. Davis, "Very High Damping in Large Space Structures," *ASME Vibration Damping Conference Proceedings*, 1988, pp. 167-171.

<sup>8</sup>B. K. Wada, and D. L. Edberg, "Adaptive Damping for Spacecraft by Temperature Control," *ASME Vibration Damping Conference Proceedings*, 1988, pp. 89-92.

<sup>9</sup>P. J. Torvik, W. Gibson, "The Design and Effectiveness of Impact Dampers for Space Applications," *ASME Vibration Damping Conference Proceedings*, 1988, pp. 65-74.

<sup>10</sup>Fanson, J., Blackwood, G., and Chu, C., "Active-Member Control of Precision Structures," *Proceedings of the 30<sup>th</sup> AIAA/ASME/ASCE/AHS Structures, Structural Dynamics, and Materials Conference*, AIAA, AIAA Paper 89-1329, Washington, DC, May 1989, pp.1480-1494.

<sup>11</sup>Peterson, L., Allen, J., Lauffer, J., Miller, A., and Skelton, R., "An Experimental and Analytical Synthesis of Controlled Structure Design," *Proceedings of the 30<sup>th</sup> AIAA/ASME/ASCE/AHS Structures, Structural Dynamics and Materials Conference*, AIAA, AIAA Paper 89-1170, Washington, DC, May 1989, pp. 91-103.

<sup>12</sup>E. F. Crawley and J. DeLuis 1987 *American Institute of Aeronautics and Astronautics Journal* 25 (10), 1373-1385. Use of piezoelectric actuators as elements of intelligent structures.

<sup>13</sup>N. W. Hagood and E. F. Crawley 1989 *Proceedings of American Institute of Aeronautics and Astronautics Guidance Navigation and Control Conference*, Boston, Massachusetts, August 1989, AIAA Paper No. 89-3436. Experimental investigation into passive damping enhancement for space structures.

<sup>14</sup>J. L. Fanson and T. K. Caughey 1987 *Proceedings of the 28<sup>th</sup> AIAA/ASME/ASCE/AHS Structures, Structural Dynamics and Materials Conference*, Monterey, California, April 1987, AIAA Paper No. 87-0902, 588-598. Positive position feedback control for large space structures.

<sup>15</sup>Hanagud, S., Obal, M.W., and Calise, A.J., "Optimal Vibration Control by the Use of Piezoceramic Sensors and Actuators," *Proceedings 28th AIAA/ASME/ASCE/AHS Structures, Structural Dynamics, and Materials Conference*, Monterey, California, April 1987, AIAA Paper No. 87-0959, pp. 987-997.

<sup>16</sup>T. Bailey and J.E. Hubbard 1985 *American Institute of Aeronautics and Astronautics Journal of Guidance Control and Dynamics* 8 (5), 605-611. Distributed piezoelectric-polymer active vibration control of a cantilever beam.

<sup>17</sup>D. Pines and A. H. von Flotow 1990 *Journal of Sound and Vibration* 142, 391-412. Active control of bending wave propagation at acoustic frequencies.

<sup>18</sup>A. D. Nasif, D. I. Jones and J. P. Henderson 1985 *Vibration Damping*, New York: John Wiley, see pp. 69-73.

# An Advanced Controls Technology Flight Experiment

R. A. Manning<sup>1</sup>, R. E. Wyse<sup>2</sup>, S. R. Schubert<sup>3</sup>

TRW Space and Technology Group

Redondo Beach, CA 90278

(310) 813-9125

## ABSTRACT

TRW has designed, fabricated, ground tested, and integrated with a host spacecraft an advanced controls technology flight experiment. The purpose of the experiment is to demonstrate advanced controls hardware and controllers for use on operational NASA and DoD spacecraft. Planned experiments include on-orbit vibration suppression, health monitoring, adaptability, and acquisition of lifetime/reliability data. The experiment structure consists of an active tripod where each leg of the tripod has piezoceramic actuators and sensors embedded within a composite material. Driving the active tripod legs is an electronics module which consists of digitally programmable analog compensators. The compensators can be reprogrammed from the ground so that the active structure can serve as an on-orbit test platform for new and robust control laws. A full set of accelerometers and thermistors provide additional data concerning the performance of the active tripod in various orbital environments. Details on the design, dynamic characteristics, ground-based environmental testing (for flight qualification), and ground-based performance testing are presented in this paper along with the level of performance that is expected from the flight experiment.

<sup>1</sup> Staff Engineer, AIAA Member, ASME Member

<sup>2</sup> Sr. Staff Engineer

<sup>3</sup> ACTEX Program Manager

## INTRODUCTION

Many future space missions will have extremely stringent pointing and alignment performance goals. Designing structures to meet these performance goals through mass and stiffness tailoring is doomed to failure. A certain amount of designed-in structural control will be required in order to to achieve their mission objectives. Utilization of advanced controls-structures interactions (CSI) technologies should be exploited whenever possible to achieve a suitable design.

Recent multidisciplinary advances in CSI technologies have yielded great promise in meeting stringent mission requirements. Some of these advances are new structural damping algorithms, such as impedance matching compensators [1] and robust controllers [2], new sensor and actuator materials [3], and new flexible electronics [4]. As these technologies become ground tested, lifetime and reliability data become available and expand our knowledge base as to their advantages and limitations. However, there is a lack of space flight experience to give spacecraft designers confidence in advanced CSI technologies.

This paper describes the development of an advanced controls technology experiment facility that is expected to be launched into orbit in late 1993. The work was performed on the Advanced Controls Technology Experiment (ACTEX) contract managed by the Air Force Phillips Laboratory. The ACTEX experiment will be a pioneering mission in the area of structural control in that it provides a number of "firsts" for space-based technology verification. It will be the first space flight of embedded piezoceramic sensors and actuators, the first on-orbit adaptive structure experiment, the first flight of digitally programmable analog electronics, the first flight of field programmable gate arrays, and the first flight of a Nitinol latch.

Achieving the objectives of the ACTEX flight experiment will demonstrate the flight-readiness of CSI hardware and algorithms. Chief among the objectives of the flight experiment is to demonstrate integrated active/passive damping using piezoceramic sensors and actuators embedded in graphite composite members. Successful launch and checkout of the ACTEX system will provide experimenters with an on-orbit test facility to conduct independent system identification and vibration suppression experiments. Another objective of the experiment is to demonstrate the concept of adaptive structures through the use of electronics that are programmable from the ground. Finally, objectives in the area of system identification are to validate preflight design and analysis tools, to monitor the long term effects of the space environment on the active structural control components, and to monitor the health of the system over long periods of time.

## EXPERIMENT DESCRIPTION

A number of conflicting requirements were placed on the design of the flight experiment; specifically, two distinct sets of requirements, one set associated with the technology demonstration objectives, and the other set associated with the host spacecraft accommodation constraints. These host spacecraft requirements, as well as all other design requirements,

are listed in Table 1. Because the flight experiment was a secondary payload, it had to fit into the existing space envelope (10" by 12" by 22"), had to have minimal effect on primary spacecraft orbital operations (by proper orbit average power scheduling), and had to fit into the paging telemetry format of the spacecraft bus. In addition, it was desirable to mount the flight experiment external to the spacecraft for maximum exposure to the space environment while mounting the electronics internal to the spacecraft for maximum reliability. Finally, power and electronics designs had to fit into the existing 30 Volt maximum spacecraft power system.

Table 1: Experiment Requirements

<b>Host Interface Requirements</b> -Head room -Low power -Telemetry format -Thermal -Drive voltage	10" maximum 16 W OAP Paging format Thermally isolated $\leq 30$ Volts
<b>Host Compatibility Requirements</b> -Small size -Low weight -Low ops impact -Location  -Schedule	10" by 12" by 22" 18# structure, 35#electronics OAP scheduling External structure, Internal electronics Deliver $\leq 12$ months
<b>Performance</b> -Demonstrate damping -Provide space testbed -Validate preflight analysis -Demo adaptive structures -Traceability -Long life effects	5-10% modal damping Other users possible On-orbit ID Uplink changes Scaleable dynamics Detailed ID and health monitoring
<b>Risk Reduction</b> -Strength -Outgassing -Radiation -Workmanship -Environment	Margins $\geq 1.0$ $TML \leq 1.0\%$ , $CVCM \leq 0.1\%$ Good to 10 kRads Extensive test program Extensive test program

The resulting flight experiment is shown schematically in Figure 1. The active tripod

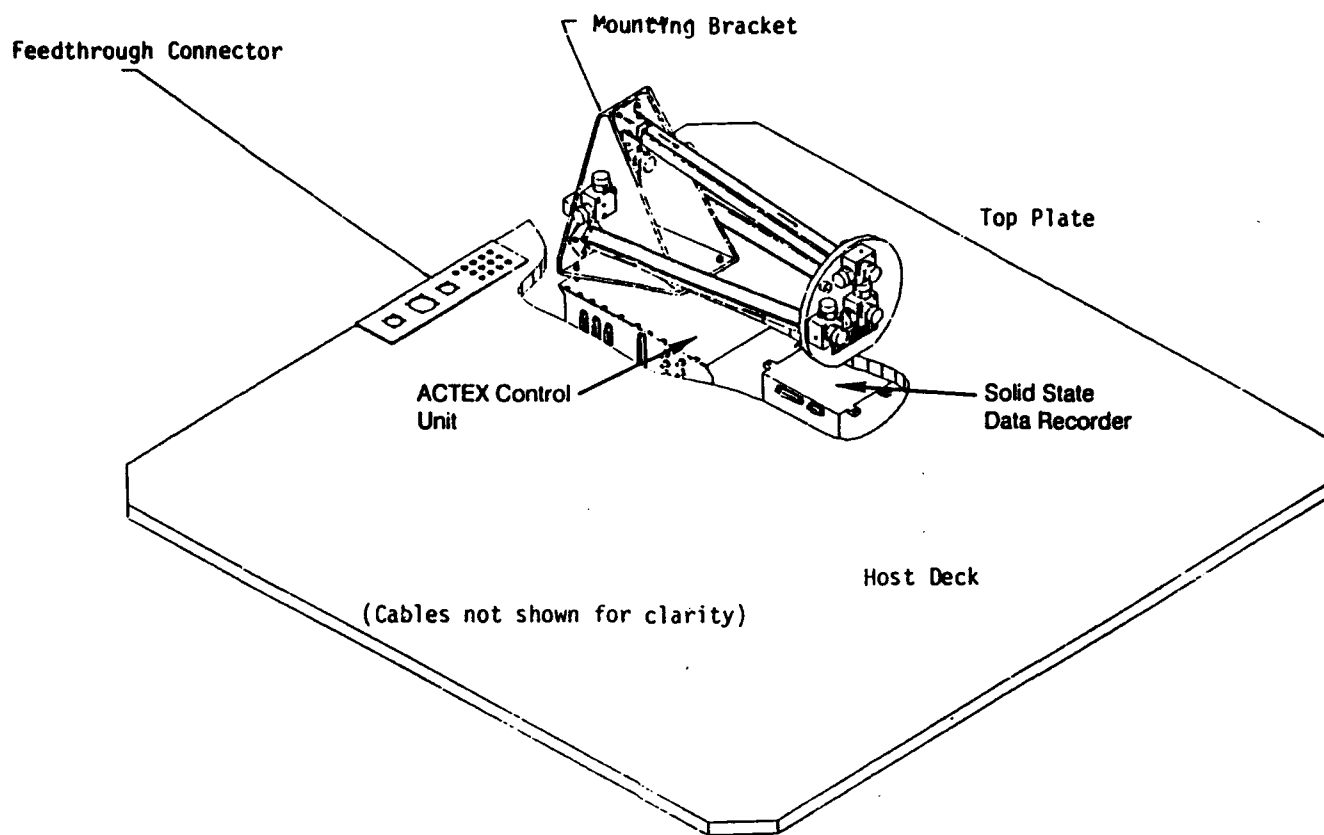


**Figure 1: ACTEX Flight Experiment Schematic**

is mounted external to the host spacecraft, on a large secondary payload deck. Internal to the spacecraft are the electronics which configure the experiment, drive the active tripod legs, and control the solid state data recorder. The tripod is connected to the electronics with a number of cables (not shown in Figure 1 for clarity) which feedthrough the secondary payload deck. A photograph of the complete ACTEX flight experiment is shown in Figure 2 (minus cables and thermal blankets for clarity).

Figure 3 contains a closeup photograph of the active tripod itself. The tripod consists of three square cross section T300 graphite composite legs with piezoceramic sensors and actuators embedded in all four faces of each leg. Members A and C are covered with multi-layer insulation (MLI) for thermal control, whereas member B (i.e., the silver leg in Figure 3) is covered with leafing aluminum paint. Twelve thermistors monitor the temperatures at various points along the active members, on the top plate, and on the bottom bracket. Six accelerometers are used to monitor the motions of the bottom bracket (i.e., monitor the input motions to the base of the tripod). Figure 4 shows a photograph of the top plate of the flight experiment. Seven accelerometers are used to monitor the motions of the top plate.

0000000000



Figure 2: Flight Experiment Hardware

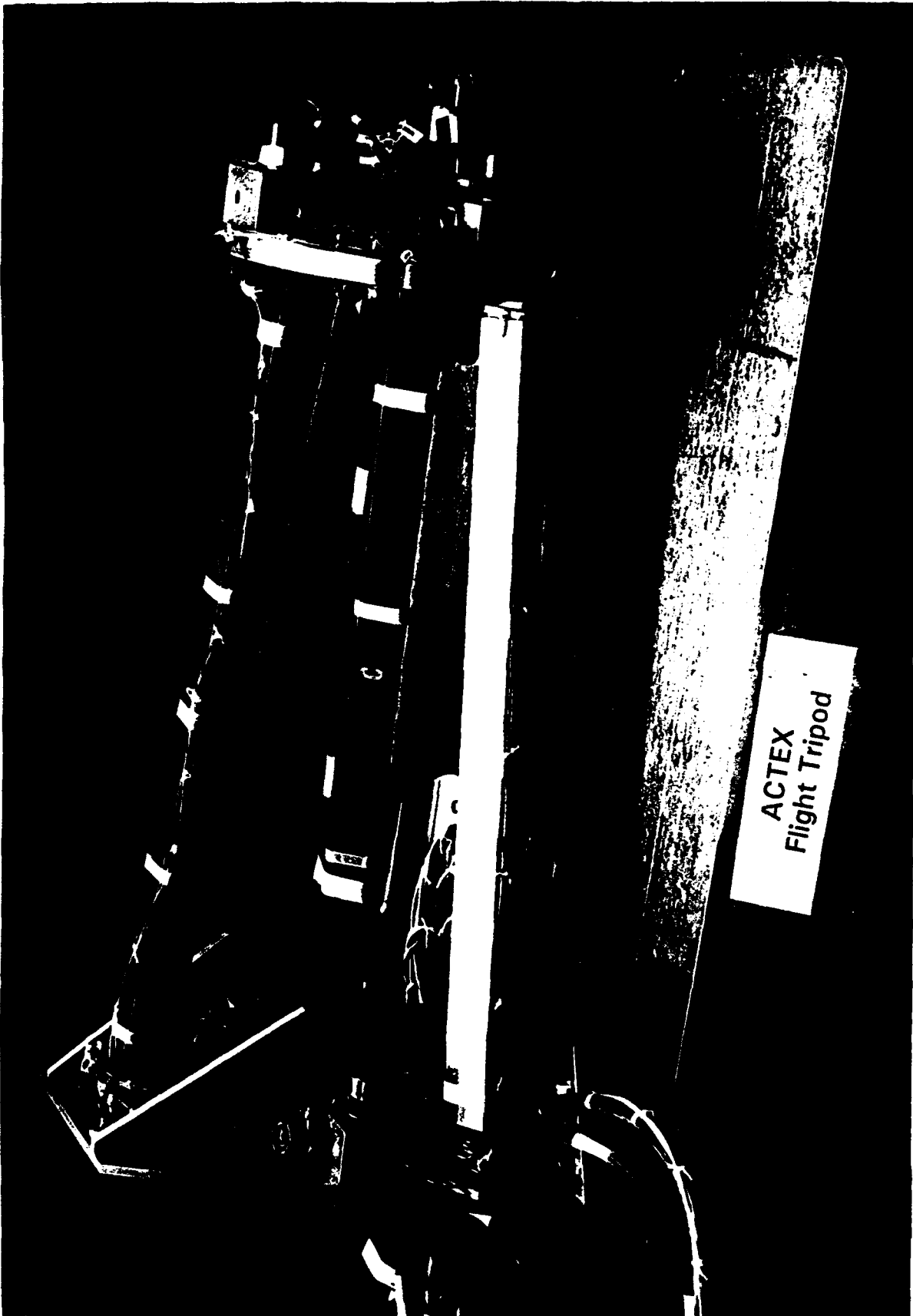


Figure 3: Active Tripod Flight Experiment



**Figure 4: Top Plate Details**

By mixing the signals of the seven accelerometers, all three translations and rotations of the top plate can be recovered for use in monitoring the open and closed loop performance of the tripod. Also contained on the top plate is a heater and redundant thermostats for active thermal control of the top plate. The active thermal control system was required in order to prevent the accelerometers from falling below their failure temperature of  $-55\text{ }^{\circ}\text{C}$ . An additional heater/redundant thermostat set are contained on the bottom bracket near the other six accelerometers.

Figure 5 contains a photograph of the bottom surface of the top plate. The active members are connected to the top plate through flexures. The flexures were designed to provide the appropriate flexibility such that the active members are closer to clamped-free boundary conditions rather than clamped-clamped. These boundary conditions enhance the controllability of the system by preventing the actuators from being located in regions of reverse curvature for the first two bending modes. Also seen in Figure 5 are the grounding beads drawn between the exterior surface of the active members and the end fittings to prevent charge differences from building up between different regions of the structure.

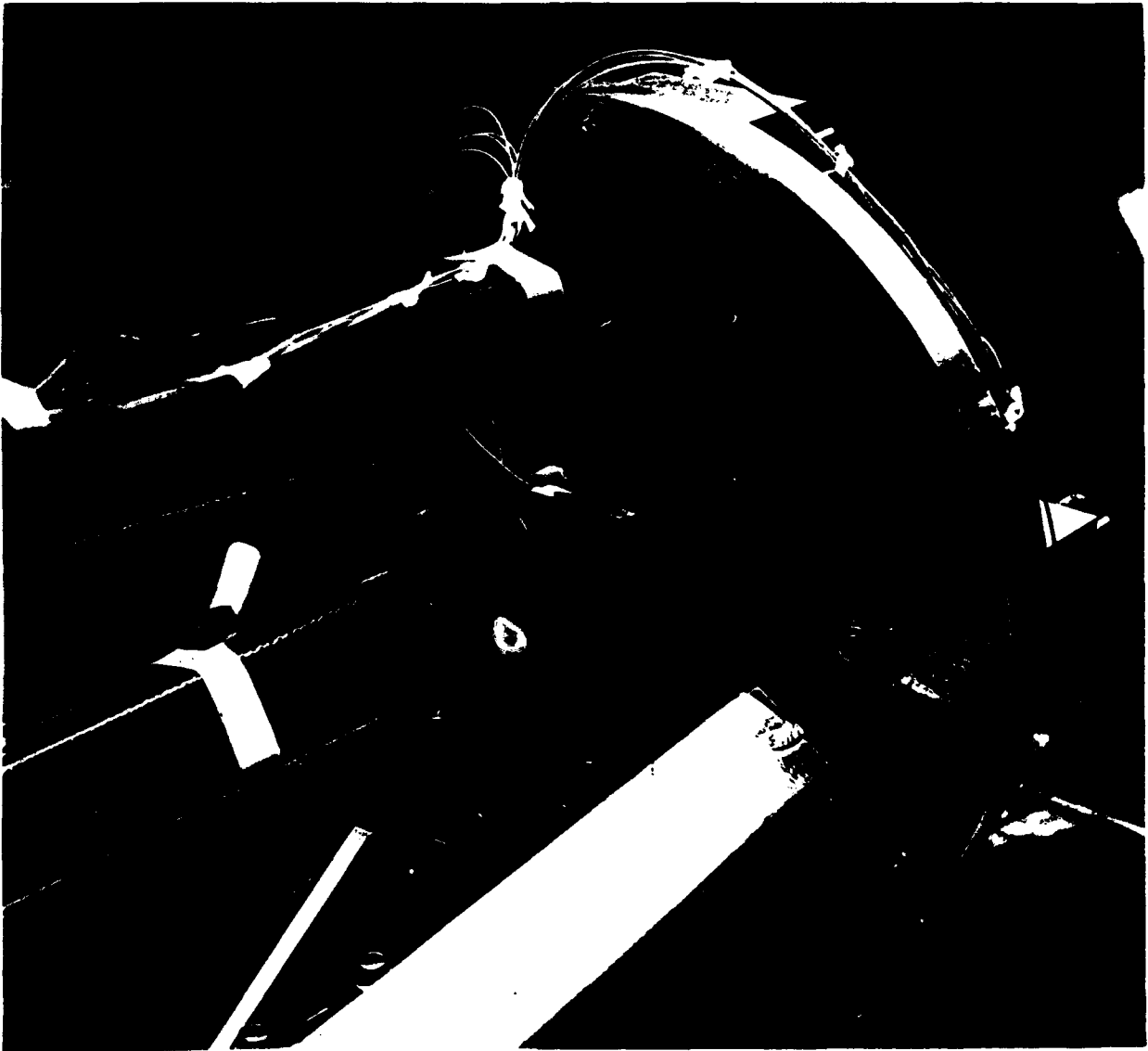


Figure 5: Bottom Surface of the Top Plate

Figures 4 and 5 also contain photographs of the Nitinol mechanisms of the ACTEX flight experiment. A Nitinol-actuated latch, attached to the center of the bottom surface of the top plate (see Figure 5), is used to take the loads during the severe environment of a Titan IV launch. Taking the launch loads with the latch relieves some of the strength requirements on the active members and enhances the experiment quality by allowing a lower frequency on-orbit system. Additional Nitinol strands are contained in the Dynamic Change Mechanism (DCM) which can be seen in Figure 4. By actuating the DCM, the Nitinol shrinks and draws the flexures up against the bottom surface of the top plate. In effect, actuating the DCM locks out one of the flexures and raises the natural frequency of the system. Ground tests showed that a 20% change in primary bending modes could be achieved by actuating the Nitinol in the DCM. Use of the DCM to change the dynamics characteristics can demonstrate the adaptivity of the tripod and electronics and can be used to demonstrate the robustness of the controllers.

## FLIGHT ELECTRONICS

The flight electronics were designed to satisfy the host interface requirements and to perform the identification, damping, and adaptivity experiments necessary to space validate adaptive structures. The functions of the electronics can be roughly broken down into control electronics, data collection/telemetry electronics, command processing electronics, and miscellaneous functional electronics. Each of these functions are described in the following paragraphs.

Figure 6 shows a block diagram of the complete electronics subsystem. At the heart of the vibration suppression capability of the active tripod are the control electronics. These circuits implement the tripod leg controllers in an analog fashion. However, the controller topology and gains are programmable via digital commands from the ground, hence the name digitally programmable analog electronics [4]. By varying the charge amplifier gains,  $K_1$  and  $K_2$  in Figure 6, the piezoceramic sensor signals can be amplified and averaged together to give a transfer function which is advantageous from a control design standpoint. By varying the digital switches, low pass and band pass filters can be enabled or disabled, thus changing the controller topology between third or fifth order rate feedback, third order positive integration, and second order Positive Position Feedback [5] controllers. Filter cut-offs are varied by changing the clock rate into the filter, in effect varying the bandwidth of the controller. Finally, the overall gain of the controllers can be changed by varying the  $K_3$  and  $K_4$  parameters (see Figure 6). The great flexibility in the digitally programmable analog electronics allows a large number of controllers to be available for space test and allows a degree of adaptiveness in the experiment.

The data collection/telemetry electronics collect data from the active members, the accelerometers, and the thermistors, and loads it into the solid state data recorder for playback at a later time. Each of the six active member signals and thirteen accelerometer signals are sampled at a 4 kHz rate. The twelve thermistors are subcommmed together onto one channel and are thus effectively sampled at a somewhat slower rate. A formatter and timing generator converts the multichannel data into serial data for loading into the data recorder. The data recorder itself has a 64 Mbit storage capacity and is semi-fault tolerant. The data

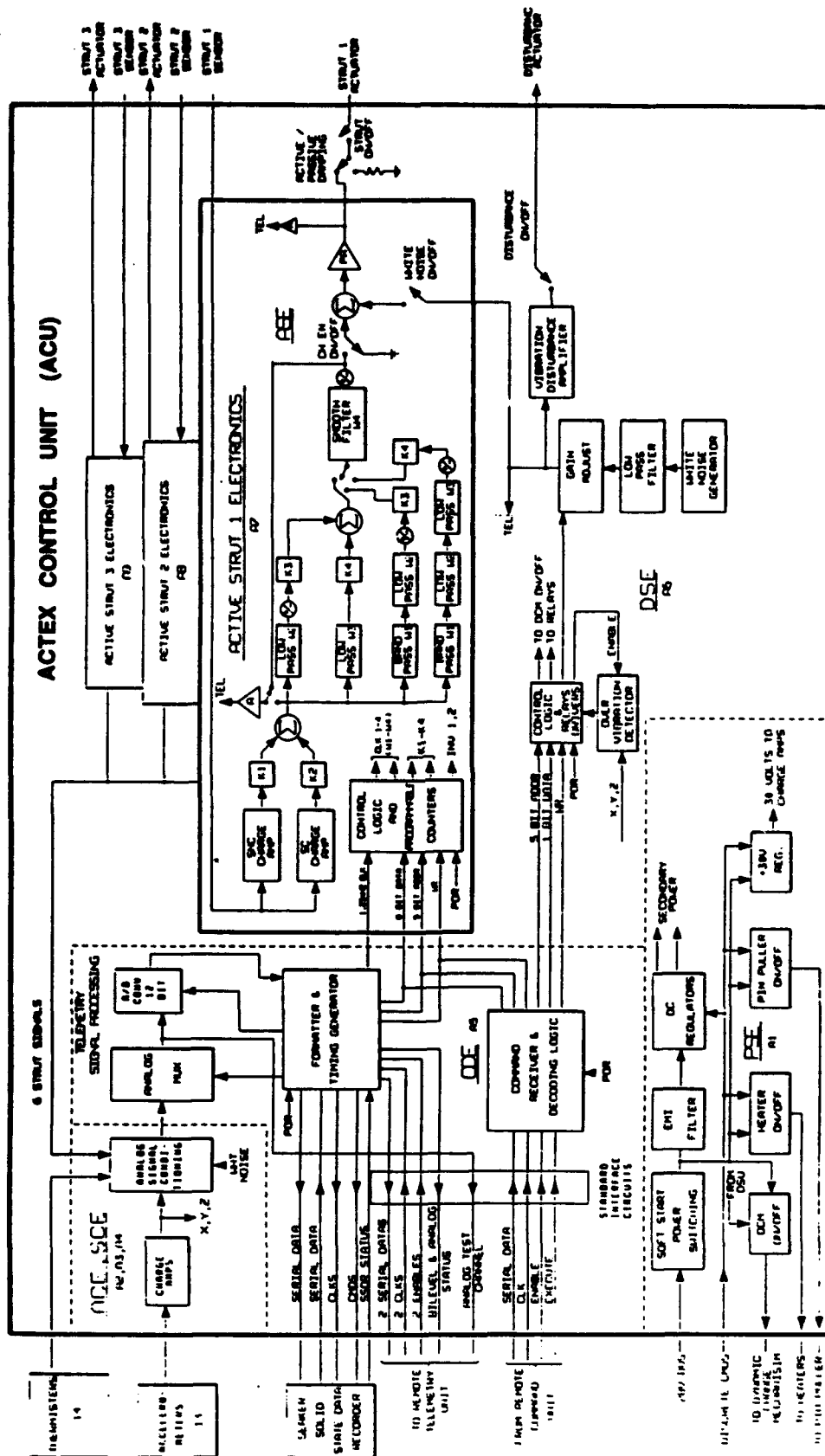


Figure 6: Electronics Functional Block Diagram

recorder monitors its own health and avoids certain blocks within the recorder when it detects a fault. Thus, end of life storage is somewhat reduced from the 64 Mbits depending on the number of faults the data recorder develops. The data collection/telemetry electronics also reads serial data out of the recorder and downlinks the data to the ground via the host spacecraft telemetry system. Digital commands uplinked from the ground control the functions which the data collection/telemetry electronics perform.

The command processing electronics is the dispatcher for setting up and communicating with the flight experiment. Ground commands for control of the overall experiment are received. This subsystem reconfigures the experiment, selects among the 80 preprogrammed experiments stored in PROM, and controls the data acquisition and readout operations. In addition, the command processing electronics can modify the experiments stored in PROM, in effect yielding a virtually unlimited number of possible experiments.

The miscellaneous electronics takes 28 Volts of fused spacecraft power and produces the  $\pm 15$  and  $\pm 5$  Volt secondary levels needed to operate the experiment. In addition, the Nitinol drivers for the latch and for the Dynamic Change Mechanism are contained within this subsystem. Finally, a white noise generator, for running system identifications and forced frequency responses, are contained within the flight electronics.

Figure 7 shows a closeup photograph of the electronics packaging. Separate "slices" were used for portions of the electronics to maintain a degree of modularity for ease of assembly and repair. The slices communicate amongst each other via an experiment bus which contains the necessary electrical connections for proper operation. The slices provide a rugged packaging method for survival of harsh environments and for protection of electronic circuits.

## GROUND TESTING AND VALIDATION

A comprehensive ground test program was conducted to verify the workmanship and integrity of the flight experiment, to demonstrate the survivability to thermal and launch environments, and to provide a catalog of system identification and damping data for comparison with on-orbit data.

Static proof tests on individual active members were run to verify design loads and proof of workmanship. Member forces were extracted from the NASTRAN finite element model and test loads were derived to attain these member forces. Strains up to  $1200\mu\text{strain}$  were observed in the regions of the piezoceramic sensors and actuators. Before and after transfer functions indicated no degradation in sensing or actuation capability following the static proof tests.

The active tripod was subjected to six thermal cycles to verify the survivability of the structure to expected thermal loads. Survival limits of testing of  $-157/+148\text{ }^{\circ}\text{C}$  for the structure were derived from thermal models of the experiment, the host spacecraft, and the orbital parameters. Temperatures of  $-89/+113\text{ }^{\circ}\text{C}$  for the structure and  $0/+40\text{ }^{\circ}\text{C}$  for the electronics

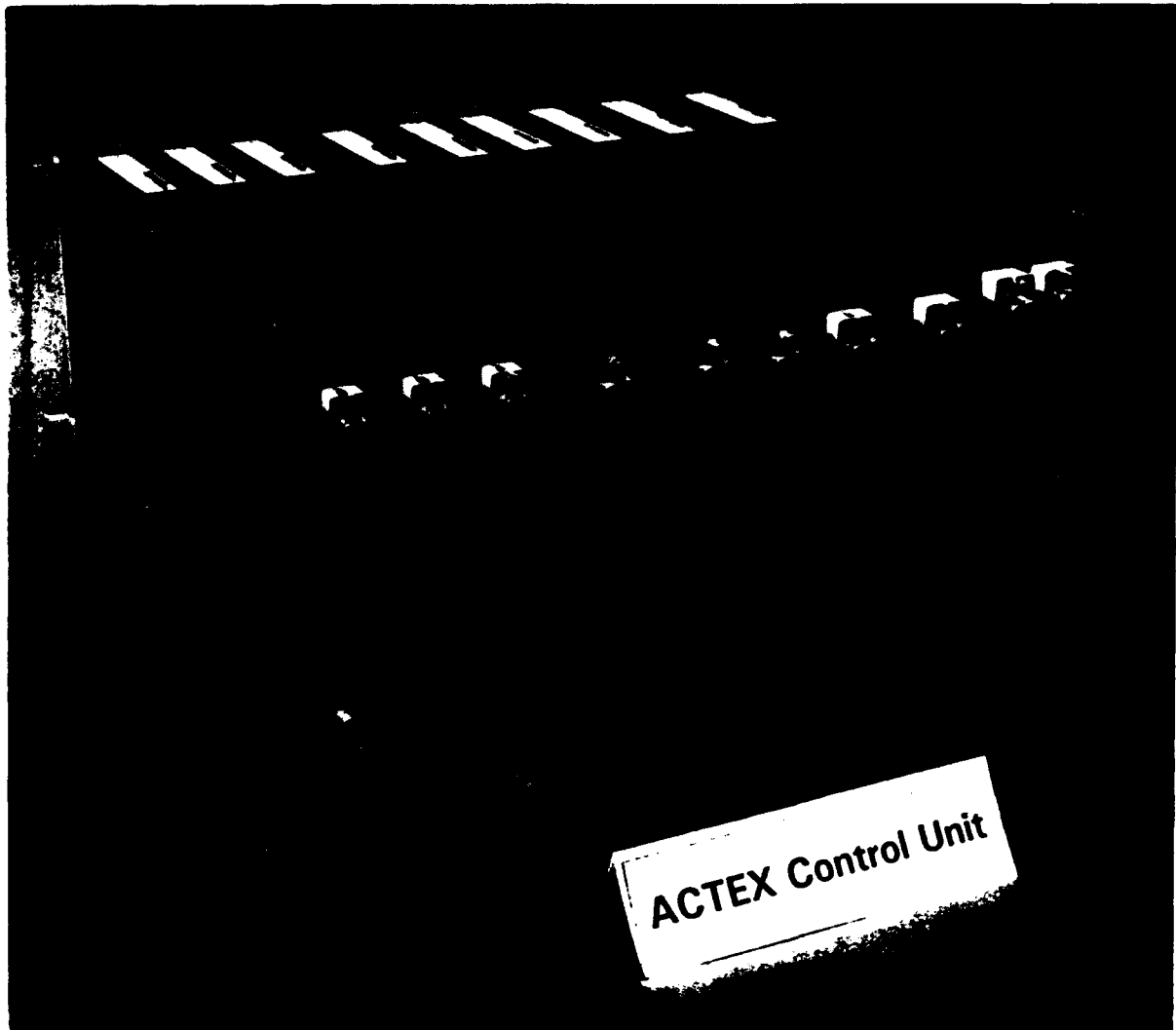
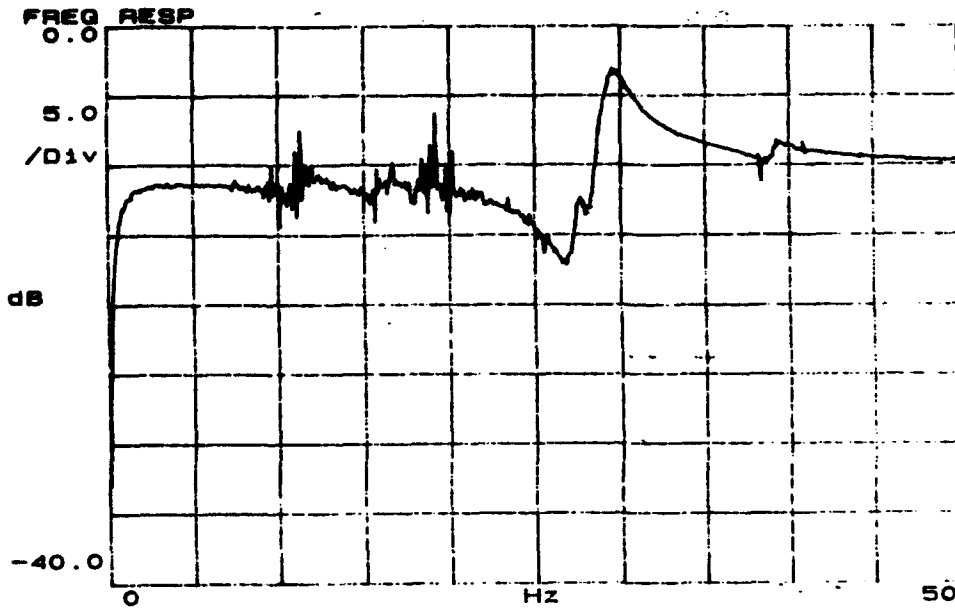


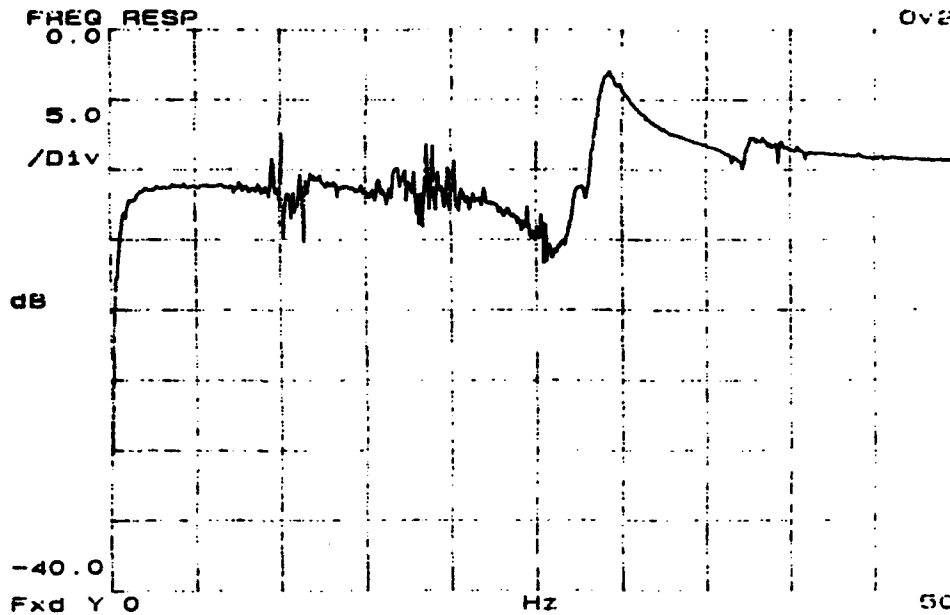
Figure 7: Electronics Packaging

were determined for flight experiment operation. Thermal cycling of the electronics at the operational limit and the active tripod at the survivable limit were conducted, with testing done before and after to verify the functionality of the system. Figure 8 contains before and after transfer functions for one channel of the active tripod. No significant deviations were observed in the data following the thermal cycling tests.

The electronics and tripod were subjected to a random vibration test with independent base inputs of  $11.1 g_{rms}$  applied axially and  $10.5 g_{rms}$  applied laterally. These input vibration levels are compatible with a secondary payload requirement on a Titan IV launch vehicle. Before and after vibration testing indicated all subsystems in working order and ready for launch.



Pre-Thermal Cycling Transfer Function, Ch. 2



Post-Thermal Cycling Transfer Function, Ch. 2

Figure 8: Before and After Thermal Cycling Transfer Functions

Transfer function and forced frequency response data were taken to characterize the dynamic behavior of the active tripod and to get a catalog of ground-based data. This data will be compared with the on-orbit data and will be used to debug the flight experiment in the event of flight anomalies. A typical averaged transfer function for the active members is shown in Figure 9. A good degree of controllability and observability are demonstrated for a lateral bending mode and the torsional mode of the structure. Open and closed loop forced frequency responses are shown in Figure 10, where only the control loop associated with the previously shown transfer function is closed. Both the torsional mode and a lateral bending mode are highly damped. The second lateral bending mode near 21 Hz is unaffected in this case because the actuator/sensor pair used for control is orthogonal to this bending mode. Either of the other two control loops can observe and control this mode however. Table 2 contains a summary of the ground-based open and closed loop damping performance that

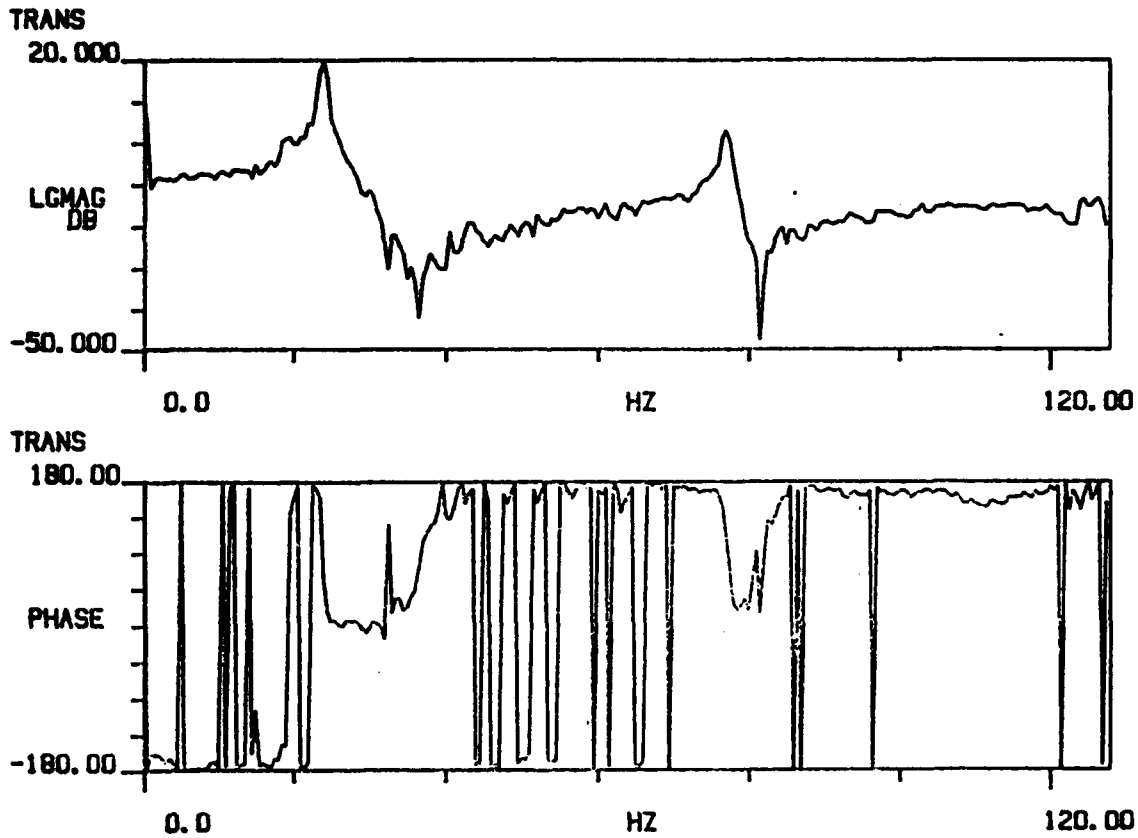


Figure 9: Typical Averaged Transfer Function

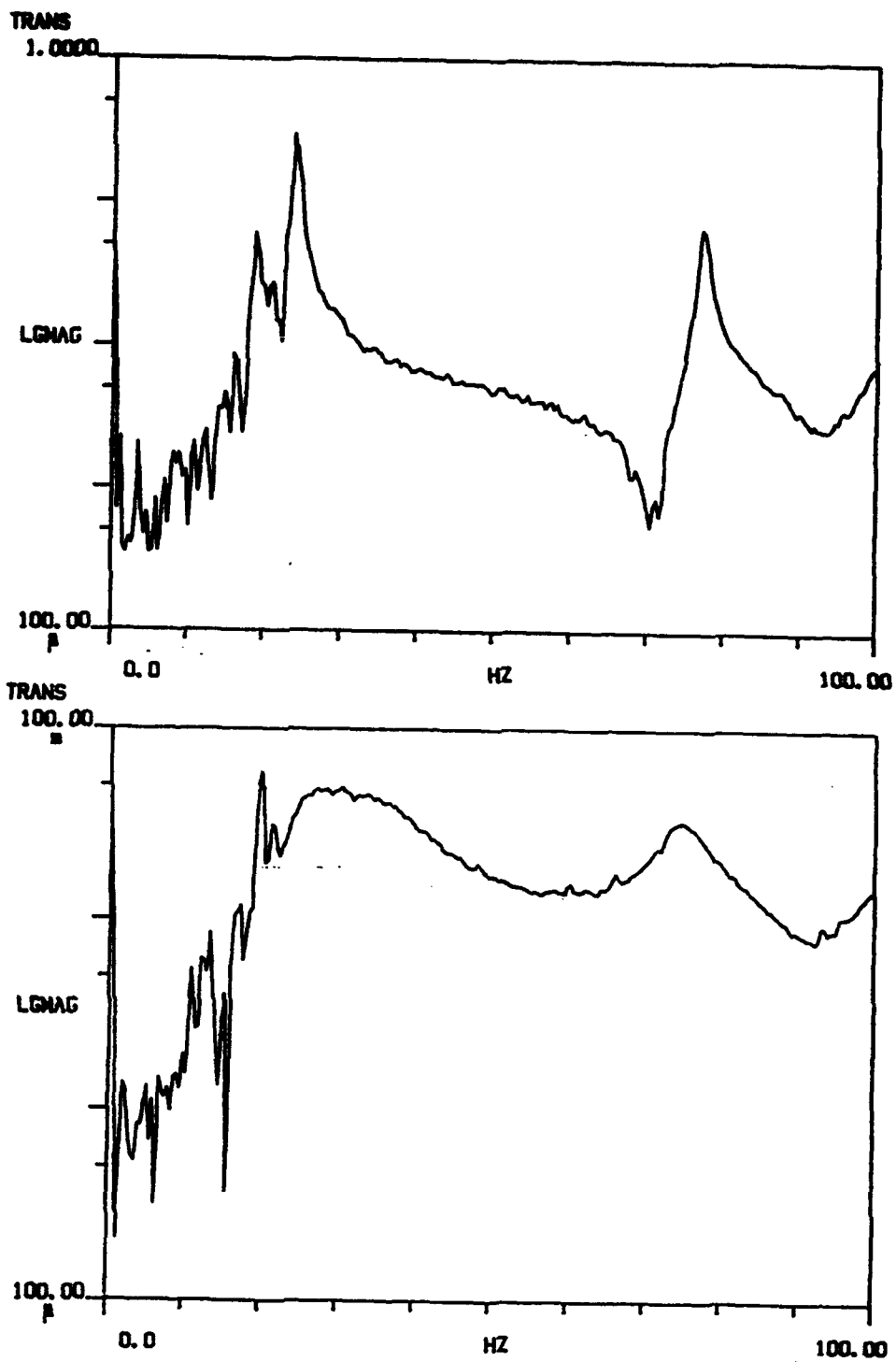


Figure 10: Open and Closed Loop Frequency Responses

was obtained on the ACTEX flight experiment. These data will be compared with both short and long term flight data as they becomes available.

Table 2: Ground Tested Damping

Mode	Open Loop		Closed Loop	
	Frequency (Hz)	$\zeta$ (%)	Frequency (Hz)	$\zeta$ (%)
Lateral Bending	21.0	1.1	20.9	16.3
Lateral Bending	23.9	0.8	27.0	22.0
Torsion	77.0	0.5	75.0	6.7

### CONCLUDING REMARKS

The description of an advanced controls technology flight experiment has been presented herein. The experiment was designed within the tight constraints of being a secondary payload on a Navy spacecraft. The structure itself consists of an active tripod with piezo-ceramic sensors and actuators embedded in the graphite composite tripod legs. Digitally programmable analog electronics are used to drive and control the active members, giving a great degree of on-orbit flexibility for control design and for a demonstration of adaptive structures. Damping levels greater than 22% were observed during closed loop testing on the ground.

The flight experiment has been fully integrated with the host and has undergone system level environmental testing with the host spacecraft. A launch date sometime late in 1993 is expected. Results regarding the system identification performance, open and closed loop damping levels, degree of adaptivity, and lifetime/reliability data will be presented when they becomes available.

### ACKNOWLEDGEMENTS

The work described in this paper was performed under the ACTEX contract from the Air Force Phillips Laboratory at Edwards Air Force Base. Dr. Alok Das was the technical monitor and Captain Maurice Martin was the contract monitor. Funding was provided by Lt. Col. Mike Obal from SDIO.

### REFERENCES

- [1] Chen, G-S., Lurie, B.J., and Wada, B.K., "Experimental Studies of Adaptive Structures For Precision Performance", *Proceedings of the 30th Structures, Structural Dynamics, and Materials Conference*, Mobile, AL, April 1989, pp. 1464-1472.
- [2] Doyle, J.C., "Analysis of Feedback Systems with Structured Uncertainties", *IEEE Proceedings*, Vol. 129, Part D, No. 6, Nov. 1982, pp. 242-250.

- [3] Cross, E., "Piezoelectric and Electrostrictive Sensors and Actuators for Adaptive Structures and Smart Materials", *Adaptive Structures*, ASME AD-Vol. 15.
- [4] Bronowicki, A.J., Mendenhall, T.L., Betros, R.S., Wyse, R.E., and Innis, J.W., "ACESA Structural Control System Design", Presented at the First Joint U.S./Japan Conference on Adaptive Structures, Maui, HI, November 13-15, 1990.
- [5] Fanson, J.L. and Caughey, T.K., "Positive Position Feedback Control for Large Space Structures", *Proceedings of the 28th AIAA Dynamics Specialists Conference*, Monterey, CA, April 9-10, 1987, pp. 588-598.

# OPTIMIZED PASSIVE VIBRATION ISOLATOR DESIGN FOR THE SPACE STATION FREEDOM EXERCISE TREADMILL

Richard W. Armentrout <sup>1</sup>  
Rotech Engineering Services Company  
and  
Harold H. Doiron  
McDonnell Douglas Aerospace - Space Systems

## ABSTRACT

Successful operations of the Space Station Freedom (SSF) require daily exercise by crewmembers to meet medical and crew health requirements while also maintaining a quiescent "microgravity" vibration environment for laboratory experiments such as large crystal growth. To meet these conflicting needs, vibration isolation systems are required for three exercise devices to be used on SSF; an exercise treadmill, a dual cycle ergometer, and a strength training device. This paper describes the preliminary design, supporting analyses, and development activities for a passive isolation system for the exercise treadmill, the largest disturbance generator of the three exercise devices. Similar isolation systems will later be developed for the much more benign disturbances of the ergometer and strength trainer.

## INTRODUCTION

Extended exposure to the zero gravity environment of orbiting manned space vehicles causes significant physiological changes in the body, for which countermeasures must be developed to prevent incapacitation of crewmembers during and after the return flights to Earth. Since crewmembers on SSF are expected to remain on-orbit for three months or more, daily treadmill exercise is required. Figure 1 illustrates the fundamental concept of an isolated exercise treadmill suspended in zero gravity. A similar restraint harness system is currently used successfully by Shuttle crewmembers to restrain themselves to the treadmill and to create "one G" forces in the body and legs during exercise. As a result of the restraint harness, footfall forces on the treadmill are similar to forces attained on Earth during normal walking or jogging exercise. These footfall impact forces are typically two times body weight, and reach as high as three times body weight for some individuals depending on their particular exercise characteristics. After subtraction of the nearly-constant restraint harness forces, the net vertical disturbing forces from the treadmill-crewmember system are approximately sinusoidal with a magnitude of about  $\pm 1.0$  body weight (BW). If the treadmill were to be bolted directly to the SSF structure, as has been standard procedure for Shuttle missions, the vibration environment at experiment locations would be on the order of hundreds of times the allowable level for the most demanding microgravity experiments planned for SSF.

Therefore, a vibration isolation system with an exercise force attenuation capability of more than two orders of magnitude is required for the SSF treadmill.

## Principles of Treadmill Isolation

The basic concept of vibration isolation for the SSF treadmill was initially proposed by astronaut William E. Thornton (1), and was envisioned for either active or passive isolation systems. The concept consists of a very soft active or passive isolator that is attached between the spacecraft and the treadmill frame to allow the crewmember-treadmill two-body system to "float" within the confines of the SSF module designated for exercise equipment. The isolation system prevents the crewmember-treadmill dynamic system from drifting too far from the center of the module, while sufficient mass (counterpoise mass) affixed to the treadmill frame ensures that the treadmill motion relative to the crewmember motion is small. In typical Earth jogging, for example, the

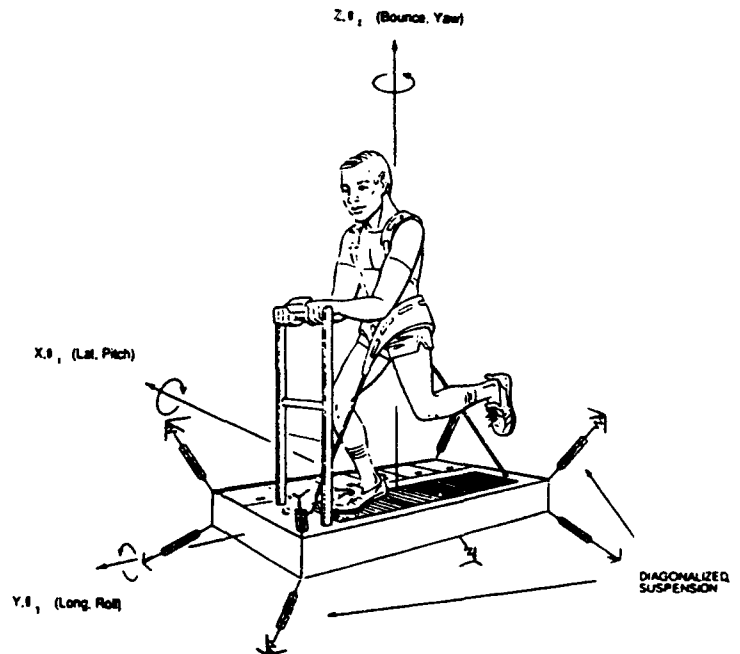


Figure 1. Passively Isolated Zero-Gravity Treadmill.

body center of mass moves approximately 1.25 to 1.5 inches zero-to-peak vertically with respect to the running surface. If the effects of the very soft isolation system are ignored compared to the relatively stiff crewmember-restraint harness system, then conservation of momentum will cause the center of mass of the two-body system to remain nearly stationary. Therefore, the relative motions of the crewmember center of mass and treadmill center of mass are determined by their mass ratios. For the case of a 200 lbm crewmember and a 1000 lbm treadmill, the mass ratio is 1:5 and the total relative motion of 1.5 inches between crewmember and treadmill center of mass during exercise is apportioned 1.25 inches to the crewmember, and 0.25 inches to the treadmill. The treadmill counterpoise mass provides a medically acceptable "feel" during exercise, while limiting the treadmill motion at the exercise frequency to approximately  $\pm 0.25$  inches. Such small motions of the treadmill frame connected to the SSF structure through a sufficiently soft passive or active device are easily limited to very acceptable transmitted disturbing forces of less than  $\pm 0.4$  lbf. The following sections describe the design procedures and supporting analyses conducted in the development of an optimized passive isolator.

## PERFORMANCE REQUIREMENTS

### General Performance Requirements

Several fundamental isolator performance objectives were established as the governing requirements for the treadmill isolator design. These performance objectives were:

1. Minimize transmission of primary exercise forces at the exercise frequencies (1.0 hz to 3.0 hz) to the surrounding SSF structure.
2. Maximize static centering stiffness at zero frequency to limit treadmill drift within its enclosure.
3. Maximize damping at the very low ( $< 0.1$  hz) isolator resonant frequencies to minimize low frequency drift oscillations.

### Transmitted Force Limits

Microgravity experiments impose strict limitations on SSF disturbances from all sources, including the treadmill. The original design requirement for the treadmill isolation system was to limit the vibration disturbance to no more than  $1.0E-5$  G at the point of treadmill attachment to the SSF structure. Subsequently, system requirements were revised in terms of a frequency dependent allowable disturbance at experiment locations from all sources of disturbance. Since this new proposed requirement has not yet allocated the treadmill portion of the total allowable disturbance, the design presented here will be based on the original requirement of less than  $1.0E-5$  G at the point of attachment.

Based on rigid body accelerations of the SSF module cluster

mass of approximately 340,000 lbm, and an assumed dynamic amplification factor of 3.0, the allowable transmitted force at 3.0 hz becomes:

$$\frac{(340000.0 \text{ lbm}) \times (1.0E-5 \text{ G})}{3.0} = \pm 1.13 \text{ lbf} \quad (1)$$

For conservatism, the value was rounded down to give an allowable steady state transmitted force limit of  $\pm 1.0$  lbf. It will be shown that the optimized passive isolator described can reduce the steady state exercise forces to less than  $\pm 0.4$  lbf, easily satisfying the preliminary transmitted force requirements mandated for SSF.

### Oscillatory Motion Limits

Oscillatory motions of the treadmill, both translational and rotational, may be disruptive to the jogging crewmember if they become excessive. The oscillatory motions are defined as the steady-state (periodic) translations and rotations induced by the crewmember at the foot strike frequency (1.0 to 3.0 hz), not the low-frequency drift motions below 0.1 hz. A preliminary set of oscillatory motion limits was established based on crew comfort and stability during exercising. These preliminary were as follows:

Translations:  $\pm 0.25$  inches vertical (Z axis)  
 $\pm 0.50$  inches lateral (X axis)  
 $\pm 0.25$  inches longitudinal (Y axis)

Rotations:  $\pm 5.0$  degrees roll (Y axis)  
 $\pm 5.0$  degrees pitch (X axis)  
 $\pm 5.0$  degrees yaw (Z axis)

### Drift Limits

Low frequency drift of the treadmill will occur due to small disturbances at frequencies much lower than the exercise frequencies and near the resonant frequency of the isolator system ( $< 0.1$  hz). Therefore, drift limits are required to prevent collision of the treadmill with the surrounding SSF structure. Packaging and stowage requirements limit the clearance gap between the treadmill and its surrounding frame to approximately 4 inches. Consequently, to be conservative, limits of  $\pm 1.0$  inch and  $\pm 10.0$  degrees were chosen as preliminary low-frequency drift limits at the isolator resonant frequency. Additionally, a maximum transient drift limit of 3.0 inches was established for the case of an extreme kickoff or stumble by the crewmember which could drive the treadmill through a transient excursion. The steady state and transient drift limits may be summarized as follows:

Steady State:  $\pm 1.0$  inch all axes  
 $\pm 10.0$  degrees all axes

Transient:  $\pm 3.0$  inches all axes

# ISOLATOR OPTIMIZATION STUDY

## General

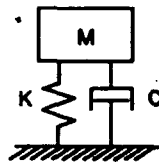
From the list of isolator performance requirements given previously, a list of specific design objectives may be developed as follows:

- 1) Maximize treadmill mass-inertia properties.
- 2) Minimize isolator dynamic stiffness at high-frequency. (1.0 to 3.0 hz exercise frequencies).
- 3) Maximize isolator dynamic stiffness and damping at low frequencies and resonant frequency (<.1 hz).
- 4) Maximize isolator static (centering) stiffness.

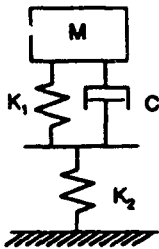
The following optimization analyses constitute an effort to develop a passive isolator which best meets all of the above performance objectives.

### Elastically-Coupled Isolator Transmissibility

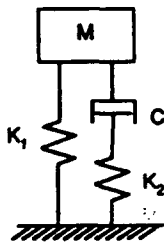
Three types of isolators are illustrated schematically in Figure 4, a conventional isolator, a series-coupled isolator, and a parallel-coupled isolator. Both the series and parallel coupled systems fall into the category of elastically-coupled isolators because of the additional stiffness element in series with the damping element. Both of these types of isolators will be shown to yield identical isolation performance that is significantly better than the conventional spring-damper system.



a. Conventional Isolator.



b. Series-Coupled Isolator.



c. Parallel-Coupled Isolator.

Figure 4. Conventional and Elastically-Coupled Isolators.

Dynamic force transmissibility of the applied exercise forces to the surrounding SSF structure is given for the conventional isolator and the two elastically-coupled isolators as

Conventional isolator:

$$TR = \frac{F_i}{F_o} = \sqrt{\frac{K^2 + \omega^2 C^2}{(K - \omega^2 M)^2 + \omega^2 C^2}} \quad (2)$$

Series coupled isolator:

$$TR = \frac{F_i}{F_o} = \sqrt{\frac{(K_1 K_2)^2 + (K_2 \omega C)^2}{(K_1 K_2 - \omega^2 M (K_1 + K_2))^2 + (\omega C (K_2 - \omega^2 M))^2}} \quad (3)$$

Parallel coupled isolator:

$$TR = \frac{F_i}{F_o} = \sqrt{\frac{(K_1 K_2)^2 + (\omega C (K_1 + K_2))^2}{(K_1 (K_2 - \omega^2 M))^2 + (\omega C (K_1 + K_2 - \omega^2 M))^2}} \quad (4)$$

where:

- $F_o$  = Force Applied to Treadmill (lbf)
- $F_i$  = Force Transmitted to Space Station (lbf)
- $\omega$  = Forcing Frequency (rad/sec)
- $M$  = Treadmill Mass (lbm)
- $K$  = Conventional Stiffness (lbf/in)
- $K1$  = Parallel Stiffness (lbf/in)
- $K2$  = Series Stiffness (lbf/in)
- $C$  = Damping (lbf-sec/in)

The transmissibility equations are plotted vs. frequency for both the conventional and series-coupled isolators in Figure 5 for a 1000 lbm treadmill mass and approximately 30% critical damping at a 0.08 hz resonance. While both isolators give the same good attenuation through the 0.08 hz resonance, the elastically-coupled system provides significantly better attenuation above resonance, where the exercise disturbances occur.

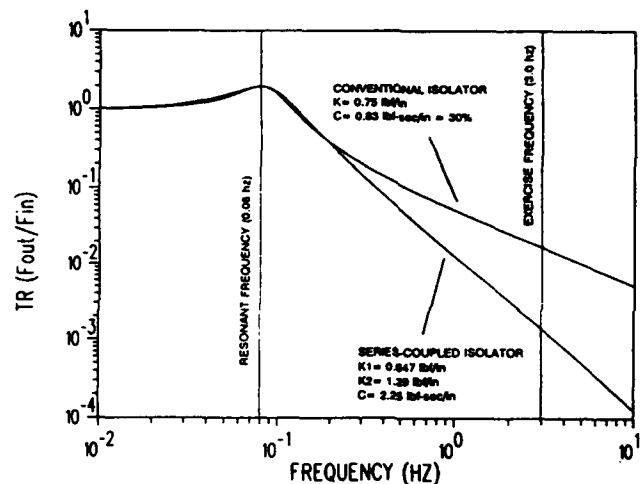


Figure 5. Conventional vs. Series-Coupled Isolator Transmissibilities at 30% Critical Damping.

Figure 6 illustrates how the series-coupled isolator actually functions as two separate isolators, one for the low-frequency regime, and another for the high-frequency regime where the exercise disturbances occur. At low frequency, the damper dynamic stiffness is low, allowing it to move for good modal damping at the drift frequencies. At high frequency, the damper stiffens and "locks up", which would normally cause high force transmissibility in a conventional system. However, the second spring of the elastically-coupled isolator serves to uncouple the damper, yielding inherently lower dynamic stiffness. The result is a frequency-biased isolator that will give good centering effects at low frequencies while allowing the treadmill to oscillate at the relatively high exercise frequency without transmitting excessive forces to the surrounding structure. This is especially beneficial in applications such as the treadmill, where the exercise excitations are at much higher frequency than the isolator resonant frequency. Consequently, the elastically-coupled isolator is the preferred configuration for passive treadmill isolation, and is examined more closely in the following sections to develop an optimized set of mass, stiffness, and damping constants that offer the best overall treadmill isolation.

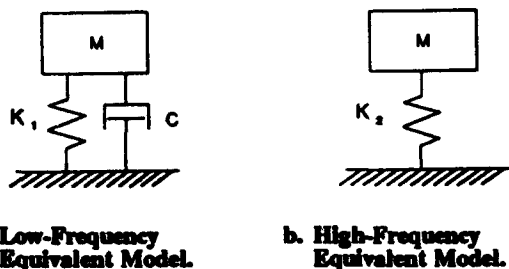


Figure 6. Low-Frequency and High-Frequency Equivalent Models for Series-Coupled Isolator.

### Exercise-Frequency Transmissibility

To minimize the percentage of the high exercise forces transmitted to the surrounding SSF structure, the isolator high-frequency dynamic stiffness must be limited to an acceptable level. At the relatively high exercise frequencies (above 1.0 Hz), the dynamic stiffness of the series-coupled isolator is simply the stiffness of the series spring,  $K_2$ . This is because the damper becomes dynamically very stiff at high frequencies, shifting all of the compliance to spring  $K_2$ . Thus, the exercise-frequency transmissibility becomes:

$$TR_{high} = \frac{F_{transmitted}}{F_{applied}} \quad (5)$$

$$= \frac{K_2 Z_{treadmill}}{F_{applied}}$$

The treadmill Z direction oscillatory motion (derived later in equations 17 through 20) is given by:

$$Z_{treadmill} = \frac{F_{applied}}{\omega^2 M_{treadmill}} \quad (6)$$

Then combining equations (5) and (6) gives the high-frequency transmissibility as:

$$TR_{high} = \frac{K_2}{\omega^2 M_{treadmill}} \quad (\text{series coupled}) \quad (7)$$

Thus, at a given exercise frequency, the high-frequency transmissibility of the treadmill on a series-coupled isolator reduces to the ratio of spring  $K_2$  to the treadmill mass.

For a parallel-coupled system, the high-frequency dynamic stiffness is the sum of the springs  $K_1$  and  $K_2$  giving:

$$TR_{high} = \frac{K_1 + K_2}{\omega^2 M_{treadmill}} \quad (\text{parallel coupled}) \quad (8)$$

Similarly, the rotational transmissibility to applied pitch and roll torques is the ratio of rotational stiffness to the respective treadmill inertias. For the roll direction, this becomes:

$$TR_{\theta_{roll}} = \frac{K_{\theta_{roll}}}{\omega^2 I_{yy}} \quad (9)$$

where:

$$K_{\theta_{roll}} = K_2 X_{ins}^2 \quad (\text{series coupled})$$

$$K_{\theta_{roll}} = (K_1 + K_2) X_{ins}^2 \quad (\text{parallel coupled})$$

$X_{ins} = X$  Distance from Isolator to Treadmill CG

The pitch and yaw transmissibilities are expressed similarly as:

$$TR_{\theta_{pitch}} = \frac{K_{\theta_{pitch}}}{\omega^2 I_{xx}} \quad (10)$$

$$TR_{\theta_{yaw}} = \frac{K_{\theta_{yaw}}}{\omega^2 I_{zz}} \quad (11)$$

Therefore, for the series-coupled isolator, the most important isolator requirement of minimizing the exercise force transmissibility becomes the relatively simple task of maintaining a heavy enough treadmill and a soft enough spring  $K_2$ . However, as will be discussed in the following sections, the other requirements to limit on-orbit weight, and to maintain adequate static centering stiffness to limit

treadmill drift, are both in direct opposition to the strategy which yields low transmissibility, forcing a necessary compromise that satisfies all three.

### Static Centering Stiffness

Like the exercise-frequency transmissibility, the ultra-low-frequency centering stiffness of the series-coupled isolator is dependent only on the isolator springs, and not the damper. This is because the damper dynamic stiffness becomes very low at low frequency, leaving only the isolator springs active. Since the ultra-low-frequency and static behavior are well below the isolator resonant frequency (around 0.05 to 0.1 hz), the centering stiffness is independent of the treadmill mass as well. This is because sub-resonant dynamic behavior that is well below the resonant frequency is mass-independent, leaving the isolator springs as the only factor in determining the static and ultra-low-frequency centering characteristics of the treadmill.

While the exercise force transmissibility is benefited by minimizing the spring stiffnesses, the reverse is true for the centering effects. Adequate centering stiffness required to prevent drifting of the treadmill into the surrounding SSF structure requires the series-combined stiffness of springs  $K_1$  and  $K_2$  to be above a minimum level.

For two springs in series, the stiffness becomes

$$K_{static} = \frac{K_1 K_2}{K_1 + K_2} \quad (\text{series coupled}) \quad (12)$$

For the parallel-coupled system, the static stiffness is simply the spring stiffness of  $K_1$

$$K_{static} = K_1 \quad (\text{parallel coupled}) \quad (13)$$

Similarly, the rotational static stiffnesses,  $K_{\theta}$ , in roll, pitch and yaw are the series combinations of the rotational stiffnesses expressed as:

$$K_{\theta static} = K_{static} x (\text{moment arm})^2 \quad (14)$$

Series-coupled:

$$K_{\theta static} = \frac{K_1 K_2}{K_1 + K_2} x (\text{moment arm})^2 \quad (15)$$

Parallel-coupled:

$$K_{\theta static} = K_1 x (\text{moment arm})^2 \quad (16)$$

### Resonant-Frequency Damping

Unlike the simple spring-damper model illustrated in Figure 4a, the modal damping of the elastically-coupled isolator is nonlinear with the damper value. This means that there is an optimum damping value at which the modal damping is highest (base motion transmissibility lowest) at the low-frequency resonance. Optimum damping occurs at the point where the partial derivative of the transmissibility at resonance with respect to the damping value is zero. Also, again unlike the conventional system, the damped natural frequency is very dependent on the damping value, making the system resonance highly coupled to damping and requiring careful selection of the optimum damping value.

### Isolator Performance Curves

An iterative solution was developed to maximize the resonant-frequency damping for a given stiffness ratio  $K_2/K_1$ . This provides an isolator design that offers the highest possible attenuation of low-frequency disturbances such as breathing and SSF base excitations. The three important isolator characteristics discussed above, exercise-frequency transmissibility, static centering stiffness, and resonant-frequency damping (transmissibility), are all plotted in Figure 7 for use in selecting isolator stiffness and damping values that yield an optimized design. The dimensionless stiffness ratio,  $K_2/K_1$ , is the abscissa variable, while the three performance parameters comprise the ordinates. Both the series-coupled and the parallel-coupled isolator configurations were found to give identical dynamic performance, and hence are both represented by the curves of Figure 7. The actual spring and damper values, however, are different for the series-coupled and parallel-coupled isolators.

In generating the three design curves, it was first necessary to select an isolator resonant frequency to be held constant throughout the calculations. This became a starting point for subsequent development of the performance data. An isolator resonant frequency of 0.08 hz was selected because it is far enough below the lower vibration modes of the SSF structure (approx. 0.12 hz and up) to help decouple the isolator from the SSF structure. Also, at 0.08 hz, the isolator resonance will be well below all exercise frequencies that begin around 1.0 hz, thus assuring inertially-controlled treadmill behavior and minimum force transmissibility to the SSF. At resonant frequencies any lower than 0.08 hz, the isolator spring stiffnesses, and hence the static centering stiffness, become too low to provide adequate treadmill centering effects. Thus, the selection of the 0.08 hz isolator resonant frequency involved a tradeoff between centering stiffness and exercise frequency transmissibility, for which 0.08 hz was chosen as the near optimum value.

Having selected a 0.08 hz resonant frequency, the next step in developing the performance curves was to compute the value of damping that minimizes the resonant transmissibility at 0.08 hz for each dimensionless stiffness ratio,  $K_2/K_1$ . This required iteration at each stiffness ratio to find the values of

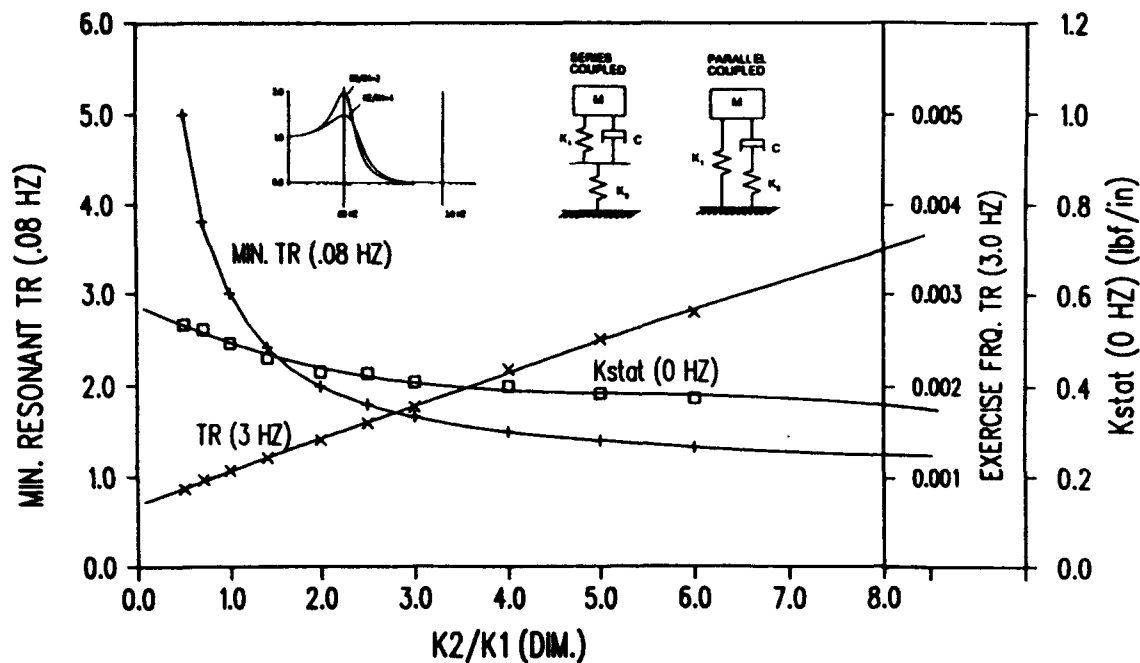


Figure 7. Elastically-Coupled Isolator Performance Curves (Series-Coupled and Parallel-Coupled).

$K_1, K_2,$  and  $C$  which yield a resonant frequency of 0.08 hz, and also provide the maximum possible modal damping. Therefore, the performance curves of Figure 7 reflect a set of iterative computations that always yield the maximum possible modal damping and a 0.08 hz resonant frequency at each dimensionless stiffness ratio.

#### Optimized Isolator Parameters

Inspection of Figure 7 reveals the expected tradeoff between exercise-frequency transmissibility and resonant-frequency transmissibility. This is understood by realizing that an increase in spring stiffness  $K_2$  relative to  $K_1$  forces more movement in the damper at low frequency, giving better modal damping at resonance. However, this also increases the high-frequency dynamic stiffness, and hence transmissibility, at the 3.0 hz exercise frequency. Conversely, reducing  $K_2$  relative to  $K_1$  provides less damper motion at resonance, raising the resonant frequency transmissibility, but also causing a beneficial reduction in the exercise-frequency transmissibility at 3.0 hz due to the loss of dynamic stiffness. Consequently, it was necessary to define a strategy for selecting a stiffness ratio of  $K_2/K_1$ , which yields the best overall isolator performance.

Surprisingly, the static centering stiffness is relatively insensitive to the stiffness ratio as long as the resonant frequency is held constant, as it was in the generation of the performance curves. Therefore, the static centering stiffness is not a major consideration in selecting an optimum stiffness ratio. It should be noted, however, that variation of the resonant frequency from 0.08 hz would strongly affect the static stiffness, as it would shift the spring rates up or down.

However, a significant change in the resonance from 0.08 hz is not recommended because it would sacrifice centering stiffness on the lower end, or increase exercise transmissibility on the upper end.

Since the performance curves reflect a strong increase in the 0.08 hz resonant frequency transmissibility below stiffness ratios of about 2.0, and this is a quantity to be minimized, it is sensible to preclude stiffness ratios below 2.0. Therefore, 2.0 becomes a logical lower bound for  $K_2/K_1$ . Also, since the exercise-frequency transmissibility increases linearly with stiffness ratio, and this too is a parameter to be minimized, it is necessary to establish an upper bound for the stiffness ratio. At  $K_2/K_1 = 4.0$ , the slope of the 0.08 hz transmissibility is very low, while the 3.0 hz transmissibility continues to rise linearly. Hence,  $K_2/K_1 = 4.0$  becomes a reasonable upper bound, beyond which there is not much additional reduction in the 0.08 hz resonant transmissibility.

The only remaining question was which stiffness ratio within the range of 2.0 to 4.0 is the optimum value. Since all values within this range would yield excellent performance, as all the transmissibilities between  $K_2/K_1$  of 2.0 to 4.0 are acceptable, an additional criterion was needed to further differentiate the relative merits of the two stiffness ratios. To narrow the selection further, it seemed sensible to examine the actual hardware to identify which of the components (the two springs or the damper) is most susceptible to manufacturing or operational variations, and then compare the performance sensitivity to such variations at stiffness ratios of 2.0 and 4.0. Since dampers are generally more subject to change over time due to wear than springs, it is instructive to investigate the sensitivity of isolator performance to variations in damping at the two stiffness ratios of 2.0 and 4.0.

Figures 8 and 9 show the effects of damping on the isolator resonant frequency and resonant transmissibility for the two stiffness ratios of 2.0 and 4.0. The exercise-frequency transmissibility and static stiffness are unaffected by damping, making it unnecessary to evaluate them in the comparisons. Inspection of Figure 8 reveals that the increase in resonant frequency with damping is greater at  $K_2/K_1=4.0$  than at  $K_2/K_1=2.0$ , making the isolator somewhat more susceptible to resonant frequency shifts at  $K_2/K_1=4.0$ . However, even the frequency shift to 0.125 hz corresponding to twice the optimum damping would not critically affect the isolator performance, leaving  $K_2/K_1=4.0$  still within the range of acceptability.

In Figure 9, the resonant transmissibilities at  $K_2/K_1=2.0$  and  $K_2/K_1=4.0$  track each other through the entire damping range, and therefore exhibit nearly the same percentage variation with damping. Consequently, there does not appear to be a significant difference in susceptibility of the isolator to loss of

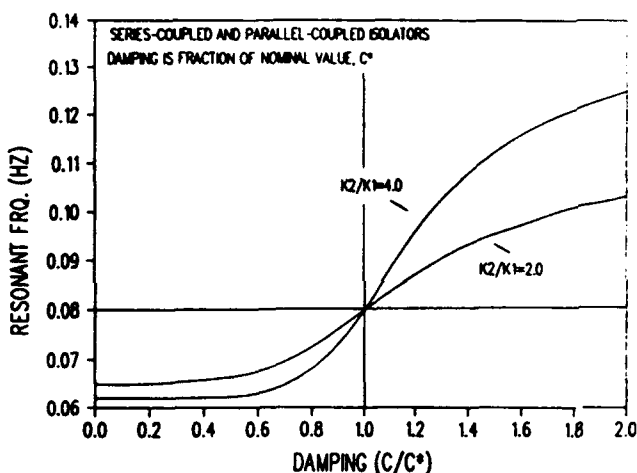


Figure 8. Effect of Damping on Elastically-Coupled Isolator Resonant Frequency at Stiffness Ratios of  $K_2/K_1=2.0$  and  $K_2/K_1=4.0$ .

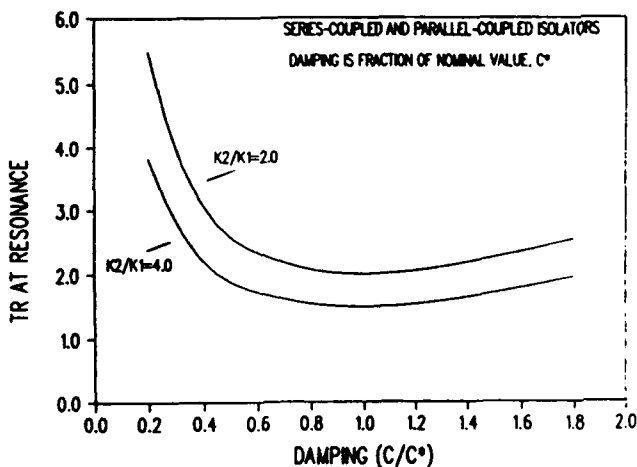


Figure 9. Effect of Damping on Elastically-Coupled Isolator Maximum Resonant Transmissibility at Stiffness Ratios of  $K_2/K_1=2.0$  and  $K_2/K_1=4.0$ .

low-frequency performance between the dimensionless stiffness ratios of 2.0 and 4.0, leaving the complete range acceptable for the isolator design. Moreover, the slope of the transmissibility curves is low near the optimum damping value, minimizing the sensitivity of isolator performance to small damping variations away from nominal.

In conclusion, any stiffness ratio between the values of 2.0 and 4.0 will yield excellent isolator performance, however, the stiffness ratio of  $K_2/K_1=2.0$  offers a slight performance advantage due to its lower exercise-frequency transmissibility and slightly higher centering stiffness. Since the stiffness ratio of 2.0 also yields acceptable low-frequency resonant damping ( $TR=2.0$ ), and does not leave the isolator overly susceptible to performance loss from damping variations, it became the preferred stiffness ratio for the treadmill isolator.

For a 1000 lbm treadmill with an isolator natural frequency of 0.08 hz, the optimum stiffness and damping values for a stiffness ratio of  $K_2/K_1=2.0$  are:

Series-Coupled:  $K_1=0.647$  lbf/in  
 $K_2=1.29$  lbf/in  
 $C=2.25$  lbf-sec/in

Parallel-Coupled:  $K_1=0.421$  lbf/in  
 $K_2=0.842$  lbf/in  
 $C=1.00$  lbf-sec/in

### TREADMILL RESPONSE TO CREWMEMBER EXERCISE (FOOTFALL) AND BREATHING FORCES

#### Measured Exercise Footfall Forces

Figure 10 shows measured foot strike forces for a 200 pound person running at approximately 6 mph (1). It is evident from

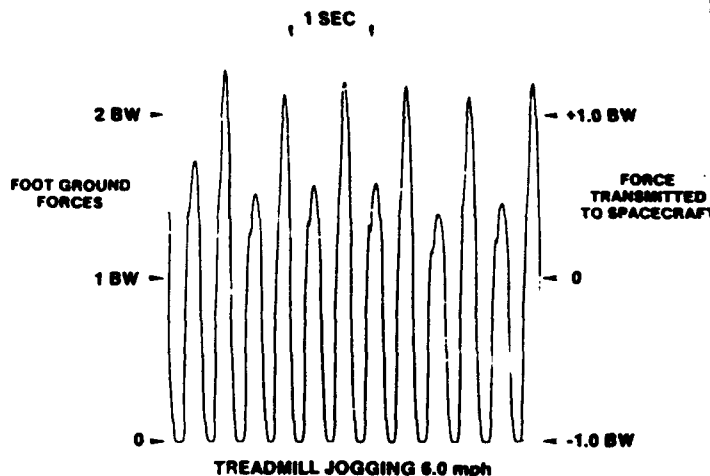


Figure 10. Measured Foot-Strike Forces for 200 lbm Crew-member Running at 6 mph (from Ref. 1).

the waveform that the forces are approximately sinusoidal, with the expected periodicity present throughout the time trace. Some asymmetry results from uneven leg contribution in this particular subject. The waveform is clipped at the bottom of each cycle as the feet briefly leave the ground during the soar phase of the gait. The fundamental frequency is near 3.0 hz for the 6.0 mph running measured. Similar data from the same reference indicates 2.5 hz and 1.5 hz for 4.0 mph jogging and 2.0 mph walking, respectively. Oscillatory force magnitude for the 4.0 mph jogging is the same as 6.0 mph running at  $\pm 1.0$  BW, while walking at 2.0 mph produced a lower excitation of approximately  $\pm 0.25$  BW.

In actual human physiology, there is wide range of footfall forces and transition frequencies from walking to running, depending on the particular subject's gait characteristics (2-4). For example, a tall long-legged runner would usually transition from walking to running at a higher speed and lower frequency. Nevertheless, the simplified exercise parameters given above are very adequate to define and analyze the treadmill dynamic characteristics for design purposes.

For purposes of analysis, the exercise forcing function may be approximated as a pure sinusoid such as that shown in Figure 11. Notice that the entire waveform has been shifted down by 200 lbf to represent the net force applied to the treadmill, including the nearly-constant restraint force. Ideally, the restraint will apply an attractive force between the crewmember and treadmill equal to one BW, regardless of the crewmember position. Such a "zero-stiffness" restraint is by definition the best approximation of gravity. For analysis purposes, the effect of the restraint is simply to shift the applied forces down by one BW so that the net treadmill forces vary symmetrically about zero, as necessary to obey conservation of momentum. The approximated exercise forcing function of Figure 11 will serve as the fundamental disturbance model for all subsequent analyses.

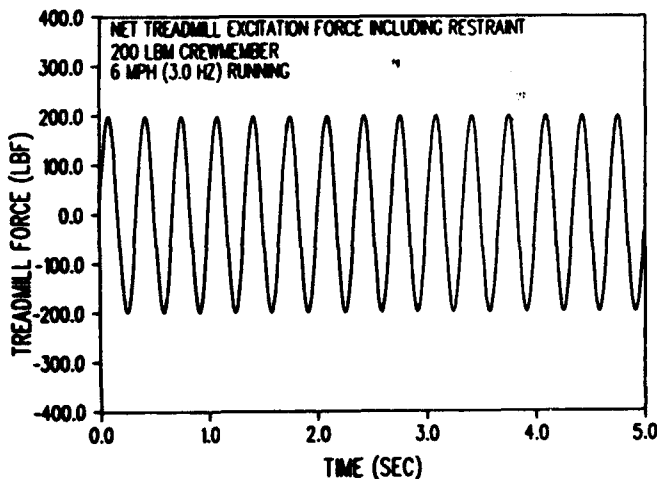


Figure 11. Sinusoidal Approximation of Net Exercise Forces for 200 lbm Crewmember Running at 6 mph (Includes 1 BW Restraint Force).

### Vertical Oscillations from Crewmember Walking/Running

On a very soft support, where the frequency of disturbance is much higher than the isolator resonant frequency, the treadmill may be treated as a free rigid body subjected to periodic excitations. For such a system, the resulting motion is non-resonant, making it dependent only on the mass, and not the supporting springs and dampers. The equation of motion for non-resonant rigid body response to periodic sinusoidal excitation is:

$$Z(t) = \frac{F \sin(\omega t)}{M} \quad (17)$$

Integrating twice gives the velocity and displacement as:

$$\dot{Z}(t) = -\frac{F \cos(\omega t)}{\omega M} \quad (18)$$

$$Z(t) = -\frac{F \sin(\omega t)}{\omega^2 M} \quad (19)$$

Dropping the time dependence gives the peak displacement as:

$$Z = \frac{F}{\omega^2 M} \quad (20)$$

For a 1000 lbm treadmill subjected to  $\pm 200$  lbf jogging excitation at 6 mph (3 hz), the peak bounce (Z) displacement is:

$$Z = \frac{(200.0 \text{ lbf})(386 \text{ lbm-in/lbf-sec}^2)}{(3.0 \text{ hz} \times 2.0 \pi)^2 (1000.0 \text{ lbm})} \quad (21)$$

$$= 0.217 \text{ in-pk}$$

This equation is plotted parametrically in Figure 12 showing the expected variation in treadmill bounce oscillation with

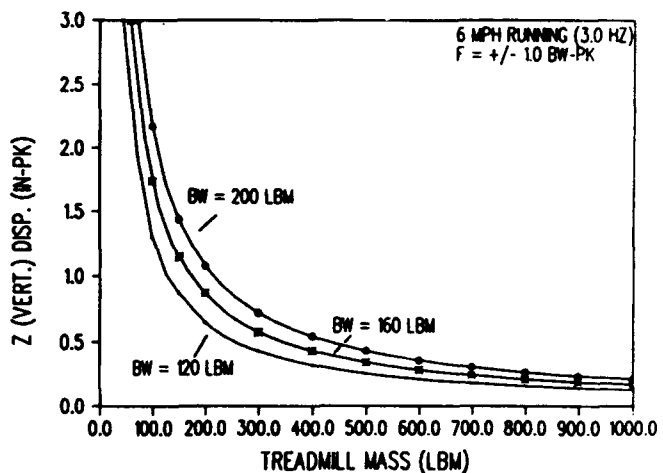


Figure 12. Peak Oscillatory Vertical (Bounce) Response vs. Treadmill Mass for Various Crewmember Body Weights During 6 mph (3.0 hz) Running.

treadmill mass for various crewmember body weights during 6 mph running. The 4 mph jogging and 2 mph walking motions are similar, except for a reduction in peak force to 0.25 BW for walking, and reductions in frequency to 2.5 hz, and 1.5 hz for jogging and walking, respectively. Therefore, to compute similar data for 4 mph and 2 mph exercise paces, the 6 mph data should be multiplied by the force and frequency conversions as follows:

$$\begin{aligned} Z_{4\text{mph}} &= \left(\frac{3.0\text{hz}}{2.5\text{hz}}\right)^2 \times Z_{6\text{mph}} \\ &= 1.44 \times Z_{6\text{mph}} \end{aligned} \quad (22)$$

$$\begin{aligned} Z_{2\text{mph}} &= \left(\frac{0.25\text{BW}}{1.0\text{BW}}\right) \times \left(\frac{3.0\text{hz}}{1.5\text{hz}}\right)^2 \times Z_{6\text{mph}} \\ &= 1.0 \times Z_{6\text{mph}} \end{aligned}$$

As indicated by equation 22, the highest treadmill motions are predicted to occur in slow (4 mph) running or jogging, where the forces are fully developed (ie. greater than walking), but the frequency is low.

#### Roll Oscillations from Crewmember Walking/Running

Like the vertical oscillations, the steady-state roll oscillations induced by the running crewmember are at a frequency much higher than the isolator roll resonant frequency, and thus are dependent only on the crewmember forces and the roll inertia of the treadmill. Equations similar to those derived previously for the bounce motion may be written for the roll motion:

$$\ddot{\theta}_r(t) = \frac{T \sin(\omega t)}{I_r} \quad (23)$$

Double integrating through velocity to displacement gives:

$$\dot{\theta}_r(t) = -\frac{T \cos(\omega t)}{\omega I_r} \quad (24)$$

$$\theta_r(t) = -\frac{T \sin(\omega t)}{\omega^2 I_r} \quad (25)$$

Dropping the time dependence gives the peak displacement as:

$$\theta_r = \frac{T}{\omega^2 I_r} \quad (26)$$

Roll torques from the running forces arise from the feet striking slightly off center by a distance of about 3 to 4 inches (6 to 8 inches foot-to-foot). This creates a sinusoidal oscillatory roll torque at half the running frequency, or approximately 1.5 hz for 6 mph running, that is the product of

the force times the 4.0 inch moment arm. The force magnitude is approximately 2.0 BW, or twice that of the vertical excitation. This is because the static 1.0 BW restraint force also contributes to roll force, whereas only the dynamic component contributes to the vertical excitations. Neglecting the small roll moments imposed by the crewmember restraint system, this becomes the only significant roll excitation to the treadmill. Figure 13 shows the simulated roll torque time history for a 200 lbm crewmember running at 6 mph (3 hz.) The brief dwell between pulses reflects the soar phase of the gait, when the feet are not in contact with the treadmill.

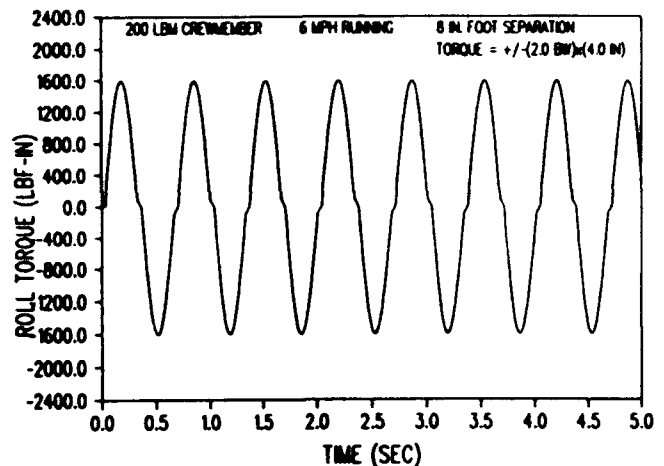


Figure 13. Simulated Roll Torque Time History for 200 lbm Crewmember Running at 6 mph (3.0 hz) with 8 in. Foot Separation.

Substituting the torque formulation into equation 26, with an assumed roll inertia of 123,000 lbm-in<sup>2</sup>, gives the oscillatory treadmill roll motion for a 200 lbm crewmember running at 6 mph (3.0 hz) as:

$$\begin{aligned} \theta_r &= \frac{(400.0\text{ lbf})(4.0\text{ in})(386.0\text{ lbm-in/lbf-sec}^2)}{(123000.0\text{ lbm-in}^2)(2.0\pi \times 1.5\text{ hz})^2} \\ &= 0.0565\text{ rad-pk} \\ &= 3.24\text{ deg-pk} \end{aligned} \quad (27)$$

The 4 mph and 2 mph roll response values are computed through multiplication by the proper ratios as follows:

$$\begin{aligned} \theta_{r,4\text{mph}} &= \left(\frac{1.50\text{hz}}{1.25\text{hz}}\right)^2 \times \theta_{r,6\text{mph}} \\ &= 1.44 \times \theta_{r,6\text{mph}} \end{aligned} \quad (28)$$

$$\begin{aligned} \theta_{r,2\text{mph}} &= \left(\frac{1.25\text{BW}}{2.0\text{BW}}\right) \times \left(\frac{1.5\text{hz}}{0.75\text{hz}}\right)^2 \times \theta_{r,6\text{mph}} \\ &= 2.5 \times \theta_{r,6\text{mph}} \end{aligned}$$

As expected, the slow jogging at 4 mph and walking at 2 mph induce larger roll responses than 6 mph running due to the lower frequency of 1.25 hz and 0.75 hz, respectively. The highest roll response is predicted to occur at walking speeds, giving a peak response for the example above of  $2.5 \times 3.24 \text{ deg-pk} = 8.1 \text{ deg-pk}$ . At 4 mph, the predicted peak roll is  $1.44 \times 3.24 = 4.66 \text{ deg-pk}$ .

While the  $\pm 8.1$  degrees at 2 mph is above the established guideline of  $\pm 5.0$  degrees for oscillatory roll motion, it will likely be tolerable for the small percentage of time spent at such a slow pace. A series of tests is underway to determine more precisely the levels of bounce, roll, and pitch motion that are tolerable for extended exercise sessions. These tests are being conducted in a 1-G apparatus designed to simulate the balance and "feel" of the 0-G system. If the 1-G tests indicate that the current levels of roll cause crew discomfort or disorientation during walking or slow running, the roll inertia may easily be increased through addition of a heavy handrail at waist level, giving a mass times distance squared increase in roll inertia. For example, a 76 lbm handrail located 40 inches above the treadmill surface would double the roll inertia to  $246,000 \text{ lbm-in}^2$ , reducing the peak-to-peak roll to  $\pm 4.05$  degrees at 2 mph, and  $\pm 2.33$  degrees at 4 mph. If the roll oscillations are still too high, an elastic restraint (bungee) can be connected from the crewmember's waist to the handrail to restrain roll.

At 6 mph, the  $\pm 3.24 \text{ deg-pk}$  roll response is well within the preliminary  $\pm 5.0$  degree limit allowed for oscillatory roll motion. This level of roll has been shown through preliminary 1-G testing to be almost unnoticeable to the exercising crewmember.

The curves of Figure 14 show the variation in oscillatory roll amplitude with roll inertia for various crewmember body weights during 6 mph running. Similar data for 4 mph jogging and 2 mph walking may be computed using the ratios of 1.44 and 2.50, respectively, as given in equation 28.

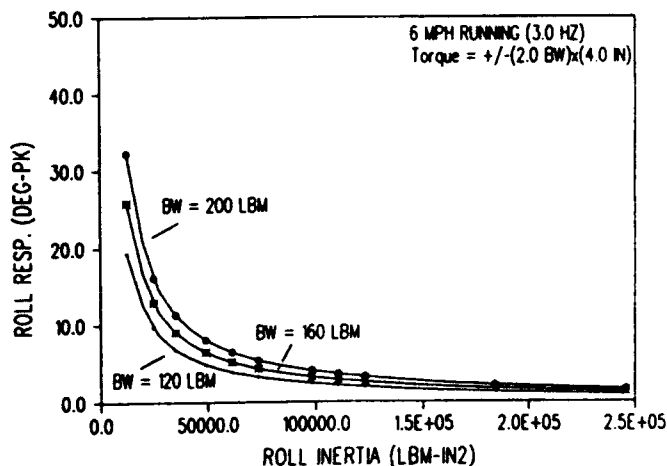


Figure 14. Peak Oscillatory Roll Response vs. Treadmill Roll Inertia for Various Crewmember Body Weights During 6 mph (3.0 hz) Running.

#### Pitch Oscillations from Crewmember Walking/Running

Oscillatory pitch torques are developed when the runner's foot contacts the running surface forward of the centerline, imposing a forward pitching moment on the treadmill. Then, under increasing foot force, the contact point passes aftward through the lateral centerline, where it creates no moment, and finally moves aft of the centerline to create an opposite backward pitch moment just before leaving the treadmill surface. This results in a complex pitch excitation torque because both the force magnitude and moment arm are changing with time. For a 200 lbm crewmember, the torques are the product of a linear moment arm variation of approximately  $\pm 12$  inches, and a sinusoidal force variation between  $\pm 400$  lbf. Like the roll torques, the 1.0 BW restraint contributes to the pitch excitations, giving applied forces that are 1.0 BW higher than the vertical disturbances.

At 6.0 mph, the pitch moment arm varies with time as follows:

$$Y(t) = 12.0in - V(t) \quad (29)$$

$$= 12.0in - (105.6 \text{ in/sec})(t)$$

The force for the 200 lbm crewmember varies sinusoidally with time as given by:

$$F(t) = -200.0(\cos(18.8t) - 1.0) \quad (30)$$

Combining equations 29 and 30 gives the effective pitch torque for the 200 lbm crewmember as:

$$T(t) = F(t) \times Y(t) \quad (31)$$

$$= -200.0(\cos(18.8t) - 1.0)(12.0 - 105.6t)$$

Figure 15 shows the simulated pitch torque time history for a 200 lbm crewmember running at 6 mph (3 hz) computed according to equation 31.

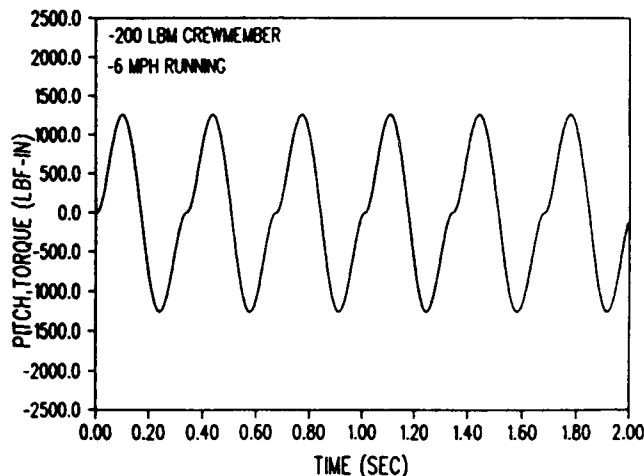


Figure 15. Simulated Pitch Torque Time History for 200 lbm Crewmember Running at 6 mph (3.0 hz).

156

The resulting oscillatory pitch motions induced in the treadmill are also at much higher frequency than the treadmill pitch resonant frequency, making them dependent only on the treadmill pitch inertia. However, since the pitch torques are not sinusoidal, the simple harmonic rigid body equations used for bounce and roll do not apply. Consequently, a transient finite difference numerical integration solution of the coupled 6-DOF equations of motion was used to compute the pitch oscillations. Figure 16 shows the rigid body dynamic model developed for the pitch computations.

The computed pitch time history is shown in Figure 17 for the 200 lbm crewmember running at 6 mph on a 1000 lbm (348,000 lbm-in<sup>2</sup> pitch inertia) treadmill. It is evident that the peak pitch magnitude is only  $\pm 0.21$  deg, which is well within the allowable pitch limit of  $\pm 5.0$  degrees.

Figures 18 through 20 show parametrically the resulting oscillatory pitch motion induced as a function of treadmill pitch inertia for various crewmember body weights during 2 mph walking, 4 mph jogging, and 6 mph running. Again, the exercise force was reduced to from 2.0 BW to 1.25 BW for the walking computations.

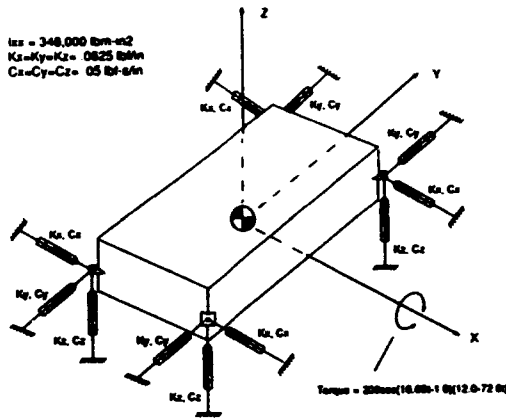


Figure 16. Six Degree-of-Freedom Rigid Body Model for Pitch Analysis.

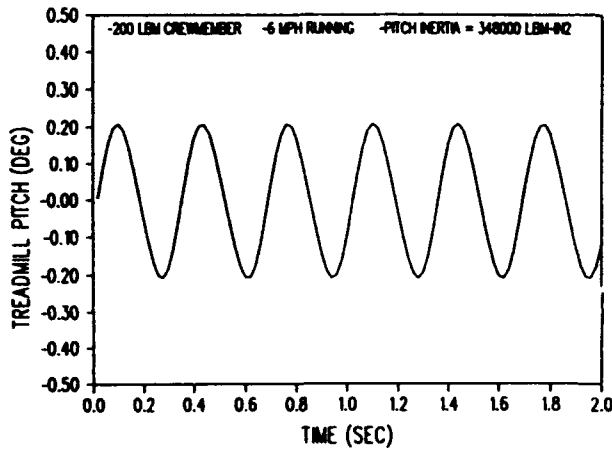


Figure 17. Computed Pitch Time History for 200 lbm Crewmember Running at 6 mph ( $I_x = 348,000$  lb-in<sup>2</sup>).

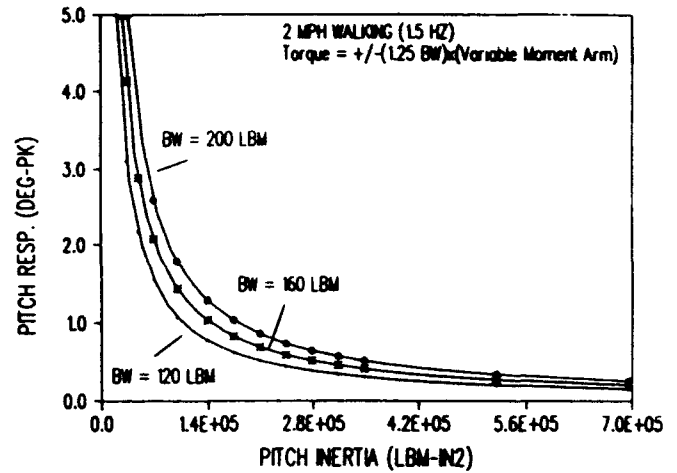


Figure 18. Peak Oscillatory Pitch Response vs. Treadmill Pitch Inertia for Various Crewmember Body Weights Walking at 2 mph (1.5 hz).

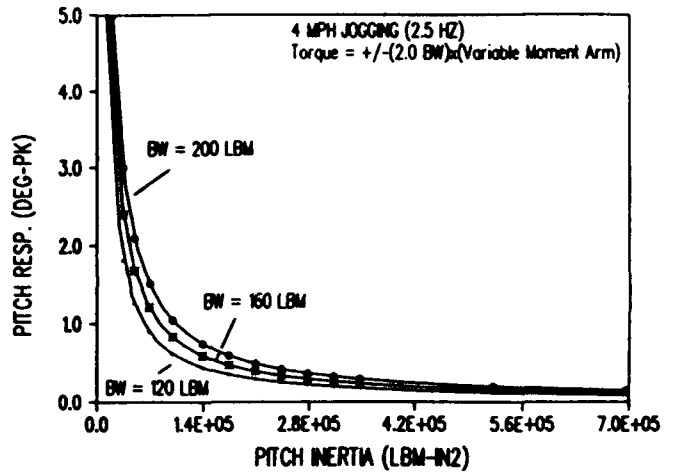


Figure 19. Peak Oscillatory Pitch Response vs. Treadmill Pitch Inertia for Various Crewmember Body Weights Jogging at 4 mph (2.5 hz).

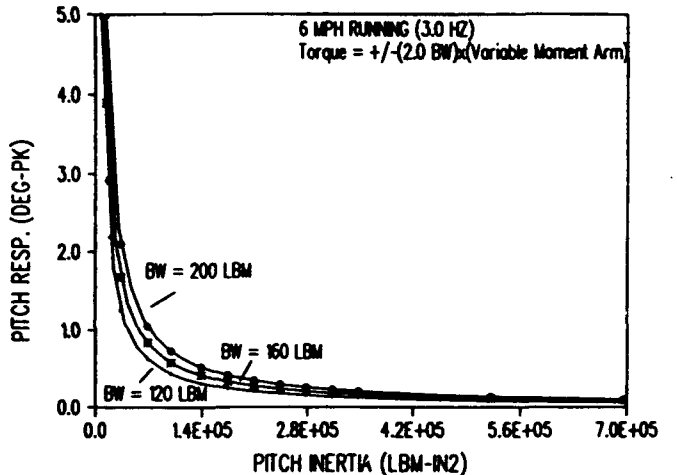


Figure 20. Peak Oscillatory Pitch Response vs. Treadmill Pitch Inertia for Various Crewmember Body Weights Running at 6 mph (3.0 hz).

157

### Transient Response to Crewmember Kick-off (Stumble)

An extreme kick-off or stumble by the running crewmember will impose high transient forces and torques of equal magnitude and opposite direction to both the treadmill and crewmember. Fortunately, conservation of both linear and angular momentum between the treadmill and crewmember will limit the transient excursions of both. This is because, as discussed previously, the momentum of the dynamic system composed of the crewmember and treadmill must remain nearly zero in the absence of significant externally applied forces (isolator spring/damper forces are equilibrated, and breathing reactions are negligible). Consequently, the combined CG of the crewmember and treadmill will remain very nearly stationary. This means that the ratio of absolute treadmill motion to absolute crewmember motion is inversely proportional to their mass ratio. Therefore, if a 200 lbm crewmember were to kick off or jump to an extreme height of 12 inches (10 inches absolute), the 1000 lbm treadmill excursion would be only 2 inches to maintain a fixed CG. Similarly, a 24 degree (20 degrees absolute) rotation of the crewmember would induce only a 4 degree rotation of the treadmill (assuming a 5 to 1 inertia ratio).

The crewmember-treadmill system was simulated with the two body dynamic model illustrated in Figure 21 to characterize the self-equilibration that must take place between the crewmember and treadmill to conserve linear and angular momentum. A two-body dynamic simulation was necessary to react internally the high crewmember-to-treadmill forces so that no net energy is imparted to the isolated system.

The optimized isolator parameters given earlier for a stiffness ratio of  $K_2/K_1=2.0$  were used to construct a series-coupled isolator model. A transient finite difference numerical integration solution was used to integrate numerically the coupled equations of motion through time. Spring and damping values between the crewmember and treadmill were chosen to give the correct running frequency of 3.0 hz, and

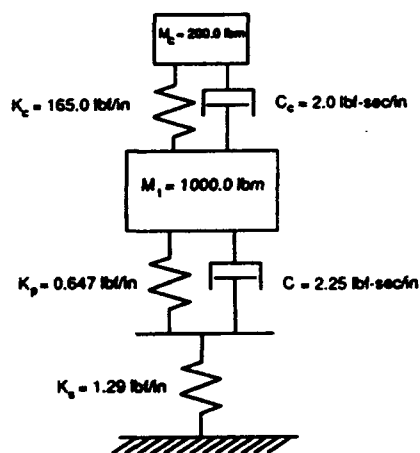


Figure 21. Two-Body Treadmill-Crewmember Dynamic Model with Series-Coupled Isolator.

to reach steady-state exercise response within several cycles. During actual running, the legs adjust over a wide range of effective stiffness and damping values to give the balance and body control needed under different circumstances. Walking, for example, requires a lower effective leg spring rate than running to yield the lower walking frequency. While the analytical model uses only a single set of dynamic parameters, it offers a very close estimate of the steady-state effects, and a reasonable estimate of the transient effects between the crewmember and treadmill.

To perform the computation, a 3.0 hz sinusoidal forcing function of 52.0 lbf was applied equally and in opposite directions to the crewmember and treadmill to sustain oscillatory running motion. Then, at  $t=3.5$  seconds, an additional triangular 600.0 lbf kick-off force of 0.5 seconds duration was applied in opposite directions to both the crewmember and treadmill masses to simulate the extreme disturbance. Since the conservation of momentum requires that there be no net external force applied to the crewmember-treadmill system, both the 52.0 lbf steady-state force and the 600.0 lbf transient disturbance were applied exactly out of phase (opposite directions) to the crewmember and treadmill as interactive forces.

Figures 22 and 23 illustrate the computed motion of both crewmember and treadmill during 6 mph jogging with the 600 lbf kick-off added. The kick-off induces a 7.5 inch excursion of the 200 lbm crewmember, while the simultaneous movement of the 1000 lbm treadmill is limited by conservation of momentum to only 1.5 inches. The corresponding forces are shown in Figures 24 and 25, where the 600 lbf kick-off adds to the internal leg forces to reach a transient peak in the legs of 950 lbf, while the transmitted SSF force is limited by the isolator to only 1.8 lbf. Therefore, even an extreme disturbance far greater than that normally expected of an astronaut is attenuated by the isolator to a reasonable level. The 1.5 inch treadmill excursion falls well below the 3.0 inch transient drift limit defined earlier.

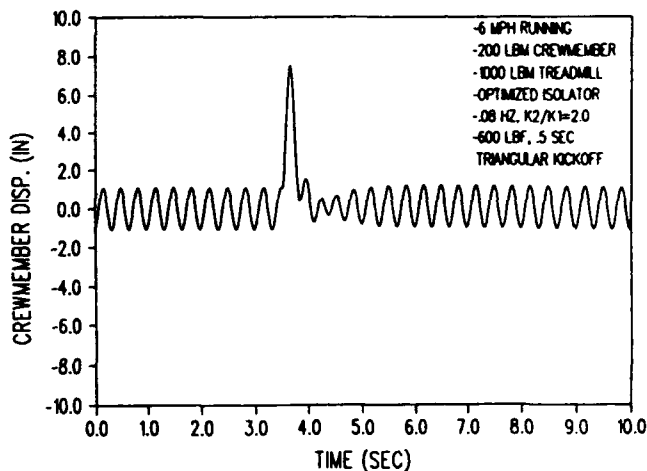


Figure 22. Transient Crewmember Absolute Response for 52.9 lbf Sinusoidal Excitation Plus 600 lbf Kick-off on Series-Coupled 6.06 hz Isolator.

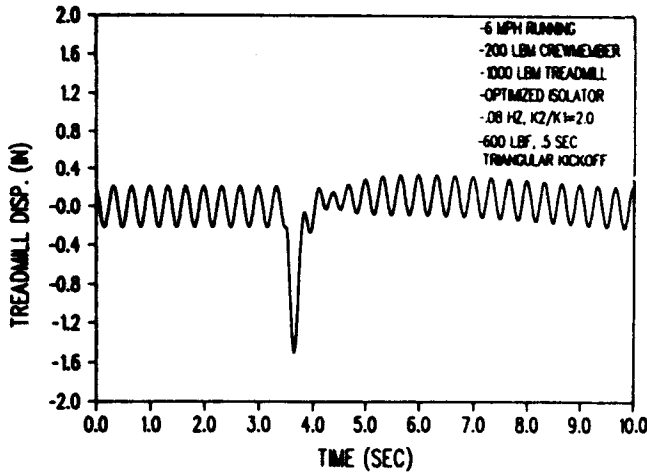


Figure 23. Transient Treadmill Absolute Response for 52.0 lbf Sinusoidal Running Excitation Plus 600 lbf Kick-off on Series-Coupled 0.08 Hz Isolator.

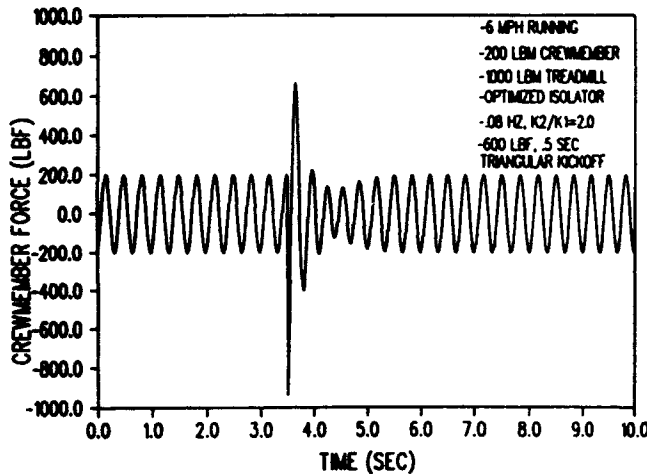


Figure 24. Transient Treadmill-Crewmember Interactive Force for 52.0 lbf Sinusoidal Running Excitation Plus 600 lbf Kick-off on Series-Coupled 0.08 Hz Isolator.

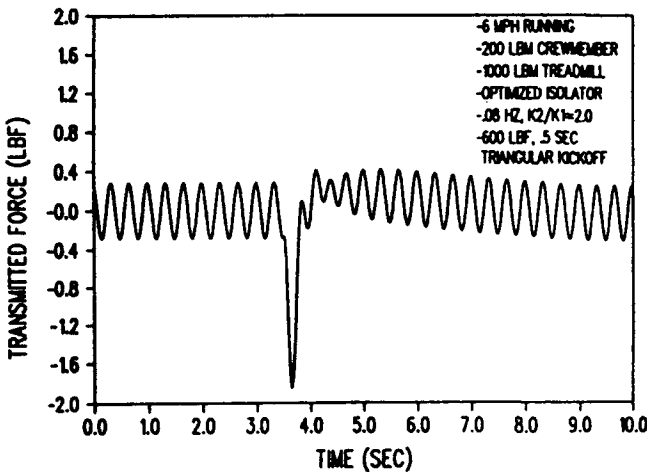


Figure 25. Transient Transmitted Space Station Force for 52.0 lbf Sinusoidal Running Excitation Plus 600 lbf Kick-off on Series-Coupled 0.08 Hz Isolator.

### Low-Frequency Response to Crewmember Breathing

Breathing forces are extremely low (approx. 0.01 lbf) and vary in frequency from approximately 0.5 to 2.0 hz., depending on running speed and cardiovascular condition. The direction of breathing reactions is usually forward, but could vary through approximately 180 degrees in both the horizontal and vertical planes due to rotation of the head.

Since the breathing frequency is significantly above the isolator resonant frequencies in lateral translation, roll, and pitch (0.5 to 2.0 hz, vs. approx. 0.08 hz), the breathing-induced treadmill motions are non-resonant, making them highly attenuated dynamically. However, a worst-case condition for crewmember breathing could occur if the crewmember were to time a sequence of head rotations that periodically induced lateral breathing pulses at the roll or pitch isolator resonant frequencies. While such a scenario is highly unlikely, it will be investigated to establish the upper bound for breathing excitations.

For a conservative estimate of the highest potential breathing-induced motions, the 0.01 lbf breathing reaction was applied laterally to the six-degree-of-freedom model at exactly the isolator roll frequency, where it will have the highest possible dynamic amplification. Figure 26 shows the analytical model developed for the breathing motions. The model consists of a 1000 lbm treadmill suspended on an optimized 0.08 hz series-coupled isolator with a stiffness ratio of  $K_2/K_1=2.0$ . A roll inertia of 473,000 lbm-in<sup>2</sup> was estimated from a homogenous 1000 lbm treadmill measuring 5 ft x 2 ft x 30 in, plus a 200 lbm crewmember, six feet tall. Isolator spring and damping rates were those corresponding to the equivalent K and C values at the roll damped natural frequency computed from a preliminary translational simulation. This gave a roll

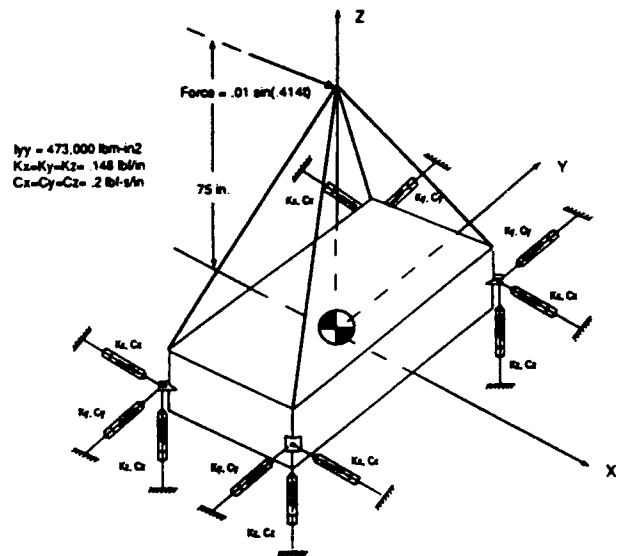


Figure 26. Six-Degree-of-Freedom Rigid Body Dynamic Model for Breathing-Induced Roll Response.

resonant frequency of 0.066 hz and overall equivalent stiffness and damping of 0.59 lbf/in and 0.805 lbf-s/in, respectively. The force was applied at a vertical moment arm of 75 inches above the treadmill CG to approximate the crewmember mouth/nose location. The computation was initiated by starting the periodic sinusoidal breathing forces beginning at time  $t=0$ , and then integrating numerically the six coupled equations of rigid body motion through time to give both the initial transient and final steady state breathing response in both roll ( $R_y$ ) and lateral translation ( $X$ ).

Figure 27 shows the resulting roll time history computed over a 200 second time interval. From the time response, it is evident that the maximum steady-state roll amplitude is only  $\pm 0.35$  degrees, which is negligible compared to the preliminary steady-state drift limit of  $\pm 10.0$  degrees.

Figure 28 shows the corresponding lateral ( $X$ ) displacement induced by the same breathing excitation. Again, the peak amplitude ( $\pm 0.026$  in) is insignificant compared to the available clearance gap surrounding the treadmill. Consequently, the maximum possible rotational and translational treadmill motions induced by crewmember breathing are attenuated by the low-frequency damping of the isolator to levels that are completely inconsequential.

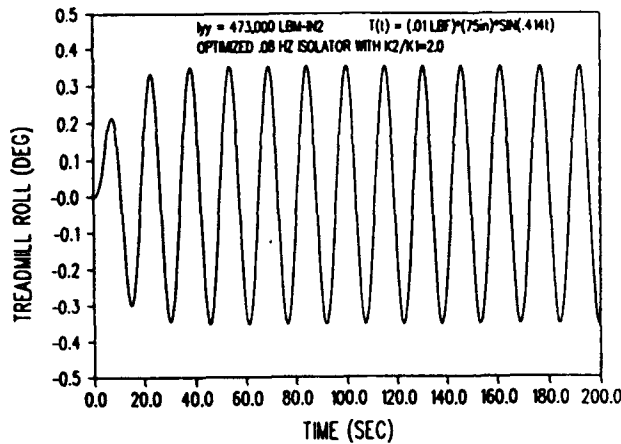


Figure 27. Treadmill Roll Response to 0.01 lbf Sinusoidal Breathing Excitation.

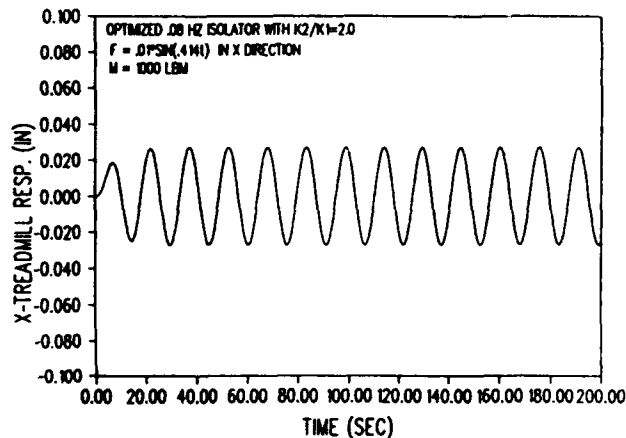


Figure 28. Treadmill Lateral Response to 0.01 lbf Sinusoidal Breathing Excitation.

## TRANSMITTED SSF FORCES AND TORQUES

### Transmitted Oscillatory Forces

With an optimized isolator having a damped natural frequency of 0.08 hz and stiffness ratio  $K_2/K_1=2.0$ , the variation of steady-state transmitted force with crewmember body weight is as shown in Figure 29 for 2.0 mph walking, 4.0 mph jogging, and 6.0 mph running. Interestingly, the transmitted forces are independent of treadmill mass, even though the oscillatory motions vary inverse linearly with mass. This is because the spring and damping values also vary linearly with mass to maintain the 0.08 hz natural frequency. Therefore, a lighter treadmill will oscillate more, but will transmit proportionately less force through its softer isolator springs, resulting in offsetting effects that render the transmitted forces independent of mass.

Inspection of Figure 29 indicates the expected severity of 4 mph jogging over walking or running because of the high force-to-frequency ratio. At 4 mph, the foot-fall forces are the same ( $\pm 1.0$  BW) as faster running, however the lower frequency results in higher treadmill displacements as predicted by equation 20. The higher oscillations induce correspondingly higher transmitted forces. Conversely, the 2.0 mph walking is less severe because the lower foot-fall forces of  $\pm 0.25$  BW. Consequently, the most severe exercise activity is a slow run or jog, where the foot-fall forces are fully developed, and the driving frequency is relatively low. Fortunately, even the 4.0 mph force of  $\pm 0.4$  lbf is well below the SSF limit of  $\pm 1.0$  lbf.

### Transmitted Oscillatory Pitch and Roll Torques

Similar data is shown in Figures 30 and 31 for the steady-state transmitted SSF roll and pitch torques expected for various exercise speeds as a function of body weight, treadmill mass, pitch and roll inertias, and the isolator moment arm from the CG. Since so many variables affect the transmitted pitch and roll torques, the variables were normalized for plotting the data in Figures 30 and 31. The applied pitch and roll torques

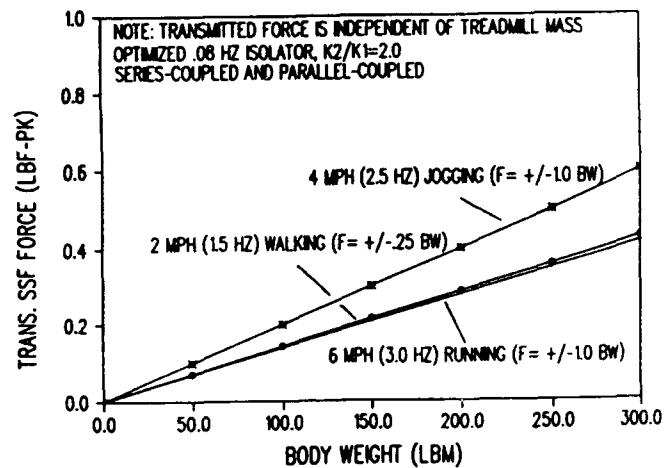


Figure 29. Transmitted SSF Oscillatory Vertical ( $Z$ ) Force vs. Crewmember Body Weight on Optimized 0.08 hz Isolator.

increase linearly with body weight and the resulting pitch motions vary inversely with the pitch and roll inertias. Also, the isolator spring rates, and hence the transmitted torques, must increase linearly with treadmill mass to maintain the 0.08 hz frequency. Thus, the abscissa variable is a normalized parametric combination of body weight, treadmill mass, and rotational inertia. Likewise, the transmitted torques vary with the square of the isolator pitch and roll moment arms (separation from CG), requiring parameterization of the transmitted pitch and roll torques with the respective moment arms squared. In the case of rotations, the 2.0 mph walking becomes more severe than 4.0 mph jogging or 6.0 mph running because the 1.0 BW restraint raises the pitch and roll forces to 1.25 BW, as opposed to 0.25 BW for vertical forces due to walking. This higher force, in combination with the lower walking frequency, makes the walking activity most severe for pitch and roll motions.

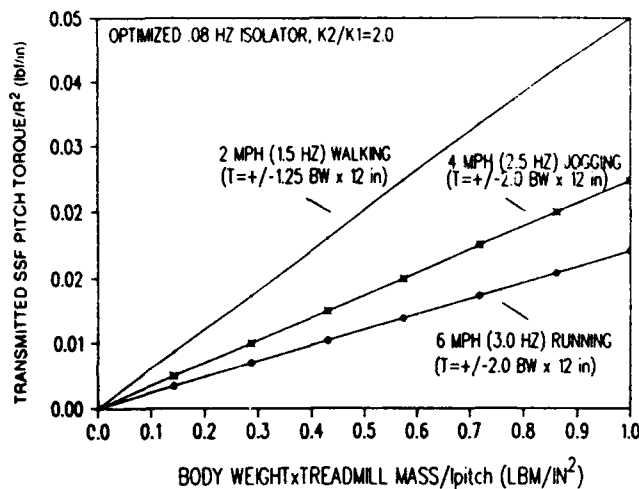


Figure 30. Transmitted SSF Oscillatory Pitch ( $R_p$ ) Torque vs. Crewmember Body Weight on Optimized 0.08 Hz Isolator.

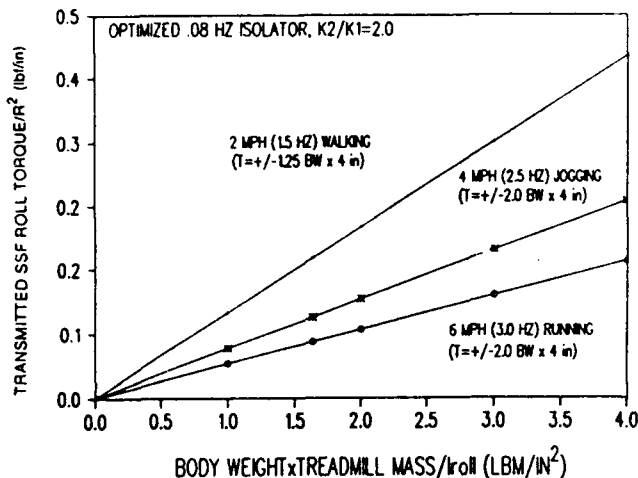


Figure 31. Transmitted SSF Oscillatory Roll ( $R_r$ ) Torque vs. Crewmember Body Weight on Optimized 0.08 Hz Isolator.

## CONCLUSIONS

The potential for reducing transmitted crewmember exercise forces to the SSF structure using a relatively simple passive isolation system has been demonstrated through a series of rigid body dynamic analyses which yield very favorable force attenuation ratios and drift control characteristics. A design optimization study was conducted to establish the mass, stiffness, and damping values which best meet the isolator performance requirements. The primary conclusions which may be drawn from the discussion presented are as follows:

1. The high crewmember exercise forces developed while running on an exercise treadmill (1.0 to 2.0 BW) may be substantially reduced by as much as a factor of 200:1 or more through a very simple, low maintenance, passive isolation system.
2. When installed on orbiting space vehicles, a passive exercise device isolator can provide sufficient centering and anti-drift characteristics to minimize off-center motion of the exercise device induced by disturbances such as crewmember breathing and sudden kick-off motions.
3. Optimum design parameters for an elastically-coupled passive isolator require a stiffness ratio near  $K_2/K_1=2.0$ , and an isolator natural frequency near 0.08 hz.

## ACKNOWLEDGEMENT

This work was performed by McDonnell Douglas Aerospace - Space Systems for the NASA Johnson Space Center under contract number NAS-9-18200.

## REFERENCES

- (1) Thornton, W.E., M.D., "A Method of Isolating Treadmill Shock and Vibration on Spacecraft," NASA Technical Memorandum No. 100474, April, 1989.
- (2) Lengel, R.C., Jr., "Proposed Space Station Treadmill Vibroacoustic Design Study," Tracor Applied Sciences Inc., Proposal No. U-AU-035-751-82-44, February 28, 1989.
- (3) Triangle Research and Development Corp., "Final Report - Vibration Isolation of Exercise Treadmill in Microgravity," NASA SBIR Contract No. NAS 9-18111, August, 1989.
- (4) Feehery, R.V., Jr., "The Biomechanics of Running on Different Surfaces," Clinics on Podiatric Medicine and Surgery - Vol 3, No. 4, New York University School of Medicine and Surgery, October, 1986.

# CONSISTENT DAMPING METHOD FOR SPACE STRUCTURAL SYSTEMS

Wan T. Tsai<sup>1,2</sup>, Joseph T. Leang<sup>1</sup>, Richard S. Chao<sup>1</sup>

## ABSTRACT

In Space Transportation Systems coupled loads analyses, two types of structural damping are commonly used: component modal damping, also known as schedule damping with zero values at the interface degrees-of-freedom (DOF's,) and diagonal system damping. Diagonal system damping is usually applied unless a damping schedule is provided. Inconsistent results have been obtained between using these damping approaches. Based upon studies of STS-45, -53, and -54, it was concluded that the phenomena were primarily caused by different treatments of the damping values at the physical interface DOF's. Since there is not yet any defined procedure for treating the interface damping, reasonable approximations may be used for flight certification analyses. This paper proposes a method of constructing the equivalent interface damping. Called Consistent Damping, this method provides for more reasonable payload responses than those calculated from the commonly applied method using the schedule damping.

## INTRODUCTION

This article proposes a new method in constructing the damping matrix for dynamic loads analyses of space structures. The proposed damping matrix includes the damping for the boundary (interface) degrees-of-freedom (DOF's) as well as for the component modal (internal) DOF's of substructures. This method simulates the damping matrix in a more realistic manner than, and is intended to replace the formation procedure of, the damping matrices being commonly applied.

In dynamic analysis of space structures, the damping matrix is usually constructed of two different approaches: system damping and schedule damping. The system damping is a diagonal matrix assembled on the system modal coordinates where all substructures are coupled together into a system. In this matrix, the damping value of each mode is the system frequency multiplied by a damping factor. On the other hand, the schedule damping is defined on the substructural coordinates. The schedule damping is composed of two portions, the component modal damping and the boundary damping. The component modal damping is obtained from substructural modal testing or other reliable means with all modes uncoupled from the boundary DOF's. For the component modal DOF's, the damping values are proportional to the component modal frequencies. For the boundary DOF's, the values are set equal to zero.

Both commonly applied approaches of establishing the damping matrix have their

---

<sup>1</sup>MTS, Structural Loads, SSD, Rockwell Int'l, 12214 Lakewood Blvd., M/C AC94, Downey, CA 90241, (213) 922-0570,-1036,-2316

<sup>2</sup>Also, Adjunct Prof., ME Dept., CA State Univ., Long Beach

advantages and disadvantages. For the system damping, the potential boundary damping is implicitly included; but the component modal damping which is defined by a more reliable manner such as the damping obtained from a substructural modal testing cannot be incorporated. On the other hand, for the schedule damping, the specifically defined component modal damping can be easily adopted; but the boundary damping is arbitrarily set equal to zero. Thus, these two methods of damping matrix assembly are on the two extremes, the advantage of one approach is the disadvantage of the other and vice versa. Their shortcomings tend to over-shallow the benefits in each approach.

The proposed damping method is to expose the shallowed portion of the damping matrix formation by combining the advantages of both system and schedule damping approaches. It not only incorporates the reliable damping for the component modal DOF's but also simulates a damping matrix with an appropriate damping for the boundary DOF's. The proposed boundary damping is physically interpretable and also consistently provides reliable responses regardless the sequence of payload coupling. This proposed consistent damping method may be reduced to either the schedule or the system damping depending upon the choice of the equivalent boundary damping. It becomes the schedule damping if the boundary damping is set equal to zero and the system damping if the coefficients of the component modal and boundary damping are the same. Therefore, the proposed method is consistent with both the commonly applied damping approaches.

The basic assumption for constructing the proposed damping is that the structural response with a uniform system damping is identical to the response with a damping that is combined by a uniform schedule damping and an equivalent uniform boundary damping on the substructural coordinates. On the basis of this assumption, the proposed consistent damping matrix is composed of two portions: a portion of schedule damping matrix for the component modal DOF's and a portion of equivalent uniform damping matrix for the boundary DOF's.

In addition to the commonly applied damping matrices, there is another approach that has been considered by Spanos, Cao, Nelson, and Hamilton (Reference 1). The approach is similar to that of the schedule damping but with an artificial set of nonzero damping values to represent the boundary DOF's. This boundary damping matrix is determined solely by using the modal frequencies that are calculated for the boundary DOF's alone; the component modal DOF's are not participated. Therefore, this type of boundary damping has no interaction between the component modal and boundary DOF's. The outcome of this artificial approach has not yet been validated and the physical meaning of this method is unclear.

Since the consistent damping matrix is fully populated on the system coordinates, the analysis may be unmanageable in some computer system and/or integration algorithm. For this reason, the off-diagonal damping elements have often been neglected in order to simplify the analysis. It has been proved by Tsai and Leang (Reference 2) that the responses using the simplified analysis may be grossly inaccurate when components of small mass and small stiffness are involved in substructures. An accurate result for this type of problems can be obtained by using the iterative method suggested in Reference 2. Therefore the proposed consistent damping matrix can be effectively implemented to analyze the structural responses when the iterative method of dynamic analysis is employed.

## REVIEW OF EXISTING APPROACHES IN DAMPING MATRIX CONSTRUCTION

Since the approach in constructing a consistent damping matrix is derived by using both system and schedule damping matrices, a review of these approaches is needed before considering the proposed method. Let  $y$  be the displacement vector;  $M$ ,  $C$  and  $K$  respectively the mass, damping and stiffness matrices; and subscripts  $b$  and  $m$  the groups of DOF's with  $b$  indicating the boundary DOF's and  $m$  the component modal DOF's. The governing differential equation on the substructural coordinates is

$$M\ddot{y} + C\dot{y} + Ky = P \quad (1)$$

All the vectors and matrices are composed of two groups involving boundary and component modal DOF's,

$$y = \begin{bmatrix} y_b \\ y_m \end{bmatrix}, \quad P = \begin{bmatrix} P_b \\ P_m \end{bmatrix} \quad (2a,b)$$

$$M = \begin{bmatrix} M_{bb} & M_{bm} \\ M_{mb} & M_{mm} \end{bmatrix}, \quad C = \begin{bmatrix} C_{bb} & C_{bm} \\ C_{mb} & C_{mm} \end{bmatrix}, \quad K = \begin{bmatrix} K_{bb} & 0 \\ 0 & K_{mm} \end{bmatrix} \quad (2c,d,e)$$

In Eqs.(2c,e),  $M_{mm}$  is a unit matrix and  $K_{mm}$  is a diagonal matrix with all diagonal elements equal to the square of the circular frequencies on the substructural coordinates. The formulation of the damping matrix  $C$  will be discussed later.

Eq.(1) is commonly analyzed on the basis of the system coordinates. Let all quantities on the system coordinates be superscribed by  $s$ . The response  $y$  is correlated to the system modal response  $y^s$  through a real transformation matrix  $\phi$ ,

$$y = \phi y^s \quad (3)$$

On the system coordinates, the differential equation is written by

$$M^s \ddot{y}^s + C^s \dot{y}^s + K^s y^s = P^s \quad (4)$$

In this,  $K^s$  is a diagonal matrix with the elements equal to the squares of circular frequencies on the system coordinates and  $M^s$  a unit matrix. The quantities in Eq.(4) are correlated to those in Eq.(1) by

$$M^s = \phi^T M \phi, \quad C^s = \phi^T C \phi, \quad K^s = \phi^T K \phi, \quad P^s = \phi^T P \quad (5a,b,c,d)$$

where the damping matrix  $C^s$  can be expressed by the form analogous to Eq.(2d),

$$C^s = \begin{bmatrix} C_{bb}^s & C_{bm}^s \\ C_{mb}^s & C_{mm}^s \end{bmatrix} \quad (6)$$

Having defined Eqs.(1-6), we can now characterize the commonly applied damping matrices. When the method of system damping is employed, the matrix  $C^s$  of Eq.(6) is considered. The submatrices  $C_{bm}^s$  and  $C_{mb}^s$  are zero and  $C_{bb}^s$  and  $C_{mm}^s$  are diagonal. Each of the nonzero diagonal elements is the corresponding circular frequency multiplied by a damping factor, say 0.02 for 1% of modal damping coefficient, 0.04 for 2%, etc. On the other hand, when the method of schedule damping is applied, the matrix  $C$  of Eq.(2d) is used. Its submatrices  $C_{bb}$ ,  $C_{bm}$  and  $C_{mb}$  are set equal to zero and  $C_{mm}$  is a diagonal submatrix with the values equal to the corresponding component modal frequencies multiplied by the designated damping coefficients. Denoted by  $C^m$ , the schedule damping is specifically defined by

$$C^m = \begin{bmatrix} 0 & 0 \\ 0 & C_{mm} \end{bmatrix} \quad (7)$$

Clearly, the schedule and system damping matrices are constructed on two different coordinate states: the substructural and the system respectively. When the schedule damping is applied, its converted matrix on the system coordinates becomes fully populated. On the other hand, when the system damping is applied, the transformed damping matrix on the substructural coordinates becomes fully populated.

### CONSTRUCTION OF CONSISTENT DAMPING MATRIX

On the substructural coordinates, the consistent damping matrix  $C^c$  is composed of two submatrices: the schedule damping  $C^m$  of Eq.(7) and a boundary damping  $C^b$ ,

$$C^c = C^m + C^b \quad (8)$$

In order to conceive the idea behind constructing the consistent boundary damping matrix  $C^b$ , let us consider a system consisting of several substructures. Suppose that the component modal damping coefficients of all substructures are identical, say  $c\%$ , and that the boundary damping coefficient is hoped to be also  $c\%$ ; then it seems to be logical to assume that the structural responses would be the same as that with the  $c\%$  of system damping coefficient on the system coordinates. The reason behind this hypothesis is that the system damping implicitly represents the damping at both internal and boundary DOF's of the substructures. When this logic is adopted as the assumption, the damping matrix of Eq.(8) must be identical to the uniform system damping matrix when they are transformed to the same coordinates. As a result, the desired  $c\%$  boundary damping matrix on the substructural coordinates can be extracted by subtracting a  $c\%$  component modal damping matrix from the transformed  $c\%$  system damping matrix. Specifically, the equivalent uniform boundary damping matrix  $C^b$  can be assembled by the following procedure:

1. Define a uniform system damping  $C^{us}$  with a damping value  $c\%$  on the system coordinates.

2. Transform  $C^{us}$  to a form on the substructural coordinates by using the inverse form of Eq.(5b)

$$C^u = (\phi^T)^{-1} C^{us} \phi^{-1} \quad (9)$$

3. Define a classic uniform schedule damping  $C^{uc}$  with  $c\%$  damping coefficient on the substructural coordinates.
4. Subtract  $C^{uc}$  from  $C^u$  to obtain the equivalent uniform damping  $C^b$  for the boundary DOF's,

$$C^b = C^u - C^{uc} \quad (10)$$

Having obtained this matrix, the consistent damping matrix  $C^c$  on the substructural coordinates can be constructed by introducing Eq.(7) and Eq.(10) into Eq.(8),

$$C^c = C^m + C^u - C^{uc} \quad (8')$$

In practical applications, the readily constructed consistent damping matrix of Eq.(8') must always be transformed into the system coordinates for numerical integrations. Therefore, determinations of  $C^c$ ,  $C^u$  and  $C^b$  on the substructural coordinates are not necessary. The needed consistent damping matrix is  $C^{cs} = \phi^T C^c \phi$  on the system coordinates. Directly expressed by using Eqs.(5b,8',9), it is

$$C^{cs} = C^{us} + \phi^T (C^m - C^{uc}) \phi \quad (11)$$

The physical meaning of this matrix can be interpreted by comparing Eqs.(7,11) with Eq.(5b). Since the uniform system damping matrix  $C^{us}$  implicitly consists of the damping for both boundary and component modal DOF's and the transformed uniform schedule damping  $\phi^T C^{uc} \phi$  only for the component modal DOF's, the subtraction of these two quantities leaves a net equivalent uniform boundary damping. Thus, the consistent damping matrix  $C^{cs}$  on the system coordinates is then defined by superimposing the equivalent uniform boundary damping to the transformed schedule damping matrix  $\phi^T C^m \phi$ .

Eq.(11) clearly indicates that the consistent damping  $C^{cs}$  is identical to the uniform system damping if  $C^m = C^{uc}$ . On the other hand,  $C^{cs}$  is naturally equal to the transformed schedule damping if  $C^{us}$  and  $C^{uc}$  are set equal to zero ( $c\% = 0$ ). These observed conclusions from Eq.(11) substantiate the definition of the consistent damping.

It must be noted that this approach in determining the consistent damping may not be applicable to non-uniform boundary damping. The reason is that the frequencies in a coupled system are not compatible with the total frequencies of the substructures. Therefore, an assigned non-uniform damping in the manner like Eq.(11) may be physically incompatible.

## ILLUSTRATIONS

Three examples are considered: a simple coupled system of four (4) DOF's and two (2)

full scale flights of space shuttle. The simple system demonstrates the detail procedure in establishing the consistent damping matrix. The full scale flight shows the potential impact on the orbital responses due to different considerations of damping matrices.

### A. Simple System of Four DOF's

The simple system consists of two substructures of uniform longitudinal bars, bars 123 and 412 as shown in Fig.(1). Each bar is composed of three-DOF's. When they are coupled together, the nodal numbers in a row are 4123. Let the mass in each substructural DOF be unity and the spring constant be  $k=1$  in bar 123 and  $k=2$  in bar 412. The physical mass and stiffness matrices for each substructure can be established. Each is then converted to the substructural coordinates of Craig-Bampton form with nodes 1 and 2 as the constrained boundary points. Upon coupling these matrices together, the mass and stiffness matrices are given by

$$M = \begin{bmatrix} 3 & 0 & 0 & 1 \\ 0 & 3 & 1 & 0 \\ 0 & 1 & 1 & 0 \\ 1 & 0 & 0 & 1 \end{bmatrix}, \quad K = \begin{bmatrix} 3 & -3 & 0 & 0 \\ -3 & 3 & 0 & 0 \\ 0 & 0 & 1 & 0 \\ 0 & 0 & 0 & 2 \end{bmatrix} \quad (12a,b)$$

To transform Eqs.(12a,b) into the system modal coordinates, a transformation matrix is required

$$\varphi = \begin{bmatrix} 0.40825 & -0.23854 & 0.06583 & 0.52163 \\ 0.40825 & 0.05109 & 0.45368 & -0.35340 \\ 0 & 0.77303 & -0.83199 & 0.45850 \\ 0 & -0.21069 & -0.72656 & -0.96318 \end{bmatrix} \quad (13)$$

On the system coordinates,  $M^s$  of Eq.(5a) is an identity matrix and  $K^s$  of Eq.(5c) is a diagonal matrix consisting of nonzero elements equal to the square of the circular frequencies,

$$K^s = \begin{bmatrix} 0 & 0 & 0 & 0 \\ 0 & 0.93801 & 0 & 0 \\ 0 & 0 & 2.19927 & 0 \\ 0 & 0 & 0 & 4.36272 \end{bmatrix} \quad (14)$$

Note that the zero frequency in  $K^s$  indicates the rigid body motion of the system. In practical applications, the rigid body modes may be eliminated. It is, however, carried out here in order to avoid a sidetrack.

Having defined Eqs.(12b,14), various damping matrices can be constructed. To signify the effective numerical digits, let the damping coefficient be 0.2, equivalent to a 10% of the critical modal damping. The classic system damping and schedule damping matrices are respectively given by

$$C^s = \begin{bmatrix} 0 & 0 & 0 & 0 \\ 0 & 0.19370 & 0 & 0 \\ 0 & 0 & 0.29660 & 0 \\ 0 & 0 & 0 & 0.41774 \end{bmatrix}, \quad C^m = \begin{bmatrix} 0 & 0 & 0 & 0 \\ 0 & 0 & 0 & 0 \\ 0 & 0 & 0.2 & 0 \\ 0 & 0 & 0 & 0.28284 \end{bmatrix} \quad (15a,b)$$

On the system coordinates, the schedule damping  $C^m$  is transformed into  $C^{ms}(-\varphi^T C^m \varphi)$ ,

$$C^{ms} = \begin{bmatrix} 0 & 0 & 0 & 0 \\ 0 & 0.13207 & -0.08533 & 0.12828 \\ 0 & -0.08533 & 0.28775 & 0.12164 \\ 0 & 0.12828 & 0.12164 & 0.30444 \end{bmatrix} \quad (16)$$

Except the elements associated with the rigid body motion, Eq.(16) reveals that the schedule damping matrix is fully populated on the system coordinates.

Now, let us consider an alternative formation of the damping matrix that is commonly used in space shuttle analyses. Let the 10% uniform damping for eigenvalues greater than unity be replaced by a damping coefficient of 20%. The damping matrix is then composed of both 10% and 20% of coefficients. The classic forms of system and schedule damping matrices become

$$C^s = \begin{bmatrix} 0 & 0 & 0 & 0 \\ 0 & 0.19370 & 0 & 0 \\ 0 & 0 & 0.59320 & 0 \\ 0 & 0 & 0 & 0.83549 \end{bmatrix}, \quad C^m = \begin{bmatrix} 0 & 0 & 0 & 0 \\ 0 & 0 & 0 & 0 \\ 0 & 0 & 0.2 & 0 \\ 0 & 0 & 0 & 0.56569 \end{bmatrix} \quad (15'a,b)$$

By using the transformation procedure of Eq.(5b), the converted schedule damping of Eq.(15'b), on the system coordinates becomes

$$C^{ms} = \begin{bmatrix} 0 & 0 & 0 & 0 \\ 0 & 0.14463 & -0.04204 & 0.18568 \\ 0 & -0.04204 & 0.43706 & 0.31958 \\ 0 & 0.18568 & 0.31958 & 0.56684 \end{bmatrix} \quad (16')$$

Eq.(16') represents the damping matrix that the boundary damping is explicitly set equal to zero. On the contrary, Eq.(15'a) represents the damping matrix that the boundary damping is implicitly inherited with nonzero values. In order to develop a consistent damping matrix that retains a 10% of boundary damping along with the 10% and 20% of component modal damping as set in Eq.(15'b), Eqs.(15a,b;15'b) are applied. By respectively designating the quantities in these equations as  $C^{us}$ ,  $C^{uc}$  and  $C^m$ ; Eq.(11) provides the consistent damping matrix  $C^s$  on the system coordinates,

$$C^m = \begin{bmatrix} 0 & 0 & 0 & 0 \\ 0 & 0.20626 & 0.04330 & 0.05740 \\ 0 & 0.04330 & 0.44591 & 0.19794 \\ 0 & 0.05740 & 0.19794 & 0.68014 \end{bmatrix} \quad (17)$$

This matrix consists of a 10% boundary damping along with 10% and 20% component modal damping for the 4DOF system.

Three types of damping matrices have been constructed in associate with a specified 10% and 20% mixed damping. They are Eq.(15'a) of system, Eq.(16') of schedule, and Eq.(17) of consistent damping, all on the system modal coordinates. Except those associated with the rigid body DOF's, the corresponding elements are different in these matrices. Accordingly, the structural responses cannot be identical. The impact of different damping on the bar responses may be evaluated when a forcing function is applied.

### B. Full Scale Flights

The dynamic liftoff analyses for two (2) flight manifests (STS-45, 54) are used to demonstrate the applications of the consistent damping method. Each manifest consists of the space shuttle vehicle (SSV) liftoff system including orbiter, external tank (ET), solid rocket booster (SRB) and the following cargo elements (or payloads or substructures) for each flight. The flight STS-45 is composed of the payloads ATLAS, SSBUV, and six side-wall mounted small payloads and STS-54 is composed of IUS/TDRS and three side-wall mounted small payloads.

For each flight, the payloads were individually modelled as substructures in the beginning of analyses. Each model was represented by hundreds or thousands of DOF's. After several stages of substructural coupling and condensations, the total number of payload models used in the liftoff dynamic analyses were about 300 to 400 DOF's. Upon coupling with the orbital model, the systems were subjected to the dynamic liftoff forcing function LR2165, one of the conditions being used for liftoff transient analyses. The analyses were performed over a range of 10.5 seconds to cover the complete liftoff events. A small time interval, which was fine enough to obtain accurate responses for frequencies up to 50Hz, was used to cover the major time span of the transient analyses.

In dynamic loads analyses of SSV/payload systems at the liftoff condition, it is customary to use 1% of damping coefficient for frequencies below 10Hz and 2% for above. An equivalent uniform boundary damping matrix must be established to accommodate the customarily applied modal damping values and to provide a yet conservative response. For these purposes, the equivalent uniform boundary damping may be assumed to be 1%. Using this value, the matrices  $C^{ms}$  and  $C^{uc}$  can be directly established. Also using 1% and 2% of damping for all substructural DOF's, the schedule damping matrix  $C^m$  can be easily composed. As a result, the consistent damping matrix is obtained from Eq.(11) and the structural responses is then evaluated from Eqs.(4,3).

Three sets of different damping matrices are considered for comparisons of payload responses in each flight: the system damping, the consistent damping with 1% of boundary

damping coefficient, and the schedule damping. The net load factors of all payloads are summarized in Table 1, 2 respectively for STS-45, 54. These Tables show that more than 85% of net load factors for both consistent and schedule damping are greater than for the system damping. Also, using the result of system damping as the basis, the percent changes of the factors for both schedule and consistent damping are provided. The factors for the schedule damping are generally much larger than for the consistent damping. This behavior is natural for the reason that the schedule, consistent and system damping methods respectively passes 100%, 99%, and 98-99% of the applied energy through the interface DOF's to the payloads. As a result, the payload responses are stronger for more energy passing through the interface DOF's. Few items which do not follow this general rule are owing to the alteration of energy paths when the interface damping values are changed.

It is known that the response of a structure has to be unique regardless the procedure that the system is coupled and the method that the structure is analyzed. In fact, as illustrated in the full scale flights, the responses computed by different approaches cannot be the same since different amount and distributions of damped energy are delivered through the interface DOF's for each analysis method. This interpretation can be substantiated by the other procedure of substructural coupling by reducing the number of the retained physical DOF's, though which is not a common approach in general applications.

To simplify the concept, the flight STS-54 is reconsidered. Ordinarily, all the payloads are first modeled individually and then all coupled simultaneously with the orbital model. Initially, the number of the retained physical DOF's for STS-54 is 34. The result of this analysis is shown in Table 2, and is repeated in Table 3 by calling it the result of one-step coupling. An alternate coupling, called two-step coupling, is introduced to re-evaluate the response. The approach is to integrate the side-wall mounted payloads into the orbiter as a complete orbital model. This updated orbital model is then coupled with the IUS/TDRS payload model for dynamic transient analysis. The number of the retained physical DOF's for this two-step coupled model becomes 16. A classic 1% and 2% schedule damping and an equivalent consistent damping along with 1% boundary damping value are separately introduced to re-analyze this two-step coupled model. The complete comparison of the net load factors for both one- and two-step analyses are shown in Table 3. From which, several response behaviors are recognized:

1. Applying different coupling procedures to the classic schedule damping method, the responses are significantly changed. The maximum difference in the percent change between one- and two-step coupling is more than 10% occurred at the  $N_2$  factor for the DXS-3S payload.
2. Applying different coupling procedures to the consistent damping method with a 1% boundary damping value, the responses are changed less significantly. The maximum difference is about 5% also occurred at the  $N_2$  factor for the DXS-3S payload.
3. Comparing the responses between the consistent and schedule damping with two-step coupling, the differences are little. They are also very close to the result of the system damping analysis.

Table 3 confirms that the payload responses are sensitive to the number of the retained physical DOF's and their damping values. It also confirms that uses of the consistent damping can effectively stabilize the scattering responses that occurs when the schedule damping is applied to different procedures of component coupling.

## DISCUSSIONS

The commonly represented term of viscous damping force, as shown in the governing differential equation, Eq.(1), is practically provided for mathematical conveniences. In fact, the damping force in dynamic loads analyses may be mostly induced by other types of forces such as the friction of dry sliding or lubricated surface, internal friction of material, and air or fluid resistance. The expressions of these forces are nonlinear with respect to the normal forces and relative velocities or displacements. The differential equation becomes difficult to solve when these nonlinear damping forces are applied. Therefore, the use of the linear viscous form is just an approximation to simulate various types of damping forces. With this recognition in minds, it seems to be understandable that it is impossible to define a viscous damping that can exactly represent the responses of payloads. Therefore, the objectives in considering the interface damping in this article are as follows:

1. To define an interface damping that is physically interpretable.
2. To define a damping method that the computed responses may be fairly unchanged regardless the procedure of coupling and the number of retained physical DOF's.
3. To define an interface damping that the designated component modal damping may be preserved.
4. To define an interface damping that may be consistent with the existing damping methods.

As a result of these objectives, the consistent damping approach attempts to simulate the interface damping by a global manner with an equivalent uniform boundary damping. It is known that the true boundary damping force cannot be simply represented by any linear viscous damping. Therefore, the proposed consistent damping method is provided simply for general applications to estimate the approximate but reliable responses for all payloads. Fortunately, these objectives are achievable on the basis of the analyses for the illustrated flights.

It is noted that the uniform value of  $c\%$  damping employed in the consistent damping may not be changed to any non-uniform values such as the mix of 1% and 2% for various frequency magnitudes. The reason for the acceptability of the uniform  $c\%$  damping is based on the implicit assumption that the damping value may remain constant in all coordinate states. This assumption may be significantly violated when the non-uniform damping values are applied since the frequencies in one coordinate state are generally different from the others. When the non-uniform damping is applied, the damping value associated with one frequency in a coordinate state may become a significantly different damping value associated with the similar frequency in another coordinate state.

## CONCLUSIONS AND RECOMMENDATIONS

1. In the case that a set of reliable component modal damping is available, the consistent damping must be applied to preserve the characteristics of the provided component modal damping and to impose a reasonable damping on the boundary DOF's. This damping which can be easily formulated is developed by combining the advantages of both system and schedule damping methods. This newly proposed method is applicable to either the Craig-Bampton or Rubin-McNeal form of substructural coupling.
2. When the damping of 1% for frequencies less than 10Hz and 2% for above is applied

to dynamic loads analyses, it has implicitly agreed in the aerospace industry that 1% is generally an acceptable and conservative damping value. For this reason, it seems to be logical to extract the proposed equivalent interface damping by using 1% damping value. This value may vary if a more reliable schedule damping is available. For example, if a test verified component modal damping indicates a lowest damping value to be 0.5%, then an equivalent uniform interface damping of 0.5% may be selected for the sake of conservative to accommodate the test verified component damping. Nevertheless, a large database is required to establish a reasonable damping from which realistic and accurate payload responses can be determined.

3. From the past experiences, the system damping is an approach that can always provide a stable and predictable result. The results of using this method have been generally agreeable with anticipated responses. Therefore, the system damping method should be applied in the case that a reliable component modal damping is absent.
4. Although the schedule damping method by using zero damping for the interface DOF's has been applied to analyze space structures for long time, the validity of such a method may be questionable. Regardless that it occasionally provide reasonable results, the responses obtained by using schedule damping for the payloads of STS-54 appear to be unstable owing to different coupling procedures. Therefore, the schedule damping method may not be a reliable approach.

## **ACKNOWLEDGEMENT**

This work has been supported by the NASA/JSC. The authors gratefully acknowledge the consistent support and constructive comments of Mr. Randy Hester and Ms. Nancy Tengler, and the encouragement of their coworkers of Dynamic Loads Analysis Group, Rockwell International; especially, Messrs. J. E. Misel, D. I. Takahashi, and L. J. Van Hofwegen.

## **REFERENCES**

1. Spanos, P. D.; T. T. Cao; D. A. R. Nelson, Jr.; D. A. Hamilton; "Efficient Loads Analyses of Shuttle-Payloads Using Dynamic Model with Linear or Nonlinear Interfaces."
2. Tsai, W. T.; Leang J. T.; "An Iterative Method in Dynamic Structural Analyses with Nonproportional Damping," Symposium of Damping '91, San Diego, CA., Feb. 12-15, 1991. Also presented at the NASA Sponsored Technical Interchange Meeting, Downey, CA., Mar. 19, 1991.

TABLE 1 NET LOAD FACTORS OF STS-45 PAYLOADS

PAYLOADS	DAMPING	Nx (% CH)	My (% CH)	Nz (% CH)	Rx (% CH)	Ry (% CH)	Rz (% CH)						
ATLAS	SYSTEM	3.282		0.799	1.876	3.048	5.071	1.749					
	1% CONSIST.	3.302	0.6	0.808	1.1	1.900	1.3	3.141	3.1	4.992	-1.6	1.700	-2.8
	SCHEDULE	3.270	-0.4	0.759	-5.0	1.898	1.2	2.824	-7.3	4.713	-7.1	1.887	7.9
SSBUV	SYSTEM	5.405		2.860	2.865	44.594	30.423	59.284					
	1% CONSIST.	5.645	4.4	2.828	1.0	3.079	7.5	46.289	3.8	29.594	-2.7	64.954	9.6
	SCHEDULE	5.851	8.3	3.453	20.7	3.056	6.7	47.557	6.6	28.444	-6.5	70.842	19.5
BAY 4P GAS	SYSTEM	3.683		4.279	2.882	50.407	14.241	31.213					
	1% CONSIST.	3.785	2.8	4.342	1.5	2.979	3.4	51.187	1.5	14.993	5.3	33.946	8.9
	SCHEDULE	3.927	6.6	4.289	0.2	2.864	-0.6	51.907	3.0	15.468	8.6	38.844	24.4
BAY 5S SEPAC	SYSTEM	4.690		4.724	7.551	138.251	113.922	38.858					
	1% CONSIST.	5.056	12.6	5.219	10.5	7.471	-1.1	138.112	-0.1	114.718	0.7	47.125	21.3
	SCHEDULE	5.667	26.2	6.010	27.2	7.636	1.1	144.173	4.3	117.712	3.3	55.335	42.4
BAY 6S GAS	SYSTEM	6.161		3.687	2.113	38.448	10.720	62.325					
	1% CONSIST.	6.349	3.1	4.328	17.4	1.983	-6.2	38.136	-0.8	11.037	3.0	64.503	3.5
	SCHEDULE	6.404	3.9	5.260	42.7	2.071	-2.0	42.884	11.5	11.102	3.6	64.939	4.2
BAY 12S GAS	SYSTEM	2.478		2.305	4.691	162.845	4.754	11.814					
	1% CONSIST.	2.558	3.2	2.532	9.8	4.941	5.3	171.904	5.6	4.840	1.8	12.324	4.3
	SCHEDULE	2.525	1.9	2.998	30.1	5.115	9.0	178.123	9.4	4.827	1.5	12.513	5.9
BAY 13S GAS	SYSTEM	3.916		2.620	1.814	40.048	24.081	26.069					
	1% CONSIST.	4.246	8.4	2.860	9.2	2.144	18.2	43.896	9.6	26.644	10.6	29.058	11.5
	SCHEDULE	4.466	14.0	2.977	13.6	2.353	29.7	48.698	21.6	27.804	15.5	31.540	21.0
BAY 13P GAS	SYSTEM	4.984		3.352	1.705	28.349	38.482	46.125					
	1% CONSIST.	5.285	6.0	3.790	13.1	1.785	4.7	32.182	13.5	44.360	15.3	52.611	14.1
	SCHEDULE	5.528	10.9	4.037	20.4	2.060	20.8	40.697	43.6	47.203	22.7	55.518	20.4

TABLE 2 NET LOAD FACTORS OF STS-54 PAYLOADS

PAYLOADS	DAMPING	Nx (% CH)	Ny (% CH)	Nz (% CH)	Rx (% CH)	Ry (% CH)	Rz (% CH)						
IUS/TDRS	SYSTEM	2.906	0.272	0.783	1.292	1.885	0.768						
	1% CONSIST.	2.901	-0.2	0.272	0.0	0.784	0.1	1.297	0.4	1.880	-0.3	0.772	0.5
	SCHEDULE	2.913	0.2	0.274	0.7	0.782	-0.1	1.310	1.4	1.891	0.3	0.790	2.9
DXS 3S	SYSTEM	3.305	3.122	6.630	266.267	9.988	30.310						
	1% CONSIST.	3.326	0.6	3.248	4.0	6.897	4.0	279.874	5.1	10.128	1.4	30.145	-0.5
	SCHEDULE	3.343	1.1	3.383	8.4	7.369	11.1	294.066	10.4	10.256	2.7	29.740	-1.9
DXS 4S	SYSTEM	3.598	3.833	2.782	40.259	8.367	31.608						
	1% CONSIST.	3.676	2.2	3.837	0.1	2.892	4.0	40.291	0.1	8.495	1.5	33.106	4.7
	SCHEDULE	3.749	4.2	3.837	0.1	3.031	9.0	40.002	-0.6	8.604	2.8	34.727	9.9
DXS 4P	SYSTEM	3.412	4.976	2.697	56.494	4.689	34.533						
	1% CONSIST.	3.467	1.6	5.029	1.1	2.817	4.4	56.121	-0.7	4.718	0.6	35.313	2.3
	SCHEDULE	3.502	2.6	5.085	2.2	2.954	9.5	58.029	2.7	4.727	0.8	35.853	3.8

TABLE 3 NET LOAD FACTORS OF STS-54 PAYLOADS

PAYLOADS	DAMPING	Nx (% CH)	Ny (% CH)	Nz (% CH)	Rx (% CH)	Ry (% CH)	Rz (% CH)						
IUS/TDRS	SYSTEM	2.906	0.272	0.783	1.292	1.885	0.768						
	1% CONS. (1)	2.901	-0.2	0.272	0.0	0.784	0.1	1.297	0.4	1.880	-0.3	0.772	0.5
	1% CONS. (2)	2.901	-0.2	0.272	0.0	0.784	0.1	1.290	-0.2	1.878	-0.4	0.769	0.1
	SCHEDULE (1)	2.913	0.2	0.274	0.7	0.782	-0.1	1.310	1.4	1.891	0.3	0.790	2.9
	SCHEDULE (2)	2.913	0.2	0.274	0.7	0.781	-0.3	1.299	0.5	1.889	0.2	0.779	1.4
DXS 3S	SYSTEM	3.305	3.122	6.630	266.267	9.988	30.310						
	1% CONS. (1)	3.326	0.6	3.248	4.0	6.897	4.0	279.874	5.1	10.128	1.4	30.145	-0.5
	1% CONS. (2)	3.302	-0.1	3.121	-0.0	6.635	0.1	266.310	0.0	10.003	0.2	30.314	0.0
	SCHEDULE (1)	3.343	1.1	3.383	8.4	7.369	11.1	294.066	10.4	10.256	2.7	29.740	-1.9
	SCHEDULE (2)	3.298	-0.2	3.117	-0.2	6.626	-0.1	266.052	-0.1	9.987	-0.0	30.183	-0.4
DXS 4S	SYSTEM	3.598	3.833	2.782	40.259	8.367	31.608						
	1% CONS. (1)	3.676	2.2	3.837	0.1	2.892	4.0	40.291	0.1	8.495	1.5	33.106	4.7
	1% CONS. (2)	3.602	0.1	3.829	-0.1	2.778	-0.1	39.950	-0.8	8.361	-0.1	31.630	0.1
	SCHEDULE (1)	3.749	4.2	3.837	0.1	3.031	9.0	40.002	-0.6	8.604	2.8	34.727	9.9
	SCHEDULE (2)	3.594	-0.1	3.815	-0.5	2.782	0.0	39.825	-1.1	8.344	-0.3	31.525	-0.3
DXS 4P	SYSTEM	3.412	4.976	2.697	56.494	4.689	34.533						
	1% CONS. (1)	3.467	1.6	5.029	1.1	2.817	4.4	56.121	-0.7	4.718	0.6	35.313	2.3
	1% CONS. (2)	3.411	-0.0	4.987	0.2	2.708	0.4	56.792	0.5	4.697	0.2	34.554	0.1
	SCHEDULE (1)	3.502	2.6	5.085	2.2	2.954	9.5	58.029	2.7	4.727	0.8	35.853	3.8
	SCHEDULE (2)	3.397	-0.4	4.972	-0.1	2.712	0.6	56.747	0.4	4.686	-0.1	34.362	-0.5

NOTE: (1)=ONE-STEP COUPLING, (2)=TWO-STEP COUPLING

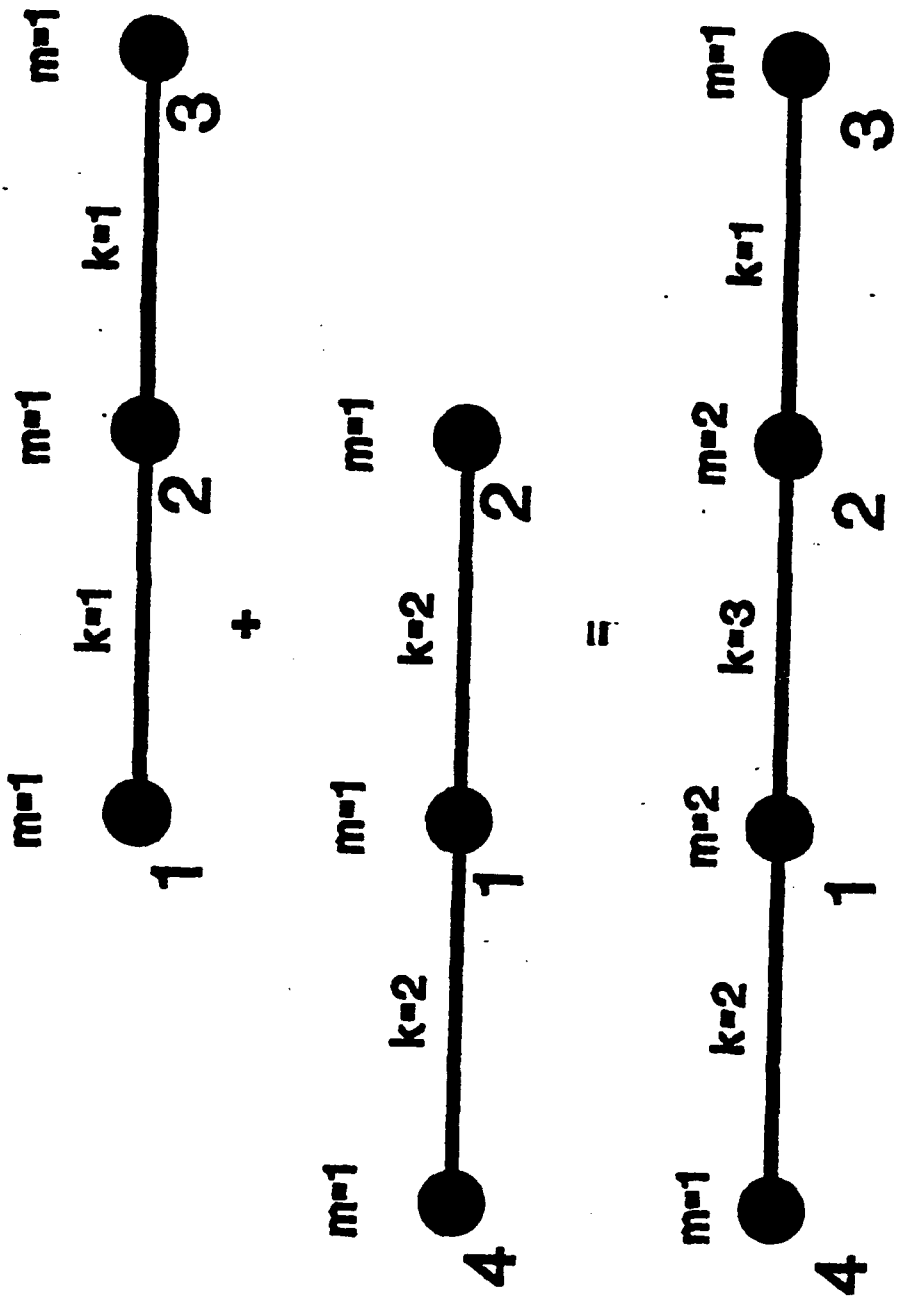


**Fig.1 4 DOF SIMPLE MODEL**

# TRANSIENT SOLUTION OF COUPLED STRUCTURAL COMPONENTS USING SYSTEM MODAL COORDINATES WITH AND WITHOUT COUPLED SYSTEM DAMPING

EDWIN E. HENKEL<sup>1</sup>, and RAYMOND MAR<sup>2</sup>

ROCKWELL INTERNATIONAL  
SPACE SYSTEMS DIVISION<sup>3</sup>

This paper presents a general methodology for the solution of the transient responses for structural modal systems with coupled system damping, i.e., system modal damping derived via the so called Triple Matrix Product method. The method presented solves the modal equations of motion, while treating the system damping properties as applied forces on the right hand side of the equations of motion. The solution approach assumes that the forces imposed by the damping properties (and all externally applied forces) are a linear function of time between any two solution time steps. With the exception of this one assumption, the solution is mathematically exact. Rapid convergence with integration time step size is demonstrated. The subject methodology was utilized and proven in the validation analysis for the STS-53 verification loads analysis cycle. The results from this analysis are compared to the more traditional treatments of system modal damping, and as will be seen, these traditional approaches prove to be inaccurate and unconservative.

## Nomenclature

A	= coefficient of integration	K	= discrete physical stiffness matrix
A'	= coefficient of integration	k	= generalized stiffness
B	= coefficient of integration	M	= physical mass
B'	= coefficient of integration	m	= generalized mass
b	= modal damping coefficient	P	= generalized force
D	= all known variables to the modal displacement solution	V	= all known variables to the modal velocity solution
C	= system generalized damping matrix	x	= physical discrete degree of freedom
c	= component generalized damping matrix	$\beta$	= modal damping coefficient
F	= coefficient of integration	$\xi$	= modal displacement degree of freedom
F'	= coefficient of integration	$\phi$	= eigenvectors
f	= physical force	$\omega$	= eigenvalues
G	= coefficient of integration	$\zeta$	= critical damping ratio
G'	= coefficient of integration	0	= null matrix
H	= generalized damping force matrix		
I	= identity matrix		

<sup>1</sup> Manager, Structural Design & Analysis

<sup>2</sup> Engineering Specialist

<sup>3</sup> Address

555 Gemini Avenue  
Houston, Texas 77058

### **Superscript**

**T** = matrix transpose

### **Subscript**

**b** = booster parameter  
**i** = modal degree of freedom  
**n** = time step  
**o** = eigenvalue/generalized mass  
**p** = launch pad parameter  
**x** = physical degree of freedom

## **Introduction**

Historically, Space Transportation System (STS)/Payload transient loads analyses have been performed in system modal coordinates with the traditional use of uncoupled system modal damping. This form of damping may also be referred to as orthogonal, classical, modal, or proportional damping (ref. 1). The damping values utilized were deemed to be conservative, usually one or two percent of critical. This "assumed" conservatism was primarily based upon modal testing performed on the STS structure. However, as the payload loads discipline has become more sophisticated, payload damping properties have become more definitive, and problems have arisen as to how to best treat the payload damping properties at the STS/Payload system modal level.

Transient loads analyses are most often performed in system modal coordinates for the purpose of mathematical expediency. That is, modal coordinates offer at least two distinct advantages: 1) the method lends itself to modal truncation, thus reducing the number of system equations to be solved, and 2) the undamped modal coordinate equations of motion are uncoupled (each modal coordinate independent from all of the others). The assumption of uncoupled system damping preserves the second mathematical convenience, lending itself to a numerically efficient and accurate solution algorithm (accurate, that is, only to the extent that the assumed proportional damping is accurate).

Craig (ref.1) cites a number of situations where proportional damping cannot properly represent the structure. These include buildings with highly damped soil interaction, offshore structures with fluid damping, and structures with discrete dampers. Methods to properly analyze

nonproportional damped systems have been suggested. These include complex eigensolutions and attempts to derive equivalent proportional damping (ref. 1).

Hasselman (ref. 2) makes the following statement: "Only under special conditions, are the equations of motion completely uncoupled by the classical modal transformation, and these conditions appear to have no physical justification. In general, and for most real structures, modal damping matrices are not diagonal, ...". Hasselman further states: "When a system mode is comprised of several subsystem modes from each subsystem, the modal coupling terms for those subsystems cannot be ignored. To do so may introduce significant error in the dissipative energy computed for that system mode, ...". Ref. 2 offers strong testimony against the traditional practice of approximating system modal damping as being diagonal.

Recognizing the above, some analyst have attempted to measure the relative importance of retaining certain off diagonal damping terms while discarding the bulk of the rest. These attempts at computational efficiency have focused mainly on modal frequency separation and off diagonal ratios to the diagonal terms. Ref. 3 demonstrated that the frequency content of the forcing function is also very important in such an exercise.

The case of a STS/Payload system is a multibody (subsystems) situation. Ideally, each body has undergone testing to determine or verify that body's modal characteristics, including damping. Since system level modal testing is not performed, the analyst must be very careful when attempting to utilize system proportional damping. In this paper will illustrate, the traditional practice can be quite inaccurate and unconservative, especially for these lightly damped problems.

Even for the bulk of the Space Station Freedom transient loads analyses, the practice has been to assume proportional damping. With its large photo voltaic and thermal control radiator arrays, this multibody system has damping characteristics that vary greatly from one body to the next, necessitating the use of coupled modal damping. Even if each body had identical damping characteristics, the use of proportional damping on such a large structure with numerous large appendages may prove to be quite inaccurate.

The system modal coordinates are derived by means of system level eigensolutions, which can be quite expensive. The eigensolution uncouples the mass and stiffness matrices (diagonalizes the undamped system equations of motion). It would, therefore, seem somewhat ludicrous to also expect diagonal damping without some similar mathematical effort and expense (this paper will not address the method of complex eigensolutions). The STS/Payload system eigensolution provides a desirable coordinate transformation to system modes. Insight into the validity of diagonal system modal damping can be gained by simply transforming this system damping back into the STS/Payload discrete physical coordinate system. This will result in a totally populated damping matrix. The physical interpretation of this is that every payload degree of freedom (DOF) will be coupled through some damping mechanism to every STS DOF. Obviously, this coupling is fictitious, the only physically allowable coupling being at the specific STS/Payload interface DOF. But again, for engineering purposes, the system diagonal damping has been utilized, the damping values deemed to be "conservative enough".

The two words "conservative enough" present a major problem, especially when the payload's damping characteristics are well defined. Definition of the system's damping characteristics based upon the component level damping parameters is not an issue. The eigensolution provides a coordinate transformation to derive the system modal damping, i.e., the Triple Matrix Product (TMP) method. The TMP damping is given as follows:

$$[C] = [\phi]^T [c] [\phi] \quad (1)$$

C is the system level TMP damping and c is the assembled substructure damping, ideally based upon some form of test data and often given as a diagonal. For the STS structure, c is defined as the free-free modal damping, the STS most often being represented in a Rubin-MacNeal (free-free modal) format. On the payload side, c is most often defined as the damping on a representative set of Craig-Bampton normal modes. Here, it is important to note that the STS damping is based upon modal testing performed with the vehicle in an unconstrained configuration, resulting in the same free-free modal coordinates used in the STS/payload system modal synthesis. Just as

important, payload modal survey testing is performed in one of the following particular constrained configuration: 1) representative of the constraints at the STS interface, 2) overconstrained at the STS interface, 3) free-free, or 4) some hybrid variation. The payload damping values in c are based upon representative test data, i.e., representative to the dynamic math model modal coordinates used to correlate the math model against the test results. Because the test force levels are typically low compared to the limit load levels of the transient analysis, this test measured damping is generally felt to be conservative, thus making the values chosen in c easily defensible. The payload Dynamic Math Models (DMM), delivered for transient loads analyses, are presently required to be overconstrained. This is to facilitate the inclusion of latch masses that are reacted through the payload structure. Ideally, the payload contractor will transform the test measured damping from the test DMM coordinates to the delivered DMM coordinates. For example, for a payload tested in a free-free configuration, the DMM damping delivered for STS coupled loads analysis would be coupled. The case where the payload contained discrete linear damping devices would also result in coupled damping.

With the use of the full TMP damping matrix, the STS and payload damping properties are preserved at the system modal level; but because this matrix is totally populated, the mathematical convenience of uncoupled equations of motion is lost. At this point, there are two options: 1) ignore the off diagonal terms, or 2) forfeit the mathematical convenience of system level diagonal damping and use a more complex and costly solution technique. The first option results in the fictitious discrete physical damping coupling mentioned above. Although the diagonal TMP damping method has been employed, it has not been known whether or not the analysis was conservative. In addition, the diagonal TMP method sometimes leads to anomalous results. This method has therefore fallen into disrepute. The second option is addressed below.

### Modal Transient Solution

The uncoupled modal equation of motion for the ith mode is given by the following:

$$m_i \ddot{\xi}_i + b_i \dot{\xi}_i + k_i \xi_i = P_i \quad (2)$$

The nomenclature follows that used in ref. 4. This equation is more conveniently rewritten as follows:

$$\ddot{\xi}_i + 2\beta \dot{\xi}_i + \omega_0^2 \xi_i = \frac{P_i}{m_i} \quad (3)$$

Because these modal equations of motion are uncoupled, each mode acts as an independent single DOF oscillator and a closed form solution approach is possible. The solution technique most often used, assumes that the applied forces vary linearly between solution time steps. With this, the incremental solution, for time step  $n+1$ , is given by the following three equations:

$$\xi_{i, n+1} = F \xi_{i, n} + G \dot{\xi}_{i, n} + A P_{i, n} + B P_{i, n+1} \quad (4)$$

$$\dot{\xi}_{i, n+1} = F' \xi_{i, n} + G' \dot{\xi}_{i, n} + A' P_{i, n} + B' P_{i, n+1} \quad (5)$$

$$\ddot{\xi}_{i, n+1} = \frac{P_{i, n+1}}{m_i} - 2\beta \dot{\xi}_{i, n+1} - \omega_0^2 \xi_{i, n+1} \quad (6)$$

Equation (4) is the solution for the modal displacement, eq. (5) for the modal velocity, and eq. (6) for the modal acceleration.  $A, B, G, F, A', B', G'$  and  $F'$  are the coefficients of integration for the  $i$ th mode. The derivation of these equations and the coefficients for underdamped, critically damped, overdamped and undamped rigid body modes can be found in ref. 4. Again, with the one assumption that the external force input,  $P$ , varies linearly between solution time steps, the solution is mathematically exact. Note that this integration algorithm is a single step method and thus has the distinct advantage of ease with which the integration time step can be changed. A simple recalculation of the coefficients is all that is necessary.

With the introduction of coupled modal damping, eq. (2) is written in matrix form.

$$\{\ddot{\xi}\} + [C] \{\dot{\xi}\} + [\omega_0^2] \{\xi\} = \{P\} \quad (7)$$

where  $m_i = 1$  and  $C$  is the full system modal damping matrix derived via the TMP method of eq. (1). Eq. (7) can be solved by means of numerous finite difference and/or iterative algorithms; however, the method of this paper treats the modal damping as if damping was an externally applied force vector on the right hand side of the equation.

$$\{\dot{\xi}\} + [\omega_0^2] \{\xi\} = \{P\} - [C] \{\dot{\xi}\} \quad (8)$$

The left hand side of eq. (8) is uncoupled. Applying the solutions of eqs. (4), (5) and (6) to eq. (8) and using matrix notation yields the following three expressions:

$$\begin{aligned} \{\xi\}_{n+1} &= [F] \{\xi\}_n + [G] \{\dot{\xi}\}_n \\ &+ [A] \{P\}_n + [B] \{P\}_{n+1} \\ &- [A] [C] \{\dot{\xi}\}_n - [B] [C] \{\dot{\xi}\}_{n+1} \end{aligned} \quad (9)$$

$$\begin{aligned} \{\dot{\xi}\}_{n+1} &= [F'] \{\xi\}_n + [G'] \{\dot{\xi}\}_n \\ &+ [A'] \{P\}_n + [B'] \{P\}_{n+1} \\ &- [A'] [C] \{\dot{\xi}\}_n - [B'] [C] \{\dot{\xi}\}_{n+1} \end{aligned} \quad (10)$$

$$\begin{aligned} \{\ddot{\xi}\}_{n+1} &= \{P\}_{n+1} - [\omega_0^2] \{\xi\}_{n+1} \\ &- [C] \{\dot{\xi}\}_{n+1} \end{aligned} \quad (11)$$

The modal velocities are solved directly by use of eq. (10).

$$\{\dot{\xi}\}_{n+1} = [I + B' \setminus C]^{-1} \{V\} \quad (12)$$

where

## Analytic Results

$$\begin{aligned} \{V\} = & [F'] \{\xi\}_n + [G'] \{\dot{\xi}\}_n \\ & + [A'] \{P\}_n + [B'] \{P\}_{n+1} \\ & - [A'] [C] \{\xi\}_n \end{aligned} \quad (13)$$

Next, the modal displacements and accelerations are solved by use of eqs. (9) and (11) respectively. Note that in this solution approach the damping is implicit, that there is no iteration on the solution time step and that finite difference solution techniques have been avoided.

An alternate approach is to solve for the right hand side generalized damping forces,  $P_d$ , directly.

$$\begin{aligned} \{P_d\}_{n+1} = & - [C] \{\xi\}_{n+1} = \\ - [C] [I + B' C]^{-1} \{V\} = & [H] \{V\} \end{aligned} \quad (14)$$

Note that solving for  $P_d$  directly saves computational effort during the recovery of modal responses; i.e., once  $P_d$  is known, the modal displacements, velocities and accelerations are solved by use of eqs. (9), (10) and (11), respectively. With this, the solution technique requires only one significant matrix multiply above and beyond the closed form solution with proportional damping. The H matrix is referred to as the generalized damping force matrix. Since, the above approach results in a single step integrator, solution time step changes are easily incorporated by recalculation of the coefficients of integration and the H matrix. It should also be noted that the calculation of the H matrix involves a matrix inverse, which involves the C matrix. This recalculation is only required when the solution time step is changed by the analyst. Also, there would not be any significant computational savings gained by nulling out those off diagonal terms within C that are deemed to be negligible. For most applications, the H matrix would still be 100% dense. Besides, any such effort will always involve an element of risk.

The above solution approach (with the treatment of unknown forces on the right hand side of the equations) has been successfully utilized before. Both refs. 5 and 6 employed this approach in the solution of transient equations of motion with response dependent nonlinear forces.

The subject integration algorithm was implemented for the validation analysis of the verification loads analysis cycle for Space Shuttle flight STS-53. The first test of this new solution scheme was solution convergence versus the integration time step size. The results presented in this paper are for the liftoff transient condition defined by forcing function case EP21658. The STS damping used was 1% critical for STS free-free modes below 10 Hz. and 2% critical above 10 Hz. The primary payload provided a damping schedule for the normal modes in its Craig-Bampton DMM. This varied mode to mode, from a minimum of 0.41% of critical to a maximum of 2.19%. The comparisons to be made are for the Load Transform Matrix (LTM) response items for the STS-53 primary payload. The first integration time step selection is the normal selection used for standard linear solutions of STS/Payload liftoff systems, the smallest time step increment being 0.002 second. Fig. 1 illustrates the comparison of LTM results for a solution of one half the standard time step selection. With the majority of the results within 0.5 percent of each other, the solution is very well converged for the standard step size selection. It should be noted here that there are some null rows in the LTM and that some response items are numerically small, e.g., absolute maximums for items 374 through 389 are less than 0.25.

A variation on the above algorithm is to place only the off diagonal generalized damping terms on the right hand side of the equations of motion; i.e., treat the diagonal part of the damping matrix, C, within the coefficients of integration. Fig. 2 illustrates the comparison for the STS-53 LTM absolute maximum results. This comparison is for the standard time step solution (as are all that follow), and again, the percent differences between the two analyses are quite small. This paper does not recommend one treatment of the diagonal damping terms over the other. However, treating the damping diagonal on the right hand side should add a slight conservatism (lower damping) over the left hand side approach. This is due to the governing assumption of right hand side forces varying linearly between solution time steps. Fig. 2 is in compliance with this statement.

The proposed integrator works extremely well. This should be no surprise, the damping forces

are being treated in the same mathematical manner as the externally applied forces. It should be noted here that we are dealing with lightly damped problems. For highly or critically damped problems, the convergence versus time step size may not be so rapid.

### Coupled versus Diagonal Damping

For the situation where one or more of the components' structural math models contained a specified damping schedule, historical practice has utilized the TMP method to derive the system level generalized damping. But then, for the sake of mathematical expediency, the off diagonal terms were discarded, forcing the generalized equations of motion to be uncoupled. For most of these analyses, the solutions appear well behaved. But occasionally, the resulting responses would be drastically out of bounds. On such occasions, it was found that retention of the full TMP damping matrix would in fact result in reasonable response levels. In fact, in order to avoid any possible analysis schedule impacts (or repetition of effort), the use of diagonalized TMP damping for STS/Payload verification loads analyses of payloads with specific damping schedules has been abandoned.

Figure 3 is a comparison of Diagonal TMP (DTMP) versus the Full TMP (FTMP) and illustrates the potential danger in the use of the DTMP. Nothing in the STS-53 analysis would appear to be anomalous had the DTMP method been employed. However, fig. 3 illustrates that the DTMP method can yield some very unconservative results, some LTM items being 20 to 25 percent lower than the FTMP numbers. A very large number of LTM items would be unconservative by 5 percent or more had the DTMP approach been used.

The structural math models used in many transient loads analysis cycles, especially the design cycles, do not specify payload damping properties. Standard practice has been to use a system level diagonal modal damping. For STS/Payload liftoff analyses, 1 percent critical damping is used on all system modes below 10 Hz. and 2 percent on all system modes above 10 Hz. and landing analyses utilize 1 percent critical damping for all system modes. But there is a hidden danger here. Although the STS has been tested and 1%-2% damping is deemed to be conservative for liftoff, the payload is usually untested at this point, and

engineering judgment is used. Historically, the judgement has been that the payload's damping characteristics will be similar to the STS, 1%-2% or more; therefore the use of 1%-2% system level diagonal modal damping has been deemed to be "conservative enough". The danger is that 1%-2% component modal damping does not equate to an equivalent 1%-2% system level diagonal modal damping. Fig. 4 presents the comparison of FTMP 1%-2% damping on the STS free-free modes and the payload Craig-Bampton normal modes versus 1%-2% diagonal system level modal damping. Note that the diagonal system results are again unconservative. This analysis was repeated, using 1% for all component modal damping versus a diagonal system level modal damping of 1%. Again, as illustrated in fig. 5, the system diagonal damping results are unconservative. The conclusion is that uniform component modal damping schedules do not transform into uniform system level diagonal modal damping! Although this may run somewhat counter to intuition, it should not be surprising. As mentioned above, diagonal system level modal damping results in fictitious coupling between substructures at non-interface DOF.

### Payload Boundary Damping

Presently the great majority of payload DMMs are delivered in Craig-Bampton formats. Eq. (15) illustrates the equations of motion for such a payload system.

$$\begin{bmatrix} M_{xx} & M_{x\xi} \\ M_{\xi x} & I_1 \end{bmatrix} \begin{Bmatrix} \ddot{x} \\ \ddot{\xi} \end{Bmatrix} + \begin{bmatrix} 0 & 0 \\ 0 & 2\zeta\omega_1 \end{bmatrix} \begin{Bmatrix} \dot{x} \\ \dot{\xi} \end{Bmatrix} + \begin{bmatrix} K_{xx} & 0 \\ 0 & \omega^2 \end{bmatrix} \begin{Bmatrix} x \\ \xi \end{Bmatrix} = \begin{Bmatrix} f_x \\ 0 \end{Bmatrix} \quad (15)$$

The x DOF are physical discrete and include at least the interface DOF to the STS system. As mentioned above, it is standard practice to require payloads to incorporate into their DMM at least all three translational DOF at the STS interfaces as discrete physical. Historically, many payload DMMs consisted of only the above Craig-Bampton mass and stiffness matrices. In these cases, it was generally assumed that payload damping was "large" compared to the STS; therefore, it would be conservative to use the STS

modal damping schedule at the system modal level. Since the boundary DOF participate in the system modes, this practice implicitly included payload boundary damping, i.e., all of the payload flexure was damped.

A more definitive payload DMM includes the damping terms of eq. (15), i.e., the  $2\zeta\omega$  terms or a schedule of per cent critical damping for each  $\omega$ . This damping is experimentally determined by the payload contractor and it is often found that specific damping values can be less than 1% critical! To preserve the payload DMM damping characteristics at the STS/Payload system modal level, it then becomes necessary to use the FTMP method. Thus the payload's flexure defined by the physical DOF of the payload's DMM remains undamped.

A legitimate concern has arisen as to the need for application of damping onto these payload physical DOF. One of the methods proposed (see ref. 7) is to transform the  $x$  DOF mass and stiffness matrices of eq. (15) into modal coordinates by use of an eigensolution. A damping schedule is imposed in these coordinates and then transformed back into the physical coordinates and added into eq. (15). The resulting payload equations of motion then appear as follows:

$$\begin{aligned} & \begin{bmatrix} M_{xx} & M_{x\xi} \\ M_{\xi x} & I \end{bmatrix} \begin{Bmatrix} \ddot{x} \\ \ddot{\xi} \end{Bmatrix} \\ & + \begin{bmatrix} (\phi_x^{-1})^T \sqrt{2}\zeta_x\omega_x (\phi_x^{-1}) & 0 \\ 0 & \sqrt{2}\zeta\omega \end{bmatrix} \begin{Bmatrix} \dot{x} \\ \dot{\xi} \end{Bmatrix} \\ & + \begin{bmatrix} K_{xx} & 0 \\ 0 & \omega^2 \end{bmatrix} \begin{Bmatrix} x \\ \xi \end{Bmatrix} = \begin{Bmatrix} f_x \\ 0 \end{Bmatrix} \quad (16) \end{aligned}$$

As a study, the above process was executed for the STS-53 primary payload, liftoff case EP21658. Being highly overconstrained (six DOF at each STS interface node for a total of 30 physical DOF), the STS-53 payload offers an excellent "acid test" against the relative importance of this boundary damping. Damping schedules,  $\zeta_x$ , of 1%, 2% and 4% were applied and compared against the  $\zeta_x$  zero results. The results for the absolute maximum LTM responses are

illustrated in fig. 6 for the 4% versus zero. A review of fig. 6 demonstrates that the additional boundary damping does in fact reduce (for the most part) the transient LTM responses, as is expected. However, the reductions are modest. The experimental measurement of such  $\zeta_x$  terms may be impossible.

If it is deemed necessary that all of the payload's flexure be analytically damped, the payload contractor has the option of measuring the structural damping in a free-free configuration. As mentioned above, this damping can then be transformed into the specific Craig-Bampton coordinate system used for the payload DMM that is used in the STS/payload coupled loads analysis. In this case, the damping matrix of eq. (15) will be totally populated. Fig. 7 illustrates the difference in LTM maximum responses for a 1%-2% damping schedule on the STS-53 payload's free-free modes versus on the payload's overconstrained modes. The great majority of these response items differ by less than one percent. It is important to note here that there are two mechanisms at work: 1) the entire structural flexure of the payload Craig-Bampton math model has been damped and 2) since some normal modes over 10 Hz. in the overconstrained payload DMM will participate below 10 Hz. in the free-free modal coordinates, the overall payload damping is impacted by that modal participation now being assigned 1% of critical versus the 2% of critical it was assigned in the overconstrained DMM. For this reason, when diagonal damping is being assigned to the payload DMM, based upon test data, it is best that the DMM coordinate system closely match the constraints utilized in the test. This payload damping matrix can then be transformed into the payload DMM coordinate system to be used in the coupled loads analysis.

### Computational Cost

The computational cost for the FTMP analysis turns out to be about 46 percent greater than for the DTMP analysis. This includes generalizing the external forces and recovery of the LTM response. Thus, with the above integration method, the mathematical convenience of discarding the off diagonal damping terms is not significant. In comparison, the FTMP solution performed by the modified Newmark-Beta method (ref. 4) required 706 percent of the DTMP computational effort. The solution time step size necessary to achieve a converged modified

Newmark-Beta solution was one-eighth that of the standard time step size, i.e., 0.00025 second versus 0.002 second.

### Coupling with Constraint Equations

Reference 5 reported a methodology of calculating booster to launch pad interface transient forces. This method did not utilize booster/pad system modes, but instead coupled the respective DMMs by use of constraint equations. These constraint equations are then manipulated to simulate the booster separating from the launch pad. The accuracy of the system modal properties is insured by observing the principles of modal synthesis (ref. 8), although system level modes are never extracted. The reported methodology utilized the same closed form integrator adopted in this report.

One advantage of the ref. 5 method was the total avoidance of TMP damping when DMMs with different diagonal modal damping schedules are to be coupled and analyzed. Since system modes are not necessary, each component is allowed its own distinct damping characteristics, the only coupling occurring at the desired interface DOF via the constraint equations. With the above reported solution procedure, the methodology of ref. 5 can be extended to include components whose

damping characteristics have been derived via the TMP method. This is illustrated for the case of the booster/payload system damping defined via TMP and the launch pad damping being the simple diagonal modal damping. First, the generalized damping forces acting on the booster, subscript b, is derived from eq. (14):

$$\{P_d\}_{b,n+1} = -[C_b]\{\dot{\xi}\}_{b,n+1} = [H_b]\{V_b + {}^1B_b \phi_b^T f\}_{n+1} \quad (17)$$

where f is the vector of unknown pad forces acting on the booster at time n+1. Substitution of this into eq. (9) yields the booster modal displacement relation for time step n+1:

$$\{\xi\}_{b,n+1} = \{D_b\}_{n+1} + [{}^1B_b]\{\phi_b^T f\}_{n+1} + [{}^1B_b][H_b]\{V_b + {}^1B_b \phi_b^T f\}_{n+1} \quad (18)$$

where D comprises all known quantities from the right hand side of eq. (9). Premultiplication of eq. (18) by  $\phi_b$  yields the booster physical displacements at the pad interface. Similar recovery of the launch pad physical boundary displacements and enforcement of the constraint equations yields the following set of equations:

$$\begin{bmatrix} I_1 & 0 & 0 & -\phi_b {}^1B_b \phi_b^T - \phi_b {}^1B_b H_b {}^1B_b \phi_b^T \\ 0 & I_1 & 0 & \phi_p {}^1B_p \phi_p^T \\ -I_1 & I_1 & I_1 & 0 \\ 0 & 0 & I_1 & 0 \end{bmatrix} \begin{Bmatrix} x_b \\ x_p \\ \Delta x \\ f \end{Bmatrix} = \begin{Bmatrix} \phi_b D_b + \phi_b {}^1B_b H_b V_b \\ \phi_p D_p \\ 0 \\ 0 \end{Bmatrix} \quad (19)$$

Equation (19) yields the launch pad, subscript p, to booster constraint forces, f, and includes the effects of the FTMP damping from the booster/payload stack (the time step subscript, n+1, was dropped). The solution proceeds time step by time step as outlined in ref. 5. The extension of this method to cases of two or more bodies with coupled damping is a trivial task.

## Summary

This paper presented a general methodology for the solution of the transient responses for structural modal systems with coupled system damping. The reported method solves the modal equations of motion, while treating the system damping properties as applied forces on the right hand side of the equations of motion. The closed form solution approach is then utilized. Rapid convergence versus the solution time step size was demonstrated, at least for the lightly damped subject problem. Comparisons were made to the more traditional treatments of system modal damping, revealing that those approaches can be unconservative and should be treated as suspect. It has also been demonstrated that the reported method is computationally very efficient, especially when compared against the NASTRAN provided method of integrating the coupled equations of motion.

## Conclusions

Although they are not new, the conclusions of this study could prove to be far reaching. Diagonal system level modal damping, as applied to STS/Payload coupled loads analyses, is a system level approximation, that may result in unconservative payload component responses.

The problem addressed in this paper can be worded as follows: given the damping (deemed conservative through testing or otherwise) for a number of components, how does the analyst proceed to execute the coupled loads analysis without unwittingly destroying that conservatism? As illustrated above, it is a simple matter for the analyst to execute a conformal transformation of this damping into the system level modal coordinates. The reported methodology will ease the computational burden from that point on.

However, with the great complexities of the STS payloads, and with the large diversity of payload contractors and their respective computing facilities, and with the fact that the payloads are also an assemblage of subcomponents (each with its respective damping properties), and knowing that a multitude of structural nonlinearities manifest themselves as damping, and with the fact that we cannot successfully model damping as we do stiffness, and knowing that damping at best

will always involve at least a degree of approximation, etc., etc., the arguments in favor using diagonal system modal damping will certainly persist.

## References

1. Craig, Jr., Roy R., Structural Dynamics, John Wiley & Sons, New York, 1981.
2. Hasselman, T. K., *Damping Synthesis from Substructure Tests*, AIAA/ASME/SAE 15th Structures, Structural Dynamics and Materials Conference, Las Vegas, Nevada, April 17-19, 1974.
3. Park, S., Park, I., and Ma, F., *Decoupling Approximation of Nonclassically Damped Structures*, AIAA Journal, 1992, Vol. 30, No. 9.
4. The NASTRAN Theoretical Manual (Level 16.0), NASA SP-221(03), general release March 1, 1979.
5. Henkel, E. E., and Mar, R., *Improved Method for Calculating Booster to Launch Pad Interface Transient Forces*, AIAA Journal of Spacecraft and Rockets, November - December 1988, Vol. 25, pp 433 - 438.
6. Chapman, J. M., *A Friction Methodology for Space Shuttle/Payload Transient Loads Analyses*, Proceedings of the Shuttle Payload Dynamic Environments and Loads Prediction Workshop, Jan. 24-26, 1984, JPL D-1347, Vol. 2, pp. 543-572.
7. Spanos, P. D., Cao, T. T., Nelson, Jr., D. A. R., and Hamilton, D. A., *Efficient Loads Analyses of Shuttle-Payloads Using Dynamic Models with Linear or Nonlinear Interfaces*, Journal of Vibration and Acoustics, July 1990, Vol. 112, pp. 366 - 373.
8. Rubin, S., *Improved Component-Mode Representation for Structural Dynamic Analysis*, AIAA Journal, Vol 13, Number 8, August 1975, pp 995 - 1006.

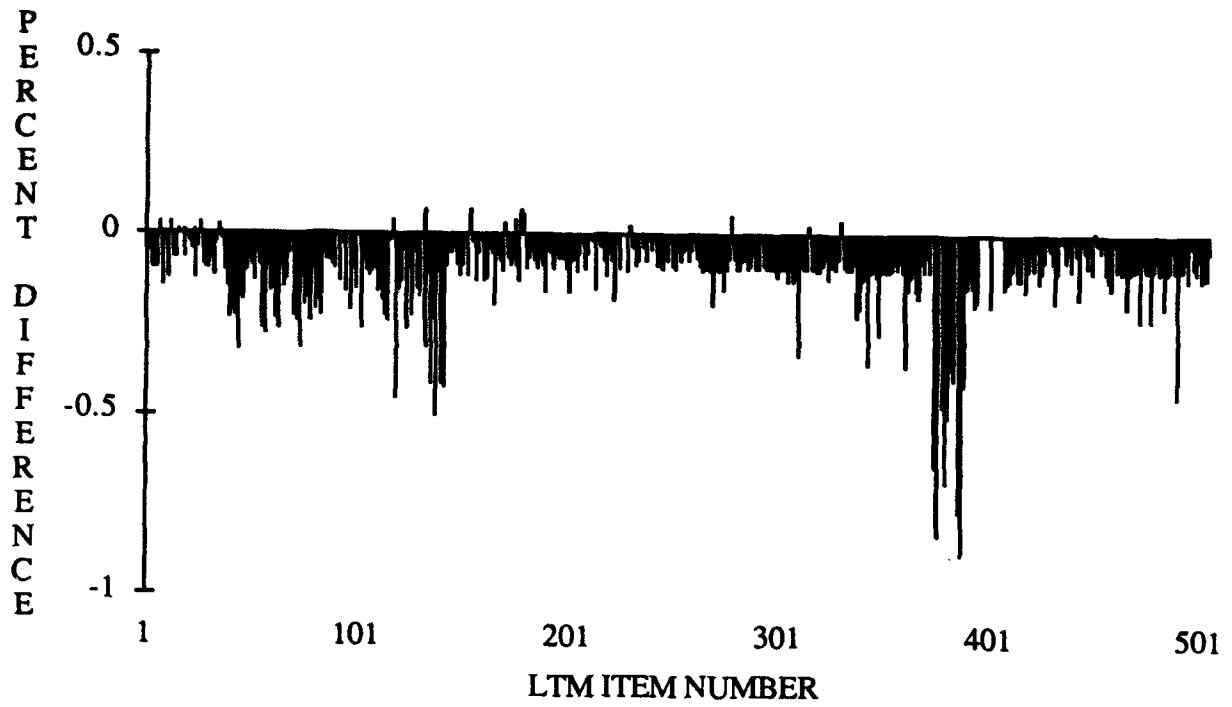


Figure 1 Standard Solution Time Step vs Half Standard Time Step

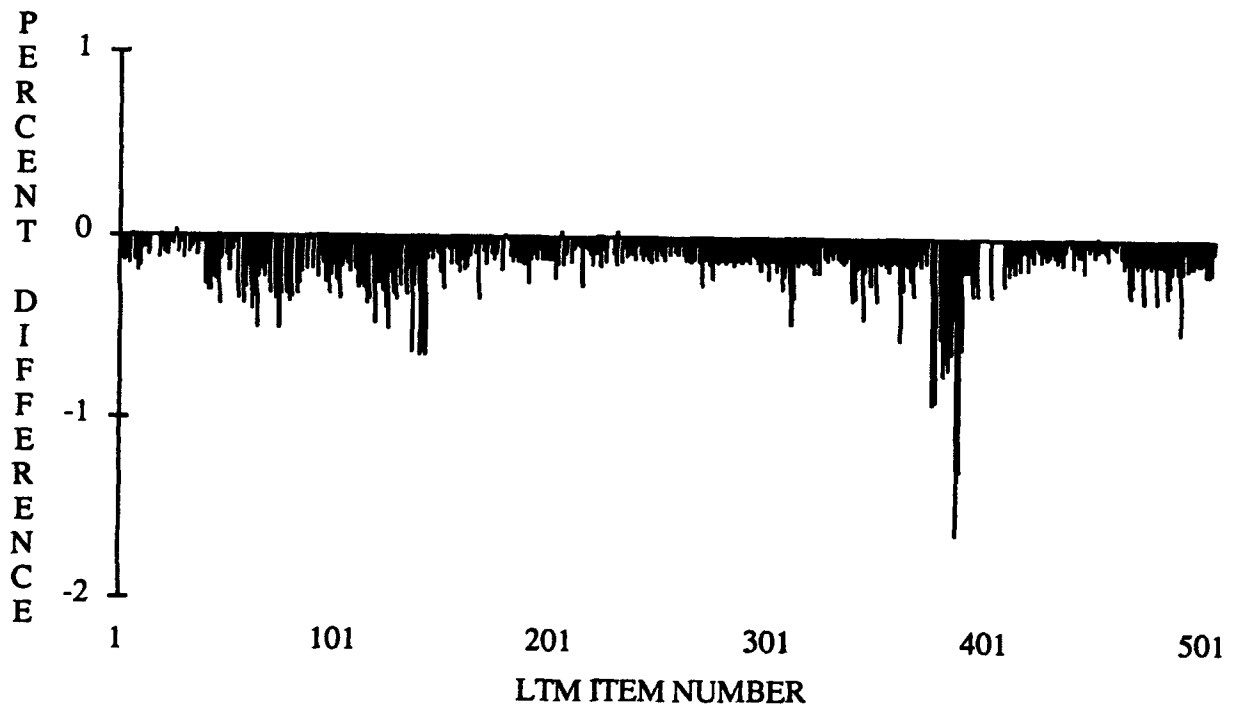


Figure 2 Right Hand Side Damping Diagonal vs Left Hand Side Damping Diagonal

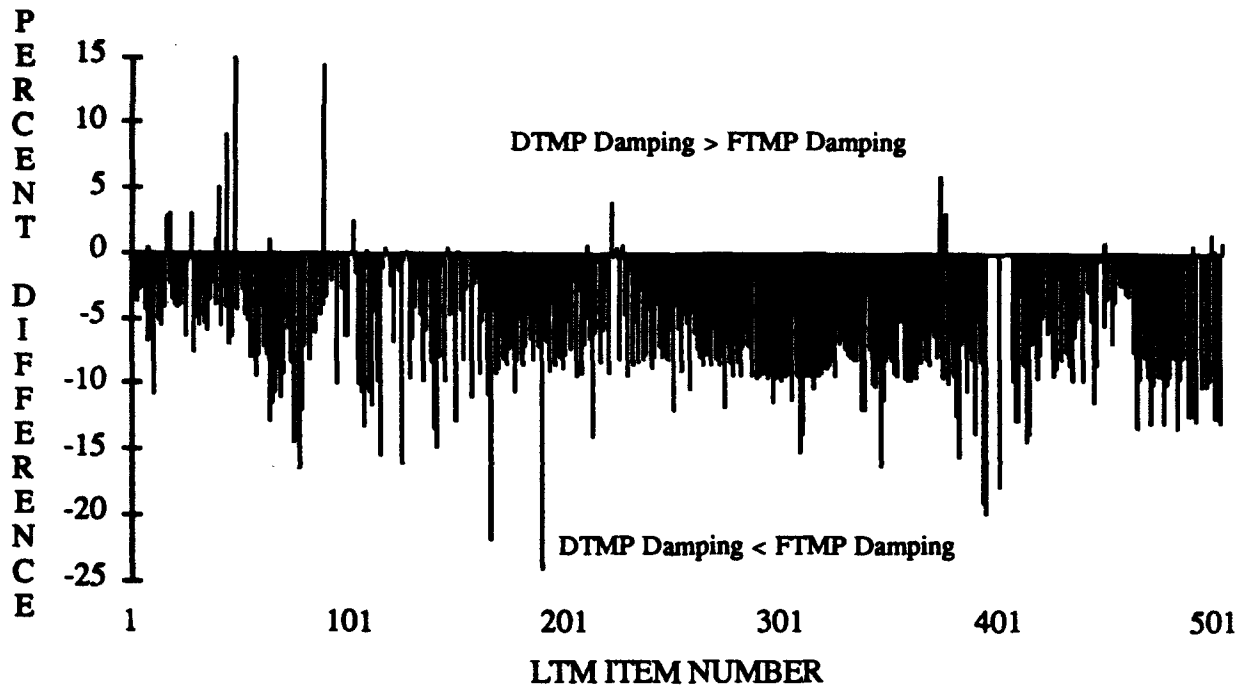


Figure 3 DTMP Damping vs FTMP Damping

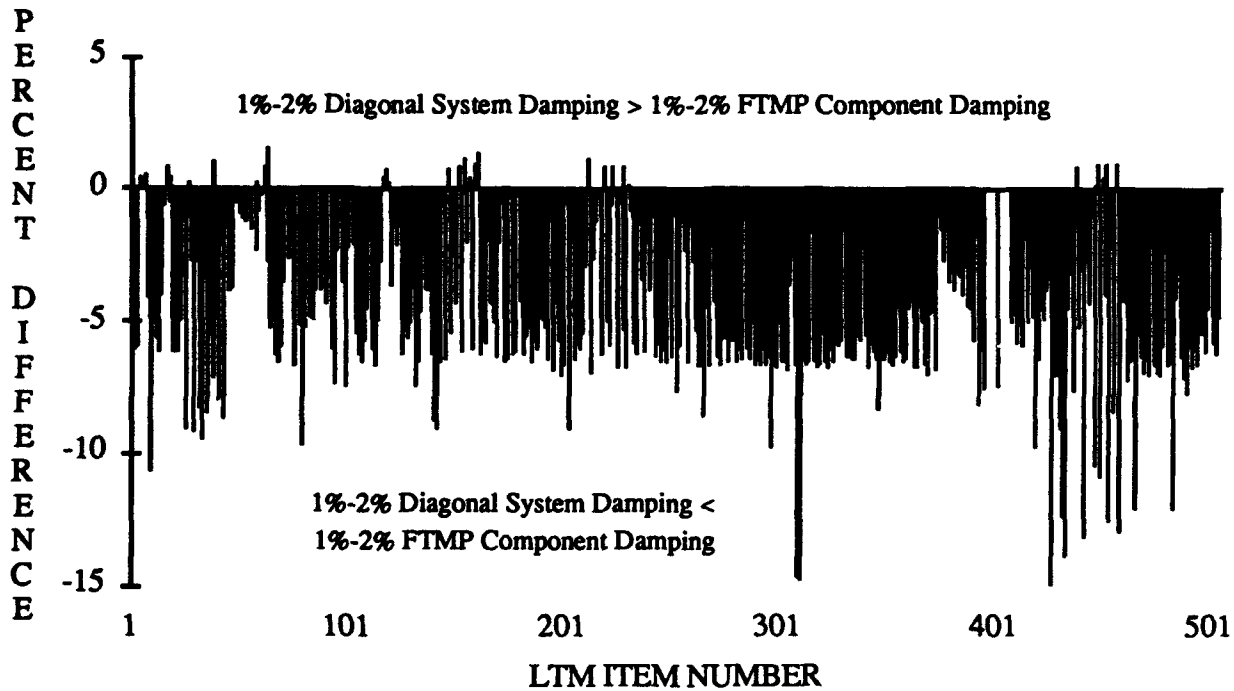


Figure 4 1%-2% Diagonal System Damping vs 1%-2% FTMP Component Damping

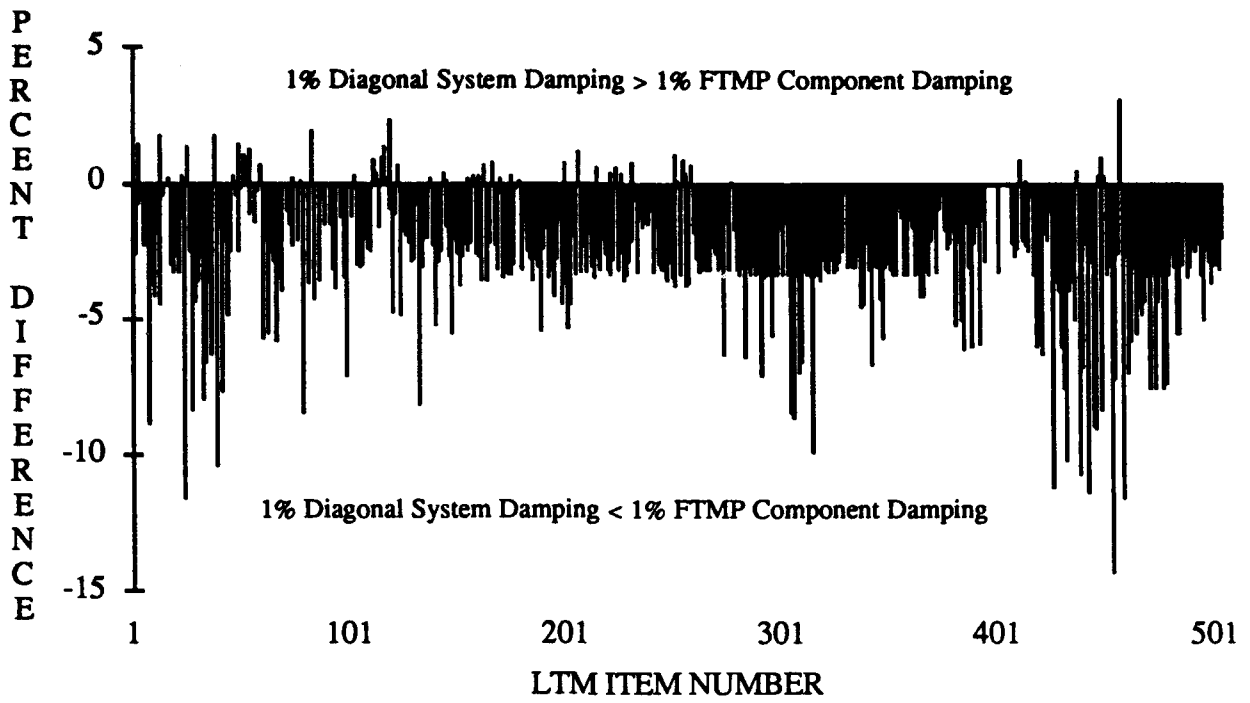


Figure 5 1% Diagonal System Damping vs 1% FTMP Component Damping

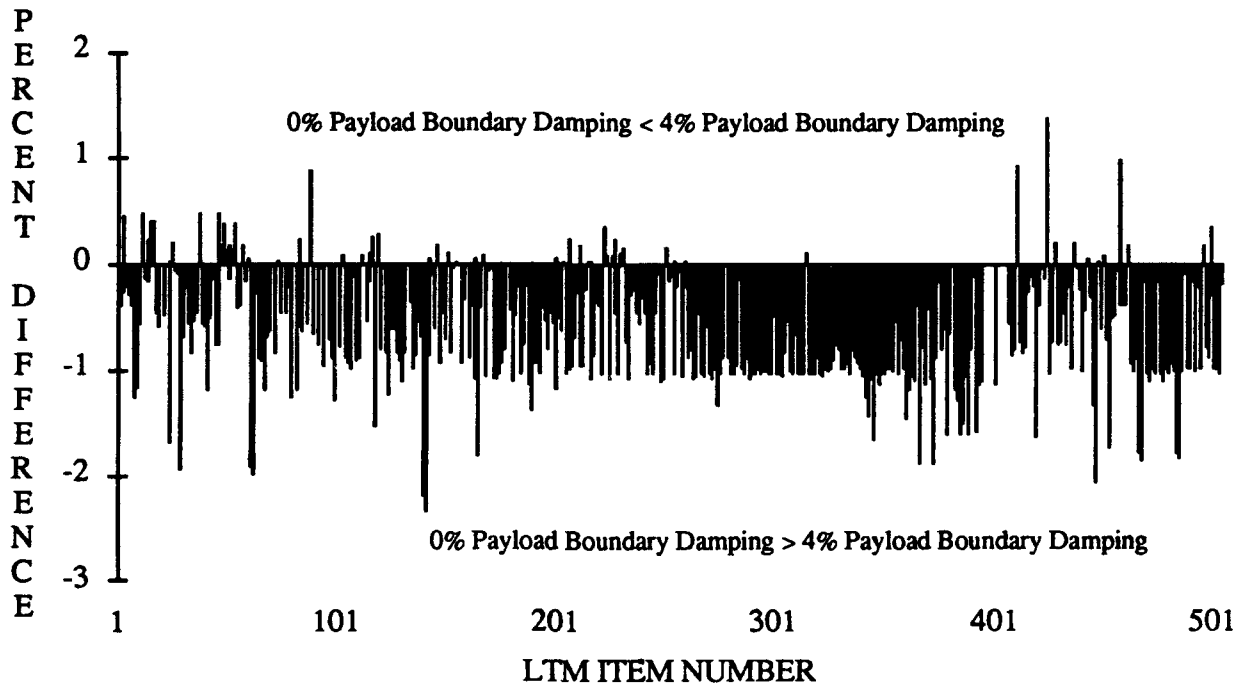


Figure 6 4% Payload Boundary DOF Damping vs 0% Payload Boundary DOF Damping

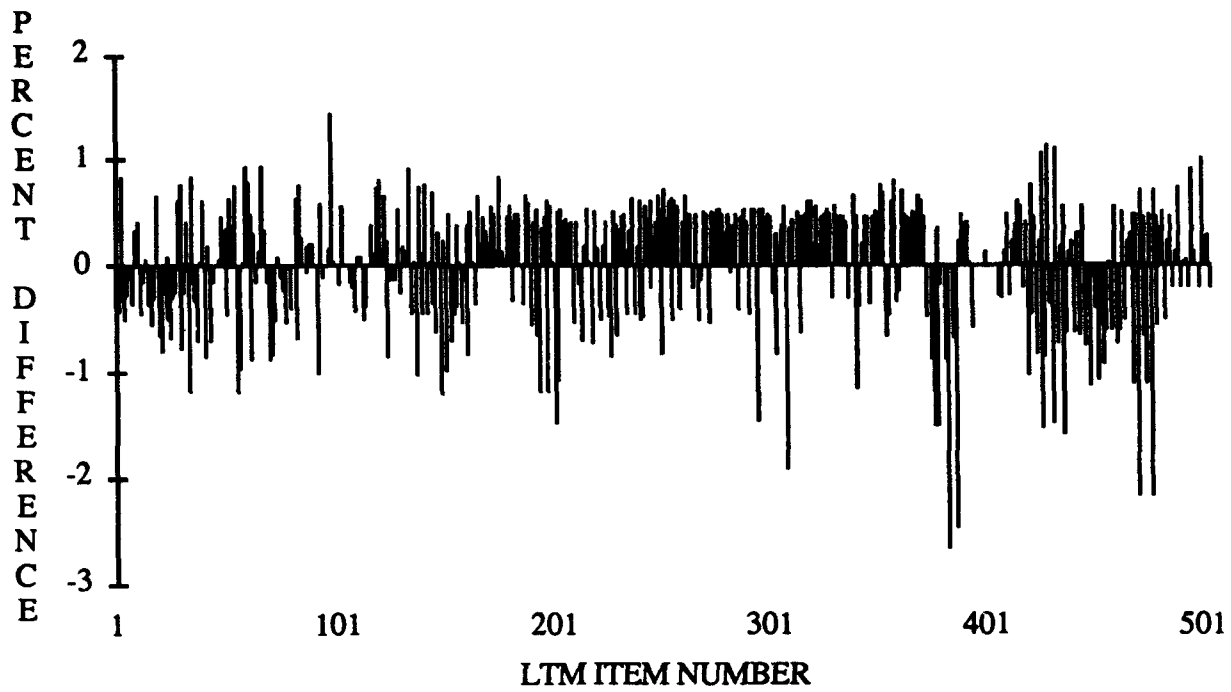


Figure 7 1%-2% Payload Free-Free Modal Damping vs  
1%-2% Payload Craig-Bampton Normal Modal Damping

# **Fourier Transform Mechanical Analysis (FTMA) Technique to Determine Dynamic Mechanical Properties of Viscoelastic Materials**

Surendra N. Ganeriwala (Suri)\*  
Philip Morris Research Center

## **ABSTRACT**

A Knowledge of the dynamic mechanical properties of the polymeric materials is necessary for optimizing their uses in suppressing and controlling noise and vibration. Conventionally, the dynamic properties are determined by measuring the response of a polymer specimen to a single frequency input at a time. The material properties over a range of frequency are obtained by repeating the experiment at many different frequencies. This paper describes a novel technique, the Fourier Transform Mechanical Analysis (FTMA), which measures the complex moduli of polymers over a range of frequency in one test by exciting the sample with a random signal (band limited white noise). A simple transfer function analysis yields the desired material functions. FTMA has many advantages over the conventional single frequency tests. The primary feature of FTMA is that a complete isotherm is obtained in just a few seconds with minimum heating and structural changes normally associated with other techniques. Many isotherms can be readily obtained by repeating the procedure at various temperatures. FTMA also, provides direct assessment of sample inertia and geometry effects. Another advantage of the FTMA over other schemes is that it can be used to easily determine the properties of moisture sensitive materials. The FTMA is a general technique which provides a procedure to determine dynamic properties of polymers without requiring to purchase a special purpose instrument.

---

\*Philip Morris USA, P. O. Box 26583, Richmond, VA 23261-6583, Tel: (804) 274-5694

## INTRODUCTION

Viscoelastic materials are increasingly used for the suppression and control of noise and vibration in many mechanical systems and structures. A comprehensive, useful understanding of the viscoelastic damping inherent in these systems can come only from studies of mechanical properties over wide ranges of frequency (time) and temperature. If materials are moisture sensitive, the effects of water activity also should be determined. A similar rule holds for plasticizers and solvents. It should be noted that the mechanical behavior of most polymers and materials that fail to crystallize when cooled from the molten state can be adequately described by the theory of viscoelasticity. But because of wide uses of polymers, viscoelasticity is often associated with polymers only. In this paper polymers and polymeric materials are synonymously used to designate viscoelastic materials.

Techniques for measuring the dynamic mechanical properties of polymers are tabulated in Figure 1 [1-9]. Although each category has advantages and disadvantages, the forced vibration methods are now preferred for basic dynamic studies and tests. There are three main reasons for this: first, material properties can be determined over a wide range of frequency using the same sample and setup. Second, measurements are made without assuming any mechanical model for materials. Third, measurement errors can be easily minimized and/or assessed.

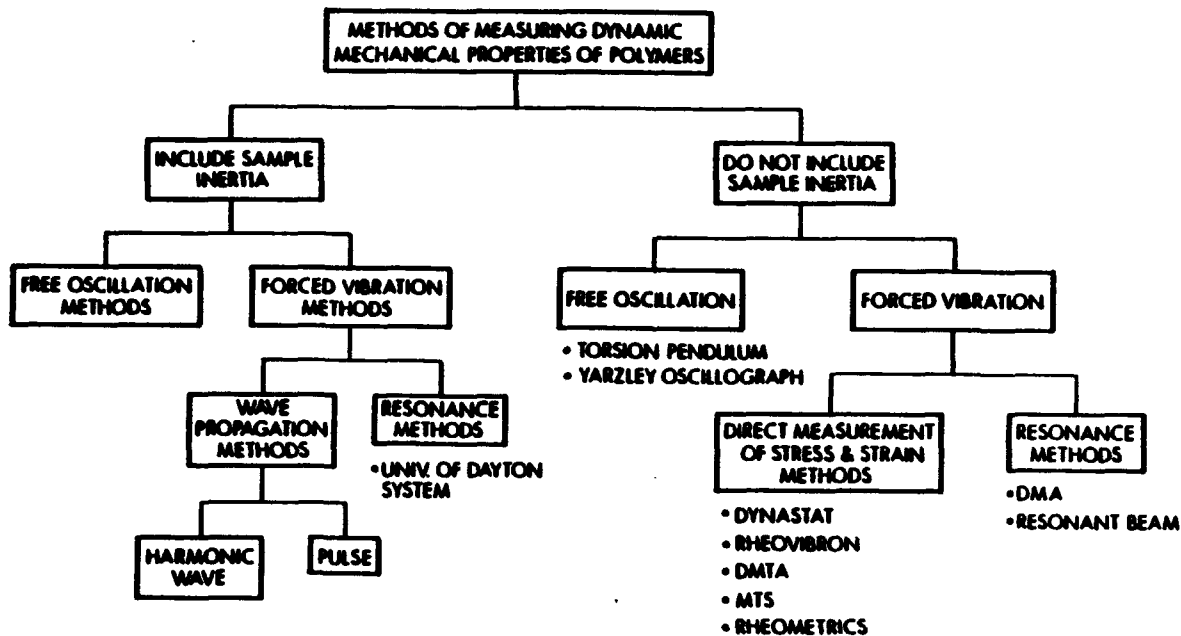


Figure 1. Common methods for measuring dynamic properties of polymeric materials.

A few of the commercially available instruments for measurements of dynamic properties are listed in Figure 1. Each instrument has some advantages and limitations depending upon the material, temperature and frequency range, accuracy, resolving power, and the information sought [8]. Typically, these instruments measure dynamic mechanical responses to sinusoidal input. To characterize the viscoelastic properties of a material, these tests are repeated over a range of temperatures and frequencies. This is sometimes done at a fixed frequency while the polymer specimen is heated or cooled and measurements are made periodically at different temperatures. Another method utilizes frequency variations while the temperature is held constant. In both procedures, the material is subjected to cyclic deformation over a period of time with uncontrolled temperature rise, loss of volatiles and other changes from energy dissipated in the material. These effects may be compounded by lags of sample from ambient temperature if heating is carried out at constant frequency. Another problem associated with temperature sweep is the inability of the material to maintain the thermodynamic equilibrium at temperature close to glass transition temperature. Thus it is difficult to obtain truly isothermal properties using most of the commercial instruments.

Another problem with these instruments is determination of mechanical properties of moisture sensitive materials. Such materials have tendency to gain moisture when subjected to mechanical excitation at constant relative humidity and temperature. This makes single frequency tests impractical for isomoisture studies over a range of frequencies.

In the past decade, the ability of designers and researchers to deal with dynamic systems has expanded greatly through the development and widespread use of new frequency analysis equipment. Spectral analysis techniques to study the behavior of polymers subjected to dynamic mechanical loads and/or deformation is called Fourier Transform Mechanical Analysis (FTMA). This paper describe how FTMA measures the complex moduli over a range of frequencies in one test by exciting the sample by a random signal (band limited white noise) [2,3]. FTMA has the following advantages over the conventional techniques.

1. For a linearly viscoelastic materials, measurements can be made over a range of frequencies in one test using white noise as an input, saving time and effort over conventional methods.

2. Because the data are sampled and manipulated automatically, the actual time to conduct a test might be short enough that temperature changes due to energy dissipation within the specimen would be negligible. Temperature could then be easily controlled as an independent variable.

3. Since FTMA measures linear viscoelastic properties over a wide range of frequency in a single test, it will be easier to determine material properties over appropriate ranges of interest without sweeping temperature and/or frequency. Thus, it will be possible to acquire the material data by maintaining the sample in thermodynamic equilibrium with the ambient at temperatures near its glass transition temperatures.

4. Many dynamic systems and structural analysis laboratories already have frequency analysis equipment and could thus conduct viscoelastic studies without purchasing additional

hardware. Others may find it preferable to purchase such general purpose equipment rather than a special purpose viscoelastic tester.

5. FTMA is a superior scheme to determine dynamic mechanical properties of moisture sensitive materials. Moisture dependent materials tend to gain moisture when deformed mechanically over a prolonged period.

6. FTMA provides a simple procedure to minimize and/or assess errors due sample geometry and wave effects.

7. The Fourier transform technique is perfectly general and the author has used it for measuring non-linear viscoelastic properties also [10].

## BASIC THEORY

### Linear Viscoelasticity Theory

A one dimensional form of constitutive equation for linear viscoelastic materials which are isotropic, homogeneous, and hereditary (non-aging) is given by [11]:

$$\sigma(t) = \int_{-\infty}^t G(t, t-t') \dot{\gamma}(t') dt' \quad (1)$$

where the kernel  $G(t-t')$  is a monotonic nonincreasing function of time known as the stress relaxation modulus,  $\sigma(t)$  is current stress, and  $\dot{\gamma}(t')$  is the strain rate history.

For the case of sinusoidal strain history Equation 1 can be transformed to yield an expression for the complex modulus,  $G^*(j\omega)$ :

$$G^*(j\omega) = G'(\omega) + jG''(\omega) \quad (2)$$

where  $j = \sqrt{-1}$ ,  $\omega$  is the frequency, and  $G'(\omega)$  and  $G''(\omega)$  are the storage modulus and loss modulus, respectively and defined as:

$$G'(\omega) = G_0 + \omega \int_0^{\infty} G(t) \sin \omega t dt \quad (3)$$

and

$$G''(\omega) = \omega \int_0^{\infty} G(t) \cos \omega t dt \quad (4)$$

$G'$  is related to the amount of energy stored and released in a cyclic oscillation and accordingly it is called the storage modulus,  $G''$  indicates the energy dissipated and is called the loss modulus. In damping applications Equation 2 is expressed:

$$G^*(j\omega) = G'(1 + j\eta) \quad (5)$$

where  $\eta$  is designated as the material damping factor defined as the ratio of  $G''$  over  $G'$ .

When the strain  $\gamma(t)$  is sinusoidal in time with an amplitude of  $\gamma_0$  :

$$\gamma(t) = \gamma_0 \sin \omega t \quad (6)$$

and stress response  $\sigma(t)$  will be

$$\sigma(t) = \sigma_0(\omega) \sin [\omega t + \delta(\omega)] \quad (7)$$

where  $\sigma_0(\omega)$  is the stress amplitude and  $\delta(\omega)$  is the phase angle between stress and strain. Both the quantities will be functions of frequency as shown in Equation 7. Note that  $\eta = \tan \delta$ . It can be shown that the storage and loss moduli are given by [1,11]

$$G'(\omega) = \frac{\sigma_0}{\gamma_0} \cos \delta \quad (8)$$

$$G''(\omega) = \frac{\sigma_0}{\gamma_0} \sin \delta \quad (9)$$

Thus, dynamic mechanical viscoelastic properties may be measured in tests with sinusoidal strain input at fixed frequency. Such tests have to be repeated at different frequencies over the range of interest to completely characterize the material.

### FTMA Formulation

When  $\gamma(t)$  is an arbitrary function of time such that its Fourier transform  $\Gamma(\omega)$  exists. Then [12]:

$$\gamma(t) = \frac{1}{2\pi} \int_{-\infty}^{\infty} \Gamma(\omega) e^{j\omega t} d\omega \quad (10)$$

and

$$\Gamma(\omega) = \frac{1}{2\pi} \int_{-\infty}^{\infty} \gamma(t) e^{-j\omega t} dt \quad (11)$$

and there are similar coupled relationships between  $\sigma(t)$  and its Fourier transform  $\Sigma(\omega)$ . Then it can be shown that [3]:

$$G^*(j\omega) = \frac{\Sigma(\omega)}{\Gamma(\omega)} \quad (12)$$

where  $\Sigma(\omega)$  is the Fourier transform of  $\sigma(t)$ . Thus according to Equation (12), the complex modulus is simply the transfer function between the input strain and output stress. Note that this relation holds for any  $\gamma(t)$  as long as its Fourier transform exists.

Equation (12) can be used to determine  $G'(\omega)$  and  $G''(\omega)$  over a range of frequency in one test if an appropriate strain input is used. White noise would seem to be ideal since it contains all frequencies, however, the resulting statistical variability of  $\Sigma(\omega)$  and  $\Gamma(\omega)$  can ruin the necessary digital calculations. The problem is avoided by calculating transfer functions from the auto and cross spectra of the input and output. In terms of the quantities of interest here the result would be

$$G^*(j\omega) = \frac{S_{\Sigma\Gamma}}{S_{\Gamma\Gamma}} \quad (13)$$

where  $S_{\Sigma\Gamma}$  is the cross spectrum between stress and strain and  $S_{\Gamma\Gamma}$  is the auto spectrum of the strain. Note that

$$S_{\Sigma\Gamma} = \Sigma(\omega)\bar{\Gamma}(\omega) \quad \text{and} \quad S_{\Gamma\Gamma} = \Gamma(\omega)\bar{\Gamma}(\omega) \quad (14)$$

where "-" denotes the complex conjugate of the respective function. Equation (13) overcomes the numerical problem of calculating  $G^*(j\omega)$  accurately when  $\Sigma(\omega)$  and  $\Gamma(\omega)$  are the results of a random process. Note that  $G^*(j\omega)$  in Equation (12) will be the complex Young's modulus if  $\sigma(t)$  and  $\gamma(t)$  are the normal stress and normal strain, respectively; and the complex shear modulus if they are the shear stress and shear strain.

### Samples and Measurements

A scheme for shear measurements is shown in Figure 2. Two identical polymer samples of length  $L$ , thickness  $h$ , and width  $W$  are bonded to two rigid metal mounts. The inner mount is attached to an impedance head (a combination force and acceleration sensor), which in turn is attached to a shaker. An accelerometer is attached to the top center of the outer mount. The stress and strain created in the polymer sample when the shaker is operated can be computed from the force and acceleration signals if the following assumptions are made:

- (1) The inertia of the polymer sample is negligible (i.e., no standing or traveling waves are set up in the specimen).
- (2) Stress and strain are distributed uniformly over the samples' cross-sectional area and thickness.
- (3) Stress concentration effects are negligible.

(4) All motion occurs in a straight line, vertically up and down.

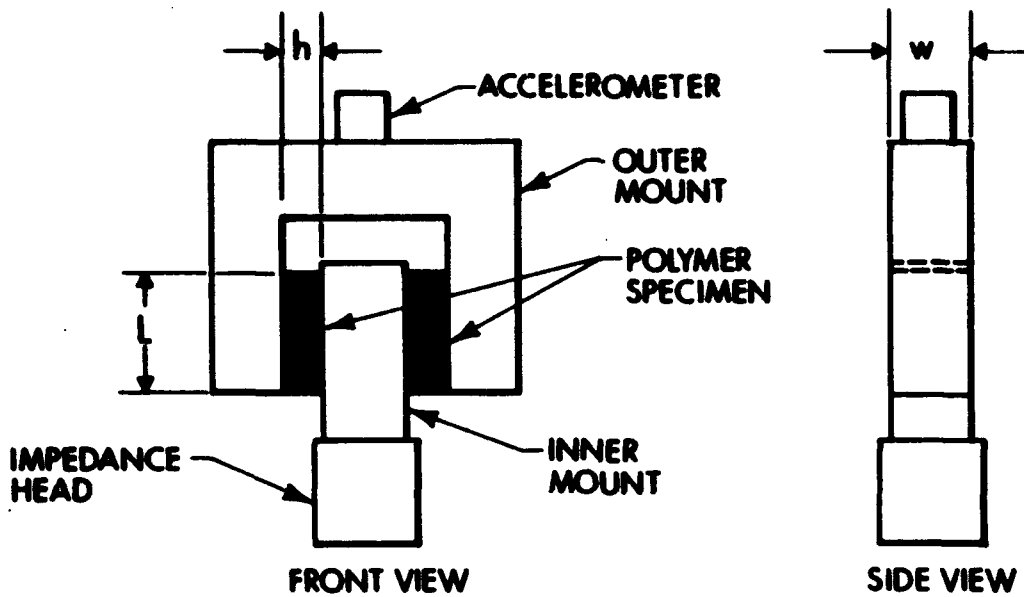


Figure 2. Typical specimen used for measuring shear properties of polymeric materials.

If  $f(t)$  is the total shear force exerted on the polymer sample then the shear stress  $\sigma(t)$  is

$$\sigma(t) = \frac{f(t)}{2LW} \quad (15)$$

and thus

$$\Sigma(\omega) = \frac{F(\omega)}{2LW} \quad (16)$$

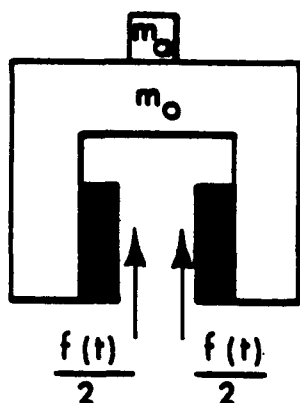
where  $F(\omega)$  is the Fourier transform of  $f(t)$ .

The force  $f(t)$  can be determined by "mass cancellation" as diagrammed in Figure 3. The equation of motion for the impedance head-inner mount assembly can be expressed:

$$f(t) = f_I(t) - (m_I + m_i) \ddot{x}_i(t) \quad (17)$$

where  $f_I(t)$  is the force measured by the impedance head,  $m_I$  the effective mass of the impedance head,  $m_i$  the mass of the inner mount, and  $\ddot{x}_i(t)$  the acceleration of the inner mount measured by the impedance head. A simple electrical circuit can be devised to multiply the  $\ddot{x}_i(t)$  signal by  $(m_I + m_i)$  and subtract the result from the  $f_I(t)$  signal, thereby producing  $f(t)$  as its output.

FREE BODY DIAGRAM OF  
POLYMER-OUTER MOUNT-  
ACCELEROMETER ASSEMBLY



FREE BODY DIAGRAM OF  
IMPEDANCE HEAD-INNER  
MOUNT ASSEMBLY

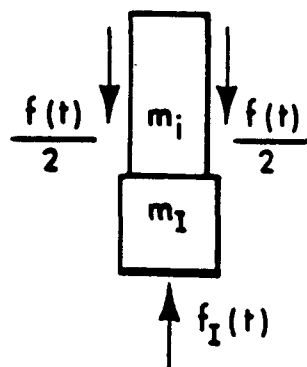


Figure 3. Free body diagrams for determining the force applied to the material.

The shear strain  $\gamma(t)$  can be obtained from the displacement of inner mount,  $x_i(t)$ , relative to that of the outer mount,  $x_o(t)$ , as

$$\gamma(t) = \frac{x_i(t) - x_o(t)}{h} \quad (18)$$

where  $x_i(t) - x_o(t)$  is found by twice integrating the acceleration difference  $\ddot{x}_i(t) - \ddot{x}_o(t)$ . This calculation is easily performed by a spectrum analyzer since integration in the frequency domain is equivalent to dividing the Fourier transform of the original signal by  $j\omega$ . Thus

$$\Gamma(\omega) = \frac{X_i(\omega) - X_o(\omega)}{h} = \frac{\ddot{X}_i(\omega) - \ddot{X}_o(\omega)}{\omega^2 h} \quad (19)$$

where the upper case letters represent the Fourier transforms of their lower case equivalents.

## EXPERIMENTAL WORK

### Sample Preparation

A specimen mounting scheme like the one shown in Figure 2 was used in an experimental study of the use of FTMA technique to measure the viscoelastic properties of polymers. The inner and outer mounts were made of aluminum. The exact dimensions varied depending on the size of the polymer specimen tested. To insure that the mounts behaved as rigid bodies, the dimensions were chosen to place the resonance frequencies of their natural

modes of vibration well above the region of interest. (The lowest frequency natural mode was found to be the "tuning fork" mode of the outer mount.) [3]

Two different elastomer compounds were used as test specimens. One compound was based on Neoprene rubber (chloroprene polymer) and the other on NBR (nitrile rubber). The surfaces of the aluminum mounts where the polymer was to be bonded were cleaned with alcohol, sand blasted, and coated sequentially with Chemelok 205 and 220 adhesives. The mounts were then placed inside a very simple mold which was then placed on a heated platen of a transfer molding press at 153°C. The elastomer was then forced into the mold cavity at a pressure of 4.14 MPa (600 psi) where it was held long enough to cure the sample (20 min. for the Neoprene and 10 min. for the NBR). In all cases the sample dimensions L, W (see Figure 2) were 25.4mm and 12.8mm respectively. Four samples of different thickness (h = 1.59mm, 3.18mm, 6.35mm, and 12.8mm) were molded from each elastomer.

### Instrumental Setup

Schematic diagrams of the entire experimental system are shown in Figure 4.

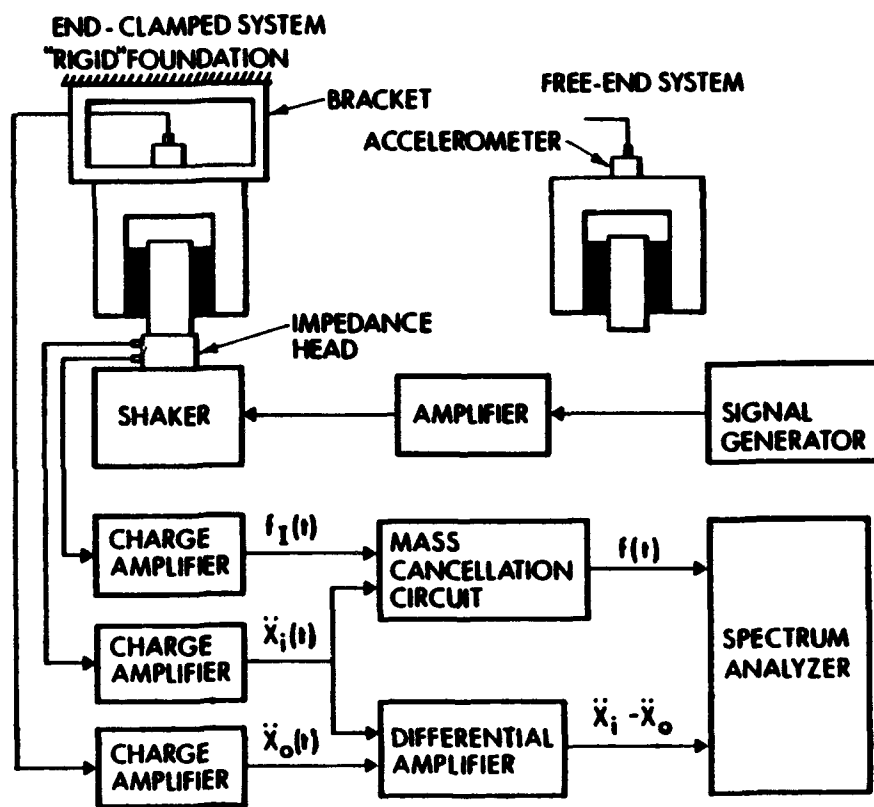


Figure 4. A schematic representation of the FTMA apparatus.

Note that two ways to strain the specimen were used: in one case the outer mount was clamped to a rigid foundation by an aluminum bracket which functioned as a stiff spring while in the other (inset in Figure 4) it was left free to vibrate. These two configurations shall be referred to as end-free and end-clamped, respectively. The end free configuration was used mainly to determine the frequency for the onset of wave effects.

The functioning of the electronic gear is also shown in Figure 4. A signal generator feeds band limited white noise into a power amplifier which drives an electro-mechanical shaker. A piezoelectric impedance head is mounted between the shaker and the inner mount. A piezoelectric accelerometer is attached to the outer mount for end-free tests and to the bracket for the end-clamped tests.

To determine viscoelastic properties over a range of temperature and moisture content, the specimen assembly was placed in a chamber with controlled temperature and humidity. In the current configuration, the environmental condition can be varied from 0°C to 100°C over a wide range of relative humidity. The chamber condition is maintained constant by a continuous supply of conditioned air from an environmental chamber. We are in the process of redesigning the sample environmental chamber to extend temperature range.

Signals from both transducers are fed through charge amplifiers. The acceleration signals  $\ddot{x}_1(t)$  and  $\ddot{x}_0(t)$  are then fed into a differential amplifier to obtain  $\ddot{x}_1(t) - \ddot{x}_0(t)$ . The force and acceleration signals  $f_1(t)$  and  $\ddot{x}_1(t)$  are fed into a mass cancellation circuit which produces  $f(t)$  as an output (see Equation (12)). The performances of the mass cancellation and acceleration difference circuits were checked to ensure the accuracy of measurements of each circuit was within 1% of the actual value. This slight difference comes from the fact that no two transducers are absolutely identical to each other, especially in phase. Such small differences also have been found in commercial instruments [4,7]. The important point is that this is always present and does not affect the repeatability of measurements.

The force and acceleration difference signals  $f(t)$  and  $\ddot{x}_1(t) - \ddot{x}_0(t)$  are then fed into a spectrum analyzer where they are Fourier transformed, and multiplied by the appropriate constants according to Equations (16) and (19).  $G^*(j\omega)$  is then computed using Equations (12) to (14).

### Measurement of Material Properties

Measurements of the viscoelastic properties of both elastomer compounds were made using a random white noise input, the calculation procedures described in the previous section, and specimens of different thickness. For comparison, tests were also run with the same equipment using a single frequency sinusoidal input, repeated at different frequencies over the range of interest. Tests were run at 25°C. A typical test took less than 5 seconds and tests were run at least 15 minutes apart.

To further check the final results, the properties of the elastomer compounds were also measured at 25°C using a Rheovibron at 3.5, 11, 35, and 110 Hz. This device actually measures the complex Young's modulus  $E^*(j\omega) = E'(\omega) + jE''(\omega)$ . According to Reference [11],  $E^*(j\omega)$  is related to  $G^*(j\omega)$  by the equation

$$E^*(j\omega) = 2(1 + \nu^*)G^*(j\omega) \quad (20)$$

where  $\nu^*$  is the complex Poisson's ratio. For most elastomers  $\nu^* = .5$  giving  $E^*(j\omega) = 3G^*(j\omega)$ .

To obtain viscoelastic properties over a wide range of frequency and temperature, the tests with random noise input were performed at 20 different temperatures from 4°C to 75°C. Each test took 4-5 sec.; consequently there could be no significant temperature rise due to internal friction in the test sample. To ensure the complete thermodynamic equilibrium of sample molecular configuration with the environment, at each temperature test specimen was equilibrated for a minimum of 30 minutes before taking a measurement. A longer dwell time was used for low temperature data.

## ERROR ANALYSIS

A highlight of the FTMA system is the capability of performing an extensive analysis of error [2,3]. The errors can be either random or systematic in nature. Random errors are minimized by using high precision instrumentations and reducing the noise. The systematic errors are evaluated both analytically and experimentally. Possible sources of systematic errors are described below for a simple shear sample. However, the same procedure can be applied to other types of sample configurations.

### Wave Effects

The foregoing treatment of stress and strain presumes no standing or traveling waves in the sample, i.e. the inertia of the sample is negligible compared to viscoelastic forces. This condition is met when the length of the shear wave propagating through the sample is much greater than the critical dimension of the sample. In shear samples, the thickness,  $h$ , is the critical dimension.

The shear wavelength  $\lambda$  is given by [13]:

$$\lambda = \frac{2\pi C}{\omega} = \frac{2\pi}{\omega} \left[ \frac{G}{\rho} \right]^{0.5} \left[ \frac{2(1 + \tan^2 \delta)}{[(1 + \tan^2 \delta)^{1/2} + 1]} \right] \quad (21)$$

where  $\omega$  is the frequency (rad/sec),  $\rho$  the mass density (kg/m<sup>3</sup>), and  $C$  is the speed of propagation of sound through the material. The other quantities have been defined earlier. The equation predicts that sample inertial effects will become significant at lower frequencies as the

thickness increases. Also that the inertial effects will show up at lower frequencies as the modulus declines (when temperature is increased). Thus, direct measurement of stress and strain with forced vibration tests is always limited to relatively low frequencies.

FTMA provides a direct method for determining the frequency at which inertial effects become noticeable. For this purpose the outer mount is detached from the "rigid" foundation and the accelerometer is mounted on it. The free body diagram of the outer mount-accelerometer assembly is shown in Figure 5. The relevant equation of motion is

$$f'(t) = (m_a + m_o) x_o(t) \tag{22}$$

where  $f'(t)$  is the force exerted on the outer mount by the specimen,  $m_a$  the mass of the accelerometer,  $m_o$  the mass of the outer mount, and  $x_o(t)$  the acceleration of the outer mount measured by the accelerometer.

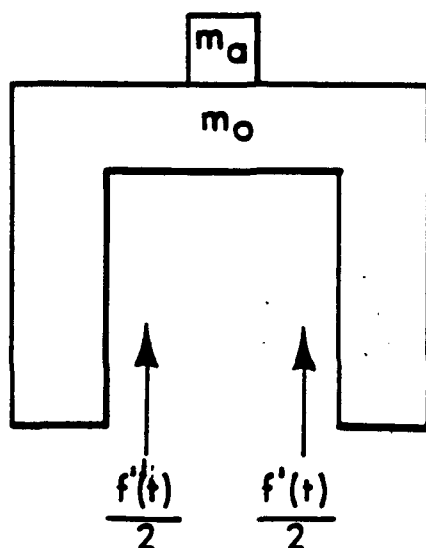


Figure 5. Free body diagram of accelerometer-outer mount assembly used for assessing the frequency for the onset of the wave effect.

As long as the inertia of the polymer sample is negligible, then  $f(t)$  should equal  $f'(t)$ . Then according to Equations 17 and 22

$$f(t) = (m_a + m_o) \ddot{x}_o(t) \tag{23}$$

If the Fourier transforms of both sides of this equation are evaluated, it follows that

$$\frac{F(\omega)}{\ddot{X}_o(\omega)} = m_a + m_o = \text{Constant} \tag{24}$$

Thus, the ratio of the force measured by impedance head to the acceleration of outer mount in end-free scheme must remain constant up to the frequency at which wave effect become significant.

The above analysis provides an alternate method for measuring the force applied to the polymer sample without any due concern for the fixture motion. However, the procedure is good only for high frequency measurements. When the sample is vibrated without a "rigid" foundation attachment, at frequencies lower than the resonance frequency of the outer mount, the sample behaves like a rigid body. The resulting force and relative acceleration are very small to be detected from the noise. Signal to noise ratio improves significantly above the outer mount resonance frequency. The data are shown in the results section.

### Bending Effects

The foregoing treatment of strain also presumes sample deformation is only simple shear, i.e. there is no bending. An approximate assessment of the effect of bending can be obtained by considering the deflection of a cantilever beam shown in Figure 6.

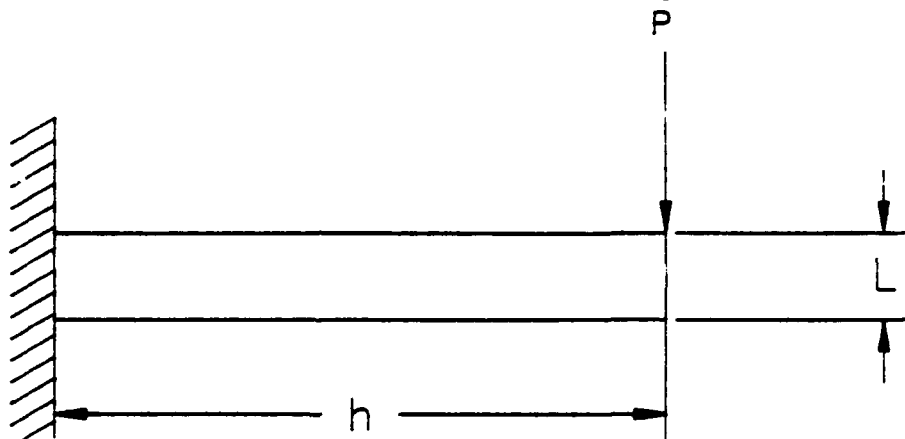


Figure 6. A cantilever beam used for estimating the error due to bending effect in measurement of strain.

The total deflection  $\Delta_T$  is a sum of deflections due to bending  $\Delta_b$  and shear  $\Delta_s$  and is given as [14]

$$\Delta_T = \Delta_s + \Delta_b \quad (25)$$

$$= 6Ph/5AG + Ph^3/3EI \quad (26)$$

where E and G are material Young's and shear moduli, A and I area and moment of inertia of the beam. For elastomers  $E = 3G$ , and for a rectangular beam  $A = bL$  and  $I = \frac{1}{12} bL^3$ . Thus Equation 21 can be expressed

$$\Delta_T = \frac{6Ph}{5AG} \left[ 1 + \frac{10}{9} \left( \frac{h}{L} \right)^2 \right] \quad (27)$$

where  $b, L,$  and  $h$  are sample dimensions. Equation (27) shows bending in the simple shear deformation is minimized when the sample length/thickness ratio is kept sufficiently large. If  $L/h$  is not large enough the strain and consequently stress distribution will not be uniform. Furthermore, Equation 19, used for shear strain calculation, will overestimate the shear strain resulting in lower modulus. Percent error in shear strain calculated from Equation 27 is summarized in Table I.

**Table I:** An estimate of the error in shear strain due the bending in samples of high length to thickness ratios.

<u>Length/Thickness</u>	<u>Error in Shear Strain</u>
2	25%
4	7%
8	1.7%
16	0.4%

This shows that sample length/thickness must be above 10 to avoid significant error in shear strain.

### **Sample Resonance and stiffness**

Sample dimensions were checked to insure that the resonance frequency was well above the highest frequency of interest. The lowest natural frequency was for the tuning fork type mode of the outer mount [3]. This frequency was about 3 time the highest frequency of measurements. Also, it is important to have sample mounting fixture stiffness much higher than the polymer being tested. This is accomplished by selecting a relatively stiff material for sample mounts, such as metals.

### **Mass Cancellation and Difference Circuits**

The performances of the mass cancellation and acceleration difference circuits were checked to ensure the accuracy of measurements of each circuit was within 1% of the actual value. Such an high accuracy requires closely phase matched sensors. Since the difference is inherent property of the measurement setup, the accuracy can be increased by programing the correction factors in computer and applying to the data. However, it is important to assess the performance these circuits.

## **RESULTS**

### **Validation of Test Data**

In order to investigate the errors caused by the wave and bending effects, samples of Neoprene and NBR compound with four different thicknesses were used . Note that all measurements described below were made using a random noise input unless otherwise stated explicitly. The Equation 24 provides a direct assessment of upper frequency for the onset of

wave effect. Figure 7 is a plot of the magnitude and phase of  $F(\omega)/\ddot{x}_0(\omega)$  versus frequency for the 1.59mm Neoprene specimen ( $L/h=16$ ). Both ratios are seen to be constant up to about 2500 Hz. Above that frequency the ratios begin to change because the inertia of the specimen was no longer negligible. Note that the phase angle appeared more sensitive to wave effects. Similar results were obtained for the other Neoprene and NBR specimens. The frequencies where the ratios began to deviate were directly proportional to the length/thickness ( $L/h$ ) ratios of the samples.

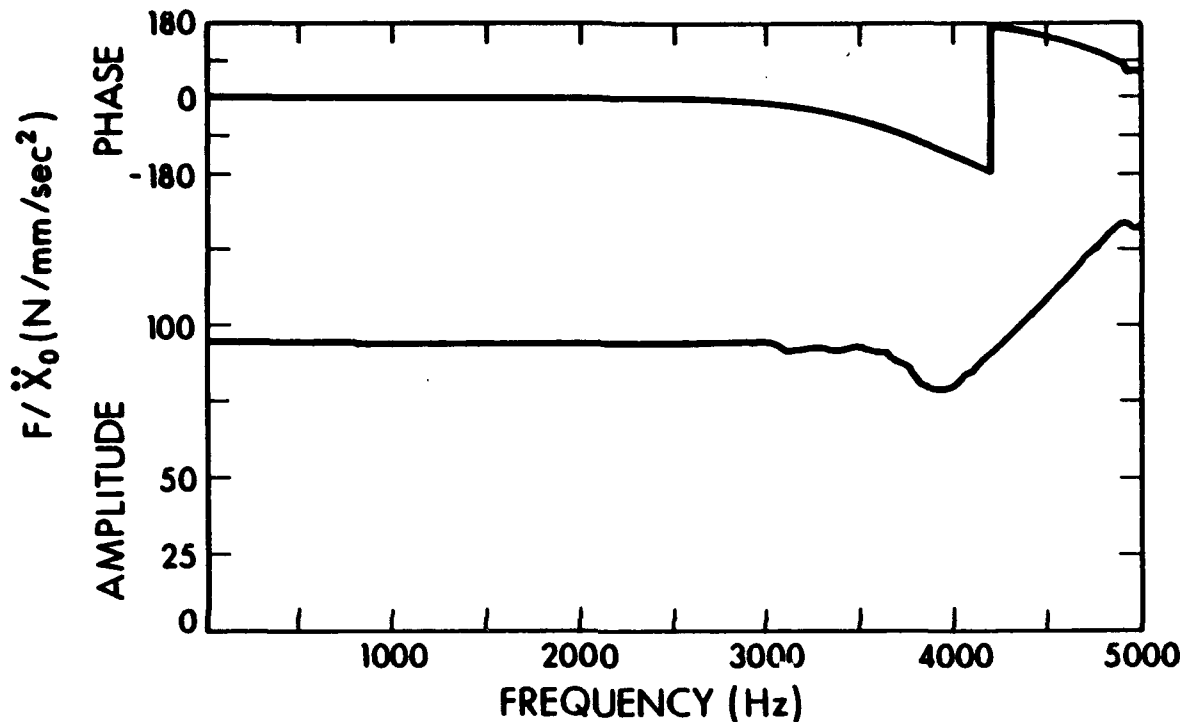


Figure 7. Acceleration impedance of a neoprene sample with 1.59 mm thickness.

The frequencies corresponding to the onset of wave effects were used in equation 21 to determine wave length/thickness ratio. In all cases the critical ratios were 14 to 16. This was midway between previous estimates; Schrag [15] estimated 20 on theoretical considerations; Ferry [1] estimated 10 on the basis of experimental results.

A quantitative determination of the inertia and bending effects was made by examining the apparent storage modulus data for four different thickness samples of the neoprene compound. The material data are plotted as functions of frequency in Figure 8. The word "apparent" is here used to indicate that the data could not be considered to represent true storage modulus yet. Results of Figure 8 indicate that the apparent modulus first increases and then decreases with frequency (in some cases it increases again). The frequency at which the local maximum occurs decreases as the specimen thickness increases, being about 2500 Hz, 1000 Hz, 400 Hz, and 175 Hz for the 1.59mm, 3.18mm, 6.35mm, and 12.8mm samples respectively. This behavior is probably caused by the onset of sample inertia effects. A detailed discussion of this phenomenon is given in references [16,17]. Also, these frequencies

were about the same as those obtained by  $F(\omega)/X_0(\omega)$  versus frequency plots of different thickness samples of both elastomers.

Figure 8 also shows that the apparent storage modulus decreases directly with the sample length to thickness ratio,  $L/h$ . At frequencies below the onset of inertia effects the apparent storage moduli for the  $L/h = 8, 4,$  and  $2$  specimens were about 3%, 8%, and 18% smaller, respectively, than the thinnest sample ( $L/h = 16$ ). These are approximately the same as theoretically predicted in Table 1 and those reported in the literature [27,28].

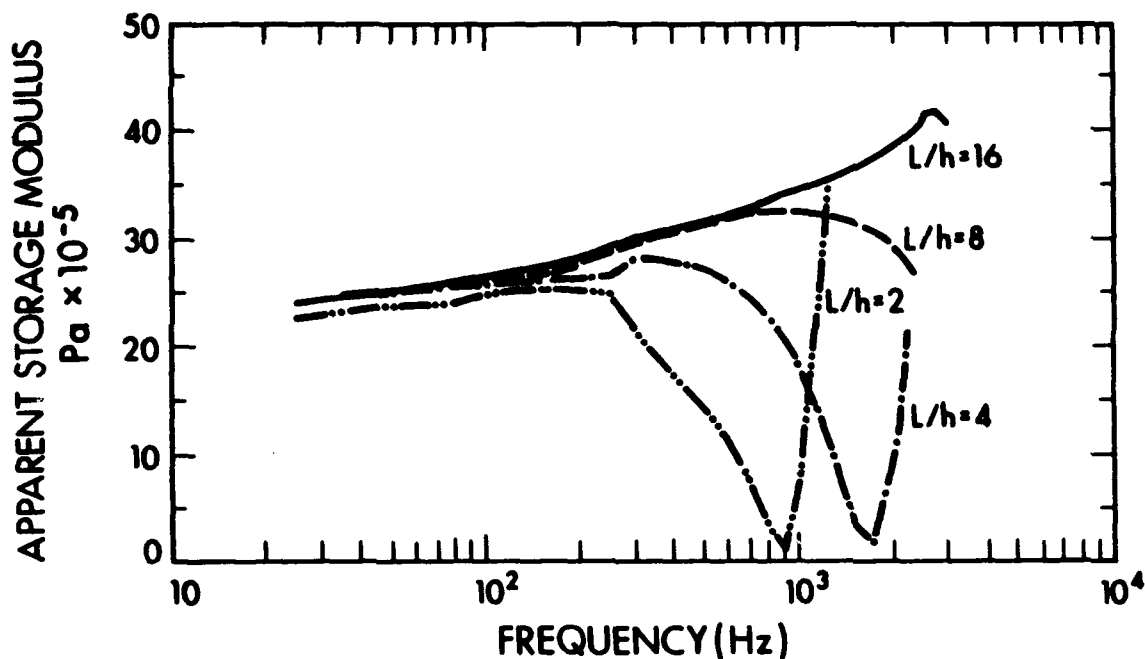


Figure 8. Apparent storage modulus of the four different thickness samples of neoprene. The data were used to assess the inertia and sample geometry effects.

#### Determination of Material Property

The foregoing analysis indicates that the FTMA provides a convenient way of estimating the sample geometry and wave effects. The samples with  $L/h = 16$  will provide sufficiently accurate material data up to 2,500 Hz. In order to check the accuracy of the data obtained by FTMA technique, measurements were also made using two other conventional methods. Figure 9 shows a typical result of directly comparing three methods for determining storage modulus on the same sample.

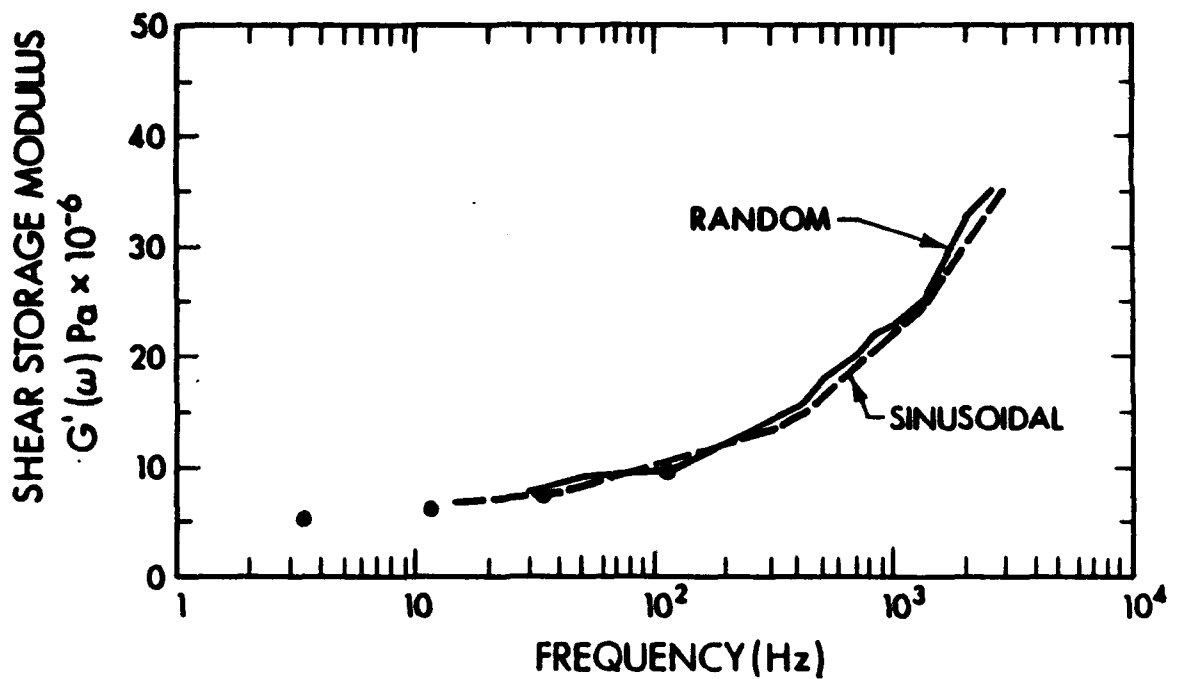


Figure 9. Comparison of the storage modulus of NBR determined by three different methods.

The points were determined with a commercial Rheovibron. The dashed line was results with forced vibration using single frequency sinusoidal inputs. The solid line shows FTMA data from random noise inputs. For further verification of FTMA technique, the loss modulus of NBR obtained by all three methods is shown in Figure 10. Again, the agreement between data is excellent.

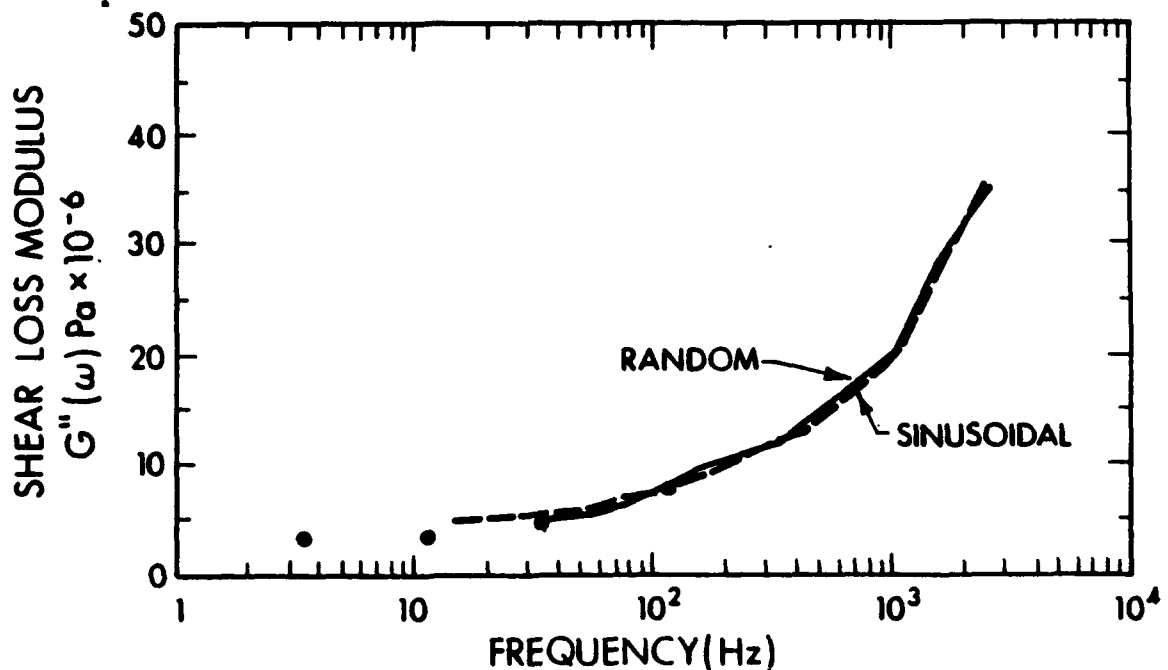


Figure 10. Comparison of the loss modulus of NBR determined by three different methods.

To determine material properties over a wide range of frequency and temperature, data were obtained at 20 different temperatures between 4°C and 74°C. Figure 11 shows NBR storage modulus versus frequency at various temperatures. Note that low temperature data showed high noise at lower frequencies. Similarly, high temperature data were distorted at upper frequency end. Accordingly, only appropriate data were kept for master curve construction. Figure 12 shows the master curve at 25°C for NBR storage modulus. Master curve was obtained by using our modeling procedure [22,23]. It compared very well with the conventional treatments. Similar results were also obtained for neoprene compound.

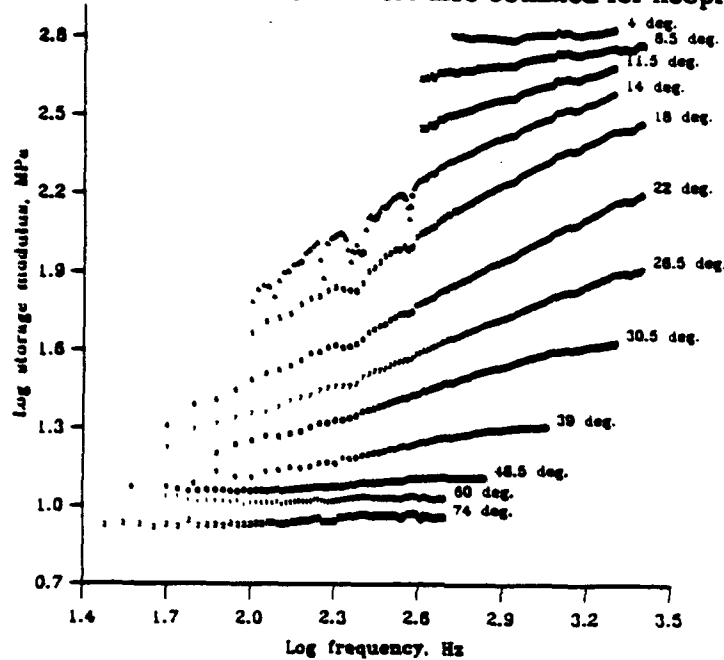


Figure 11. Storage modulus of NBR at various temperatures determined using FTMA.

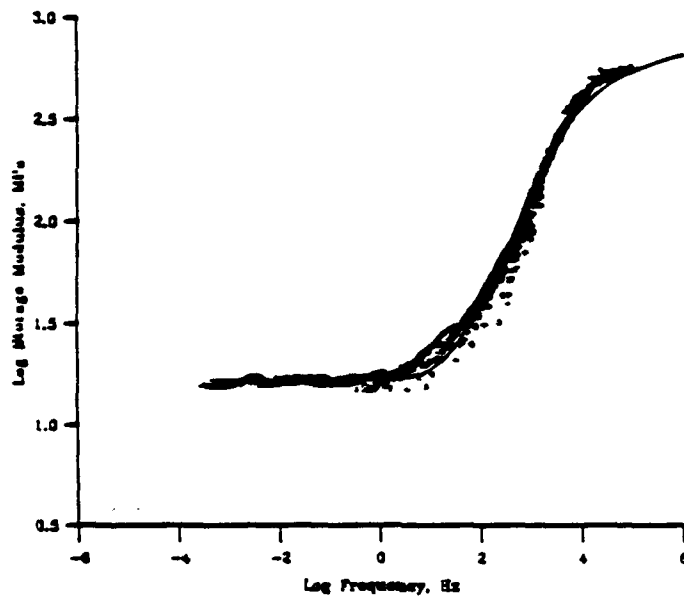


Figure 12. Storage modulus master curve for NBR at 25°C. The shift factors and line were determined using our constitutive equation.

## DISCUSSION

FTMA is a forced vibration test method based on direct measurement of stress and strain spectra. As with all forced vibration methods, FTMA is subject to spurious wave effects at high frequencies. The lower frequency limit is determined by transducers, signal conditioners, etc. The lower limit in this research was 35 Hz as determined by the inherent properties of the piezoelectric transducers. With different transducers and signal conditioners, FTMA should measure material properties down to much lower frequencies.

The primary feature of FTMA is the fact that a complete isotherm is obtained in just a few seconds. This saves time and effort compared to commercial single frequency instruments. It also gives better data in the case of sensitive materials, such as natural products, which may change during long exposure in a test chamber. Changes induced by energy dissipation within the sample are minimized. Another feature of FTMA is the fact that it readily provides direct assessment of sample inertia, bending and geometry effects. This would be very difficult with single frequency instruments.

The Fourier transform technique is perfectly general. It may be used also to study non-linear viscoelastic properties [10]. The moisture sensitive materials have tendency to exchange moisture when subjected to mechanical loading. The FTMA can be used to determine the viscoelastic properties of such materials because of short duration of the test. FTMA has great potential for applications in conjunction with a coupled theory of the effects of both temperature and strain histories on mechanical material properties.

## CONCLUSIONS

1. The Fourier transform mechanical analysis (FTMA) techniques can be used to measure the linear isothermal viscoelastic properties of polymers over a wider range of frequencies in a shorter period of time than is possible with currently used techniques.
2. An approximate sample length to thickness ratio of 8 or higher is required to avoid errors caused by bending effects like out of plane motion.
3. The shear stress wave length to sample thickness ratio must be 15 or more to avoid sample inertia effects.
4. The shear storage and loss moduli data obtained by random signal excitation compared well with those obtained using conventional sinusoidal signals, and with data obtained using a Rheovibron.
5. The viscoelastic measurement can be performed using standard vibration measuring equipment. Thus, the purchasing of a special purpose instrument can be avoided.

## ACKNOWLEDGEMENT

The helpful support and encouragement of Philip Morris management and the individual assistance of J. L. Banyasz and H. A. artung are gratefully acknowledged.

## REFERENCES

1. Ferry, J. D. *Viscoelastic Properties of Polymers*; 3rd. ed., John-Wiley & Sons Inc.: New York, 1980; Chs. 6, 7.
2. S. N. Ganeriwala and H. A. Hartung, in *Sound and Vibration Damping with Polymers*, Eds. R. D. Corsaro and L. H. Sperling, ACS Symposium Series 424, American Chemical Society, Washington D. C., (1990); also, J. Acoust. Soc. Am., in Communications.
3. Ganeriwala, S. N. Ph.D. Thesis, The University of Texas at Austin, 1982.
4. D. I. G. Jones, in *Proceedings of Damping '91*, Ed. J. Pearson, L. Rogers, 13-15 February 1991, San Diego, California, pp. EBD-1 to EBd-18.
5. Gehman, S. D. *Rub. Chem. Tech.* 1957, 30, 1202-1250.
6. Abolafia, O. R. *Survey of methods used to determine the dynamic mechanical properties of polym.*, U. S. Dept. of Commerce, office of Tech. Serv., Tech. rep. 2060, Sept. 1954.
7. Ward, I. M. *Mechanical Properties of Solid Polymers*, Wiley-Interscience, Inc.: New York, 1983; Chs. 5-7.
8. Boyer, R. F. *Polymer Characterization*, Ed. Craver, C. D.; Advances in Chemistry Series 203; ACS: Washington, D. C., 1983; pp. 3-25.
9. Medalia, A. I. *Rub. Chem. Tech.*, 1978, 51, 3, 437-523.
10. Ganeriwala S. N. and Rotz C. A., *Polym. Eng. Sci.* 1987, Jan., 27, 2, pp. 165-178.
11. Christensen, R. M. *Theory of Viscoelasticity an Introduction*, 2nd. ed., Academic Press Inc.: New York; 1982; Ch. 1.
12. Greenberg, M. D. *Foundation of Applied Mathematics*, Prentice-hall: Englewood Cliffs, N. J.; 1978; ch. 5.
13. Fitzgerald, E. R., Personal Communications, Department of Mechanical Engineering, The Johns Hopkins University, Baltimore, Maryland.
14. Popov, E. P. *Introduction to mechanics of solids*; Prentice-Hall, Inc.: Englewood Cliffs, N. J.; 1968; pp. 484-487.
15. Schrag, J. L. *Trans. Soc. Rheo.*, 1977, 21, 3, 399-413.
16. Harris, C. M. and Crede, C. E. Ed. *Shock and Vibration Handbook*, 2nd. ed., McGraw-Hill Book Co.: New York; 1976; ch. 30, pp. 52-56.
17. Snowdon, J. C. *J. Sound Vib.*, 1965, 2, (2), 175-103.
18. Parsons, J. S., Yates, Wallace, and Scholoss, *The measurement of dynamic properties of materials using Transfer Impedance Technique*, Report 2981, Naval Ship R & D center, Washington, D. C., April, 1969.
19. Ganeriwala S. N. and Hartung H. A., in *Constitutive Laws for Engineering Materials: Recent Advances and Industrial and Infrastructure Applications*, Eds. C. S. Desai, E. Krempl, G. Frantziskonis, and H. Saadatmanesh, ASME book Series, ASME Press, New York, (1991). and *J. Chem. Phys.*, in Progress.
20. Ganeriwala S. N., in *Proceeding of Proceedings of Damping '93*, Ed. J. Pearson, L. Rogers, February 23-25, 1993, San Francisco, California.
21. Ganeriwala, S. N. *Vibro-Acoustic Characterization of Materials and Structures*, Ed. P. K. Raju, NCA-Vol. 14, ASME, New York, 1992, pp. 1-12.

## **DYNAMIC COMPRESSIBILITY APPARATUS**

**Wayne T. Reader**  
**Vector Research Company, Inc.<sup>1</sup>**

**Fred Schloss**  
**Wilcoxon Research<sup>2</sup>**

**N. Scott Emery**  
**Vector Research Company, Inc.<sup>1</sup>**

### **ABSTRACT**

Foam rubbers manufactured with very lossy viscoelastic polymers are frequently used as light weight damping layers. This paper describes an apparatus assembled to measure the complex dynamic compressibility  $K = K' (1 + i\eta)$  of such damping materials, where  $K'$  is the elastic modulus and  $\eta$  is the loss factor ( $\tan \delta$ ). The modulus and loss factor are characterized for frequencies 50 Hz to 10 kHz by driving a rigid mass against a specimen of the foam. The principles which govern operation of the apparatus are described, as are the limitations faced by the technique. Measurements are presented for a variety of foam rubber specimens.

---

1 Suite 700, 2101 East Jefferson Street, Rockville, MD 20852.  
Tel: (301) 816-5500; Fax: (301) 816-5517.

2 Wilcoxon Research, 21 Firstfield Road, Gaithersburg, MD 20878.  
Tel: (301) 330-8811; Fax: (301) 330-8873

## INTRODUCTION

Foam rubbers manufactured with very lossy viscoelastic polymers are used as light weight damping layers and, particularly for submerged structures, as sound isolation layers. In either application, the dynamic compressibility may characterize the acoustic performance of the foam or may define quality assurance parameters during manufacture.

A simple apparatus has been assembled, primarily from commercially available components, to determine the complex compressibility as a function of frequency over the range 50 - 10,000 Hertz. This paper describes the theoretical basis for the technique, components of the apparatus, and operation of the equipment to determine the compressibility of several available foam rubbers.

## THEORETICAL BASIS

Figure 1 illustrates the principle forming the basis of the technique. The foam rubber layer of thickness "h" is sandwiched between a rigid mass, M, and a rigid immobile base. The mass is driven by a force, F(t), and its induced acceleration is  $\ddot{x}(t)$  determined. The driven motion of the mass/foam system is assumed equivalent to the motion of the simple harmonic oscillator depicted in Figure 1.

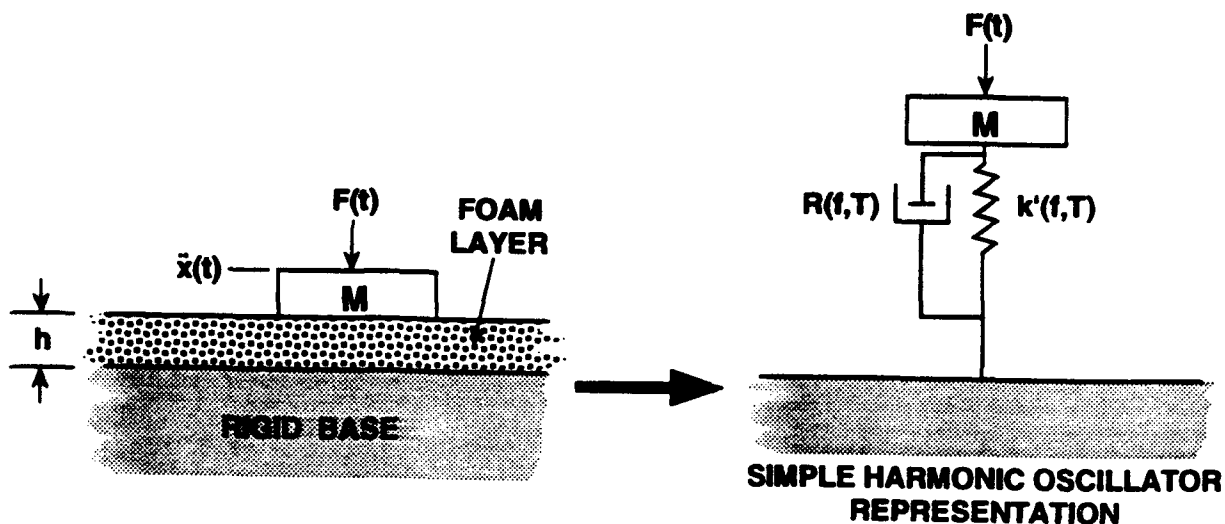


Figure 1. Measurement of the compressibility of a foam layer.

In essence, the foam layer is characterized as a spring with stiffness  $k'(f,T)$  in parallel with a dashpot characterized by a damping coefficient  $R(f,T)$ . Both the stiffness and damping coefficients are assumed to depend upon frequency,  $f$ , and temperature,  $T$ , in deference to the frequency and temperature dependence of the viscoelastic polymer used to manufacture the foam.

### COMPLEX STIFFNESS OF A SIMPLE HARMONIC OSCILLATOR

The motion of the simple harmonic oscillator is described by the equation:

$$M \ddot{x}(t) + R(f,T) \dot{x}(t) + k'(f,T) x(t) = F(t) \quad (1)$$

where  $x(t)$ ,  $\dot{x}(t)$ , and  $\ddot{x}(t)$  are the displacement, velocity, and acceleration, respectively, of the mass.

The harmonic excitation equation (1) can be solved for the complex stiffness:

$$\bar{k}(f,T) = \omega^2 \left[ M - \frac{F_0}{\ddot{x}_0} \right] \quad (2)$$

where  $F_0$  and  $x_0$  are the phasor amplitudes of the harmonic force and displacement, and  $\bar{k}(f,T)$  represents the complex stiffness:

$$\bar{k}(f,T) = k'(f,T) \left[ 1 - \frac{i\omega R(f,T)}{k'(f,T)} \right] \quad (3)$$

Complex stiffness can also be represented:

$$\bar{k}(f,T) = k'(f,T) (1 - i\eta) \quad (4)$$

Here, the complex stiffness is presented in terms of the elastic stiffness  $k'(f,T)$  and loss factor  $\eta(f,T)$  of the foam.

Combining Eq (4) and (2) yields for the stiffness:

$$k'(f,T) (1-i\eta) = \omega^2 \left[ M - \frac{F_o}{\ddot{x}_o} \right] \quad (5)$$

Equation (5) forms the basis for determining the foam stiffness and, as will be seen, the compressibility. Measurement of the amplitude and phase of the ratio  $F_o/\ddot{x}_o$  in conjunction with the mass  $M$  are sufficient to determine the elastic and loss components of the compressibility.

### CONVERSION OF STIFFNESS TO COMPRESSIBILITY

The compressibility  $K$  is defined as the inverse of the bulk modulus  $B$ , i.e.  $K = 1/B$ . Applying the definition of the bulk modulus, the compressibility is given by:

$$K = - \frac{1}{V} \frac{\partial V}{\partial P} \approx - \frac{\frac{\Delta V}{V}}{\Delta P} \quad (6)$$

where  $\Delta V/V$  is the volume strain produced by the change in hydrostatic pressure  $\Delta P$ . Applying equation (6) to the apparatus of Figure (1):

$$K \approx - \left[ V \frac{\Delta P}{\Delta V} \right]^{-1} = - \left[ h \cdot \frac{\Delta P}{\Delta x} \right]^{-1} \quad (7)$$

Recognizing that  $\Delta P/\Delta x$  is equal to the stiffness per unit area  $k_A(f,T)$ , the compressibility is found to be

$$K(f,T) \approx - [h \cdot k_A(f,T)]^{-1} \quad (8)$$

This latter equation explicitly displays the dependence of the compressibility upon the frequency and temperature.

Combining Eq (7) and (2), the compressibility is found to be given by:

$$K(f,T) = - \frac{A}{\omega^2 h} \left[ M - \frac{F_o}{\ddot{x}_o} \right]^{-1} \quad (9)$$

## APPARATUS AND MEASUREMENT PROCEDURES

### EQUIPMENT

A schematic of the dynamic compressibility apparatus is shown in Figure 2. Test specimens are sandwiched between a rigid steel base and an aluminum drive mass,  $M_A$ . The aluminum mass is driven by a Wilcoxon Research Model F3 shaker containing an integral model Z602WA impedance head. The shaker's input signal is a swept sine function generated by an HP 3562A Dynamic Signal Analyzer and amplified by a Bogen Model HTA-125A Power Amplifier.

The F3/Z602WA accelerometer and force gage generate acceleration and force data which are collected and processed by the signal analyzer. The accelerometer and force gage are powered by an HP E3611 DC power supply. Data are plotted on an HP 7550A Graphics Plotter and are stored on disk by an HP 9836 CU computer via the system's HP-IB interface.

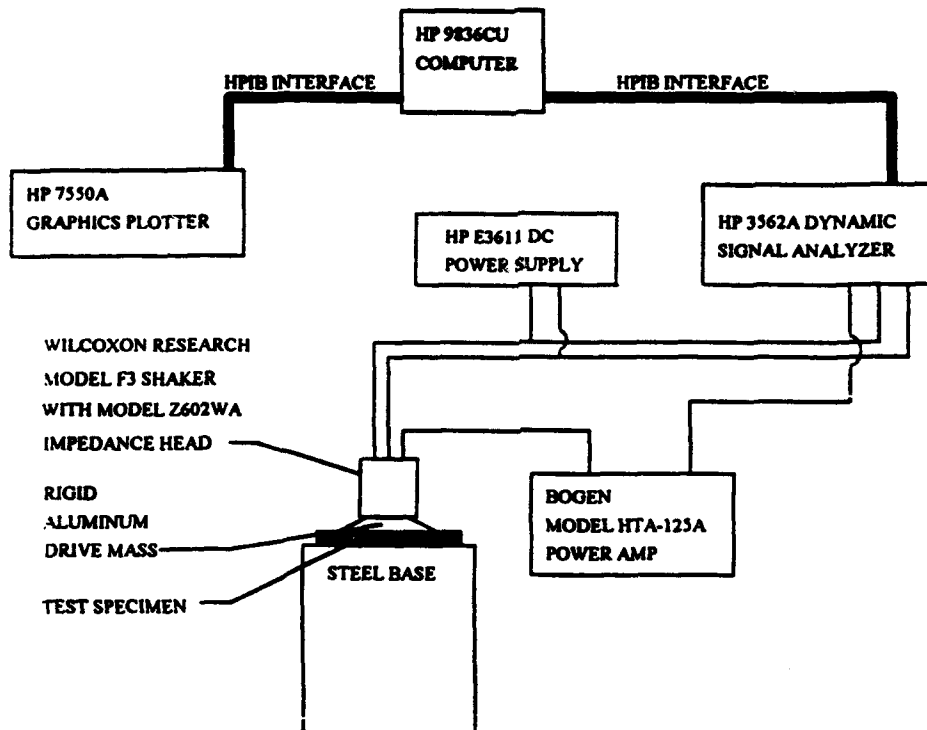


Figure 2. Dynamic compressibility equipment schematic.

## CALIBRATION OF THE APPARATUS

Equation (5) provides the basis for calibration of the apparatus. If the mass is driven through the vibration generator while the unit is freely suspended without contacting the foam, the analyzer output  $[F_o/\ddot{x}_o]$  represents the calibration factor CF of the apparatus. For this condition, Eq (5) becomes:

$$\left[ \frac{F_o}{\ddot{x}_o} \right]_o = CF = M \quad (10)$$

Hence the system sensitivity is simply:

$$\text{System Sensitivity} = CF/M \quad (11)$$

The mass M to be used here is the total mass between the force gage used to measure the force and the foam. Hence:

$$M = M_{FG} + M_A \quad (12)$$

where  $M_{FG}$  is the mass below the force gage internal to the impedance head, and  $M_A$  is the mass of area A added between the impedance head and the foam layer.

## MEASUREMENT TECHNIQUE

There are 3 steps to measuring the dynamic compressibility of a foam material: calibration, data collection, and calculation of compressibility. Calibration involves determining the frequency response, force divided by acceleration, of the mass-shaker system while it is freely suspended without contacting foam. Data collection is the measurement of a foam's frequency response. The material's compressibility is calculated from the foam's frequency response and the mass-shaker's impedance.

The calibration factor,  $CF(f)$ , shown in Figure 3 is the mass-shaker system's impedance,  $F/\ddot{x}$ . So that the inertial forces of the driven mass are the only forces present,  $CF(f)$  is measured with the F3 in the horizontal position and without a foam test specimen. The shaker is driven by a sine function swept between 20 and 10,000 Hz at a rate of 19.4 seconds per decade. Each data point is the average of 5 measurements. No data is collected above 10 kHz because the driven mass has a fundamental resonance slightly above 10 kHz.

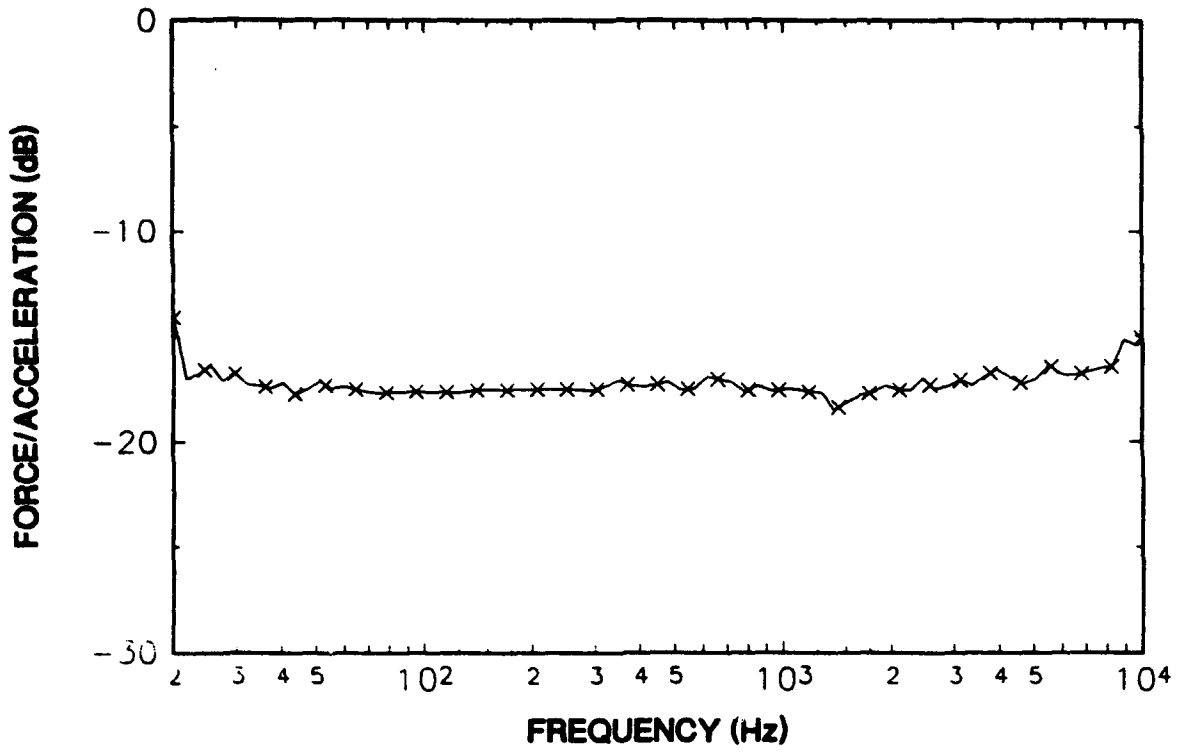


Figure 3. Calibration factor, CF.

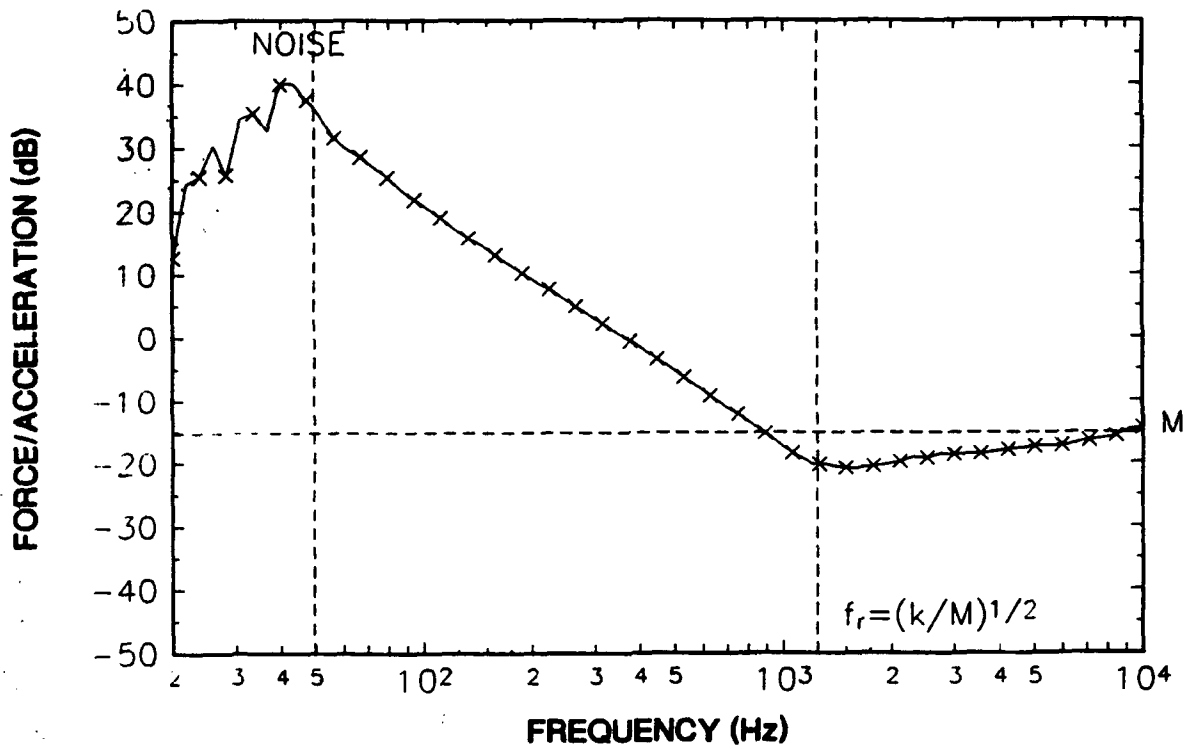


Figure 4. Measured frequency response of a typical foam.

It will be shown below that this is not a critical limit, since foam/mass resonances of samples tested occur below 10 kHz.

Test specimens are secured between the steel base and the rigid drive mass with double sided tape. For thin specimens, multiple foam layers may be tested to insure test accuracy. The shaker's input signal parameters during data collection are identical to the input signal parameters during calibration; 10-10,000 Hz at 19.4 seconds per decade with 5 averages. The frequency response,  $F/\bar{x}$ , of a typical foam is shown in Figure 4. The minimum value of  $F/\bar{x}$  which occurs at 400 Hz is due to the foam/mass resonance.

The next step is calculating the material's compressibility. The intermediate value  $R_w$  is calculated on the signal analyzer by subtracting the calibration curve,  $CF(f)$ , from the foam's frequency response curve and multiplying the resulting curve by  $(j\omega)^2$ .  $|R_w|$  of the tested foam specimen is shown in Figure 5. The compressibility, shown in Figure 6, is calculated using equation 13:

$$K(f,T) = \left[ \frac{A}{mh} \right] \frac{CF}{|R_w|} \quad (13)$$

Where  $h$  is the material thickness in cm,  $A$  is surface area of the rigid drive mass in  $cm^2$ ,  $m$  is the total mass below the force gage.

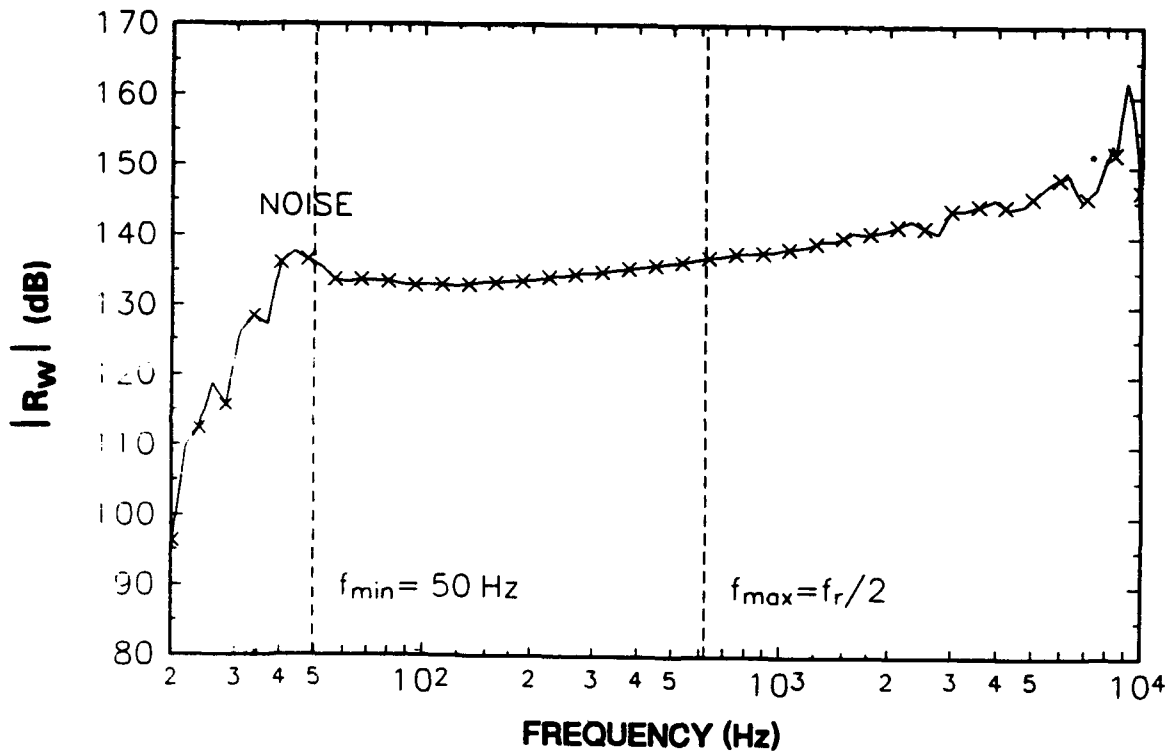


Figure 5. Calculated  $|R_w|$  of a typical foam.

The loss factor,  $\eta$ , of the foam is the imaginary component of  $R_w$  divided by the real component of  $R_w$  or simply  $\tan \delta$ , where  $\delta$  is the phase angle associated with  $R_w$ . The loss factor of the tested sample is shown in Figure 7. The foam's loss can be accurately measured only in the frequency range in which the foam/mass system is stiffness controlled. As the frequency exceeds resonance, the system becomes mass controlled. Thus, the loss factor can only be determined at frequencies significantly below the foam/mass resonance. In Figure 7, the maximum frequency at which the loss factor is usable is marked with a dotted line at 200 Hz. It may be seen that as the system approaches resonance the phase angle approaches 90 degrees, i.e. the apparent loss factor approaches  $\infty$ . Therefore, to remain within the stiffness controlled regime, the data used to compute the compressibility and loss factor will be restricted to those below  $f/2$ , i.e. one-half the resonant frequency.

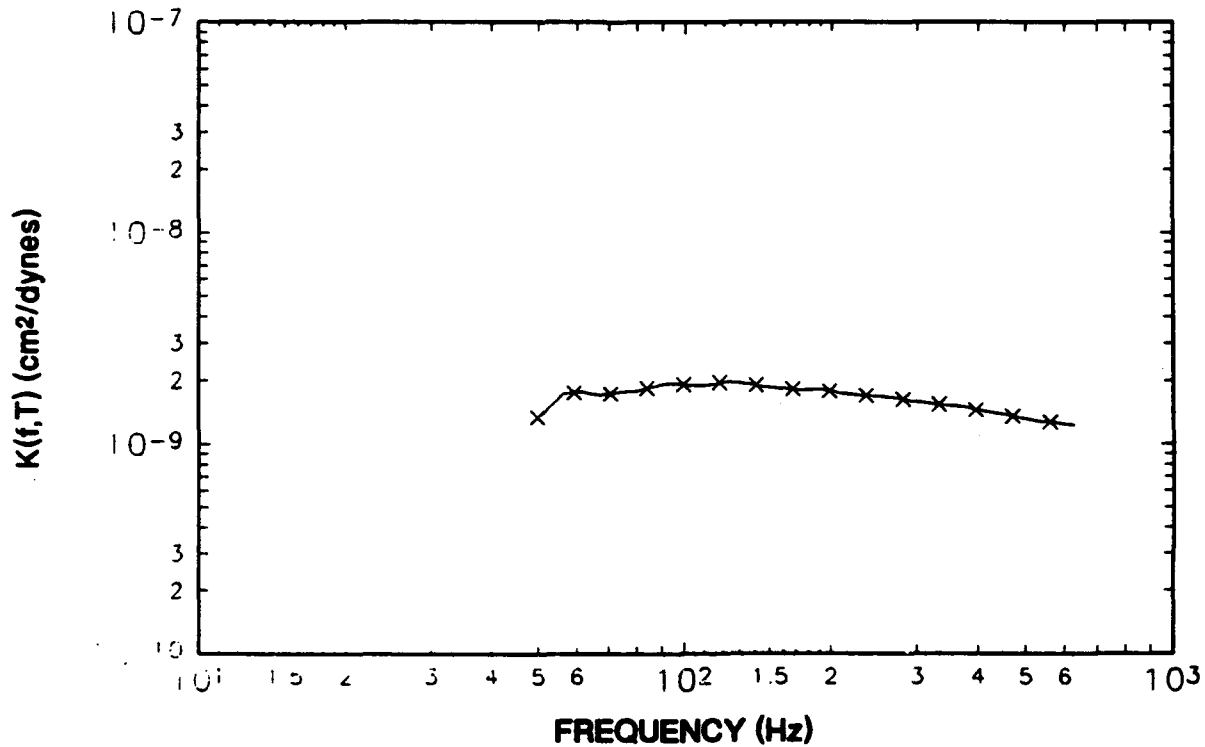


Figure 6. Dynamic compressibility of a typical foam.

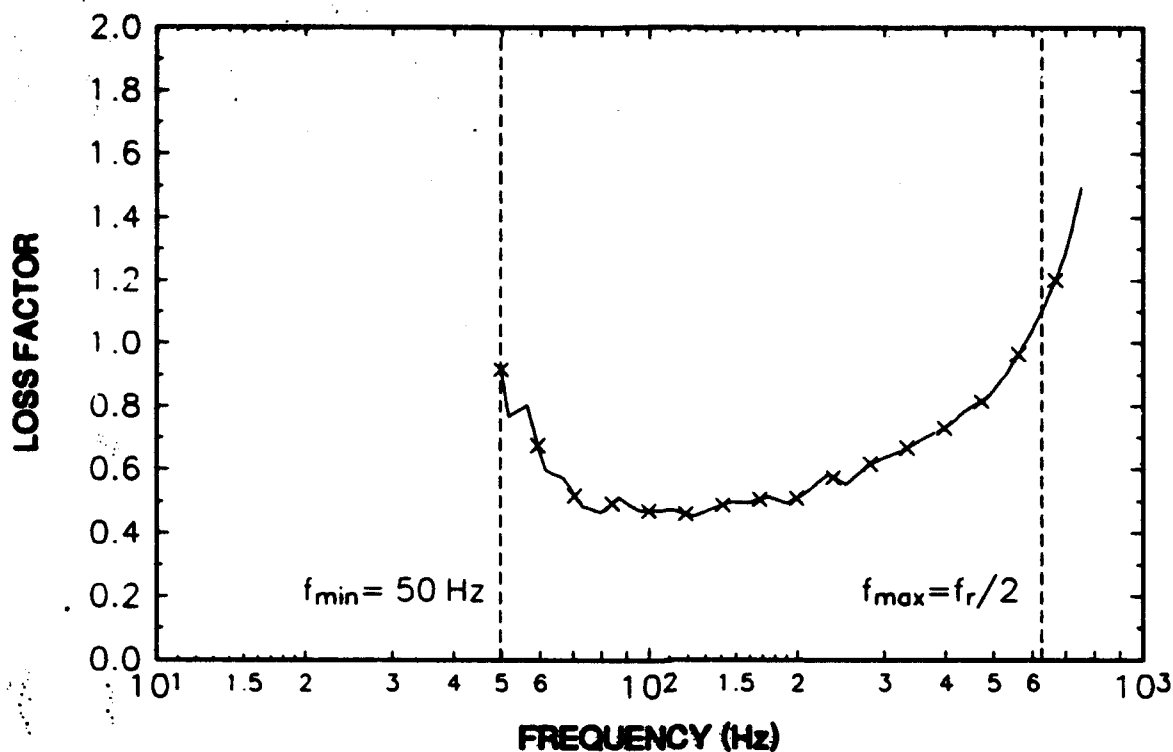


Figure 7. Loss factor ( $\tan \delta$ ) of a typical foam.

#### LIMITATIONS OF THE TECHNIQUE

The apparatus, as configured, suffers several limitations. The lower frequency limit of 50 Hz is essentially controlled by the resonant frequency of the vibration generator. Below its resonance frequency of approximately 50 Hz, the generated force falls off very quickly with decreasing frequency. A larger generator would decrease the lower frequency limit.

The upper frequency limit is controlled by the foam/mass resonance. As illustrated in Figure 8, the ratio  $F_0/\bar{x}_0$  approaches the mass  $M$  after passing through the resonance frequency of the foam/mass system. Therefore, as can be seen from Eq (8), the difference  $[M - F_0/\bar{x}_0]$  approaches zero. This upper limit can be raised by decreasing the mass and therefore raising the resonance frequency; however, increases approaching an order of magnitude will be very difficult to achieve because the resonance frequency is proportional to the square root of the mass.

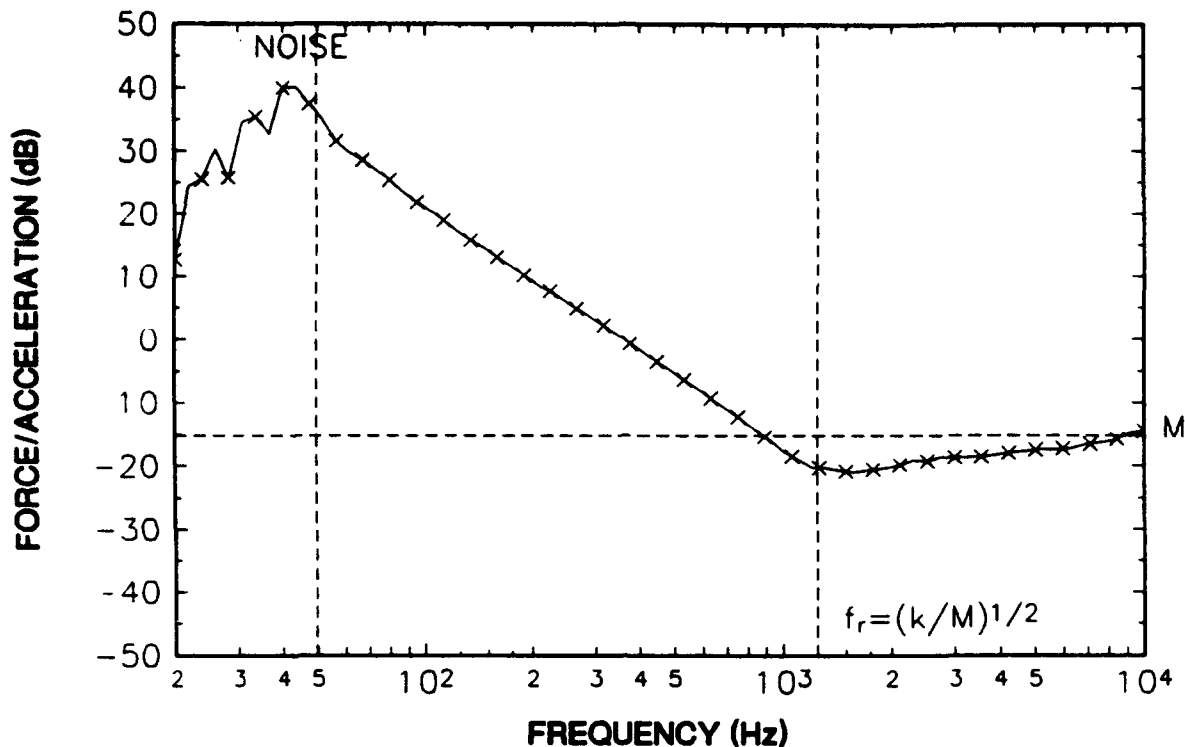


Figure 8. Measured frequency response of a typical foam showing effect of foam mass resonance on collected data.

## COMPRESSIBILITY MEASUREMENTS

The typical foam used as the example above provides an example of a material with a high mass/foam resonance relative to the Rubatex and Lauren foams presented below. Thus, compressibility and loss data of the typical foam can be obtained over a relatively broad frequency range. In addition the tested foam has a significant loss factor compared to the loss factor of the Rubatex and Lauren foams. In addition to the typical foam used as the example above, two series of test have been run to demonstrate determination of dynamic compressibility of foams. The first set of tests was performed on three commercially available foams manufactured by Rubatex. The second set of tests was performed on single and multiple layers of a silicone foam manufactured by Lauren Manufacturing.

## RUBATEX FOAMS

The three 1/2" thick Rubatex foams tested were R-415N, R-416H, and G-207N. Compressibilities and loss factors are shown in Figures 9 and 10 respectively. Due to the relatively small stiffness of the Rubatex foams, the frequency range is limited to between 50 and 200 Hz.

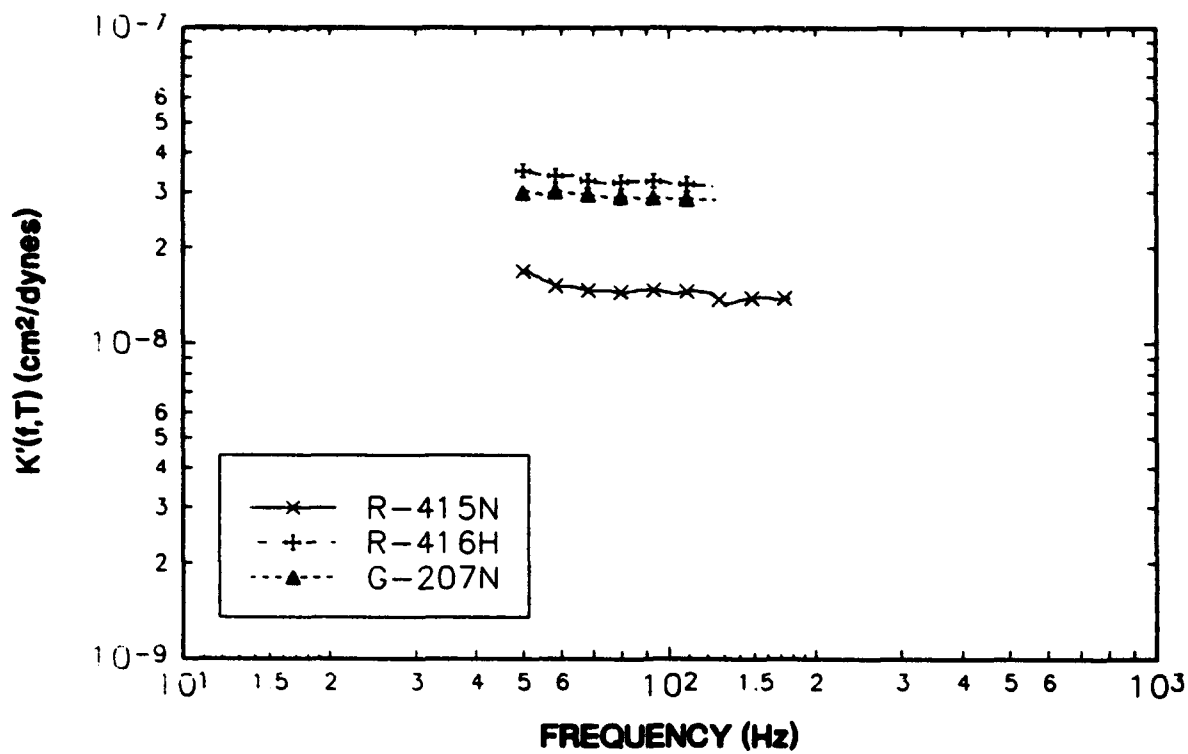


Figure 9. Compressibility of tested Rubatex foams.

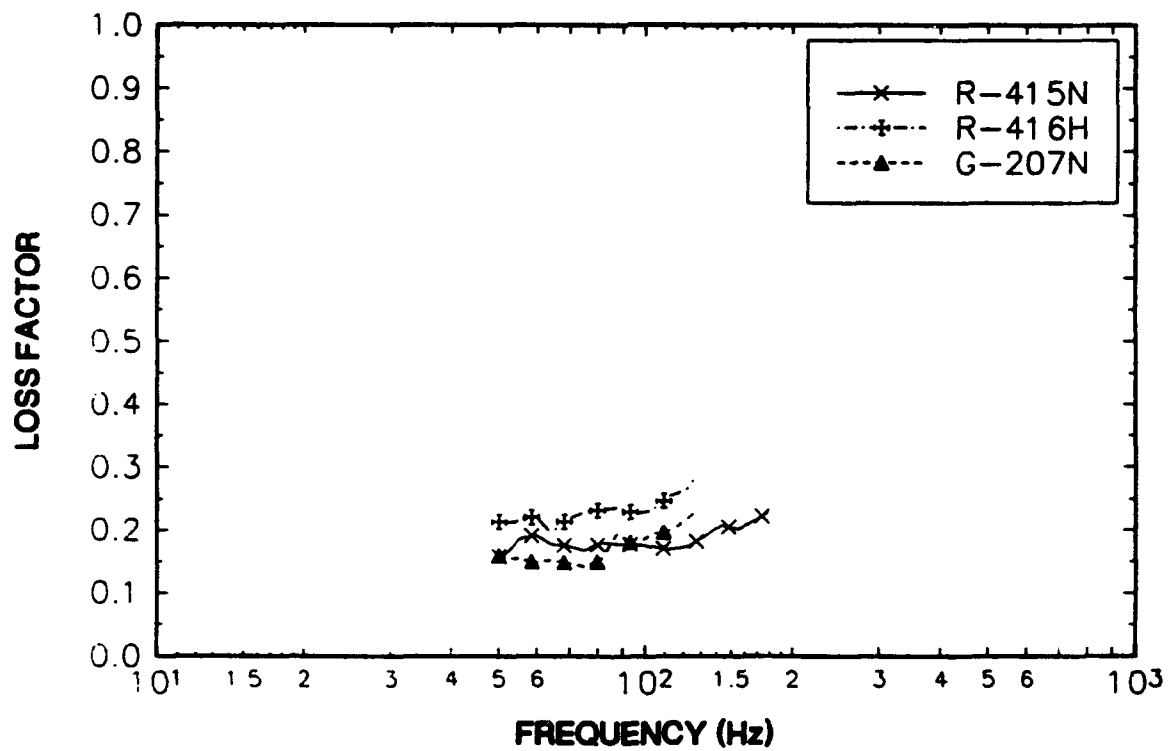


Figure 10. Loss factor of tested Rubatex foams.

## LAUREN SILICONE FOAM

For the series of tests performed on the Lauren silicone foam, the objective was to demonstrate the effect of material thickness on the compressibility measurement process. Figure 11 shows the effect of thickness on the system's frequency response and the foam/mass resonance. Three cases were run: one layer, two layers, and four layers. Each case effectively doubled the foam thickness of the previous case. Ignoring damping, this is analogous to placing 1, 2 and 4 springs of equal stiffness in series. As would be expected for a simple spring mass system, the mass/foam resonance is reduced by a factor of the  $\sqrt{2}$  and the foam's effective stiffness is decreased by approximately 6 dB for each doubling of the foam thickness. Only the frequency range of the material's compressibility shown in Figure 12 is affected by the number of layers since the material's thickness is a parameter in the compressibility calculation. The material's loss factor is shown in Figure 13.

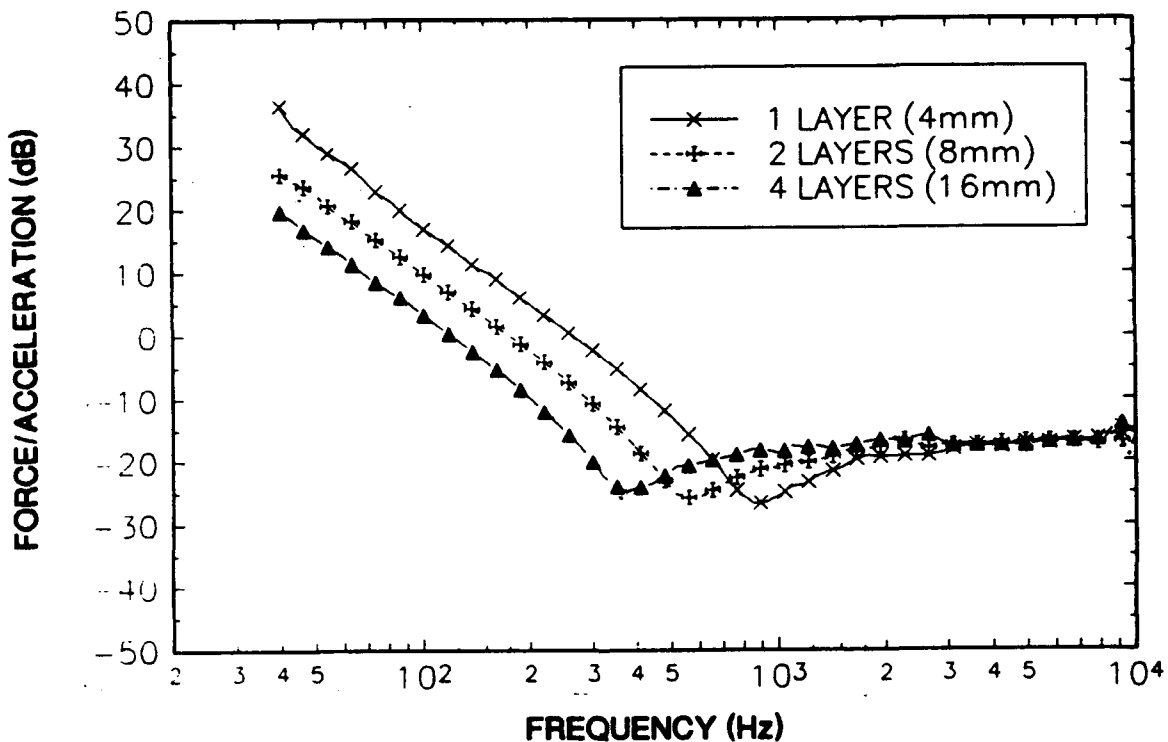


Figure 11. Frequency response of Lauren silicone foam showing effect of sample thickness on collected data.

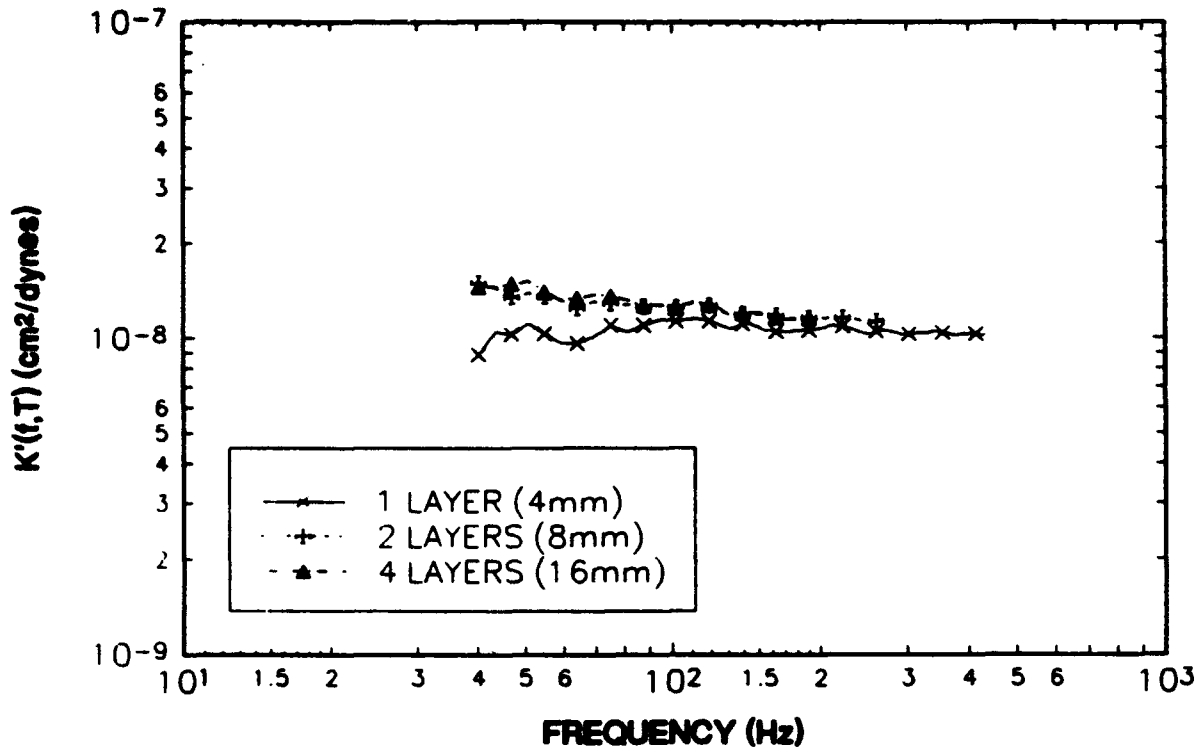


Figure 12. Compressibility of Lauren silicone foam.

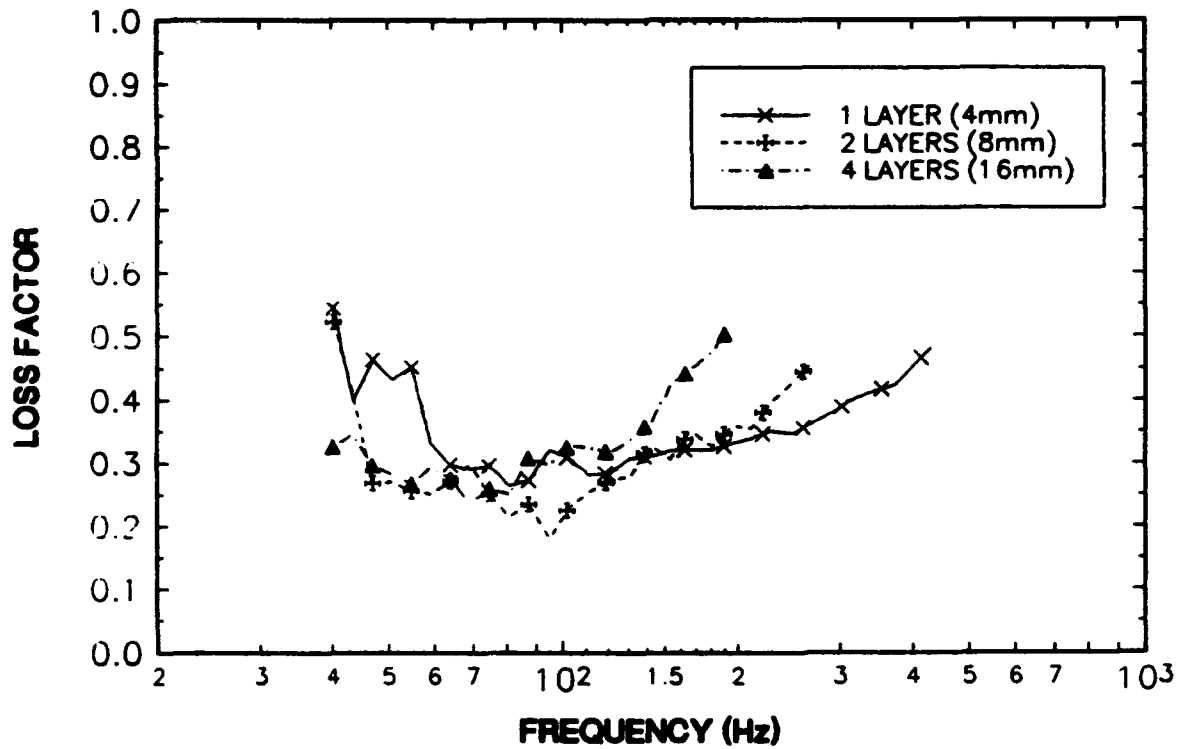


Figure 13. Loss factor of Lauren silicone foam.

## CONCLUSIONS

A system has been developed which determines a foams' compressibility,  $K(f,T)$ , and loss factor,  $\eta(f,T)$ , for frequencies below the resonance of the foam mass system. The compressibilities of five foams have been presented: a typical foam with a relatively high stiffness, three commercially available foams from Rubatex, and a silicone foam from Lauren Manufacturing.

It has been shown that the system's lower frequency limit is determined by the F3/Z602WA's resonant frequency of approximately 50 Hz, and the upper limit is defined by the foam/mass resonance. The foam/mass resonance is controlled by both the driven mass and the foam stiffness. The doubling of the silicone foam's thickness, which effectively reduces the system stiffness by a factor of 2, clearly demonstrates the relationship between foam stiffness and the foam/mass resonance. Since the foam stiffness is a material property, a light driven mass must be used to yield a desirably large frequency range.

# DYNAMIC DUROMETER MEASUREMENT OF YOUNG'S MODULUS AND LOSS FACTOR

Walter M. Madigosky and Ralph B. Fiorito  
Naval Surface Warfare Center\*

## ABSTRACT

The Shore hardness tester is used extensively throughout industry to determine the static modulus of materials. The new apparatus described here extends the capability of an indenter type tester into the dynamic regime, and provides a measurement of the dynamic shear or Young's modulus and loss factor as a function of frequency. The instrument, model and data of typical rubber samples are given and compared to other dynamic measurements.

## INTRODUCTION

The standard durometer has been used to measure the static "hardness" or resistance of materials to indentation. Various static models have been developed to quantify these measurements by relating the static Young's modulus and Poisson ratio of a viscoelastic material to the force of indentation, the penetration depth, and size (radius) of the indenter.

To our knowledge, an equivalent satisfactory dynamic model in which the indentation force is time dependent has not been developed analytically. Various empirical models, however, have been examined to model the interaction of transducers placed in contact with a viscoelastic slab to excite shear and compressional waves in the material. R. von Gierke<sup>1</sup> e.g. has produced such a model to examine the acoustic properties of living tissue. He assumes the transducer behaves as a hemispherical radiator whose diameter equals that of the cylindrical transducers used in his experiments. In this model, the radiation impedance of a vibrating sphere is related to the complex dynamical shear and compressional moduli of the material. This model, under certain approximations, can be used to infer the dynamic Young's modulus,  $E'$ , and loss factor,  $\delta$ . To perform these measurements the amplitude and phase of the driving force and acceleration of the transducer which is in contact with the material are measured.

We are examining the validity and applicability of such models experimentally by comparing the predicted results for  $E'$  and  $\delta$  to those obtained by more conventional methods such as those developed by Madigosky and Lee<sup>2</sup>, or other type of dynamic mechanical testing apparatus such as the dynamic mechanical thermal analyser (DMTA).

The goal of this study is to develop a model and simple apparatus which will allow a dynamical measurement of  $E'$  and  $\delta$  of a material in a manufacturing environment.

\*10901 New Hampshire Avenue, Silver Spring, MD. USA, 20903-5000, (301) 394-2464

## THEORY

The theoretical model we will first examine for measuring the dynamic response of a viscoelastic material to intrusion by a perturbing force is that developed by von Gierke to examine the acoustic properties of living tissue. The theory considers the medium to be homogeneous, isotropic, compressible, and viscoelastic. The probe perturbing the medium is a cylindrical transducer placed in contact with the surface of the medium. The transducer-medium interaction is modeled as a hemispherical radiator whose diameter equals that of the transducer.

The complex impedance of the medium which is defined as the ratio of force over velocity is related analytically to the complex shear and compressional moduli of the material which are defined as:

$$\mu = \mu_1 + j\omega\mu_2 = \mu_1(1 + \delta_S) \quad (1)$$

$$\lambda = \lambda_1 + j\omega\lambda_2 = \lambda_1(1 + \delta_L) \quad (2)$$

where  $\omega\mu_2/\mu_1 \equiv \delta_S$  is the shear loss factor and  $\omega\lambda_2/\lambda_1 \equiv \delta_L$  is the compressional loss factor.

The Young's Modulus is related to the shear modulus by

$$E \equiv E'(1 + j\delta_S) \equiv 3\mu \quad (3)$$

so that

$$E' \equiv 3\mu_1 \quad (4)$$

The radiation impedance  $Z_S$  of the sphere is

$$Z_S = -4\pi\rho\omega a^3 \cdot \frac{j/3 \cdot \left\{ \left(1 - 3j/ah - 3/a^2 h^2\right) - 2(j/ah + 1/a^2 h^2) \cdot \left[ \frac{3 - a^2 k^2 / (jak + 1)}{\left(1/a^2 h^2 + j/ah\right) a^2 k^2 / (jak + 1)} + [2 - a^2 k^2 / (jak + 1)] \right] \right\}}{\quad} \quad (5)$$

where  $a$  = radius of the sphere,

$$k^2 = \rho\omega^2 / (2\mu + \lambda) \quad (6)$$

and

$$h^2 = \rho\omega^2 / \mu \quad (7)$$

We have examined several limiting cases of  $Z_S$

a.  $\lambda_1 \gg \mu_2, \omega\lambda_2, \lambda_2 \approx 0$

This limit is achieved when  $ak \ll 1$ , then

$$Z_S \rightarrow Z_2 \equiv -2\pi\rho\omega a^3 j/3 \cdot (1 - 9j/ah - 9/a^2 h^2) \quad (8)$$

b. high loss materials ( $\omega\mu_2 \gg \mu_1$ )

$$Z_S \rightarrow Z_3 \equiv -2\pi\rho\omega a^3 j/3 \cdot (1 + 9(\mu_2/(2\rho\omega a^2))^{1/2} - 9j(\mu_2/2\rho\omega a^2)^{1/2} \cdot [1 + (2\mu_2/\rho\omega a^2)]^{1/2}) \quad (9)$$

c. low loss materials ( $\omega\mu_2 \ll \mu_1$ )

$$Z_S \rightarrow Z_4 \equiv -2\pi\rho\omega a^3 j/3 \cdot (\omega - 9\mu_1/\rho\omega a^2 - 9j[(\mu_1/\rho a^2)^{1/2} + \mu_2/\rho a^2]) \quad (10)$$

$Z_2$  and  $Z_4$  will be of primary interest for the materials with properties in the frequency range of interest (50 -1000 Hz).

A comparison of the real part of  $Z_S, Z_2$  and  $Z_4$  as a function of frequency when the sphere radius  $a = 1$  mm shows that the formulas for  $Z_2$  and  $Z_4$  are in excellent agreement with  $Z_S$  over a wide frequency range, and diverge from  $Z_S$  only at very high frequency.

Since it is straightforward to interpret  $Z_4$ , we will use it as the basis for an experimental method to obtain  $\mu_1$  and  $\mu_2$ .

The impedance  $Z_4$  can be interpreted as that of a simple oscillator. To see this, consider the equation of a forced harmonic oscillator

$$m\ddot{x} + k^*x = F \quad (11)$$

Here,  $k^*$  is complex to account for the case of viscous damping. The impedance of the oscillator  $Z \equiv F/\dot{x}$  can be obtained by assuming  $x = x_0 \exp(j\omega t)$  and  $F = F_0 \exp(j\omega t)$  and  $\dot{x} = j\omega x$ .

$$Z = mj(\omega - k'/\omega m - jk''/\omega m) \quad (12)$$

where  $k^* = k' + jk''$

Comparing  $Z$  to the equation for  $Z_4$  we see that  $Z_4$  behaves like an oscillator with mass  $\equiv m = 2\pi a^3 \rho / 3$  (which is half the mass of a sphere), stiffness  $\equiv k' = 6\pi a \mu_1$  and frictional resistance  $\equiv k'' = 6\pi a^2 \rho \cdot [(\mu_1/\rho)^{1/2} + \mu_2/ap]$  as observed by von Gierke.

If then, a hemispheric impedance head of real mass  $M$  is placed in contact with the viscoelastic material, and it is assumed that the impedance of the material is ideally modeled by that of the radiating sphere model under the approximation  $Z_S = Z_4$  for the frequency range of interest, the acceleration measured by such an impedance head is given by:

$$F/\ddot{x}_{\text{measured}} = M + Z_4/j\omega = (M + m) - k^*/\omega^2 \quad (13)$$

Then, in view of the interpretation of  $k'$  and  $k''$  given above, we may write:

$$k' = 6\pi a \mu_1 = \omega^2 (M + m - \text{Re}(F/\ddot{x}_{\text{meas}})) \quad (14)$$

$$k'' = 6\pi a^2 \rho = \omega^2 [(\mu_1/\rho)^{1/2} + \mu_2/ap] = \omega^2 m \text{Im}(F/\ddot{x}_{\text{meas}}) \quad (15)$$

We can then use these equations to calculate  $E' = 3\mu_1$  and  $\delta = \omega\mu_2/\mu_1$ .

Similarly the expression for  $Z_2$  can be inverted to produce these values by solving for the variable  $1/h$  in equation (8).

## EXPERIMENT

We have performed experiments on a variety of viscoelastic materials to test the validity and applicability of the model given above.

To do this we employ a compact Wilcoxon piezoelectric shaker- impedance head to which we can attach indentors of various diameters, a Hewlett-Packard noise generator / spectrum analyzer which drives the shaker with white noise and measures the real and imaginary parts of the acceleration (amplitude and phase of the driving force). With the help of a computer, the complex impedance of the excited material is calculated and the real and imaginary parts are used to produce the Young's modulus and loss factor as described above.

Tables I. and II. show a comparison of experimental results on generic nitrile and urethane rubber samples using the method described above and those obtained using a dynamic mechanical thermal analyser (DMTA) made by Polymer Laboratories. The DMTA was used to measure the Young's modulus and loss factor as a function of temperature using the frequencies 0.3, 1, 3, 10 and 30 Hz. The data was then shifted to the frequency domain by using the standard Williams-Landel-Ferry (WLF) technique.

**Table I. Comparison of Results on Nitrile Rubber**

F(Hz)	Dynamic Durometer Method		DMTA Method	
	E (m Pa)	Loss Factor	E (m Pa)	Loss Factor
50	4.3	0.3	7.5	0.2
100	5.3	0.47	7.7	0.25
200	7.0	0.34	7.9	0.3
300	7.5	0.31	8.5	0.33
400	7.8	0.25	8.9	0.35
500	8.1	0.27	9.5	0.4

**Table II. Comparison of Results on Urethane Rubber**

F (Hz)	Dynamic Durometer Method		DMTA Method	
	E (m Pa)	Loss Factor	E (m Pa)	Loss Factor
200	54	0.15	63	0.085
300	59	0.16	66	0.090
400	61	0.10	68	0.094
500	62	0.11	70	0.097
600	70	0.17	74	0.100

These results indicate the good agreement between the two types of measurement. Further studies are being done to test the effect of indenter surface area and the effect of static contact pressure of the indenter.

In addition to the dynamic modulus measurements on cured materials, a study of the change in dynamic modulus as a function of time was made on a two component polyurethane (Techthane 13, Seaward International) as it changed from a viscous mixture to a cured solid. The results are given in Table III. A small disc, 0.8 cm diameter, was used. As can be seen from the data, this technique may be used to accurately determine the rate of cure and the state of cure in materials.

**Table III. Dynamic Cure Test of Polyurethane**

Time ( hours )	Young's Modulus (kPa)	Loss Factor
1	4	1.7
2	51	0.9
3	320	0.68
5	610	0.52
6	770	0.42
7	850	0.41
19	1150	0.38
31	1620	0.37
43	1850	0.37
53	1890	0.36
94	1980	0.34
182 ( 8 days )	2150	0.33

Similar rate and state of cure measurements can be obtained on epoxies and vulcanized rubbers, thus replacing current methods which provide only relative data.

#### REFERENCES

1. H. von Gierke et. al. , Physics of Vibrations in Living Tissues, J.Appld. Physiology, 4, p. 886-900, 1952.
2. W. Madigosky and G. Lee, Improved Resonance Technique for Materials Characterization, J. Acoust. Soc. Am. 73, p. 1374-77, 1985.

**Integrated Direct Complex Stiffness  
Test System for  
Viscoelastic Material Properties  
(Work in Progress)**

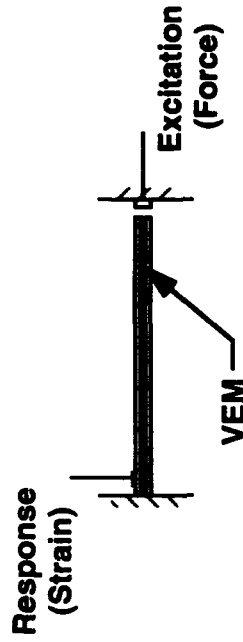
**Bradley R. Allen  
David A. Kienholz  
Bryce L. Fowler  
CSA Engineering, Inc.  
Palo Alto, CA**

**Presented at Damping '93  
February 24-26, 1993**

# Introduction

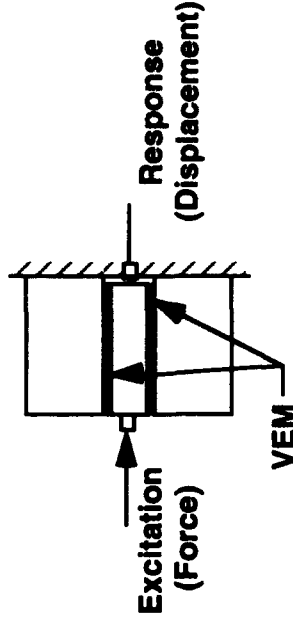
- Viscoelastic material (VEM) complex moduli are measured by two techniques:

## Indirect (resonant)



- Uses flexible sandwich beam
- Measures modal properties via resonant frequency response
  - Natural frequencies
  - Modal damping factors
- Infers VEM properties from modal properties via beam theory
- Temperature controlled by air convection and radiation

## Direct (non-resonant)

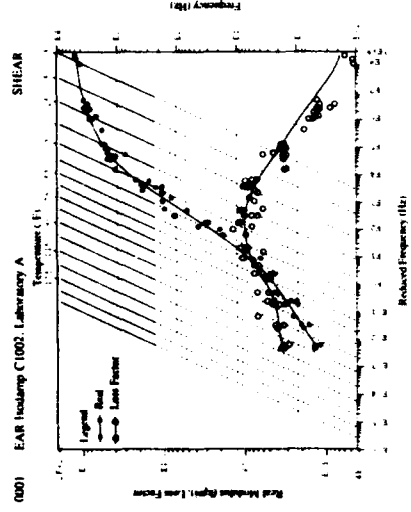
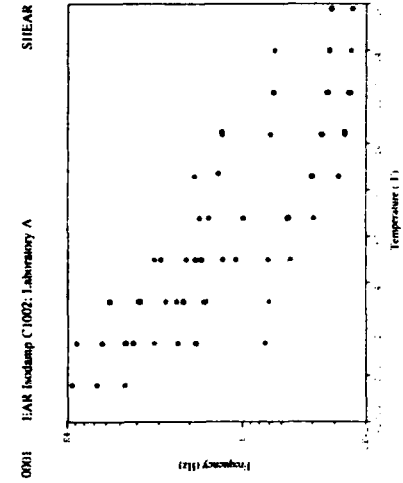


- Specimen rigid except for VEM
- Dynamic shearing displacement and force measured directly
- Complex stiffness measured in real time from force/displacement
- Temperature control by forced convection from liquid flowing through internal passages

# Indirect Measurement Technique (Beam Tests)

- Results are "backed out" from raw data using beam theory
  - Uncertainty can be large under highly damped conditions
- Each specimen gives data at only a few (resonant) frequencies
- Temperature control is slow and uncertain: air convection/radiation
- Method is well understood (ASTM E75 G80)
- Useful as spot check on data from other methods

88-3

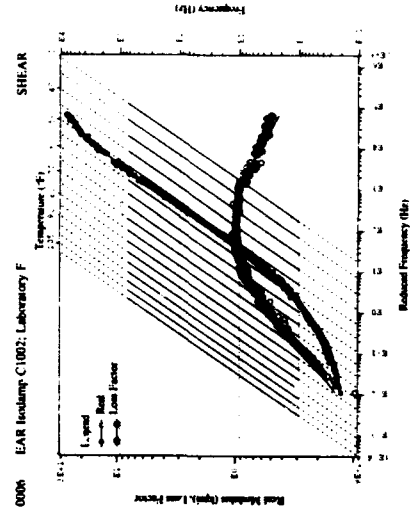
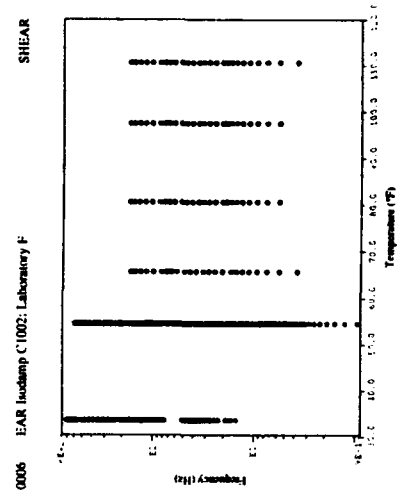


232

# Advantages of Direct Measurement Method

- Yields heavily populated data curve: 400-800 frequency points per specimen per temperature
- Measurement accuracy is best under highly damped conditions
- Large frequency range: 0.1 to 1000 Hz
- Broadband input with FFT processing gives fast data acquisition

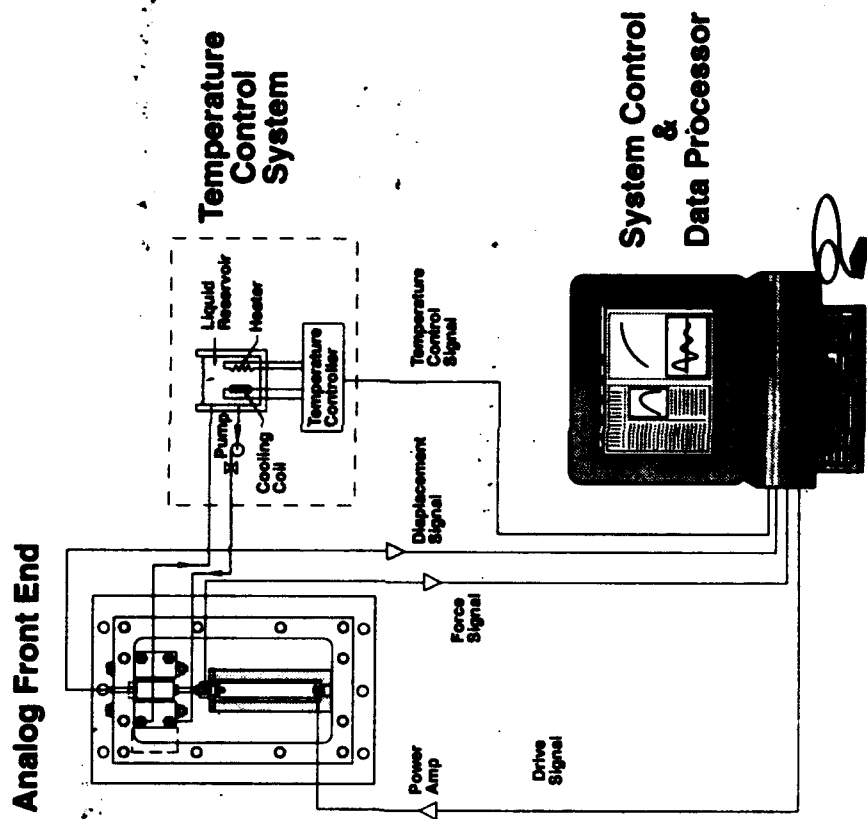
CD-4



# Characteristics of Direct Complex Stiffness (DCS) Test Method

- **Uncertainty is reduced to measurement accuracy: no modeling assumptions**
- **Transducing is more demanding than for resonant test method**
  - **Calibration is critical**
  - **Signal-to-noise ratio must be high**
- **Measured force is predominantly due to material stiffness**
- **Ratio of fixture stiffness/specimen stiffness must be very high**
- **Specimen stiffness changes dramatically with frequency: 1000:1 is common**

# Schematic of CSA's DCS Test System



235

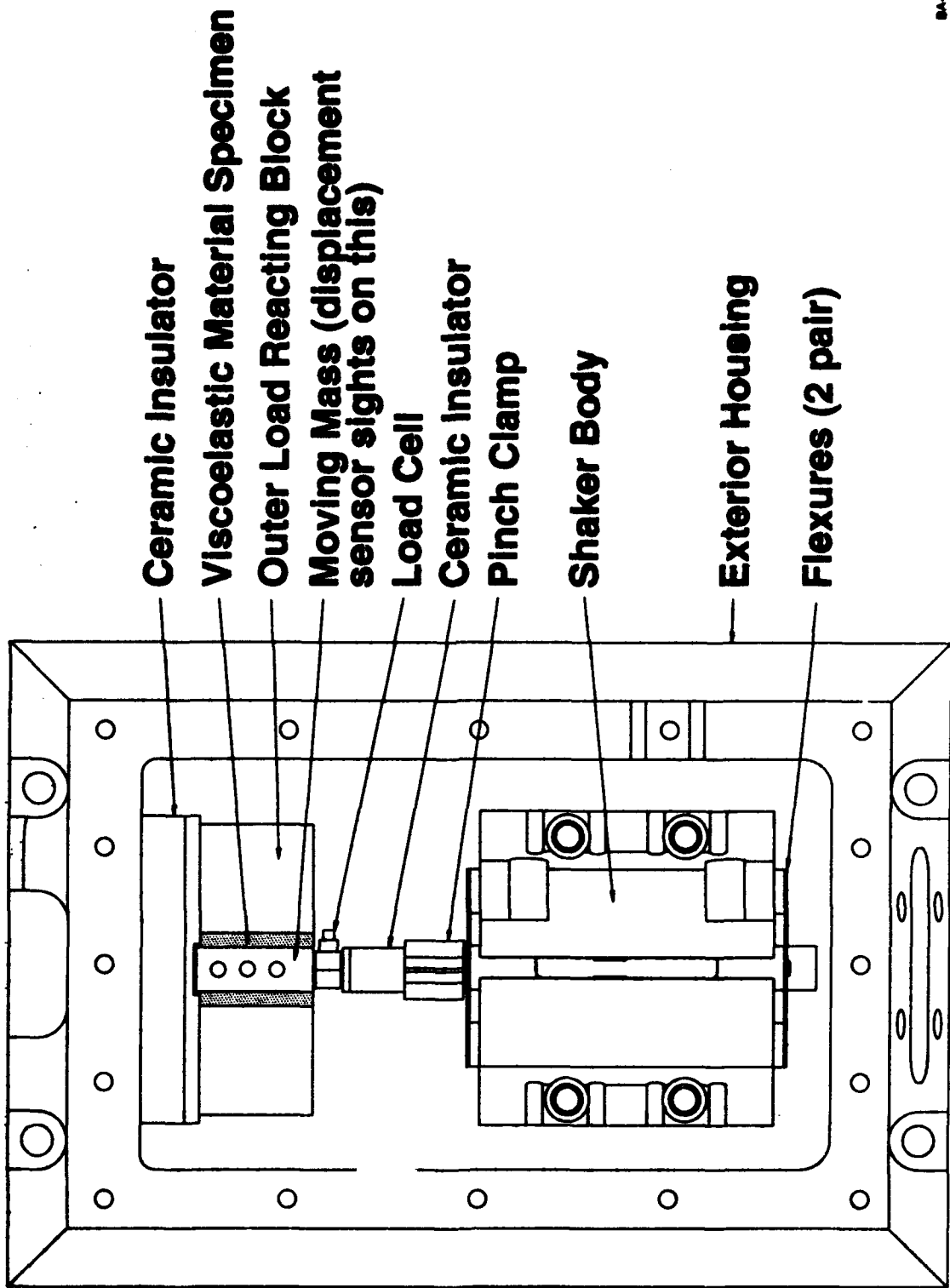
# Advantages of CSA's DCS System

- Liquid forced convection combines good dynamic AND good thermal performance
  - Rigid, compact fixturing keeps resonances high, allows wide test bandwidth
  - External liquid reservoir gives fast, accurate temperature control even with stiff, massive fixture
- Compact, high-force magnetic actuator allows wide range of allowable specimen stiffness; completely covers glass transition region
- Rapid data acquisition
  - Broadband input with FFT processing - all frequencies acquired simultaneously
  - Fast temperature changes between measurements
- Complex modulus displayed immediately; suitable for user inspection and characterization processing

# Specifications

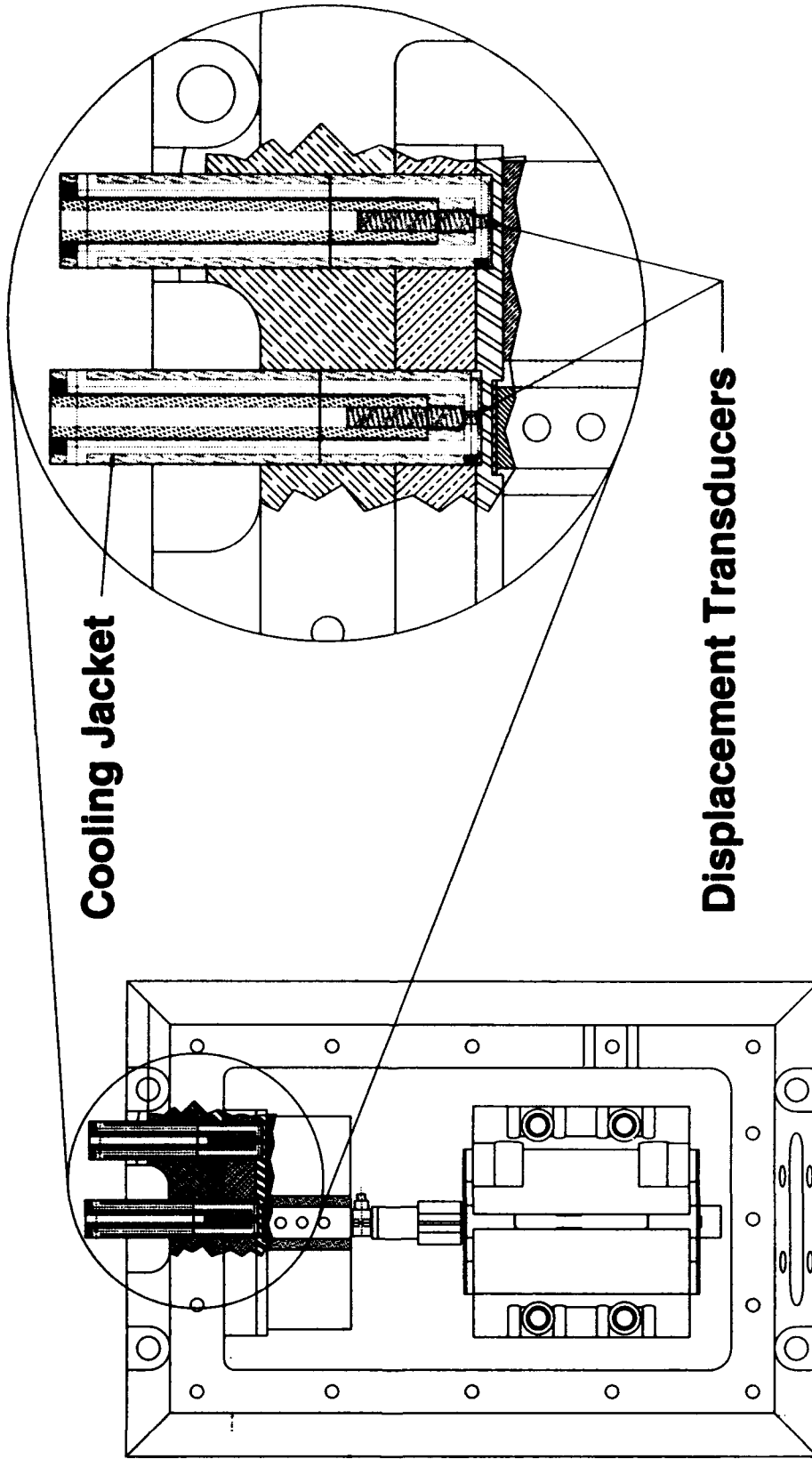
- **Temperature range: -85 to 475 °F**
- **Peak excitation force: 150 lbf**
- **Bandwidth: 0.1 to 500 Hz**
- **Dynamic range**
  - **Input force: 10,000/1**
  - **Response displacement: 10,000/1**
- **Maximum specimen stiffness: 1,000,000 lbf/in**
- **Minimum specimen stiffness: 10 lbf/in**
- **Specimen area: 0.25 - 6.00 sq. in.**
- **Specimen thickness: 0.002 - 0.250 in.**

# Analog Front End (Top View)



BA-DPC93-023-BA 1

# Displacement Sensing by Differential Eddy Current Probes

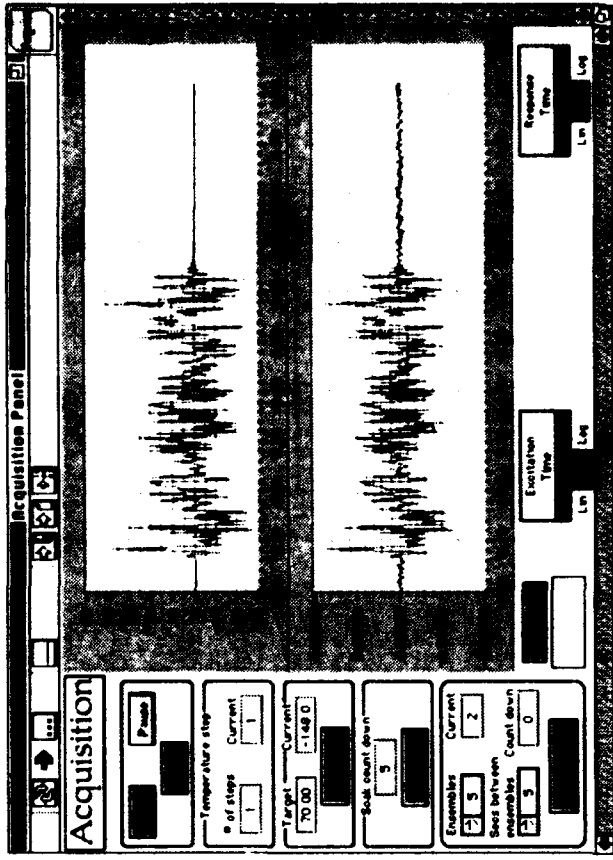


- Prototype currently being upgraded
- Will improve strain threshold and resolution

BA-DPG93-023-BA(1)

# Data Acquisition Software

- Programmed in Labview
- Measurement process controlled by Macintosh
  - Temp. control, input waveform, data acquisition and processing
  - All time and frequency functions displayed
  - Process can be automated
- Real-time data reduction to VEM complex modulus, ready for user inspection or exporting to other programs
  - Corrects for measured compliance of fixture
  - Corrects for measured inertia force on center block
- Exports data to characterization and database software



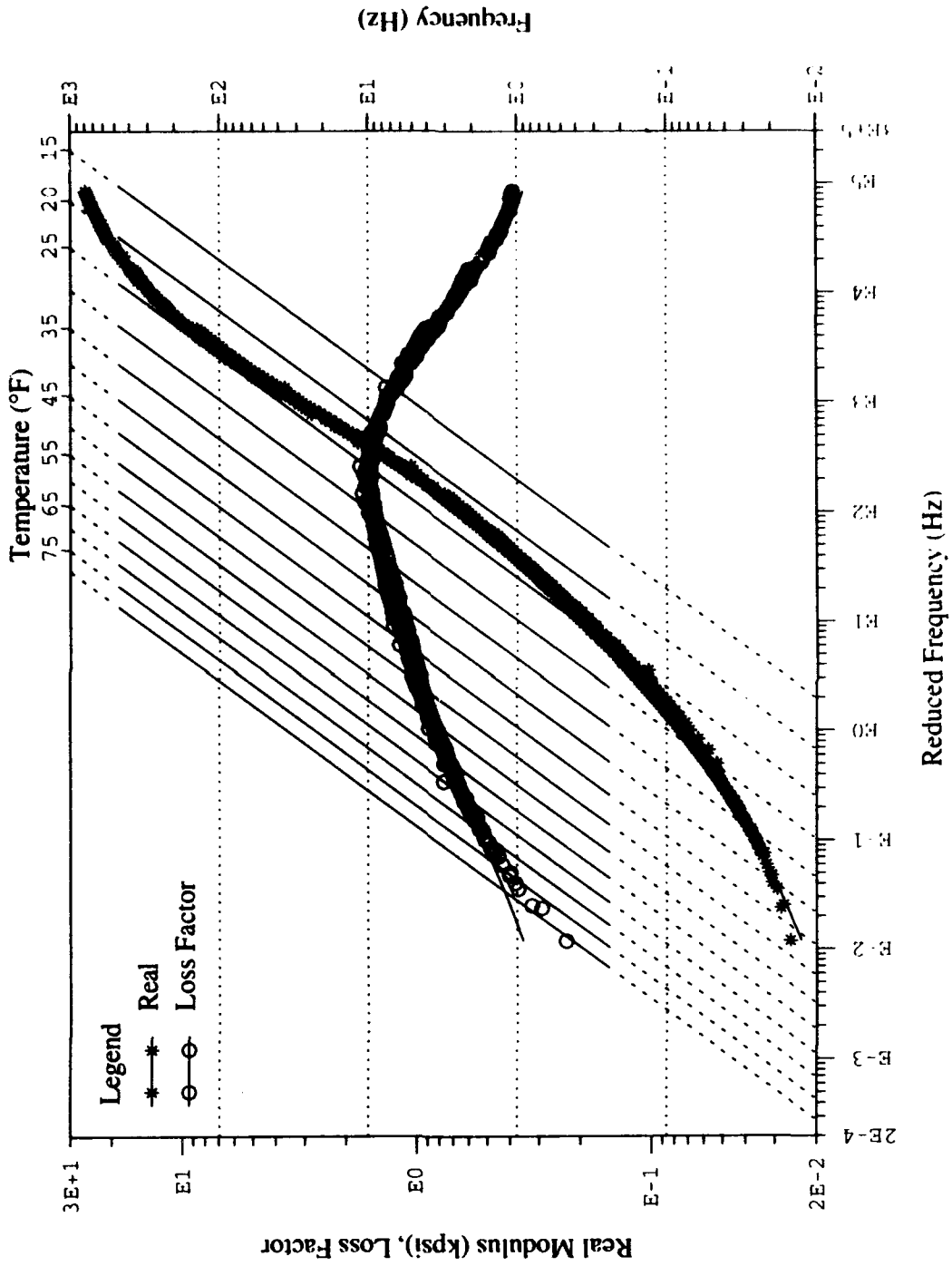
# Data Reduction Features

- **Multi-tasking environment allows characterization during data acquisition**
- **Characterization allows on-line quality control**
  - **Indicates data acquisition errors immediately, while test is still set up**
  - **Indicates coverage of reduced frequency range, tells user if additional temperatures are needed**

# Characterized Data Ready for Database

1211 SMRD 100B37-T2B

SHEAR



BA-OPG83-023-BA-11

242

**VARIATIONS IN THE DAMPING OF SPACE STRUCTURES  
IN 1 G AND 0 G**

**Andrew S. Bicos \***  
McDonnell Douglas Aerospace

and

**Edward F. Crawley, Mark S. Barlow,  
Marthinus C. van Schoor, and Brett Masters**  
Space Engineering Research Center  
Massachusetts Institute of Technology

**ABSTRACT**

An experimental study of the changes in the modal damping of space structural test articles from one- to zero-gravity is presented. Deployable, erectable, and rotary modules was assembled to form three one- and two-dimensional structures, in which variations in bracing wire and rotary joint preload could be introduced. The ground experimental measurements, which were made on a springwire suspension system with a nominal plunge frequency of one Hertz, are compared with measurements made on the Shuttle middeck under conditions of zero-gravity. The degree of change in linear modal damping as well as the change in nonlinear nature of the response is examined. Trends in modal damping is presented as a function of force amplitude, joint preload, reassembly, shipset, suspension, and ambient gravity level.

---

\* McDonnell Douglas Aerospace, 5301 Bolsa Ave., Huntington Beach, CA 92647, (714) 896-1534

## INTRODUCTION

In order to accurately predict the dynamic loads and open loop response of a structure, accurate numerical models must be created. If the structure is to be an element of the plant in a robust closed-loop control system, an even higher premium is placed on the accuracy of the structural model. It is becoming apparent that it is now far easier to create a numerical structural dynamic model with great precision, than to assure its *a priori* accuracy within any stated bounds. Accuracy is degraded as a result of poor modeling due to inexact elements and boundary conditions, mismodeling by the analyst, and non-modeling of features such as damping and weak nonlinearities.

In the normal engineering evolution of a structural model, the inaccuracies are reduced by iterative comparison with experimental data. The poor modeling of stiffness inherent in a first generation or *a priori* model (i.e., one made from drawings and handbook properties before any hardware exists) is often noted by comparison with component or element testing. This information is then incorporated into a second generation model (i.e., one which includes updated component information based on measurements). Performing modal testing and identification then yields frequency, mode shape and damping data that can be used to further refine and update the model, producing what can be called a third generation model.

Such an orderly evolution of models is not always as straightforward for space structures, due to the complications introduced by the ground testing necessary as part of the prelaunch third generation model improvement. Gravity loads the structure, causing droop and local stiffness changes; gravity alters preload on potentially nonlinear joints; and gravity necessitates suspension, which alters the structure's dynamics while introducing its own. One of the remaining issues in open-loop modeling is to understand the degree to which the presence or absence of gravity influences the dynamics of space structures. In order to address this issue, the Middeck 0-gravity Dynamics Experiment (MODE) program was established at the MIT Space Engineering Research Center (SERC) with McDonnell Douglas Aerospace (MDA) as a coporate participant.

The main objectives of this research program are: to study suspension and gravity influences on the structural dynamics of a modular truss system by comparing the measured response in ground and orbital tests; and to quantify the suspension and gravity induced perturbations using analytical models of the suspension and nonlinear effects. Further objectives are to examine the repeatability of measured modal properties from test to test and from test article to test article.

The experimental approach is to test three nominally identical shipsets of a model of a space structure, called the structural test article or STA, at two sites on the ground. In addition, testing of one shipset has been carried out in the micro-gravity of the Shuttle middeck. The on-orbit data were taken during the STS-48 mission in September of 1991. All scheduled tests were performed during two days of on-orbit testing.

The difficulty in directly comparing such on-orbit structural dynamic test results with ground test results is due primarily to the complicating effects of gravity on the ground tests. Five classes of gravity influences can be identified: the need for a suspension and its complication of the dynamics; the direct effect of gravity loading on nonlinearities; the direct structural stiffening or destiffening due to gravity loading; the gravity deformation of the structure, which leads to dynamic perturbations about a deformed equilibrium; and the direct gravity influence on some inertial sensors and actuators. The degree of each influence depends on the stiffness of the test article, inherent nonlinearities, and the geometry of the suspension [Pinson, Hanks, 1983, Rey 1992]. The specific objective of the MODE program is to examine the first two gravity influences, those of suspension and nonlinearity.

In order to span several typical geometries and structural forms, the structural test article (STA) designed for MODE utilized a versatile set of modules, allowing several configurations to be assembled. These modules included deployable truss modules, erectable truss hardware, a rotary joint,

rigid appendages, and a flexible appendage. By assembling various modules, straight and L-shaped trusses were formed and tested. A controlled degree of nonlinearity was introduced into the truss modules and the rotary joint. The preload on one deployable bay controlled the nonlinearity of the joints and bracing wires; similarly, the preload on the rotary joint controlled the friction and propensity for axial rotation. The remainder of this paper begins with a description of the test hardware and the experimental procedures used.

The next section of this paper describes the ground test results, which were comprehensively reported in two earlier documents [Barlow, 1992 and Crawley, et al., 1992]. Ground vibration testing was performed at MIT and McDonnell Douglas on two different shipsets, under highly controlled test conditions. For each of two shipsets, three configurations and several modes, variations were introduced by changing the stiffness of the suspension system, the force level, the joint preload, and by assembly/reassembly of the structure. The pertinent features and conclusions of this ground test program are presented.

The on-orbit structural dynamic test results will then be presented. The orbital test results of three configurations are compared with the ground results for the same shipset, for variations in forcing level and preload. The ground data used for these comparisons will be for the softest successfully tested suspension system, which most closely replicates the free-free orbital test conditions.

The ground and orbital test results will be compared with linear analytical models that incorporate the presence (or absence, as appropriate) of the suspension and gravity stiffening. The nonlinearities of the test articles are also identified as a function of force amplitude and preload. The presence of the measured nonlinearities will be reported, but detailed nonlinear modeling and correlation with nonlinear experimental results await a future report.

### Configurations

In order to examine the influence of gravity on the dynamics of space structures, a representative STA was designed and fabricated. The STA was built up from erectable and deployable modules, which could be arranged to produce several configurations, as shown in Fig. 1. Each module was fashioned after a typical space structural form, and was included in the hardware set for a specific reason.

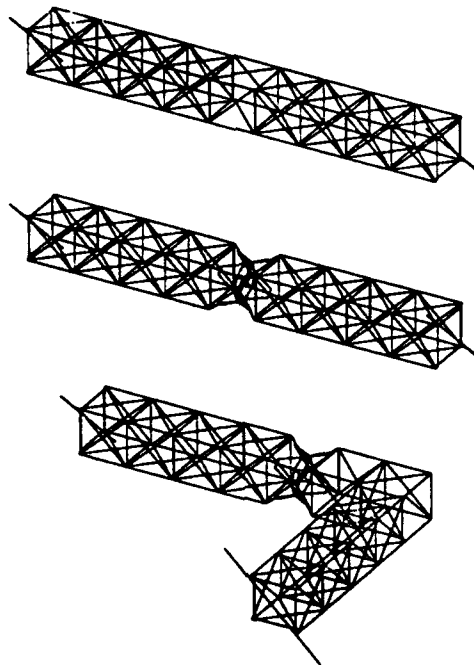


Figure 1. STA baseline, alpha and L configurations.

The simplest arrangement of the modules is called the baseline configuration. For this structure, two four-bay deployable modules (i.e., modules which are capable of being deployed and restowed by utilization of hinging joints and locking mechanisms) are connected in the center bay with erectable hardware components (i.e. hardware that can be assembled from individual components to form a truss section) to form a straight truss. The objective of the tests of this configuration was to determine the impact of gravity and suspension influences on a straight truss composed of primarily deployable hardware, and to examine the influence of preload in the diagonal bracing wires of the deployable hardware on the measured ground and orbital modal parameters.

A slightly more complicated configuration, called the alpha configuration, is formed by replacing the erectable hardware of the center bay of the baseline with a rotary joint modeled after the Solar Array Rotary Joint (SARJ) or Alpha Joint of Space Station Freedom. Although this configuration still forms a straight truss, the additional mass and internal dynamics of the rotary joint substantially change the behavior of the system. The purpose of testing this configuration was to evaluate the influence of 1-g test methods on a truss with a rotary joint that contains a frictional interface with operating bearings.

A more complex configuration includes both deployable modules, erectable hardware, and the rotary joint to form a planar truss called the L configuration. Due to its shape and mass distribution, the L configuration was the most difficult to test in a 1-g field. Tests on this configuration were performed to provide the greatest challenge to the testing of a planar structure in a gravity field.

The three configurations of the structural test article are composed of several different modules. These modules include two deployable truss modules, erectable truss hardware, a rotary joint, and two rigid appendages. The modules are scaled models built by the AEC/Able Engineering Company for MDA, who supplied two shipsets to MIT (denoted STA 1 and STA 2). A third shipset, STA 3, was retained at MDA for testing.

Two deployable truss modules form the bulk of each configuration. The deployable truss resembles one of the designs proposed for the Space Station Freedom solar array truss structure. Weighing approximately eight pounds, each section is four bays in length with a nominal bay comprised of an eight inch cubic section. Each Lexan longeron hinges at its midpoint (via a knee joint) and at its attachment points with the batten frames. The batten frames remain rigid when the truss is collapsed. The hinge arrangement allows the truss segment to fold like an accordion for stowage. All hardware that connects the Lexan rods is made of 6061 aluminum. Tension is maintained throughout the deployable module by the use of pretensioned cables which run diagonally between the batten stations. When the longerons lock in their over-center deployed position, the tension in these cables reaches 25 lb. The cables are tensioned to prevent possible slop in the hinge and knee joints from entering the system dynamics. The preload maintains local longeron "string" modes above 40 Hz. Typical preload on the longerons is 28 lb. This loading is 50% of the estimated buckling load of the longerons and represents a compromise between sufficient preload to prevent slop at the joints and excessive preload that might destiffen a longeron.

A single bay of one of the two deployable modules includes a mechanism that allows for varying the preload level in the wires. The purpose of this feature is to permit the study of preload on the joints and its influence on the truss dynamics. Provisions for preloads of 24, 13, and 7 lb were incorporated into the truss design and were denoted as the high preload, or preload 1 (PL1), the medium preload, or preload 2 (PL2), and the low preload, or preload 3 (PL3). Preload 1 corresponds to the same preload as in the wires of the unadjustable bays. As the preload on this bay is reduced, it is possible for the joints to become unloaded as the cables begin to slacken. Both cable slackening and joint motion are expected to contribute to changes in the truss dynamic behavior. In summary, the deployable hardware consists of one module with four bays in which the wire pretension is fixed, and one module that contains one bay in which the preload is adjustable and three bays in which it is fixed.

Erectable truss hardware forms the next largest portion of the structure. Although scaled down in size, the erectable components are identical to hardware used by the NASA Langley Research Center for their Dynamic Scaled Model Technology structure [Gronet, et al. 1989]. Erectable hardware

consists of spherical nodes with 26 holes to which standoffs may be mounted. Longerons, diagonal, and batten members terminate in lugs that slip into these standoffs and are secured by tightening a locking collar. Erectable segments are connected to the deployable hardware using standoffs incorporated into the two end batten frames of each of the deployable modules. Erectable longerons and diagonals are connected to the standoffs on the deployable modules to form the baseline configuration, and are incorporated together with the alpha joint in the L configuration.

The alpha joint was intended to approximate the dynamics of the SARJ proposed for Space Station Freedom. The 2.5 lb module is constructed around two aluminum disks that are connected at their centers by an axle, and at a radius of 2.75 in by 5.5 mm diameter stainless steel ball bearings. The two plates are free to rotate relative to each other on the bearings. The disk assembly has Lexan struts terminating in erectable-style lugs and locking sleeves to allow connection with erectable standoffs. The disk/strut module is sized as an eight inch cubic bay. Friction between the two plates is adjustable through the use of a cam mechanism set by a tensioning lever; the tight position is denoted as alpha joint tight (AT) and the loose position as alpha joint loose (AL). In the AT setting no relative rotation occurs, while in the AL setting the two plates can rotate relative to one another, constrained only by bearing friction. The alpha joint was used in the alpha and L configurations.

Rigid appendages have been added to the ends of each configuration to lower the system fundamentals below 10 Hz. These appendages are dumbbell-shaped and each weighs approximately 16 lb.

### **Sensors and Actuator**

Several sensor types were utilized to measure the structural response to the force input created by a single proofmass actuator. Accelerations were sensed by piezoresistive accelerometers, and the input force by a load cell. All electrical signals were routed off the STA through a single umbilical. Thirty-three pairs of 28 gauge stranded wire were loosely braided and wraps in a fire resistant woven shell to form an 8 ft length of bundled wire. As in space flight hardware, cables connecting the sensor location to the umbilical attachment points were routed along the structure and tie-wrapped in place.

Excitation was provided by a proof-mass actuator. The shaker used a 1.0 lb throw-mass and interchangeable springs to permit both ground and orbital testing. The mass and spring mounted to the support platform that in turn mounted to the load cell. Total weight of the actuator is approximately 1.8 pounds. For the spring selected for ground testing, the shaker's spring-mass resonance occurred at 4.0 Hz, while resonance occurred at 2.3 Hz with the space spring. Due to the change in springs from ground to orbit, the actual force differed slightly between ground and orbit for the same commanded voltage. The forcing amplitudes will be referred to as low, medium and high, but the actual value of measured forcing for any particular test varied. The excitation acted in the vertical direction on the corner of the end batten frame of the deployable module that contained the bay with adjustable preload.

Eleven accelerometers were placed on the truss in locations and orientations so as to make observable the modes of interest for each of the structural configurations. Three accelerometers were placed on the end batten frame that supported the proofmass actuator, three at the batten frame four bays away at the far end of the same deployable module, three at the first batten frame of the second deployable module, and two at the far end of the second deployable module. Four strain gauges also instrumented the adjustable bay, for a total of sixteen channels of data.

Signal conditioning, data acquisition, and data storage were provided by an Experiment Support Module, or ESM. Sixteen channels of sensor signals were simultaneously sampled by 12 bit A/D's at 500 Hz and stored on a Write Once Read Many (WORM) disk. Sensor signals are amplified and low pass filtered using eight-pole tunable Bessel filters with a corner frequency of 250 Hz.

### **Test Procedures and Data Reduction**

Testing on the ground and on orbit followed the same basic procedures. A structural

configuration was assembled and suspended (on earth) or tethered (on orbit). The umbilical and actuator were attached, and the test protocol performed.

For the ground testing of the STA, a soft mechanical suspension system was selected to support the structure while approximating free-free boundary conditions. A suspension system consists of steel wires hung from coil springs, attached to a rigid support frame. Three spring sets were used providing nominal system plunge frequencies of 1, 2, and 5 Hz. An overall spring-wire length of 120 in was maintained, which yielded a sway frequency of 0.28 Hz. Other suspension resonances (including transverse (violin string) wire modes, axial modes of the springs, and compound pendulum modes of the spring/wire) were sufficiently separated from the STA resonances to not complicate the identification of STA frequencies and damping ratios [Crawley, et al. 1992].

On the middeck, tests were performed in a shirt-sleeve room temperature and pressure environment. Although a suspension system was not required, it was impossible for the STA to truly free float on the Shuttle. Residual velocity from the release by the crew, air circulation, and gravity gradient accelerations, as well as occasional firings of the vernier reaction control system, would cause contact of the STA with the cabin walls. To prevent such an impact, an elastic tether system was used, which consisted of four tethers of 0.0625 in square elastic surrounded by Nomex sheathing. The tethers were positioned to provide restoring forces in three orthogonal directions to prevent drift. After being attached to an STA longeron via a Nomex and velcro cuff, each tether was attached to a prepositioned velcro pad mounted on the middeck interior. Based on video data, the frequency of the STA on this tether "suspension" was 0.025 Hz, about a factor of forty below the lowest ground suspension frequency, and three hundred below the STA fundamental.

The test procedure was the same for all configurations. Sine sweep testing was performed. As each protocol was conducted, signal time histories for each excitation frequency were stored. Post-test data reduction consisted of reducing the time history data to a single amplitude harmonic coefficient for each data channel at the tested excitation frequency by employing a harmonic balance technique. Next, estimates of natural frequency and damping ratio were determined using the circle fit method [Ewins, 1984]. Implicit in the use of this method is the assumption that the dynamic behavior is dominated by a linear resonance. For every forcing amplitude of each mode, channels with clean signals were selected for use in the determining modal parameters. Parametric data from each channel were then averaged to determine the modal values. In this manner, channels which had saturated or experienced small signals were removed from the parameter determination algorithm.

## TEST RESULTS

### Test Matrix Selection

This section will briefly review the parameter matrix explored in ground and orbital testing, then go on to present the principal ground test results, before presenting the orbital test results and comparisons between the two.

As described above, combinations of the hardware modules allowed for variation in configuration, deployable bay joint preload, and alpha joint preload. Any number of modes could be tested at multiple force levels. Three different shipsets were available to test on various suspension systems on the ground and in micro-gravity on orbit. Assemble and reassemble repeatability tests could also be conducted. Considering all of these parameters, the resulting test matrix has seven dimensions: configurations, preloads, modes, force level, shipsets, suspension/gravity, and assembly/raassembly. Because of the limited nature of on-orbit test time, a specific subset of the multidimensional test matrix was completed on orbit.

Prior to and following the orbital testing, the hardware was the subject of extensive ground testing. The ground test matrix included tests on STA 1 at MIT, for the same submatrix of configurations, modes, forcing levels, and deployable bay and alpha joint preloads as were tested on orbit. In addition, the ground testing filled out the overall matrix by testing two different shipsets at

two different sites: STA 1 at MIT and STA 3 at MDA. For both shipsets, assembly/reassembly testing was performed, and in the MIT tests, three different suspension systems were employed.

### Ground Test Results

This section will present the data on the ground testing of the three configurations of the two nominally identical shipsets of the STA studied. In the evaluation of ground testing technologies, several different suspensions were used, which differed primarily in suspension stiffness. Three different structural configurations were tested to assess the influence of different structural modules and difficulties associated with testing structures that are essentially one dimensional (baseline and alpha configurations) versus two dimensional (L configurations). To assess the influences of small mechanical variations in the structure, several permutations of each configuration were tested varying such parameters as bay preload and alpha joint tension. Several modes were tested for each configuration — generally, the lowest flexible mode and one or two higher modes. For each mode, several force levels were used for each test to examine the extent of the structural nonlinearities. For all of the configurations, assembly/reassembly tests were performed to determine the repeatability of modal measurements after reassembly of the structural components. Tests on two nominally identical shipsets of the same hardware at two different facilities using nominally identical protocols were intended to identify test article to test manufacturing and test technique variations. Reference Barlow [1992] contains a summary of the configurations and permutations tested for each suspension system.

Although tests were performed with several different suspension systems, the 1 Hz system is considered the nominal system, since it provides approximately an order of magnitude separation in frequency from the fundamental. Tests utilizing the 2 and 5 Hz suspensions were intended to test the limits of the modal separation argument. Since a softer suspension is generally considered superior, a 0.5 Hz suspension was also utilized. However, soft mechanical suspensions have numerous practical problems. Soft springs are long and relatively massive. For the STA configurations tested, the largest STA mass was approximately 47 lb; each 0.5 Hz spring weighed over 2 lb leading to a suspension mass fraction approaching 20%. Due to the large mass and low stiffness of the 0.5 Hz springs, the internal dynamics of the springs occurred at low frequencies. Axial surge modes for these springs began at 3.5 Hz and appeared at harmonic intervals of 3.5 Hz. This pattern places a surge mode near almost every mode of the STA (i.e. at approximately 7 Hz, 10.5 Hz, 21 Hz, 28 Hz, etc.). Because the 0.5 Hz suspension system interfered and coupled to the STA dynamics, no data from these tests will be presented. Practically speaking, once the desired plunge frequencies of a suspension system drop much below 1 Hz, a mechanical spring should no longer be used due to internal dynamic influences. For such applications, a system such as pneumatics which does not utilize a mechanical spring must be considered [Kienholz, 1989].

Multiple modes were tested for every structural configuration. Figure 2 contains mode shape data from a finite element model of all the configurations tested. For the baseline configuration, the three lowest global flexible modes (torsion, bending, and shearing) were tested. Between the torsion and bending modes, several local modes caused by the large rotary inertia of the rigid appendages existed. Since the strain energy for these modes was concentrated in only a few elements, they were not included in the test matrix. Torsion and bending, the two lowest flexible modes, were tested with the alpha configuration. These two modes were selected since they were the most likely to be influenced strongly by the presence of the alpha joint. For the L configuration, the third, fourth, and fifth global flexible modes were tested. The first mode exhibited scissors-like motion which would not have been properly excited by the actuator due to its position. Furthermore, ground testing of this mode would have been very difficult had the actuator been moved. The untested second mode was very similar to the third which was tested. The third mode was tested since it produced larger modal displacements at the sensor positions. The next two tested modes both had coupled leg bending and torsion but had different strain energy distributions.

In order to assess the nonlinear behavior of each structure, several force levels were also tested for each configuration. Force amplitude spanned about one order of magnitude. For each configuration tested, the number of forcing levels and the values of each are given in Table 1.

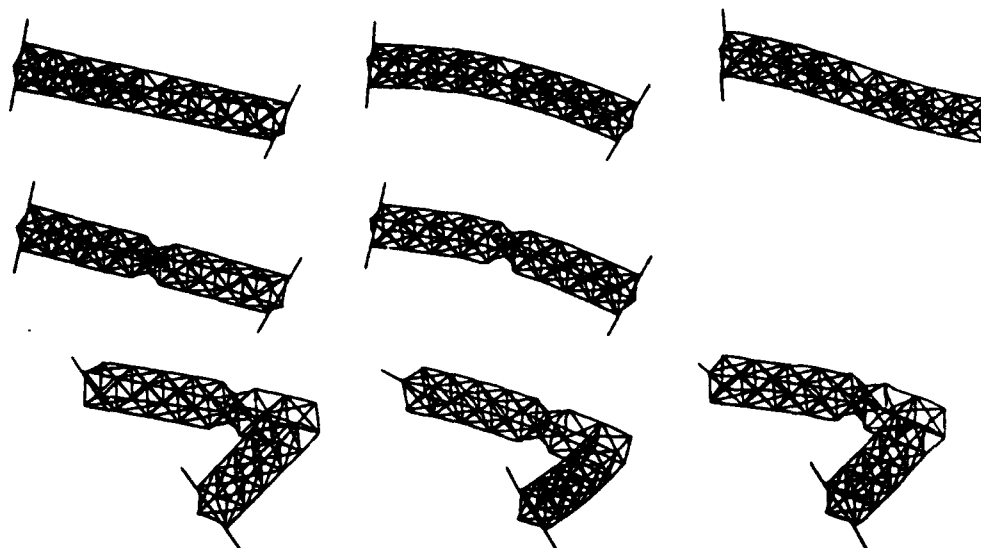


Figure 2. Mode shapes of the three STA configurations.

Table 1. Excitation force amplitudes used in the STA ground tests.

Config.	Mode	Type	Approx. Freq. (Hz)	Amplitude 1		Amplitude 2		Amplitude 3	
				MIT (lbf)	MD (lbf)	MIT (lbf)	MD (lbf)	MIT (lbf)	MD (lbf)
Baseline	1	Torsion	7.75	0.046	0.025	0.224	0.100	0.396	0.400
	2	Bending	20.0	0.044	0.025	0.208	0.100	0.368	0.400
	3	Shearing	29.0	0.043	0.025	0.204	0.100	0.362	0.400
Alpha	1	Torsion	7.25	0.046	0.038	0.227	0.180	0.276	0.322
	2	Bending	10.5	0.043	0.038	0.130	0.180	0.380	0.322
L	1	Torsion	7.75	0.047	0.038	0.263	0.180	0.471	0.322
	2	Bending	25.5	0.039	0.038	0.226	0.180	0.404	0.322
	3	Bending	30.5	0.030	0.038	0.223	0.180	0.399	0.322

Due to the complex nature of many of the structural modules, repeatability tests were performed. Deployable, erectable, and alpha joint modules were each tested after disassembly and reassembly to determine the repeatability of modal results. Testing of the repeatability of the dynamics of the erectable hardware was performed at MIT and MDA. At MIT, STA 1 was repeatedly disassembled and reassembled in the L configuration. The deployable modules and the alpha joint were not collapsed or disassembled — only the erectable hardware was removed. The position of each individual strut remained unchanged after reassembly. At MDA, STA 3 was repeatedly disassembled and reassembled in the baseline configuration, once with the strut location unchanged, and once with the locations randomly changed. Testing of the repeatability of the dynamics of the deployable modules and alpha joint were performed on STA 1 at MIT. After the initial tests of the alpha joint (alpha tension tight and loose), the structure was removed from the suspension and disassembled: the deployable segments were collapsed, the alpha joint was removed, and the alpha joint halves were separated. The structure was reassembled, suspended, and tested. The alpha configuration was again removed from its suspension. Again, the alpha joint was removed and disassembled, but the deployable modules remained extended. After reassembly, the structure was again tested.

#### Baseline Configuration

The tested modes of the baseline configuration were torsion, bending, and shearing, which were tested at three different excitation force levels (listed for all configurations in Table 1). The frequency and damping ratio of all tested modes for all tests of the baseline are given in Table 2.

**Table 2. Measured modal parameters of the baseline configuration (ground data).**

	Suspension	STA - Rep.	Frequency			Damping Ratio		
			Low Force	Med. Force	High Force	Low Force	Med. Force	High Force
<i>Torsion</i>								
High	1 Hz	1-1	7.74	7.70	7.67	0.24	0.40	0.54
Preload	2 Hz	1-2	7.77	7.72	7.70	0.22	0.39	0.54
	5 Hz	1-3	7.94	7.90	7.88	0.23	0.35	0.47
	1 Hz	3-1	7.69	7.66	7.64	0.20	0.33	0.40
	1 Hz	3-2		7.57	7.55		0.26	0.34
	1 Hz	3-3		7.57	7.56		0.27	0.33
Med.	1 Hz	1-1	7.71	7.66	7.64	0.27	0.42	0.57
Preload	1 Hz	3-1	7.66	7.62	7.61	0.22	0.37	0.48
	1 Hz	3-2		7.53	7.52		0.28	0.37
	1 Hz	3-3		7.54	7.53		0.31	0.37
	1 Hz	3-3		7.58	7.54		0.67	0.86
Low	1 Hz	1-1		7.58	7.54		0.67	0.86
Preload	2 Hz	1-2	7.69	7.59	7.54	0.28	0.64	0.87
	5 Hz	1-3	7.86	7.76	7.71	0.27	0.66	0.83
	1 Hz	3-1	7.49	7.44	7.44	0.28	0.68	0.72
	1 Hz	3-2		7.39	7.35		0.47	0.65
	1 Hz	3-3		7.38	7.36		0.57	0.69
	1 Hz	3-3		7.38	7.36		0.57	0.69
<i>Bending</i>								
High	1 Hz	1-1	20.43	20.37	20.33	0.41	0.39	0.62
Preload	2 Hz	1-2	20.45	20.43	20.40	0.29	0.39	0.64
	5 Hz	1-3		20.50	20.48		0.38	0.55
	1 Hz	3-1	20.55	20.53	20.48	0.25	0.31	0.33
	1 Hz	3-2		20.65	20.60		0.28	0.30
	1 Hz	3-3		20.74	20.68		0.27	0.28
Med.	1 Hz	1-1	20.48	20.41	20.31	0.58	0.48	0.52
Preload	1 Hz	3-1	20.51	20.48	20.43	0.26	0.33	0.34
	1 Hz	3-2		20.61	20.56		0.29	0.31
	1 Hz	3-3		20.69	20.63		0.31	0.29
	1 Hz	3-3		20.29	20.18		0.55	0.52
Low	1 Hz	1-1	20.29	20.18	20.12	0.55	0.52	0.44
Preload	2 Hz	1-2		20.33	20.30		0.47	0.59
	5 Hz	1-3	20.45	20.41	20.22	0.28	0.36	0.62
	1 Hz	3-1	20.38	20.41	20.46	0.35	0.34	0.36
	1 Hz	3-2		20.59	20.50		0.27	0.32
	1 Hz	3-3		20.56	20.52		0.32	0.40
	1 Hz	3-3		20.56	20.52		0.32	0.40
<i>Shearing</i>								
High	1 Hz	1-1	29.42	29.33	29.28	0.25	0.27	0.28
Preload	2 Hz	1-2	29.42	29.36	29.32	0.21	0.23	0.28
	5 Hz	1-3	29.48	29.40	29.34	0.28	0.23	0.27
	1 Hz	3-1	29.19	29.12	29.04	0.16	0.20	0.26
	1 Hz	3-2		29.02	28.96		0.21	0.21
	1 Hz	3-3		29.04	28.95		0.21	0.29
Med.	1 Hz	1-1	29.34	29.26	29.22	0.26	0.27	0.29
Preload	1 Hz	3-1	29.14	29.07	28.97	0.14	0.21	0.28
	1 Hz	3-2		28.95	28.88		0.25	0.31
	1 Hz	3-3		28.98	28.89		0.21	0.31
	1 Hz	3-3		29.14	29.10		0.30	0.33
Low	1 Hz	1-1		29.14	29.10		0.30	0.33
Preload	2 Hz	1-2	29.31	29.22	29.14	0.20	0.25	0.25
	5 Hz	1-3	29.32	29.21	29.15	0.29	0.28	0.35
	1 Hz	3-1	28.79	28.87	28.93	0.32	0.23	0.20
	1 Hz	3-2		28.84	28.87		0.20	0.41
	1 Hz	3-3		28.77	28.65		0.29	0.44
	1 Hz	3-3		28.77	28.65		0.29	0.44

Examining Table 2, one can see that the structure is weakly nonlinear since the frequencies and damping ratios are different for different excitation force levels. Each mode shows the same softening trend to varying degrees; as the excitation force is increased, the frequency of the mode decreases. In the torsion mode, an increase in damping ratio with increasing force is also generally observed, although in the bending mode the damping tends to rise and then fall with increasing excitation. The shearing mode follows the same trends as the torsion mode. Since both the shearing and torsion modes store much of their strain energy in the shearing of the bay faces, it is not unexpected that their behavior is similar; bending strains longerons and can be expected to display slightly different behavior.

The change in modal properties with preload was examined by next testing with the medium and low preloads on the one bay of deployable hardware. As in the high preload test, the modes generally soften and show increased damping with increasing force (except for the second mode which has its highest damping at the lowest amplitude). Compared to the high preload, the trends were qualitatively similar, but the modal frequencies decrease and damping increases as preload diminishes.

Two physical mechanisms are likely to cause such nonlinear modal behavior: slackening of the tensioning cables and accumulated microfriction. For the low preload test of the baseline torsion mode, the cables of the adjustable bay displayed flexural deformations as the structure was excited, indicating that some amount of slackening was occurring. However, softening occurs even at the highest preload, as evidenced in Table 2. Such behavior might be explained by microfriction at the joints. With increasing amplitude there is increasing friction breakage, resulting in softening and increased dissipation. A more thorough modeling of the nonlinear nature of the response is beyond the scope of the current paper.

Trends in the resonance of the torsion and bending modes of the baseline configuration are displayed in Figure 3, which shows the damping ratio (in percent) versus the change in frequency normalized by a reference (in percent). The first test of STA 1 at MIT with the high preload and low excitation amplitude, which is considered the most linear case, has been chosen as the reference in this and subsequent similar figures. Following a line of constant preload in Figure 3a, the trend with increasing excitation level is very clear. Frequency steadily drops and damping steadily rises with increasing force. By comparing the shift from the solid lines of high preload to the dashed lines of low preload, the shift downward in frequency and upward in damping is also apparent (the medium preload shows the same trends, but has been omitted for clarity).

Also visible in Figure 3a is a trend not previously discussed, which is the change in modal properties with suspension stiffness. As might be expected, the suspension stiffens the torsion mode (at approximately 7.7 Hz) slightly in going from 1 to 2 Hz, and more markedly in the change from 2 to 5 Hz. The damping ratio is largely unaffected by the change in suspension. The shift in modal frequencies can be attributed to the stiffer suspension system having an impact on the "free-free" boundary condition of the suspended test article. In the lower right corner of Figure 3a, the frequencies predicted by ADINA [ADINA, 1987; Crawley, 1992; Rey, 1992] for the free-free (0-g) case, as well as the STA on 1, 2 and 5 Hz suspensions are shown. Although there is an absolute error in the prediction, the trend of stiffening with suspension frequency is remarkably well predicted. It should be emphasized that no experimentally measured component or modal properties were used to update the ADINA model, so that the results shown are "honest" first generation prediction.

The modal results from the testing of STA 3 at MDA are shown in a constant format in Figure 3. Three assembly tests are shown, two of which have only partial data. The results should be nominally identical to each other and to the 1 Hz suspension STA 1 results obtained at MIT. In fact, the same trends are observed, softening and dampening with increasing force and decreasing preload. Even the "slope" of the curve of  $\Delta\zeta/\Delta\omega$  is preserved. However, there is noticeable scatter among nominally identical reassembly tests at MDA, and between the average of those results and the MIT STA 1 results. Clearly some variation with shipset and reassembly is evident.

The complementary trend plot for the bending mode (Figure 3b) of the baseline configuration shows that the data now falls in a smaller cluster, but the trends are less apparent. At the high preload, the general trend of increased damping and decreased frequency with increased force is apparent,

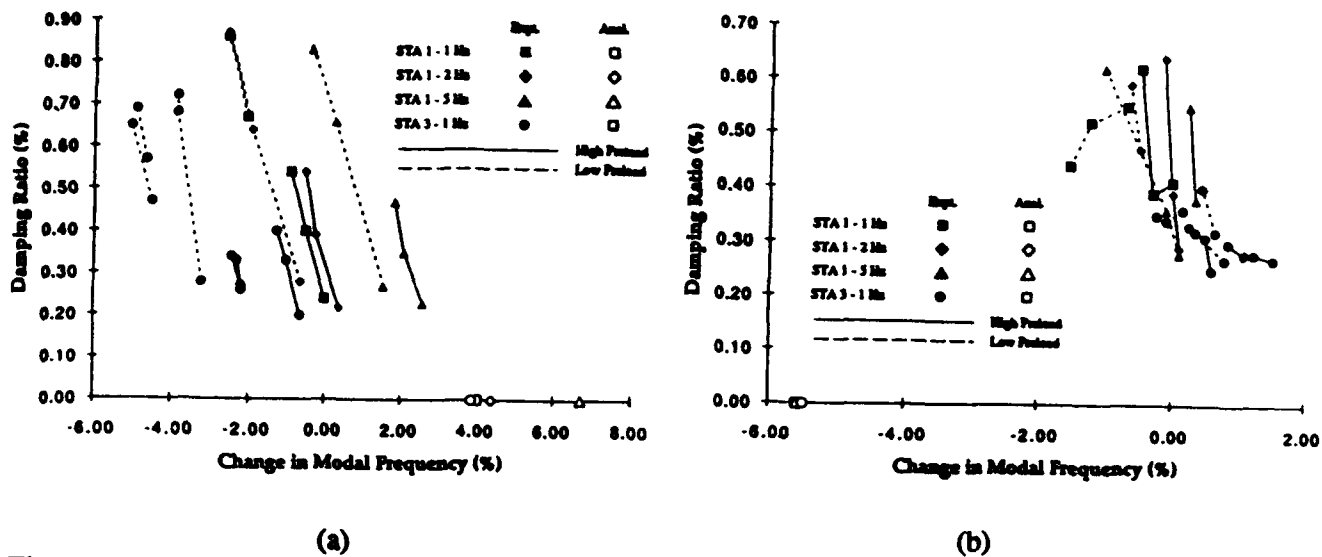


Figure 3. Trends in modal resonance of baseline configuration for torsion and bending mode.

although not as monotonic as in the torsion mode. The "slope" of the trends for STA 1 and STA 3 are quite different, even though their absolute parameters are more similar than in the torsion mode. The trend of increasing frequency with increasing suspension frequency is also present, to a lesser degree than in the first mode, but to a greater degree than predicted by the ADINA results. The low preload results are more problematical, with the trends with force amplitude and preload somewhat unclear.

#### Alpha Configuration

The alpha configuration added the complication of a massive rotary joint in the middle of the truss. It was tested in the torsion and bending modes with the alpha joint tight (which essentially eliminated relative motion between the two faces) and with the joint loose (which allowed some relative motion at higher amplitudes). All testing of the alpha configuration was performed with the preload in the adjustable bay of the deployable module set at its high value.

The assembly/reassembly testing for the alpha configuration was performed on STA 1 at MIT. Initially, the alpha configuration was assembled and hung, the joint was locked, and the alpha tight test was performed. The alpha joint was then loosened and the alpha loose protocol was conducted. The structure was removed from the suspension and completely disassembled (alpha joint halves were separated and deployable modules were collapsed). The structure was reassembled, hung, and tested. Finally, the structure was removed from the suspension and the alpha joint was removed and completely disassembled and then reassembled. In this second disassembly/reassembly, the deployable modules were not collapsed, but remained deployed. Once reassembled, the structure was tested for the third time.

Table 3 contains natural frequency and damping ratio data for the alpha configuration for all test conditions. As occurred with the baseline tests, the modes soften and dampen with increased force levels. The torsion mode of the alpha tight test shows a marked increase in damping with force, while the bending mode softens without much change in damping. Comparing the torsion mode of the alpha tight and loose tests, the tight case is only weakly nonlinear, while the loose case shows a violent shift in frequency downward. The weakly nonlinear response of the truss observed in the variations of the joint preload discussed above and the alpha tight testing has been replaced by what might be called a moderately nonlinear response in the alpha loose tests. It is speculated that at the higher amplitude excitation in the torsional mode, the frictional interface in the bearings is breaking in the loose alpha joint. Since the torsion mode would carry torque across the alpha, this mode would be

**Table 3. Measured modal parameters of the alpha configuration (ground data).**

	Suspension	STA - Rep.	Frequency			Damping Ratio		
			Low Force	Med. Force	High Force	Low Force	Med. Force	High Force
<b>Torsion</b>								
Tight	1 Hz	1-1	7.52	7.45	7.42	0.48	0.54	1.19
	1 Hz	1-2	7.50	7.44	7.39	0.37	0.53	1.13
	1 Hz	1-3	7.53	7.44	7.42	0.32	0.78	1.09
	2 Hz	1-4	7.57	7.48	7.46	0.31	0.77	1.05
	5 Hz	1-5	7.74	7.63	7.60	0.18	0.67	0.99
	1 Hz	3-1	7.38	7.31		0.35	0.58	
Loose	1 Hz	1-1	7.41	7.16		1.37	2.50	
	1 Hz	1-2	7.28	6.96		1.91	2.68	
	1 Hz	1-3	7.23	7.14		1.45	4.90	
	2 Hz	1-4	7.43	7.08		0.56	3.62	
	5 Hz	1-5	7.60	7.20		0.60	3.93	
	1 Hz	3-1	7.20			1.09		
<b>Bending</b>								
Tight	1 Hz	1-1	10.88	10.56		1.02	1.45	
	1 Hz	1-2	10.80	10.67	10.64	1.14	1.13	1.91
	1 Hz	1-3	11.09	10.82	10.74	1.56	0.91	1.17
	2 Hz	1-4	10.86	10.81	10.73	1.11	2.22	1.61
	5 Hz	1-5		10.85	10.76		0.84	0.89
	1 Hz	3-1	10.62	10.84	10.29		2.06	0.93
Loose	1 Hz	1-1	10.74	10.59		1.04	1.41	
	1 Hz	1-2	10.84	10.71	10.64	1.57	1.21	2.07
	1 Hz	1-3		10.85	10.72		1.19	0.96
	2 Hz	1-4		10.67	10.89		1.61	1.60
	5 Hz	1-5	11.09	10.87	10.75	0.90	0.73	0.77
	1 Hz	3-1	10.47	10.38	10.23	0.54	0.92	0.68

particularly susceptible to be influenced by slipping at the interface. The bending mode, which carries bending moment across the alpha, as opposed to torque around the longitudinal axis as in the torsion mode, is less influenced by the loosening of the joint.

The trend plots for the torsion and bending modes of the alpha configuration are shown in Figure 4. For the alpha tight many of the same trends are visible as was the case in the torsion mode of the baseline configuration. The modes soften and dampen with increasing force, and stiffen with increasing suspension stiffness. The three assembly repeatability tests on STA 1 at MIT nearly overlap, and once again for the torsion mode, the STA 3 data from MDA is a few percent softer. However, the loosening of the alpha joint changes the situation dramatically. The drop in frequency and rise in damping with increasing force is more than several percent in each test. Further, it should be noted by comparison of Table 3 with Figure 4a that the two force level plots shown in Figure 4a correspond only to the low and medium force levels. The high force level shifted the resonance so much, that it was moved outside of the test window. The repeatability of reassembly shown in the 1 Hz suspension data has also dropped noticeably.

The trends for the bending mode of the alpha configuration are again less clear, as shown in Figure 4b. The trend of softening with force amplitude is apparent, but the damping trend is down then up as force increases. The reassembly repeatability is quite good, and the change in frequency with change in suspension small, but the damping appears to rise with the 2 Hz suspension and fall with the 5 Hz suspension. The few tests from STA 3 suggest that it is several percent softer. Note that the ADINA results overpredict this frequency by as much as ten percent.

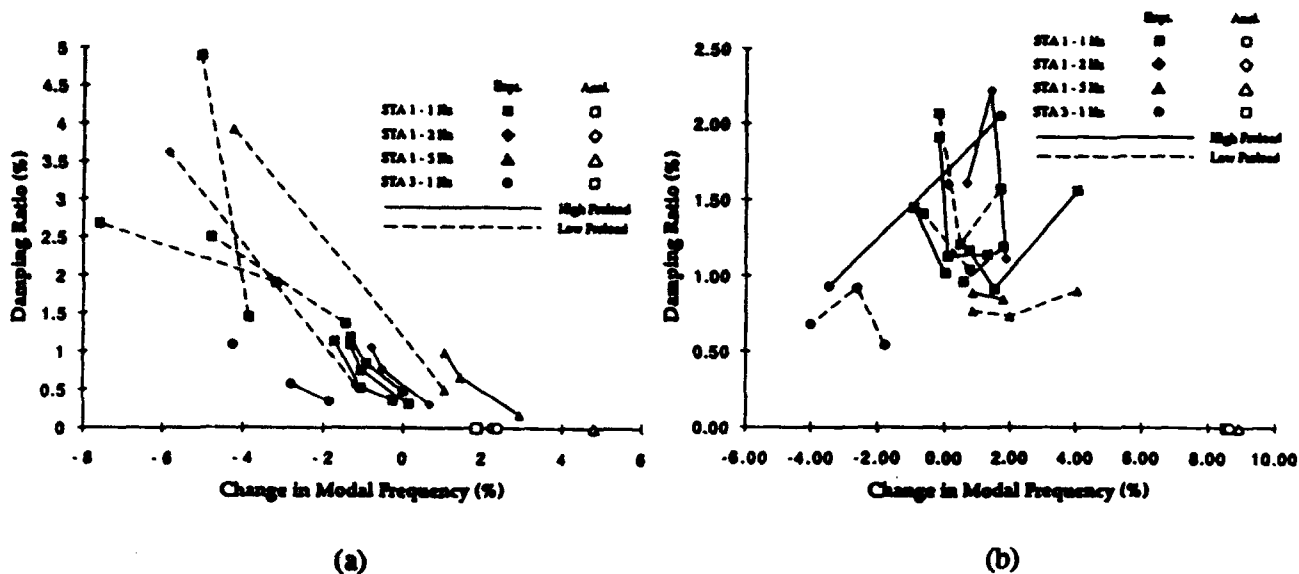


Figure 4. Trends in modal resonance of alpha configuration for the torsion and bending modes.

### L Configuration

The L configuration was chosen not so as to introduce any new hardware, but so as to present a slightly more complex geometry, more difficult to suspend in a gravity field. The geometric complexity of the L coupled the dynamics, producing the three modes chosen for testing (Figure 2). The L configuration was tested with alpha tight and loose, and a repeatability of assembly test was performed on STA 1 at MIT. After the first assembly and test, the erectable portion of the structure was removed, then replaced without struts being returned to the same location purposefully. Thus, although performed on the L configuration, this was a test to assess the repeatability of assembly of the hardware, as were the tests performed on the baseline configuration of STA 3 at MDA (discussed above).

For the three tests performed on this configuration, estimated modal parameters can be found in Table 4. As would be expected, the trends reflect aspects of the behavior of the baseline and alpha configurations discussed previously. The first mode tested (the third global or torsion mode) exhibits the softened and dampening trend of the bending mode of the baseline, without much change in damping when the alpha is loosened. The STA 1 second mode has an unusual trend of decreasing in stiffness and damping with increasing force. The STA 3 data is quite different in absolute value and trend. The third mode results are closely clustered, and generally mimic the first mode.

### Analysis of Experimental Variance

For the three configurations and eight modes discussed above, five experimental variations were introduced, in forcing level, joint preload, reassembly, shipset, and suspension. In the above discussion, an attempt was made to point out the trends associated with these variations. But in fact, of the five variations, only one - the modal changes due to suspension system - is deterministic in a linear model. Two are truly statistical in nature: the variation with shipset, and with reassembly. Two others, the sensitivity to preload and forcing level, are in principle deterministic if one were in possession of a highly detailed nonlinear structural model. In the absence of such a model, the variation due to force level and preload can be considered a statistical variation in model parameters. This introduces the option of examining the statistics of the 240 test cases represented in Tables 2, 3 and 4 in order to extract the sample variances associated with the physical variations.

**Table 4. Measured modal parameters of the L configuration (ground data).**

Suspension	STA - Rep.	Frequency			Damping Ratio			
		Low Force	Med. Force	High Force	Low Force	Med. Force	High Force	
<i>Torsion</i>								
Tight	1 Hz	1-1	7.88	7.78	7.74	0.39	0.76	0.88
	1 Hz	1-2	7.87	7.77	7.72	0.42	0.89	0.92
	1 Hz	1-3	7.87	7.76	7.73	0.44	0.76	0.90
	2 Hz	1-4	7.99	7.86	7.82	0.37	0.73	1.01
	1 Hz	3-1	7.95	7.84		0.36	0.71	
Loose	1 Hz	1-1	7.76	7.83	7.57	0.51	0.77	0.71
	1 Hz	3-1	7.67	7.59		1.26	1.07	
<i>Bending</i>								
Tight	1 Hz	1-1	25.85	25.76	25.72	0.39	0.33	0.33
	1 Hz	1-2	25.85	25.76	25.72	0.39	0.35	0.35
	1 Hz	1-3	25.81	25.70	25.65	0.43	0.35	0.32
	2 Hz	1-4	25.44	25.39	25.32	0.44	0.57	0.62
	1 Hz	3-1	25.22	25.07	24.91	0.42	0.60	0.57
Loose	1 Hz	1-1	25.83	25.76	25.73	0.37	0.32	0.37
	1 Hz	3-1	25.55	25.30	25.02	0.37		0.82
<i>Bending</i>								
Tight	1 Hz	1-1	31.68	31.49	31.46	0.54	0.81	1.30
	1 Hz	1-2	31.67	31.45	31.46	0.52	0.70	1.40
	1 Hz	1-3	31.72	31.48	31.45	0.58	0.69	1.25
	2 Hz	1-4		31.55	31.34		0.96	0.65
	1 Hz	3-1	31.21	31.11	31.04	0.42	0.37	0.42
Loose	1 Hz	1-1	31.77	31.58	31.59	0.45	0.84	1.27
	1 Hz	3-1	31.50	31.30	31.20	0.38	0.46	0.42

**Table 5. Sample variance for structural variations.**

Category	Statistical Set	N	$\Delta\omega/\omega$ (%)		$\zeta$ (%)	
			$S_{\Delta}$	$ \pm\Delta _{\max}$	$S_{\Delta}$	$ \pm\Delta _{\max}$
Forcing Level	All Data	162	.54	1.90	.19	.54
	Baseline	78	.35	1.10	.11	.32
	$\alpha$ & L	84	.68	1.90	.25	.54
Preload	All Data	166	.99	3.41	.40	2.07
	Baseline	84	.68	1.76	.08	.22
	$\alpha$ & L	82	1.23	3.41	.57	2.07
Reassembly	All Data	111	.54	2.21	.22	1.54
	Baseline & L	81	.32	.79	.04	.11
	$\alpha$	30	.91	2.21	.42	1.54
Ship Set	All Data	96	.85	2.15	.19	.45
	Baseline	50	.61	1.18	.08	.16
	$\alpha$ & L	46	1.06	2.15	.26	.45
All Variations	All Data	240	1.25	4.69	.45	3.59
	Baseline	122	.92	2.82	.13	.43
	$\alpha$ & L	118	1.53	4.69	.64	3.59

The variances in the data of Table 5 were extracted in the following way. For a given mode, the data for like test conditions were averaged, and then the delta from the average for each otherwise nominally identical case was calculated. For the frequency, the delta was normalized by the average, and expressed as percent. For the damping ratio, which is already a small quantity, and already normalized by the frequency in the equations of motion, the delta is just the difference from the average expressed in percent. For example, in order to examine variation with force level, the frequency measured for the low, medium and high force amplitude for each row in Table 3 was averaged, and the delta from that average for that row calculated. This had the effect of introducing a zero mean data set of normalized deltas which identified only the variation under study, and suppressed all other variations. The sample variance of these deltas was then calculated.

These sample variances are shown in Table 5, along with the statistically less significant absolute value of the maximum or minimum delta. In examining the statistics, it was found that there was a noticeable difference in the statistics of the sample that excluded the alpha joint in its dynamics versus those that included the alpha joint. Therefore for each variation, the statistics of all the data in the set, and of the data taken without and with the alpha joint, are shown separately.

The statistical data is remarkably constant. The variance in frequency is about one-half percent for variation in forcing level (over one order of magnitude) and reassembly, and about one percent for variation in preload and shipset. In each case, the data set that excludes the alpha joint shows about 60% of the average variance, while the data set that includes the alpha is commensurably larger. Note that for the variation in reassembly, the L configuration data has been included in the nonalpha category, since the disassembly/reassembly that was done on this configuration was of the erectable hardware.

The variance in the damping ratio is also very consistent. A sample variance of 0.2% is found for variation in forcing, reassembly, and shipset, while twice that variance is found for change in preload. This compares with an average damping ratio of 0.7%. However, the difference between the variance for the non-alpha and alpha tests is more apparent in the damping ratio. The non-alpha cases average less than 0.1% damping variance (compared to an average of 0.4%), while the alpha cases average around 0.4% variance (compared to an average of 1%).

The statistics for all variations are presented at the bottom of Table 5. Roughly speaking they indicate that about one percent variance should be expected in frequency and one-half percent in damping ratio for all manufacturing and experimental variation. By way of contrast, statistics of the agreement between experiment and analysis are shown in Table 6. For this comparison all the data for a mode have been averaged, the delta formed with the ADINA prediction as described above, and the mean and variance of the difference calculated for the significantly smaller data set. The variance in frequency is consistently about five percent between the first generation model (i.e. no experimental data used to update the model) and the experimental value. If sufficient data were included in the set, presumably the mean error in frequency would approach zero, unless there is some consistent bias in our modeling of structures. The predicted damping ratio of the structure is of course zero, so the statistics on damping in Table 6 are just the statistics of the experimentally observed damping.

Table 6. Comparison of ADINA predictions and mean experimental ground data.

Statistical Set	N	$\Delta\omega/\omega$ (%)				$\zeta$ (%)			
		$\bar{\Delta}$	$S_{\Delta}$	+ $\Delta_{max}$	- $\Delta_{max}$	$\bar{\Delta}$	$S_{\Delta}$	+ $\Delta_{max}$	- $\Delta_{max}$
All Data	21	1.35	4.57	8.52	-5.82	.70	.41	1.63	.24
Baseline	9	-.55	4.99	6.43	-5.82	.37	.08	.49	.24
$\alpha$ & L	12	2.77	3.83	8.52	-2.14	.95	.29	1.63	.42

## Orbital Test Results

The baseline configuration was tested in its first torsion, bending and shearing modes, with high, medium and low bay preload. The alpha configuration was tested in its first torsion and bending modes, and the L in a torsion and two bending modes. The alpha and L configurations were always tested with the high deployable bay preload, and with the alpha joint in either the tight and loose settings. In general the test articles were driven at low, medium and high force amplitudes, which were approximately linearly spaced over one decade (Table 7). In some cases selected amplitudes were omitted to conserve test time. Only one shipset (STA 1) was tested on orbit and no assembly/assembly testing was performed.

### Baseline Configuration

The first torsion, bending and shearing modes of the baseline configuration were excited on orbit. Representative transfer functions for the baseline configuration with high preload (PL1) are shown in Figure 5. The three symbols indicate the transfer function for low medium and high excitation force levels (Table 7). For all plots shown in this and subsequent figures, the transfer functions for the torsion, bending and shearing modes are from the measured force input to an accelerometer at the actuator end, center and far end of the truss respectively. Identified modal parameters for the baseline configuration are listed in Table 8.

Low forcing of the torsion mode (first mode) displays a clear and nearly linear resonance (Figure 5). As the force level is increased, the resonance quickly begins to appear nonlinear. Due to the structural nonlinearity, the mode softens and becomes more damped with increased forcing amplitudes.

For these and subsequent nonlinear transfer functions, the linear parameters reported in Tables 8, 9 and 10 can be interpreted as best linear approximation of the modal parameters. For the bending mode (second mode), distinct resonances remain for all force levels. The apparent resonance changes only slightly as the excitation force is increased. Damping, on the other hand, more than doubles between low and medium forcing levels, and continues to increase for the third amplitude. The third or shearing mode appears to possess a relatively linear resonance, with a slight softening and increase in damping. The response of this first configuration with a tight preload can be characterized as weakly nonlinear in bending and shearing, and moderately nonlinear in torsion.

Table 7. Force amplitudes used in STA 1 excitations for ground and space testing.

Config.	Mode	Type	Apprx. Freq. (Hz)	Amp.1		Amp.2		Amp.3	
				Ground (lbf)	Space (lbf)	Ground (lbf)	Space (lbf)	Ground (lbf)	Space (lbf)
Baseline	1	Torsion	7.75	0.046	0.052	0.224	0.296	0.396	0.530
	2	Bending	20.00	0.044	0.046	0.208	0.228	0.368	0.407
	3	Shearing	29.00	0.043	0.046	0.204	0.223	0.362	0.397
Alpha	1	Torsion	7.25	0.046	0.051	0.227	0.303	0.276	0.547
	2	Bending	10.50	0.043	0.048	0.130	0.257	0.380	0.462
L	1	Torsion	7.75	0.047	0.048	0.263	0.292	0.471	0.526
	2	Bending	25.50	0.039	-	0.226	0.224	0.404	-
	3	Bending	30.50	0.030	-	0.223	0.221	0.399	-

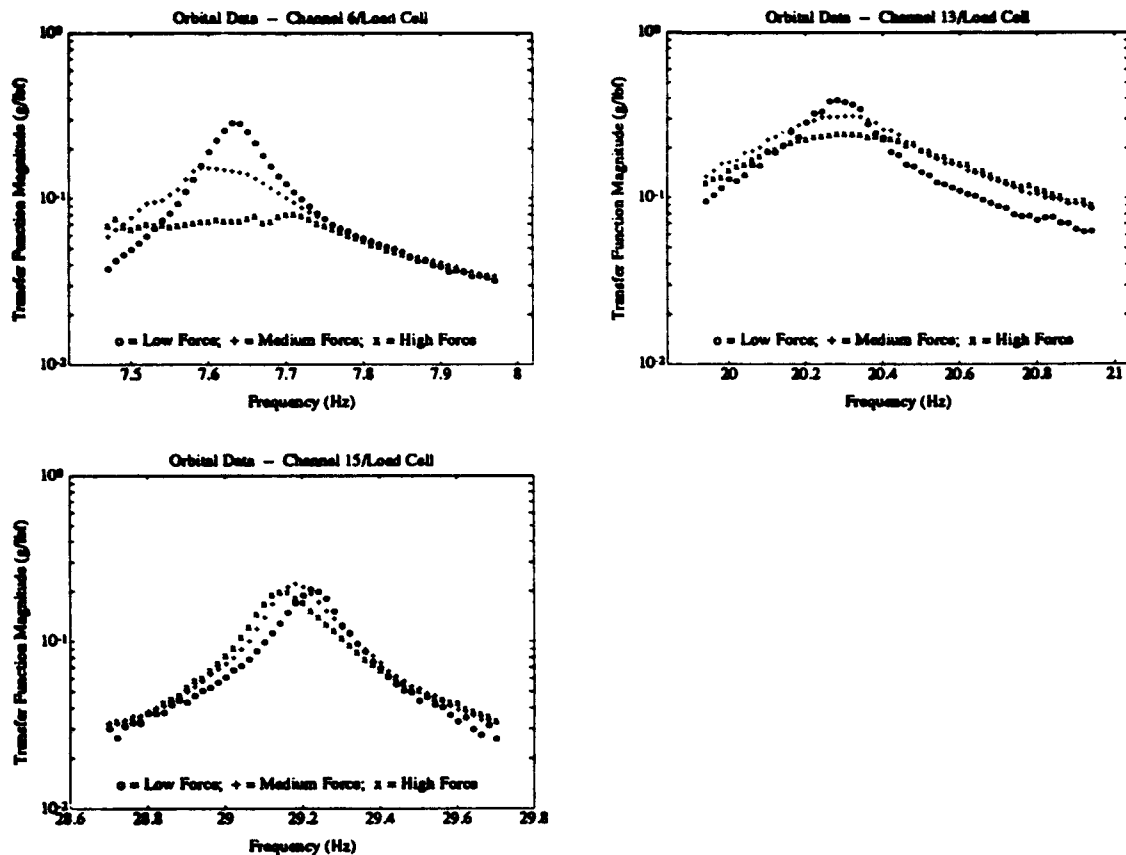


**Figure 5. Transfer functions for the torsion, bending, and shearing modes of the baseline configuration with high preload (space data).**

A comparison of the low and high amplitude excitation of torsion modes for high bay preload for ground and orbital tests can be found in the first of the three transfer functions of Figure 6. From the figure and Table 8, it is obvious that the modes of the space data occurred at lower frequencies and, where calculable, larger damping ratios. Upon comparison, it is evident that the nonlinearities manifest themselves much more strongly in the orbital data.

Similar comparisons can be made for the bending and shearing mode. For the bending mode (see Figure 6), the space frequencies are again lower than those of the ground data but by a much smaller percentage. Even though they are similar at low force levels, the space damping levels become almost double the levels seen in ground testing at the highest force level. The ground and orbital modes seem to exhibit the same characteristics with the exception that the orbital data are generally more damped. Figure 6 also contains a comparison of the shearing modes of ground and orbital tests. Although the space data was softer, only very slight changes in damping were present.

On-orbit data was obtained for the one deployable bay with medium and low preload. The results for the medium (PL2) preload are generally intermediate to the high and low cases, and are listed in Table 8. Figure 7 contains transfer function plots of the low preload (PL3) for medium and high forcing levels for space and ground; estimated modal frequency and damping are listed in Table 8.

As can be seen in the first transfer function in Figure 7, the two tested amplitudes for the first mode have resonances that are barely within the left boundary of the test window. It is significant to note that although certain test windows did partially or completely miss the intended modes, all windows were based on preflight ground test data. Each space test window was selected by referring to several ground tests and estimating the amount of expected shifting. Therefore, a missed orbital test mode indicates a significant and unexpected shift in frequency.

**Table 8. Predicted and measured modal parameters of the baseline configuration.**

	Suspension	Pred. Freq. (Hz)		Frequency (Hz)			Damping Ratio (%)		
		Full	Guyan	Low Force	Med. Force	High Force	Low Force	Med. Force	High Force
<i>Torsion</i>									
High	1 Hz	8.05		7.74	7.70	7.67	0.24	0.40	0.54
Preload	0-g	7.68	8.04	7.63	7.59	7.57	0.40	0.92	2.3
Med.	1 Hz	NA		7.71	7.66	7.64	0.27	0.42	0.57
Preload	0-g	NA		7.61	7.57	7.53	0.34	1.2	2.7
Low	1 Hz	NA		-	7.58	7.54	-	0.67	0.86
Preload	0-g	NA		-	7.52	7.50	-	1.6	2.7
<i>Bending</i>									
High	1 Hz	19.29		20.43	20.37	20.33	0.41	0.39	0.62
Preload	0-g	19.26	19.31	20.27	20.27	20.29	0.47	0.98	1.18
Med.	1 Hz	NA		20.48	20.41	20.31	0.58	0.48	0.52
Preload	0-g	NA		20.24	20.21	20.23	0.46	0.99	1.15
Low	1 Hz	NA		20.29	20.18	20.12	0.55	0.52	0.44
Preload	0-g	NA		20.24	20.22	20.22	0.51	0.85	1.12
<i>Shearing</i>									
High	1 Hz	28.68		29.42	29.33	29.28	0.25	0.27	0.28
Preload	0-g	28.27	28.68	29.22	29.18	29.14	0.22	0.24	0.28
Med.	1 Hz	NA		29.34	29.26	29.22	0.26	0.27	0.29
Preload	0-g	NA		29.18	29.14	28.10	0.23	0.23	0.27
Low	1 Hz	NA		-	29.14	29.10	-	0.30	0.33
Preload	0-g	NA		-	29.08	29.06	-	0.24	0.28

**Table 9. Predicted and measured modal parameters of the alpha configuration (high deployable bay preload).**

	Suspension	Pred. Freq. (Hz)		Frequency (Hz)			Damping Ratio (%)		
		Full	Guyan	Low Force	Med. Force	High Force	Low Force	Med. Force	High Force
<i>Torsion</i>									
Tight	1 Hz	7.66		7.52	7.44	7.41	0.39	0.71	1.14
	0-g	7.69	7.70	7.35	7.30	7.28	0.51	1.05	2.1
Loose	1 Hz	NA		7.31	7.08	-	1.58	3.36	-
	0-g	NA		7.21	6.74	7.19	1.21	NDR	NDR
<i>Bending</i>									
Tight	1 Hz	11.57		10.85	10.68	10.69	1.24	1.16	1.54
	0-g	11.78	11.58	-	10.62	10.59	-	2	1.8
Loose	1 Hz	NA		10.79	10.72	10.68	1.31	1.91	1.52
	0-g	NA		-	10.40	10.15	-	2.7	2.44

**Table 10. Predicted and measured modal parameters of the L configuration (high deployable bay preload).**

	Suspension	Pred. Freq. (Hz)		Frequency (Hz)			Damping Ratio (%)		
		Full	Guyan	Low Force	Med. Force	High Force	Low Force	Med. Force	High Force
<b>Torsion</b>									
Tight	1 Hz	7.90		7.87	7.77	7.73	0.42	0.78	0.92
	0-g	8.12	8.00	7.34	-	-	-	-	-
Loose	1 Hz	NA		7.76	7.63	7.57	0.51	0.77	0.71
	0-g	NA		-	-	-	-	-	-
<b>Bending</b>									
Tight	1 Hz	25.16		25.84	25.74	25.70	0.4	0.34	0.33
	0-g	25.29	25.28	-	-	-	-	-	-
Loose	1 Hz	NA		25.83	25.76	25.73	0.37	0.32	0.37
	0-g	NA		-	-	-	-	-	-
<b>Bending</b>									
Tight	1 Hz	30.78		31.69	31.47	31.46	0.55	0.73	1.32
	0-g	31.30	31.15	-	-	-	-	-	-
Loose	1 Hz	NA		31.77	31.58	31.59	0.45	0.84	1.27
	0-g	NA		-	-	-	-	-	-

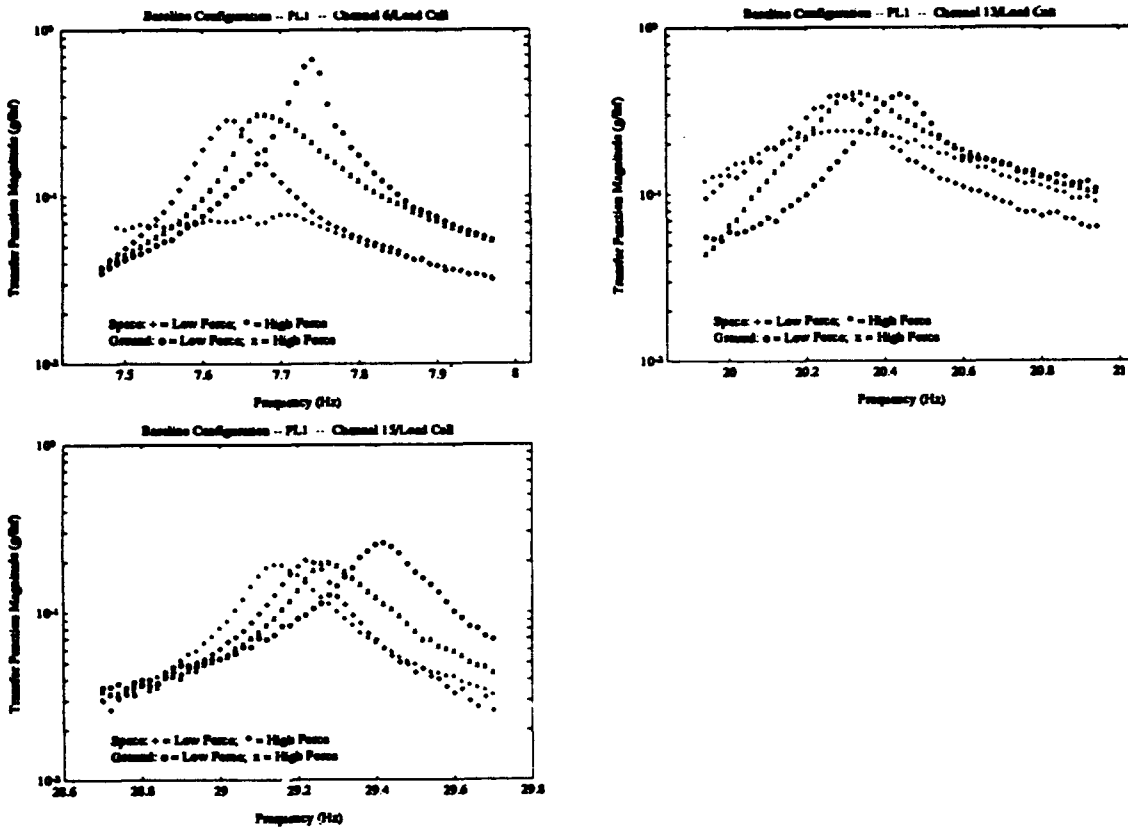


**Figure 6. Transfer functions for the torsion, bending, and shearing modes of the baseline configuration with high preload (space vs. ground data).**

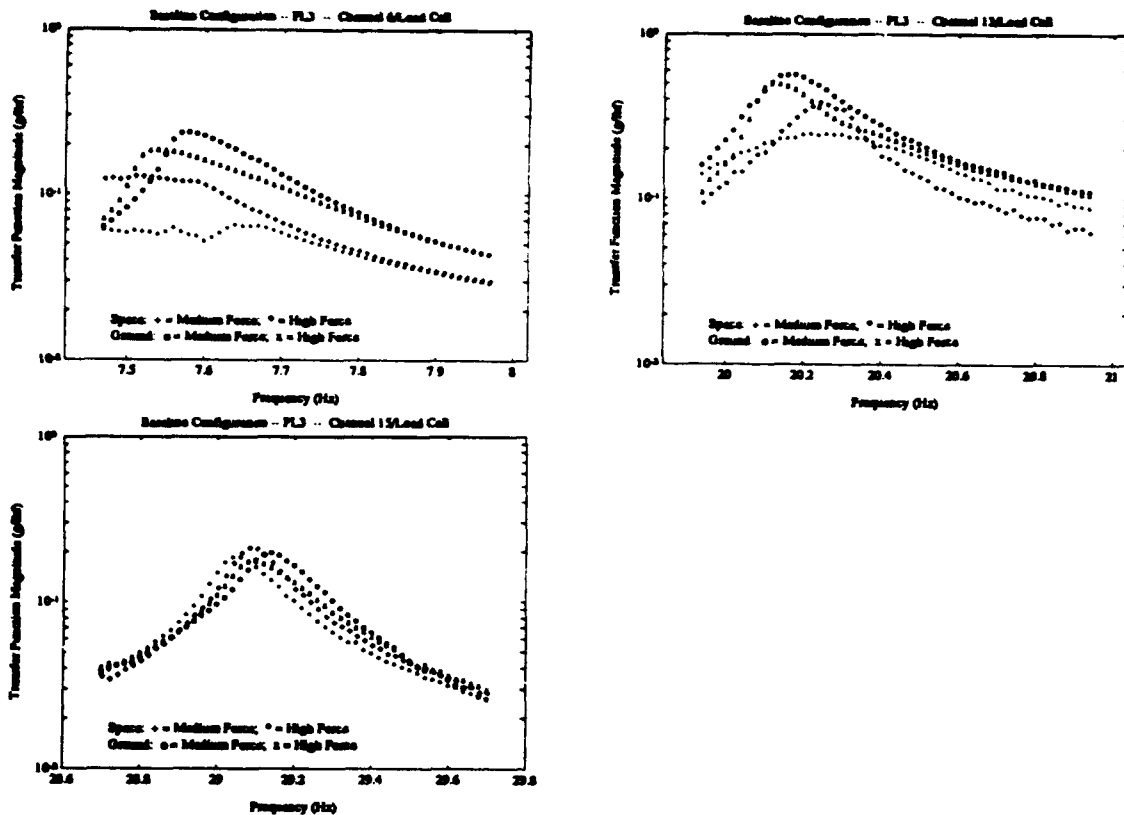


**Figure 7. Transfer functions for the torsion, bending, and shearing modes of the baseline configuration with low preload (space vs. ground data).**

The influence of reduced bay preload can be observed by comparing the space traces for medium and high excitation for low preload in Figure 7 with the traces for medium and high excitation for high preload in Figure 5. The magnitude curves for the torsion mode indicate a continued softening and dampening, as well as increasing structural nonlinearity. The behavior of the bending mode was remarkably unchanged with preload in orbit, still with notable increase in damping but little change in frequency with increased force amplitude. Shearing is slightly softer but no more damping at low preload, and again softened slightly and experienced a small increase in damping with increased force.

Comparative plots of ground vs. orbital data can also be found in Figure 7 for torsion, bending, and shearing modes, respectively. For the torsion mode, the space data are softer and more damped than the ground data. With low preload, even the ground response is moderately nonlinear, with a distinct nonsymmetric resonance. For the bending mode, the frequency increased slightly in space, but the damping was greater. Only small differences exist for the shearing mode. The space data are softer and slightly less damped than the ground test equivalents.

Two physical mechanisms are likely to cause the nonlinear behavior observed in the baseline configuration: slackening of the tensioning cables and accumulated microfriction. Stranded cables such as those used in the bay possess highly nonlinear stiffness as they come slack, and are noticeably nonlinear when preloaded up to significant fractions of their yield stress, well above the stress at which they were preloaded, even at the high preload settings. Microfriction is an alternate explanation. With increasing amplitude, there is increasing friction breakage, resulting in softening and increased dissipation. A more thorough analysis of the nonlinear response awaits a detailed set of measurements on the nonlinear behavior of the truss components.

In order to more easily visualize the influences of gravity, preload and force level, the trends in the three modes of the baseline configuration are shown in Figures 8a, 8b and 8c. The damping ratio (in percent) is plotted versus the change in frequency normalized by a reference frequency (in

percent). The first test of STA 1 at MIT with high preload and low excitation level was considered the reference. The lines connect tests of constant bay preload, and the symbols indicate tests of different force amplitudes. For the case of the torsion mode in Figure 8a, the trends are quite clear. Both on earth and in space, increasing force amplitude softens and damps the system. The rate at which damping increases in space is greater. Decreasing bay preload softens the system, but does not strongly affect damping. Finally the absence of gravity softens and damps the response.

The bending mode trends are displayed in Figure 8b. The ground data show only a weak trend of decrease in frequency with force level, and no organized sensitivity to damping ratio. On the other hand, the space data show a strong increase in damping with force level for all preloads, a trend not seen on the ground. The trends for shearing, shown in Figure 8c, are like those for torsion, but more subtle. Increasing force and decreasing preload slightly soften and dampen the mode. On orbit the mode softens, but does not show a significant change in damping.

It is now appropriate to apply the tests of statistical significance to the changes observed between earth and orbit. Based on the extensive ground assembly/ reassembly testing presented above, it was determined that the standard deviation due to reassembly was about one half percent in frequency and one quarter percent in damping ratio. Examining Figure 8 and comparing the shifts in frequency and damping ratio for equivalent test conditions, it can be concluded that: for torsion, both the shift in frequency and damping is significant; for bending, only the change in damping is significant; and for shearing, the change in frequency is marginally significant

#### **Alpha Configuration**

The additional feature of the alpha configuration was the relatively massive articulated rotary joint that replaced the center bay of erectable hardware. This configuration was tested in the torsion and bending modes, with the alpha joint tight and loose. Testing of the alpha configuration was performed with the preload in the adjustable bay of the deployable module in the high preload setting, so that it was closest to that of the other, unadjustable bays.

The alpha configuration was first tested in the alpha tight setting. Representative transfer functions may be found in Figure 9. For the second mode, the low force data is unreliable due to a saturation of the accelerometer. Estimates of natural frequencies and damping ratios for the tested modes are contained in Table 9. The first plot of Figure 9, for the torsion mode, bears remarkable resemblance to the torsion mode of the baseline, Figure 5. Softening, dampening and increasing nonlinearity are present with increased force amplitude. Comparison of the modal parameters in Tables 8 and 9 for the space data of the baseline high preload and the alpha tight show only a slight drop in frequency and the same range of damping. Obviously the presence of the tight alpha joint in the middle of the truss, at a node of the torsion mode, has only a slight impact on the parameters of that mode.

By way of contrast, the bending mode has dropped almost a factor of two in frequency, due to the large mass of the alpha joint at an antinode of bending mode. For a fixed damping and a drop in two of frequency, one would expect an increase in two of damping ratio. The data reveal more or less the expected factor of two in damping ratio. Thus, other than the addition of mass, the alpha joint in its tight preload has a small effect on the dynamics of the STA.

Ground and orbital test data are overplotted for the torsion mode in Figure 10. Although similar at lower force levels, the relative appearance of the two curve sets changes with increased forcing amplitude; the ground data display smooth transitions while the orbital curves exhibit more irregular behavior. Generally, however, the space data are softer and more damped than the ground data. For the bending mode, the parameters in Table 9 show that the space data are slightly softer and more damped than the ground data. Again these are the same trends seen in the baseline high preload case.

The alpha configuration with loose preload was tested next. For this test, transfer function data are plotted in Figure 11, while parametric estimates are given in Table 10. The torsion mode appears to exhibit jump phenomena for the two upper amplitudes. For low forces, the static friction within the alpha joint is thought to be sufficient to keep the joint locked, producing essentially linear behavior and the familiar modal peak. However, as the forcing level is increased, the joint may begin to slip

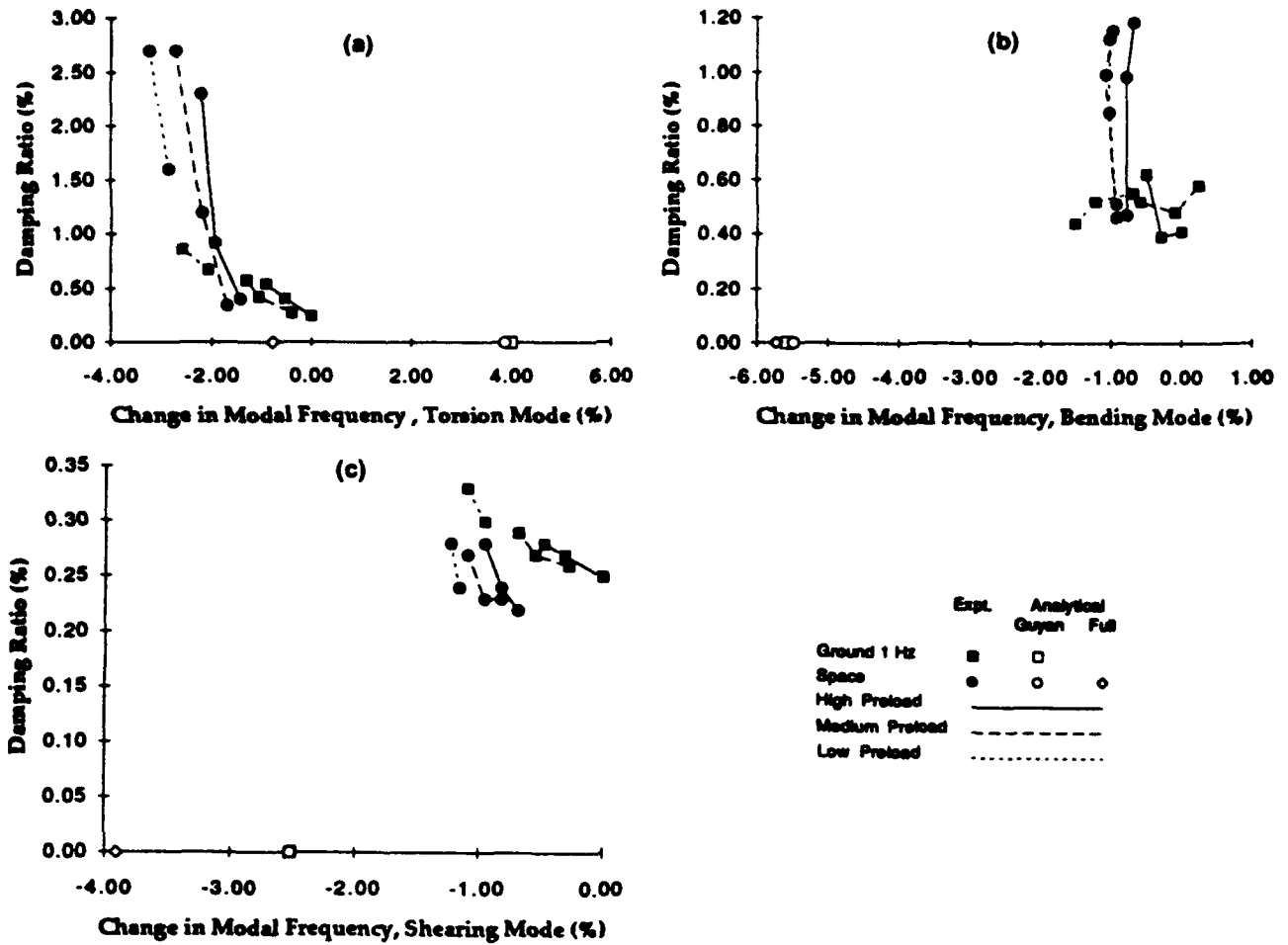


Figure 8. Trends in modal parameters of baseline configuration (space vs. ground data).

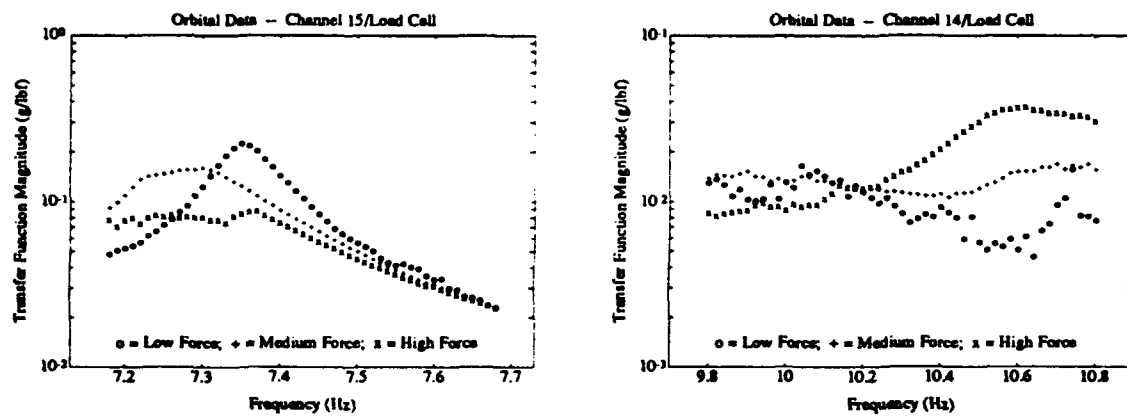
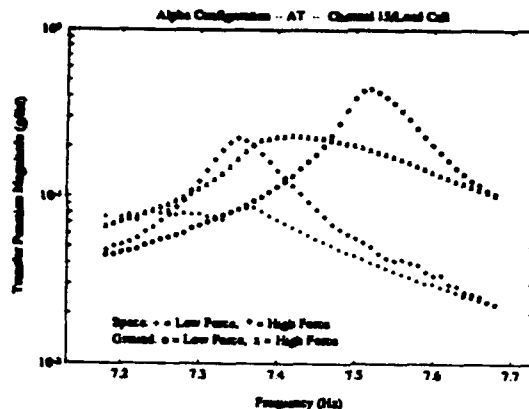


Figure 9. Transfer functions for torsion and bending modes of the alpha configuration with alpha tight (space data).

9



**Figure 10. Transfer functions of the torsion mode of the alpha configuration with alpha tight (space vs. ground data).**

causing the discontinuities in the plot. For these jumps, no damping estimate can be calculated. For the force amplitudes where jump occurred, the parameter table will contain the jump frequencies. It is worth noting that no indications of jumping occurred for the alpha tight tests of this configuration. Unlike the torsion mode, the bending mode appears only weakly nonlinear, with evidence of slight softening with increasing excitation. The low force trace is again unreliable due to saturation.

The orbit and ground results can be compared by examining Figures 11 and 12. Upon comparison with ground results, the orbital torsion data are markedly different except for the low amplitude. The ground data softened and became much more damped but saw no jump phenomena. On the other hand, the orbital data had a clear peak for the low force level but displayed jumps for higher amplitudes. During ground testing, gravity may have preloaded the alpha joint enough to prevent rotations and jumps from occurring. As a result, damping increased but jumps were not in evidence.

The trend plots for the alpha configuration are shown in Figure 13. For the torsion mode in Figure 13a, only the on orbit data which did not show a jump are presented. The statistically significant softening and dampening influence of zero-gravity on the torsion mode is quite apparent. Likewise, statistically valid decrease in stiffness and damping are present in the bending modes, as can be seen in Figure 13b.

### **L Configuration**

Finally, the most challenging configuration, the L configuration, was tested with the alpha joint tight and loose in a torsion and two bending modes. The narrow test windows specified prior to flight did not manage to catch a single mode well enough to produce modal estimates, due to unexpectedly large frequency shifts. A low force sine sweep was performed up to 30 Hz via a manual protocol. Coarse location of the torsion mode was identified, and is compared with the ground results in Table 10. Since this mode dropped 7%, and the other modes dropped enough to be outside the test windows, it can be concluded that qualitatively significant softening of the two dimensional configuration occurred in 0-g.

## **CONCLUSIONS**

The variations in modal properties with force amplitude, joint preload, reassembly, shipset, suspension, and gravity were measured for the structural configurations of a scaled model of typical erectable, deployable and articulated space structures. Trends and statistical information were

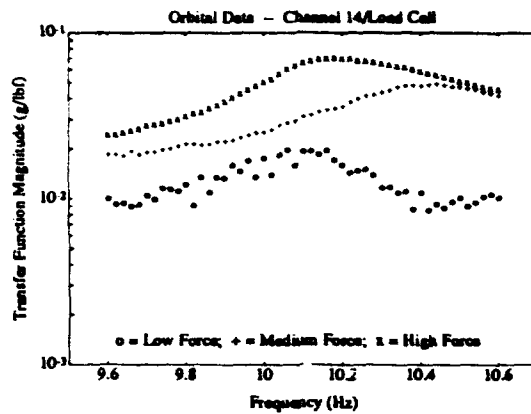
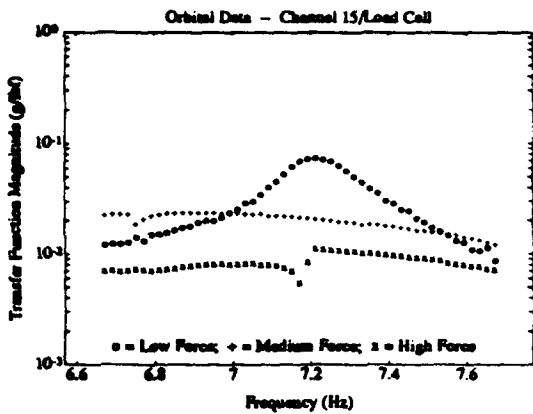


Figure 11. Transfer functions for torsion and bending modes of the alpha configuration with alpha loose (space data).

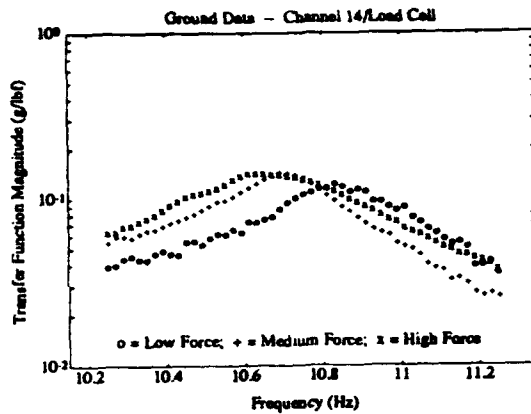
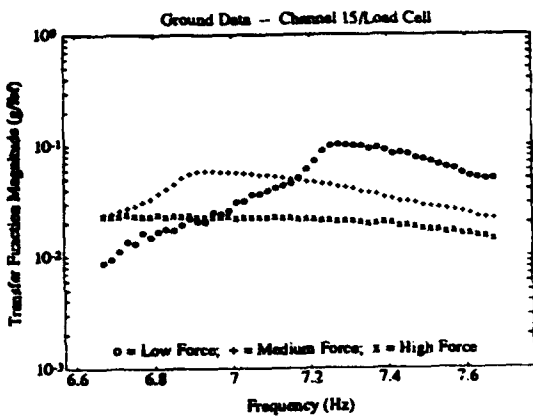


Figure 12. Transfer functions for torsion and bending modes of the alpha configuration with alpha loose (ground data).

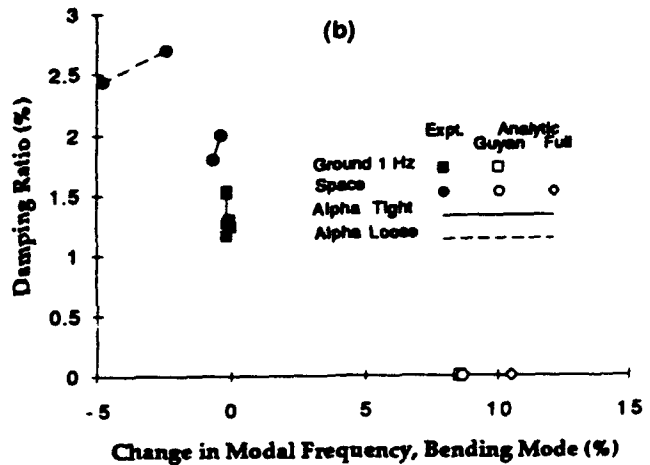
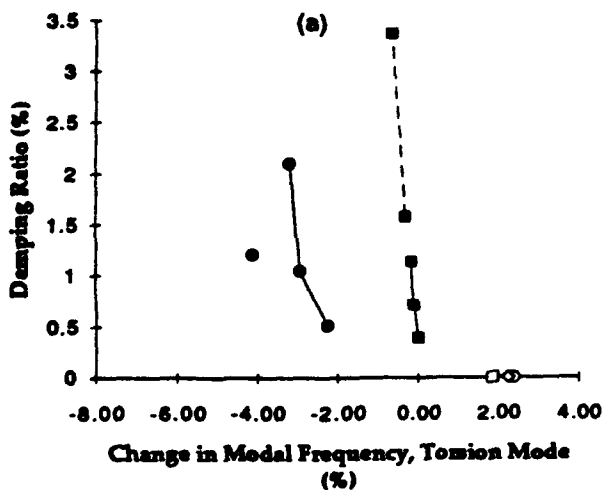


Figure 13. Trends in modal parameters for the torsion and bending modes of the alpha configuration (space vs. ground data).

extracted from the approximately two billion data measurements made. While these trends and statistics are particular to this test article, it is sufficiently representative that they can be generalized to similar hardware. Significant differences between 1 g and 0 g identified modal parameters were measured. Generally, data taken in orbit showed lower resonant frequencies and higher damping ratios. Gravity preload of the structure and the presence of a suspension, resulted in higher frequencies and lower damping ratios for ground test data.

Repeatability of modal parameters to reassembly of certain components was investigated. Although the deployable modules appeared to have fairly good repeatability, the alpha joint was seen to cause poor repeatability with its introduction into the truss system. From multiple tests of the L configuration, the erectable hardware was found to have good repeatability characteristics. Variation from one shipset to the second revealed, by and large, the same trends in the data, but an absolute difference which ranged between zero and several percent in frequency. In some cases this caused the data from the two shipsets to lie within the scatter of each taken individually, while in other cases it created noticeably distinct sets.

The choice of suspension system stiffness had noticeable and relatively predictable impacts on the measured response of the STA. Both natural frequencies and damping ratios were affected by the suspension system. As suspension stiffness was increased, natural frequencies generally increased while damping ratios dropped. Frequency shifting was most pronounced on the lower modes and stiffer suspensions.

The STA exhibited weakly, moderately and strongly nonlinear structural behavior. Deployable joints, tensioning cables, and the alpha joint all contributed to the overall nonlinear behavior of the truss. As a result, modes generally softened and experienced increased damping levels as the excitation force was increased. In both test environments, as the adjustable bay preload was decreased, the nonlinear behavior became stronger. A dramatic difference was seen between tests where the alpha joint was tight and loose; strongly nonlinear behavior occurred with the alpha joint loose in the torsion mode, while the STA displayed only moderately nonlinear behavior with the joint tight. The jump phenomenon witnessed for the orbital test of the alpha configuration with loose preload was not seen on earth; no indication of this behavior could be deduced based on ground tests.

A trend was seen in the data that indicated that the differences between one- and zero-gravity are stronger at lower frequencies and diminish at higher frequencies. For first or torsion modes, the change in transfer function magnitude with increasing force was often abrupt, causing a resonant peak to be indiscernible. In the alpha loose tests, jumps occurred on orbit for which no indication could be found in the ground data. Although higher modes were also different in orbital tests, these differences were largely due to smaller shifts in frequency and changes in damping ratio. Unfortunately, it is often the first few modes of a structure that are most important for loads, dynamics and control analyses.

With few exceptions, the orbital test data produced modes that were softer than those of the applicable ground tests. Two mechanisms for this destiffening are elimination of suspension stiffening of the boundaries and gravity preload of the structure. To evaluate the influence of the first mechanism on the ground test results, several variants in suspension stiffness were used. It was found that the finite element model correctly predicted the linear stiffening of the STA due to 1, 2 and 5 Hz suspensions. However, the linear model under-predicted the destiffening due to the removal of the suspension altogether. Therefore, it can be concluded that the absence of gravity loading directly on the structural elements was the cause of the destiffening. However, the finite element model also captured the "linear" gravity geometric stiffening, such as that which leads to buckling. The inference is that the softening in space must be due to gravity loading on the nonlinear elements of the structure.

In general, the space data were also more damped than the 1-g suspended data. Again, two mechanisms exist to explain the change in damping between the ground and orbital tests. Measured damping can be due to transmission of energy out of the structure or true dissipation. Comparing the transmission paths present in the middeck and ground facilities, one finds the same umbilical, same atmosphere, and a much less intrusive suspension on the middeck. Thus, the transmission losses must

be the same or less on orbit. This is substantiated by the relatively similar damping measured at high preloads and low excitation amplitudes. Therefore, the increase in damping is once again due to internal mechanisms, probably dominated by the nonlinear elements. When testing in 0-g, no gravity field exists to preload the joints and wires of the deployable structure. With the gravity-induced bias removed, the joints would be able to participate more freely and increase the effective damping of the structure. Also, with the gravity-induced preload on the alpha joint removed, the joint would be freer to introduce damping, especially when in the AL setting. Thus, the potentially nonlinear elements (the joints, wires and alpha joint) are the likely source of the softening and dampening that occurs on orbit.

The variance in all the data due to the variations in forcing, preload, reassembly, and shipset was on the order of one percent in frequency, and one-half percent in damping ratio. These are slightly lower and higher for the subsets of the data that exclude the alpha joint and include the alpha joint, respectively. The variance in the damping ratio is of the order of one-half percent, again lower for the non-alpha configurations and higher for the configurations which include the alpha. These variances provide valuable guidance in the evaluation of structural dynamic predictions, and closed-loop controller robustness. For example, they indicate that any structural dynamic prediction that agrees with experiment by better than one percent on average is the result of luck or tuning the model to the specific test article and test conditions present. The one percent rule essentially establishes a lower bound in the error of any *a priori* prediction of structural resonance. For the evaluation of the robustness of closed-loop control, it establishes a minimum variance in frequency and damping that should be considered in robust design and prediction of likely achieved closed loop performance.

#### ACKNOWLEDGEMENTS

This work was supported by the NASA IN-STEP Flight Experiments Program, and the NASA Langley Research Center, Reference No. NAS1-18690, with Dr. Sherwin Beck as monitor; by the NASA Headquarters Grant No. NAGW-1335 to the MIT Space Engineering Research Center, with Dr. Robert Hayduk as technical monitor, and by NASA Head Quarter Grant No. NAGW-2014 with Mr. Samuel Venneri as technical monitor.

McDonnell Douglas Aerospace was instrumental in the supply of the structural test article, and the funding at McDonnell Douglas of the experiments performed there.

#### REFERENCES

ADINA User's Manual, ADINA R&D, Watertown, MA 1987

Barlow, Mark S., "Modeling and Ground Modal Identification of Space Structures," S.M. Thesis, MIT Cambridge, MA., January 1992

Crawley, E.F., Barlow, M.S., van Schoor, M.C., Bicos, A.S., "Variation in the Modal Parameters of Space Structures," Proceedings of the 33rd AIAA/ASME/ ASCE/AHS Structures, Structural Dynamics and Materials Conference, Dallas, TX, April 1992.

Ewins, D.J., "Modal Testing: Theory and Practice," Research Studies Press 1984, pp. 158-168.

Gronet, M.J., Crawley, E.F., Dienhols, D., "Design, Analysis, and Testing of a Hybrid-Scale Structural Dynamic Model of the Space Station." AIAA Paper No. 89-1340, 1989

Kienholz, D.A., Crawley, E.F. and Harvey, I.J., "Very Low Frequency Suspension Systems for Dynamic Testing," AIAA Paper No. 89-1194, 1989.

Pinson, L.D. and Hanks, B. R. "Large Space Structures Raise Testing Challenges," *Astronautics and Aeronautics*, Vol. 21, No. 10, 1983, p. 34.

Rey, D.A., "The Effects of Suspension Systems and Gravity on Ground Based Tests of Controlled Space Structures," S.M. Thesis, MIT Cambridge MA, August 1992.

# IMPACT OF INTERFACE STIFFNESS AND DAMPING ON PAYLOAD RESPONSES IN SPACE SYSTEMS

Wan T. Tsai<sup>1</sup>

Rockwell International, Downey, CA

## ABSTRACT

This paper presents a new method in coupling payloads to launch vehicles. The study in developing this method was initiated by the strange response phenomenon frequently encountered in dynamic loads analyses of space transportation system. When the mass of a small payload is slightly altered, the responses of other larger payloads at distance away may be significantly changed. The reliability in the highly sensitive response changing phenomenon has been suspected. After careful examinations of the system integration and analysis methodology, the strange response phenomenon may be partially induced by the existing coupling approach in treating the interface stiffness and damping. This paper summarizes the theory of the newly proposed coupling method and uses it to analyze payload responses. The analysis results confirm our initial speculation that the strange responses may diminish when proper interface stiffness and damping values are applied. Using the new coupling method, the interface joints between the payloads and launch vehicle can be re-designed to reduce the payload responses. Such a re-design process in considering the effect of interface stiffness and damping cannot be done when the existing coupling approach is applied.

## INTRODUCTION

This paper proposes a new method in coupling payloads to space transportation systems. The proposed method enables analysts to determine the payload responses in a more realistic manner by accounting for the physical properties at the interfaces between payloads and launch vehicles. As a tool, the proposed method also provides the capability in re-designs of the interface joints so that the payload responses can be effectively reduced and therewith the orbital capabilities can be increased. The ability in re-designing interface joints for increasing the orbital capabilities is not available when the existing coupling method is applied.

In transient analyses of space transportation systems, a strange response phenomenon has been frequently encountered. When the mass

---

<sup>1</sup>Sr. Engineering Specialist. Also Adjunct Professor, Cal. State Univ., Long Beach.

of a small payload is slightly changed, the responses of other larger payloads at distance away may be significantly altered. One way in interpreting this phenomenon is that the change of small payload mass effectively alters the system frequencies. As a result, some of the altered frequencies may happen to coincide with those in the frequency enriched forcing function to induce resonances. Another way in interpreting this phenomenon, after careful studies of the system integration and system analysis methodology, is that the existing coupling approach in treating the interface stiffness and damping may not be fully adequate to represent the true condition. This paper investigates the impact of interface stiffness and damping variations on payload responses. The effect of frequency will be briefly illustrated by a simple example.

In practical applications, two corresponding interface degrees-of-freedom (DOF's), one in the payload and one in the launch vehicle, are commonly integrated into one in finite element analyses. This coupling procedure is equivalent to assuming the interface DOF's to be rigidly connected. The stiffness and damping effects on the joint are ignored. Using this coupling method, the response of a major payload may be drastically changed owing to the mass change of a distant small payload. Other inconsistent payload responses such as those due to different number of interface DOF's are also frequently observed. These types of strange phenomena leave a question about the reliability of the payload responses that are computed by using the existing coupling method.

In fact, the displacements of those two corresponding interface DOF's cannot be the same since the joint is a fictitious point integrated from two elastic bodies. Specifically, any joint is either composed of an idealized point inside the trunnion and another idealized point outside the latch or composed of two idealized points aparted by a bolt of some length. The idealized DOF's on both payload and launch vehicle can never be truly tied together into one single DOF. Additionally, there may be some free-play at the interface between two corresponding bodies and also possible an elasto-plastic layer of material placed at the interface. The realistic connection is elastically formed and also inherent with damping between these two bodies.

To accommodate the reality of interface connections, a new procedure of coupling payloads to launch vehicles is proposed to evaluate the impact of the interface stiffness and damping on payload responses. The proposed method retains the interface DOF's on both payload and launch vehicle as two separate DOF's in the coupled system. An elastic element is introduced to connect those two DOF's. The spring constant and damping values of the element are estimated from the

physical properties between these two bodies. Using this new concept of coupling, the payload responses are more rational than using the existing coupling method.

This new method is illustrated by three examples, a two-DOF, a four-DOF, and a full scale coupled systems. Both the simple two- and four-DOF coupled systems are to develop the basic phenomena in dynamic analyses. The full scale system is to validate the basic phenomena developed from the simple systems. The interface properties for both two- and four-DOF systems are selected arbitrarily for reference purposes. For the full scale flight analysis, the properties are estimated by considering the mechanical components and local damping characteristic of the joint.

The importance in applications of damping to dynamic loads analyses had been well recognized. Many simulations were proposed in the 1960's and 1970's when the design of nuclear power plants was popular. The method of triple-matrix-product (TMP) in the component damping simulation with neglected off-diagonal damping elements in the system modal coordinates was one of the most favorite approaches. This approach has been considered as the standard method and widely accepted in the aerospace industry for more than twenty years. However, it was pointed out by Tsai and Leang (Ref.1) in 1989 that the approach was incompatible for applications because of the neglected off-diagonal damping elements. Since then, the off-diagonal damping elements in the system modal coordinates are retained and the approach is called the full-TMP method in the aerospace industry. Prior to Ref.1, Tsai (Ref.2) recognized the deficiency of the diagonalized TMP and attempted to simulate a system diagonal damping through use of Gaussian Least Square technique. It appears that the component damping cannot be completely simulated by using a diagonalized system damping matrix. After deep involvement in structural analysis with damping effects, Tsai et al. (Ref.3) recognized that the interface damping was very important to payload responses. They proposed the method of consistent damping in order to simulate an equivalent interface damping matrix. Since it is simple in application, this method may be well accepted in the near future after clarifications of some detail items.

The newly proposed coupling method intends to use the physical properties at the interface joint. This method has not been known before the initiation of this study. Apparently, Belvin (Ref.4) proposed earlier a similar concept which was not known to the author until this paper was nearly complete. The specific structure of a space truss was considered in Ref.4. The nonlinear low frequency friction induced detail response from the truss joints was the objective in the analysis. Unlike Ref.4, the present paper

emphasizes the basic phenomenon development when the coupled structure is treated as a linear system. It attempts to capture the global response phenomena for all payloads instead of focusing in detail simulation of joint non-linearity for a specific structure.

#### APPROACHES OF SUBSTRUCTURAL COUPLING

In the existing approach of structural coupling, two interface DOF's, one in each sub-structure, are coupled into one. This approach is equivalent to assuming that the joint is rigidly connected and no damping is applied to the interface joint. On the contrary, the proposed coupling approach assumes the two interface DOF's to remain as two separate DOF's after coupling. They are connected by an equivalent member of finite stiffness and non-zero damping. The limiting case of the proposed method is the existing approach when the value of stiffness is set equal to infinity and the value of damping is set equal to zero. Following is the formulation of the proposed approach. The formulation of the existing approach is also provided for comparisons.

Let the superscripts 1 and 2 respectively represent the quantities for sub-structures 1 and 2, the governing differential equations for both uncoupled sub-structures are given by

$$M^i \ddot{x}^i + C^i \dot{x}^i + K^i x^i = P^i, \quad i=1,2 \quad (1)$$

where  $\dot{x} = dx/dt$ ,  $x$  and  $P$  respectively are the displacement and forcing vectors and  $M$ ,  $C$  and  $K$  respectively are the mass, damping and stiffness matrices. The quantity  $x$  may be either the physical or modal displacements.

To distinguish the quantities associated with the boundary (interface) and internal DOF's, let the subscripts  $b$  and  $i$  be designated respectively as the corresponding measures. By arranging the interface DOF's to be close to each other between two sub-structures, Eq. (1) can be rewritten into the form

$$\begin{bmatrix} M_{ii}^1 & M_{ib}^1 \\ M_{bi}^1 & M_{bb}^1 \end{bmatrix} \begin{bmatrix} \dot{x}_i^1 \\ \dot{x}_b^1 \end{bmatrix} + \begin{bmatrix} C_{ii}^1 & C_{ib}^1 \\ C_{bi}^1 & C_{bb}^1 \end{bmatrix} \begin{bmatrix} x_i^1 \\ x_b^1 \end{bmatrix} + \begin{bmatrix} K_{ii}^1 & K_{ib}^1 \\ K_{bi}^1 & K_{bb}^1 \end{bmatrix} \begin{bmatrix} x_i^1 \\ x_b^1 \end{bmatrix} = \begin{bmatrix} P_i^1 \\ P_b^1 \end{bmatrix} \quad (1a)$$

$$\begin{bmatrix} M_{bb}^2 & M_{bi}^2 \\ M_{ib}^2 & M_{ii}^2 \end{bmatrix} \begin{bmatrix} \dot{x}_b^2 \\ \dot{x}_i^2 \end{bmatrix} + \begin{bmatrix} C_{bb}^2 & C_{bi}^2 \\ C_{ib}^2 & C_{ii}^2 \end{bmatrix} \begin{bmatrix} x_b^2 \\ x_i^2 \end{bmatrix} + \begin{bmatrix} K_{bb}^2 & K_{bi}^2 \\ K_{ib}^2 & K_{ii}^2 \end{bmatrix} \begin{bmatrix} x_b^2 \\ x_i^2 \end{bmatrix} = \begin{bmatrix} P_b^2 \\ P_i^2 \end{bmatrix} \quad (1b)$$

## Existing Coupling Method

The existing coupling method assumes the displacements at any two corresponding interface DOF's to be identical,  $x_b^1 = x_b^2 (=x_b)$ . The governing differential equation of the coupled system becomes

$$\begin{bmatrix} M_{i1}^1 & M_{ib}^1 & 0 \\ M_{bi}^1 & M_{bb}^1 + M_{bb}^2 & M_{bi}^2 \\ 0 & M_{ib}^2 & M_{i1}^2 \end{bmatrix} \begin{bmatrix} \dot{x}_1^1 \\ \dot{x}_b^1 \\ \dot{x}_1^2 \end{bmatrix} + \begin{bmatrix} C_{i1}^1 & C_{ib}^1 & 0 \\ C_{bi}^1 & C_{bb}^1 + C_{bb}^2 & C_{bi}^2 \\ 0 & C_{ib}^2 & C_{i1}^2 \end{bmatrix} \begin{bmatrix} \dot{x}_1^1 \\ \dot{x}_b^1 \\ \dot{x}_1^2 \end{bmatrix} + \begin{bmatrix} K_{i1}^1 & K_{ib}^1 & 0 \\ K_{bi}^1 & K_{bb}^1 + K_{bb}^2 & K_{bi}^2 \\ 0 & K_{ib}^2 & K_{i1}^2 \end{bmatrix} \begin{bmatrix} x_1^1 \\ x_b^1 \\ x_1^2 \end{bmatrix} = \begin{bmatrix} P_i^1 \\ P_b^1 + P_b^2 \\ P_i^2 \end{bmatrix} \quad (2)$$

In common practices, the damping sub-matrices related to the interface DOF's ( $C_{bi}$ ,  $C_{ib}$  and  $C_{bb}$ ) are set equal zero for Craig-Bampton form of coupling. However, they may be non-zero values if the damping is defined on the free-free modal coordinates and is retained as such throughout all transformations.

Note in order to keep the concept simple for development of the basic phenomena, all DOF's are retained without truncation so that any additional correction process induced from truncations is not the issue of this article.

## Proposed Coupling Method

Let K and C respectively be the stiffness and damping sub-matrices associated with the equivalent members between the retained interface DOF's, the new form of governing differential equations of the coupled system can be written by

$$\begin{bmatrix} M_{i1}^1 & M_{ib}^1 & 0 & 0 \\ M_{bi}^1 & M_{bb}^1 & 0 & 0 \\ 0 & 0 & M_{bb}^2 & M_{bi}^2 \\ 0 & 0 & M_{ib}^2 & M_{i1}^2 \end{bmatrix} \begin{bmatrix} \dot{x}_1^1 \\ \dot{x}_b^1 \\ \dot{x}_b^2 \\ \dot{x}_1^2 \end{bmatrix} + \begin{bmatrix} C_{i1}^1 & C_{ib}^1 & 0 & 0 \\ C_{bi}^1 & C_{bb}^1 + C & -C & 0 \\ 0 & -C & C_{bb}^2 + C & C_{bi}^2 \\ 0 & 0 & C_{ib}^2 & C_{i1}^2 \end{bmatrix} \begin{bmatrix} \dot{x}_1^1 \\ \dot{x}_b^1 \\ \dot{x}_b^2 \\ \dot{x}_1^2 \end{bmatrix} + \begin{bmatrix} K_{i1}^1 & K_{ib}^1 & 0 & 0 \\ K_{bi}^1 & K_{bb}^1 + K & -K & 0 \\ 0 & -K & K_{bb}^2 + K & 0 \\ 0 & 0 & K_{ib}^2 & K_{i1}^2 \end{bmatrix} \begin{bmatrix} x_1^1 \\ x_b^1 \\ x_b^2 \\ x_1^2 \end{bmatrix} = \begin{bmatrix} P_i^1 \\ P_b^1 \\ P_b^2 \\ P_i^2 \end{bmatrix} \quad (3)$$

The responses of Eq.(3) with K set equal to infinite and C set equal to zero are identical to those obtained from Eq.(2). In fact, the payload responses will not be affected by C if K approaches to infinity since the relative velocities,  $\dot{x}_b^1$  and  $\dot{x}_b^2$  will be identical and the magnitude of C becomes immaterial.

## ILLUSTRATIONS

Three examples are considered: a two-DOF coupled system, a four-DOF coupled system, and a full scale flight.

## Two-DOF Coupled System

The two-DOF coupled system consists of a large mass  $M$  and a small mass  $m$ . Mass  $m$  is attached to mass  $M$  which in turn is supported by a rigid base driven by a sinusoidal forcing function of frequency  $\Omega$ , as shown in Fig.1. Mass  $M$  is to simulate the launch vehicle and mass  $m$  to simulate a payload. The frequency of mass  $M$  is  $\omega$ . The purpose of this example is to determine mass  $M$  response owing to the variation of the mass, frequency and damping values of  $m$ . Using the dimensionless quantities, the peak response accelerations of mass  $M$  is shown in Figs.2a,b with the ratio of forcing to natural frequencies,  $\Omega/\omega$  as the abscissa,  $r$  as the frequency ratio of masses  $m$  to  $M$ , and  $\zeta_2$  as the damping coefficient of mass  $m$ . The damping coefficient of mass  $M$  is assumed to be 5% throughout all considerations.

When  $m/M=0$ , the response acceleration of mass  $M$  is naturally identical to the one when a single mass is considered, regardless the frequency variation of mass  $m$  (see Fig.2a.) The response difference becomes significant as the value of  $m/M$  increases. The zone that has the greatest difference is near  $\Omega/\omega=1$ . Except for the case of  $\alpha=0$ , the zone near  $\Omega/\omega=1$  has two peaks. They are caused by the resonance owing to the shifted frequencies<sup>2</sup>.

At  $m/M=0.05$ , the response change at mass  $M$  is mild as  $\zeta_2$  varies over the range from 0.05 to 0.15 (see Fig.2b.) However, the response is altered drastically when  $\zeta_2=0$ . The critical zone is at  $\Omega/\omega$  near the  $r$ -values. Sharp spikes are seen in comparing with the case of  $m=0$  when  $r=0.5$ , 1.0, and 1.5. These results clearly indicate that the responses are very sensitive when a zero interface damping value is used.

In comparing the responses for different damping values, it is noted that the responses for  $\zeta_2=0$  may not always be greater than those for other non-zero values of  $\zeta_2$ . As a result, the response using a damping value of  $\zeta_2=0$  may not be conservative. Furthermore, based upon the engineering intuition, there is no joint absolutely free from energy dissipations. Thus, it is not realistic to assume  $\zeta_2=0$  at the interface joint for dynamic loads analyses. To obtain the

---

<sup>2</sup>A two-DOF coupled system formed by two uncoupled single-DOF's has two frequencies. The greater one of them is always greater than the greater frequency of the uncoupled single-DOF and the smaller one of them is always smaller than the smaller frequency of the uncoupled single-DOF. The magnitude of the shifted frequency depends upon the mass ratio of both uncoupled single-DOF's and is shifted most significantly when both uncoupled single-DOF's have the same frequency.

responses in a somewhat more realistic manner, reasonable damping values must be used at the interface DOF's.

#### Four-DOF Coupled System

This example illustrates the procedure in coupling the sub-structures using Eqs.(1-3). The four-DOF coupled system shown in Fig.3 also simulates the launch vehicle to payload coupling from a different point of view. Nodes 1 and 2 together as a unit, say unit 1, attempts to simulate the launch vehicle and nodes 3 and 4 together, say unit 2, to simulate a payload. Nodes 2 and 3 are to be tied together so that both units are coupled into a system. The axial acceleration responses of all nodal points are interested when node 1 is subjected to an axial force of a Heaviside step function.

Physical DOF's are employed in this example since both units are of simple structures. The mass and stiffness matrices of both units 1 and 2 are given by

$$M^1 = \begin{bmatrix} 600 & 0 \\ 0 & 10 \end{bmatrix}, \quad M^2 = \begin{bmatrix} 10 & 0 \\ 0 & 100 \end{bmatrix}, \quad K^1 = K^2 = 10^6 \begin{bmatrix} 1 & -1 \\ -1 & 1 \end{bmatrix}$$

To signify the effect of interface stiffness and damping, the internal damping values in both units are assumed to be zero. Thus, the system by using the existing coupling method,  $x_3 = x_2$ , as used in Eq.(2), is given by

$$\begin{bmatrix} 600 & 0 & 0 \\ 0 & 20 & 0 \\ 0 & 0 & 100 \end{bmatrix} \begin{bmatrix} \dot{x}_1 \\ \dot{x}_2 \\ \dot{x}_4 \end{bmatrix} + 10^6 \begin{bmatrix} 1 & -1 & 0 \\ -1 & 2 & -1 \\ 0 & -1 & 1 \end{bmatrix} \begin{bmatrix} x_1 \\ x_2 \\ x_4 \end{bmatrix} = \begin{bmatrix} 278200 \\ 0 \\ 0 \end{bmatrix} \quad (4)$$

The response accelerations of all nodal points are shown in Fig.4a. Nodes 1 and 4 oscillate primarily at the same frequency of 12.1 Hz, but on different magnitudes and different phases. The oscillations of nodes 2 and 3 are composed of two distinct frequencies, 12.1 Hz and 51.4 Hz. They always oscillate between the magnitudes of nodes 1 and 4. The oscillations do not decay since no damping is introduced.

In contrast to Eq.(4), both component units can be integrated together by using the proposed coupling method. By substituting the component mass and stiffness matrices into Eq.(3), the new form of governing differential equation for the four-DOF coupled system is

$$\begin{bmatrix} 600 & 0 & 0 & 0 \\ 0 & 10 & 0 & 0 \\ 0 & 0 & 10 & 0 \\ 0 & 0 & 0 & 100 \end{bmatrix} \begin{bmatrix} \dot{x}_1 \\ \dot{x}_2 \\ \dot{x}_3 \\ \dot{x}_4 \end{bmatrix} + \begin{bmatrix} 0 & 0 & 0 & 0 \\ 0 & C & -C & 0 \\ 0 & -C & C & 0 \\ 0 & 0 & 0 & 0 \end{bmatrix} \begin{bmatrix} \dot{x}_1 \\ \dot{x}_2 \\ \dot{x}_3 \\ \dot{x}_4 \end{bmatrix} + 10^6 \begin{bmatrix} 1 & -1 & 0 & 0 \\ -1 & 1+k & -k & 0 \\ 0 & -k & 1+k & -1 \\ 0 & 0 & -1 & 1 \end{bmatrix} \begin{bmatrix} x_1 \\ x_2 \\ x_3 \\ x_4 \end{bmatrix} = \begin{bmatrix} 278200 \\ 0 \\ 0 \\ 0 \end{bmatrix} \quad (5)$$

In this, C and k ( $=K/10^6$ ) are the single element sub-matrices. The response sensitivity of the system can then be determined by varying the values of C and k.

In order to make a direct comparison with the result of Eq.(4), C=0 is assumed. Two values of k are used, the stiff interface spring of k=10 and the mild interface spring of k=1. For the case of k=10, the responses of all DOF's (Fig.4b) are almost identical to those computed from Eq.(4). This substantiates our initial statement that the existing coupling method assumes the interface DOF's to be rigidly connected. For the case of mild interface spring k=1, the system frequencies are changed. Nodes 1 and 4 primarily oscillate at a frequency of 11.7 Hz and nodes 2 and 3 at the composed frequencies of 11.7 Hz and 51.8 Hz (Fig.4c). Regardless the change of frequencies, the response magnitudes of all DOF's remain about the same as for those computed from Eq.(4) except that the response of node 3 appears to be much stronger than that of node 2 when k=1 is applied.

Now, the cases with non-zero values of C are considered, also by using k=1 and k=10. For the case of mild spring (k=1), C=316 is assumed. The responses magnitudes diminish drastically as the time increases (Fig.4d). This is the type of responses being anticipated. On the other hand, when the stiff spring (k=10) is considered, C=1000 is applied. The response accelerations are insignificantly different from those of zero-damping (Fig.4b) even though the C-value is more than three (3) times the value for the mild spring. This substantiates the earlier observation of Eq.(3) that the interface damping value has little effect on the responses if the interface spring is very rigid.

As a summary of this example, the effect of the interface damping is very important to the payload responses. However, the degree of such an effect diminishes as the stiffness value increases. Therefore, the interface stiffness must be presented when the interface damping is considered.

### Full Scale Flight

The full scale flight model uses the complete sets of mass and

stiffness matrices provided by the payload contractor and launch vehicle model developer. Originally, the flight had three payloads. After completion of the dynamic loads analysis, a small payload of weight less than 0.03% of the total system weight was added and the system was re-analyzed. In both analyses, the system is subjected to a synthesized forcing function. The 1% of full-TMP component damping for the internal DOF's is applied except for payload 1 which has a set of damping schedule provided by the payload contractor.

Prior to considerations of various interface stiffness and damping values, the NASTRAN DMAP set-up for the proposed coupling method is verified against the existing method by assuming all interface stiffness to be  $9 \times 10^9$  lb/in and interface damping to be zero. This interface stiffness value is fairly large since all the stiffness elements of the physical DOF's are in the order of magnitudes of  $10^5$  to  $10^7$ .

The interface stiffness and damping values for the true flight are estimated by using the design detail of joints. The effect of material properties and member sizes are included in the estimates. The interface stiffness values are also in the order of magnitudes of  $10^5$  to  $10^7$  depending upon the types of connections. The corresponding interface damping values vary from 1% to 5%. The best estimated basic interface stiffness and damping values are respectively denoted by  $K_b$  and  $C_b$ .

In addition to the verification case of using the artificial interface stiffness of  $9 \times 10^9$  lb/in, this paper provides ten (10) analysis cases for all payloads, one using the existing coupling method and nine (9) using the suggested coupling method. The analyses by using the suggested coupling method consist of the variations of two parameters: interface stiffness and damping. The interface stiffness uses the previously indicated basic value of  $K_b$  and the interface damping uses  $C_b$ . A variation using one-tenth of  $K_b$  ( $K_b/10$ ) and three additional damping variations of 0,  $10C_b$  and  $100C_b$  are also considered. Note that the damping value of  $100C_b$  is prepared for reference purposes. Another case using the mixed damping composed of  $C_b$  for all payloads except  $100C_b$  for the added small payload is also considered.

The peak responses of the interface loads are summarized in Tables 1, 2 and 3. Table 1 is a comparison for the results using the proposed to the existing coupling methods. Three sets of interface stiffness values are considered in applications of the proposed coupling method:  $K=9 \times 10^9$ ,  $K_b$ , and  $K_b/10$ . All the analyses use zero interface damping. The results from these variations show that:

1. The loads are sensitive to the interface stiffness. The

discrepancy is greater when the interface stiffness is lower.

2. The interface loads using the suggested coupling method may go either higher or lower than those using the existing coupling method. This proves that the responses using the existing coupling method may not be conservative if the interface damping were truly zero.

Table 2 reveals the comparisons at the variation of interface damping:  $C=0$ ,  $C_b$ ,  $10C_b$  and  $100C_b$ . Two groups of interface stiffness,  $K_b$  and  $K_b/10$ , are considered. The responses with the mixed damping are also provided. The results from these variations indicate that:

1. The interface damping values are important to the payload responses when low interface stiffness values are applied.
2. By increasing the damping values, the interface loads are almost always decreasing. For the case of  $K_b/10$ , some interface loads at  $100C_b$  may decrease to less than one-half the interface loads at  $C=0$ .
3. At the mixed damping condition, some interface loads are increased and some decreased. The interface loads for the added small payload are most affected and always decreased. The interface loads for the other payloads are also significantly changed but may be either increased or decreased.

Table 3 represents the change of interface loads from the case with to the case without the added small payload. By comparing the overall root mean square (RMS) responses, we find:

1. The change of interface loads is larger in using the proposed coupling method than using the existing method when the zero interface damping value is applied. Such a change become smaller when the damping values are increased. Therefore, the responses computed by using the existing method may not be conservative since the true interface stiffness is not infinite and the true interface damping is not zero.
2. When the zero interface damping is applied, the change of interface loads is severer for the lower than for the higher interface stiffness. However, the degree of severity may reverse when the interface damping value is higher. Effectively, the added payload or the payload weight change may not induce any significant impact on the interface loads of other payloads if the interface joint design has low stiffness and high damping values.

## DISCUSSIONS

The illustrations demonstrate that the interface stiffness and damping are sensitive to payload responses. The degree of sensitivity depends upon the magnitude of interface stiffness and damping values. When these values fall in a certain range, the

effect of a small payload mass on a large payload response becomes less sensitive than the effect when the existing coupling method is applied.

With the best estimate of interface stiffness and damping values by using the true joint connections, the magnitude of the values seems to be in the sensitive range. The payload responses may be significantly different between using the existing and the proposed coupling method. To validate the responses obtained from using the existing coupling method, it is strongly recommended that the physical interface stiffness and damping values be test evaluated. These values are then applied to compute the payload responses by using the suggested coupling method. The responses determined from the existing method can then be justified if they are little different from those computed by applying the test verified interface stiffness and damping to the proposed coupling method.

The suggested coupling method enables engineers to design a set adequate stiffness and damping for the interface joint so that the payload can respond in a specified manner. This capability does not exist when the existing coupling method is applied.

#### **SUMMARY**

Compiled from the illustrations, some basic important phenomena are recognized.

1. An added payload or modifying the weight of a payload generally change the responses of the other payloads. The change is more significant when the added payload or the modified payload weight is heavier.
2. The payload responses are generally decreased when the interface damping is increased. The effect of the interface damping is more significant when the interface stiffness is lower.
3. When the interface damping of the added payload is increased and the interface damping of the other payloads remains unchanged, the response of the added payload is generally decreased; but the responses of the other payloads may be either increased or decreased. Therefore the interface loads obtained from using the existing coupling method of zero interface damping may not be conservative.
4. From the point of view of considering the effect of frequency, use of zero interface damping may be easy to cause false responses that are similar to local resonances. These false responses go away when proper interface damping is applied.

## ACKNOWLEDGMENT

The author is grateful to the support of all coworkers in the Dynamic Loads Group. He particularly appreciates Mr. L. J. Van Hofwegen for the set-up of NASTRAN DMAP. This work could not have occurred without the support of NASA/JSC. However, the content of this paper represents the opinion of the author only.

## REFERENCES

1. Tsai, W. T., J. T. Leang, "An Iterative Method in Dynamic Structural Analyses with Nonproportional Damping," Damping '91, San Diego, CA, Feb. 13-15, 1991. Also Presented at the NASA Technical Interchange Meeting, Downey, CA, Mar. 19, 1991.
2. Tsai, W. T., "Considerations of Synthesized System Damping in Dynamic Analysis of Space Structures," Damping '89, W. Palm Beach, FL., Feb. 8-10, 1989.
3. Tsai, W. T., J. T. Leang, R. S. Chao, "Consistent Damping Method for Space Structural Systems," Presented at the NASA Technical Interchange Meeting, Downey, CA, May 19-20, 1992. Also presented at DAMPING '93, San Francisco, CA, Feb. 24-26, 1993.
4. Belvin, W. K., "Modeling of Joints for Dynamic Analysis of Truss Structures," NASA Technical Paper 2661, 1987.

TABLE 1. EFFECT OF INTERFACE STIFFNESS WITH INTERFACE DAMPING

		EXISTING	K=9*E9		Kb		Kb/10
		LOAD(lb)	LOAD(lb)	(%)	LOAD(lb)	(%)	LOAD(lb)
I/F LOADS FOR THE CASE WITHOUT ODERACS:							
P/L 1	Y	16993	16911	0.1	16716	-1.0	14789 -12.5
	X	35353	35281	-0.2	34853	-1.4	35279 -0.2
	Z	19118	18999	-0.6	19354	1.2	19096 -0.1
	Z	12871	12829	-0.3	13146	2.1	18004 39.9
	X	35038	35007	-0.1	35178	0.4	33464 -4.5
	Z	20006	19831	-0.9	18835	-5.9	20846 4.2
P/L 2	Z	14828	14776	-0.4	14167	-4.5	16799 13.3
	X	3041	2978	-2.1	2885	-5.1	2503 -17.7
	Y	16912	16881	-0.2	16159	-4.5	12517 -26.0
	Y	6036	6031	-0.1	5851	-3.1	5266 -12.8
	Z	1477	1472	-0.3	1439	-2.6	1215 -17.7
	Z	8339	8349	0.1	8221	-1.4	6631 -20.5
P/L 3	Z	2428	2430	0.1	2441	0.5	1832 -24.5
	X	2565	2576	0.4	2556	-0.4	2546 -0.7
	Y	4461	4487	0.6	3650	-18.2	10143 127.4
	Y	2625	2656	1.2	2269	-13.6	4554 73.5
	Z	820	821	0.1	865	5.5	2101 156.2
	Y	2389	2396	0.3	2217	-7.2	5601 134.4
Z	1256	1273	1.4	1259	0.2	2223 77.0	

I/F LOADS FOR THE CASE WITH ODERACS:

P/L 1	Y	16866	16872	0.0	16616	-1.5	15080 -10.6
	X	32571	32452	-0.4	32251	-1.0	34648 6.4
	Z	18729	18639	-0.5	19045	1.7	18739 0.1
	Z	13222	13251	0.2	13433	1.6	16611 25.6
	X	35600	35509	-0.3	35382	-0.6	34359 -3.5
	Z	21689	21521	-0.8	20584	-5.1	21641 -0.2
P/L 2	Z	15150	15091	-0.4	14299	-5.6	16709 10.3
	X	3368	3289	-2.3	3254	-3.4	2921 -13.3
	Y	14821	14736	-0.6	12142	-18.1	9995 -32.6
	Y	5216	5175	-0.8	4533	-13.1	3921 -24.8
	Z	1358	1348	-0.7	1227	-9.6	1024 -24.6
	Y	7158	7117	-0.6	5878	-17.9	5260 -26.5
P/L 3	Z	2131	2121	-0.5	1768	-17.0	1679 -21.2
	X	2627	2662	1.3	2664	1.4	2851 8.5
	Y	3132	3156	0.8	3498	11.7	7032 124.5
	Y	2207	2220	0.6	2376	7.7	3792 71.8
	Z	799	809	1.3	783	-2.0	1041 30.3
	Y	1790	1813	1.3	1618	-9.6	3210 79.3
P/L 4	Z	1**5	1063	-4.7	1049	-5.9	1824 63.6
	Y	2482	2457	-1.0	2373	-4.4	7887 217.8
	Z	606	602	-0.7	656	8.3	1244 105.3
	Y	3726	3739	0.3	3656	-1.9	5106 37.0
	Z	1223	1219	-0.3	1179	-3.6	3433 180.7
	X	2877	2909	1.1	2993	4.0	3651 26.9
Y	3848	3775	-1.9	4537	17.9	12459 223.8	

TABLE 2. EFFECT OF INTERFACE DAMPING

		STIFFNESS Kb				STIFFNESS Kb/10				MIXED Cb				
		C=Cb		C=10Cb		C=Cb		C=10Cb		C=Cb		C=10Cb		
		LOAD(lb)	LOAD(lb) (%)	LOAD(lb)	LOAD(lb) (%)	LOAD(lb)	LOAD(lb) (%)	LOAD(lb)	LOAD(lb) (%)	LOAD(lb)	LOAD(lb) (%)	LOAD(lb)	LOAD(lb) (%)	
I/F LOADS FOR THE CASE WITHOUT COERCERS:														
P/A	1	Y	16716	16713	-0.0	16681	-0.2	16407	-1.8	14789	14583	-1.4	13683	-7.5
		X	34853	34854	0.0	34849	-0.0	34708	-0.2	35279	35069	-0.6	33828	-4.1
		Z	19354	19355	0.0	19364	0.1	19433	0.4	19096	19014	-0.4	18621	-2.5
		X	13146	13141	-0.0	13092	-0.4	12632	-3.0	18004	17297	-3.9	14491	-19.5
		X	35178	35174	-0.0	35141	-0.1	34813	-1.0	33464	33301	-0.5	32203	-3.8
		Z	18835	18834	-0.0	18829	-0.0	18756	-0.4	20846	19737	-5.3	17609	-15.5
		Z	14167	14165	-0.0	14147	-0.1	13939	-1.6	16799	16057	-4.4	13768	-18.0
		X	2885	2884	-0.0	2879	-0.2	2828	-2.0	2503	2514	0.4	2420	-3.3
		Y	16159	16137	-0.1	15951	-1.3	14429	-10.7	12517	11680	-6.7	7843	-37.3
		Z	1439	1437	-0.1	1420	-1.3	1281	-11.0	5266	4924	-6.5	3335	-36.7
P/A	3	Y	8221	8210	-0.1	8111	-1.3	7312	-11.1	1215	1147	-5.6	836	-31.2
		Z	2441	2438	-0.1	2413	-1.1	2198	-10.0	1832	1724	-5.9	1287	-29.7
		X	2556	2556	0.0	2553	-0.1	2523	-1.3	2546	2516	-1.2	2318	-9.0
		Y	3650	3646	-0.1	3618	-0.9	3478	-4.7	10143	8546	-15.7	4228	-58.3
		Y	2269	2266	-0.1	2245	-1.1	2104	-7.3	4354	3789	-16.8	2309	-49.3
		Z	865	864	-0.1	850	-1.7	756	-12.6	2101	1814	-13.7	951	-54.7
		Y	2217	2214	-0.1	2192	-1.1	1989	-10.3	5601	4674	-16.6	1995	-64.4
		Z	1259	1258	-0.1	1249	-0.8	1174	-6.8	2223	1873	-15.7	1261	-44.2
		X	16616	16613	-0.0	16590	-0.2	16370	-1.5	15080	14984	-0.6	13727	-9.0
		X	32251	32254	0.0	32282	0.1	32521	0.8	34648	34465	-0.5	33540	-3.2
P/A	2	X	19045	19046	0.0	19054	0.0	19110	0.3	18739	18735	-0.0	18446	-1.6
		Z	13433	13428	-0.0	13382	-0.4	13212	-1.6	16611	16062	-3.3	14038	-15.5
		X	35382	35377	-0.0	35332	-0.1	34913	-1.3	34359	34020	-1.0	32558	-5.2
		Z	20584	20582	-0.0	20563	-0.1	20355	-1.1	21641	19963	-7.8	17457	-19.3
		Z	14299	14298	-0.0	14291	-0.1	14172	-0.9	16709	15898	-4.9	13672	-18.2
		X	3254	3252	-0.1	3241	-0.4	3132	-3.7	2921	2870	-1.7	2744	-6.1
		Y	12142	12127	-0.1	11991	-1.2	10916	-10.1	9995	8516	-14.8	6159	-38.4
		Y	4533	4526	-0.2	4469	-1.4	4006	-11.6	3921	3427	-12.6	3162	-19.4
		Y	1227	1226	-0.1	1212	-1.2	1103	-10.1	1024	965	-5.8	790	-22.9
		Y	5878	5871	-0.1	5802	-1.3	5257	-10.6	5260	4706	-10.5	3176	-39.6
P/A	3	X	1768	1766	-0.1	1749	-1.1	1620	-8.4	1679	1530	-8.9	1278	-23.9
		X	2664	2661	-0.1	2655	-0.3	2585	-3.0	2851	2810	-1.4	2514	-11.8
		Y	3498	3496	-0.1	3474	-0.7	3268	-6.6	7032	6305	-10.3	3714	-47.2
		Y	2376	2375	-0.0	2364	-0.5	2266	-4.6	3792	3365	-11.3	2445	-35.5
		Z	783	783	0.0	778	-0.6	759	-3.1	1041	961	-7.7	727	-30.2
		Z	1618	1615	-0.2	1594	-1.5	1494	-7.7	3210	2682	-16.4	1656	-48.4
		Z	1049	1049	0.0	1044	-0.5	1002	-4.5	1824	1647	-9.7	1195	-34.5
		Y	2373	2373	0.0	2370	-0.1	2343	-1.3	7887	6699	-15.1	2876	-63.5
		Z	656	655	-0.2	655	-0.2	640	-2.4	1244	1061	-14.7	651	-47.7
		Y	3656	3655	-0.0	3653	-0.1	3623	-0.9	5106	4380	-14.2	3636	-28.8
P/A	4	Y	1179	1179	0.0	1177	-0.2	1153	-2.2	3433	2914	-15.1	1223	-64.4
		X	2993	2992	-0.0	2986	-0.2	2923	-2.3	3651	3534	-3.2	2850	-21.9
		Y	4537	4529	-0.2	4458	-1.7	3954	-12.8	12459	10536	-15.4	4935	-60.4
		X	16799	16799	-1.9	16799	-1.9	16799	-1.9	16799	16799	-1.9	16799	-1.9
		X	34954	34954	0.9	34954	0.9	34954	0.9	34954	34954	0.9	34954	0.9
		X	16228	16228	-2.3	16228	-2.3	16228	-2.3	16228	16228	-2.3	16228	-2.3
		X	33447	33447	-2.7	33447	-2.7	33447	-2.7	33447	33447	-2.7	33447	-2.7
		X	19071	19071	-11.9	19071	-11.9	19071	-11.9	19071	19071	-11.9	19071	-11.9
		X	15971	15971	-4.4	15971	-4.4	15971	-4.4	15971	15971	-4.4	15971	-4.4
		X	2619	2619	-10.3	2619	-10.3	2619	-10.3	2619	2619	-10.3	2619	-10.3

TABLE 3. EFFECT OF ADDITIONAL ODERACS PAYLOAD ON INTERFACE LOADS

	EXISTING K=9*E9	C=0	STIFFNESS Kb			STIFFNESS Kb/10				MIXED Cb	
			Cb	10Cb	100Cb	C=0	Cb	10Cb	100Cb		
I/F LOADS FOR THE CASE WITHOUT ODERACS:											
P/L 1	Y	16893	16911	16716	16713	16681	16407	14789	14583	13683	9301
	X	35353	35281	34853	34854	34849	34788	35279	35069	33828	28354
	Z	19118	18999	19354	19355	19364	19433	19096	19014	18621	16680
	Z	12871	12829	13146	13141	13092	12632	18004	17297	14491	12676
	X	35038	35007	35178	35174	35141	34813	33464	33301	32203	27476
	Z	20006	19831	18835	18834	18829	18756	20846	19737	17609	15452
	Z	14828	14776	14167	14165	14147	13939	16799	16057	13768	10815
P/L 2	X	3041	2978	2885	2884	2879	2828	2503	2514	2420	2310
	Y	16912	16881	16159	16137	15951	14429	12517	11680	7843	4561
	Y	6036	6031	5851	5843	5770	5177	5266	4924	3335	2204
	Z	1477	1472	1439	1437	1420	1281	1215	1147	836	766
	Y	8339	8349	8221	8210	8111	7312	6631	6174	4191	1957
	Z	2428	2430	2441	2438	2413	2198	1832	1724	1287	954
P/L 3	X	2565	2576	2556	2556	2553	2523	2546	2516	2318	2018
	Y	4461	4487	3650	3646	3618	3478	10143	8546	4228	2466
	Y	2625	2656	2269	2266	2245	2104	4554	3789	2309	1783
	Z	820	821	865	864	850	756	2101	1814	951	853
	Y	2389	2396	2217	2214	2192	1989	5601	4674	1995	1750
	Z	1256	1273	1259	1258	1249	1174	2223	1873	1241	1069

I/F LOADS FOR THE CASE WITH ODERACS:

P/L 1	Y	16866	16872	16616	16613	16590	16370	15080	14984	13727	9342	14799
	X	32571	32452	32251	32254	32282	32521	34648	34465	33540	28183	34954
	Z	18729	18639	19045	19046	19054	19110	18739	18735	18446	16388	18627
	Z	13222	13251	13433	13428	13382	13212	16611	16062	14038	12668	16228
	X	35600	35509	35382	35377	35332	34913	34359	34020	32558	27518	33447
	Z	21689	21521	20584	20582	20563	20355	21641	19963	17457	15143	19071
	Z	15150	15091	14299	14298	14291	14172	16709	15898	13672	10699	15971
P/L 2	X	3368	3289	3254	3252	3241	3132	2921	2870	2744	2361	2619
	Y	14821	14736	12142	12127	11991	10916	9995	8516	6159	4146	9024
	Y	5216	5175	4533	4526	4469	4006	3921	3427	3162	2123	3902
	Z	1358	1348	1227	1226	1212	1103	1024	965	790	766	948
	Y	7158	7117	5878	5871	5802	5257	5260	4706	3176	1816	4852
	Z	2131	2121	1768	1766	1749	1620	1679	1530	1278	956	1443
P/L 3	X	2627	2662	2664	2661	2655	2585	2851	2810	2514	2338	2460
	Y	3132	3156	3498	3496	3474	3268	7032	6305	3714	2311	6741
	Y	2207	2220	2376	2375	2364	2266	3792	3365	2445	1810	2870
	Z	799	809	783	783	778	759	1041	961	727	821	1446
	Y	1790	1813	1618	1615	1594	1494	3210	2682	1656	1644	3590
	Z	1115	1063	1049	1049	1044	1002	1824	1647	1195	1048	1475

PERCENT OF CHANGE: WITH TO WITHOUT ODERACS

P/L 1	Y	-0.2	-0.2	-0.6	-0.6	-0.5	-0.2	2.0	2.7	0.3	0.4	1.5
	X	-7.9	-8.0	-7.5	-7.5	-7.4	-6.5	-1.8	-1.7	-0.9	-0.6	-0.3
	Z	-2.0	-1.9	-1.6	-1.6	-1.6	-1.7	-1.9	-1.5	-0.9	-1.8	-2.0
	Z	2.7	3.3	2.2	2.2	2.2	4.6	-7.7	-7.1	-3.1	-0.1	-6.2
	X	1.6	1.4	0.6	0.6	0.5	0.3	2.7	2.2	1.1	0.2	0.4
	Z	8.4	8.5	9.3	9.3	9.2	8.5	3.8	1.1	-0.9	-2.0	-3.4
	Z	2.2	2.1	0.9	0.9	1.0	1.7	-0.5	-1.0	-0.7	-1.1	-0.5
P/L 2	X	10.8	10.4	12.8	12.8	12.6	10.7	16.7	14.2	13.4	2.2	4.2
	Y	-12.4	-12.7	-24.9	-24.8	-24.8	-24.3	-20.1	-27.1	-21.5	-9.1	-22.7
	Y	-13.6	-14.2	-22.5	-22.5	-22.5	-22.6	-25.5	-30.4	-5.2	-3.7	-20.8
	Z	-8.1	-8.4	-14.7	-14.7	-14.6	-13.9	-15.7	-15.9	-5.5	0.0	-17.3
	Y	-14.2	-14.8	-28.5	-28.5	-28.5	-28.1	-20.7	-23.8	-24.2	-7.2	-21.4
	Z	-12.2	-12.7	-27.6	-27.6	-27.5	-26.3	-8.4	-11.3	-0.7	0.2	-16.3
P/L 3	X	2.4	3.3	4.2	4.1	4.0	2.5	12.0	11.7	8.5	15.9	-2.2
	Y	-29.8	-29.7	-4.2	-4.1	-4.0	-6.0	-30.7	-26.2	-12.2	-6.3	-21.1
	Y	-15.9	-16.4	4.7	4.8	5.3	7.7	-16.7	-11.2	5.9	1.5	-24.3
	Z	-2.6	-1.5	-9.5	-9.4	-8.5	0.4	-50.5	-47.0	-23.6	-3.8	-20.3
	Y	-25.1	-24.3	-27.0	-27.1	-27.3	-24.9	-42.7	-42.6	-17.0	-6.1	-23.2
	Z	-11.2	-16.5	-16.7	-16.6	-16.4	-14.7	-17.9	-12.1	-3.7	-2.0	-21.2
RMS AVG		12.4	12.8	15.2	15.2	15.1	14.5	20.8	20.5	11.3	5.2	15.4

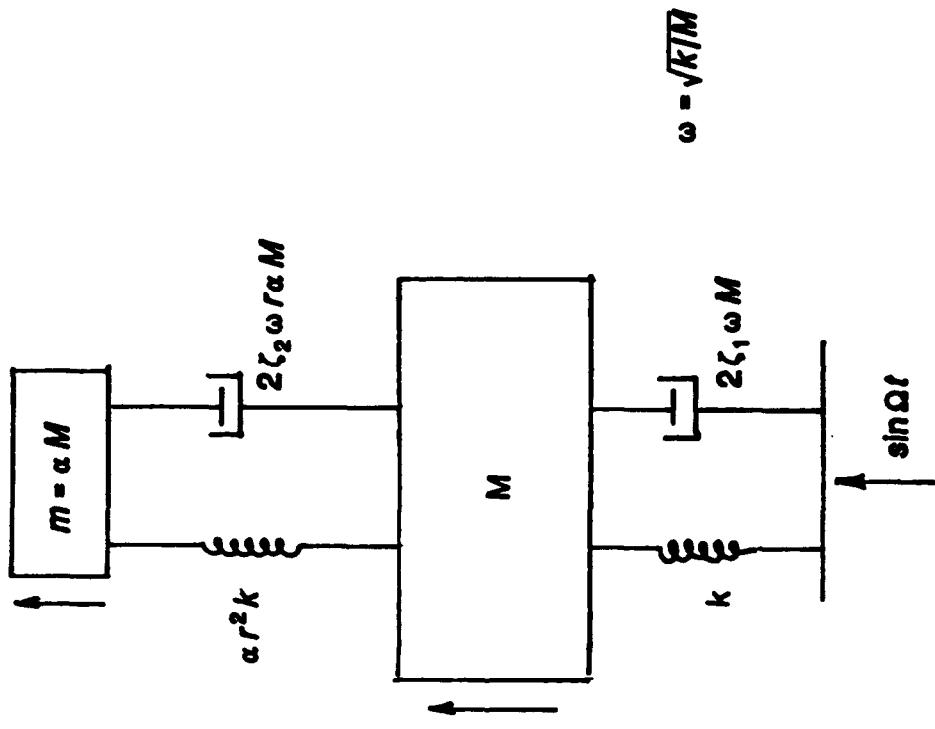


FIG.1 TWO DEGREE-OF-FREEDOM SYSTEM

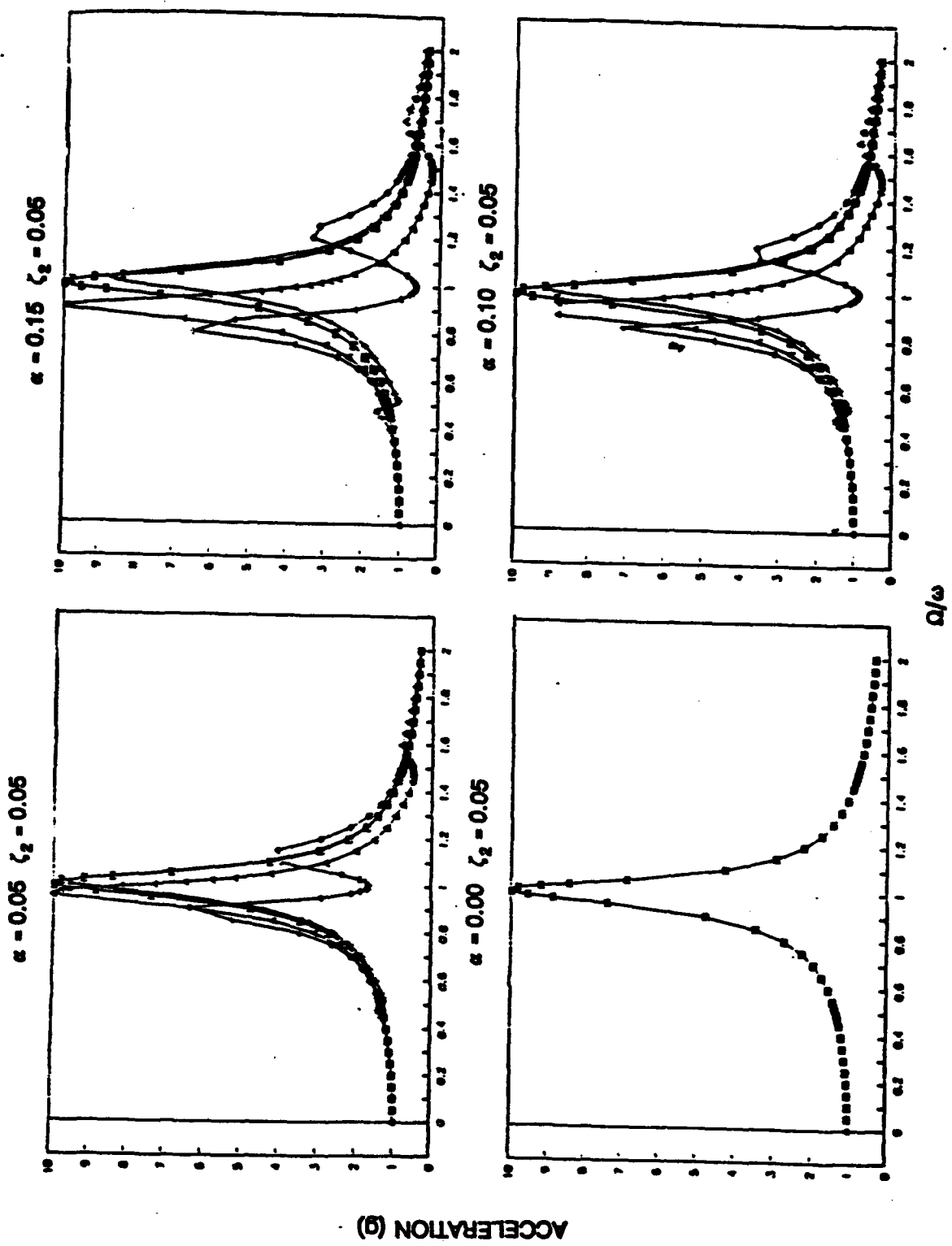


FIG.2a LARGE MASS RESPONSES

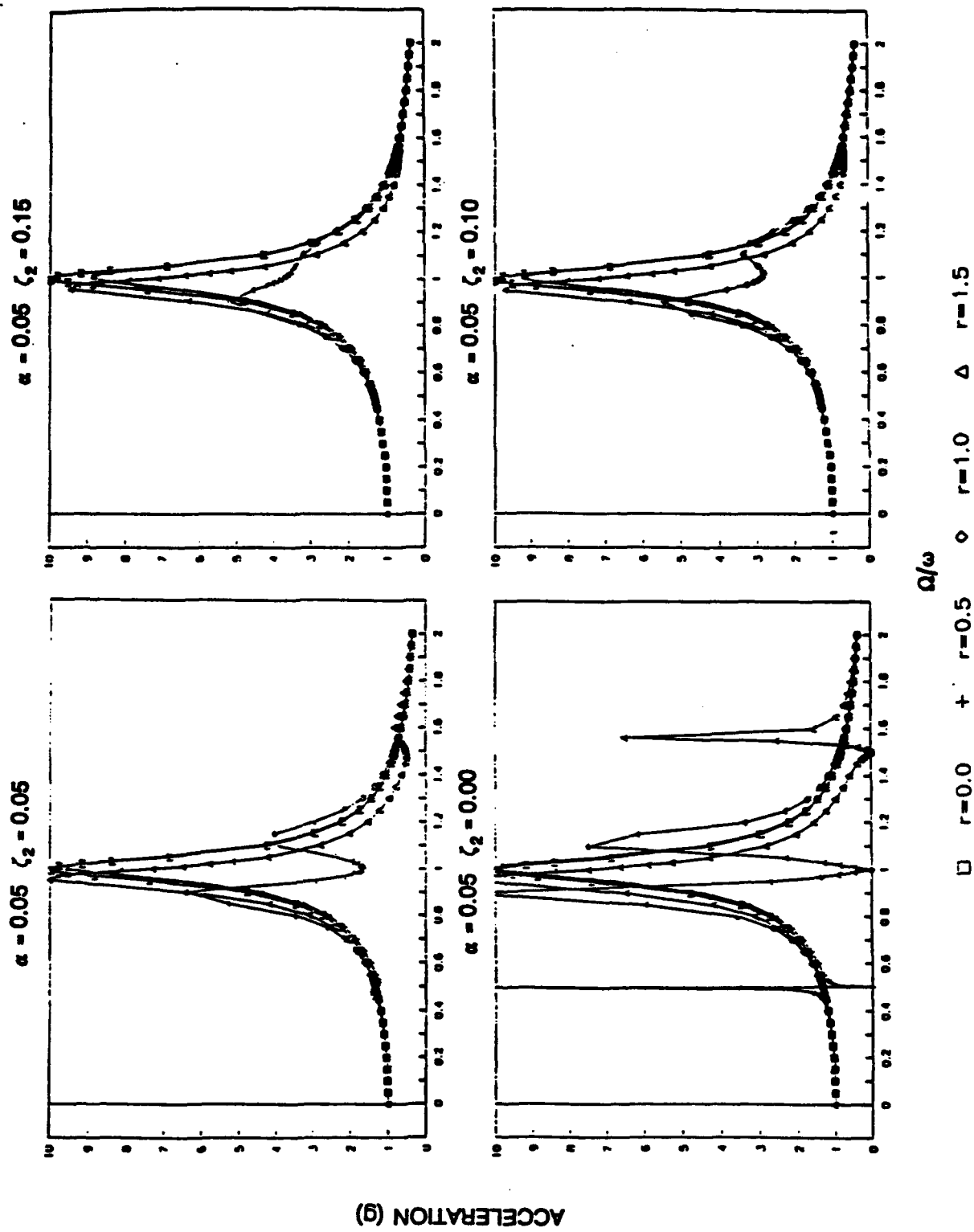


FIG.2b LARGE MASS RESPONSES

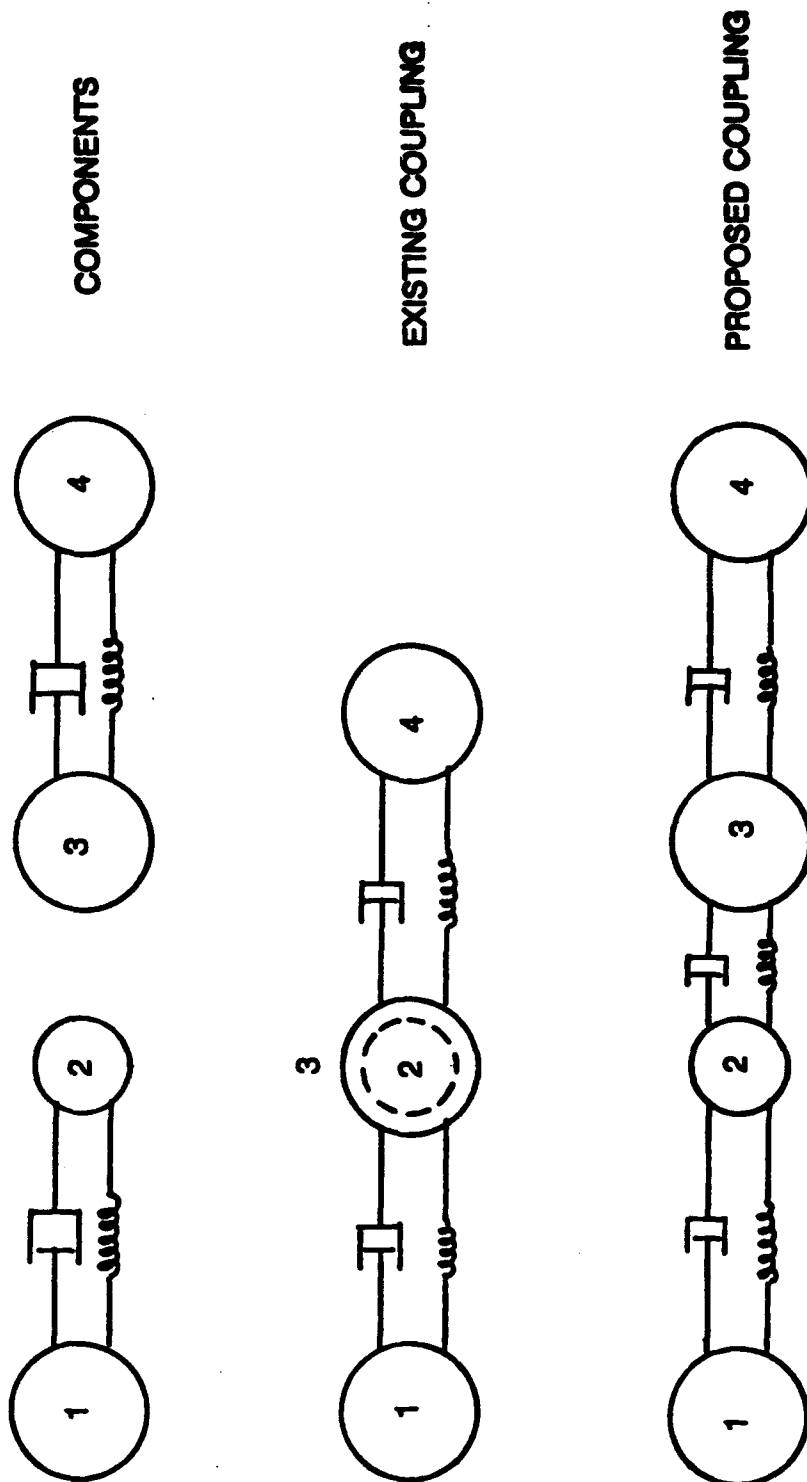
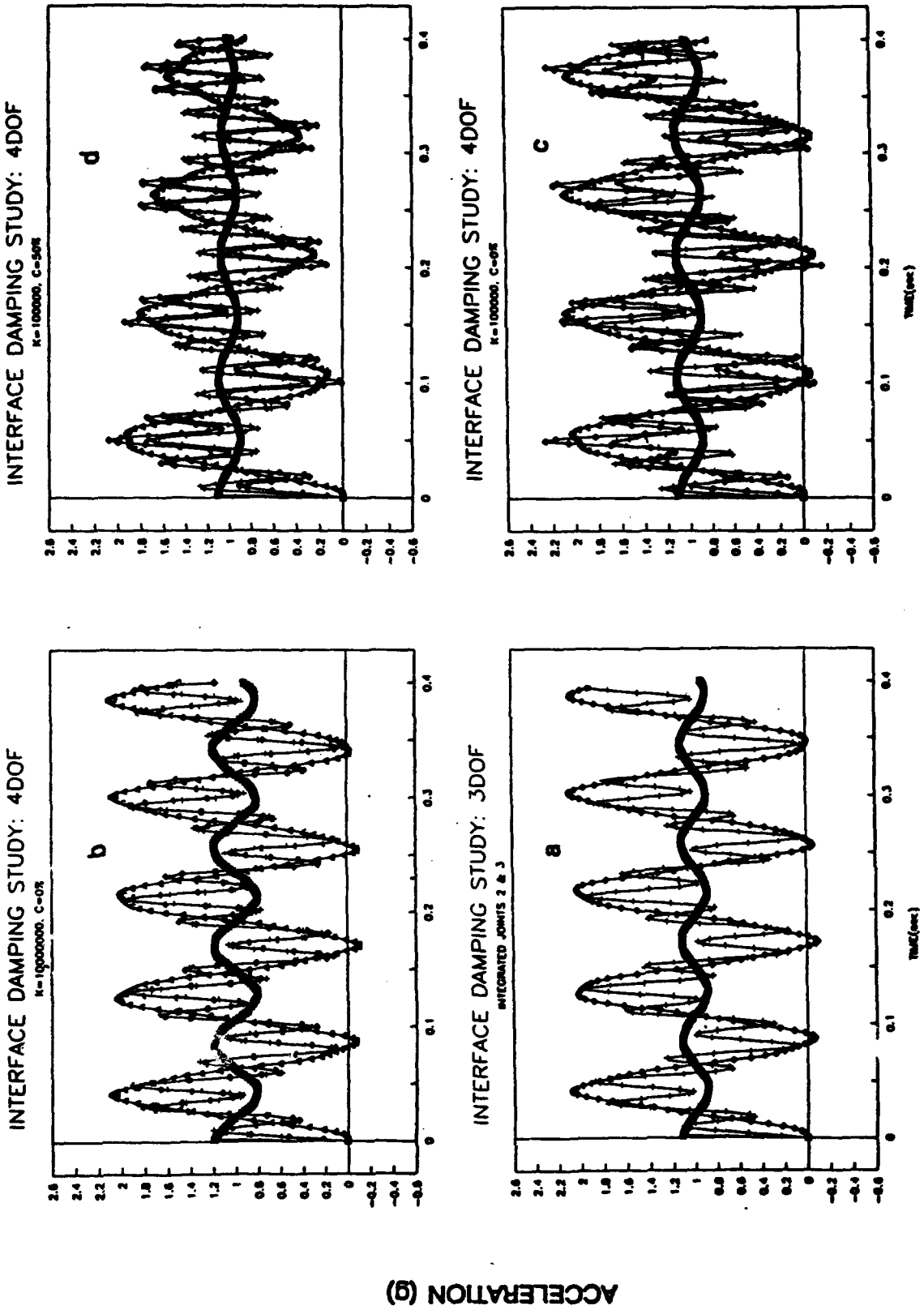


FIG.3 FOUR DEGREE-OF-FREEDOM SYSTEM



ACCELERATION (g)

FIG.4 4-DOFS: INTERFACE CONNECTIONS

# MODAL PARAMETER ESTIMATION EFFECTS ON DAMPING MATRIX IDENTIFICATION

A.Agneni, L.Balis-Crema, A.Castellani, F.M.Onorati

Università degli Studi di Roma "La Sapienza"  
Dipartimento Aerospaziale <sup>1</sup>

## ABSTRACT

This paper deals with the effects that some errors, relative to modal parameter estimates carried out from experimental data, can have on mass, stiffness and damping matrix identification. For the damping matrix, the hypothesis of proportionality with respect to mass and stiffness matrices, is considered; thus the real eigenvectors can diagonalize all the matrices: mass, stiffness and damping too.

Numerical simulations regard errors in natural frequency, damping ratio and residue evaluations: a particular attention is paid to the possible truncation of the impulse response at the end of the observation time.

Some numerical tests, carried out both on a 3-DOF lumped system and on a cantilever beam, represented by a finite element model reduced to a 10-DOF system, give a quantitative evaluation of the different experimental errors and confirm the sensitivity of the identification process especially with regard to residue estimates.

## NOMENCLATURE

$c_i(t)$	i-th damping component (Ns/m)
$e(\tau_w)$	impulse response envelope at the end of the observation window
$k_i$	i-th stiffness component (N/m)
$m_i$	i-th mass component (kg)
$\{r_{p,j;m}\}$	residue vector (column vector) relative to the m-th mode
$r_{j,j;m}$	residue in the driving point of the m-th mode
$\{u_{p;m}\}$	eigenvector (column vector) relative to the m-th mode
$\{u_{p;m}^*\}$	eigenvector normalized with respect to unitary modal masses
$[C_a]$	damping matrix derived from the analytical model
$[C_a^*]$	damping matrix derived from analytical model with incomplete set of modes
$[C_e]$	damping matrix evaluated from experimental data

---

<sup>1</sup> Via Eudossiana, 16 - 00184 Roma (Italy)  
FAX 06 44585335

$[C_x]$	damping matrix evaluated from experimental data with incomplete set of modes
$[I]$	identity matrix
$[K]$	stiffness matrix
$[K_a]$	stiffness matrix derived from the analytical model
$[K_i]$	stiffness matrix derived from analytical model with incomplete set of modes
$[K_e]$	stiffness matrix evaluated from experimental data
$[K_x]$	stiffness matrix evaluated from experimental data with incomplete set of modes
$[M]$	mass matrix
$[M_a]$	mass matrix derived from the analytical model
$[M_i]$	mass matrix derived from the analytical model with incomplete set of modes
$[M_e]$	mass matrix evaluated from experimental data
$[M_x]$	mass matrix evaluated from experimental data with incomplete set of modes
$ \epsilon_{(*)} $	magnitude of the relative error on (*) expressed in per cent
$\sigma$	decay rate (rad/s)
$[\sigma_{a,i}]$	diagonal matrix formed by decay rates derived from the analytical model
$[\sigma_e]$	diagonal matrix formed by decay rates
$[\sigma_{e,i}]$	diagonal matrix formed by decay rates evaluated from experimental data
$\sigma_N$	standard deviation of the added random noise
$\tau_w$	observation window length (s)
$\omega_d$	damped angular frequency (rad/s)
$\omega_{d,m}$	damped angular frequency of the m-th mode (rad/s)
$\omega_n$	natural angular frequency (rad/s)
$\omega_{n,m}$	natural angular frequency of the m-th mode (rad/s)
$[\omega_n]$	diagonal matrix formed by the natural angular frequencies
$[\omega_{n,a}]$	diagonal matrix of natural angular frequencies derived from the analytical model
$[\omega_{n,e}]$	diagonal matrix of natural angular frequencies evaluated from experimental data
$[\Phi]$	matrix of eigenvectors normalized with unitary modal mass
$[\Phi_a]$	matrix of eigenvectors derived from the analytical model
$[\Phi_e]$	matrix of eigenvectors evaluated from experimental data

## INTRODUCTION

An accurate evaluation of mass, stiffness and damping matrices, obtained by using experimental data, allows one to compare and to update the numerical model, which is generally derived by a finite element code [1,2]. In fact a reliable numerical model permits to predict the system response to generic forces, the consequences of structural modifications and the effects of connecting two or more structures together.

This paper especially deals with the damping matrix identification when it is considered proportional to mass and stiffness matrices. Thus, the matrix of real eigenvectors not only diagonalizes the mass and stiffness matrices, but also the damping matrix.

The importance of natural frequency, damping ratio and especially of residue estimates - with which the eigenvector matrix can be achieved - is pointed out by the effects produced in the identification of the matrices mentioned above. This problem is particularly important for those structures, as some aerospace ones, whose vibration modes are characterized by

light damping and low natural frequencies. In fact, in this case, residue estimates, if gained by a direct approach performed in the frequency domain, starting from truncated impulse responses, could be affected by bias errors [3-7].

Numerical tests, carried out on a lumped system with three degrees of freedom and on a continuous beam structure, whose experimental data (frequency response functions) is simulated by a finite element model and analyzed by the NASTRAN code, illustrate the problem, showing how important the errors, due to a poor modal parameter estimation, are.

For this last numerical simulation, two approaches have been used in order to point out the effects of the residue evaluation. In the first case, frequency response functions have been directly synthesized in the frequency domain so that no bias effects are present in the residue estimates, in the second one frequency response functions are derived from the impulse responses and therefore errors in residue evaluations (in magnitude and in phase) can be present if the time functions are truncated at the end of the time observation window.

The same approach has been applied on an incomplete model too, that is a structure of which a limited number of modes has been considered, in particular the examples reported in this paper are relative to a model in which only 6 modes out of 10 have been maintained. In the incomplete model identification the Error Matrix Method [1,2] has been used.

## THEORETICAL CONSIDERATIONS

Mass, stiffness and damping matrices can be directly obtained by manipulating frequency response functions gained from experimental data [8,9], otherwise their estimates require the evaluation of residues, natural frequencies and damping ratios.

In the case of light damping, the following relationship links the eigenvector relative to the generic  $m$ -th mode  $\{u_{p;m}\}$  with the relative residue vector - evaluated in  $p$  when the driving force is applied in the  $j$ -th point,  $\{r_{p;j;m}\}$  - and with a scale factor  $A_m$ :

$$\{u_{p;m}\} = \frac{1}{A_m} \frac{r_{p;j;m}}{u_{j;m}} \quad \begin{cases} p = 1, \dots, N \\ m = 1, \dots, M \end{cases} \quad (1)$$

where  $N$  is the number of DOFs of the model,  $M$  is the number of modes and  $j$ , as said before, represents the exciting point.

Supposing that scale factors are normalized with respect to unitary modal masses, they result only dependent on damped angular frequencies, thus  $u_{j;m}$  in function of the driving point residue is given by:

$$u_{j;m} = (\omega_{d,m} r_{j;j;m})^{1/2} \quad (2)$$

If Eq.(2) is substituted into Eq.(1), the mode shapes - normalized, as said before, with respect to unitary modal masses - are equal to:

$$\{u_{p;m}\} = \left[ \frac{\omega_{d,m}}{r_{j,j;m}} \right]^{1/2} \{r_{p,j;m}\} \quad (3)$$

Of course, for a complete model, as many normalized eigenvectors as the modes are achieved and therefore the matrix  $[\Phi]$ , whose columns are the vectors  $\{u_{p;m}\}$ , is completely known and result square.

When proportional damping is considered or when the Basile hypothesis is valid, that is when the natural frequencies are sufficiently separated and the damped natural angular frequency, for each excited mode, is much greater than the relative decay rate [10,11], the modes are real (or practically real) and therefore mass, stiffness and damping matrices are given by the following relationships:

$$[M] = [\Phi]^{-T} [I] [\Phi]^{-1} \quad (4)$$

$$[K] = [\Phi]^{-T} [\omega_n^2] [\Phi]^{-1} \quad (5)$$

$$[C] = [\Phi]^{-T} [2\sigma_n] [\Phi]^{-1} \quad (6)$$

where  $[\omega_n^2]$  indicates the diagonal matrix of the square natural modal angular frequencies and  $[\sigma_n]$  is the diagonal matrix of the modal decay rates.

The possible errors in the evaluation of each fundamental mode propagate in the identification of all the terms of mass, stiffness and damping matrices, as it is possible to see from the previous equations. Errors on natural frequencies are generally very small, whereas the ones on damping ratios and especially on residues (in magnitude and phase) could be significant. Since we are particularly interested in studying light damped structures, damped angular frequency estimates result good enough, therefore a particular attention must be paid to residue evaluations, in fact normalized eigenvectors are practically dependent on them.

If a fitting is used on frequency response functions and these ones are obtained from impulse responses truncated at the end of the time window, biased estimates of the magnitude and phase residue could be achieved [3]. This type of error, is difficult to predict because the frequency response function behaviour, especially near the resonance, depends not only on how much truncated the envelope is, but it also depends on how the truncation happens at the end of the observation window [4]. In this case more reliable results can be gained either by using an exponential window in the time domain - so that impulse responses become untruncated [6,7] - or by correcting magnitude and phase of the residues with an analytical relationship derived from the Poisson sum formula [5]. Obviously no problems arise if the estimation process is carried out in the time domain, for instance by the Ibrahim

approach [12], by fitting impulse responses with complex exponential functions (Prony method) [13] or by fitting, with linear least square method, instantaneous envelopes and total phases derived from time functions through the Hilbert transform [3,14].

Obviously, if frequency response functions are synthesized in the frequency domain we must face an opposite situation: fittings in the frequency domain do not involve bias in residue estimates, whereas approaches in the time domain could provide not negligible errors [15,16].

In order to evaluate the effect of using an incomplete model ( $M < N$ ), the Error Matrix Method has been used [1,2]; this method, proposed in order to localize the differences between experimental data and numerical models, is based on the hypothesis that the errors are essentially present in the theoretical model and not in measurements. On the other hand, in this paper the approach is utilized to point out the effect due to experimental errors in modal parameter estimation on the overall identification process.

Indicating the mass, stiffness and the damping matrices evaluated from experimental data with  $[M_x]$ ,  $[K_x]$  and  $[C_x]$ , and likewise with the subscript 'a' the matrices relative to the analytical model, the correction matrices are defined by the following relationships:

$$[\Delta M] = [M_x] - [M_a] \quad (7)$$

$$[\Delta K] = [K_x] - [K_a] \quad (8)$$

$$[\Delta C] = [C_x] - [C_a] \quad (9)$$

By the Error Matrix Method, these correction matrices can be approximated by:

$$[\Delta M] = [M_a] [[M_a^*]^{-1} - [M_x^*]^{-1}] [M_a] \quad (10)$$

$$[\Delta K] = [K_a] [[K_a^*]^{-1} - [K_x^*]^{-1}] [K_a] \quad (11)$$

$$[\Delta C] = [C_a] [[C_a^*]^{-1} - [C_x^*]^{-1}] [C_a] \quad (12)$$

where the inverse matrices, which have reduced rank in the case of an incomplete model, can be evaluated as follows:

$$[M_a^*]^{-1} = [\Phi_a] [\Phi_a]^T \quad (13)$$

$$[M_x^*]^{-1} = [\Phi_x] [\Phi_x]^T \quad (14)$$

$$[K_a^*]^{-1} = [\Phi_a] [\omega_{n,a}^2]^{-1} [\Phi_a]^T \quad (15)$$

$$[K_x^*]^{-1} = [\Phi_x][\omega_{n,x}^2]^{-1}[\Phi_x]^T \quad (16)$$

$$[C_a^*]^{-1} = [\Phi_a][2\sigma_{n,a}]^{-1}[\Phi_a]^T \quad (17)$$

$$[C_x^*]^{-1} = [\Phi_x][2\sigma_{n,x}]^{-1}[\Phi_x]^T \quad (18)$$

In this approach it is possible to use an incomplete model in the overall updating process, even if obviously the problems due to incompleteness of the experimental data are of basic importance and can cause the updating method to fail.

## NUMERICAL SIMULATIONS

A set of numerical tests is presented in order to simulate the effects due to experimental errors in the identification of mass, stiffness and damping matrices, both on a lumped system and on a cantilever beam.

Even if data has been obtained from numerical tests, modal parameters (natural frequencies, damping ratios and residues) have been estimated by fitting frequency response functions by a Rational Fraction Least Square fitter, that is processing numerical data likewise the experimental ones.

In all the cases presented, as said before, the damping matrix has been introduced as proportional, that is:

$$[C] = \alpha[M] + \beta[K] \quad (19)$$

In the first case a lumped three degree of freedom system has been considered, where the coefficients  $\alpha$ ,  $\beta$  of the previous equation had the values 0.01 and 0.0001 respectively, whereas the natural frequencies and the damping ratios of the same system are presented in Tab.1.

Table 1 - Natural frequencies and damping ratios of 3-DOF model.

$f_{n1}$ (Hz)	$f_{n2}$ (Hz)	$f_{n3}$ (Hz)
5.2846	21.7238	31.2466
$\zeta_1$	$\zeta_2$	$\zeta_3$
0.0018	0.0069	0.0098

From the previous table the envelopes of the three modes, if their initial amplitudes were unitary, at the end of the observation time ( $\tau_w$ ) would result equal to:

1st mode	$e_1(\tau_w) = \exp(-\sigma_1 \tau_w) = 0.5481$
2nd mode	$e_2(\tau_w) = \exp(-\sigma_2 \tau_w) = 8.5625 \cdot 10^{-5}$
3rd mode	$e_3(\tau_w) = \exp(-\sigma_3 \tau_w) = 4.0576 \cdot 10^{-9}$

so that only the first impulse response is truncated, whereas the other two are completely damped. In a first step residue estimates have been corrected with the method based on the Poisson sum formula in order to eliminate the errors due to truncation (actually only the residues relative to the first mode presented remarkable errors).

The identification of [M], [K] and [C] matrices has been obtained introducing natural angular frequencies, decay rates and eigenvectors estimates - these last ones derived from the residues evaluations mentioned above - into Eqs.(4) to (6). The estimated values of mass, stiffness and damping components, along with the relative errors, are presented in the following Tables (Tabs.2 to 4).

Table 2 - Estimated mass components and their relative errors.

$m_1$	$m_2$	$m_3$
0.99998	1.99998	0.99998
$ \epsilon_{m1} $ (‰)	$ \epsilon_{m2} $ (‰)	$ \epsilon_{m3} $ (‰)
0.0175	0.0079	0.0226

Table 3 - Estimated stiffness components and their relative errors.

$k_1$	$k_2$	$k_3$
5828	11656	23311
$ \epsilon_{k1} $ (‰)	$ \epsilon_{k2} $ (‰)	$ \epsilon_{k3} $ (‰)
0.0240	0.0071	0.0150

Table 4 - Estimated damping components and their relative errors.

$c_1$	$c_2$	$c_3$
0.5928	1.1856	2.3411
$ \epsilon_{c1} $ (%)	$ \epsilon_{c2} $ (%)	$ \epsilon_{c3} $ (%)
0.0054	0.8369	0.0059

Therefore the identification of a complete model, in an ideal noise free condition, permits a very accurate evaluation of mass, stiffness and damping matrices if good modal parameter estimations (especially of residues) are available.

On the contrary, in a second case the effect of the truncation of the impulse response at the end of the observation time has been considered.

In Tabs.5 to 7 the estimated values of mass, stiffness and damping components, along with the relative errors, are presented.

Table 5 - Mass components estimates with relative errors in presence of truncation.

$m_1$	$m_2$	$m_3$
1.0297	2.2343	1.0645
$ \epsilon_{m1} $ (%)	$ \epsilon_{m2} $ (%)	$ \epsilon_{m3} $ (%)
2.966	11.716	6.453

Table 6 - Stiffness components estimates with relative errors in presence of truncation.

$k_1$	$k_2$	$k_3$
5952	11563	23382
$ \epsilon_{k1} $ (%)	$ \epsilon_{k2} $ (%)	$ \epsilon_{k3} $ (%)
2.140	0.787	0.304

Table 7 - Damping components estimates with relative errors in presence of truncation.

$c_1$	$c_2$	$c_3$
0.6064	1.1555	2.3488
$ \epsilon_{c1} $ (%)	$ \epsilon_{c2} $ (%)	$ \epsilon_{c3} $ (%)
2.297	2.538	0.522

It is worth noting how important the effect due to the truncation of the first mode is: errors propagate towards all the elements of mass, stiffness and damping matrices, in particular very significant errors have been found in mass component estimates, as already verified in a previous work [17].

Thereafter a continuous cantilever beam has been considered; it has been supposed of aluminum, 1m long and with square section (1cm  $\times$  1cm). The beam, represented by a finite element model, has been analyzed by the NASTRAN code.

In this case also, the damping matrix has been considered proportional both to the mass and to the stiffness matrices, following the Eq.(19); the coefficients have been chosen equal to  $\alpha=10^{-2}$  and  $\beta=10^{-6}$ , in order to obtain damping ratios consistent with those ones of an aluminum beam. A reduced 10-DOF model is presented: natural frequencies, damping ratios and values assumed by the envelopes of each mode at the end of the time window (considering unitary the initial amplitudes) are reported in Tab.8.

Table 8 - Natural frequencies, damping ratios and envelope truncations of the cantilever beam modes (the time window width is:  $\tau_w=1.28$  s).

$f_{n1}$ (Hz)	8.1875	$\zeta_1$	$1.2292 \cdot 10^{-4}$	$e_1(\tau_w)$	0.9919
$f_{n2}$ (Hz)	50.739	$\zeta_2$	$1.7508 \cdot 10^{-4}$	$e_2(\tau_w)$	0.9310
$f_{n3}$ (Hz)	140.648	$\zeta_3$	$4.4752 \cdot 10^{-4}$	$e_3(\tau_w)$	0.6028
$f_{n4}$ (Hz)	272.743	$\zeta_4$	$8.5977 \cdot 10^{-4}$	$e_4(\tau_w)$	0.1517
$f_{n5}$ (Hz)	445.851	$\zeta_5$	$1.4025 \cdot 10^{-3}$	$e_5(\tau_w)$	$0.6545 \cdot 10^{-2}$
$f_{n6}$ (Hz)	657.035	$\zeta_6$	$2.0654 \cdot 10^{-3}$	$e_6(\tau_w)$	$1.8202 \cdot 10^{-5}$
$f_{n7}$ (Hz)	899.321	$\zeta_7$	$2.8262 \cdot 10^{-3}$	$e_7(\tau_w)$	$1.3258 \cdot 10^{-9}$
$f_{n8}$ (Hz)	1155.74	$\zeta_8$	$3.6316 \cdot 10^{-3}$	$e_8(\tau_w)$	$2.1880 \cdot 10^{-15}$
$f_{n9}$ (Hz)	1392.28	$\zeta_9$	$4.3746 \cdot 10^{-3}$	$e_9(\tau_w)$	$5.3271 \cdot 10^{-22}$
$f_{n10}$ (Hz)	1560.49	$\zeta_{10}$	$4.9029 \cdot 10^{-3}$	$e_{10}(\tau_w)$	$1.8915 \cdot 10^{-27}$

Some significant elements of the mass, stiffness and damping matrices are presented in Tabs.9 to 11 in order to show the efficiency of the identification process. The actual values derived with the numerical model have been indicated with NASTRAN,  $FRF_s$  indicates the estimates obtained from frequencies response functions directly synthesized in the frequency domain, whereas  $FRF_{FR}$  stands for evaluated components from frequencies response functions achieved Fourier transforming the relative impulse responses, consequently these last could be subjected to errors due to truncation effects.

Table 9 - Comparison of some mass matrix elements estimates (10-DOF beam).

$m_{ij} 10^2$	NASTRAN	FRF <sub>s</sub>	FRF <sub>IR</sub>
$m_{11}$	2.7000	2.7000	2.6723
$m_{28}$	0.0	$1.1177 \cdot 10^{-4}$	$7.1934 \cdot 10^{-2}$
$m_{33}$	2.7000	2.7010	2.3331
$m_{55}$	2.7000	2.7009	2.4380
$m_{69}$	0.0	$7.1772 \cdot 10^{-5}$	$5.8163 \cdot 10^{-2}$
$m_{77}$	2.7000	2.7005	2.3901
$m_{1010}$	1.3500	1.3497	1.0914

Table 10 - Comparison of some stiffness matrix elements estimates (10-DOF beam).

$k_{ij} 10^{-6}$	NASTRAN	FRF <sub>s</sub>	FRF <sub>IR</sub>
$k_{11}$	1.0984	1.0984	1.0984
$k_{19}$	$9.4987 \cdot 10^{-5}$	$1.2109 \cdot 10^{-4}$	$-3.4301 \cdot 10^{-4}$
$k_{33}$	0.8386	0.8388	0.8365
$k_{410}$	$7.7792 \cdot 10^{-4}$	$7.8701 \cdot 10^{-4}$	$-4.3784 \cdot 10^{-4}$
$k_{55}$	0.8373	0.8374	0.8364
$k_{82}$	$1.3474 \cdot 10^{-3}$	$1.4378 \cdot 10^{-3}$	$1.0975 \cdot 10^{-3}$
$k_{99}$	0.5761	0.5761	0.5762

Table 11 - Comparison of some damping matrix elements estimates (10-DOF beam).

$c_{ij}$	NASTRAN	FRF <sub>s</sub>	FRF <sub>IR</sub>
$c_{11}$	1.0987	1.0987	1.0986
$c_{19}$	$9.4987 \cdot 10^{-5}$	$1.3230 \cdot 10^{-4}$	$-3.3247 \cdot 10^{-4}$
$c_{33}$	0.8389	0.8390	0.8367
$c_{410}$	$7.7792 \cdot 10^{-4}$	$7.8391 \cdot 10^{-4}$	$-4.4169 \cdot 10^{-4}$
$c_{55}$	0.8375	0.8377	0.8367
$c_{82}$	$1.3475 \cdot 10^{-3}$	$1.4350 \cdot 10^{-3}$	$1.1017 \cdot 10^{-3}$
$c_{99}$	0.5764	0.5764	0.5764

It appears that mass element evaluations are very accurate, when the experimental estimates - gained from unbiased FRF<sub>S</sub> - are precise, on the contrary significant errors arise as a consequence of the truncation (very high for the first three modes) of the uncorrected FRF<sub>IR</sub>. In particular, it has been noticed a general trend of the off diagonal mass matrix elements, which should be zero in the actual model, to assume values of the same order of the diagonal terms. The effect of the truncation on stiffness and damping elements, as it results from the evaluations indicated with FRF<sub>IR</sub>, turned out to be limited at least for the more significant elements.

In a fourth case, the effects due to different errors in the experimental evaluation of modal parameters are presented; in particular, changes of the actual values, in order to simulate estimates from experimental data, have been considered for the first and the fourth natural frequencies, for the last two f<sub>n</sub>'s, for the damping ratios relative to the first three modes, for the driving point residues and finally for all them together, as indicated in the following Table (Tab.12).

Table 12 - Errors introduced on natural frequencies, damping ratios and residue estimations.

a	f <sub>n1</sub> =9 (Hz)	f <sub>n4</sub> =300 (Hz)	
b	f <sub>n9</sub> =1500 (Hz)	f <sub>n10</sub> =1700 (Hz)	
c	ζ <sub>1</sub> =2.4 10 <sup>-4</sup>	ζ <sub>2</sub> =2.5 10 <sup>-4</sup>	ζ <sub>3</sub> =6.0 10 <sup>-4</sup>
d	a random noise, with zero mean value and standard deviation (σ <sub>N</sub> ) equal to 10% of the residue amplitude, has been added to the driving point residue estimation		
e	a+b+c+d		

In Tabs.13 to 15 evaluations of some significant elements of mass, stiffness and damping matrices have been reported: the letters 'a' to 'e' indicate the simulation of different errors, as it has been specified in the previous Table.

Table 13 - Estimations in some mass matrix elements when errors are considered.

m <sub>ij</sub> 10 <sup>2</sup>	a	b	c	d	e
m <sub>11</sub>	2.6866	2.6533	2.7000	2.8473	2.8333
m <sub>28</sub>	-5.0831 10 <sup>-2</sup>	1.6349 10 <sup>-2</sup>	1.1175 10 <sup>-4</sup>	1.3149 10 <sup>-1</sup>	7.8388 10 <sup>-2</sup>
m <sub>55</sub>	2.6427	2.6602	2.7008	2.9346	2.8735
m <sub>69</sub>	-3.2098 10 <sup>-2</sup>	2.6179 10 <sup>-2</sup>	7.1770 10 <sup>-5</sup>	1.0023 10 <sup>-1</sup>	6.3808 10 <sup>-2</sup>
m <sub>1010</sub>	1.3073	1.3484	1.3497	1.4197	1.3738

Table 14 - Estimations in some stiffness matrix elements when errors are considered.

$k_{ij} 10^{-6}$	a	b	c	d	e
$k_{11}$	1.0988	1.1393	1.0984	1.2330	1.2335
$k_{19}$	$3.1286 10^{-4}$	$-8.9018 10^{-3}$	$1.2109 10^{-4}$	$4.7430 10^{-2}$	$4.7629 10^{-2}$
$k_{55}$	0.8389	0.8796	0.8374	0.9834	0.9850
$k_{82}$	$2.9390 10^{-3}$	$-8.1224 10^{-3}$	$1.4379 10^{-3}$	$3.5170 10^{-2}$	$3.6724 10^{-2}$
$k_{99}$	0.5762	0.5902	0.5761	0.6410	0.6411

Table 15 - Estimations in some damping matrix elements when errors are considered.

$c_{ij}$	a	b	c	d	e
$c_{11}$	1.0987	1.0987	1.0988	1.1899	1.1900
$c_{19}$	$1.3230 10^{-4}$	$1.3230 10^{-4}$	$2.1583 10^{-4}$	$5.6262 10^{-2}$	$5.6345 10^{-2}$
$c_{55}$	0.8377	0.8377	0.8380	0.9380	0.9383
$c_{82}$	$1.4350 10^{-3}$	$1.4350 10^{-3}$	$7.0123 10^{-4}$	$4.3898 10^{-2}$	$4.3159 10^{-2}$
$c_{99}$	0.5764	0.5764	0.5767	0.6266	0.6269

The more significant errors have been found in the matrix elements which are derived from misestimated driving point residues (case 'd' in Tabs.13 to 15).

A general trend of the errors to spread towards all the terms of the spatial matrices has been noticed. These results confirm the importance of the effects that the errors on residue evaluations have on the identification process.

In the last case the identification of the spatial matrices from an incomplete model, considering only 6 out of 10 modes of the beam model, by using the Error Matrix Method is presented. Hereafter this method has been applied in order to evaluate the effects produced by an "experimental" model whose modal parameters have been estimated with unnegligible errors; in fact the experimental errors yield an "updating" of the spatial matrices, achieved from the "analytical" model, towards values which mislead the identification process.

Although truncations are smaller than the ones of the complete case (reported in Tab.8), in fact the observation window length is doubled with respect to the previous example, three out of six modes result highly truncated as it is shown in Tab.16, where the envelopes (always considered with unitary initial amplitude) are presented.

Table 16 - Envelope truncations when only 6 modes are considered and with  $\tau_w=2.56$  s.

$e_1(\tau_w)$	$e_2(\tau_w)$	$e_3(\tau_w)$	$e_4(\tau_w)$	$e_5(\tau_w)$	$e_6(\tau_w)$
0.9839	0.8667	0.3634	$2.3012 \cdot 10^{-2}$	$4.2838 \cdot 10^{-5}$	$3.3091 \cdot 10^{-10}$

A comparison between two different conditions for the incomplete model has been considered: Modes<sub>C</sub> indicates matrix element estimates, carried out considering the first 6 modes, from synthesized frequency response functions, whereas Modes<sub>T</sub> stands for values achieved from impulse response functions (i.e., where truncation effects are considered), and corrected with the Error Matrix Method. Some significant elements of spatial matrices are presented in Tabs.17 to 19.

Table 17 - Some elements of mass matrix by incomplete model without or with truncation.

$m_{ij} \cdot 10^2$	$m_{11}$	$m_{28}$	$m_{33}$	$m_{55}$	$m_{69}$	$m_{77}$	$m_{1010}$
Modes <sub>C</sub>	2.700	$9.81 \cdot 10^{-6}$	2.701	2.701	$5.46 \cdot 10^{-5}$	2.701	1.350
Modes <sub>T</sub>	2.590	$2.51 \cdot 10^{-1}$	1.270	1.526	$-6.8 \cdot 10^{-1}$	1.330	$1.85 \cdot 10^{-1}$

Table 18 - Some elements of stiffness matrix by incomplete model without or with truncation.

$k_{ij} \cdot 10^6$	$k_{11}$	$k_{19}$	$k_{55}$	$k_{82}$	$k_{99}$
Modes <sub>C</sub>	1.0984	$9.478 \cdot 10^{-5}$	0.8373	$1.349 \cdot 10^{-3}$	0.5761
Modes <sub>T</sub>	1.0977	$-1.121 \cdot 10^{-3}$	0.8336	$9.224 \cdot 10^{-4}$	0.5756

Table 19 - Some elements of damping matrix by incomplete model without or with truncation.

$c_{ij}$	$c_{11}$	$c_{19}$	$c_{55}$	$c_{82}$	$c_{99}$
Modes <sub>C</sub>	1.0987	$1.011 \cdot 10^{-4}$	0.8375	$1.348 \cdot 10^{-3}$	0.5764
Modes <sub>T</sub>	1.0979	$-1.117 \cdot 10^{-3}$	0.8338	$9.468 \cdot 10^{-4}$	0.5758

Table 14 - Estimations in some stiffness matrix elements when errors are considered.

$k_{ij} 10^{-6}$	a	b	c	d	e
$k_{11}$	1.0988	1.1393	1.0984	1.2330	1.2335
$k_{19}$	$3.1286 10^{-4}$	$-8.9018 10^{-3}$	$1.2109 10^{-4}$	$4.7430 10^{-2}$	$4.7629 10^{-2}$
$k_{55}$	0.8389	0.8796	0.8374	0.9834	0.9850
$k_{82}$	$2.9390 10^{-3}$	$-8.1224 10^{-3}$	$1.4379 10^{-3}$	$3.5170 10^{-2}$	$3.6724 10^{-2}$
$k_{99}$	0.5762	0.5902	0.5761	0.6410	0.6411

Table 15 - Estimations in some damping matrix elements when errors are considered.

$c_{ij}$	a	b	c	d	e
$c_{11}$	1.0987	1.0987	1.0988	1.1899	1.1900
$c_{19}$	$1.3230 10^{-4}$	$1.3230 10^{-4}$	$2.1583 10^{-4}$	$5.6262 10^{-2}$	$5.6345 10^{-2}$
$c_{55}$	0.8377	0.8377	0.8380	0.9380	0.9383
$c_{82}$	$1.4350 10^{-3}$	$1.4350 10^{-3}$	$7.0123 10^{-4}$	$4.3898 10^{-2}$	$4.3159 10^{-2}$
$c_{99}$	0.5764	0.5764	0.5767	0.6266	0.6269

The more significant errors have been found in the matrix elements which are derived from misestimated driving point residues (case 'd' in Tabs.13 to 15).

A general trend of the errors to spread towards all the terms of the spatial matrices has been noticed. These results confirm the importance of the effects that the errors on residue evaluations have on the identification process.

In the last case the identification of the spatial matrices from an incomplete model, considering only 6 out of 10 modes of the beam model, by using the Error Matrix Method is presented. Hereafter this method has been applied in order to evaluate the effects produced by an "experimental" model whose modal parameters have been estimated with unnegligible errors; in fact the experimental errors yield an "updating" of the spatial matrices, achieved from the "analytical" model, towards values which mislead the identification process.

Although truncations are smaller than the ones of the complete case (reported in Tab.8), in fact the observation window length is doubled with respect to the previous example, three out of six modes result highly truncated as it is shown in Tab.16, where the envelopes (always considered with unitary initial amplitude) are presented.

Table 16 - Envelope truncations when only 6 modes are considered and with  $\tau_w=2.56$  s.

$e_1(\tau_w)$	$e_2(\tau_w)$	$e_3(\tau_w)$	$e_4(\tau_w)$	$e_5(\tau_w)$	$e_6(\tau_w)$
0.9839	0.8667	0.3634	$2.3012 \cdot 10^{-2}$	$4.2838 \cdot 10^{-5}$	$3.3091 \cdot 10^{-10}$

A comparison between two different conditions for the incomplete model has been considered: Modes<sub>C</sub> indicates matrix element estimates, carried out considering the first 6 modes, from synthesized frequency response functions, whereas Modes<sub>T</sub> stands for values achieved from impulse response functions (i.e., where truncation effects are considered), and corrected with the Error Matrix Method. Some significant elements of spatial matrices are presented in Tabs.17 to 19.

Table 17 - Some elements of mass matrix by incomplete model without or with truncation.

$m_{ij} \cdot 10^2$	$m_{11}$	$m_{28}$	$m_{33}$	$m_{55}$	$m_{69}$	$m_{77}$	$m_{1010}$
Modes <sub>C</sub>	2.700	$9.81 \cdot 10^{-6}$	2.701	2.701	$5.46 \cdot 10^{-5}$	2.701	1.350
Modes <sub>T</sub>	2.590	$2.51 \cdot 10^{-1}$	1.270	1.526	$-6.8 \cdot 10^{-1}$	1.330	$1.85 \cdot 10^{-1}$

Table 18 - Some elements of stiffness matrix by incomplete model without or with truncation.

$k_{ij} \cdot 10^6$	$k_{11}$	$k_{19}$	$k_{55}$	$k_{82}$	$k_{99}$
Modes <sub>C</sub>	1.0984	$9.478 \cdot 10^{-5}$	0.8373	$1.349 \cdot 10^{-3}$	0.5761
Modes <sub>T</sub>	1.0977	$-1.121 \cdot 10^{-3}$	0.8336	$9.224 \cdot 10^{-4}$	0.5756

Table 19 - Some elements of damping matrix by incomplete model without or with truncation.

$c_{ij}$	$c_{11}$	$c_{19}$	$c_{55}$	$c_{82}$	$c_{99}$
Modes <sub>C</sub>	1.0987	$1.011 \cdot 10^{-4}$	0.8375	$1.348 \cdot 10^{-3}$	0.5764
Modes <sub>T</sub>	1.0979	$-1.117 \cdot 10^{-3}$	0.8338	$9.468 \cdot 10^{-4}$	0.5758

The possibility of spatial matrix identifications by incomplete, but correct, models, that is in the ideal hypothesis of error free modal parameter estimates, has been pointed out by the very accurate evaluations of all the terms of mass, stiffness and damping matrices. On the contrary truncation effects resulted quite important in the mass matrix estimation, whereas stiffness and damping elements have been evaluated with less significant errors. It is worth noting that high errors have been introduced by truncation: so that both the cross orthogonality check (between "experimental" and "numerical" eigenvectors) and the Modal Assurance Criterion have not been satisfied.

## CONCLUDING REMARKS

Some problems concerning the spatial matrix identifications, starting from modal parameter estimates are presented.

Simulations of possible experimental errors have been carried out: the effects of natural frequency, damping ratio, residue evaluations and in particular of impulse response truncations at the end of the observation window have been considered. A peculiar attention has been paid to the possible identification by incomplete models using the Error Matrix Method, also in presence of truncation effects.

The numerical tests confirm the relevant effects of the experimental errors in the identification process: in particular as regards the residue errors due to both truncation problems and random additive noise. The effects of experimental errors in residue estimations can result completely misleading in the identification process of mass, stiffness and damping matrices. Actually, it is possible to note that a large number of modes, with respect to the considered ones, presented large errors due to truncation effects.

## ACKNOWLEDGMENTS

This work is sponsored in part by Consiglio Nazionale delle Ricerche under grant CTB 91.2073.CT11 : "Analisi dinamica combinata vibrazioni temperatura di materiali aerospaziali" and in part by Ministero della Università e della Ricerca Scientifica e Tecnologica (M.U.R.S.T.) research project: "Stima del fattore di smorzamento da segnali molto rumorosi".

## REFERENCES

- [1] Ewins D.J., He J., Lieven N.A.J., "A Review of the Error Matrix Method (EMM) for Structural Dynamic Model Comparison", *Proceedings of the International Conference on 'Spacecraft Structures and Mechanical Testing'*, Noordwijk, The Netherlands, 1988. ESA SP-289, pp.55-62.
- [2] Lieven N.A.J. and Ewins D.J., "Effect of Incompleteness and Noise on Error Matrix Calculations", *International Modal Analysis Conference (IMAC X)*, 1992, pp.1406-1413.

- [3] Agneni A., Balis Crema L., "Damping Measurements from Truncated Signals via Hilbert Transform", *Mechanical System and Signal Processing*, 1989, Vol.3 n.1, pp.1-13.
- [4] Agneni A., Balis Crema L., and Paolozzi A., "Impulse Response Identification of SDOF System from Time-Truncated Signals", *Proceedings of the Florence Modal Analysis Conference*, Florence, 1991, pp.741-748.
- [5] Agneni A., Balis Crema L., and Paolozzi A., "On the Use of Poisson's sum Formula to Avoid Truncation Effects", *Proceedings of the Florence Modal Analysis Conference*, Florence, 1991, pp.645-654.
- [6] Cafeo J.A., Trethewey M.W., "Impulse Tests Truncation and Exponential Windows Effects on Spectral and Modal Parameters", *Proceedings of the 8th International Modal Analysis Conference*, Kissimee, 1990, pp.234-240.
- [7] Trethewey M.W., Cafeo J.A., "Signal Processing Aspects of Structural Impact Testing", *The International Journal of Analytical and Experimental Modal Analysis*, 1992, Vol.2 n.2, pp.129-149.
- [8] Shye K. and Richardson M., "Mass, Stiffness and Damping Matrix Estimates from Structural Measurements", *Proceedings of International Modal Analysis Conference*, London, 1987, pp. 756-761.
- [9] SMS, Structural Measurements Systems, Modal Analysis System. *Operating Manual, "Theory of Operation"*, 1985, Ch.12, pp.12-25 to 12-33.
- [10] Imbert J.F., "Analyse des Structures par Elements Finis", *Cepadues-Editions*, Toulouse, 1984, pp. 413-414.
- [11] Mazet R., "Mécanique Vibratoire", *Librairie Polytechnique Ch. Béranger*, Paris, 1955, pp. 216-218.
- [12] Ibrahim S.R., Pappa R.S., "Dynamic Analysis: a Parametric Study of the Ibrahim Time Domain Modal Identification Algorithm", *The Shock and Vibration Bulletin*, Bulletin 5 Part 3 of 3 Parts, 1981, pp.43-71.
- [13] Marple Jr. S.L., "Digital Spectral Analysis with Applications", *Prentice-Hall*, New Jersey, 1987, Ch.11, pp.303-349.
- [14] Agneni A., Balis Crema L., "A new Proposal for Time Domain SDOF Components Estimation", *Aerotecnica-Missili e Spazio*, 1986, Vol.65 n.4, pp.167-175.
- [15] Gade S., Herlufsen H., "Errors on Impulse Response Function Estimates and their Corrections", *15th International Seminar on Modal Analysis*, Leuven, 1990, pp.1005-1015.
- [16] Agneni A., "Bias in Modal Parameters due to Aliasing in the Time Domain", *MECCANICA*, 26, 1991, pp.221-228.
- [17] Agneni A., Balis Crema L. "Residue estimation effects on mass and stiffness matrix identification", *Structural Dynamics and Vibrations - 1993*. ASME, PD-vol.52, pp.159-164.

# THE RELATION BETWEEN INTERNAL FRICTION IN METALS AND ELASTIC WAVE VELOCITIES

Capecchi Augusto  
Institute of Construction Science  
Genoa University - Italy

## ABSTRACT

This paper highlights the dependence of internal friction on the velocity of elastic waves in metals at ambient temperature and vanishing amplitude. The corresponding diagrams, similarly shaped for each metal, allow conclusions to be drawn on the reliability of the test results and the different test methods.

The experimental data, in fact, seem to be at odds with the predictions of the anelastic-relaxation theory and, in particular, with those of thermo-relaxation; the inverted dependence of I.F. on the velocity of elastic waves instead suggests that a viscous mechanism may be responsible for the dissipation phenomena.

## INTRODUCTION

The physical and mechanical properties of a metal or alloy at almost any temperature can be readily found from tables. It is impossible, however, to find any information on internal friction, even for principal structural metals at ambient temperature.

Wishing to investigate the problem further, I started to study the phenomena and discovered that the written information currently available is rather fragmentary and often contradicting. Furthermore, there seems to be some debate as to whether internal friction is actually a property of the material or not.

From an experimental point of view, there doesn't even appear to be any agreement on the type of specimens to use for the measurements, nor on the test methods to adopt.

Some applications, in fact, require an accurate chemical-physical characterisation of the specimen, implying a considerable reduction in dimensions and mass in order to be able to carry out heat treatment and vacuum doping. Others instead consider it necessary to use specimens of larger mass in order to reduce the influence of the supports (1).

Others again, in their attempt to increase the sensitivity of the antennas for researches into gravitational waves, use magnetic levitation to eliminate mechanical supports. This, however, means operating at cryogenic temperatures. Even in these rather refined studies there still doesn't appear to be any design methods or theories for obtaining the maximum values of the amplification factor  $Q$  (2).

Yet again, some researchers make use of specimens with distributed mass or added concentrated masses indifferently, maintaining that the results obtained with both systems are comparable.

Furthermore, some test methods have been developed and published that, in my opinion, are extremely unreliable. In particular, I refer to the direct and reverse torsion pendula, in which it is impossible to determine how much energy is dissipated in the specimen and how much, instead, flows to the supports (4)(5).

All this opens the debate on the need for specimens to be excited only in self-balanced modes and supported at the nodes, at least to prevent the forces undoubtedly present in these sections from being transmitted to the supports. Other problems are linked to the need to measure the temperature, under vacuum, of specimens with a reduced mass without any additional contacts for the thermocouples.

In addition, the specimens need to be securely positioned, with steady contacts, when using condenser exciting and measuring techniques (6), in that the other armature of the condenser must be placed at a distance of approximately 1/10 mm from a flat portion of the specimen.

Problems also arise with the need to compare results relating to the three types of vibration possible in bounded specimens, i.e. longitudinal, torsional and flexural, in terms of, for example, frequency.

When examining the above problems, two principal factors emerge: the impossibility of predicting the outcome of a test and the consequent impossibility of judging the absolute reliability of the result.

When carrying out tests under similar conditions on the same specimen, the only true statement that can be made is that the lowest value of the I.F. will be less incorrect, in that any type of error will lead almost certainly to an increase.

A comment should also be made at this point about the only physical mathematical theory on I.F.; one which determines the main cause of dissipation of flexural vibrations in thermo-elastic relaxation and allows its calculation (7)(8) (9).

Zener's theory however does not seem to have any reliable experimental proof, in that the results produce different progressions, justifying the hypothesis that the same type of dissipation mechanism is present in the three types of stresses, contrary to that stated by the theory.

This paper summarises the results obtained by the author.

### **SPECIMEN TYPES**

The fundamental condition necessary for operating in a correct manner is that of minimising the influence of supports, such that the amount of energy flowing towards the outside becomes negligible. In order to obtain this state, first of all the excited modes must be self-balanced in order not to transmit the forces present in the nodal sections to the supports.

This condition, though necessary, is not sufficient on its own, in that the displacements in the nodes are zero but not the rotations, nor are the strains in the plane of the cross section of the specimen.

With a bar in flexure, the rotation in the nodal sections causes interaction with the suspensions, even if filiform. This can be proved by just placing the bar horizontally, supporting the two nodal sections on wires, or vertically, and exciting it in the same manner though with only one section suspended, observing that the values measured decrease.

A great degree of attention has, therefore, been paid to reducing

interaction with the supports and to identifying the mechanical oscillators that would lessen the induced errors.

In order to eliminate the error in the determination of nodal sections and their coincidence with the supports, specimens in the form of rings are used. Suspended at one section, these correspond to a nodal section and the results, for the same thickness and frequency, are reduced when compared to bars.

Furthermore, in order to prevent rotation at the supports, consideration should be given to the use of specimens that have nodal axes that intersect at the support. Of these, the most simple, including from a construction point of view, is the thin disc type supported at the centre and, if possible, at the middle plane. In excitation modes that only provide nodal diameters (without nodal circles), the axis of the disc is not subjected to rotation and its middle plane is not displaced.

Using these specimens, the values reduce further with respect to those obtained with rings of the same thickness and frequency. In particular, they eliminate the peak zone, the focal point of the thermo-elastic theory. On the contrary, the use of discs, but excited with a nodal circle and supported on it at three points acting on the middle plane, creates notable interaction with the supports due to second order effects; consequently, the results could be wrong in excess.

In order to establish a more direct comparison between the results of the discs supported at the centre and those on bars, it was decided to construct cross-shaped specimens with four equal arms at right angles. These are cut from sheets using a specially designed machine. The specimens are supported at the centre point and excited such that the two aligned arms have positive bending and the remainder negative. The specimens are thus self-balancing and possess the above mentioned properties for the centre (10).

The results obtained on the cross-shaped specimens, made up of four beams joined together, have entirely confirmed the results obtained with the discs and, consequently, after this test, their use can no longer be justified (11).

Therefore, it can be concluded that bars, at least for certain frequencies and thicknesses, even if self-balanced, introduce errors that cannot be tolerated in the measurements.

In spite of this, it seems that the beams can be used, with great care, at relatively high or very low frequencies, as if the interaction with the suspensions is subjected to a resonance far of which the results would seem to be acceptable (12).

For measurements relating to longitudinal and torsional vibrations, the optimum situation is represented by the bar supported vertically at the centre, paying special care in the making supports (13).

#### **TEST METHODS**

The best method of measuring low I.F. values is to excite the specimen at one of its natural frequencies, compatible with the applied supports, then measuring the free-decay of the free oscillations after switching-off the excitation.

The most simple and economic method of exciting and measuring

without contact is, without doubt, inducing eddy currents even through a telephonic earpiece, after removing the membrane. These transducers can, of course, assume more complex forms, by switching off the permanent magnetic field of the excitation in order to limit its influence on the free oscillations, or with suitable coil shapes for exciting torsional vibrations. The usefulness of these transducers lies in the non-critical nature of their positioning, within a few millimetres, while their linearity has no influence. Linear electro-magnetic systems are also available for measuring, though these are rather costly and less sensitive, plus optical systems which have the advantage of annulling mutual effects. The condenser excitation and measuring system does present a series of difficulties, such as the need for steady positioning of the specimen, with the inevitable interaction with the supports, the need for a rather high vacuum which precludes the use of large specimens, the need to position the mobile electrode with extremely fine adjustment from the outside, and finally the ad hoc electronics which I had to improve substantially (14). Personally speaking though I think that the first of these conditions is the one that constitutes a notable source of error. Other flexural test method, though not in common use, make use of a vibrator to impart a sinusoidal motion to the centre of the beam while measuring the amplitude at the free ends, thus obtaining the Q-factor immediately. Due to the inevitable interaction with the machine, this particular method introduces quite substantial errors and specimens are difficult to work (15).

#### **PHYSICAL-MATHEMATICAL REFERENCES**

As already stated, in thermo-elastic relaxation damping in flexure is mainly due to a thermal dissipation phenomenon. This is because, in solids, a positive variation in the volume leads to a reduction in temperature, and viceversa. In the presence of flexure, the temperature reduces at the extrados and increases at the intrados.

Therefore, during flexural vibration of a bar, a thermal flow is created which alternates between its sides in the bending plane. The phenomenon has the tendency to become adiabatic at high frequencies, in that the time available before the reversal of the flow is too short, while it tends to be isothermic at low frequencies, in that the reduced deformation velocity does not create any thermal gradients.

For a given thickness of vibrating beam, the damping should have the characteristic bell-shaped progress versus frequency and show a peak. By varying the thickness of the beam, a family of identical curves should be obtained, translated in frequency. For each thickness, the theoretical progress in a bilogarithmic diagram should consist instead of two half lines at right angles to each other and inclined at  $\pm 45^\circ$ , linked by a curve near to the peak value.

For longitudinal vibrations, the positive and negative volume change zones, i.e. in tension or compression, are at a distance equal to half of the wavelength and, as a result, it is generally

impossible to hypothesise the existence of a thermal flow. In round bars in torsion, there are no volume variations whatsoever, and as a result no thermal flows can be hypothesised here either.

Zener also attempted to extend the thermo-relaxation relaxation theory to cover these cases, resorting to the hypotheses of intergranular thermal flows caused by grain anisotropy.

While it is certain that the dimensions of the grain could influence the damping, this interpretation of the phenomenon is by no means acceptable.

It must be pointed out that the thermo-elastic relaxation theory has never been criticised, even though the experimental tests in flexure are based only on the use of beams, either with or without added masses, with limited coverage of the progress especially in the peak zones which, as the evidence shows, disappear when working with oscillators that do not interact with the suspensions.

After a series of attempts in which I either maintained the test frequency constant and varied the thickness, or maintained the thickness constant and varied the frequency, I came to the conclusion that the thermal phenomena undoubtedly present are not in the quantities calculated by Zener and, therefore, are not the main factors responsible for flexural damping.

Important progress in our research could have been made by taking into account the work of Kolsky on the velocity of continuous elastic waves in bounded specimens (16). As the excitation of a vibration at a point in a continuum is always associated with a strain wave that travels in the medium, it becomes very important to know the speed at which these waves propagate.

In particular, the propagation of a monochromatic wave in a bar normally takes place at speeds that may vary, for example in aluminium alloys, from 0 to approximately 5000m/s.

In order to determine the test velocity, the first step is to establish whether the waves are flexural, torsional or longitudinal and, for each type, to take into account the ratio between the transversal dimensions of the bar and the wavelength.

Under normal test conditions, it can be stated that the velocity of extensional waves very rarely shifts from the maximum value measured; for torsional waves, the velocity is constant and equal to approximately 2/3 of the maximum value while, in flexural waves only, it is possible to vary the velocity from 5 to 1000 m/s, at least in the indicated material.

In order to understand the significance of wave velocity, despite the excitation of a standing wave in a bar of finite length, reference should be made to the incident wave on the end face of the bar and the reflected wave. The overlapping of these two counterrunning waves generates the stationary wave which then perfectly identifies the propagation speed of the constituent waves.

As the velocity is given by the product of the frequency and the wavelength, when the latter is identified from the resonance of the specimen and determined from the length of the bar and the excitation mode, it is possible easily and accurately to calcu-

late the velocity, by the resonance frequency. Consideration must be given to the significance of the velocity of the propagation wave, constant for a given test, with respect to that of the oscillation velocity of a point. The latter oscillates around its equilibrium position and the velocity value is sinusoidal.

This oscillation velocity is not necessarily linked to the wave velocity, as it has already been stated that, with longitudinal and torsional vibrations, a variation in the excitation frequency (and consequently in the average oscillation velocity of the point) does not cause variations in propagation velocity.

This is due to the fact that the axial and torsional rigidity only depend on the section and, in order to follow higher modes, the mass diminishes between two nodal sections which gradually come together.

The flexural situation is quite different in that the velocity increases with the frequency. In fact, the specimen is capable of oscillating on its higher modes, both increasing its flexural rigidity, through a reduction in the free deflection span between nodal sections, and reducing the mass between the same sections, which gradually come together.

In order to understand the physical aspects of the propagation velocity of a wave, reference should be made to the relative movement of two homologous points in two adjacent sections of the bar.

If the speed were infinite, the movement of the points would be synchronous and identical, though with a finite speed, the movement of the points would be out of phase, creating local strain which moves along the bar.

It thus appears clear that the propagation velocity is that of the translation of the strain along the bar, even though, when exciting standing waves in the specimens, the phenomenon does not appear.

Given that the principal damping mechanism demonstrates an inverse dependence on the thus defined velocity, it could be hypothesized that a viscous damping exists, and that larger dissipation phenomena could result from a slower movement of the strain. A dynamic rheological modelling in this direction is at present being studied by the author.

## **RESULTS**

In the excitation of torsional vibrations, the velocity is constant and equal to the velocity of a "shear" wave in an unbounded medium. With longitudinal vibrations, the reduction is very small as the frequency increases (0.4% for a variation from 414 to 22725 c/s) and equals the velocity of a continuous wave in a bar of infinite length.

The "bar" velocity defines, together with the density, the longitudinal modulus of elasticity, while the shear velocity defines the tangential modulus of elasticity, in the same link.

In fact, these two decisively high velocity values correspond to more or less constant values of damping, near to the minimum measurable.

Viceversa, in the excitation of flexural vibrations in reliable tests, the velocity range extends from values not too far from the shear velocity up to the minimum allowed by experimentation, a few metres per second. Further reduction of the frequency becomes prohibitive due to the unacceptable dimensions of the specimens and the introduction of a flexural-torsional instability phenomena.

This considerable reduction in velocity is accompanied by a substantial increase in the damping value which, for aluminium alloys, reaches approximately two logarithmic decades. Consequently, a bilogarithmic damping/velocity graph is obtained, showing the characteristic progress of a low velocity zone with a high and constant damping value, followed by a 45° descent and then a final horizontal zone of minimum value.

We have been able to draw this graph for the principal metals, all similar in layout, but with different values and extensions in the two horizontal sections. It is interesting to note that all the values obtained with the three wave types can be inserted perfectly in these graphs.

In order to verify the identity or otherwise of the flexural and torsional damping origin, torsional tests were carried out on rectangular cross section bars, varying the ratio between the sides of the section (17). In these cases, the velocity is not the same as that of the shear wave but, on reduction of the torsional rigidity, produces a reduction in the propagation velocity, that can be calculated from the product of the wave length and frequency.

Mathematically speaking, it has been demonstrated that this velocity reduces that of the shear wave in accordance with the ratio between the sides of the section. In this manner, it was possible to fully explore the velocity range already studied in the flexural tests, and the results obtained with the two wave types show a perfect coincidence at the same velocity.

The graph of damping versus velocity has proved to be completely incompatible with the family of curves predicted by the Zener theory, and it seems to further negate the validity of the numerical predictions of the theory.

The results of the research include graphs obtained from aluminium alloys, copper, brass, steel and tantalum; these graphs should be considered only representative of the behaviour of those metals. Results deemed to be correct and significant obtained by other researchers also appear.

In particular, experiments using several differently shaped oscillator were carried out mainly on the aluminium alloys.

#### **ADDITION OF CONCENTRATED MASSES**

All the results were obtained using distributed mass oscillators, in that it is considered that the addition of concentrated masses leads to results that may differ considerably for the same thickness and frequency.

In order to understand the difference between the two cases, from the physics point of view, it is sufficient to examine the motion of a distributed mass oscillator in free vibration. The energy

possessed by the system is transformed from kinetic energy into strain potential energy twice in each oscillation and viceversa. During the cycle, all the possessed energy is available for dissipation into the material; with additional masses, instead, a part of the energy is stored by the mass and consequently temporarily subtracted from the dissipation phenomena caused by the oscillator strains.

In general, therefore, it can be stated that the addition of masses causes smaller damping values than a distributed mass oscillator.

For a free-free beam in flexure with two nodal sections, the addition of a mass at each end and one at the centre, in the appropriate ratio, allows the position of the nodal sections to remain unchanged. Operating in this manner though has shown that the damping values are decisively less than those obtainable on a beam of the same material and cross section, the longer length of which allows it to vibrate at the same frequency.

However, it does not seem possible to compare the results obtained for oscillators with and without added masses beforehand.

Moreover, this phenomenon has never been the subject of detailed research, with the preference being to exclude the possibility of working with added masses.

It is evident, however, that if in some way it could be made comparable, this method would allow the exploration of frequency ranges difficult to reach with distributed mass specimens.

### CONCLUSIONS

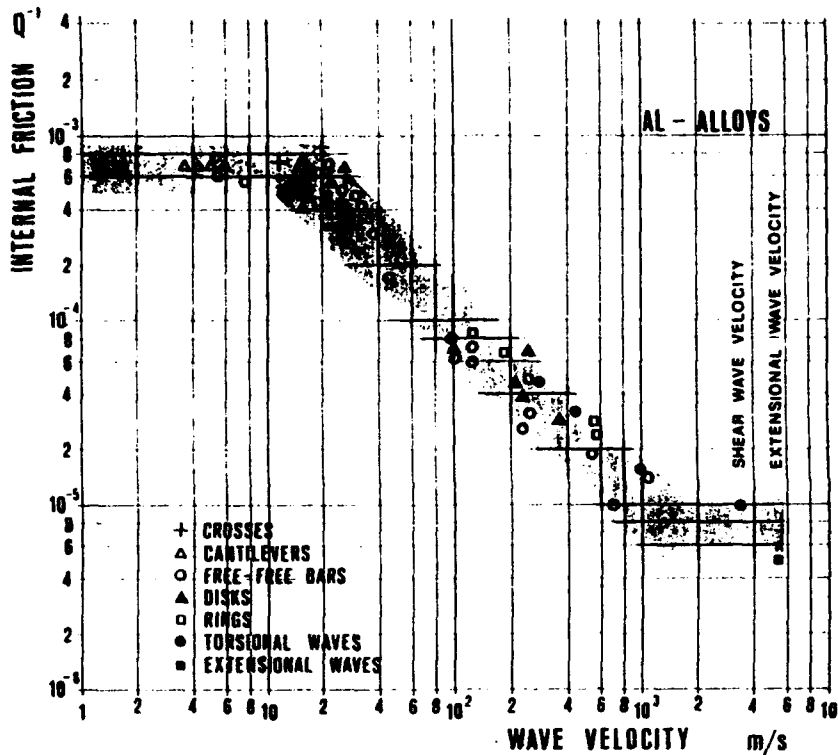
From the above results, it should be noted that the introduction of elastic wave velocity, as a fundamental parameter of damping, has enabled the following conclusions to be drawn:

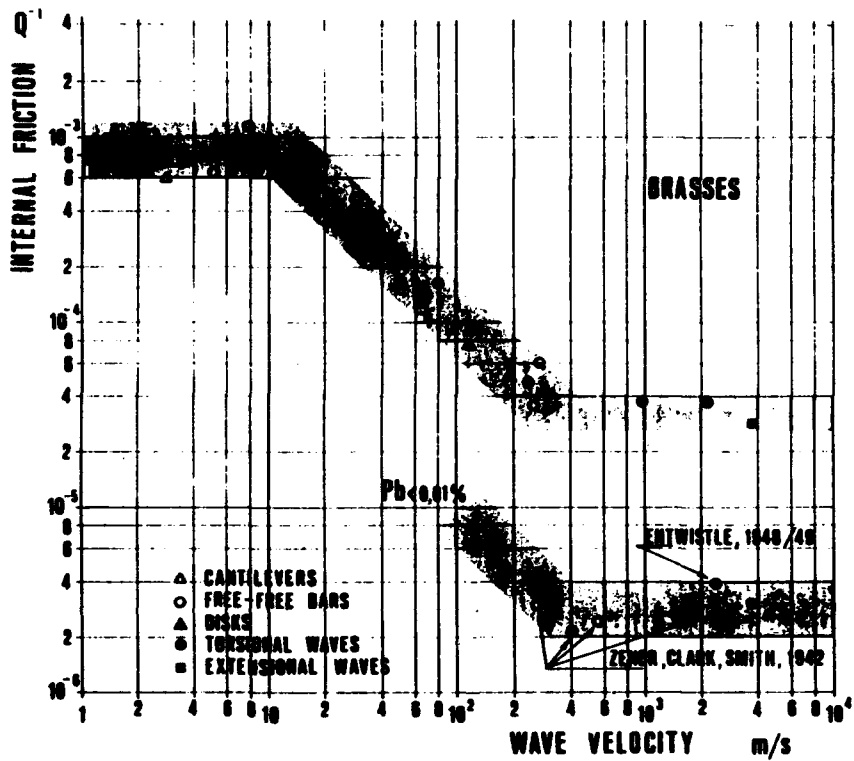
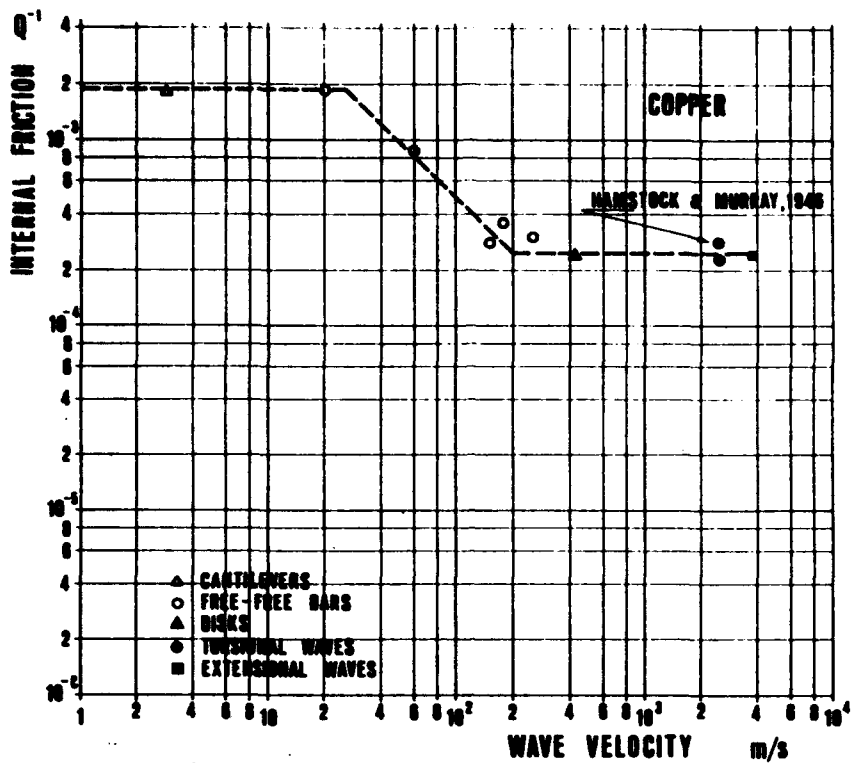
- in each metal a single graph can be drawn of the results relating to longitudinal, torsional and flexural waves
- the damping of a metal can be characterised as a function of the velocity of the wave associated to vibration, giving the designer, for the first time, reliable values.
- the reliability of a test result or method can be confirmed on the basis of the value deducible from the graphs
- the dissipation mechanisms for the various types of wave, and consequently vibration, are the same.
- the thermo-elastic relaxation theory is not capable of explaining the relaxation phenomena
- it can be rationally assumed that damping has a viscous type origin
- it is possible to determine whether or not damping is a characteristic of the material, or whether it is linked to a structural aspect.

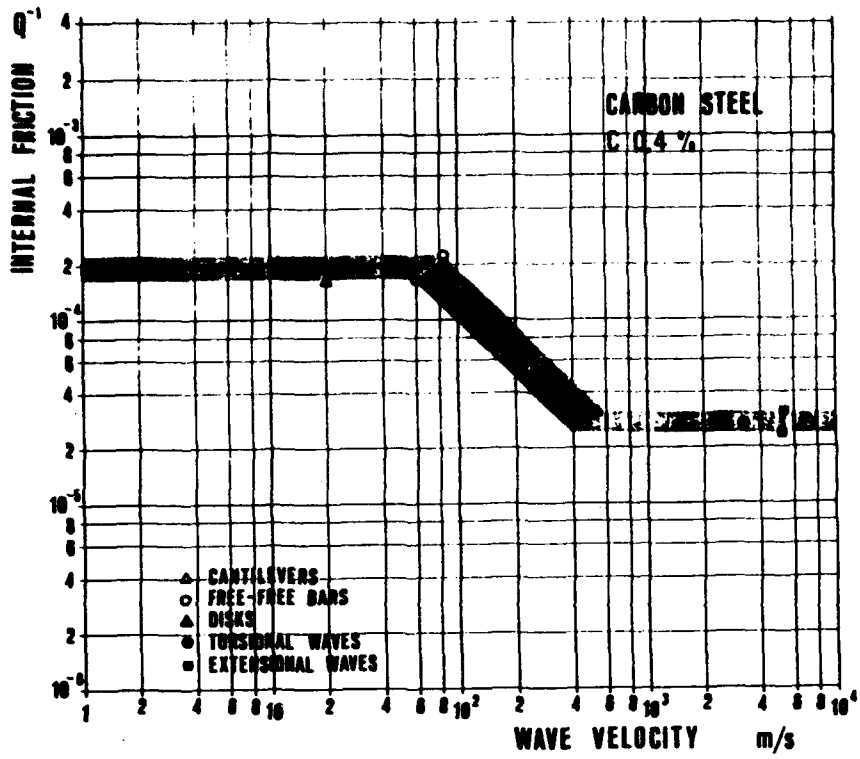
### BIBLIOGRAPHY

- (1) FROMMER L. MURRAY A., J. Instr. Met. 70,1
- (2) 2° Meeting on General Relativity, Trieste 1979
- (3) BERRY B.S., J. Appl. Phys. 26,884  
J. Appl. Phys. 26,1221
- (4) KE T.S., Phys.Rev. 71,8,533

- (5) KOIWA M., J. Phys. E: Sci. Instr. vol.13,27, 1980
- (6) BORDONI P.G., Il Nuovo Cimento, vol.IV, n3-4, 177
- (7) ZENER C., Phys. Rev. 52,230
- (8) ZENER C., Phys. Rev. 52,90
- (9) ZENER C., Phys. Rev. 53,100
- (10) CAPECCHI A., J.de Phys.,C8-305, 48, 1987
- (11) CAPECCHI A., Atti Convegno AIAS, L'Aquila 1988, 321
- (12) CAPECCHI A. CAPURRO M., Atti Conv.AIAS, Genova 1984
- (13) CAPECCHI A., Atti Conv.AIMETA, Roma 1989, 255
- (14) CAPECCHI A. CARRERA G., Atti Conv.AIAS, Amalfi 1990
- (15) GRANICK N. STERN J.E., NASA TN D-2893
- (16) KOLSKY H., Stress Waves in Solids, Clarendon Press
- (17) CAPECCHI A., Atti Conv. AIAS, Genova 1992, 303
- (18) ENTWISTLE K.M., The Damping Capacity of Metals, in "The Physical Examination of Metals", Arnold Pubbl., London
- (19) ZENER C. CLARK H. SMITH C.S., Trans.AIME,CXLVII,1942,90
- (20) HAMSTOCK R.F. MURRAY A., J.Instr.Met.,72,97







# **SOME FREQUENCY AND DAMPING MEASUREMENTS OF LAMINATED BERYLLIUM BEAMS**

**John Andriulli and Dr Lynn Rogers  
Oak Ridge National Lab**

**ABSTRACT:** A quantum leap in vibration performance of beryllium structure has been experimentally investigated. Laminations, segmentation, and sandwich syntactic foam core have been demonstrated to have both high specific flexural structural stiffness and high damping for reduced vibratory response. Acquisition cost, weight, machinability and environmental benefits are also expected. Applications to structure of optical and inertial navigation equipment would lead to reductions in jitter levels and other vibratory response measures.

**Introduction:** Figure 1 conceptually shows the three types of beams which were fabricated and tested. Each beam was nominally 0.5 x 10. inches with total thickness dependent on the number of layers and their individual thicknesses. The bottom beam illustrates continuous layers of metal bonded together with a structural adhesive. The top beam shows a syntactic foam core with continuous laminated face sheets. The middle beam indicates a syntactic foam core with the face sheets composed of layers which are segmented. A set of three beams was fabricated using aluminum and another set using beryllium.

**Fabrication:** The aluminum and the beryllium were nominally 5 mil foil. The surface of the aluminum was wiped with a solvent for surface preparation. The surface preparation of the beryllium was: i) clean with trichloroethane, ii) 10 % sulfuric acid and deionized water dip, iii) rinse and gently agitate in deionized water, iv) wipe dry, v) dip in 2% sulfuric/2% nitric/1-2% hydroflouric acid and deionized water, vi) rinse/agitate in deionized water and vii) wipe dry. Some beams were fabricated with a precured foam core and others with uncured. During cure, the foam would become liquid and require a dam to contain. The exact temperature, pressure and vacuum of cure were not controlled or recorded. The thicknesses of individual lamina were not determined. The complex modulus of the structural adhesive and of the foam was not determined. The adhesive was selected for its damping properties as well as strength and stiffness characteristics. The storage, processing and cure cycle of the adhesive were not in exact compliance with the manufacturer's recommendations.

**Testing:** The specimens were clamped in a vise and tested as 8. inch long cantilever beams. Excitation was by an instrumented hammer impacting

3.25 inches from the root. Response was measured by a 1.9 gram accelerometer mounted 1.75 inches from the tip. No undamped beam was tested for the purpose of establishing the threshold of spurious damping. Corrections for the mass of the accelerometer and its lead wire were not made.

**Results:** Figure 2 shows the frequency response functions obtained from the six beams. Averages from five strikes were used. Coherence was examined and was above 0.95 at modal frequencies. The horizontal scale is linear in frequency from 0 to 1600 hz. The vertical scale is 80dB. It is obvious that all modes are highly damped. Testing was performed at room temperature only.

Figure 3 presents the modal loss factors (reciprocal of Q) and frequencies for the first three modes of each beam. Modal damping was calculated by the half power point bandwidth method and then corrected for the exponential window applied to the response acceleration to obtain the values reported here. It may be seen that Q's (dynamic magnification factor) of ten and lower are common, with values as low as three achievable.

**Discussion:** Experimental data has shown the practicality of laminated beryllium for applications subjected to vibratory disturbances. The laminated metal, with or without a syntactic foam core, has a higher specific flexural section stiffness due to the lower density of the adhesive and of the foam. Also, heroic levels of modal damping have been demonstrated, probably much higher than would be used in applications. In many applications, the RMS response is the quantity of concern; in this case the RMS to give acceptable performance at minimum weight would probably be the proper merit function. It is well known that methods exist such that modal frequencies and damping are design parameters. Attendant benefits in performance, acquisition cost, and weight are practical. Attractive potential applications are structures of optical and navigational equipment, such as turrets, yokes, etc.

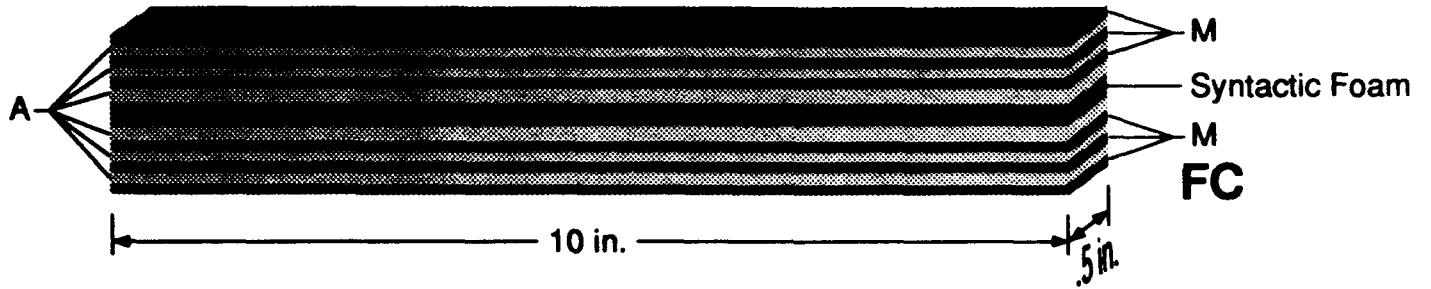
This concept provides a *quantum leap in capability*; as such, it is mandatory that the most basic design criteria be used. Intermediate or derived criteria such as a specified minimum natural frequency may severely limit the improvements achievable.

Newer beryllium processing based on ingot metallurgy is said to be lower in cost than that based on powder. Moreover, aluminum-beryllium alloys, whose specific extensional modulus is approximated by the rule of mixtures, are said to have cost, machinability, and environmental benefits.

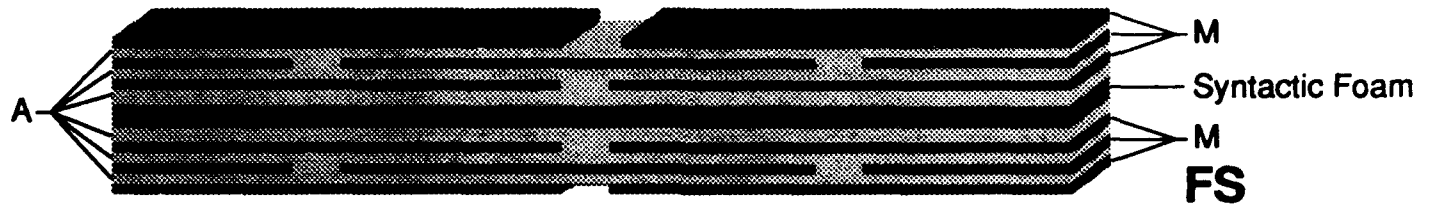
**Almost any kind of structure can be economically built up of small, segmented sections. Flat sheets and plates can obviously be laid up with multiple layers of a checkerboard or honeycomb pattern or other with the seams staggered or offset. Single and double curvature shells can also be laid up, possibly with some forming required. Substructure can also be laminated, tapered and bonded. Tubular and truss elements can also be laminated. Joints can be bonded or mechanically fastened.**

**ACKNOWLEDGEMENT:** Support is gratefully acknowledged for this project by the Advanced Metallic Structures office at Wright-Patterson Air Force Base, by Dexter Aerospace Materials Division in Pittsburg CA, and by Manufacturing Sciences Corporation in Oak Ridge TN.

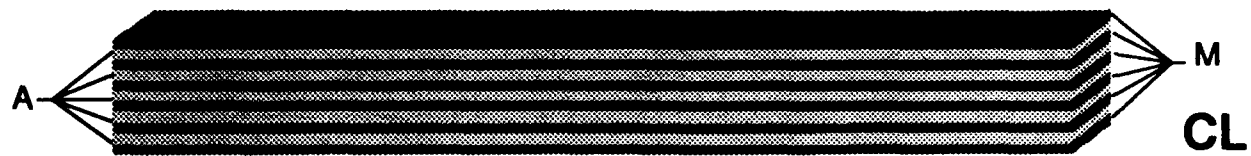
### Continuous Face Sheets



### Segmented Face Sheets



### Laminated Face Sheets



A = Adhesive  
C = Continuous  
F = Foam

L = Laminated  
M = Metal  
S = Segmented

Fig. 1. Passively damped laminated syntactical structures.

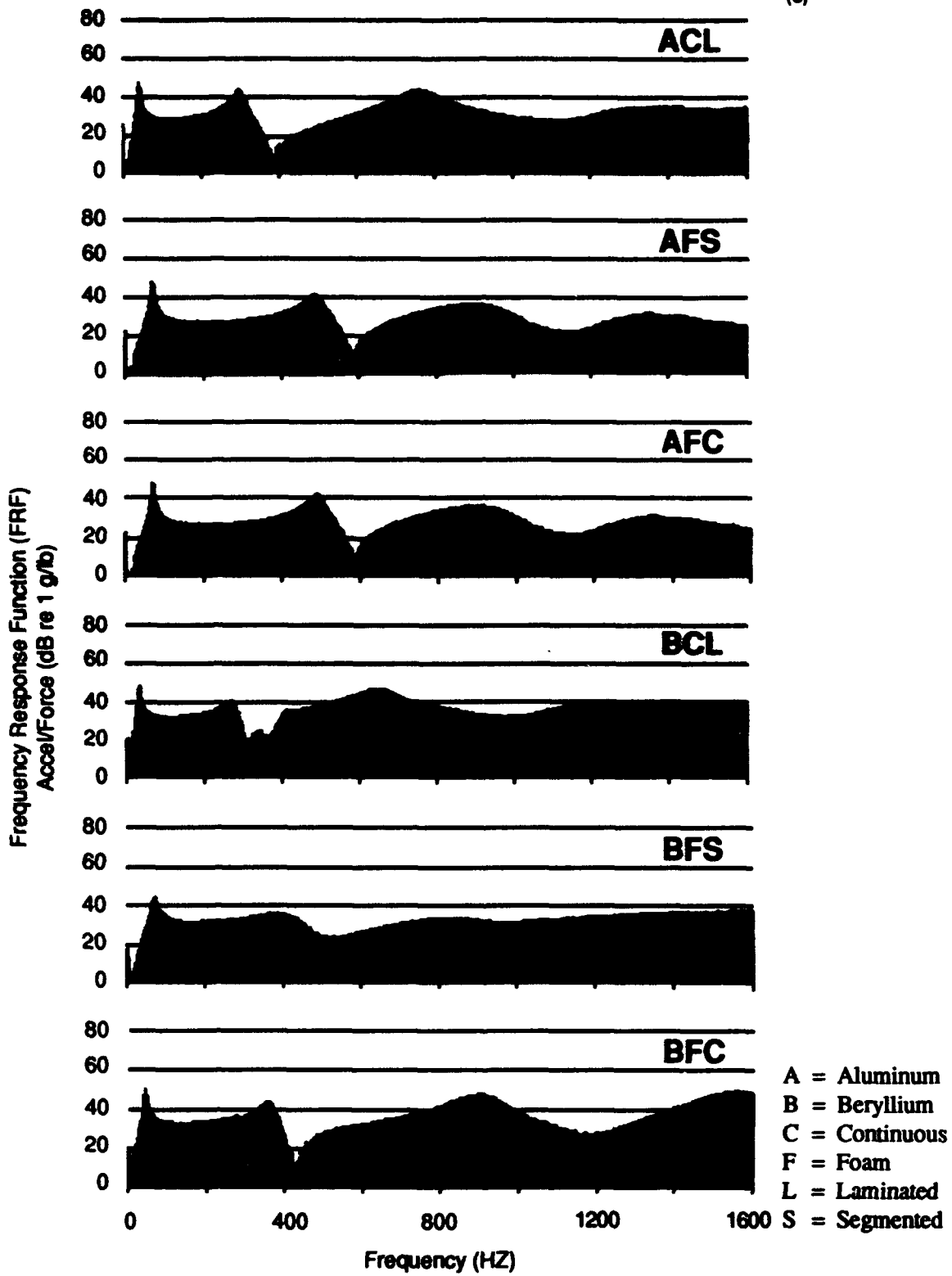


Fig. 2. Frequency response function for aluminum and beryllium - syntactic foam core laminates, cantilever beam specimens.

# FREQUENCY AND DAMPING MEASUREMENTS OF LAMINATED BEAMS

	<u>MODE 1</u>		<u>MODE 2</u>		<u>MODE 3</u>				
	<u>FREQ</u>	<u>DAMP</u>	<u>FREQ</u>	<u>DAMP</u>	<u>FREQ</u>	<u>DAMP</u>			
ACL	41.9	0.0423	23.6	298.	0.0733	13.6	758.	0.117	8.55
AFS	68.1	0.0785	12.7	479.	0.104	9.62	1256.	0.123	8.13
AFC	70.3	0.0391	25.6	489.	0.079	12.7	879.	0.234	4.27
BCL	32.5	0.0589	17.0	264.	0.163	6.13	642.	0.164	6.10
BFS	70.3	0.152	6.58	382.	0.390	2.56	814.	0.347	2.88
BFC	40.9	0.070	14.3	353.	0.0967	10.3	904.	0.109	9.17

A = ALUMINUM  
 B = BERYLLIUM  
 C = CONTINUOUS

F = FOAM  
 L = LAMINATED  
 S = SEGMENTED

Fig 3 Modal Frequencies and Damping

# **ACCURATE CHARACTERIZATION OF PASSIVE DAMPING MATERIALS WITH DATABASE STORAGE AND RETRIEVAL ON DIFFERENT COMPUTER PLATFORMS**

by

Bryce Fowler  
CSA Engineering, Inc.  
2850 West Bayshore Rd.  
Palo Alto CA 94303-3843  
415-494-7351  
FAX: 415-494-8749

and

Dr. Lynn Rogers  
Oak Ridge National Laboratory  
3945 North Lake Shore Drive  
Jamestown OH 45335-1119  
513-675-2258

## **Abstract**

An approach to successfully characterize a wide range of viscoelastic material data is discussed. Computer programs that implement the characterization process and allow the database storage and retrieval of materials based on dynamic properties are also discussed.

## **Introduction**

There is a growing number of very successful, high payoff applications of viscoelastic damping to vibration. A particular opportunity exists for more accurate design and analysis of modal frequencies and damping, especially for precision structure. A crucial factor in the advancement and application of damping technology is accurate and efficient smoothing, interpolation, modeling, presentation, storage, retrieval and dissemination of complex modulus design data for viscoelastic damping materials (VEM). Computerized modeling is essential for automated design. If needed, modeling facilitates interconversion between the various dynamic mechanical properties (DMP) such as compliance, creep, and relaxation, and other characteristics such as retardation spectra, relaxation spectra and relative molecular weight distributions.

(VEM). Computerized modeling is essential for automated design. If needed, modeling facilitates interconversion between the various dynamic mechanical properties (DMP) such as compliance, creep, and relaxation, and other characteristics such as retardation spectra, relaxation spectra and relative molecular weight distributions. Typically, a set of DMP data for damping materials is generated for screening purposes or for engineering applications and, therefore, justifiably does not cover temperature and frequency ranges in a scientific manner. It is challenging to analyze a set of data and interpret it in such a way to be useful to the designer while providing assurances against its misuse.

## Complex Modulus

The approach described in the present document exploits the property of the frequency response functions of linear systems that, once any part of the complex valued function (i.e., magnitude, phase, real, or imaginary) is specified, any other part is uniquely determined; this is called the "Kramers-Kronig" (KK) relationship [1].

The model or equation used as a basis for fitting complex modulus data is a ratio of factored polynomials of fractional order

$$G(j\omega_R) = G_e \prod_{\ell=1}^N [1 + (j\omega_R/z_\ell)^\beta] / [1 + (j\omega_R/p_\ell)^\beta] \quad (1)$$

$$z_\ell < p_\ell$$

$$0 < \beta \leq 1$$

It has been found convenient to rewrite this equation using different notation

$$G(j\omega_R) = G_e \prod_{\ell=1}^N [1 + a_\ell (j\omega_R/r_\ell)^\beta] / [1 + (1/a_\ell) (j\omega_R/r_\ell)^\beta] \quad (2)$$

where

$$\prod_{\ell=1}^N a_\ell^2 = G_g/G_e; a_\ell > 1 \quad (3)$$

$$z_\ell = r_\ell a_\ell^{-1/\beta}$$

$$p_\ell = r_\ell a_\ell^{1/\beta}$$

If each ratio pair in E2 is envisioned as a stair step of asymptotes, the  $a$ 's determine the height of the riser, and the  $r$ 's "slide" that step (and that step alone) right and left.

This equation inherently satisfies the KK relation, which is essential to the present approach. The equation is parametric and therefore easily represented on computers,

especially with modern computational power. The basic theory for perfectly accurate data for perfectly thermorheologically simple (TRS) materials is straightforward. The difficulty lies in choosing values for parameters in the presence of statistical variation in actual data and numerical sensitivities such that the complex modulus is accurately represented. Interactive computer graphics have greatly improved the efficiency and accuracy of the process of choosing, adjusting, and converging on proper values. The approach is an iterative one, and presumes an estimate of the temperature shift function. Using this estimate, the magnitude of the complex modulus is fit by appropriately selecting values for parameters in E1. Any lack of fit of the loss factor curve to experimental data is used to adjust the slope of the temperature shift function.

A set of tabulated complex modulus data together with parameter values (provided they have been determined) defining the temperature shift function and the complex modulus model are displayed in a spreadsheet window.

One of the earliest steps is to examine the wicket plot (loss factor as a function of magnitude) of the set of data. Accurate data for a TRS VEM should plot as a curve of vanishing width; this is a necessary but not a sufficient condition. Individual points of the set of data can be edited interactively. Estimates of the maximum loss factor and the rubbery and the glassy asymptotes are made using the wicket plot. Data points having loss factor greater than 0.7 times the maximum loss factor are taken to define the transition region. Experience has shown that almost any approach is both satisfactory and robust in the transition.

The characterization software now calculates the slope of the TSF (STSF) in the center of the transition (which is typically very close to the final value) and displays a reduced frequency plot. The STFS at the maximum and minimum experimental temperatures are then interactively adjusted based on appearance and judgment. The resulting TSF is an initial estimate. The TSF is now represented by points of STSF as a function of temperature; these points are taken as knots and cubic splines used to represent the continuous STSF, and then the integral used to represent the TSF. The knots are chosen to result in equal increments of log TSF.

The experimental magnitude points are empirically fit (smoothing spline) as a function of reduced frequency. The magnitude from E2 is fit to a large number of discrete points determined from the spline. The  $r_i$ 's are evenly spaced logarithmically to give equal length steps. The  $a_i$ 's are chosen to progressively fit discrete values given by the empirical curve fit. Adjustments are made until the magnitude from E2 converges on the discrete points. Any lack of agreement between the loss factor curve from E2 and the experimental loss factor is used to adjust values of the STSF knots.

Equal horizontal spacing of the steps is a recent innovation. In the past, equal vertical height of the steps was used. While this was satisfactory in fitting the magnitude, there were major difficulties in fitting the loss factor satisfactorily. In addition to the step spacing, a change has been made in the interactive approach to interactively determining the values for  $Ge$  and  $Gg$ . The revised approach is an empirical,

graceful and self-consistent extrapolation. The necessity of these changes is due to the statistical variation in the data, especially the slope of the magnitude, and the numerical sensitivity of the process in the rubbery and glassy regions. The characterization procedure is now much more robust and is considered mature.

## Implementation

A three-tiered implementation of a viscoelastic material database has been implemented. Using low-level calls, searches for characterized VEM's may be conducted based on property constraints (e.g., modulus and loss factor at specified temperature and frequency) and/or other criteria (e.g., available thicknesses, type, etc.)

1. An interactive graphical program that runs on a Macintosh personal computer is used to perform all characterization.
2. A VEM database engine which may be compiled and run on any computer that supports ANSI FORTRAN 77 is utilized. The engine consists of FORTRAN callable subroutines that search a VEM database created from VEM characterization data files. A textual command-line interface with a well-defined syntax is supplied for both interactive and batch execution. Reports are in the form of tables.
3. Stand-alone graphical programs have been written for MS-DOS, Macintosh, and X Window UNIX machines to provide X-Y plots using data and commands generated by the database engine.

Displays from the characterization program were shown in the slides presented at the conference. They are repeated at the end of this paper.

## References

- [1] L. Rogers, "An Accurate Temperature Shift Function and a New Approach to Modeling Complex Modulus," Presented at 60th Shock and Vibration Symposium, Virginia Beach VA, Nov 1989.
- [2] L. Rogers, "Graphical Presentation of Damping Material Complex Modulus," Standard, ISO/TC108/WG13, Aug 1987.
- [3] B. L. Fowler, "VEM Characterization Program," Proc. of DAMPING '91, San Diego CA, Feb 1991, USAF-WL-TR-91-3078, Paper DBA, Aug 1991.
- [4] B. L. Fowler, "VEM Database Program," Proc. of DAMPING '91, San Diego CA, Feb 1991, USAF-WL-TR-91-3078, Paper GDC, Aug 1991.

**Accurate Characterization of Passive Damping  
Materials with Database Storage and Retrieval on  
Different Computer Platforms**

**Bryce L. Fowler**  
CSA Engineering, Inc.  
Palo Alto, CA

**Dr. Lynn C. Rogers**  
Oak Ridge National Lab  
Oak Ridge, TN

**Presented at Damping '93  
San Francisco, CA  
February 24-26, 1993**

**Motivation**

- **Accurate design of precision structures**
- **Computer modelling**
  - **Design/Automation/Efficiency**
- **Smoothing and interpolation of experimental data**
- **Accuracy and efficiency in finding values for complex modulus**
- **Facilitate interconversion of dynamic mechanical properties**

## Introduction

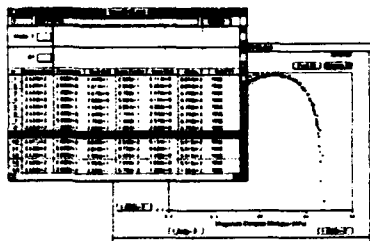
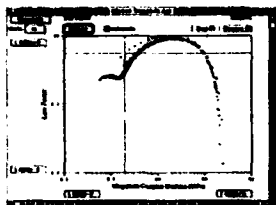
- Equations used in characterization are parametric
  - Easily represented on computers
- Difficulty lies in choosing parameters so equations accurately represent VEM
- Interactive computer graphics have greatly improved the process of choosing and adjusting correct parameter values

## VEMINT MAC

- Data and parameters displayed in spreadsheet window

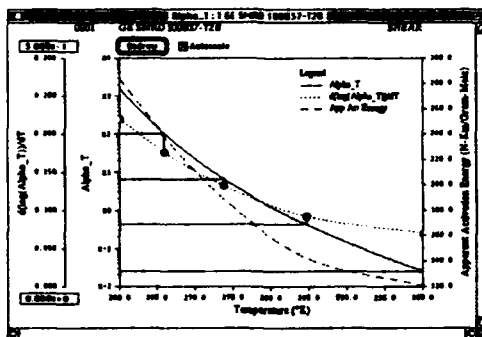
CE SHRD 100037-120							
CE SHRD 100037-120						SHEAR	
		Modulus	Phase	Alpha	Yield Pt		
		6.08e-6	5.24e-5	5.78e-3			
		2.49e-7	-8.26e-5	5.35e-3			
		1.66e-7	-8.05e-5	3.99e-3			
		8.29e-5	3.55e-4	1.53e-3			
		8.59e-2	5.24e-2	9.89e-2			
		1.66e-1	7.24e-1	1.11e+0			
SI	Temp	Tabulated values		Mod	Phase	Alpha	Yield Pt
1	2.99e+2	1.25e+0	2.08e-1	3.75e-1	7.80e-2	2.64e-2	FALSE
2	2.99e+2	2.50e+0	2.34e-1	4.53e-1	1.06e-1	2.64e-2	FALSE
3	2.99e+2	3.75e+0	2.59e-1	5.16e-1	1.33e-1	2.64e-2	FALSE
4	2.99e+2	5.00e+0	2.79e-1	5.47e-1	1.52e-1	2.64e-2	FALSE
5	2.99e+2	6.25e+0	2.97e-1	5.94e-1	1.76e-1	2.64e-2	FALSE
6	2.99e+2	7.50e+0	3.12e-1	6.09e-1	1.90e-1	3.05e-2	TRUE
7	2.99e+2	8.75e+0	3.28e-1	6.41e-1	2.10e-1	3.05e-2	TRUE
8	2.99e+2	1.00e+1	3.40e-1	6.56e-1	2.23e-1	3.05e-2	TRUE
9	2.99e+2	1.12e+1	3.54e-1	6.72e-1	2.37e-1	3.05e-2	TRUE
10	2.99e+2	1.25e+1	3.64e-1	6.72e-1	2.46e-1	3.05e-2	TRUE
11	2.99e+2	1.37e+1	3.79e-1	6.88e-1	2.60e-1	3.05e-2	TRUE
12	2.99e+2	1.50e+1	3.88e-1	7.03e-1	2.72e-1	3.05e-2	TRUE
13	2.99e+2	1.62e+1	3.99e-1	7.19e-1	2.86e-1	3.05e-2	TRUE

## Interactive Displays



## Temperature Shift Function (TSF)

- Spline fit of slope of log (TSF) versus temperature
- Spline knots equally spaced on log (TSF) scale
- Enables Collocation method



## Complex Modulus

- Ratio of factored polynomials is given by

$$G(j\omega_R) = G_e \prod_{l=1}^N \frac{1 + \left(\frac{j\omega_R}{z_l}\right)^\beta}{1 + \left(\frac{j\omega_R}{p_l}\right)^\beta}$$



$$0.5 \leq \beta \leq 1.0$$

$$= G_e \prod_{l=1}^N \frac{1 + a_l \left(\frac{j\omega_R}{r_l}\right)^\beta}{1 + \frac{1}{a_l} \left(\frac{j\omega_R}{r_l}\right)^\beta}$$



## Initialization

- Logarithmically evenly-spaced values between  $f_{Rmin}$  and  $f_{Rmax}$  calculated
- Smoothing spline fit to magnitude  $G^*$  versus reduced frequency
- $r_i$ 's initialized about evenly-spaced reduced frequency points with step sizes calculated to extend curve from rubbery to glassy asymptotes

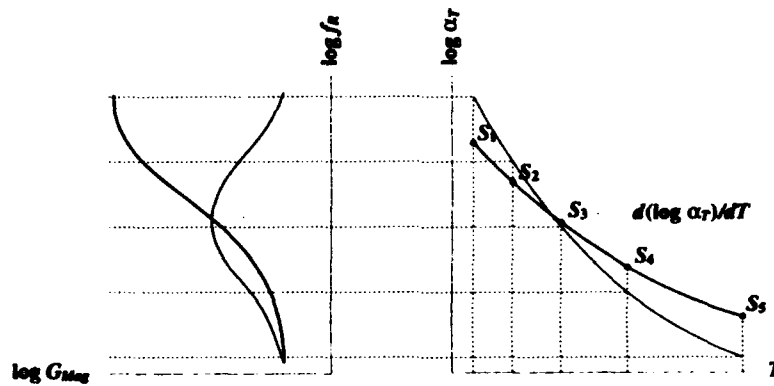
## Collocation

- Smoothing spline is fit through  $\eta$  versus reduced frequency
- TSF is iteratively adjusted using lack of fit of  $\eta_{curve}$

$$S_{new_i} = S_{old_i} \frac{\arctan(\eta_{curve_i})}{\arctan(\eta_{exp_i})}$$

- After all TSF knots are adjusted, smoothing splines are refit, and  $r_i$  and TSF adjustments are repeated

## Iterating TSF



## Observations

- Anything works in center of transition
- At ends of Wicket and Reduced Frequency plots, statistical variation in modulus and its slope, and numerical sensitivities provide challenges to determining the temperature shift function and to fitting  $G^*$  data
- Developed an empirical, graceful, self-consistent extrapolation (Still requires some user interaction)

## Database Fields

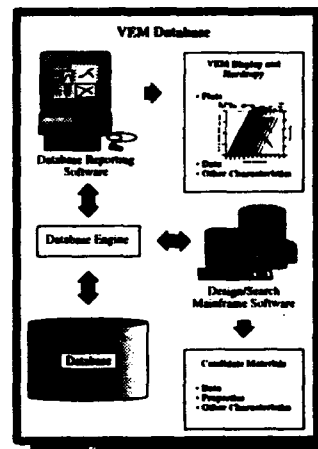
### • Measured Properties

(All are temperature and/or frequency dependent)

- Shear modulus
- Loss factor
- Outgassing characteristics
- \*Creep characteristics
- \*Non-linear effects
- \*Pre-load effects
- \*Strain effects

### • Other Properties/Information

- Sources
- Availability
- Type (adhesive, rubber, etc.)
- Available forms (liquid, sheets, etc.)
  - Thicknesses
- Density
- Application techniques
- Test conditions and apparatus
- Environmental resistance
- Cost
- Quality of data



## VEM Database Mainframe Module

- Database file architecture – FORTRAN 77 sequential access
  - (EXP) file holds experimental data and characterization parameters
  - (INF) file hold all other material information
- Command line interface with batch capability
- Data import and export in ASCII
- Linkable to other software projects

## Example

```
VEM Database v1.00
VEM_DB* OPEN VEMFILE
VEM_DB-Warning-VEMFILE Rfp not found
Create new database file: Y
VEM_DB Info 'VEMFILE' created
VEM_DB* REPORT C1002
VEM_DB-Info-File C1002.Dat added to VEMFILE
VEM_DB* REPORT 10011
VEM_DB-Info-File 10011.DAT added to VEMFILE
VEM_DB* GET POINT 1
Enter temperature 295
Enter frequency 100
Enter lower modulus 2
Enter upper modulus 100
Enter lower loss factor .5
Enter upper loss factor 2
VEM_DB* GET POINT 2
Enter temperature 295
Enter frequency 1000
Enter lower modulus 10
Enter upper modulus 200
Enter lower loss factor .5
Enter upper loss factor 2
VEM_DB* BATCH POINTS 1, 2
VEM_DB-Info: 1 material found
VEM_DB* SHOW REPORT
Report#
1
VEM_DB* SHOW REPORT 1
Materials in Report 1
END C1002
VEM_DB* REPORT REPORT 1 VEMFILE
VEM_DB* GET
Quitting VEM_DB
```

## **Status**

- **Software mature (version 1.3+)**
- **24 VEMs fit (30+ data sets)**
- **User's manual written**
- **No sponsorship for further development**
- **Have ideas for improvements**
- **Platforms**
  - **Characterization**
    - **Macintosh**
  - **Database (text)**
    - **FORTRAN**
  - **Database plots**
    - **Macintosh**
    - **PC**
    - **Unix w/ X Window**

## **How do I get a copy?**

- **Software, manuals, VEM data**
- **USAF will request approval for unlimited distribution**
- **Any individual approved by the USAF may procure a copy**
- **There probably will be a charge for the cost of distribution**

**RESULTS OF RECENT ANALYSIS OF THE FREQUENCY-  
TEMPERATURE BEHAVIOR OF POLYISOBUTYLENE**

by

David I.G. Jones<sup>\*</sup>  
Wright Laboratory

**ABSTRACT**

This paper reports the results of analyses conducted by several organizations and researchers to re-evaluate complex modulus data for Polyisobutylene, as provided by Ferry, Grandine and Fitzgerald in 1956. The original data was analyzed with a Williams-Landel-Ferry (WLF) type of shift function relationship. Recently renewed interest in frequency-temperature analysis and in shift factor issues has provided an incentive for re-examination of the matter. The original Ferry, Landel, Fitzgerald data was provided to a number of researchers, who undertook to carry out their own temperature-frequency analysis, using available software, and provide the results to the author for comparative evaluation. The shift factors, when plotted on a logarithmic scale versus inverse absolute temperature, show that the WLF and Arrhenius types of shift function models are practically indistinguishable and that, in particular, scatter in the data at the extreme upper and lower temperatures precludes a clear choice between these models. The good agreement between shift factors determined by each investigator indicates that, when low scatter data is available, all data reduction algorithms tend toward the same solution. Major differences arise, presumably, only when scatter is high.

---

\* Senior Research Engineer, Flight Dynamics Directorate (WL/FIBG)  
Wright-Patterson AFB, OH 45433. Tel: (513) 255-5229 X 414.

## INTRODUCTION

The process of obtaining optimized reduced-frequency "master curves" for complex modulus properties of polymeric damping materials is currently carried out in a number of ways. These range from manual estimation of shift factors, through the direct application of an Arrhenius shift factor relationship and various Williams-Landel-Ferry (WLF) type relationships, to highly computerized statistical processes which permit the data to direct its own shift factor relationships. The differences between master curves and shift factor-temperature relationships, as obtained by each approach, can be quite considerable, particularly if the data has some scatter. On the other hand, it is difficult to believe that differences in the various estimates can be great when the scatter is low. To determine whether or not this was the case, a two-part program was initiated, and several investigators of complex modulus testing and analysis were asked to participate. The first task was to find a set of complex modulus data which covered a reasonably wide range of frequencies and temperatures and which was accurate and had little scatter. The Ferry, Grandine, Fitzgerald data for Polyisobutylene [1] was selected. Each laboratory analyzed the data, by their usual methods, and returned the data to the author. The second task, which was to evaluate the effects of varying degrees of scatter, has not yet been accomplished.

## PROGRAM ORGANIZATION

The program emerged as a result of meetings which took place at Wright-Patterson Air Force Base in late 1989 and early 1990, to review the state of the art in measurement and temperature-frequency analysis of polymer complex modulus data. It was agreed that different software algorithms seemed sometimes to lead to different results, and it was surmised that such differences were strongly related to the degree of scatter in the data. In order to verify the accuracy of this hypothesis, it was decided in the first instance to evaluate the complex modulus properties of Polyisobutylene, as provided by Ferry, Grandine and Fitzgerald [1], this being a case where the scatter was quite modest. Each investigator agreed to apply their frequency-temperature algorithms to this data set, and the author agreed to compare the results. The participants in this program are listed in Table 1. The complex modulus data for Polyisobutylene, used in this analysis, are summarized in Table 2.

## WICKET PLOT ANALYSIS

In order to verify that the complex modulus data was of high quality, a plot of log loss factor versus log modulus was prepared, as in Figure 1. This plot is currently known as a Wicket Plot. It is seen that scatter is relatively low, apart from a few points which are mainly at high frequencies, and that the points in general tend to follow a single, unique curve, with two apparent relaxation peaks. The range of modulus values is quite wide, being over three decades. Another format of the wicket plot is shown in Figure 2, in the form of a plot of loss factor (linear scale) versus log modulus, as provided by the Naval Surface Weapons Laboratory. This form of the plot is more sensitive to errors

in the loss factor, the erroneous points clearly standing out. A third form of the wicket plot is a version of the Cole-Cole plot, consisting of a plot of loss modulus (linear scale) versus storage modulus (linear scale). Figure 2 illustrates such a plot for the current data. It is seen that the linear modulus scale compresses most of the data points into the lowest 5 percent of the horizontal scale, thereby completely obscuring the lowest of the two peaks seen clearly in Figures 1 and 2. Use of the Cole-Cole form of the wicket plot both unduly emphasizes data in the high modulus range and unduly neglects data in the low modulus range. This form of the wicket plot is not recommended for most evaluations of complex modulus data.

TABLE 1. PARTICIPANTS IN THE PROGRAM

Anatrol Corporation, 10895 Indeco Drive, Cincinnati, OH 45245 (Mr. A.D. Nashif and Mr. T. Lewis)

CSA Engineering Inc., 2850 W. Bayshore Road, Palo Alto, CA 94303-3843 (Dr. C.D. Johnson and Mr. B. Fowler)

Naval Surface Warfare Center, Carderock Division, Code 1945.1, Bethesda, MD 20084-5000 (Mr. R.J. Deigan and Dr. J.J. Dlubac)

University of Manchester, Dynamics Research Group, Department of Engineering, Simon Building, Oxford Road, Manchester M13 9PL, England (Prof. G.R. Tomlinson and Dr. S.O. Ojadiji)

Vector Research Corporation, 2101 East Jefferson Street, Suite 700, Rockville, MD 20852 (Dr. Wayne T. Reader)

Wright Laboratory, Flight Dynamics Directorate (WL/FIBGD), Wright-Patterson Air Force Base, OH 45433 (Dr. D.I.G. Jones)

#### TEMPERATURE-FREQUENCY ANALYSIS

Temperature-frequency analysis of the data was performed by each participant by means of their usual software and methodology.

Figures 4 and 5 show the master curves resulting from manually estimated shift factors (Wright Laboratory), using the full data set and the data set with most widely scattered points culled, respectively. The shift factors do not differ greatly in each case.

Figure 6 shows the master curves prepared by Anatrol Corporation, using an Arrhenius shift factor relationship to reduce the data, of the form:

$$\log \omega(T) = T_A (1/T - 1/T_0) \quad (1)$$

with  $T_A = 7500^\circ\text{R}$  ( $4167^\circ\text{K}$ ) and  $T_0 = 50^\circ\text{F}$  ( $10^\circ\text{C}$ ). The "ratcheting" of the reduced data points at high modulus values are believed to result from possible small systematic errors in the modulus values, arising

because of high specimen stiffness. This often happens in direct stiffness tests, but proof is not here possible because the original tests were conducted in only one way.

Figure 7 shows the master curves provided by the University of Manchester. Figure 8 shows the plot of log shift factor versus temperature difference, based on a reference temperature  $T_0$  of 10°C. Both the master curves and the shift factor-temperature relationship are represented analytically by polynomials in the reduced frequency and temperature difference, respectively.

Figures 9 to 16 show the master curves provided by the Naval Surface Warfare Center, with shift factors estimated in several ways, as indicated, along with plots of the corresponding shift factors versus temperature.

Figure 17 shows the master curves provided by CSA Engineering, with shift factors estimated by an advanced statistical computer code [2]. Figure 18 shows the temperature "knots" used in the data reduction process.

Figures 19 and 20 show the master curves and corresponding shift factors provided by Vector Research Corporation. The loss factor scale in Figure 19 is linear.

Other data used in the comparative analysis was provided by Bagley [3] and Ferry, Grandine and Fitzgerald [1].

#### EVALUATION OF THE RESULTS

Each participant in the program used his software algorithms to analyze the PIB data in various ways, ranging from simple to complicated. One of the problems facing users of such analyzed data has been the perceived discrepancies between such evaluations. The purpose of this investigation was to determine the reason(s) for such discrepancies and the expected order of magnitude. The shift factors determined by each participant are summarized in Table 3, for each temperature at which data was available. It is seen that each participant, for various reasons, chose a different reference temperature  $T_0$ . These differences can be eliminated, for comparative purposes, by choosing a single reference temperature (25°C in this case) and subtracting the shift factor at 25°C from each value of log shift factor. This procedure does not alter the shape of the plot of log shift factor versus temperature, but merely shifts it vertically, and shifts the master curves horizontally along the reduced frequency scale without changing the shape of the master curves. The software, in some instances, may not allow the user to do this conveniently, but it is merely a programming matter which can be fixed if desired. Nevertheless, the resulting array of values of log shift factor is much easier to understand and compare, as Table 4 shows. The values of log shift factor versus temperature, all at the 25°C reference temperature, show the range of estimates for each participant. Table 4 also shows the average value at each temperature. The average values of log shift factor are plotted against inverse absolute temperature in Figure 21. Added are lines representing an Arrhenius

fit of the form given in equation (1) and with  $T_0 = 25^\circ\text{C}$  ( $297^\circ\text{K}$ ) and  $T_A = 4235^\circ\text{K}$ . Also plotted are the extreme upper and lower limits of estimated values of log shift factor. These form a band of uncertainty around the Arrhenius fit, with peak errors of about half a decade at the temperature extremes.

Figure 22 shows the result of an attempt to fit a WLF equation of the form:

$$\log a(T) = \frac{-C_1 (T-T_0)}{C_2 + T-T_0} \quad (2)$$

by plotting  $(T-T_0)/\log a(T)$  against  $T-T_0$ , to give a straight line of the form:

$$\frac{T - T_0}{\log a(T)} = - \frac{C_2}{C_1} - \frac{(T-T_0)}{C_1} \quad (3)$$

It is seen that the average value of log shift factor gives a reasonably good straight line fit, but the lines corresponding to the upper and lower limits of log shift factor show that the error bounds are quite wide, so it is by no means certain that a good fit of the data can be obtained using the WLF equation. Even so, a fit with  $C_1 = 7.93$  and  $C_2 = 184^\circ\text{K}$  does seem to fit the average data quite well.

Figure 23 possibly puts the matter in better perspective. The range of values of the  $1000/T$  scale is now from 0 to 7, even though no data exists below a value of about 2 or above a value of about 5. It would be quite difficult to obtain such data.

It is seen that the Arrhenius and WLF fits differ by no more than half a decade within the range of test temperatures, but deviate rapidly outside that range. Clearly, extrapolation outside the range of test temperatures could be dangerous, while the uncertainty within the range of test temperatures makes the choice between WLF and Arrhenius fits quite difficult. The Arrhenius fit has the clear and great advantage of simplicity, while the WLF fit is well accepted, widely understood (perhaps) and familiar. What is certain is that it would be very difficult to definitively settle the issue on the basis of the data currently available for Polyisobutylene, and recourse will have to be made to tests at very high and very low temperatures and for many more materials.

## CONCLUSIONS

It was a goal of this investigation to determine the range of variability of shift factor estimates obtained by various data reduction algorithms used by different organizations and individuals. This goal has been achieved, and it has been shown that for data having low scatter the master curves and shift factor estimates do not vary greatly. Another goal was to determine which type of shift factor versus temperature relationship, Arrhenius or WLF, best fitted the data. This goal was not fully accomplished, but it was shown that within the range of test temperatures the difference was not great. A further goal is to determine

the role of data scatter in creating differences between the master curves and shift factor estimates. This has not yet been accomplished, but is recommended for future research.

#### REFERENCES

1. J.D. Ferry, L.D. Grandine, Jr. and E.R. Fitzgerald, "The Relaxation Function of Polyisobutylene in the Transition from Rubber-Like to Glass-Like Behavior", J. Appl. Phys., 24(7), pp 911-916, July 1956.
2. R.L. Bagley, "The Thermorheologically Complex Material", Int. J. Engrg. Sci., 29(7), pp 797-806 (1991).
3. B.L. Fowler, "VEM Characterization Program", Proc. DAMPING '91 Conference, WL-TR-91-3078, Vol. I, pp DBA1-12, August 1991.



TABLE 3. VALUES OF LOG SHIFT FACTOR: VARIOUS REFERENCE TEMPERATURES

TEMP (°C)	CSA	ANATROL	MANCHESTER	NSWC	BAGLEY	VECTOR	WL/FULL	WL/CULLED	FITZGERALD
-44.6	+2.18	+3.99	+3.89	+3.80	-4.10	+2.61	+4.40	+4.30	+4.75
-40.4	+1.80	+3.62	+3.51	+3.35	-4.70	+2.10	+3.85	+3.85	+4.23
-34.7	+1.34	+3.13	+3.00	+2.90	-5.02	+1.59	+3.34	+3.30	+3.69
-29.8	+0.95	+2.73	+2.59	+2.40	-5.42	+1.12	+2.85	+2.85	+3.22
-25.0	+0.58	+2.36	+2.21	+2.00	-5.76	+0.74	+2.30	+2.48	+2.84
-19.9	+0.21	+1.97	+1.82	+1.65	-6.03	+0.34	+2.30	+2.11	+2.45
-14.8	-0.15	+1.60	+1.46	+1.30	-6.33	0	+2.00	+1.85	+2.08
- 9.9	-0.45	+1.26	+1.13	+1.05	-6.57	-0.29	+1.70	-	+1.78
- 5.0	-0.74	+0.93	+0.82	+0.80	-6.74	-0.54	+1.34	+1.30	+1.51
- 0.1	-1.00	+0.62	+0.54	+0.50	-7.01	-0.81	+1.18	+1.08	+1.22
+ 4.9	-1.26	+0.31	+0.26	+0.20	-7.22	-1.08	+0.90	+0.85	+0.98
+ 9.8	-1.50	0	+0.01	0	-7.40	-1.32	+0.70	+0.60	+0.72
+14.8	-1.73	-0.28	-0.23	-0.20	-7.61	-1.54	+0.40	+0.40	+0.51
+19.8	-1.95	-0.56	-0.45	-0.45	-7.85	-1.75	+0.15	+0.18	+0.27
+25.0	-2.16	-0.84	-0.67	-0.75	-8.11	-1.97	0	0	0
+30.2	-2.37	-1.11	-0.87	-1.00	-8.37	-2.23	-0.23	-0.23	-0.21
+34.9	-2.54	-1.35	-1.05	-1.10	-8.59	-2.38	-0.30	-0.51	-0.42
+40.0	-2.71	-1.60	-1.22	-1.20	-8.75	-2.53	-0.60	-0.70	-0.62
+50.0	-3.02	-2.07	-1.55	-1.55	-9.05	-2.85	-0.85	-1.00	-0.99
+59.8	-3.29	-2.50	-1.85	-1.80	-9.30	-3.04	-1.18	-1.30	-1.31
+80.0	-3.76	-3.31	-2.43	-2.20	-	-3.52	-1.78	-2.00	-1.90
+99.9	-4.13	-4.02	-3.01	-2.40	-	-3.71	-2.40	-	-2.29

TABLE 4. VALUES OF LOG SHIFT FACTOR: REFERENCE TEMPERATURES = 25°C

TEMP (°C)	CSA	ANATROL	MANCHESTER	NSWC	BAGLEY	VECTOR	WL/FULL	WL/CULLED	FITZGERALD	AVG
-44.6	+4.34	+4.83	+4.56	+4.55	+4.01	+4.58	+4.40	+4.30	+4.75	+4.48
-40.4	+3.96	+4.46	+4.18	+4.10	+3.41	+4.08	+3.85	+3.85	+4.23	+4.01
-34.7	+3.50	+3.97	+3.67	+3.65	+3.09	+3.56	+3.34	+3.30	+3.69	+3.53
-29.8	+3.11	+3.57	+3.26	+3.15	+2.69	+3.09	+2.85	+2.85	+3.22	+3.09
-25.0	+2.74	+3.20	+2.88	+2.75	+2.35	+2.71	+2.30	+2.48	+2.84	+2.69
-19.9	+2.37	+2.81	+2.49	+2.40	+2.08	+2.31	+2.30	+2.11	+2.45	+2.37
-14.8	+2.02	+2.44	+2.13	+2.05	+1.78	+1.97	+2.00	+1.85	+2.08	+1.76
- 9.9	+1.71	+2.10	+1.80	+1.80	+1.54	+1.68	+1.70	-	+1.78	+1.76
- 5.0	+1.43	+1.77	+1.49	+1.55	+1.37	+1.43	+1.34	+1.30	+1.51	+1.47
- 0.1	+1.16	+1.48	+1.21	+1.25	+1.10	+1.16	+1.18	+1.08	+1.22	+1.20
+ 4.9	+0.90	+1.15	+0.93	+0.95	+0.89	+0.89	+0.90	+0.85	+0.98	+0.94
+ 9.8	+0.67	+0.84	+0.68	+0.75	+0.71	+0.65	+0.70	+0.60	+0.72	+0.70
+14.8	+0.44	+0.56	+0.44	+0.55	+0.50	+0.43	+0.40	+0.40	+0.51	+0.47
+19.8	+0.22	+0.28	+0.22	+0.30	+0.26	+0.22	+0.15	+0.18	+0.27	+0.23
+25.0	0	0	0	0	0	0	0	0	0	0
+30.2	-0.21	-0.27	-0.20	-0.25	-0.26	-0.26	-0.23	-0.23	-0.21	-0.24
+34.9	-0.38	-0.51	-0.38	-0.35	-0.48	-0.41	-0.30	-0.51	-0.42	-0.42
+40.0	-0.55	-0.76	-0.55	-0.45	-0.64	-0.56	-0.60	-0.70	-0.62	-0.60
+50.0	-0.86	-1.23	-0.88	-0.80	-0.94	-0.88	-0.85	-1.00	-0.99	-0.94
+59.8	-1.13	-1.66	-1.18	-1.05	-1.19	-1.07	-1.18	-1.30	-1.31	-1.23
+80.0	-1.60	-2.47	-1.76	-1.45	-	-1.55	-1.78	-2.00	-1.90	-1.81
+99.9	-1.97	-3.18	-2.34	-1.65	-	-1.74	-2.40	-	-2.29	-2.22

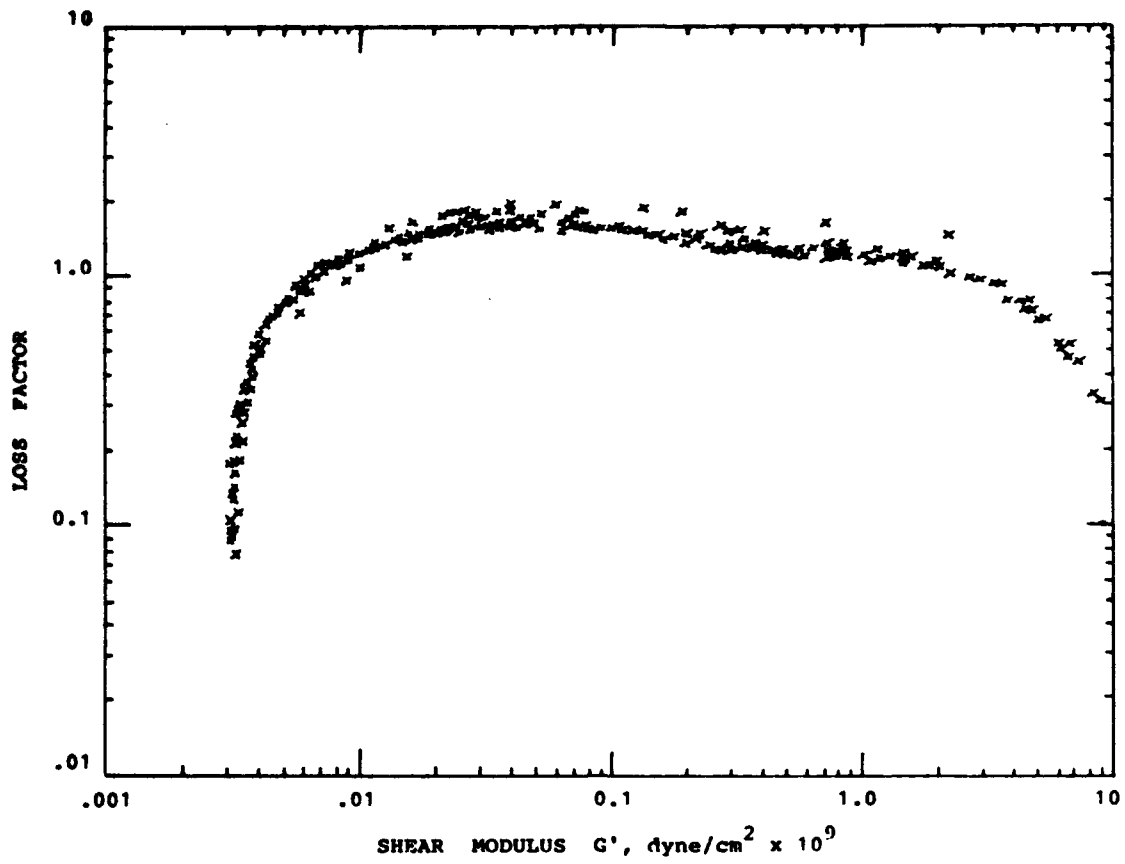


Figure 1. Wicket Plot for Polyisobutylene

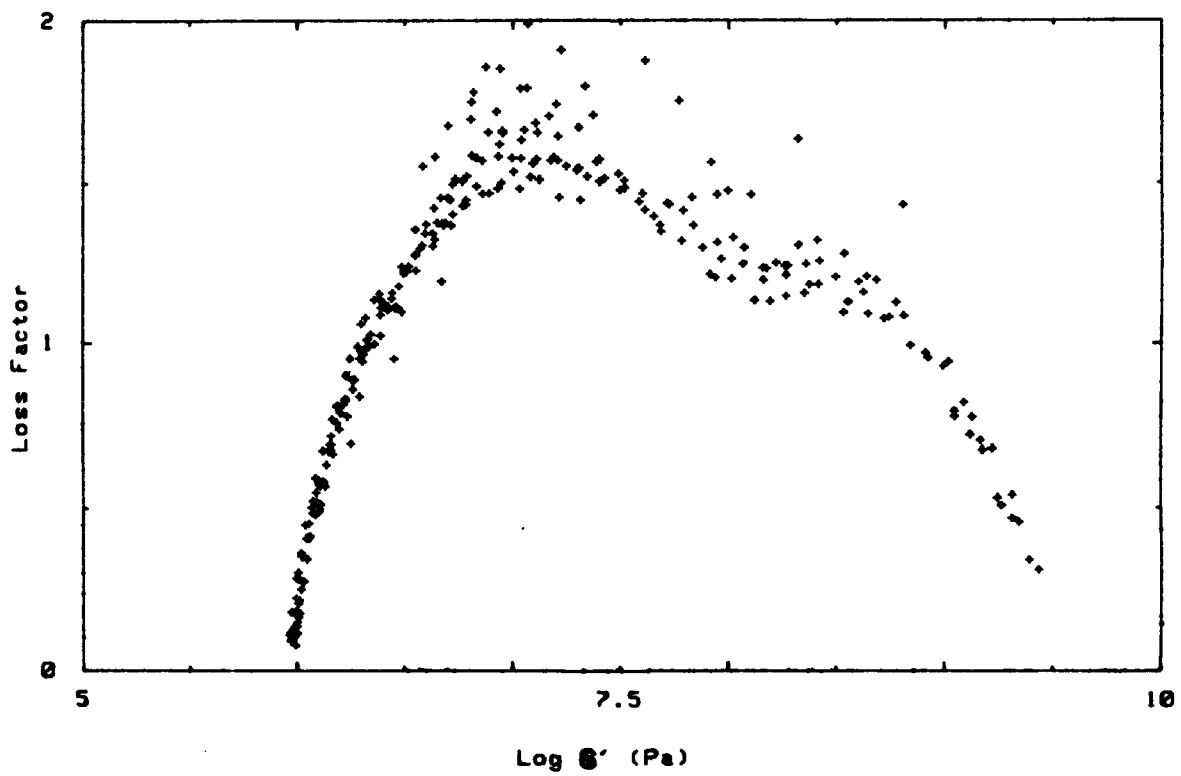


Figure 2. Wicket Plot with Linear Loss Factor Scale

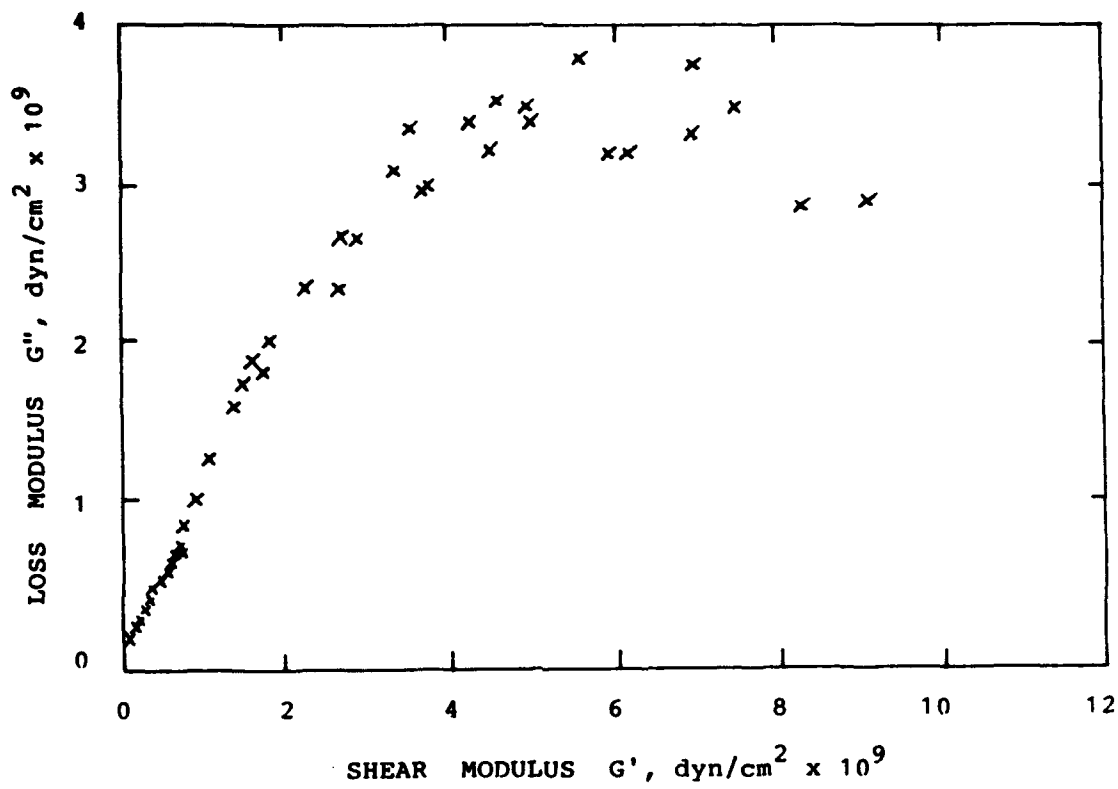


Figure 3. Cole-Cole Type Plot

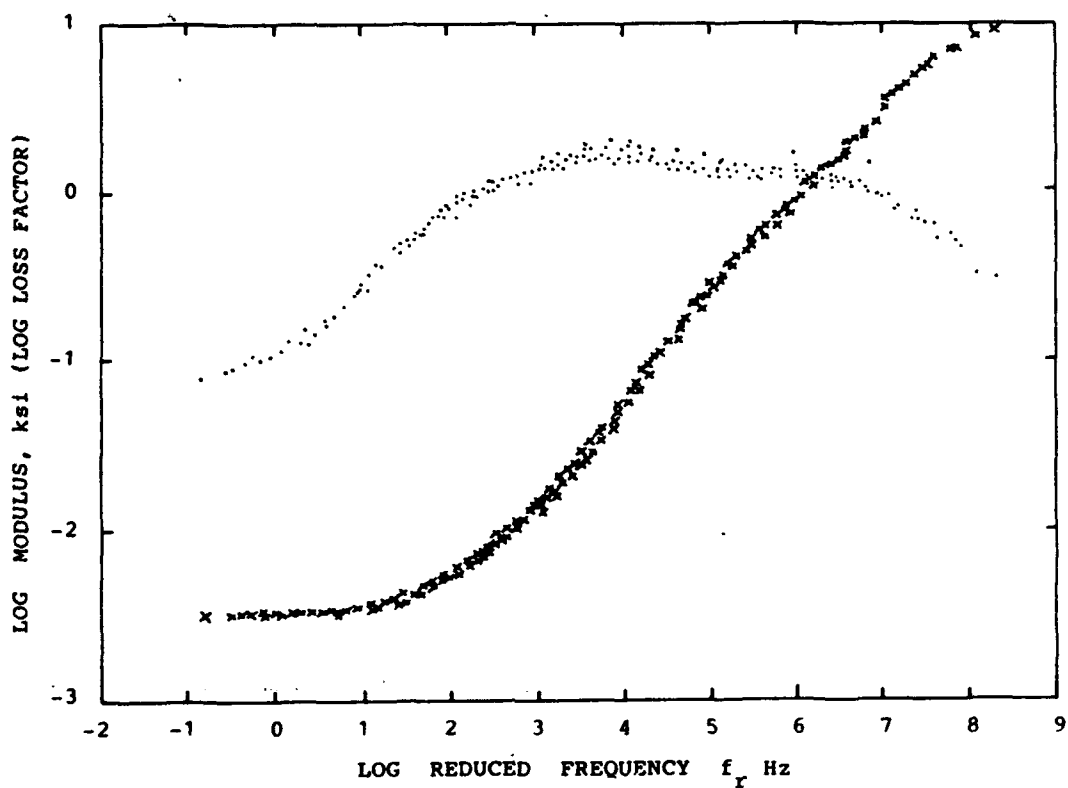


Figure 4. Master Curves for Polyisobutylene (WL/Manual/All Points)

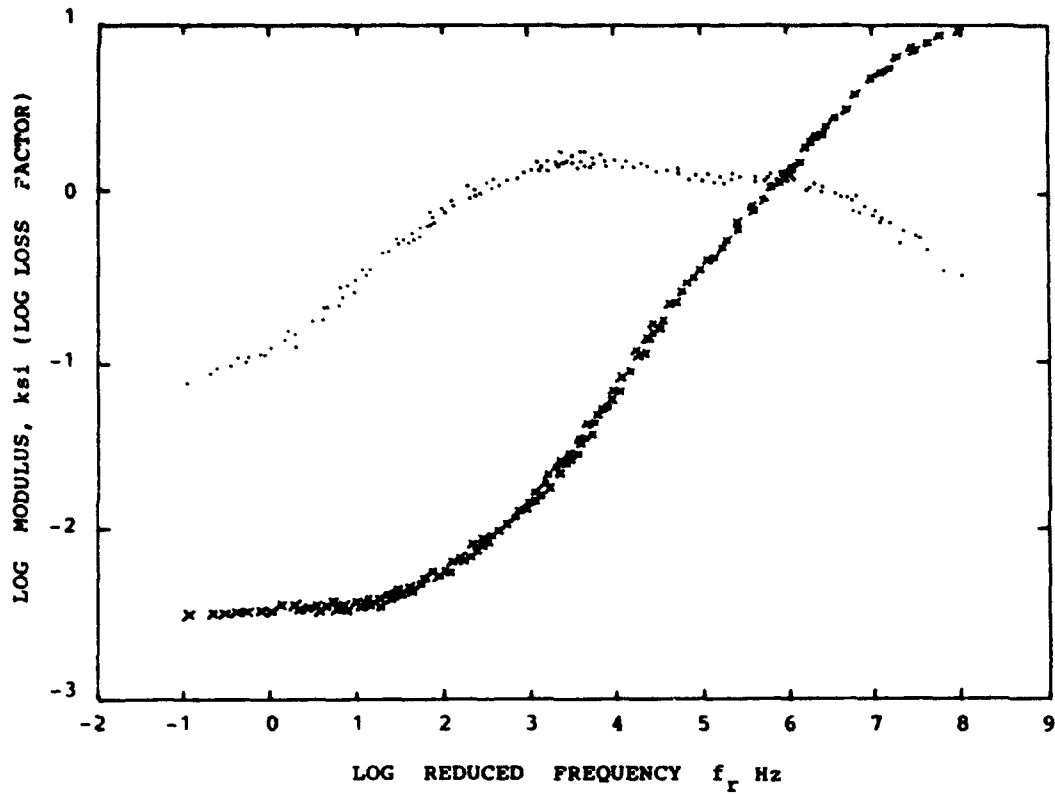


Figure 5. Master Curves for Polyisobutylene (WL/Manual/Culled)

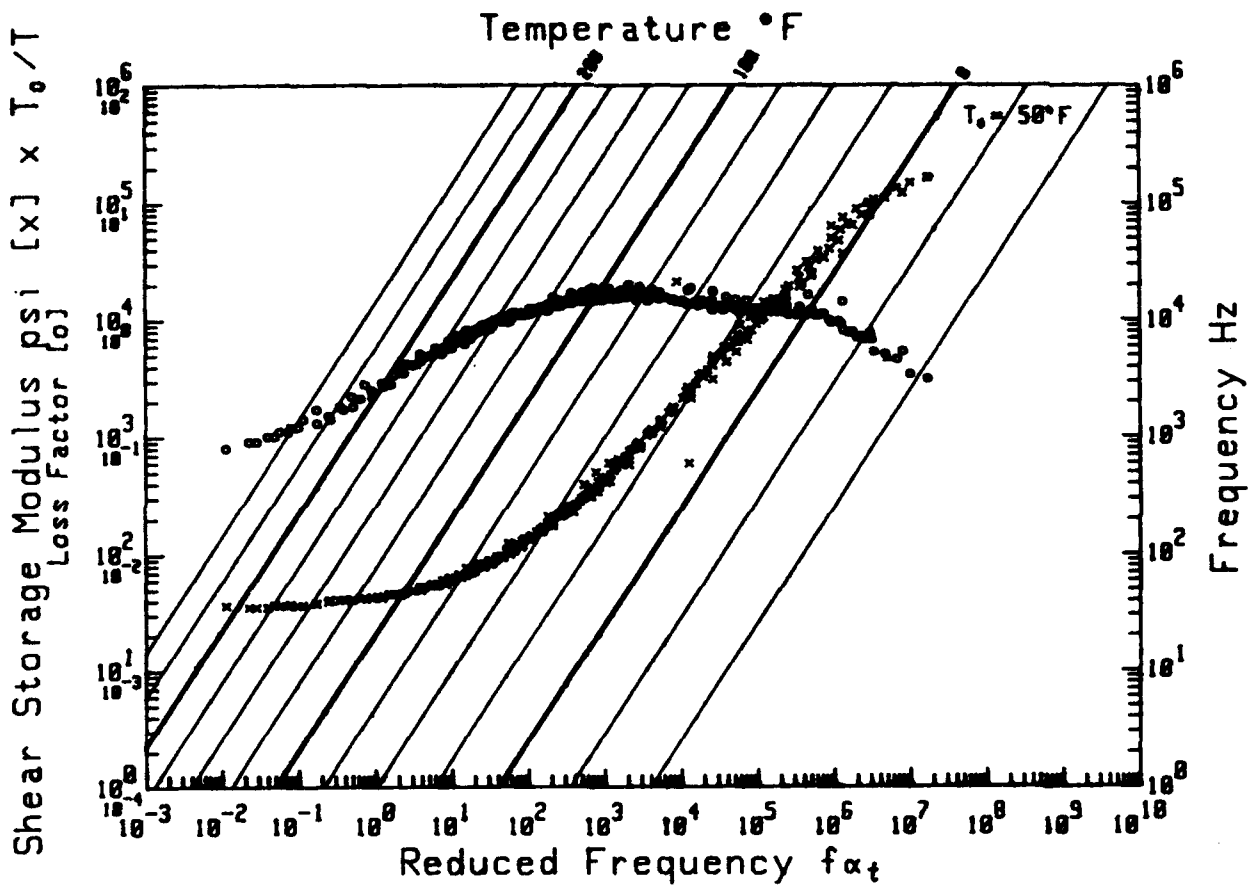


Figure 6. Master Curves for Polyisobutylene (Anatrol)

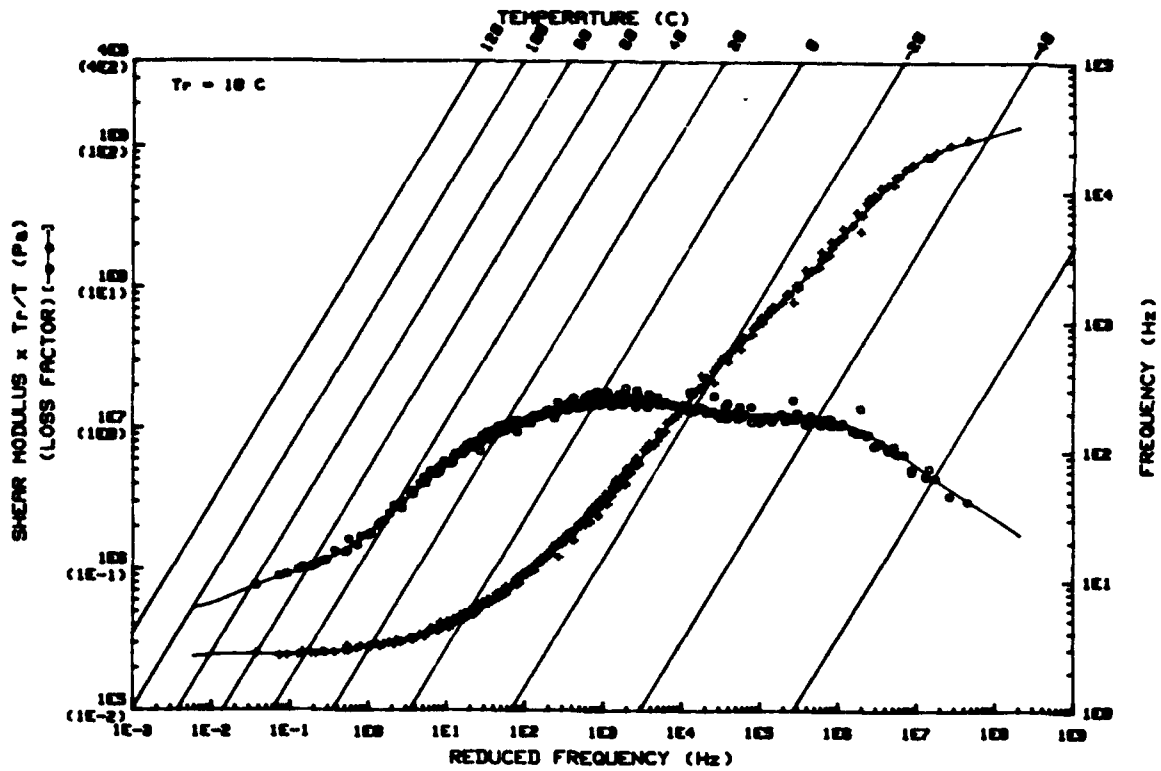


Figure 7. Master Curves for Polyisobutylene (Manchester)

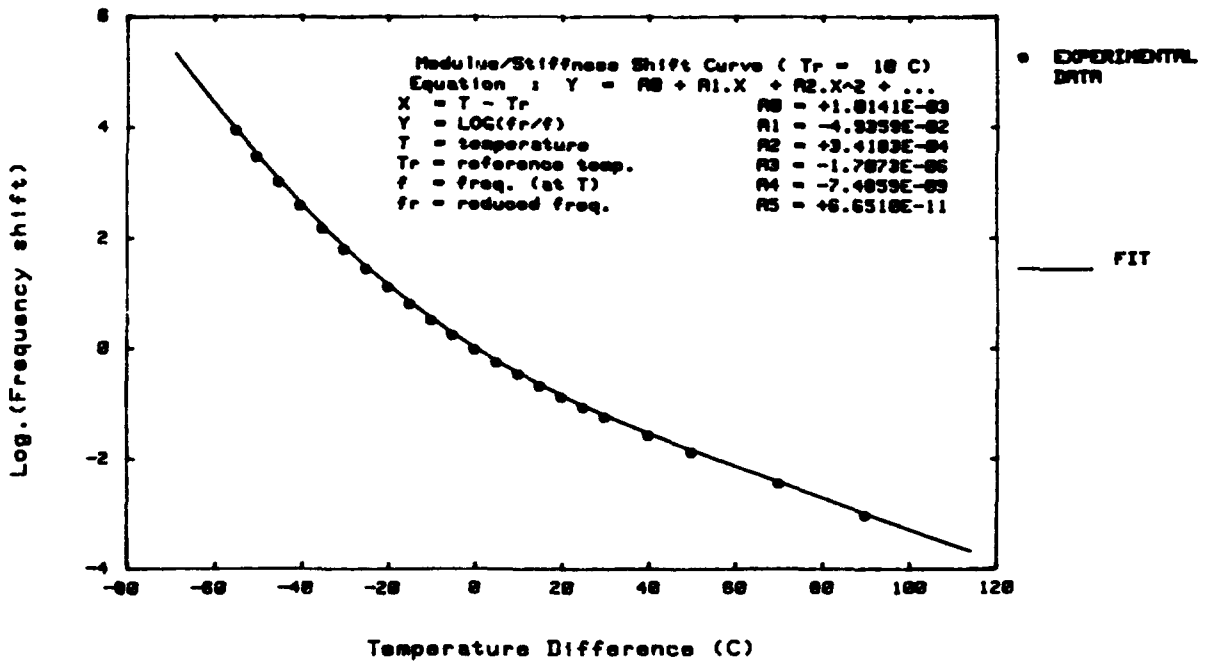


Figure 8. Log Shift Factor Versus Temperature (Manchester)

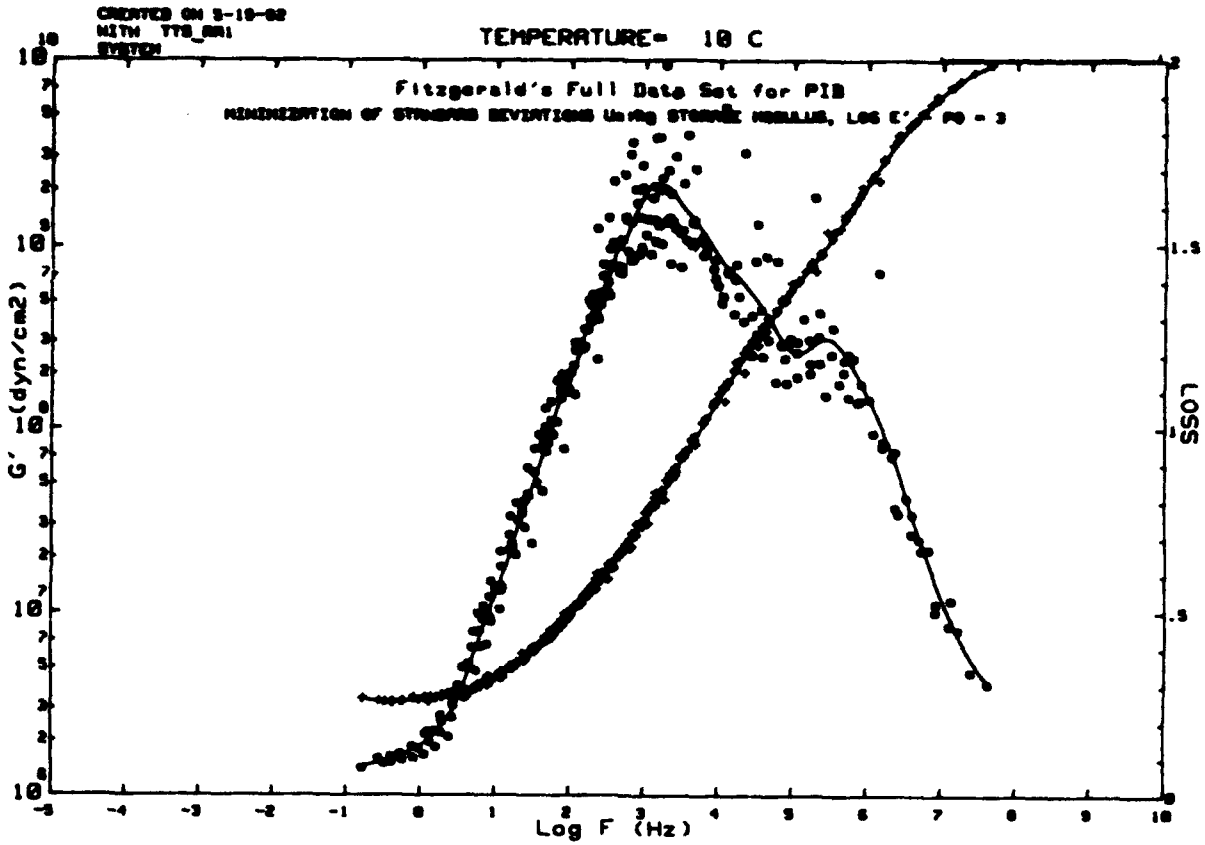


Figure 9. Master Curves for Polyisobutylene (NSWC)

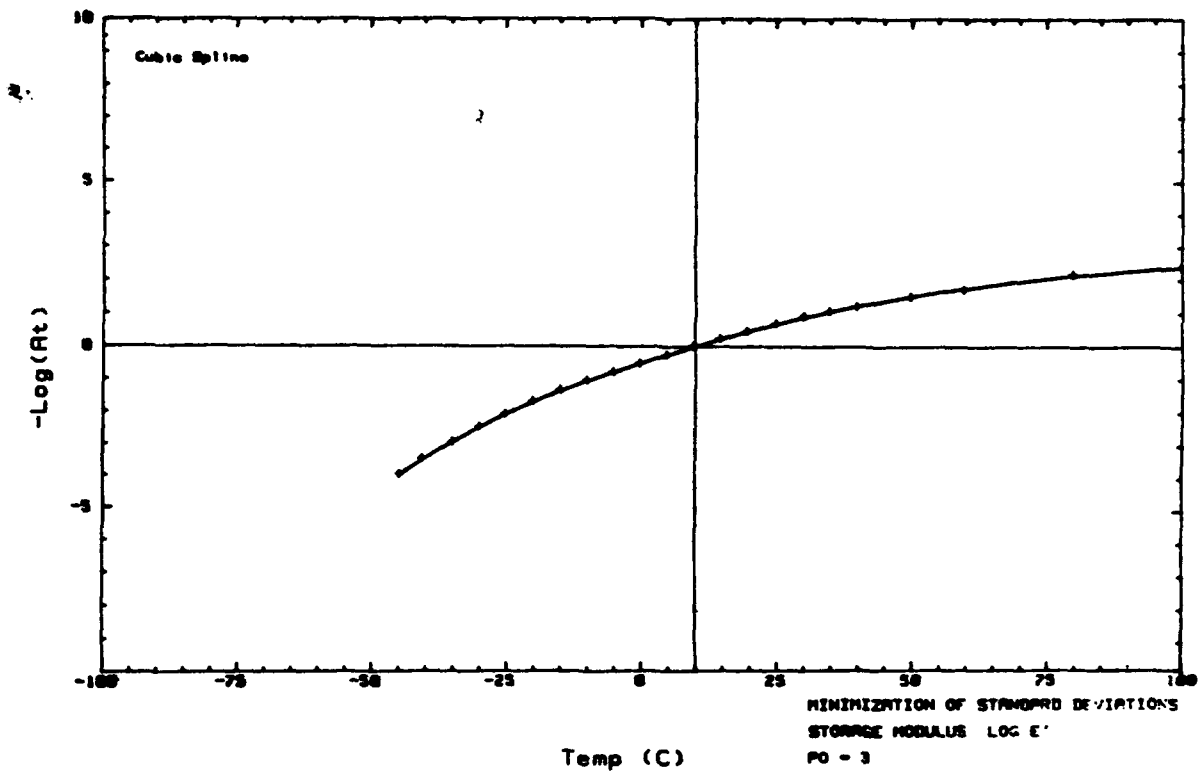


Figure 10. Log Shift Factor Versus Temperature (NSWC)

346

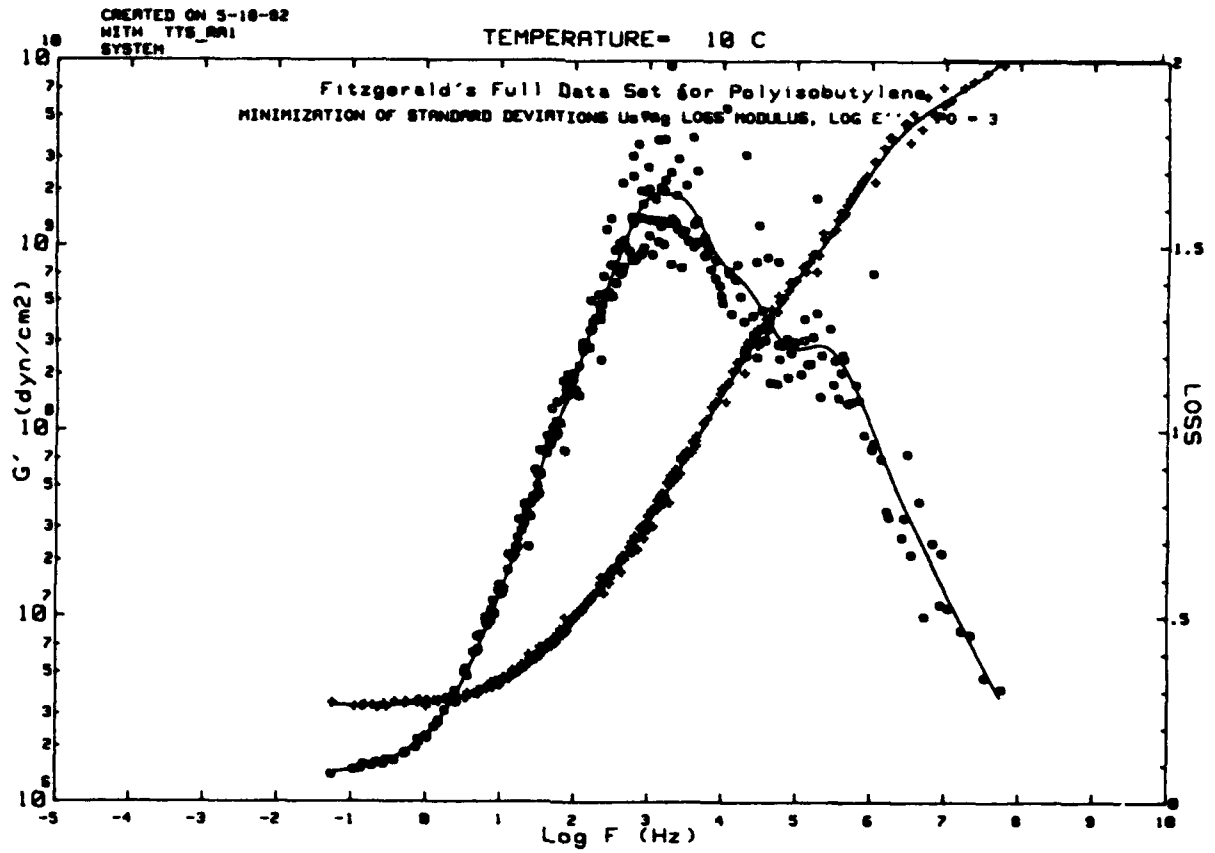


Figure 11. Master Curves for Polyisobutylene (NSWC)

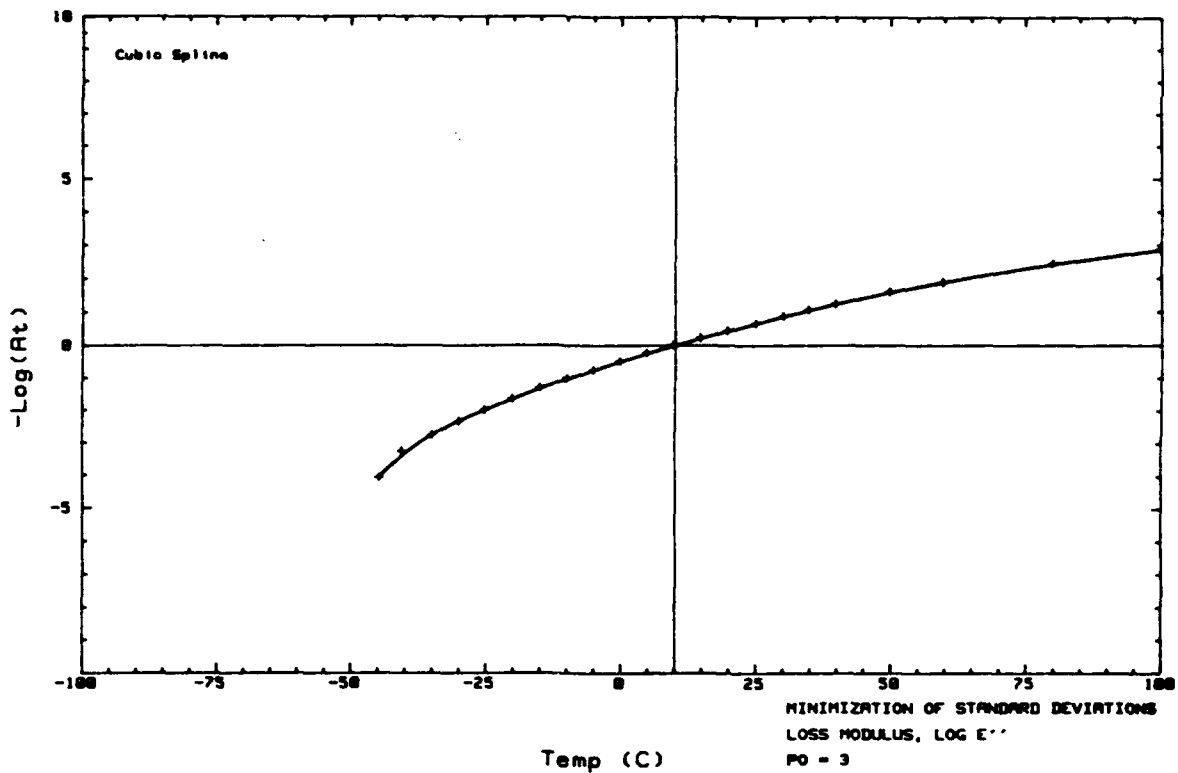


Figure 12. Log Shift Factor Versus Temperature (NSWC)

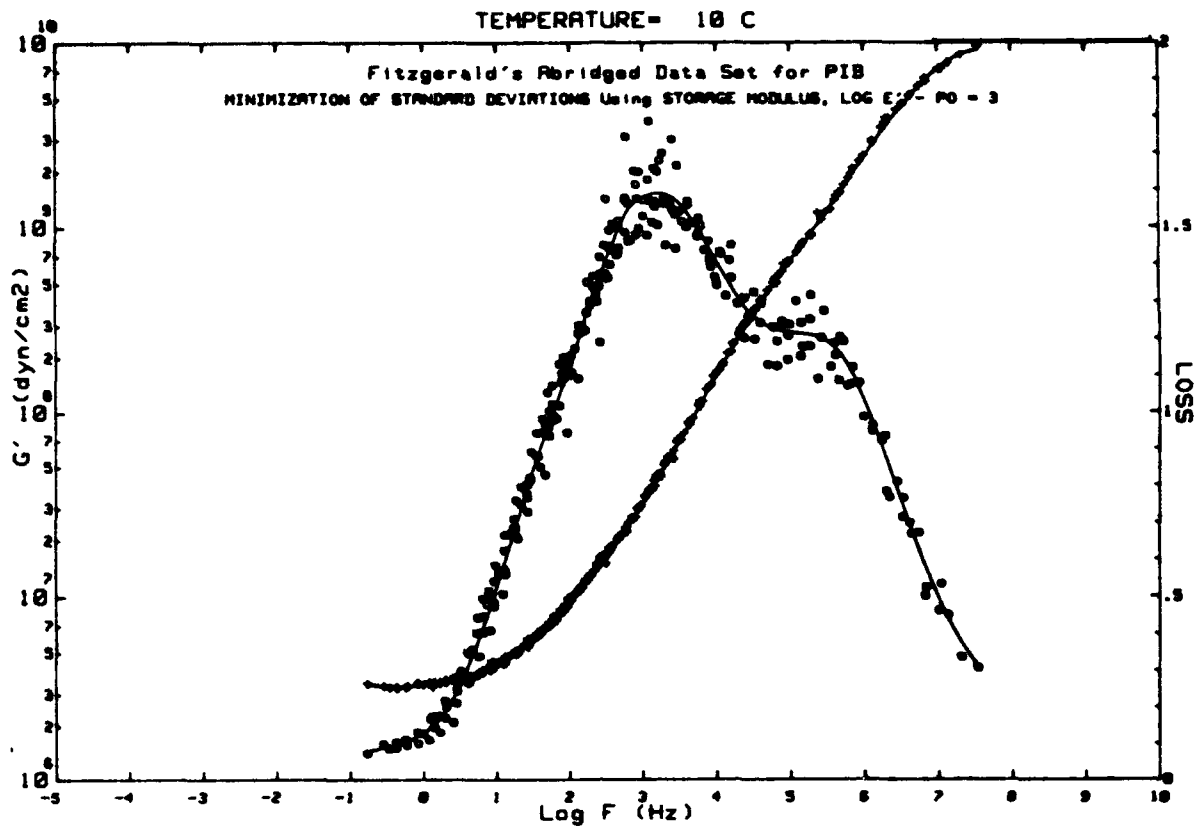


Figure 13. Master Curves for Polyisobutylene (NSWC)

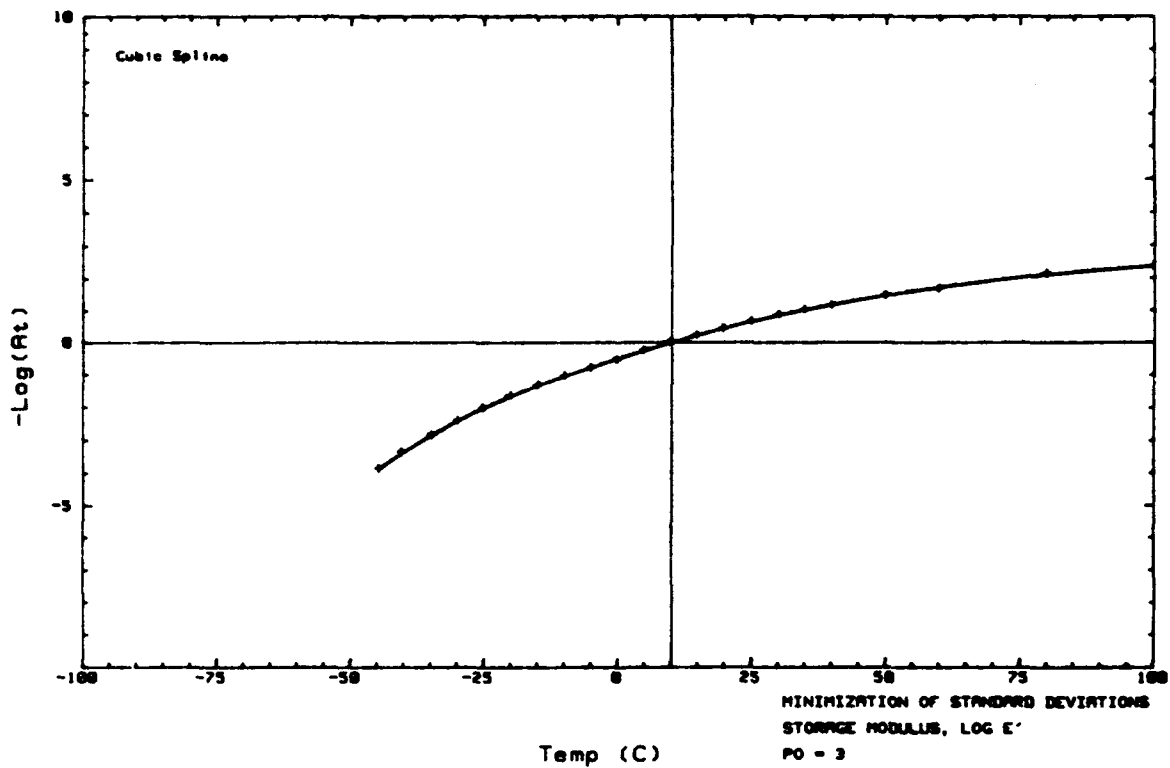


Figure 14. Log Shift Factor Versus Temperature (NSWC)

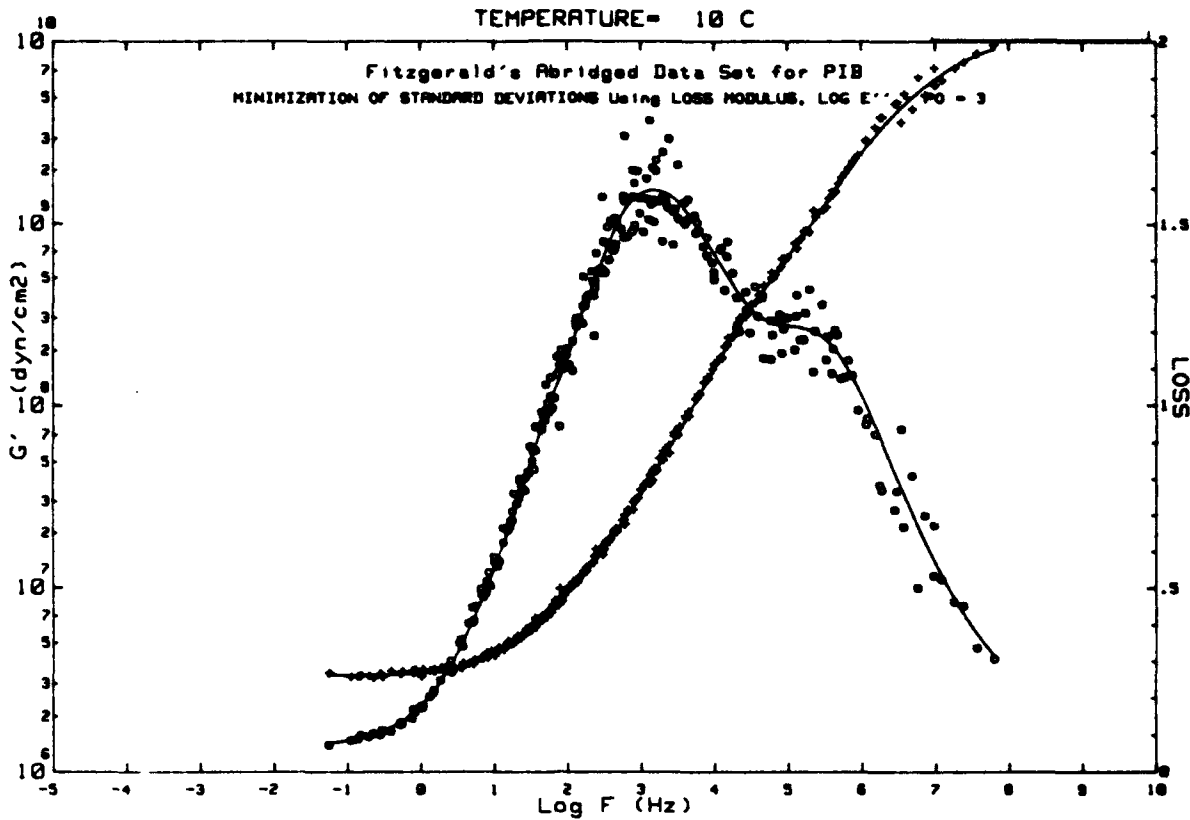


Figure 15. Master Curves for Polyisobutylene (NSWC)

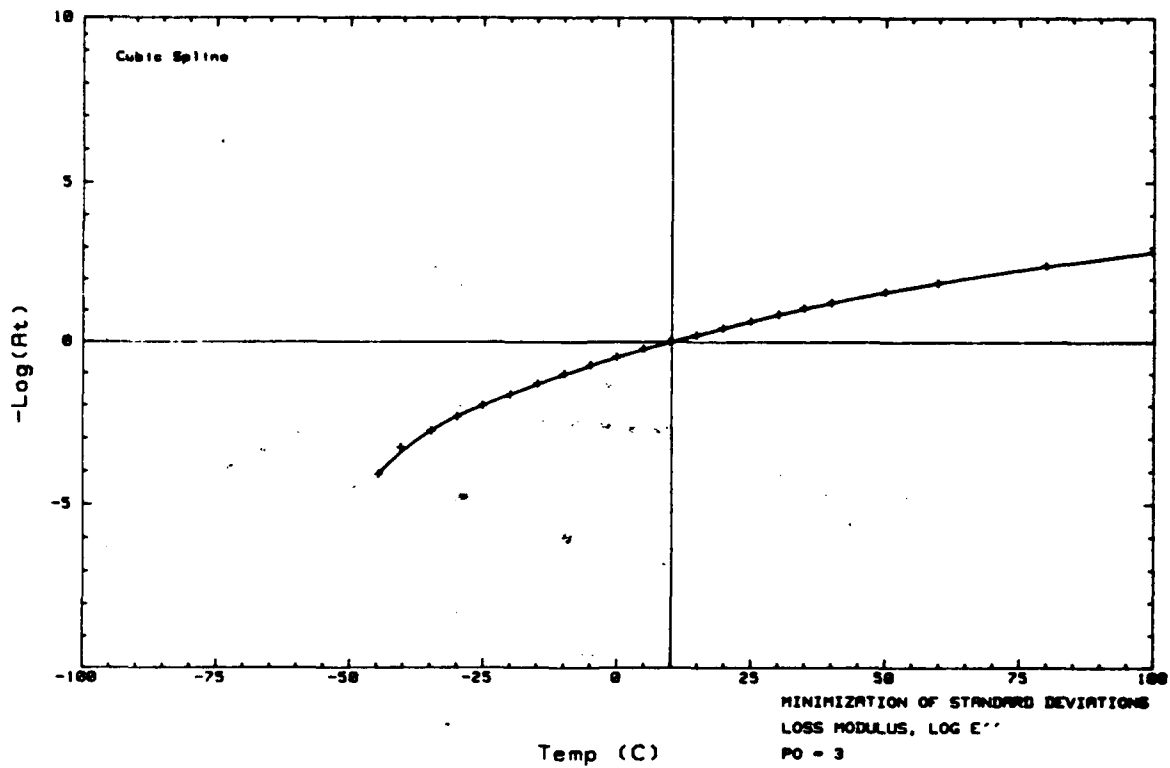


Figure 16. Log Shift Factor Versus Temperature (NSWC)

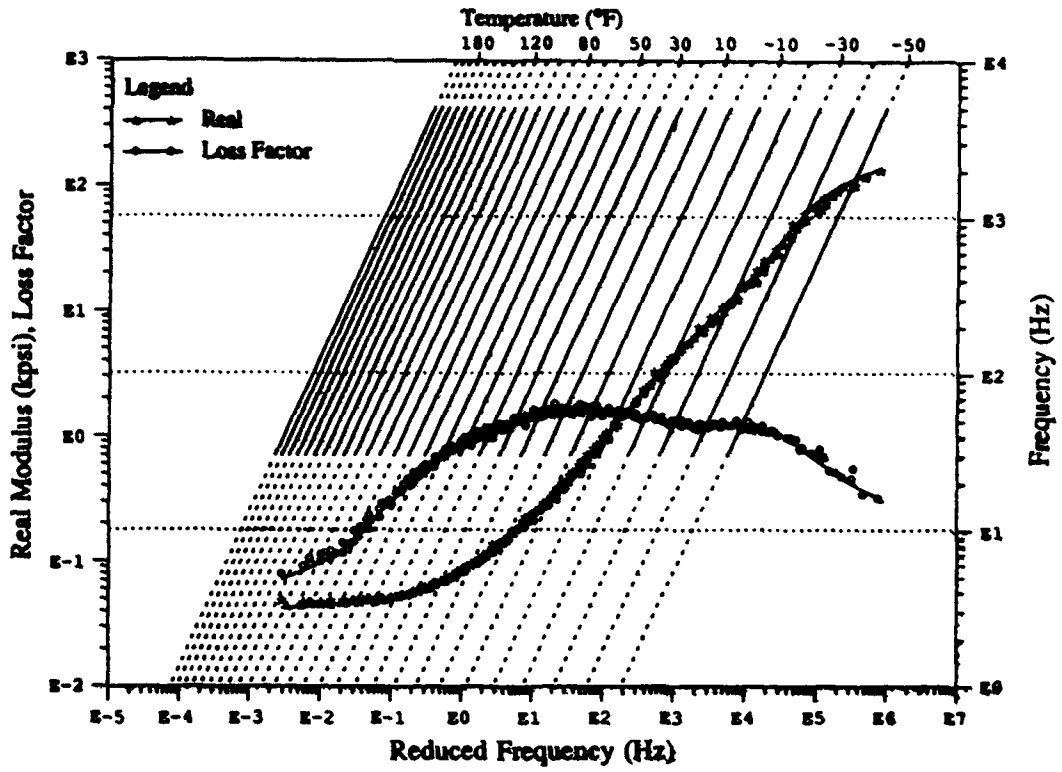


Figure 17. Master Curves for Polyisobutylene (CSA)

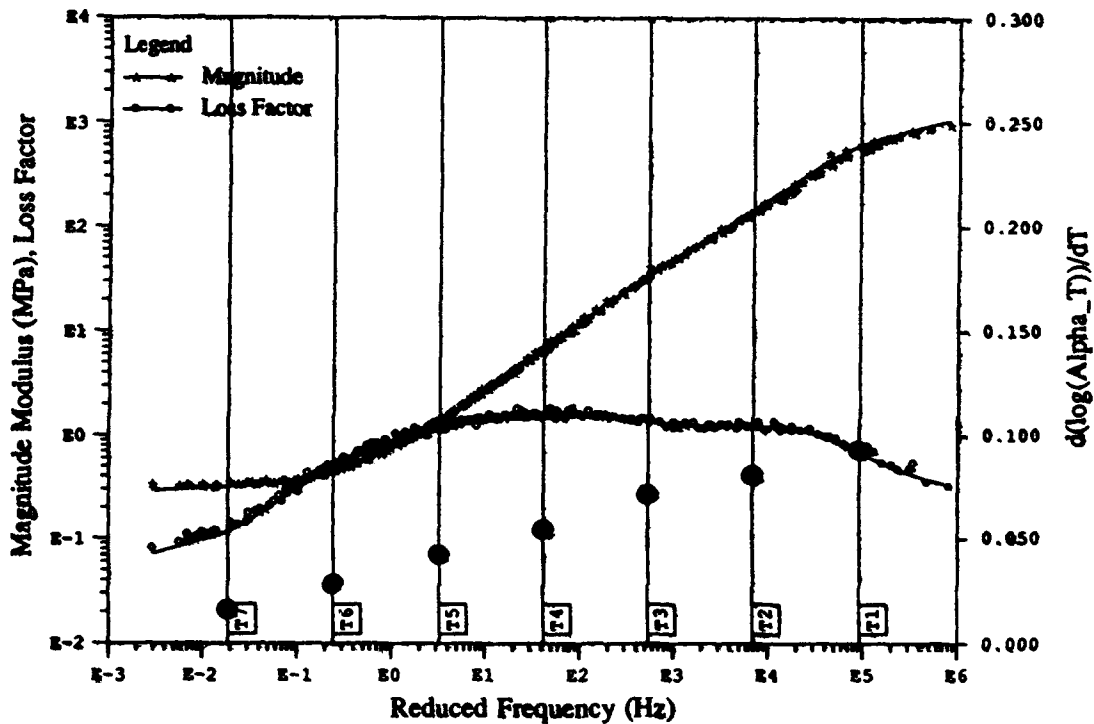


Figure 18. Master Curves for Polyisobutylene with "Knots" (CSA)

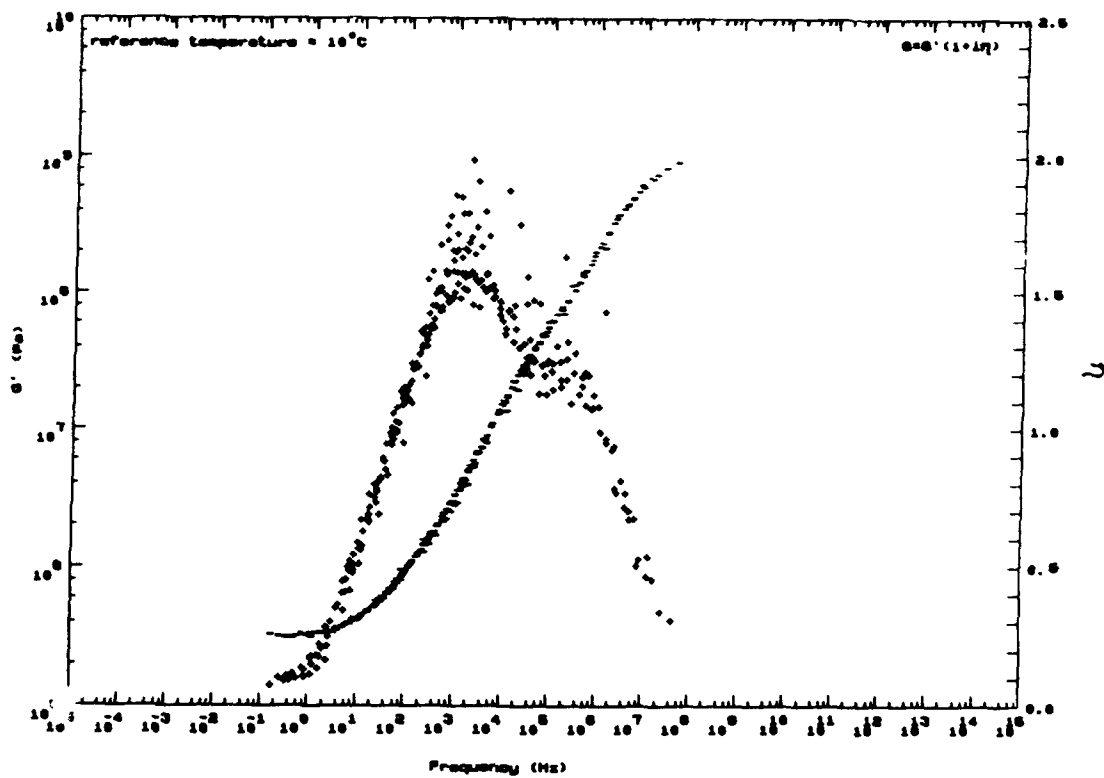


Figure 19. Master Curves for Polyisobutylene (Vector Research)

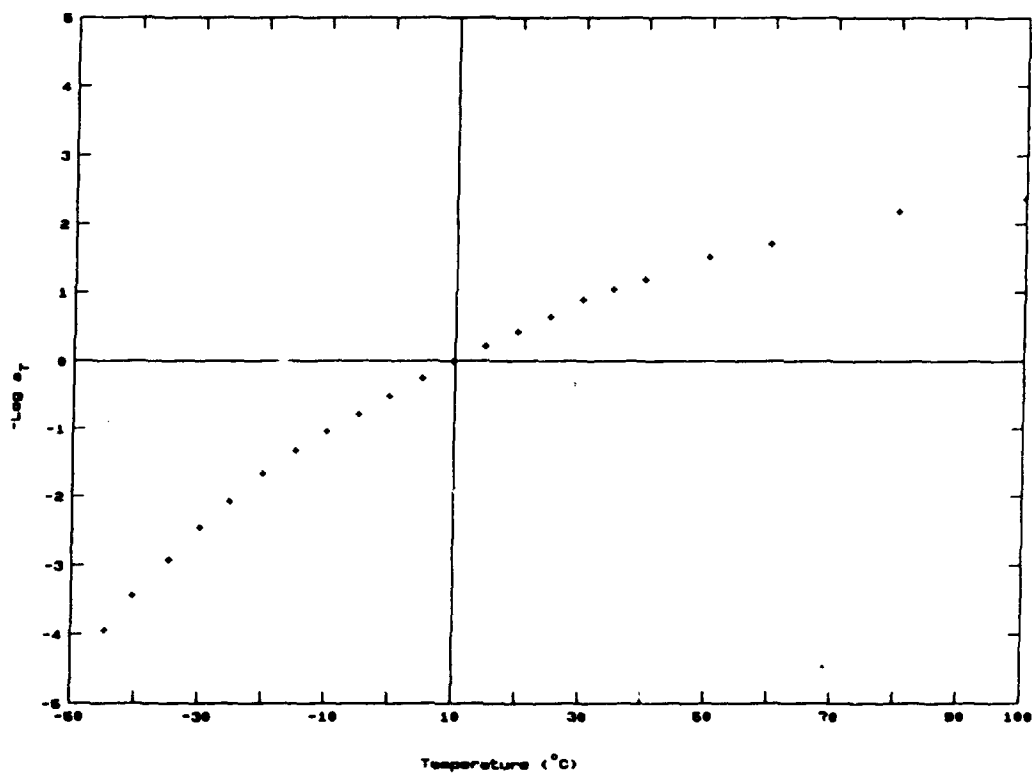


Figure 20. Log Shift Factor Versus Temperature (Vector Research)

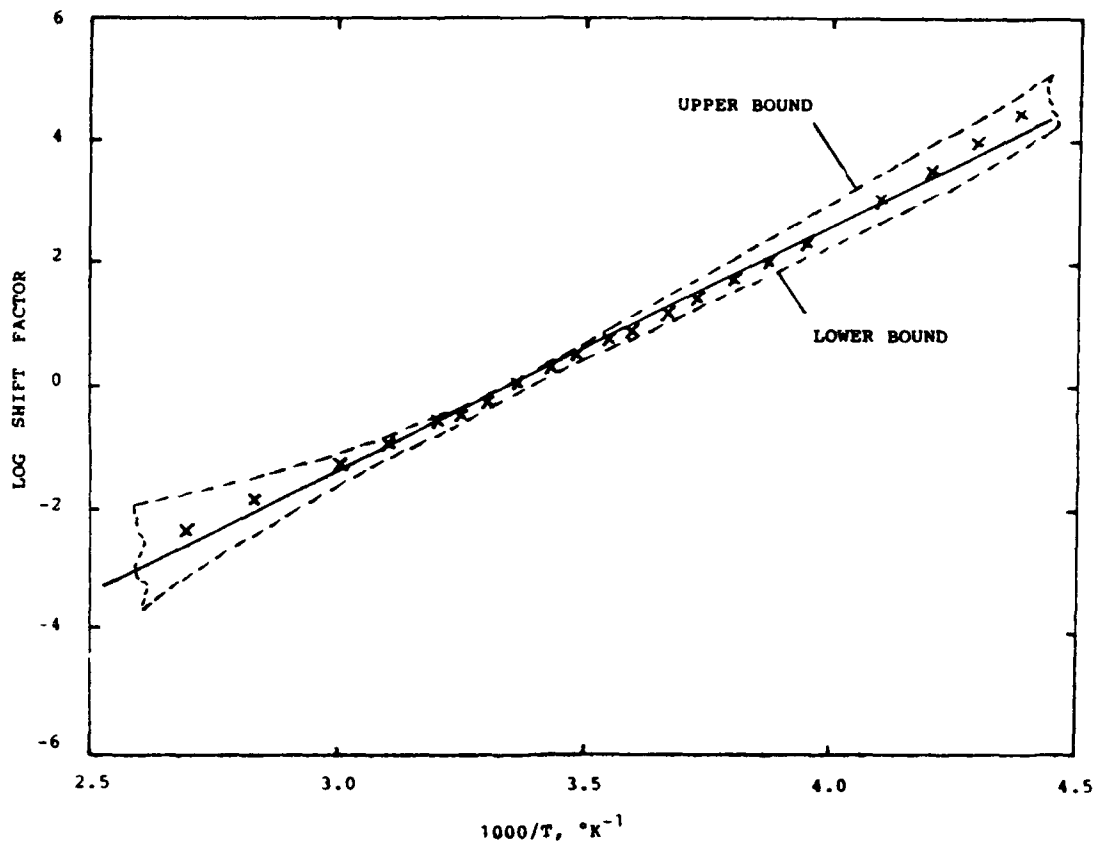


Figure 21. Plot of Log Shift Factor versus 1000/T

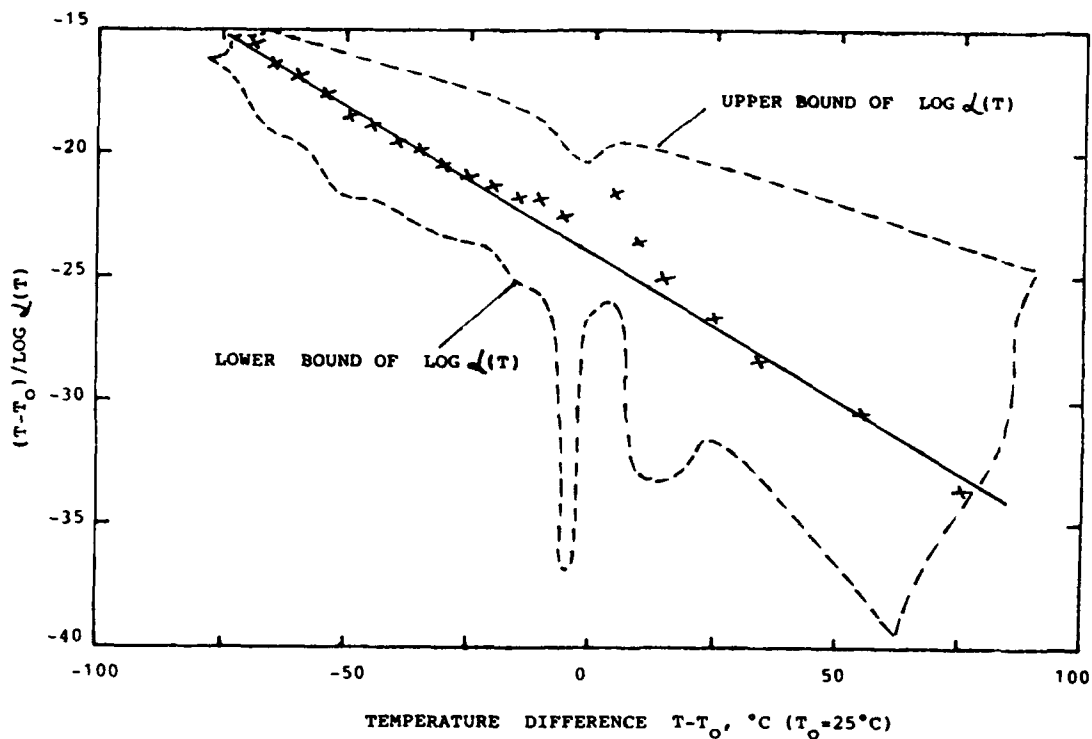


Figure 22. Plot of  $(T-T_0)/\text{Log } d(T)$  Versus  $T-T_0$

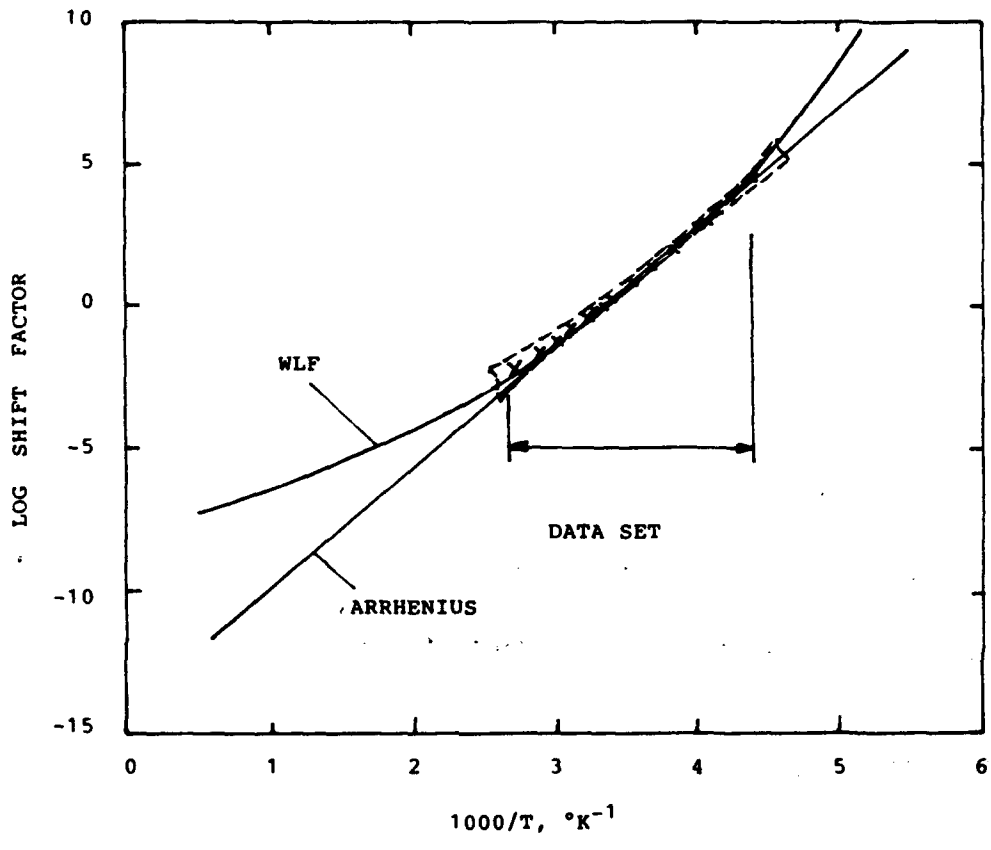


Figure 23. Plot of  $\text{Log} \alpha(T)$  Versus  $1000/T$

# **Estimation of Dynamic Properties of Rubber Materials and Their Applications to Vibration Isolator**

**Chun-Hwa Ryu, Gyu-Seop Lee,  
Hyeong-Oh Kweon and Sang-Kyu Park**

**Institute of Research and Development  
UNISON INDUSTRIAL CO., LTD.**

## **ABSTRACT**

Rubber has high elongation of as much as 1000 percent and possesses high internal damping. Furthermore rubber can be easily processed into various shapes and can be well adhered to metal.

However, rubber is difficult to analyze accurately because it consists of organic compound and additional ingredients.

In this paper, a procedure of measuring modulus of elasticity and loss factor of rubber specimens according to Korean Industrial Standard will be introduced, and its results will be compared with the theoretical values.

## **1. INTRODUCTION**

Rubber has high elongation and large internal damping in comparison with metal. Rubber can be well adhered to metal and processed into various shapes with the intended spring constant in arbitrary direction. Because of these material properties rubber is widely used for application to vibration isolation systems.

However, it is difficult to analyze material properties accurately because rubber consists of organic compound and additional ingredients. Variations in manufacturing procedures cause many changes in the material properties of the rubber. In order to use rubber material efficiently as a vibration isolator, precise and exact knowledge of complex Young's modulus which is consisted of Young's modulus and loss factor is necessary.

In this paper, according to the test method for rubber specimen of Korean Industrial Standard[1,2], Young's modulus and loss factor of rubber are measured experimentally and compared with the theoretical values.

## 2. THEORETICAL BACKGROUND

### STATIC YOUNG'S MODULUS

For such a material as rubber, the shear modulus  $G$  is about  $10^8$  N/m<sup>2</sup> and the bulk modulus  $B$  is about  $10^{10}$  N/m<sup>2</sup>. Because the bulk modulus is much larger than the shear modulus, Poisson's ratio  $\nu$  is about 0.5 as shown in equation (1).

$$\nu = \frac{3B - 2G}{6B + 2G} \approx 0.5 \quad (1)$$

and the Young's modulus  $E$  is as follow.

$$E = 2(1 + \nu)G \approx 3G \quad (2)$$

The apparent Young's modulus  $E_a$  is defined by

$$E_a = E(1 + \beta S^2) \quad (3)$$

where  $S$  is the shape factor and  $\beta$  is constant determined by chemical compositions[3]. For specimen with diameter  $D$  and height  $L$ , the shape factor  $S$  is.

$$S = \frac{D}{4L} \quad (4)$$

The apparent Young's modulus  $E_a$  for the rubber of cylindrical type changes as follow

$$E < E_a < B \quad (5)$$

If the dynamic displacement is small, the stiffness  $K$  of the rubber is assumed to be.

$$K = E_a \frac{A}{L} \quad (6)$$

## THE COMPLEX YOUNG'S MODULUS

When external force is applied to viscoelastic materials, a part of energy due to the external force is dissipated and the rest of that is stored with elastic energy because viscoelastic materials have damping as well as stiffness. The dynamic properties of viscoelastic materials of rod type is expressed by the apparent Young's modulus  $E_a$  and loss factor  $\gamma$ . The above factors are expressed with the complex Young's modulus  $E^*$  defined by equation(7).

$$E^* = E_a(1 + j\gamma) \quad (7)$$

The model for analyzing dynamic properties of rubber is considered as shown in Fig.1.

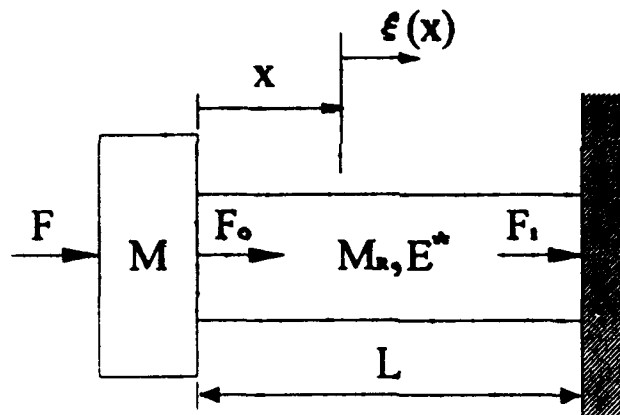


Fig.1 Model composed by added mass and rubber rod

The equation that describes the longitudinal vibration of a long rod with uniform cross sectional area  $A$  is expressed by equation (8).

$$E^*A \frac{\partial^2 \bar{\xi}(x,t)}{\partial x^2} dx = \rho A dx \frac{\partial^2 \bar{\xi}(x,t)}{\partial t^2} \quad (8)$$

where  $\bar{\xi}(x,t)$  is displacement of the rod at the point  $x$ ,  $t$  is time, and  $\rho$  is the density of the rod material.

If external force varies sinusoidally, the second partial derivative of  $\bar{\xi}(x,t)$  with respect to  $t$  is equated to  $(j\omega)^2 \xi(x) e^{j\omega t}$  and equation (8) is written as.

$$\frac{\partial^2 \xi(x)}{\partial x^2} + \left(\frac{n^*}{L}\right)^2 \xi(x) = 0 \quad (9)$$

where  $\left(\frac{n^*}{L}\right)^2$  is  $\frac{\omega^2 \rho}{E^*}$

Depending on boundary conditions, solutions of equation (9) are obtained as follows.

Case (1) Boundary Conditions :  $\xi(L) = 0, \frac{\partial \xi(0)}{\partial x} = \frac{-F_0}{E^*A}$

$$\xi(x) = \frac{F_0 L}{E^* n^* A} \left[ \tan n^* \cos\left(\frac{n^* x}{L}\right) - \sin\left(\frac{n^* x}{L}\right) \right]$$

$$\frac{\xi(0)}{F_0} = \frac{L \tan n^*}{AE^* n^*} \quad (10)$$

Case (2) Boundary Conditions :  $\frac{\partial \xi(L)}{\partial x} = -\frac{F_1}{E^*A}, \xi(L) = 0$

$$\xi(x) = \frac{F_1 L}{E^* n^* A} \sin n^* \left(1 - \frac{x}{L}\right)$$

$$\frac{\xi(0)}{F_1} = \frac{L \sin n^{\circ}}{AE^{\circ}n^{\circ}} \quad (11)$$

Case (3) Boundary Conditions :  $\xi(L) = 0$ ,  $E^{\circ}A \frac{\partial \xi(0)}{\partial x} = -F - \omega^2 M \xi(0)$

$$\xi(x) = \frac{FL \left[ \sin n^{\circ} \cos\left(\frac{n^{\circ}x}{L}\right) - \cos n^{\circ} \sin\left(\frac{n^{\circ}x}{L}\right) \right]}{E^{\circ}n^{\circ}A (\cos n^{\circ} - \gamma n^{\circ} \sin n^{\circ})}$$

$$\frac{\xi(0)}{F} = \frac{L \sin n^{\circ}}{AE^{\circ}n^{\circ}(\cos n^{\circ} - \gamma n^{\circ} \sin n^{\circ})} \quad (12)$$

where  $\gamma$  is  $M/M_n$ .

### 3. TEST METHODS[1, 2]

According to Korean Industrial Standard, the forced vibration test methods of rubber can be broadly classified into two categories ; resonant test method, nonresonant test method.

#### RESONANT TEST METHOD

The accelerance of the vibration system shown in Fig. 1 is expressed by equation (13).

$$\left| \frac{\xi(0)}{F} \right| = \frac{1/K}{[(1 - (\omega/\omega_n)^2)^2 + (\eta \omega/\omega_n)^2]^{1/2}} \quad (13)$$

By measuring the external force  $F$  and displacement  $\xi(0)$ , accelerance curves can be obtained for different frequencies. Considering  $K = M\omega_n^2$  and

using equation (13), the loss factor of rubber  $\eta$  can be calculated.

$$\eta = \frac{1}{(K|\xi(0)/F|_{\max})} \quad (14)$$

From equations (3) and (6), Young's modulus of rubber specimen is written as;

$$E_a = K \frac{L}{A} \quad (15)$$

$$E = E_a/(1 + \beta S^2) \quad (16)$$

### NONRESONANT TEST METHOD

Using the nonresonant test method without added mass  $M$ , the Young's modulus  $E$  and loss factor is evaluated as follows.

$$\frac{F_1}{\xi(0)} = |K^*|(\cos \delta + j \sin \delta) = \frac{AE_a(1 + j\eta)}{L} \quad (17)$$

$$E_a = \frac{L |K^*| \cos \delta}{A} \quad (18)$$

$$E = \frac{L |K^*| \cos \delta}{A(1 + \beta S^2)} \quad (19)$$

where  $\eta$  is  $\tan \delta$ .

### TEST USING CONTINUOUS MODEL

Because rubber has large nonlinearity and Young's modulus and the loss factor change with frequencies, the resonant test method describes material properties at specific frequency only. Also because mass of rubber specimen is not considered, nonresonant test method has large error at high frequencies.

Using equation (11) and (12), the following equation (20) is obtained.

$$\frac{F}{F_1} = \cos n^* - \gamma n^* \sin n^* \quad (20)$$

where the parameter  $n^*$  is a complex quantity and is written as

$$n^* = p + jq \quad (21)$$

$$\operatorname{Re}\left(\frac{F}{F_1}\right) = \cos p \cosh q - \gamma (p \sin p \cosh q - q \cos p \sinh q) \quad (22)$$

$$\operatorname{Im}\left(\frac{F}{F_1}\right) = -\sin p \sinh q - \gamma (p \cos p \sinh q + q \sin p \cosh q) \quad (23)$$

Substituting  $\left(\frac{n^*}{L}\right)^2 = \frac{\omega^2 \rho}{E^*}$  into equation (21), values of  $p$  and  $q$  are determined.

$$p = \frac{\omega L}{D_{zw}} \left( \frac{\rho (D_{zw} + 1)}{2E_a} \right)^{1/2}$$

$$q = -\frac{\omega L}{D_{zw}} \left( \frac{\rho (D_{zw} - 1)}{2E_a} \right)^{1/2}$$

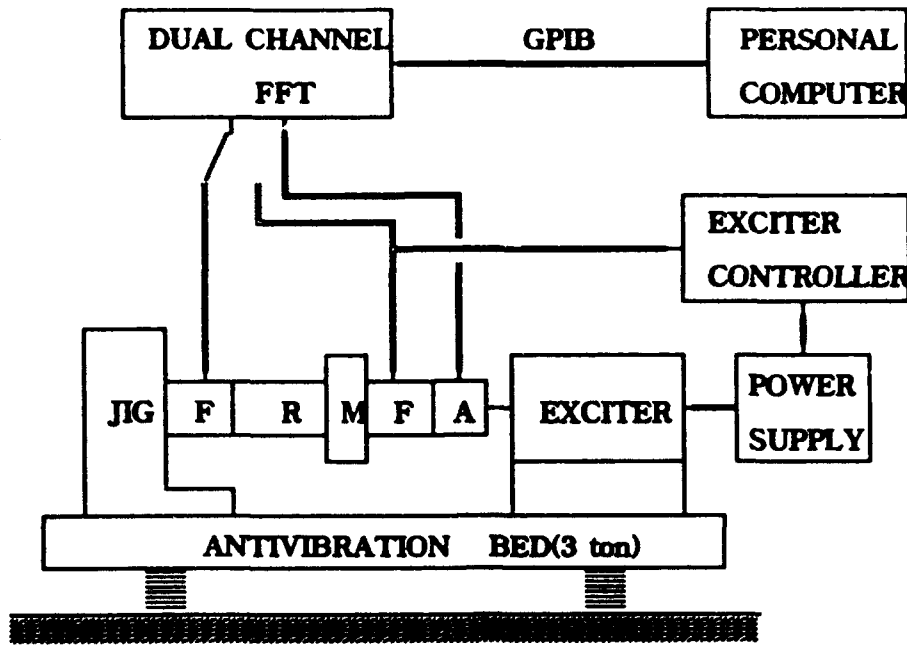
where  $D_{zw}$  is  $(1 + \eta^2)^{1/2}$

Solving equation (22) and (23), we can obtain Young's modulus and loss factor.

#### 4. EXPERIMENTAL APPARATUS

##### DYNAMIC TEST

The schematic diagram of the test rig is illustrated in Fig.2. The test apparatus was installed on antivibration bed with natural frequency 3.15 Hz. added mass is 84.8 g and Neoprene rubber, general vibration isolator rubber, was used as specimen. The test specimens have cylindrical shapes and the geometry of the test specimens is shown in Table 1.



F : Force Transducer      R : Rubber Specimen  
M : Added Mass              A : Accelerometer

Fig.2 Schematic view of test rig

Table 1. Geometry of test specimens

Specimen	Unit Density [kg/m <sup>3</sup> ]	Length [m]	Shape Factor S	Diameter [m]
Duro 40	1100	0.040	0.1563	0.025
		0.030	0.2083	
		0.250	0.2500	
		0.020	0.3125	
Duro 60	1350	0.040	0.1563	
		0.030	0.2083	
		0.025	0.2500	
		0.020	0.3125	

The instruments used for the vibration measurement are shown in Table 2.

Table 2. Instruments

Equipment	Maker	Specifications
Exciter System	B&K	Max. Force : 1780 N Frequency Range : 0~100 kHz 4802(4817), 2708, 1050
Force Transducer	B&K	Force Range : -4~16kN Frequency Range : 20kHz, 8201
Accelerometer	B&K	Frequency Range : 0.2~3500Hz Acceleration Range : $10^{-5}$ ~60g, 4370
FFT	B&K	Dual Channel 2034
Charge Amp.	B&K	Sensitivity : 0.1~10.99 pC/m/sec <sup>2</sup> , 2635

## 5. RESULTS AND DISCUSSION

### TEST RESULTS BY RESONANT METHOD

Apparent Young's modulus  $E_a$  and loss factor  $\eta$  determined by resonant method for different specimens are shown in Table 3.

Table 3. Apparent Young's modulus  $E_a$  and loss factor  $\eta$  determined by resonant test method

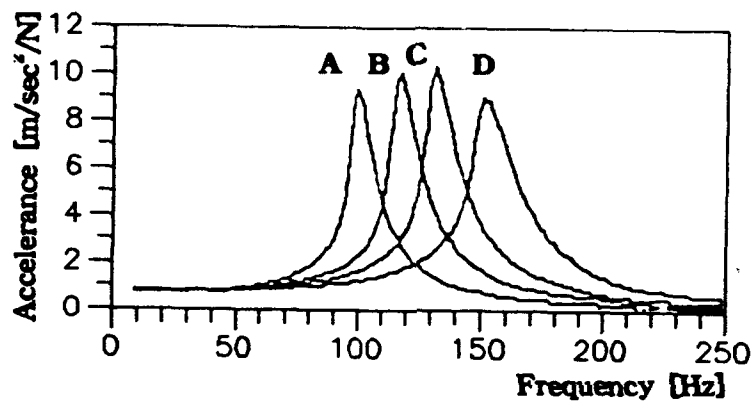
Specimen	Length [m]	Stiffness [ $10^4$ N/m]	Apparent Young's Modulus [ $10^9$ N/m <sup>2</sup> ]	Loss Factor $\eta$
Duro 40	0.040	3.347	2.727	0.012
	0.030	4.660	2.848	0.097
	0.025	5.831	2.970	0.095
	0.020	7.732	3.150	0.108
Duro 60	0.040	11.578	9.434	0.176
	0.030	16.197	9.899	0.198
	0.025	20.196	10.653	0.180
	0.020	28.534	11.626	0.194

Using least square method, Young's modulus  $E$  and constant  $\beta$  was calculated from Table 3 and the results are given in Table 4.

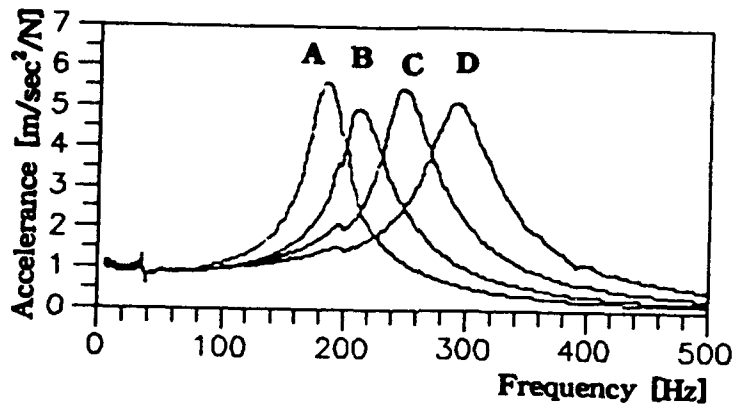
**Table 4** Young's modulus E and constant  $\beta$

Specimen	Young's Modulus [ $10^8 \text{N/m}^2$ ]	$\beta$	Max. Error [%]
Duro 40	2.595	2.222	6.2
Duro 60	8.660	3.527	6.5

The accelerance curves obtained by resonant test method are shown in Fig. 3.



(a) Duro 40



(b) Duro 60

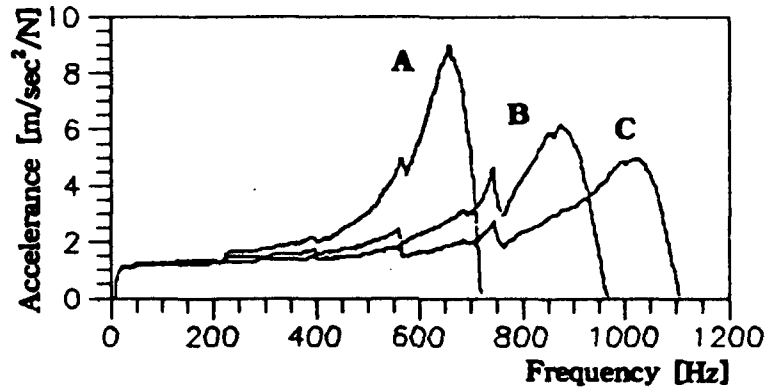
A : length 40 mm, B : length 30 mm  
 C : length 25 mm, D : length 20 mm

**Fig. 3** Accelerance curve obtained by resonant test method

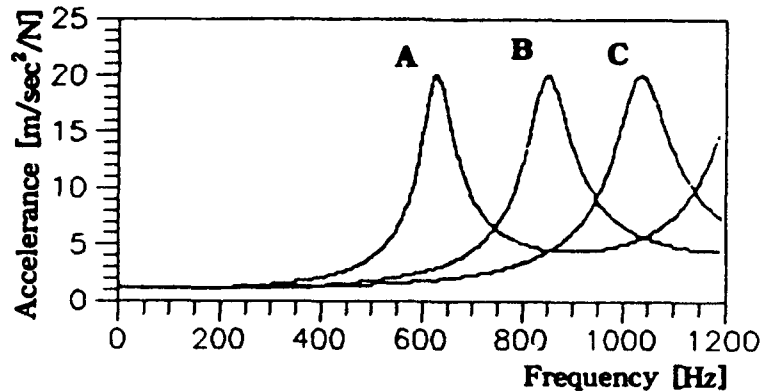
## TEST RESULTS BY NONRESONANT TEST METHOD

The accelerance curve obtained by nonresonant test method is shown in Fig. 4(a). In the figure, Young's modulus  $E$  increase with frequency. This is due to inertia effect of rubber specimen.

Comparing the peak points of nonresonant test results with those of simulation results for specimen with duro 40 is described in Table 5. Simulation results obtained using continuous model confirm the effect(Fig4.(b)). Young's modulus and loss factor used for the simulation were obtained by resonant test method.



(a) Nonresonant test results



(b) Simulation results

A : length 40 mm, B : length 30 mm, C : length 25 mm

Fig.4 Nonresonant test results and simulation results

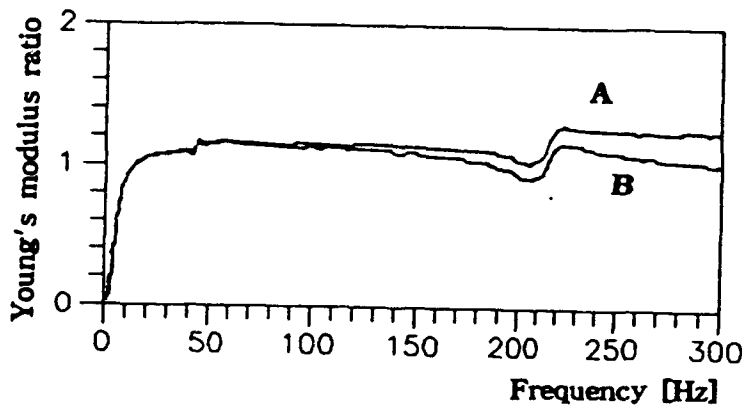
Table 5 Peak points at nonresonant test results and simulation results

Specimen Duro 40 Length [m]	Peak Points at nonresonant test results [Hz]	Peak Points at Simulation Results [Hz]
0.040	670	626
0.030	888	850
0.025	1034	1040

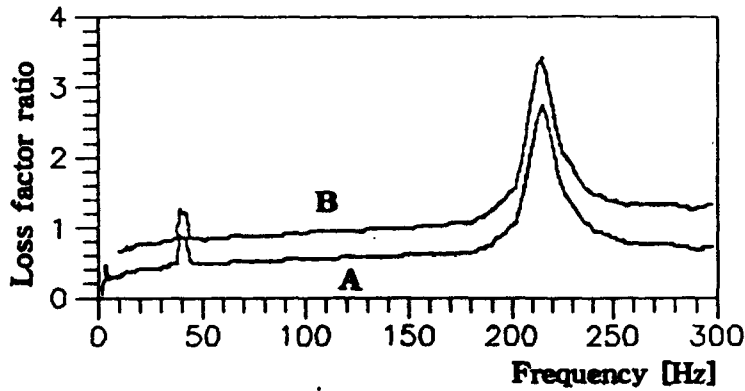
Inertia effect of rubber on the Young's modulus and loss factor is shown in Fig. 5. As frequency increases, Young's modulus is overestimated and loss factor is underestimated. In Fig. 5 the peaks in the neighborhood of 40 Hz and 220 Hz are test errors due to the mobility of jig.

In order to gain consistent data, at resonant point calculated by resonant test, comparing nonresonant test results with the simulation results are described in Table 6. In Table 6, Young's modulus ratio and loss factor ratio are ratio to Young's modulus and loss factor calculated by resonant test method.

In the range between 100 - 300 Hz, Young's modulus calculated using nonresonant test method is overestimated by 10 - 25%. Using continuous model, Young's modulus is overestimated within 10%. This phenomena is due to nonlinear properties of specimen. Loss factor is underestimated within 10%. the error in loss factor of nonresonant test method is larger than that of continuous model.



(a) Young's modulus ratio



(b) Loss factor ratio

A : Nonresonant/Resonant, B : Continuous/Resonant

Fig. 5 Inertia effect of rubber specimen on nonresonant test results

Table 6. Young's modulus ratio and loss factor ratio of nonresonant test method and continuous model at resonant point

Specimen		Resonant Point [Hz]	Nonresonant Test Method		Continuous Model	
Hardness	Length [mm]		Young's Modulus Ratio	Loss Factor Ratio	Young's Modulus Ratio	Loss Factor Ratio
Duro 40	40	100	1.23	0.74	1.07	0.80
	30	118	1.22	0.75	1.05	0.82
	25	132	1.13	1.02	1.06	0.90
	20	152	1.17	1.05	1.05	0.86
Duro 60	40	186	1.26	0.90	1.10	0.86
	30	220	1.25	1.55	1.08	0.78
	25	250	1.24	1.10	1.07	0.81
	20	292	1.12	0.95	1.05	0.89

## 6. CONCLUSION

The test methods for rubber specimen according to Korean Industrial Standard have been presented and discussed. The conclusions are as follows.

- (1) Using resonant test method, Young's modulus and rubber constant  $\beta$  can be calculated within error 6%.
- (2) Using nonresonant test method, apparent Young's modulus is overestimated due to inertia effect of rubber specimen while loss factor is underestimated.
- (3) Analyzing rubber specimen with continuous model, mass effect occurring at nonresonant test method can be reduced.

## 7. REFERENCES

1. KS M 6604, " Testing Method for Rubber Vibration Isolators," 1985.
2. KS M 6665, " Testing Method for Dynamic Properties of Rubber Materials for Vibration Isolators," 1985.
3. Gent, A. N., and Lindley, B. B., "The compression of bonded rubber blocks," Proceedings of Institution of Mechanics Engineers, pp.111-117, Vol.173, 1959.
4. J.C. Snowdon, "Longitudial Vibration of Internally Damped Rods," JASA, Vol.36, No.3, 1965, pp.502-510.
5. J.C. Snowdon, "Vibration & Shock in Damped Mechanical Systems," John Wiley & Sons, 1968.
6. T. Pritz, "Apparent Complex Young's Modulus of a Longitudial Vibrating Viscoelastic Rod," Journal of Sound and Vibration 77(1), 93-100, 1981.